UNIVERSITAT DE
BARCELONA

Optimization of the use of diamond indicator minerals in diamond exploration in kimberlites

Jingyao Xu

ADVERTIMENT. La consulta d'aquesta tesi queda condicionada a l'acceptació de les següents condicions d'ús: La difusió d'aquesta tesi per mitjà del servei TDX (**www.tdx.cat**) i a través del Dipòsit Digital de la UB (**diposit.ub.edu**) ha estat autoritzada pels titulars dels drets de propietat intel·lectual únicament per a usos privats emmarcats en activitats d'investigació i docència. No s'autoritza la seva reproducció amb finalitats de lucre ni la seva difusió i posada a disposició des d'un lloc aliè al servei TDX ni al Dipòsit Digital de la UB. No s'autoritza la presentació del seu contingut en una finestra o marc aliè a TDX o al Dipòsit Digital de la UB (framing). Aquesta reserva de drets afecta tant al resum de presentació de la tesi com als seus continguts. En la utilització o cita de parts de la tesi és obligat indicar el nom de la persona autora.

ADVERTENCIA. La consulta de esta tesis queda condicionada a la aceptación de las siguientes condiciones de uso: La difusión de esta tesis por medio del servicio TDR (**www.tdx.cat**) y a través del Repositorio Digital de la UB (**diposit.ub.edu**) ha sido autorizada por los titulares de los derechos de propiedad intelectual únicamente para usos privados enmarcados en actividades de investigación y docencia. No se autoriza su reproducción con finalidades de lucro ni su difusión y puesta a disposición desde un sitio ajeno al servicio TDR o al Repositorio Digital de la UB. No se autoriza la presentación de su contenido en una ventana o marco ajeno a TDR o al Repositorio Digital de la UB (framing). Esta reserva de derechos afecta tanto al resumen de presentación de la tesis como a sus contenidos. En la utilización o cita de partes de la tesis es obligado indicar el nombre de la persona autora.

WARNING. On having consulted this thesis you're accepting the following use conditions: Spreading this thesis by the TDX (**www.tdx.cat**) service and by the UB Digital Repository (**diposit.ub.edu**) has been authorized by the titular of the intellectual property rights only for private uses placed in investigation and teaching activities. Reproduction with lucrative aims is not authorized nor its spreading and availability from a site foreign to the TDX service or to the UB Digital Repository. Introducing its content in a window or frame foreign to the TDX service or to the UB Digital Repository is not authorized (framing). Those rights affect to the presentation summary of the thesis as well as to its contents. In the using or citation of parts of the thesis it's obliged to indicate the name of the author.

DEPARTAMENT DE MINERALOGIA, PETROLOGIA I GEOLOGIA APLICADA

FACULTAD DE CIENCIAS DE LA TIERRA

UNIVERSITAT DE BARCELONA

Optimization of the use of diamond indicator minerals in diamond exploration in kimberlites

Memoria de tesis doctoral presentada por:

Jingyao Xu

Esta tesis ha sido realizada dentro del programa de doctorado en Ciencias de la Tierra de la *Universitat de Barcelona*

Dirigida por: ***Dr. Joan Carles Melgarejo Draper***

La doctoranda

El director y tutor

Jingyao Xu

Joan Carles Melgarejo Draper

Barcelona, marzo de 2019

CONTENTS

ACKNOWLEDGMENTS

First of all, I would like to thank Dr. Joan Carles Melgarejo, director of the doctoral thesis. Thank you for your confidence during these years. I have learned a lot during these years from you, as how to write a paper, how to solve a problem, more and more. I do not have sufficient words to express my gratitude and not only as director but as a friend and person. Thank you so much!

I would like to thank to my family for their unconditional support and for being there always giving me strength to keep going. Thanks to my mother, Qingmin Yao who always worry about my health and gives me infinitive love. Thanks to my father Jiangnan Xu for all the support otherwise I couldn’t have been stayed ten years in Spain. I would also like to thank my friend Juan Carlos Ruiz Alarcon, who gives me the biggest help in those most difficult moments in these ten years, and the accompaniment during ten years.

This research was supported by the CGL2006-12973 and CGL2009-13758 projects of the Ministerio de Ciencia e Innovación of Spain, the AGAUR 2014SGR01661 and 2017SGR707 (Generalitat de Catalunya), and a FI grant to Jingyao Xu (coded FI_B 00904, Departament d’Educació i Universitats, Generalitat de Catalunya).

Author acknowledge the Scientific and Technical Centres of the University of Barcelona (CCiTUB) for assistance with SEM-EDS (Javier García Veigas, Eva Prats Miralles and David Artiaga Torres), EMPA (Xavier Llovet) and Raman (Tariq Jawhari Colin). Thank thin section laboratory of University of Barcelona (Dolors Barsó, Vicenç Planella and Montserrat Sibila). Thank Montgarri Castillo for her assistance with LA-ICP-MS at GEMOC (Macquarie University). Thanks to Gus Formadas of Diavik Mine for sending us many good samples.

Thanks to colleagues in the department, to let me share the day to day throughout this time and make me feel at home. Thanks to Josep Roqué, Thomas Aiglsperger, Lisard Torró, Sandra Amores, Núria Pujol, Cristina Villanova, Marc Campeny, Júlia Farré, Lídia Butjosa, Montgarri Castillo, Saleh Lehbib, Jorge Macridachis. Thank you very much to Joaquín Proenza, Maite García, to Salvador Galí, Pere Enrique and to the professors and colleagues of the department. Thank you Esperanza Tauler, I would not have started this PhD thesis without your encouragement.

Thanks to all of you!

SUMMARY

Ti-rich minerals occur in xenoliths of metasomatized mantle peridotites, MARID and PIC. Xenocrysts produced by disaggregation during the intrusion have equivalent compositions.

Early crystallization in the first intrusive stage in kimberlites and related rocks produces olivine phenocrysts that may have trapped inclusions of co-crystallizing rutile, Mg-rich ilmenite to geikielite and chromite. Geikielite may replace Ti-bearing minerals of the xenocrystic suite, producing a suite of magnesian ilmenites of intermediate compositions that follow an Mg enrichment trend depending on the grade of interaction xenocrysts/magma. Phlogopite microphenocrysts can start to crystallize in this stage.

A second magmatic stage produces saturation in pyrophanite, that can precipitate or react with all the above Ti-rich minerals, producing crystallization of a suite of intermediate manganoan ilmenites whose compositions depend on that of the replaced Ti-mineral and the grade of interaction of the magma with the above crystals. Lately in this stage, qandilite-ulvöspinel-magnetite start to crystallize, together with perovskite, along with phlogopite microphenocrysts. Finally, the crystallization of ulvöspinel-magnetite crystals may be produced in disequilibria, inducing the development of atoll textures.

Groundmass phlogopite crystallize in the late magmagtic stage. Monticellite can be formed in this stage. Interstitial glass can be produced at the end of this stage.

Subsolidus hydrothermal processes are widespread in most of the kimberlites, with replacement of the early minerals by hydrous and carbonic fluids of kimberlitic provenance. Olivines and glass are replaced by serpentines and carbonates. A sequence of ilmenites (geikielite followed by pyrophanite) can precipitate directly or replace the above Ti-bearing minerals. Spinels and perovskites may also be replaced by Ti hydrogarnets and late perovskite or kassite accompanied by aeschynite.

The composition of the replacing ilmenite depends on that of the replaced mineral. Hence, these ilmenites can retain Nb, Cr, Zr when replacing rutile or perovskite, chromite or crichtonite. Therefore, the trace composition of ilmenite cannot be used to extract petrogenetic information.

Mg- or Mn-ilmenites cannot be used as DIM because they are very late minerals formed during the intrusion.

When plotting the composition of these minerals in the existing IUGS classification diagrams there is an extensive overlap among kimberlites and related rocks. Thus the existing classification diagrams are not useful and we propose some amendments to the existing classification.

CHAPTER 1

GENERAL INTRODUCTION

1. GENERAL INTRODUCTION

Kimberlites are great scientifically and economically interesting because of their deep origin in mantle and because they are principal primary deposits of diamond. However, high amounts of different xenoliths and intensive alteration obscure their original magma chemistry and properties (Mitchell, 1986; Sparks, 2013), making it difficult to understand the nature of the complex kimberlitic rocks.

1.1. KIMBERLITES AND RELATED ROCKS

Kimberlites and related rocks are encountered during diamond exploration. Related rocks include lamproite, orangeite, melilitite, carbonatite, minette, camptonite, monchiquite, sannaite, aillikite, alnöite, damtjernite, melnoite, etc (Scott Smith *et al.*, 2018). Kimberlite is the main primary source of diamonds and together with lamproite form the principal primary diamond deposits.

1.1.1. Kimberlites

Kimberlite (also called as Group I kimberlite) is defined as a group of volatile-rich (dominantly CO_2) potassic ultrabasic rocks by IUGS recommendation (Le Maitre, 2002). Kimberlite is recently defined as volatile-rich ($H_2O \geq 5\%$ and $CO_2 \geq 10$ wt%), K-rich ($K_2O \leq 3$ wt%; $Na_2O \leq 0.5$ wt%; Na_2O / $K_2O < 0.5$) and olivine-rich (~50 modal%) ultrabasic igneous rock by Scott Smith *et al.* (2018). They show typically an inequigranular texture with macrocrysts (>1mm) set in a finer-grained matrix (Mitchell, 1997; Le Maitre, 2002; Scott Smith *et al.*, 2018). They derived from depleted asthenospheric mantle sources at depth from 150 - 400 km (Mitchell, 2006).

Kimberlites are hybrid rocks that contain xenoliths and xenocrysts from distinct sources (Mitchell, 1986; Le Maitre, 2002): mantle rocks (peridodite, eclogite), deep crustal rocks (for instance granulites) and shallow crustal rocks (such as country rocks; Scott Smith *et al.*, 2018), which are incorporated during emplacement of kimberlite melt from deep mantle to the surface. The common and diverse xenoliths and xenocrysts are settled together with primary phases crystallizing from the kimberlite magma.

Macrocrysts (> 1 mm) are dominated by olivine, and less frequently by Cr-poor or Cr-rich pyrope, Mg-ilmenite, Cr-spinel, Cr-diopside, other types of clinopyroxene, orthopyroxene, phlogopite, zircon and also diamond (Scott Smith *et al.*, 2018). Microphenocrysts as primary mineral (~0.5 - 1 mm) are dominated by olivine and less commonly by phlogopite and Mg-Cr-Ti spinel (Scott Smith *et al.*, 2018). Groundmass (mainly < 0.2 mm) is composed of typical primary minerals such as monticellite, phlogopite - kinoshitalite, perovskite, spinel (qandilite - Mg-chromite – ulvöspinel - magnetite s.s.), apatite, carbonate (calcite and/or dolomite) and serpentine (Scott Smith *et al.*, 2018).

Many kimberlites are particularly susceptible to weathering (Scott Smith *et al.*, 2018). Alteration and xenoliths obscure their original magma chemistry and properties (Sparks, 2013).

1.1.2. Orangeites

Orangeites were previously named as “micaceous kimberlite” (Wagner, 1914) and later, were termed as “group II kimberlite” (Skinner, 1989; Woolley *et al.*, 1996; Le Maitre, 2002). Orangeite is ultrapotassic, peralkaline volatile-rich (dominantly H_2O) rocks, characterized by phlogopite macrocrysts and microphenocrysts, together with “tetraferriphlogopite” to phlogopite groundmass micas (Le Maitre, 2002). Recently, orangeites have been proposed to be included into the lamproites (var. Kaapvaal) due to their petrographic similarity and common petrogenesis (Scott Smith *et al.*, 2018). They have typically abundant phlogopites as essential mineral together with diopside (Scott Smith *et al.*, 2018). Orangeites derived from metasomatized (enriched) deep lithospheric mantle (Mitchell, 2006).

1.1.3. Lamproites

Lamproites are peralkaline ultrapotassic rocks which are dominant by one together with presence of two or more following minerals (Le Maitre, 2002): titanian, Al-poor phenocrystic phlogopite (TiO_2 2%-10%; Al_2O_3 5%-12%), groundmass poikilitic titanian tetraferriphlogopite (TiO_2 5% -10%), titanian potassium richterite (TiO_2 3%-5%; K_2O 4% – 6%), forsteritic olivine, Al-poor, Na-poor diopside (Al_2O_3 < 1% and Na_2O < 1%), non-stoichiometric iron-rich leucite (Fe_2O_3 1% – 4%), Fe-rich sanidine (typically Fe_2O_3 1% -5%). Lamproites are recently defined as peralkaline ultrapotassic ($K_2O/Na_2O > 3$; molar $K_2O/N_2O/Al_2O_3 > 1$), H_2O bearing, silica-undersaturated, mafic mantle derived igneous rocks (Scott Smith *et al.*, 2018).

Lamproites are derived from metasomatized (enriched) deep lithospheric mantle (Mitchell, 2006). Only olivine macrocryst-rich lamproites have the potential to carry macrodiamonds but as a very rare constituent (Scott Smith *et al.*, 2018).

1.1.4. Lamprophyres

Lamprophyres are a group of alkaline silica-undersaturated mesocratic to melanocratic, porphyritic igneous rocks (Scott Smith *et al.*, 2018). Common minerals presented in lamprophyres are: phenocrysts and groundmass of phlogopite-biotite and/or amphibole, clinopyroxene and olivine present or absent, with feldspar (commonly alkali feldspar) in groundmass (Scott Smith *et al.*, 2018). Lamprophyres are divided into three groups (Scott Smith *et al.*, 2018):

a) Calc-alkaline lamprophyres which are composed of clinopyroxene, amphibole and mica. Groundmass carbonate and quartz may be found in groundmass. This group include: 1) minette (biotite and orthoclase dominant); 2) kersantite (biotite and plagioclase dominant); 3) vogesite (hornblende and orthoclase dominant) and 4) spessartite (hornblende and plagioclase dominant). They are suggested to be associated with basalt and shoshonite.

b) Alkaline lamprophyres which are composed of pyroxene, amphibole, primary carbonate and minor melilite. This group include: 1) camptonite (plagioclase > alkali feldspar); 2) monchiquite (feldspathoid present, feldspar absent) and 3) sannaite (alkali feldspar > plagioclase feldspar). They are suggested to be associated with alkali basalt and/or nephelinite.

c) Ultramafic lamprophyres which are composed of phlogopite, olivine, clinopyroxene, amphibole and primary carbonate. This group include: 1) aillikite (carbonate-rich); 2) alnöite (melilite-bearing) and damtjerinite (nepheline and/or alkali feldspar-bearing). They are suggested to be associated with nephelinite, melilite and carbonatite-ijolite-suite rocks.

1.2. KIMBERLITE VOLCANISM

1.2.1. Generation in deep mantle

Kimberlite magma originated at a depth between 150-400 km (Mitchell, 2006) fit into the diamond stability field or “diamond window”, and temperature at 1350-1450 ºC (Priestley *et al.*, 2006). Two possible source of kimberlite magma have been suggested. Becker and Le Roex (2006) proposed that kimberlite were originated by partial melting of subcontinental lithospheric or deeper astenospheric mantle previously metasomatized by basaltic magmas in an ocean island context. However, Mitchell (2006) and Scott Smith *et al.* (2018) proposed that kimberlite derived from depleted asthenospheric mantle. Russell *et al.* (2012) proposed that the primary parental melts of kimberlite is carbonatitic, then it is modified by the assimilation of orthopyroxene during ascent. Kimberlite melt is produced by ~0.5% melting of carbonated lherzolite at the pressures conditions of the upper asthenosphere (i.e., 6.0–8.6 GPa at ~190–285 km and ~1400–1500 °C; Soltys *et al.*, 2018) .

Orangeites (group II kimberlite, renamed to lamproite recently), lamproites and other potassic rocks are derived from metasomatized (enriched) lithospheric mantle (Becker and Le Roex, 2006; Mitchell, 2006; Scott Smith *et al.*, 2018), in the lower part of the lithospheric mantle in the garnet stability field about 150-200km in depth (Mitchell, 2006; Giuliani *et al.*, 2015). (Mitchell, 2006) suggested that archetypal kimberlite and lamproites (including orangeites) are derived from different depths and sources, therefore they have no genetic relationship (Fig. 1.1.).

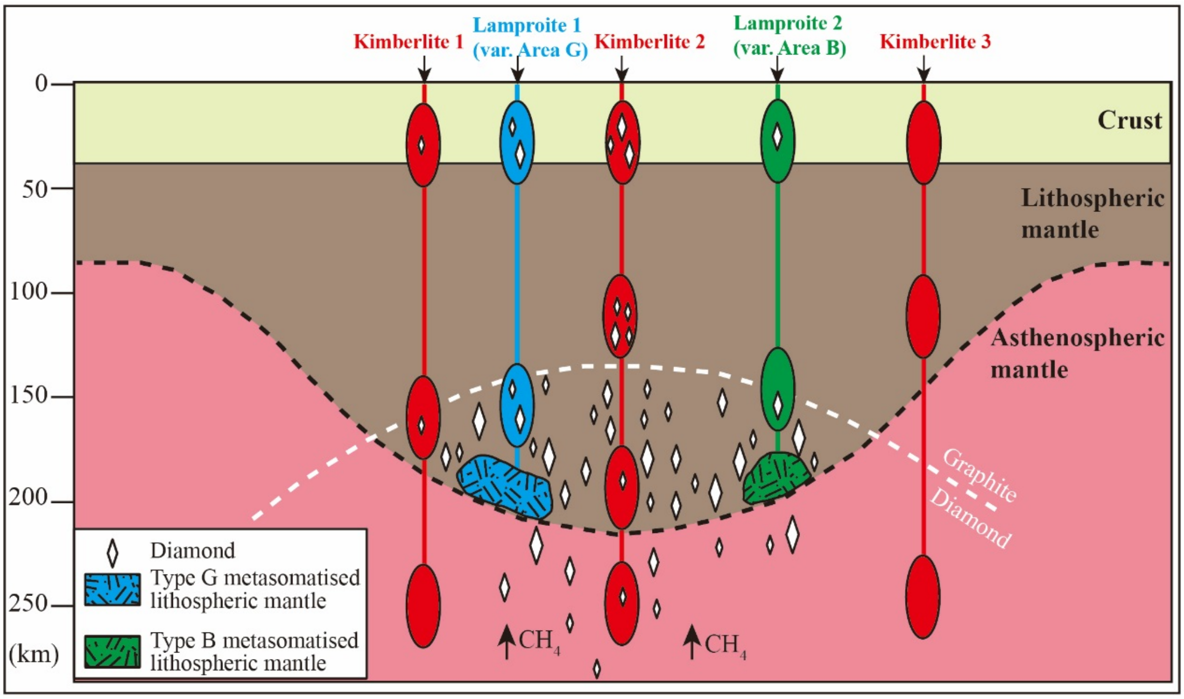

Fig. 1.1. Origin of kimberlite and lamproite (after Mitchell, 2006; Scott Smith, 2017). Ovals are separate kimberlite and lamproite melt with different diamond contents. Kimberlite melt originated in asthenospheric mantle. Lamproites are originated from different metasomatized lithospheric mantle that generated specific lamproite melts in each different area (lamproite var. Area G or B).

1.2.2. Magma ascent

Kimberlite magma ascent rapidly from >150 km along narrow dykes at velocity of several meters per second, reaching surface in ascent times of several hours (Sparks *et al.*, 2006; Sparks, 2013). A dyke is essential to enable starting kimberlite ascent (Sparks, 2013), bubble nucleation of melt supersaturated in CO_2 generate high pressure that fragment mantle host rocks and initiate magma ascent (Lensky *et al.*, 2006). Physiochemical conditions and magma properties change during magma ascents including incorporation and resorption of mantle and crustal xenoliths, crystallization, cooling, degassing, changes of oxidation state (Sparks, 2013).

Kimberlite melt was alkali-rich carbonatitic when it started ascent, which lead to its high buoyancy, low density, ultra-low viscosity and high mobility (Sharygin *et al.,* 2017). The viscosity of kimberlite magma decreases by more than three times during its ascent from mantle to crust (Persikov *et al.,* 2015). Decrease in the temperature of the ascending kimberlite magma from 200 km can be 90 - 140 °C (Sparks, 2013). Kimberlite melts has viscosity about 35 Pa · s can be generated by partial melting (< 1 wt%) of carbonated peridotite in the mantle at depths of 250 - 350 km (at ~ 8.5 GPa and ~ 1350 °C). While the viscosity of near-surface kimberlite melts is much lower (~10 Pa · s, at ~50 MPa and 1200 °C; Persikov *et al.,* 2015). The viscosity of 10 Pa · s is as low as the viscosity of honey at room temperature and pressure, in contrast to the high viscosity of basalt about ~ 600 Pa · s during its eruption (Persikov *et al.*, 2015). Low viscosity of near-surface kimberlite melt is also suggested as by Sparks *et al.*(2006) to be 0.1-1 Pa · s, while high viscosity of 10^3 - 10^4 Pa · s is suggested by other works (Brown *et al.*, 2012; Gernon *et al.*, 2012).

Stalling of kimberlite magma may lead to fractional crystallization, loss of volatile and loss or gain xenocrysts, and the result is the generation of a diversity of differentiated kimberlite magmas (Sparks, 2013). Multiple pulses of magma result in separate units or mixing. Magma mixing is manifested as bimodal mineral compositions, disequilibrium mineral assemblages, textural heterogeneities and crystal in both normally and reversed zoning (Sparks, 2013). Assimilation of mantle and crustal material may affect the whole rock geometry by introducing large amounts of xenoliths and xenocrysts (Mitchell, 2008; Sparks, 2013). Mitchell (2008) suggested that there is no hypabyssal kimberlites that could represent the initial primary kimberlite magma composition; all kimberlites are hybrid and contaminated magmas.

1.3. KIMBERLITE STRUCTURE AND ROCK TYPES

Each single kimberlite body is formed by multiple separate batches of magma (Scott Smith *et al.*, 2018) which form one phase of kimberlite which has a different origin and ascent history, showing different characteristics (for example, different mantle and crustal xenolith and xenocryst composition and content, including different diamond content, different groundmass mineralogy (Scott Smith *et al.*, 2018). Different patches magma from the same pipe could be different magmatism of millions of years (Ranger *et al.*, 2018). Each phase may include several textural varieties (facies) due to variation in one emplacement event (Scott Smith *et al.*, 2013). A lot of different terminologies for geological units and lithofacies of kimberlite have been established, changed and discussed for many years (Mitchell, 1986; Skinner and Marsh, 2004a; Cas *et al.*, 2008; Scott Smith *et al.*, 2013, 2018; Sparks, 2013).

Kimberlite magma form different kinds of bodies near surface. Three types of kimberlite bodies termed Class 1, 2 and 3 are described by Skinner and Marsh (2004) which were lately described by Scott Smith (2008) as type c, a and b respectively (Fig. 1.2): Class 1 (classical) shows 3 zones including crater facies (pyroclastic and re-sedimented volcaniclastic), pipe or diatreme facies and root zone (hypabyssal kimberlite and breccias); Class 2 is dish-shaped crater without considerable pipe and root zone; Class 3 is pipe filled with re-sedimented volcaniclastic kimberlite. Formation of class

1 and 3 is suggested to be related to water-rich magma while class 2 is relative to CO_2-rich (Skinner and Marsh, 2004a).

However, two kinds of end member body types have been proposed recently (Scott Smith *et al.*, 2018): volcanic pipes and intrusive sheets. Volcanic pipes show two different types in kimberlites: Fort à la Corne-type and Kimberley-type pyroclastic kimberlite (FPK and KPK; Scott Smith *et al.*, 2013). FPKs (formerly pyroclastic kimberlite) are shallow bowl-shaped craters similar to subaerial basaltic pyroclastic rocks (Scott Smith *et al.*, 2018). KPKs (formerly tuffisitic kimberlite) have infilled diatreme zone (deep pipes) which are unique to kimberlite (Scott Smith *et al.*, 2018).

The classic model of kimberlite (for KPK kimberlite type) divides three textural genetic groups of rocks: crater facies, diatreme facies and hypabyssal facies (Mitchell, 1986; Fig. 1.3). Crater facies include lavas, pyroclastic rocks and epiclastic rocks. Diatreme facies rocks also be termed as tuffisitic kimberlites (TK), tuffisitic kimberlite breccias and volcanoclastic kimberlite (Mitchell, 1986). Hypabyssal facies rocks include sills, dykes, root zone and "blow" (Mitchell, 1986). Hypabyssal kimberlite are found both linked and unrelated to known pipes (Mitchell, 1986, 2008). These facies terms from the classic model have been widely using for many years, Scott Smith *et al.*, (2018) propose avoid them. Using of textural-genetic classification is suggested instead of facies terms (Scott Smith *et al.*, 2013, 2018): a) coherent kimberlite (CK) including a1) intrusive (intrusive coherent kimberlite (ICK) or hypabyssal kimberlite (HK)) or a2) extrusive coherent kimberlite (ECK); b) volcaniclastic kimberlite (VK) including b1) pyroclastic kimberlite (PK, divide into Fort à la Corne-type and Kimberley-type pyroclastic kimberlite (FPK and KPK)), b2) resedimented volcaniclastic kimberlite (RVK) or b3) epiclastic volcaniclastic kimberlite (EVK).

Other discrimination in four basic kimberlite rock types for kimberlites are also provided (Sparks *et al.*, 2006) including two types of volcaniclastic rock: massive volcaniclastic kimberlite (MVK, it is widely called as Tuffisitic Kimberlite Breccia or TKB) and layered volcaniclastic kimberlite (LVK); marginal wall-rock breccias and magmatic kimberlite (MK).

Depth of pipe structures is estimated to be originally 1 - 3 km, tipical contact angle between pipe and country rock is 70 - 90º (Sparks, 2013). Typical dimensions of cross-sectional areas of kimberlite pipe are commonly around 10^3 - 3×10^5 m^2 and volumes of fill are about 10^6-2×10^8 m^3 (Sparks *et al.*, 2006). A four stage model for kimberlite erupting magma has been provided (Sparks *et al.*, 2006): 1) initially overpressured resulting in explosive cratering and the pipe grows from the top downward by failure of pipe walls; 2) underpressure cause rock bursting at depth, down-faulting, ejecting by explosive flow; 3) form fluidized bed of pyroclasts with pipes; 4) hydrothermal metamorphism and alteration.

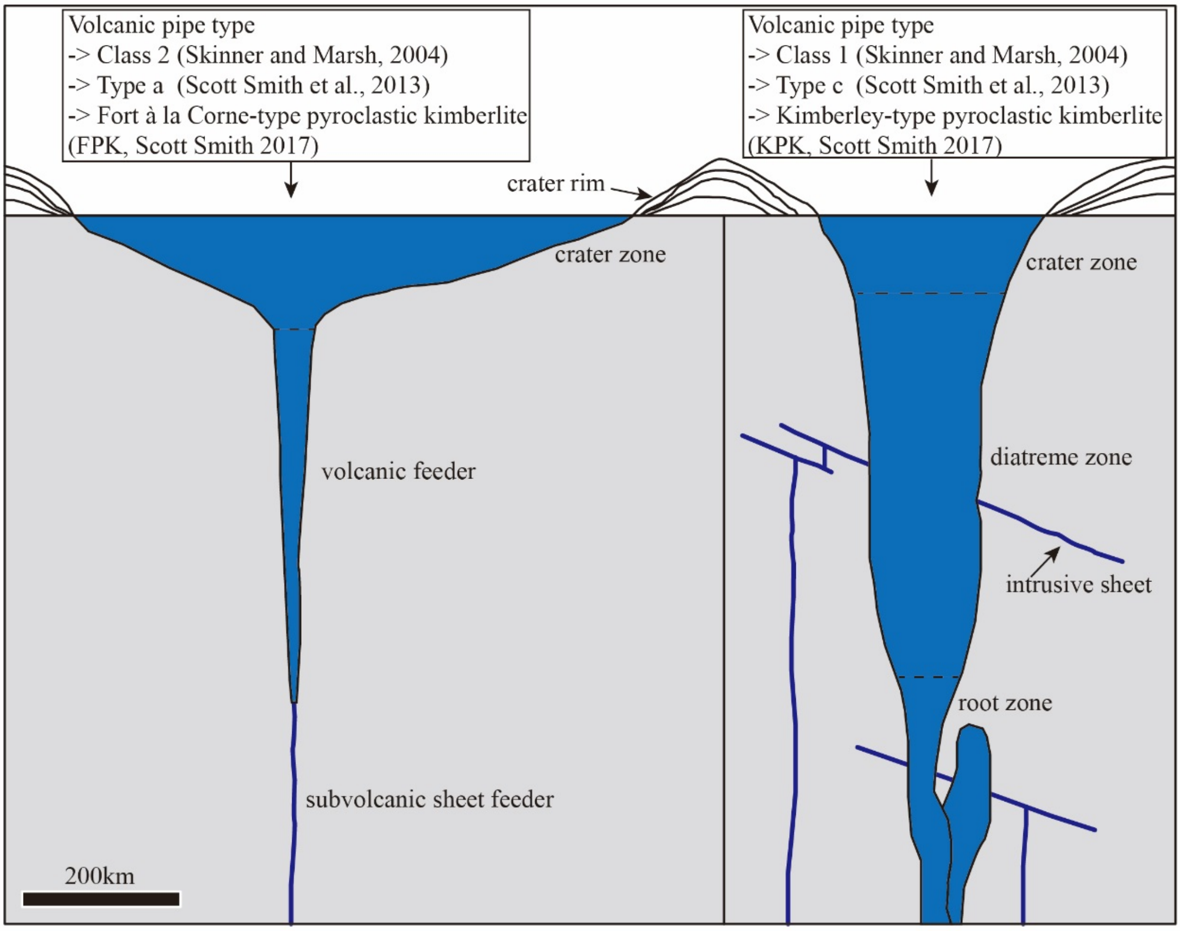

Fig. 1.2. Different classification and terminology of kimberlite body types after (after Skinner and Marsh, 2004; Scott Smith *et al.*, 2013; Scott Smith, 2017).

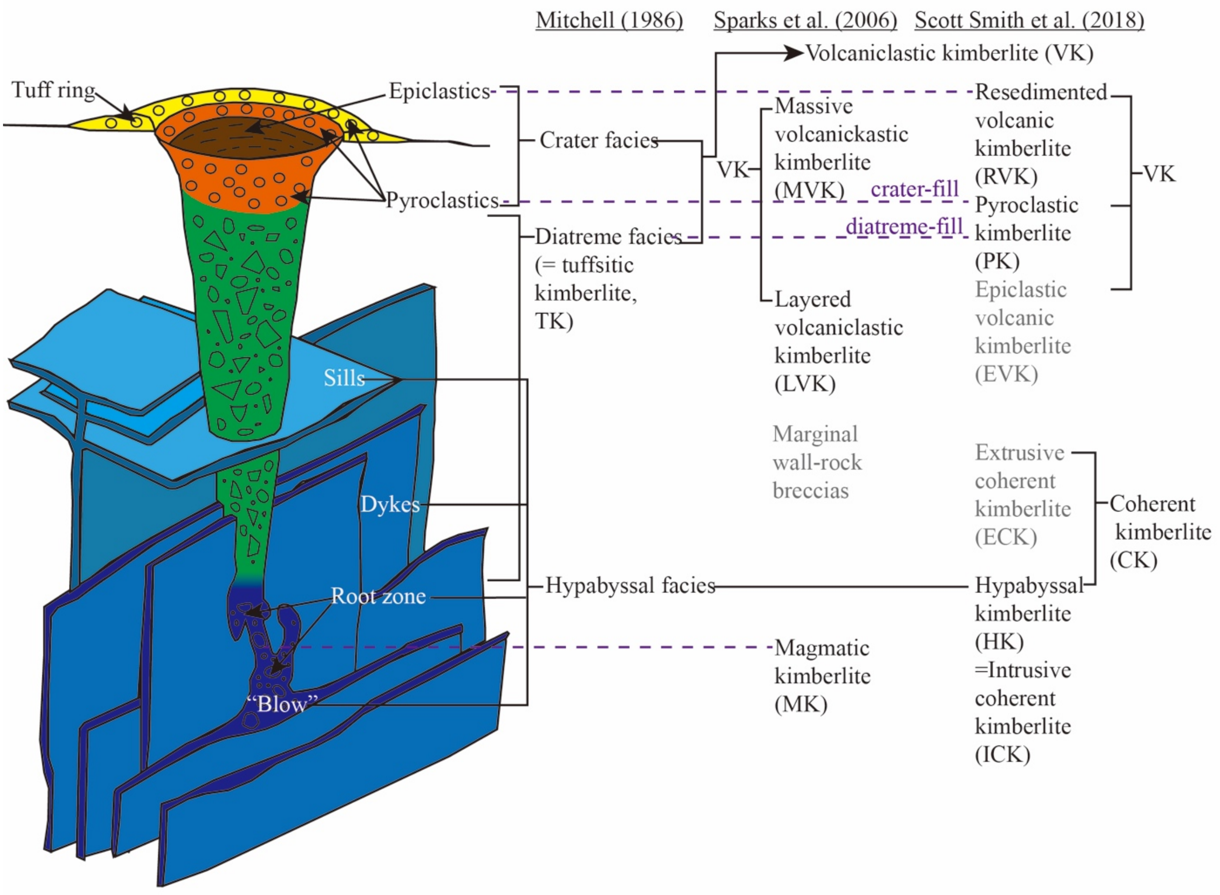

Fig. 1.3. Model of and idealized Kimberley-type kimberlite magmatic system (Mitchell, 1986) and different classification and terminology of kimberlite rock types or genetic or textural-genetic group of kimberlite rocks (Mitchell, 1986; Sparks *et al.*, 2006; Scott Smith *et al.*, 2018). Gray letters are types not illustrated in the scheme of the model.

1.4.KIMBERLITE ALTERATION

Extensive alteration occurs in most kimberlites. Serpentine is a major alteration mineral found in most kimberlite replacing olivine and other primary minerals (Sparks, 2013). Diopside, calcite, chlorite, talc, clay minerals also are found as alteration minerals in kimberlite (Sparks, 2013). Alteration temperature is suggested between 250 and 400 ºC (Buse *et al.*, 2010) comparable to ocean floor hydrothermal system.

There are different opinions about the origin of alteration minerals, for instance, serpentine. Alteration and the formation of serpentine could be originated by deuteric magmatic fluids (Mitchell *et al.*, 2009; Mitchell, 2013) and also external fluids (Wyatt *et al.*, 2004; Sparks, 2013; Afanasyev *et al.*, 2014), or a combination of these two agents during the decrease of the temperature, as suggested by the occurrence of different generations of serpentine (Giuliani *et al.*, 2017).

Silicic basement lithic could favour the diopside formation (Porritt *et al.*, 2012). Diopside is considered as matrix component of MVK and characteristic of tuffsitic kimberlite (Mitchell *et al.*, 2009), however, diopside is also considered as secondary alteration mineral in pyroclastic kimberlite (Porritt *et al.*, 2012).

1.5. KIMBERLITE OCCURRENCES

About 5000 kimberlites have been found in all continents (Janse and Sheahan, 1995; Faure, 2010; Fig. 1.4). Kimberlite intrusions commonly grouped in clusters of similar age (Sparks *et al.*, 2006). Most kimberlites occur within ancient craton regions of continents (Sparks *et al.*, 2006). Kimberlite have been dated giving ages from early Proterozoic to early Tertiary (Sparks *et al.*, 2006). Mitchell, (1986) noted that economically important kimberlites are found in cratons older than 2.4 Ga.

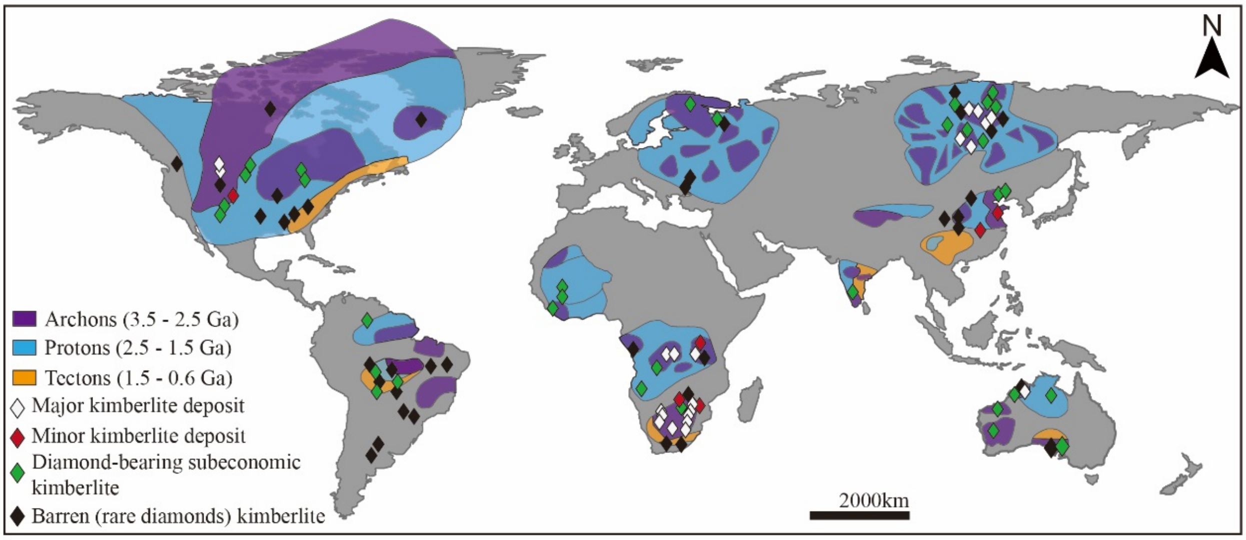

Fig. 1.4. World map showing locations of cratons and kimberlite deposits (after Janse, 2007; Robles-Cruz, 2008).

1.6. KIMBERLITES AND DIAMONDS

Diamonds formed in peridotite and eclogite in the deep roots of ancient cratons (Harlow and Davies, 2005) beneath about 140 km into diamond stability field in upper mantle, transitional zone (410 - 660 km) and lower mantle (Stachel *et al.*, 2005). Diamond petrogenesis is linked to the migration of fluids (melts or volatile- bearing fluids; Carmody *et al.*, 2014) and supposed to involve carbonate-bearing, volatile-rich brines (Kopylova *et al.*, 2010a). Kimberlite is the principal primary source of diamond; together with lamproite (Scott Smith, 2017; Scott Smith *et al.*, 2018), they carry diamond from deep mantle to near surface. Diamonds are found as xenocrysts or within mantle xenoliths in kimberlites. Not all kimberlites contain diamonds, only about 10% kimberlites are diamondiferous (Janse and Sheahan, 1995) and even the most diamond-rich kimberlites only contain ~ 70 ppb diamond (Carmody *et al.*, 2014).

1.7. KIMBERLITE INDICATOR MINERALS (KIMS) AND DIAMOND INDICATOR MINERALS (DIMS)

Kimberlite indicator minerals (KIMs) are used as tracer minerals for the exploration for kimberlite. The most commonly used KIMs are picroilmenite, peridotitic pyrope garnet, eclogitic garnet, Cr-diopside, chrome spinel, and less commonly olivine (Scott Smith et al., 2018). These minerals are more common than diamond in source rock and kimberlite, moreover, they are resistant to alteration processes and have high specific gravities thus allowing them to concentrate along with diamond during both the industrial separation processes of diamond and the formation of secondary diamond deposits in placers (Scott Smith et al., 2018). Diamond indicator minerals (DIMs) are KIMS whose chemical composition reveals a provenance from mantle with higher diamond-bearing potential (Scott Smith et al., 2018). Minerals commonly used as DIMs are, for instance, Cr-rich pyrope (Sobolev *et al.*, 1973), G-9 and G10 garnet (Dawson and Stephens, 1975). Further works proposed their use as DIMs based on Cr content of chromite (Gurney *et al.*, 1993) and the Ni content of G-9 and G-10 garnet (Griffin and Ryan, 1995). Ilmenite also has been discussed for its use as DIM based on its Mg, Fe^{3+} and Cr content (Mitchell, 1973, 1986; Haggerty, 1975a; Moore, 1987; Gurney and Zweistra, 1995; Schulze *et al.*, 1995), based on Mn content (Kaminsky *et al.*, 2000, 2001, 2006) and also based on trace elements such as Zr and Nb content (Griffin *et al.*, 1997; Carmody *et al.*, 2014).

1.8. RELATION BETWEEN KIMBERLITE AND RELATED ROCKS

Orangeite and lamproite

The contrast between macrocrystic and micaceous kimberlites is associated to the amount of mantle components that were incorporated into a compositionally uniform parental mafic silicate melt (Tappert et al., 2019). The assimilation of xenocrystic magnesite and incorporation of xenocrystic olivine from dunitic source rocks were the key processes that modified the parental silicate melt and created the unique hybrid (carbonate-silicate) character of kimberlites (Tappert et al., 2019). Kimberlites derived from same parent magma exhibit different composition as result of different degree of mantle contamination is also reported by le Roex (2003). Kimberlite in the same cluster are derived from the same parent melt is also reported by Giuliani (2018).

MARID-veined peridotites is supposed to be the mantle source for orangeite magmas in southern Africa (Giuliani et al., 2015). The formation of lamproite or kimberlite is supposed to be related to interaction with different mantle metasomatized rock. Close spatial association and contemporaneous emplacement of kimberlite and lamproite is proposed to be related to a unifying petrogenetic model which involves the interaction of a silica-poor carbonatite melt with differently metasomatised wall rocks in the lithospheric mantle (Shaikh et al., 2018). The metasomatised wall rock is phlogopite-rich and MARID-type metasomatic veins for lamproite, while is relatively refractory for kimberlite (Shaikh et al., 2018).

Aillikite and carbonatite

Carbonate component in the aillikitic source could have been produced by evolved kimberlite melts (Nosova *et al.*, 2018). Carbonatite magma is produced by kimberlite and other deeply derived carbonated silicate melts, such as aillikites, exsolve their carbonate components within the shallow lithosphere in ascent to the Earth’s surface (Tappe *et al.*, 2017).

1.9.MANTLE METASOMATISM AND KIMBERLITE

Mantle metasomatism could be originated by subduced ocean crust as well as by interaction of kimberlite melt (or failed proto kimberklite melt) with mantle peridotite. Cr-rich megacryst clinopyroxene and garnet is also suggested to be associated to failed kimberlite as percolation of kimberlite melt into depleted mantle (as harzburgite) to form lherzolite (Bussweiler *et al.*, 2018). High

Fe-Ti-bearing carbonate-silicate early kimberlite melt ascent from the base of the SCLM interacted with peridotites of the SCLM and converted the carbonate-silicate kimberlite melt to the silicate-bearing kimberlite melt (Kargin *et al.*, 2017)**.** This interaction form low-Cr megacrysts (as low-Cr and Fe-Ti-rich garnet and low-Cr clinopyroxene) in peridotites and metasomatism of the SCLM leading to the formation phlogopite-garnet-peridotites with ilmenite (Kargin *et al.*, 2017). During the ascent forming Cr-rich clinopyroxene and low-Cr and -Ti phlogopite megacrysts in clinopyroxene-phlogopite rocks (Kargin *et al.*, 2017). New pulses of kimberlitic melts ascent through the clinopyroxene–phlogopite metasomatic rocks formed late high-Ti clinopyroxene spongy rims and zones and high-Ti-Cr phlogopites along veinlets veinlet networks (Kargin *et al.*, 2017). Metasomatism produced by interaction of protokimberlite melt with mantle peridotite could create some diamond populations (Ashchepkov *et al.*, 2013).

Saline high-density fluid (HDF) is found as inclusion in diamond and is supposed to be originated from subducted ocean crust, which cause mantle metasomatism and leading to kimberlite eruption (Timmerman *et al.*, 2018; Weiss and Goldstein, 2018).

CHAPTER 2

OBJECTIVES

2. OBJECTIVES

There are a lot of publications about chemical study of whole rock or mineral chemistry of diamond indicator minerals obtained from concentrates (Wyatt et al., 2004), but textural data obtained by whole rock petrography are comparatively lesser. Many earlier publications studied mineral textures but there is a lack of good quality photos (Mitchell, 1986, 1995) of each generation or lack detailed textural description.

During the last years, several studies published by the Consolidated Research Group of Mineral Resources at the University of Barcelona demonstrated that the use of mineral chemistry without a detailed petrographic study in kimberlites and related rocks could produce erroneous conclusions. Some general studies exist on the petrogenetic and economic information that can be obtained from the petrographic study of some the different minerals, based on the study of hundreds of kimberlites (i.e., in the case of the spinels, the synthesis of Roeder and Schulze, 2008) but there are not enough information on the rest of the minerals. Moreover, a lot of kimberlite-like intrusions are named as kimberlite while most of them might be classified as lamproites or ultramafic lamprophyres (Mitchell, 1997; Tappe et al., 2006). The classification of these rocks is a non-solved problem.

Kimberlite and related rocks are hybrid rocks as they are a mixture of materials of different sources from mantle to the surface; therefore, a whole rock analysis or an analysis of concentrates of minerals will mix many different information and not be representative neither of the kimberlite magma nor of the different sources. Therefore, the objectives of this thesis are:

1) to establish the textural-compositional types of the common minerals components of the macrocrystic suite and the groundmass in kimberlites and related rocks: spinel group minerals, ilmenite group minerals, rutile, perovskite, crichtonite-group minerals, mica group minerals, clinopyroxene group minerals, titanium garnets and djerfisherite from a population of 79 different worldwide kimberlites and related rocks, considered as representative of the different.
2) to establish a common paragenetic sequence for these different rocks from worldwide;
3) to select whose of the proposed indicator minerals can be effectively used in occurrences of these rocks and in diamond exploration;
4) to examine the possibility of use of the mineral associations and the corresponding mineral chemistry in the kimberlite classification.

CHAPTER 3

GEOLOGICAL SITUATION OF THE SELECTED SAMPLES

3. GEOLOGICAL SITUATION OF THE SELECTED SAMPLES

3.1 GENERAL DISTRIBUTION

Thousands of kimberlites and related rocks are known across all the continents (Janse and Sheahan, 1995), but these deposits are subject to many restrictions for sampling from mining companies or governments, and many of them occur in remote regions. Some of the samples were collected in situ by our Research Group during field trips in Angola, India, Botswana and China, other were donated by prospectors or diamond mining companies, and some of them were acquired in the mineral collector market. The resulting samples cover most of the continents, except Australia and Antarctica. Samples from 79 intrusions of kimberlites and related rocks from 11 countries have been studied: 3 from Angola, 13 from Botswana, 11 from South Africa, 1 from Lesotho, 12 from Canada, 11 from USA, 1 from Venezuela, 2 from Guinea, 9 from Russia, 13 from India and 3 from China (Fig. 3.1). 79 samples including 68 kimberlite, 1 ultramafic lamprophyre (UML), 3 orangeites and 7 lamproites. Among 68 kimberlite samples, 21 are volcaniclastic rocks and 47 are coherent rocks.

Coherent rocks were preferred because they have minor contamination in crustal elements and therefore reflect more the original magma composition.

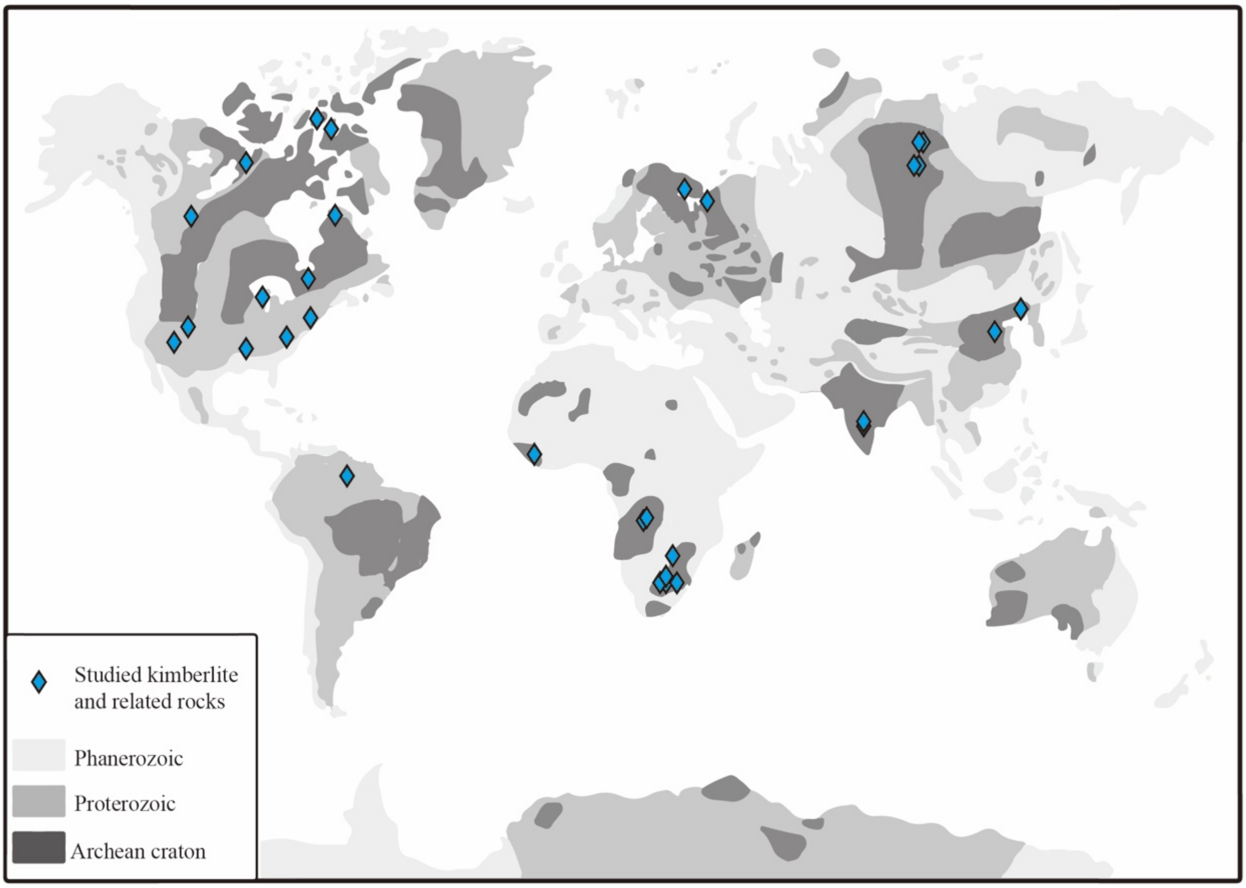

Fig. 3.1. Localization of studied kimberlites and related rocks. Craton map adapted from (Tang et al. (2013).

3.2. AFRICAN KIMBERLITES

30 samples from Africa are studied including 2 from Western Africa and 28 from the south part of Africa.

Two kimberlites from Banankoro of Guinea were obtained as representative from the Man Craton in the Western Africa Craton (Fig. 3.2a). $^{40}Ar/^{39}Ar$ phlogopite age determination from the Banankoro rocks returned ages of 139 ± 3 Ma (Skinner *et al.*, 2004).

Most of the kimberlites from the Congo craton are located in the Lucapa corridor, a tectonic structure trending NE-SW across Angola and Congo (de Carvalho, 1983). Most of these kimberlites are found in the Congo and the NW Angola (Reis, 1972; Egorov *et al.*, 2005), in the Lunda Norte province (Ustinov *et al.*, 2018), where more than 2000 showings have been prospected in the last years; however, some kimberlite outcrops have been described in the central area of Huambo (Boyd and Danchin, 1974) and at the SW (i.e., Roman'ko *et al.*, 2005; Egorov *et al.*, 2007). However, mining operations are only active currently in some kimberlites of the Lundas, and the rest of the sectors are very remote. Selected samples from three kimberlites (Cucumbi, Tchiuzo and Cacuilo) from Angola were taken as representative of the kimberlites from this domain (Fig. 3.2b). Nearby kimberlite from Catoca is about 133 Ma using U-Pb of perovskite (Castillo-Oliver *et al.*, 2016). Most of the kimberlites of this domain suffered a very low erosion and therefore crater facies use to be generally very well preserved (Zuev *et al.*, 1988).

10 samples from Orapa, Letlhakane, Damtshaa and Karowe mines from Botswana are located at the edge of the Zimbabwe Craton. Orapa AK1 kimberlite age is reported as 93.1 Ma (Davis, 1977). These four mines are distributed across a relatively reduced area, less than 40 km in diameter.

Other three samples from the Jwaneng mine in Bostwana were selected as representative the Kaapvaal Craton, together with other kimberlites from classic mines in South Africa and Lesotho. Jwaneng kimberlite is reported as 240 Ma (Kinny *et al.*, 1989). One sample was studied from the pipe 200 from Lesotho. 88-95 Ma is given as the ages for other kimberlites from Lesotho (Hoese, 2009). Ten coherent rocks from South Africa were studied, including seven kimberlites from Riverton, Bulfontein kimberlite (91-94 Ma, Davis, 1977), Big Hole (92 Ma, Davis, 1977), Dutoitspan (80 Ma Davis, 1977), Monastery (83 ± 3 Ma, Kramers and Smith, 1983) and Kaalvallei (called Kaalvallei "A" in this work, 85 Ma, Viljoen *et al.*, 1994). One lamproite from Kaalvallei (called Kaalvallei "B" in this work) was also studied. Finally, three orangeites from South Africa have been studied in this work including Helam (147-150 Ma by Allsopp and Barrett, 1975; classified by Hammond and Mitchell, 2002), Roberts Victor (92.2 Ma by Davis, 1977, classified by Mitchell, 1995) and Bellsbank (118Ma by Smith *et al.*, 1985, classified by Mitchell, 1995).

3.3. RUSSIAN KIMBERLITES

Eight kimberlites from Russia were studied in this work. Five of them are located in the Siberian Craton, including Udachnaya, Obnazhonnaya, Mir, Pobeda and Leningrad (Fig. 3.3a). Udachnaya kimberlite age is reported as 353-367 Ma (Kinny *et al.*, 1997), Mir kimberlite is 361 Ma (Davis, 1978).

Three are located in the East European Platform, in the Kola peninsula and the Timan aulacogen, including Emakowskaya, Lomonosovskaya and Pionerskaya (Fig. 3.3b). Lomonosovskaya kimberlite is reported as 340-380 Ma (Beard *et al.*, 1998).

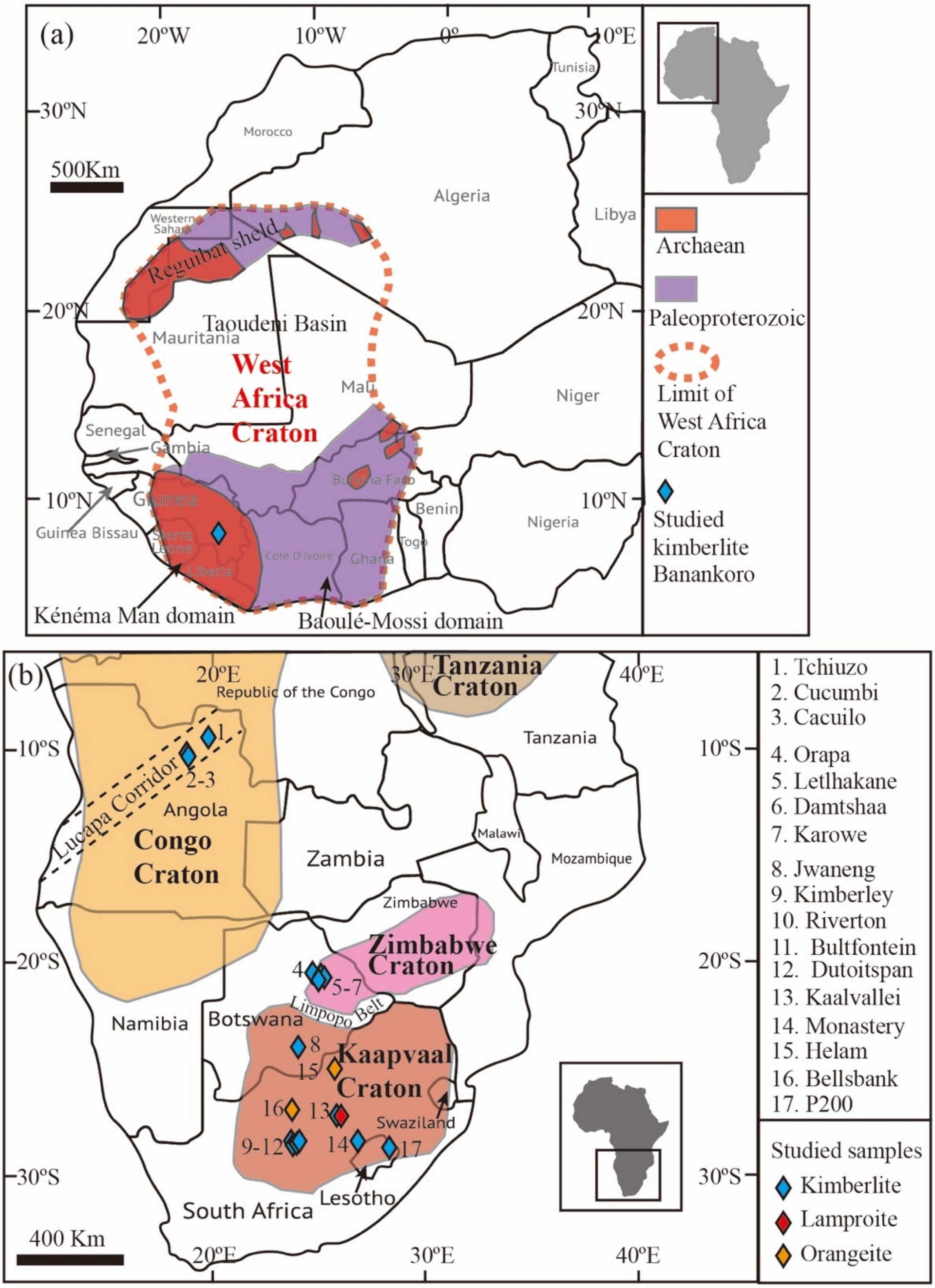

Fig. 3.2. Localization of samples from Africa. (a) Localization of studied Banankoro kimberlite in West Africa Craton (adapted from Begg et al., 2009). (b) Localization of studied kimberlite and related rocks from Southern Africa (adapted from Begg et al., 2009; Farr and Farr, 2018; Motsamai et al., 2018; Fitzpayne et al., 2019).

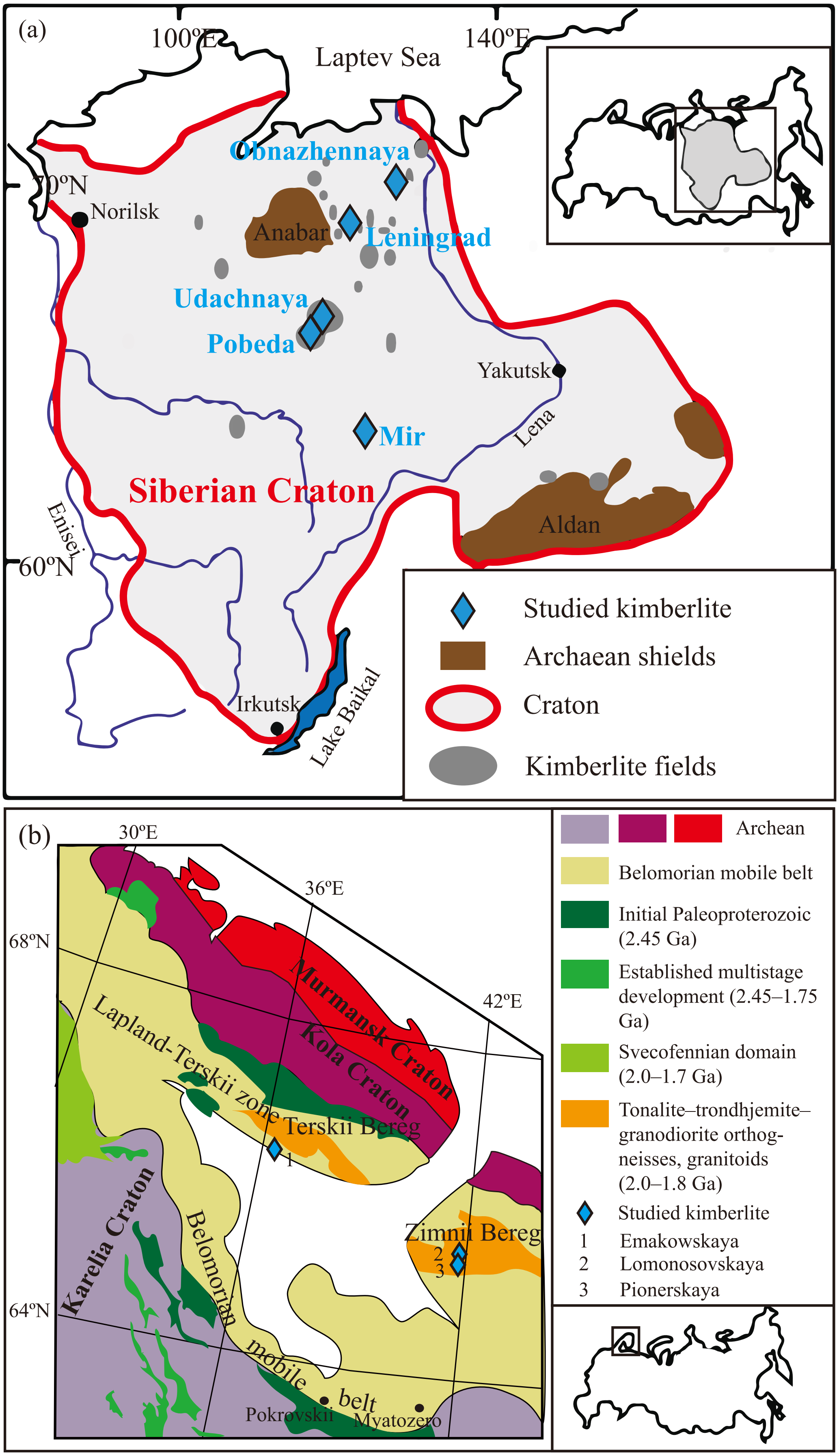

Fig. 3.3. Localization of samples from Russia in (a) Siberian Craton (adapted from Ionov et al., 2018) and (b) East European Platform (adapted from Samsonov et al., 2009).

3.4. INDIAN KIMBERLITES

13 Mesoproterozoic coherent rocks from India are studied in this work (Fig. 3.4) which are located in Eastern Dharwar Craton in Raichur kimberlite field (RKF) and Wajrakarur kimberlite field (WKF). Nine of them are kimberlites including Siddanpalli SK-1 (1089 ± 14 Ma , Chalapathi Rao *et al.*, 2013), SK-2 and SK-3 kimberlites from RKF, Chigicherla CC-4 (1117 ± 14 Ma, Chalapathi Rao *et al.*, 2013) and CC-5 (1134 ± 8 Ma, Chalapathi Rao *et al.*, 2013), Kalyandurg KL-3 (1101 ± 11 Ma, Chalapathi Rao *et al.*, 2013) and KL-4, Wajrakarur P-1 and Lattavaram P-3 kimberlites from WKF. Four lamproites from WKF are studied in this work including Chigicherla CC-1, Wajrakarur P-2 (1092 ± 15 from Kumar *et al.*, 1993, classified by Kaur and Mitchell, 2013), Lattavaram P-4 (classified by Shaikh *et al.*, 2018) and Mulligiripally P-5 (1083 ± 12 Ma from Chalapathi Rao *et al.*, 2013, classified by Kaur *et al.*, 2013) lamproites.

3.5. CHINESE KIMBERLITES

Three kimberlites from China are studied in this work including Red Flag #1 (457-484 Ma, Dong, 1994), and Shengli (470 ± 4 Ma, Yang *et al.*, 2009) kimberlite from Mengyin, Shandong province and Wafangdian (400-500 Ma, , Huang *et al.*, 1992) kimberlite from Liaoning province. They are located in Northern China Craton (Fig. 3.5).

3.6. SOUTH AMERICAN KIMBERLITES

One kimberlite sample from Guaniamo from Venezuela is also studied. This kimberlite is about 710 Ma (Channer *et al.*, 2001) and located in Amazonian Craton (Fig. 3.6). It is a very altered kimberlite, and there are complex mineral associations, including pyrochlore (Sharygin *et al.*, 2009).

3.7. NORTH AMERICAN KIMBERLITES

12 kimberlites are studied from Canada in Northern America. Five kimberlites are from Northwest Territories including Somerset island (100 Ma, Smith *et al.*, 1988), Drybones Bay (441 ± 0.8 Ma, Heaman, 2003), Diavik (54.8 ± 0.3 Ma, Graham *et al.*, 1999), Pointe Lake (51.5 ± 1 Ma, Creaser *et al.*, 2004) and Snap Lake (552.9 ± 6.9 Ma, Heaman *et al.*, 2004), the four latest kimberlites are located within Slave craton (Fig. 3.7). One kimberlite from Jackson inlet is located in Rae Craton. Four samples are from Superior Craton including one UML from Torngat (classified by Tappe *et al.*, 2004a) and three kimberlites from Seed, Notre Dâme du Nord (126.6 ± 1 Ma, Heaman *et al.*, 2004) and Bucke Township (115.4 ± 1.5 Ma, Heaman and Kjarsgaard, 2000). One kimberlite from Birch Mountains from Alberta is 77.6 ± 1 Ma (Eccles *et al.*, 2004). 9 kimberlites and 2 lamproites are studied from samples from USA, including Lake Ellen (206 ± 9 Ma, Paces *et al.*, 1990), Alhambra Rock, Norris, Chicken Park (614.5 ± 2.1 Ma, Heaman *et al.*, 2003), Gate-Adah, Kelsey Lake, Laramie Co., Menominee and Sloan #2 (380 Ma, Smith *et al.*, 1979) kimberlites and Kelsey Lake (classified in this work) and Murfreesboro (106 ± 3 Ma, Gogineni *et al.*, 1978, classified by McCandless *et al.*, 1994) lamproites (Fig. 3.7).

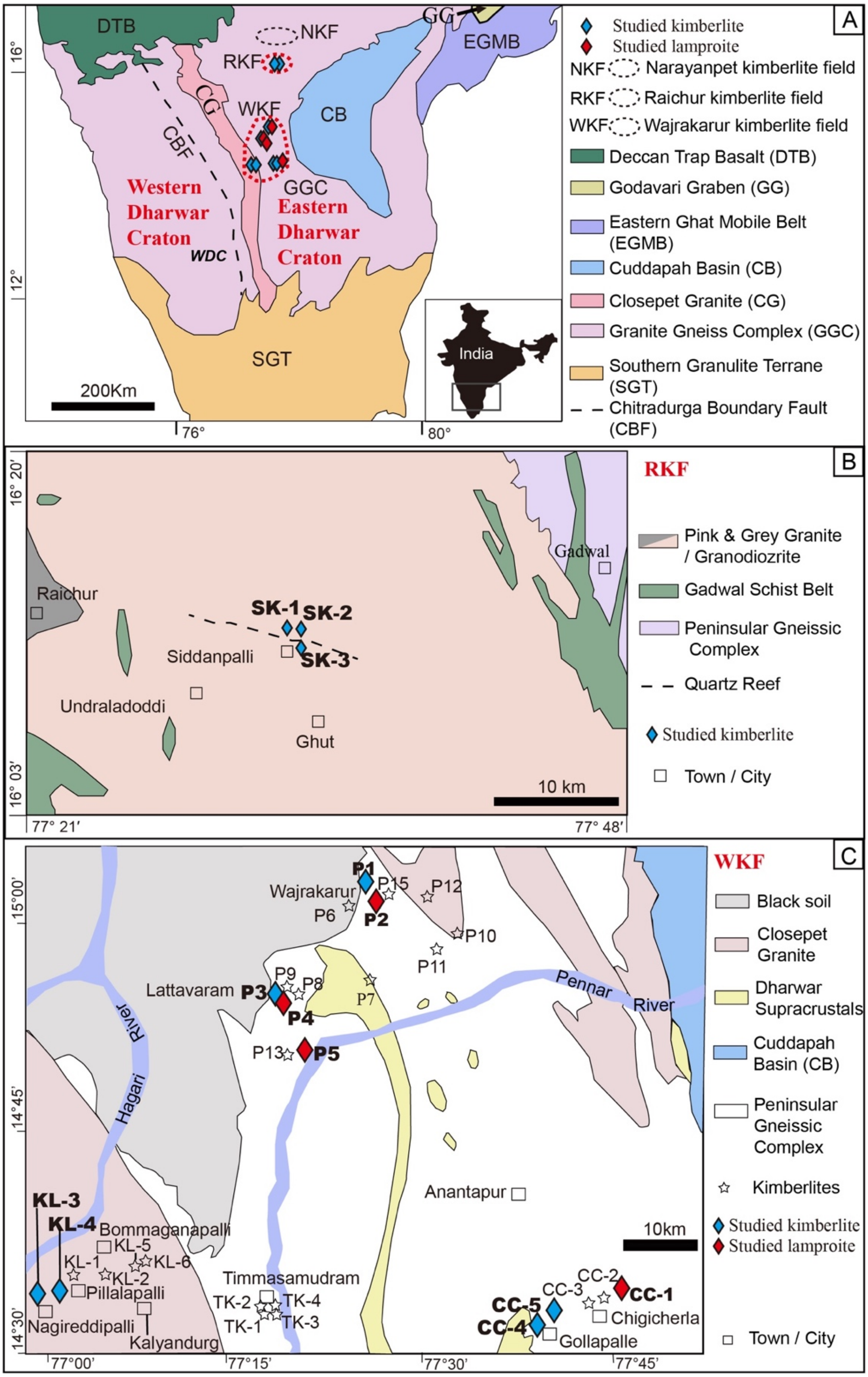

Fig. 3.4. Localization of studied Indian samples. (a) Simplified geological map of Southern India showing locations of Narayanpet kimberlite field (NKF), Raichur kimberlite field (RKF) and Wajrakarur kimberlite field (WKF). Modified after Dongre et al. (2015). (b) Geological setting of the Siddanpalli kimberlites in the RKF, showing the kimberlites studied. Adapted from (Sridhar et al., 2004). (c) Geological setting of the WKF, showing the kimberlites studied, adapted from Nayak and Kudari (1999).

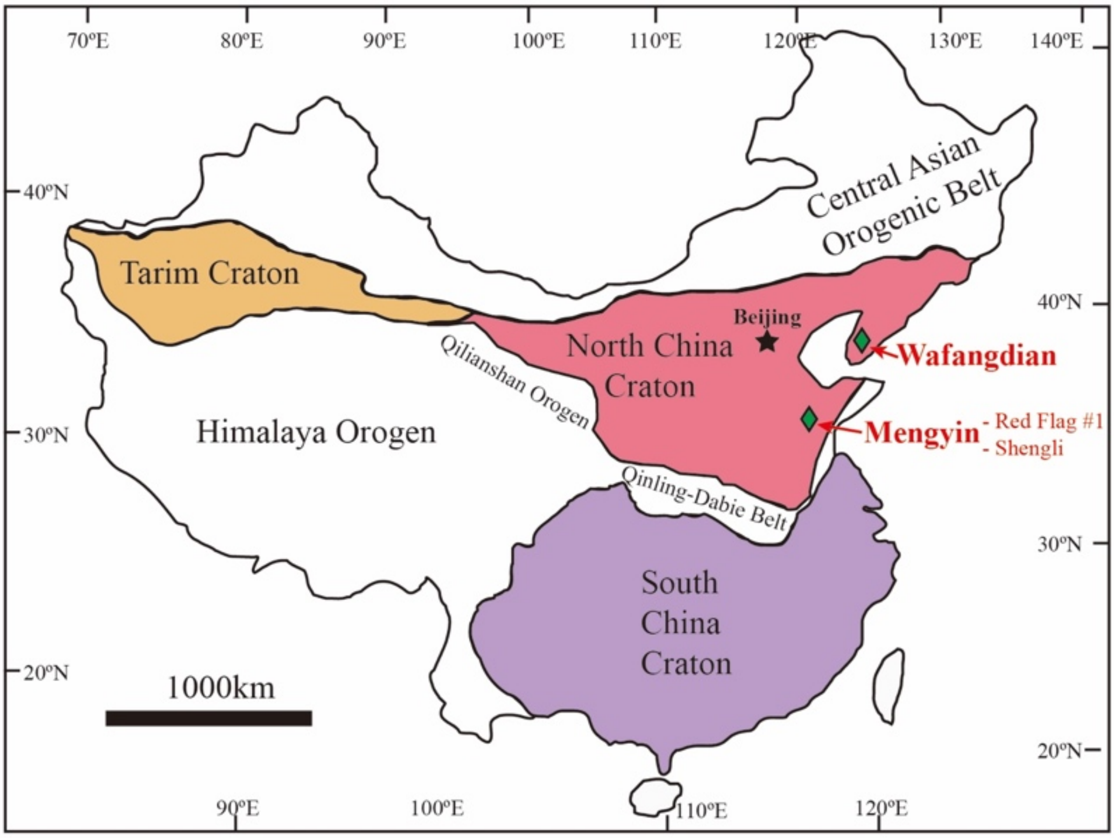

Fig. 3.5. Localization of studied kimberlite from China (adapted from Yang et al., 2009).

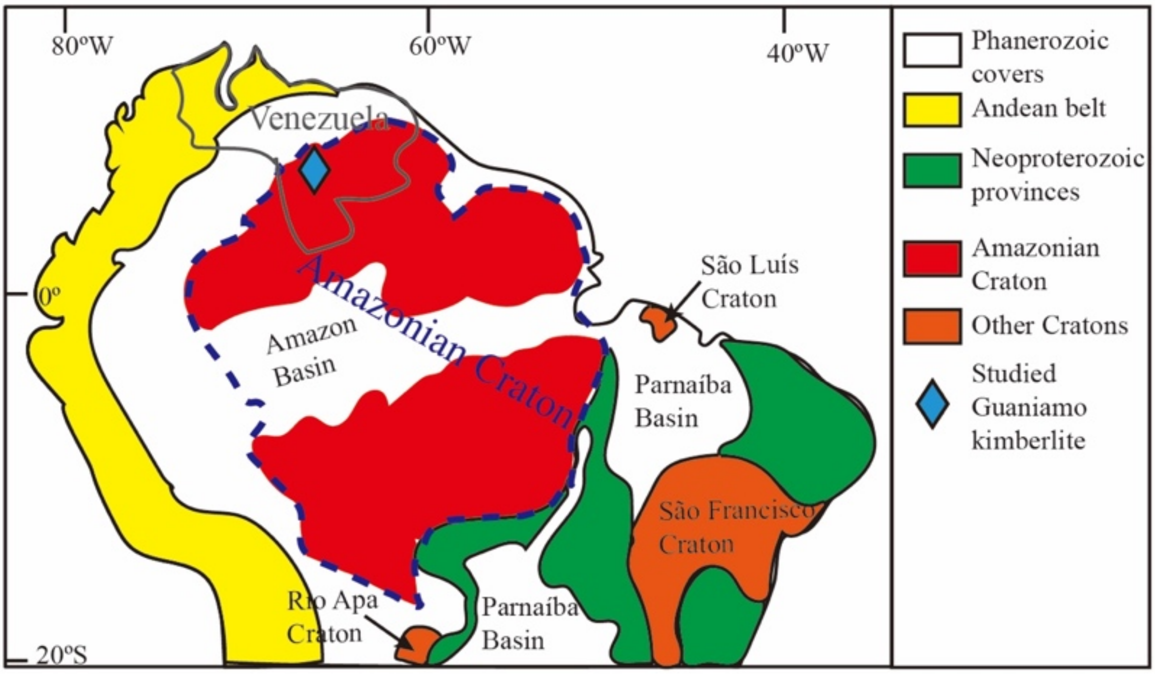

Fig. 3.6. Localization of sample from Venezuela in Amazonian Craton (adapted from Cordani et al., 2009).

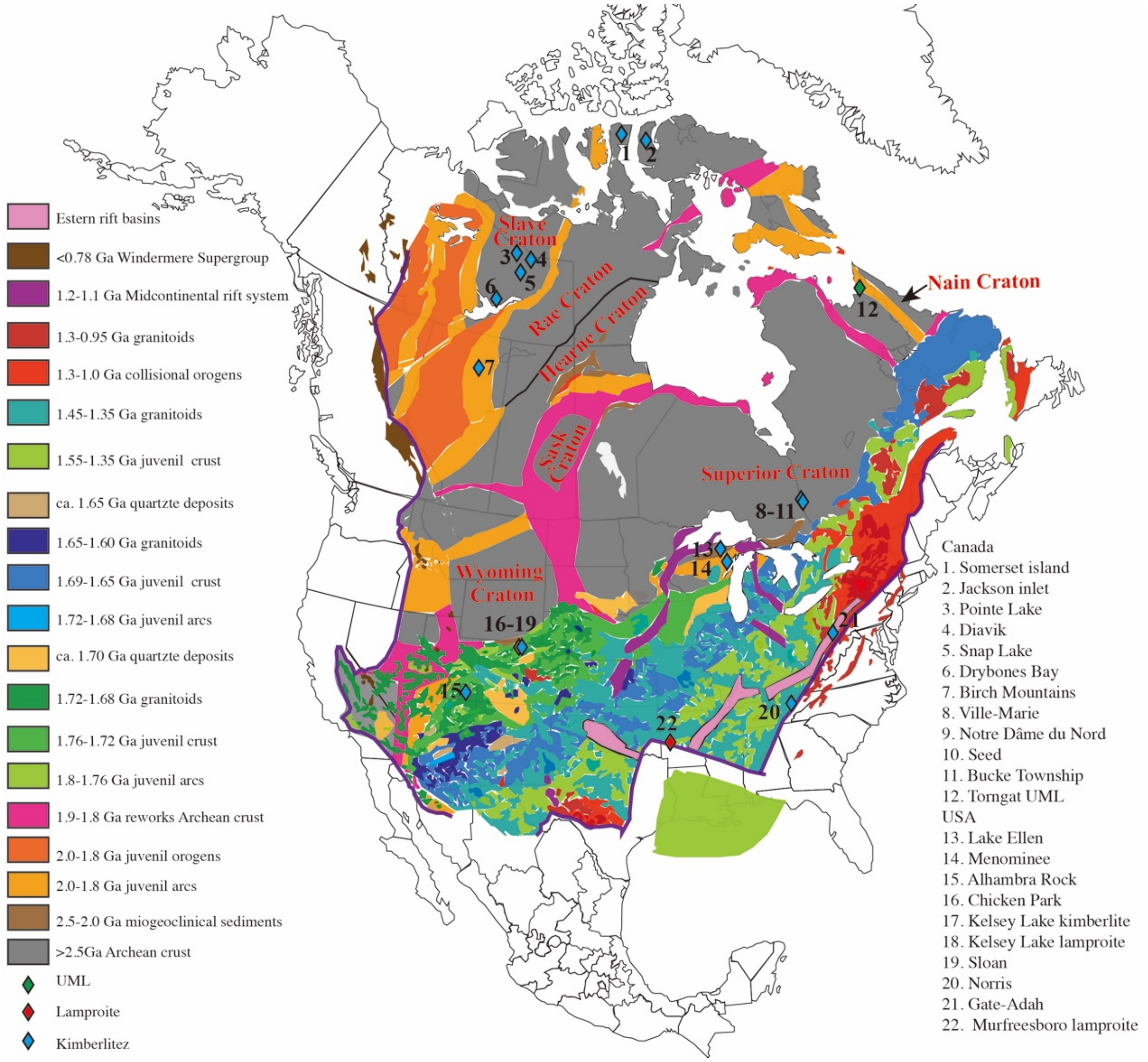

Fig. 3.7. Localization of studied kimberlite and related rocks from North America (adapted from Whitmeyer and Karlstrom, 2007).

CHAPTER 4

METHODOLOGY

4. METHODOLOGY

Samples from 79 kimberlites have been studied. A set of thin (30 μm) and thick (100μm) sections was obtained. This work has been developed following the next methodologies:

a) petrographic study in thin and polished section was carried out by optical microscope for the mineral identification and textural characterization, by using transmitted and reflected light optical mineralogy;

b) mineralogical and textural characterization was complemented by scanning electron microscopy (SEM-EDS), accompanied with the determination of the qualitative or semiquantitative chemical characterization of the composition of the mineral phases;

c) determination of the quantitative composition of the mineral phases and structural formula of the minerals by electronic microprobe (EMPA);

d) identification of selected mineral phases using Raman spectroscopy;

e) in situ trace elements analysis (in perovskite and mathiasite) by Laser Ablation Inductively Coupled Plasma Mass Spectrometry (LA-ICP-MS);

f) in situ U-Pb dating (in perovskite and mathiasite) by LA-ICP-MS.

Thin and thick sections were studied by optical transmitted and reflective light microscope at the Department of Mineralogy, Petrology and Applied Geology, Faculty of Earth Sciences, University of Barcelona.

The analysis of EMPA, SEM-EDS and Raman have been carried out at the Centres Científics i Tecnològics de la Universitat de Barcelona (CCiTUB), Spain.

The analysis of trace elements and U-Pb dating using LA-ICP-MS have been carried out in GEMOC laboratories (Macquarie University, Sydney).

4.1. OPTICAL MICROSCOPY IN TRANSMITTED AND REFLECTED LIGHT

Most of the kimberlites and related rocks have a fine-grained groundmass, made up of complex mineral associations; moreover, in many of the cases the minerals can be partially altered, with staining of secondary minerals, thus making complicate the study with transmitted light. This approach can be more effective with the macrocrysts and the coarsely-grained xenoliths. However, transmitted light is extremely valuable in order to select the most interesting areas for detailed exploring with other methods, in particular, SEM or microRaman.

Reflected light petrography can be very helpful in order to identify many ore minerals, but also helping locate the occurrences in the surface of minerals that should be identified by using other methods, as SEM or microRaman.

4.2. SEM-EDS

Accurate petrographic and textural studies were complemented by using scanning electron microscopy (SEM), the latter employing an E-SEM-Quanta 200 FEI-XTE-325/D8395 (FEI, Hillsboro, USA) scanning electron microscope, equipped with a BSE detector and coupled to a Genesis EDS microanalysis system. The operating conditions were 20–25 kV (in some cases, up to 30 Kev), 1 nA beam current and 10 mm of working distance of the sample to the detector. Exploration of samples and obtaining images were carried out under back-scattered mode (BSE) by using the Z contrast differences between minerals.

4.3. EMPA

The compositional study was carried out using an electron microprobe (EMPA) JEOL JXA-8230 (JEOL, Tokyo, Japan), equipped with five wavelength dispersive spectrometers (WDS) and an energy dispersive spectrometer (EDS), at the CCiTUB. The operating conditions were: accelerating voltage of 20 kV combined with a beam current of 15 nA.

Calibration standards, analytical crystals and analytical lines used for the analyses of olivine, rutile, ilmenite and spinel group minerals were, respectively, the following: wollastonite (Si, TAP, *K*α), corundum (Al, TAP, Kα), chromite (Cr, PETL, *K*α), periclase (Mg, TAPH, *K*α), V (V, LIFH, *K*α), rhodonite (Mn, LIFH, *K*α), Fe_2O_3 (Fe, LIFH, *K*α), Ni (Ni, LIFH, *K*α), sphalerite (Zn, LIFH, *K*α), rutile (Ti, PETJ, *K*α), wollastonite (Ca, PETL, *K*α), Nb (Nb, PETL, *L*α), $ZrSiO_4$ (Zr, PETL, *L*α). The Fe^{3+}/Fe^{2+} relation of ilmenite and spinel group minerals were calculated by charge balance and stoichiometry.

In the case of the analyses of phlogopite, the calibration standards, analytical crystals and analytical lines used were, respectively, the following: wollastonite (Si, TAP, *K*α), corundum (Al, TAP, *K*α), Cr_2O_3 (Cr, PETJ, *K*α), rutile (Ti, PETJ, *K*α), periclase (Mg, TAPH, *K*α), albite (Na, TAPH, *K*α), apatite (F, TAPH, *K*α), barite (Ba, LIFH, *L*α), V (V, LIFH, *K*α), rhodonite (Mn, LIFH, *K*α), Fe_2O_3 (Fe, LIFH, *K*α), Co (Co, LIFH, *K*α), Ni (Ni, LIFH, *K*α), celestine (Sr, PETL, *L*α), ZrSiO4 (Zr, PETL, *L*α), orthoclase (K, PETL, *K*α), wollastonite (Ca, PETL, *K*α).

When analysing perovskite, LIMA and kassite, the calibration standards, analytical crystals and analytical lines used for the analyses were, respectively, the next: wollastonite (Si, TAP, *K*α), corundum (Al, TAP, *K*α), rutile (Ti, PETJ, *K*α), CeO_2 (Ce, PETJ, *L*α), LaB_6 (La, PETJ, *L*α), periclase (Mg, TAPH, *K*α), albite (Na, TAPH, *K*α), Ta (Ta, LIFH, *L*α), Fe_2O_3 (Fe, LIFH, *K*α), rhodonite (Mn, LIFH, *K*α), REE-1 (Pr, LIFH, *L*b), REE-4 (Nd, LIFH, *L*α), barite (Ba, LIFH, *L*α), wollastonite (Ca, PETL, *K*α), orthoclase (K_2O, PETL, *K*α), Nb (Nb, PETL, *L*α), $ZrSiO_4$ (Zr, PETL, *L*α), celestine (Sr, PETL, *L*α).

The working conditions for aeschynite (calibration standards, analytical crystals and analytical lines) were the following, respectively: celestine (Sr, PETJ, *L*α), YAG (Y_2O_3, PETJ, *L*α), ZrO_2 (Zr, PETJ, *L*α), Nb (Nb, PETJ, *L*α), wollastonite (Ca, PETJ, *K*α), UO_2 (U, PETJ, *M*b), ThO_2 (Th, PETJ, Mα), albite (Na, TAPH, *K*α), periclase (Mg, TAPH, *K*α), corundum (Al, TAPH, *K*α), wollastonite (Si, TAPH, *K*α), fluorite (F, TAPH, *K*α), barite (Ba, LIFH, *L*α), rutile (Ti, LIFH, *K*α), LaB_6 (La, LIFH, *L*α), CeO_2 (Ce, LIFH, *L*α), REE-4 (Nd, LIFH, *L*b), Cr_2O_3 (Cr, LIFH, *K*α), REE-1 (Pr, LIFH, *L*b), rhodonite (Mn, LIFH, *K*α), REE-3 (Sm, LIFL, *L*b), Fe_2O_3 (Fe, LIFL, *K*α), REE-3 (Gd, LIFL, *L*b), REE-1 (Er, LIFL, *L*α), REE-1 (Dy, LIFL, *L*b), Hf (Hf, LIFL, *L*α), Ta (Ta, LIFL, *L*α), PbS (Pb, LIFL, *L*α).

The rutine of analysis of Ti-rich garnets (respectively, calibration standards, analytical crystals and analytical lines) were the next: wollastonite (Si, TAP, *K*α), corundum (Al, TAP, *K*α), Cr_2O_3 (Cr, PETJ, *K*α), rutile (Ti, PETJ, *K*α), periclase (Mg, TAPH, *K*α), albite (Na, TAPH, *K*α), barite (Ba, LIFH, *L*α), rhodonite (Mn, LIFH, *K*α), Fe_2O_3 (Fe, LIFH, *K*α), celestine (Sr, PETL, *L*α), $ZrSiO_4$ (Zr, PETL, *L*α), orthoclase (K_2O, PETL, *K*α), wollastonite (Ca, PETL, *K*α).

Finally, calibration standards and analytical crystals used for the analyses of djerfisherite were the next (respectively): wollastonite (Si, TAP, *K*α), corundum (Al, TAP, *K*α), periclase (Mg, TAPH, *K*α), albite (Na, TAPH, *K*α), SRM1158 (Ni, LIFH, *K*α), Co (Co, LIFH, *K*α), SRM1158 (Fe, PETL, *K*α). chalcopyrite (Cu, LIFH, *K*α), FeS_2 (S, PETL, *K*α), PbS (Pb, PETL, *M*α), NaCl (Cl, PETL, *K*α), orthoclase (K, PETL, *K*α), *wollastonite* (Ca, PETL, *K*α).

4.4. RAMAN

Micro Raman analyses were obtained at the CCiTUB by using a HORIBA Jobin Yvon LabRam HR 800 dispersive spectrometer (HORIBA, Kyoto, Japan), equipped with an Olympus BXFM optical microscope. Non-polarized Raman spectra were obtained by applying a 532 nm laser; the pixel size was 1 µm. The exposure time was 5 s with 3 scans and the laser power on the sample was 2.5 mW for anatase; in the case of kassite the exposure time was 5 s with 10 scans and laser power on the sample was 5 mW. Finally, when analysing garnets the exposure time was 20 s with 5 scans and laser power at sample was 1.25 mW.

4.4. IN-SITU TRACE-ELEMENT ANALYSIS BY LA-ICP-MS

Trace elements (Na, Mg, K, Sc, V, Fe, Rb, Sr, Y, Zr, Nb, Ba, REE, Hf, Ta, Th, U and Pb) of perovskite and mathiasite grains were analysed on polished sections of 100 µm thick using a New Wave Research UP-213 laser ablation microsampling system attached to an Agilent 7700cx 300 ICP-MS at the GAU (Macquarie University). NIST 610 glass was used for calibration and each analysis was normalised using the Ca and Ti values determined by electron microprobe for perovskite and mathiasite, respectively. Samples were analysed in runs of 16 analyses comprising 12 analyses of unknowns bracketed by two analyses of the standard at the beginning and end of each run. Moreover, one analysis of the USGS BCR-2 standard was included in each run as a secondary standard to monitor the accuracy of the measurements. The ablation or total counting time for each analysis was 120 s. Typical detection limits range from 5 to 50 ppb for V, Rb, Sr, Y, Zr, Nb, REE, Hf, Ta, Th, U and Pb, up to 100 ppb for Ba and Sc and 100 ppb to 1 ppm for Na and Mg. The relative precision and accuracy for a laser microprobe analysis is 1 - 10%. The spot size is 15 - 40 µm.

4.5. IN SITU U–PB DATING USING LA-ICP-MS

The analyses were carried out using a New Wave Research UP-213 laser ablation microsampling system coupled to an Agilent 7500 ICP-MS system at the GAU (Macquarie University). Measurements of U–Pb were done *in situ* on thick (100 µm) polished sections, using a spot size ranging from 30 to 40 µm. Each analytical run consisted of 8–12 analyses of unknowns, bracketed by two analyses of a primary standard (zircon GJ-1, ~ 609 Ma) at the beginning and the end of each run. Additionally, two near-concordant zircons (91500, ~1065 Ma, (Wiedenbeck *et al.*, 1995); Mud Tank, 732 ± 5 Ma, (Black and Gulson, 1978)) were analysed as secondary standards after the first two GJ-1 analyses in order to assess the accuracy and precision of the method. As already suggested by Storey *et al.*, (2007) for titanite, and demonstrated by Batumike *et al.* (2008) for perovskite, strict matrix matching of the sample and the external standard is not essential for U–Pb dating by LA-ICP-MS. Typical acquisitions consisted of 60 s background measurement followed by 120 s of sample ablation. The ablation was done in He instead of Ar, since it leads to efficient sample transport, signal stability and better reproducibility of U/Pb fractionation. The laser was set to give a 2.5mJ/cm^2 energy, using 5 Hz repetition rate for all the analyses. Avoidance of cracks and inclusions was achieved by selecting the stable parts of the ablation signal, with data collected in time-resolved mode. This also enabled termination of the analysis if the laser drilled into the kimberlite matrix. The U–Pb isotope ratios were obtained from raw signals using the software GLITTER (Griffin *et al.*, 2008). The common-Pb correction was done using a regression technique, as described by (Batumike *et al.*, 2008). The upper intercept of the regression line defined by the raw data on a Tera–Wasserburg plot is taken as the ^{207}Pb/^{206}Pb of the common-Pb component. The lower intercept gives the crystallisation age of the perovskite population, and hence the kimberlite. The slight scatter observed in some of the data may reflect heterogeneity in the composition of the common-Pb component due to intrinsic variations of the Pb composition of the mantle. Pb loss can also occur in highly altered perovskites (Donnelly *et* *al.*, 2012), giving unrealistically young ages. However, as discussed later, these problematic ages can be identified by anchoring the upper intercept to the present-day ^{207}Pb/^{206}Pb terrestrial value. Isoplot 4.0 software (Ludwig, 2003) is used for the U–Pb plots and the regression calculations.

CHAPTER 5

SPINEL GROUP

5. SPINEL GROUP

5.1. INTRODUCCION

Spinel group minerals

Minerals of the spinel supergroup are defined by the last IMA nomenclature (Bosi *et al.*, 2019) as minerals of general formula AB_2X_4 where A and B represents cations (including vacancy) and X anions with a cubic close packing whereas cations in tetrahedral (T) and octahedral (M) sites (Hill *et al.*, 1979; Fig. 5.1). The X anion uses to be O (the oxyspinels), but some minerals have S or Se (respectively, the sulfospinels or thiospinels and the selenospinels; Bosi *et al*,. 2019). However, for the purpose of this kimberlite study, only the oxyspinels are relevant.

In the oxyspinels, whit Z occupied by O^{-2}, there are several possibilities to build mineral structures depending on the cation charge valence: the most common is with A filled by divalent cations and B with trivalent cations (2-3 spinels), but in some cases A can be filled with tetravalent cations and therefore B is occupied with divalent cations (4-2 spinels, Biagioni and Pasero, 2014).

The "2-3 spinels" are grouped as a function of the dominant B^{3+} cation (Al, Cr, Fe, and V), forming four different groups. "4-2 spinels", are rarer than the former group, having Fe^{2+}, Mg^{2+}, and Mn^{2+} as B cation, whereas the A cation uses to be represented by a tetravalent cation (Si, Ti, and Ge). The resulting oxide spinels are indicated in Table 5.1.

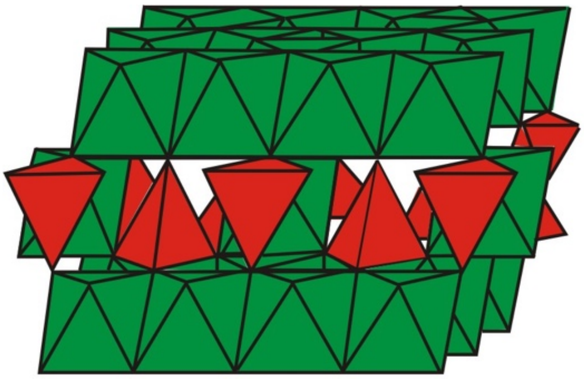

Fig. 5.1. The spinel structure. Note the existence of a sandwiched layer of mixed cations coordinated tetrahedrally (red) or octahedrally (green), between layers of octahedral cations (green).

Table 5.1. Classification of the oxides of the spinel supergroup of minerals (spinel subgroup and ulvöspinel subgroup).

species	structural formula	symmetry	cation in A	cation in B
Spinel subgroup (2-3)				
Spinel	$MgAl_2O_4$	Iso. *m*3*m* (4/*m* 3 2/*m*) : *Fd*3*m*		Al
Hercynite	$Fe^{2+}Al_2O_4$	Iso. *m*3*m* (4/*m* 3 2/*m*) : *Fd*3*m*		
Thermaerogenite	$CuAl_2O_4$	Iso. *m*3*m* (4/*m* 3 2/*m*) : *Fd*3*m*		
Galaxite	$Mn^{2+}Al_2O_4$	Iso. *m*3*m* (4/*m* 3 2/*m*) : *Fd*3*m*		
Gahnite	$ZnAl_2O_4$	Iso. *m*3*m* (4/*m* 3 2/*m*) : *Fd*3*m*		
Dellagiustaite	$V^{2+}Al_2O_4$	Iso. *m*3*m* (4/*m* 3 2/*m*) : *Fd*3*m*		
Deltalumite	$(Al_{0.67}\square_{0.33})Al_2O_4$			
Thermaerogenite	$CuAl_2O_4$			
Magnetite	$Fe^{2+}Fe^{3+}{}_2O_4$	Iso. *m*3*m* (4/*m* 3 2/*m*) : *Fd*3*m*		Fe^{3+}
Magnesioferrite	$MgFe^{3+}{}_2O_4$	Iso. *m*3*m* (4/*m* 3 2/*m*) : *Fd*3*m*		
Maghemite	$(Fe^{3+}{}_{0.67}\square_{0.33})Fe^{3+}{}_2O_4$			
Titanomaghemite	$(Ti^{4+}{}_{0.67}\square_{0.33})Fe^{3+}{}_2O_4$			
Jacobsite	$Mn^{2+}Fe^{3+}{}_2O_4$	Iso. *m*3*m* (4/*m* 3 2/*m*) : *Fd*3*m*		
Franklinite	$Zn^{2+}Fe^{3+}{}_2O_4$	Iso. *m*3*m* (4/*m* 3 2/*m*) : *Fd*3*m*		
Cuprospinel	$Cu^{2+}Fe^{3+}{}_2O_4$	Iso.		
Trevorite	$Ni^{2+}Fe^{3+}{}_2O_4$	Iso. *m*3*m* (4/*m* 3 2/*m*) : *Fd*3*m*		
Chromite	$Fe^{2+}Cr^{3+}{}_2O_4$	Iso. *m*3*m* (4/*m* 3 2/*m*) : *Fd*3*m*		Cr
Magnesiochromite	$MgCr_2O_4$	Iso. *m*3*m* (4/*m* 3 2/*m*) : *Fd*3*m*		
Zincochromite	$ZnCr_2O_4$	Iso		
Manganochromite	$Mn^{2+}Cr_2O_4$			
Cochromite	$(Co,Ni,Fe)(Cr,Al)_2O_4$			
Coulsonite	$Fe^{2+}V^{3+}{}_2O_4$			V^{3+}
Magnesiocoulsonite	MgV_2O_4	Iso.		
Vuorelainenite	$Mn^{2+}V^{3+}{}_2O_4$			
Guite	$Co^{2+}Co^{3+}{}_2O_4$			Co^{3+}
Hausmannite	$Mn^{2+}Mn^{3+}{}_2O_4$			Mn^{3+}
Hetaerolite	$Zn^{2+}Mn^{3+}{}_2O_4$			
Ulvöspinel subgroup (4-2)				
Ulvöspinel	$Ti^{4+}Fe^{2+}{}_2O_4$		Ti	
Qandilite	$Ti^{4+}Mg^{2+}{}_2O_4$			
Brunogeierite	$Ge^{4+}Fe^{2+}{}_2O_4$		Ge	
Ringwoodite	$Si^{4+}Mg^{2+}{}_2O_4$		Si	
Ahrensite	$Si^{4+}Fe^{2+}{}_2O_4$			
Filipstadite	$(Fe^{3+}{}_{0.5}Sb_{0.5})Mn^{2+}{}_2O_4$		Sb	
Tegengrenite	$(Mn^{3+}{}_{0.5}Sb_{0.5})Mg^{2+}{}_2O_4$			

Spinels in kimberlites

Despite spinels can be formed in many geological environments, they are a common constituent of kimberlites and related rocks (i.e., Griffin *et al.*, 1994; Mitchell, 1995, 1997). Spinels are a relatively stable oxidised mineral, and therefore they are relatively resistant compared with most of other kimberlite components, during many subsolidus processes experimented by the kimberlite.

Processes including hydrothermalism and weathering; in addition, their high hardness allows them to be preserved after erosion and transport. Moreover, they can be accumulated as a placer mineral because of the high density. These facts determined the spinels to be in the focus of many research to evaluate its role as indicator mineral of kimberlites.

Spinel group minerals in kimberlites have very complex compositions because there are almost continuous solid solutions between the most of the abovementioned endmembers, thus making complicate the representation of these compositions in the classical spinel diagrams. Moreover, the composition in a zoned crystal commonly varies continually between different endmembers, sometimes following one or more different trends. This is why different authors suggested the use of a specific nomenclature for these spinels, although this can be partly contradictory with the IMA rules. However, in order to make easy the comparison of the spinels from this study with those from the exiting literature (i.e., Mitchell, 1986, 1995; Roeder and Schulze, 2008), the following names and abbreviations are used in this work for the studied cases of spinel group minerals:

Spinel: this term is used to refer to all spinel group minerals.

Chromite: this term is used when Cr predominates in the octahedral position (Cr series predominates among Al, Ti, magnetite and Cr series), including MCC and AMC.

MCC: chromite including magnesiochromite and chromite, Al<0.4 apfu (atoms per formula unit).

AMC: aluminous magnesian chromites. Chromite which has higher Al content than MCC (chromite with Al >0.4 apfu).

MUM spinels: the ensemble of magnesian ulvöspinel-ulvöspinel-magnetite, as MUM described by (Mitchell, 1986) and similar to Mum for magnesio-ulvöspinel-magnetite described by (Roeder and Schulze, 2008). MUM innclude UM and Qan.

Qan: qandilite, spinel in which Ti serie predominates and the qandilite component predominates.

UM: magnesian ulvöspinel-ulvöspinel-magnetite excluding those classified as qandilite.

Sp: spinel *sensu strictu* (*s.s.*) in which $MgAl_2O_4$ predominates. Al serie predominantes and >80%. It is similar to the old term "pleonaste" as described by (Mitchell, 1986, 1995; Roeder and Schulze, 2008). Spinel *s.s.* replace pleonaste in this work because pleonaste is a variety of spinel *s.s.* following the IMA rules.

UMS: ulvöspinel-magnetite bearing spinel, Al predominates in the octahedral position but Al series <80%

Mag: magnetite.

5.2. SPINEL PARAGENESES

Two main textural types of spinels are classically differentiated in kimberlites and related rocks: a) primary, as fine-grained crystals scattered in the groundmass and supposed to have crystallized from the kimberlite magma (i.e., Roeder and Schulze, 2008), and b) as a coarser macrocrysts derived from mantle xenoliths (Haggerty, 1975a). For the purpose of accurate description and discrimination, we have grouped the spinel group minerals found in the studied kimberlites in the following textural positions:

1) spinel as a component of xenolith
2) Spinel xenocrysts
3) Primary magmatic spinels in kimberlite groundmass or mantling/replacing other oxides
4) Spinels formed during late-stage hydrothermal processes and post-magmatic alteration
5) Spinel/ilmenite exsolutions
6) Spinel in reaction rim replacing garnet xenocrysts

In any case, the most suitable spinels to get direct information on the kimberlite magma are the primary magmatic spinels from groundmass, and therefore only these spinels will be described in detail in this study (section 5.3), although we will provide some general data from the rest.

5.2.1 Spinel as a component of xenoliths

Spinel is found in xenoliths which have been sampled by kimberlite magma during its ascent from the kimberlite source in the lower mantle, across the asthenosphere and the lithosphere (Haggerty, 1975a). This means that spinel-bearing xenoliths could have a provenance within the spinel domain, and therefore they will be normally xenoliths from upper mantle and crustal sources. For instance, chromite may be found in peridotitic xenoliths or in glimmerites, magnetite in granitic xenoliths, ulvöspinel-magnetite in basaltic xenoliths of country rock, etc. These spinels can provide valuable information about the conditions of formation of the hosting rock, and can be considered as a suitable tool to measure the vertical distribution of rock types in the lithospheric mantle sampled by the intrusion of kimberlites or other related rocks (i.e., O’Reilly and Griffin, 2006; Malkovets *et al.*, 2007). In addition, they can assess the nature of the metasomatic processes affecting the sampled mantle before these intrusions (Haggerty, 1995). Finally, the study of the trace element composition (in terms of elements as Zn, Ga, Ni) of the mantle spinel coexisting with garnet, olivine and pyroxene has been proposed as a criteria for diamond exploration (Griffin *et al.*, 1994; Kaminsky *et al.*, 2010).

However, the contribution of xenolithic spinel to the kimberlite formation is lesser and therefore they are not included in the present study, although they are many results in our database (see appendix). Their composition is normally far of the composition of the spinels from the groundmass. In most of the peridotite xenolith cases, this spinel corresponds to Ti-poor chromite, and is not zoned and occurs as rounded grains with equilibria textures with the host rocks. Crustal rocks use to have magnetite.

5.2.2. Spinel xenocrysts

Spinel xenocrysts are found either as anhedral macrocrysts to microcrysts, rounded or angulate discrete crystals. Its composition are very variable depending on its source rock. In many cases, it is possible to correlate their compositions with those of the accompanying xenoliths. Spinel xenocrysts are in disequilibria with the kimberlite magma and therefore they are replaced by a thin reaction rim of chromite and/or ilmenite. However, they do not have zoning internally. Use of spinel xenocrysts in kimberlite petrogenesis and diamond exploration can have the same considerations as those indicated for the mantle xenoliths in the above section.

5.2.3. Late hydrothermal spinels

Pure magnetite occur as a replacement product of all of the textural types (xenocrysts, phenocrysts, xenoliths, groundmass) of the ferromagnesian minerals, as olivine and humite groups, but also pyroxenes. Normally magnetite occurs in this type of association as fine-grained single crystals or aggregates filling veins in the replaced mineral or replacing completely the ensemble of it. Magnetite is found in this paragenesis in close association with serpentine-group minerals, calcite and other hydrous minerals. Therefore, this magnetite and the accompanying minerals are considered as a product of late-stage hydrothermal processes and post-magmatic alteration, and therefore they do not provide information about the crystallization during the magmatic stages and cannot supply information about the diamond mineralization.

5.2.4. Spinel exsolutions in ilmenite

Exsolution textures of ilmenite and spinels have also been found in the studied rocks. However, due to the extremely thin width exsolution of the spinels, the components cannot be analysed by EMPA in order to obtain the corresponding accurate chemical compositions. Moreover, ilmenite-spinel exsolution-like textures have been found in many samples, but most of them are not clearly an exsolution and could be explained by replacement of Fe^{3+}-rich ilmenite by secondary spinel along the ilmenite cleavage.

5.2.5. Reaction rims on garnet

Garnet xenocrysts, such as pyrope, may be found replaced by a reaction rim composed by spinels, many times together with phlogopite. These spinels use to have a MUM composition, being similar to that of the groundmass spinel, but sometimes have higher Al content. The compositions of these spinels and that of phlogopite are influenced by the composition of the replaced garnet xenocryst. For instance, AMC is found in a reaction rim replacing Cr very rich pyrope (up to 12.4 wt% Cr_2O_3) in the Snap Lake kimberlite. These spinels are explained as a result of decompression reactions involving the garnet during their ascent from the mantle within the kimberlite melt (i.e., Armstrong, 1995).

5.3. TEXTURAL PATTENS OF PRIMARY SPINELS

We will describe in this section only the spinels that provide textural evidences of being a result of magmatic crystallization, thus excluding many of the textural types described in the section 5.2. The composition of primary spinel has been proposed as a source of petrogenetic information, in particular on the magma genesis (Schulze, 2001; Roeder and Schulze, 2008). Primary spinels occur in kimberlites in the following textural positions:

A)Groundmass euhedral crystals.
B)Inclusions in olivine phenocrysts.
C)In veinlets crosscuting xenocrysts.
D)Rims that mantle or replace other pre-existing oxides (eg. ilmenite, chromite, magnetite

xenocrysts).

E) Inclusions in groundmass phlogopite.

F) Spinel-phlogopite clasts (globular bodies).

5.3.1. Groundmass euhedral spinel crystals

Groundmass spinels are one of the principal groundmass components in nearly all kimberlites, although their modal content in the groundmass (<1-15%) is extremely variable in different kimberlite. They often occur as ultra-fine-grained (<0.1mm, size classification of (Scott Smith *et al.*, 2018)), euhedral to subhedral crystals (Fig. 5.2a). Many of them are zoned, showing a core of chromite mantled by magnesian ulvöspinel-ulvöspinel-magnetite (Fig. 5.2a). They use to be mantled by other minerals, thus indicating an early crystallization during the kimberlite sequence.

Atoll spinels (Mitchell, 1986) represent a textural variety of these discrete crystals in the groundmass. They are found in a large number of kimberlites. The crystal sections resemble an atoll island, with a central island (spinel) surrounded by a barrier of reef (spinel). The core and the outermost rim is separated by a gap (the so-called “lagoon” by (Roeder and Schulze, 2008)) which is commonly filled by fine-grained minerals as serpentine and calcite, sometimes with magnetite, Ti-rich hydrogarnets and chlorite (Fig. 5.2b-d). For a long time these spinels as an ensemble have been considered as primary, and its formation should be produced in four steps (Armstrong *et al.*, 1997):

a) Early euhedral spinels were formed in the melt;
b) As a result of a supersonic ascent of the melt an its rapid emplacement into the upper crust, a large grade of overcooling took place and the spinel continued growing as a skeletal crystal over the above crystal substract;
c) A cruciform pattern can be seen in the places of directional growth of the {111} planes;
d) The interstitial melt crystallises;
e) Late hydrothermal alteration produces the replacement of the “lagoon” minerals by secondary minerals, and may produce minor dissolution of the spinels.

5.3.2. Spinels as inclusions in olivine microphenocrysts

In some kimberlites, spinels may also be found as euhedral inclusion in fresh olivine microphenocrysts that outstand in the groundmass. In case of these olivine crystals have a clear compositional zoning, the spinel crystals are found in the internal zone or rims. Therefore, the spinels growth simultaneously with the olivine crystals and therefore they can be considered as primary magmatic (Fig. 5.2e). In the majority cases they are chromite which has similar composition as core of groundmass spinel.

In the case of inclusions in olivine which is altered to serpentine or chlorite, chromite is considered as primary inclusion when its composition is similar to some groundmass spinel (Fig. 5.2f).

5.3.3. Spinels in veinlets crosscutting xenocrysts

Spinels may also occur in thin veinlets which crosscut xenocrysts, such as olivine and ilmenite, accompanied by phlogopite and other groundmass minerals (Fig. 5.3a). Both phlogopite and spinels have the same composition than the corresponding groundmass minerals, and therefore we have segguest this association in veinlets as the result of percolation of kimberlite magma throughout small cracks in the host minerals.

5.3.4. Spinels mantling oxides

Spinels also commonly occur as a thin reaction rim mantling or replacing other pre-existing xenocrysts of oxide minerals (Fig. 5.3b-c), such as chromite, ulvöspinel, magnetite (Fig. 5.3e-f), ilmenite (Fig. 5.3b), rutile and crichtonite group minerals. These spinel crystals use to develop cockade textures on the replaced mineral. In many of these associations these spinels occur intimately intergrown with perovskite (Fig. 5.3c-d).

5.3.5. Spinels as inclusions in phlogopite microphenocrysts

Euhedral spinel crystals are also found as inclusions in phlogopite microphenocrysts (Fig. 5.4a-b). These spinels can be concentrated following growth zones of the mica zoning. These included spinels have identical compositions to those of groundmass spinel, and therefore this texture is interpreted as groundmass spinel trapped by the growth of post crystallizing phlogopite.

5.3.6. Spinels in spinel-phlogopite globular bodies

Some kimberlites have this type of texture, but it is rare. These use to be rounded bodies, with a distinct texture from the rest of the groundmass (Field and Scott Smith, 1998). They can have fine-grained spinel grouped in dense “clouds” embedded in phlogopite. These bodies are called as “spinel-phlogopite clast” or “magmaclast” in some works (Xu *et al.*, 2018b). These bodies can be minority, as in Udachnaya in Russia (Kopylova *et al.*, 2016) but in some cases they may achieve up to 40 volume % of the rock, as in the Anuri kimberlite in Nunavut (Canada; Masun *et al.*, 2004), but use to be fine-grained (less than 1 cm in diameter, in general. These authors interpret the texture as pyroclastic juvenile lapilli. Unfortunately, there is no a systematic study of differences in compositions between these bodies and the rest of the groundmass in the abovementioned kimberlites, although some authors indicate the occurrence of different trends of the spinels in these bodies when compared with the rest of the kimberlite (i.e., Masun *et al.*, 2004).

These bodies are found in two kimberlites in this work, in Banankoro and Benfontein. The origin of these bodies is uncertain, but they are primary. Spinels found in spinel-phlogopite spherical bodies have finer grain size than those of the surrounding groundmass (mostly ≤ 1µm, Fig. 5.4c-d). Spinels in these globular bodies are often euhedral and we have interpreted them as precipitated from a magma which must be different to that was crystallizing the kimberlite groundmass. Hence, these textures suggest the existence of magma mixing and therefore the spinels from both occurrences (groundmass and globular) were analysed separately.

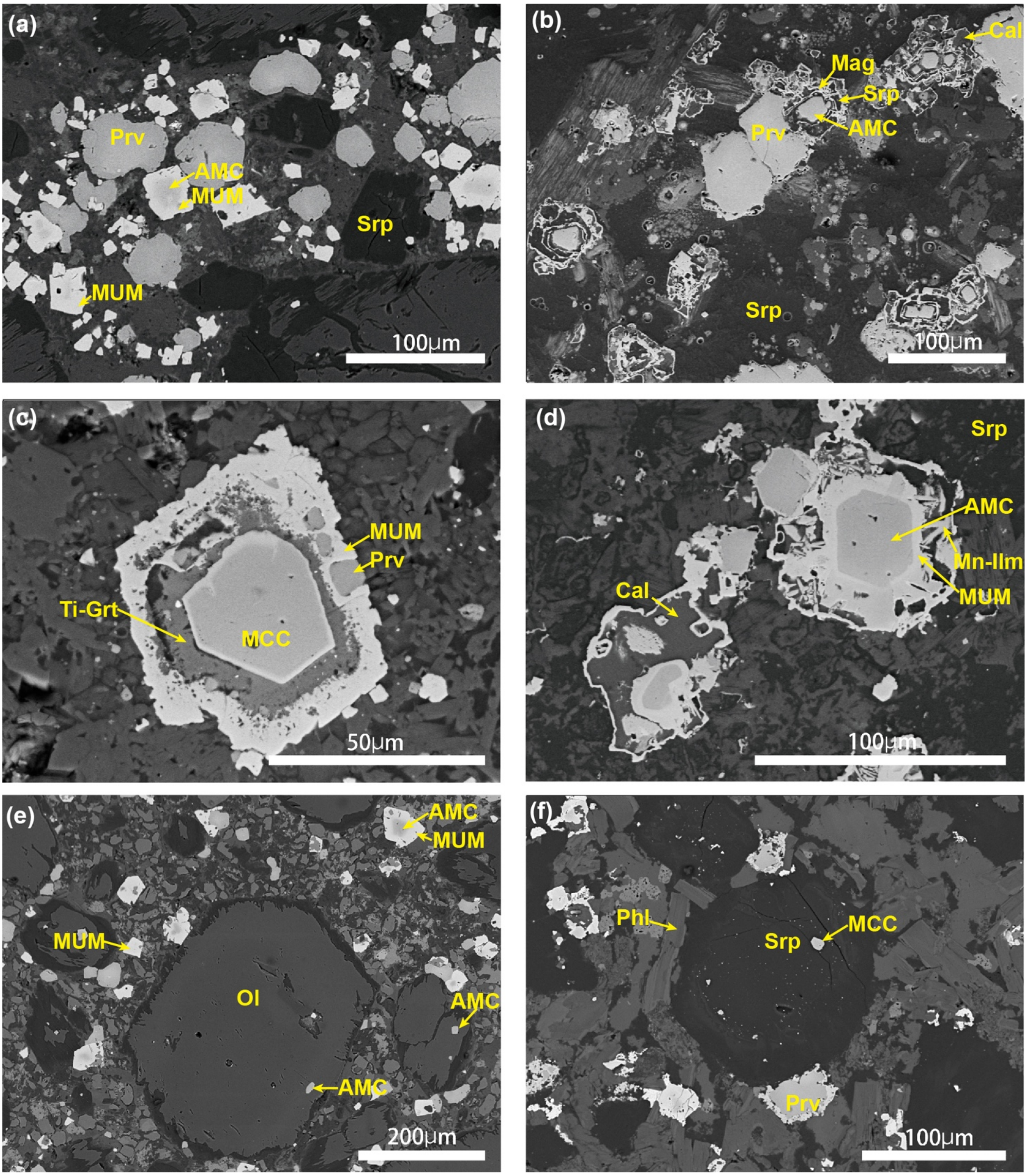

Fig. 5.2. Back-scattered electron (BSE) imagings of primary spinels. (a) Groundmass perovskite (Prv) and spinels with AMC core and MUM rim, in AK6 Karowe kimberlite. (b) Groundmass atoll spinel with AMC core and outmost rim of Mag, "lagoon" is filled with serpentine (Srp) and calcite (Cal), Laramie kimberlite. (c) Groundmass atoll spinel with core of MCC and rim of MUM, "lagoon" infilled by Ti.-rich hydrogarnet (Ti-Grt), CC-1 Chigicherla lamproite. (d) Groundmass atoll spinel with core of AMC and rim of MUM, "lagoon" infilled by serpentine, calcite and Mn-rich ilmenite (Mn-Ilm), CC-5 Chigicherla kimberlite. e) Groundmass atoll spinel with core of AMC and rim of MUM, AMC also found as inclusion in fresh olivine (Ol), P200 Lesotho kimberlite. (f) MCC found as inclusion in altered olivine, Banankoro kimberlite.

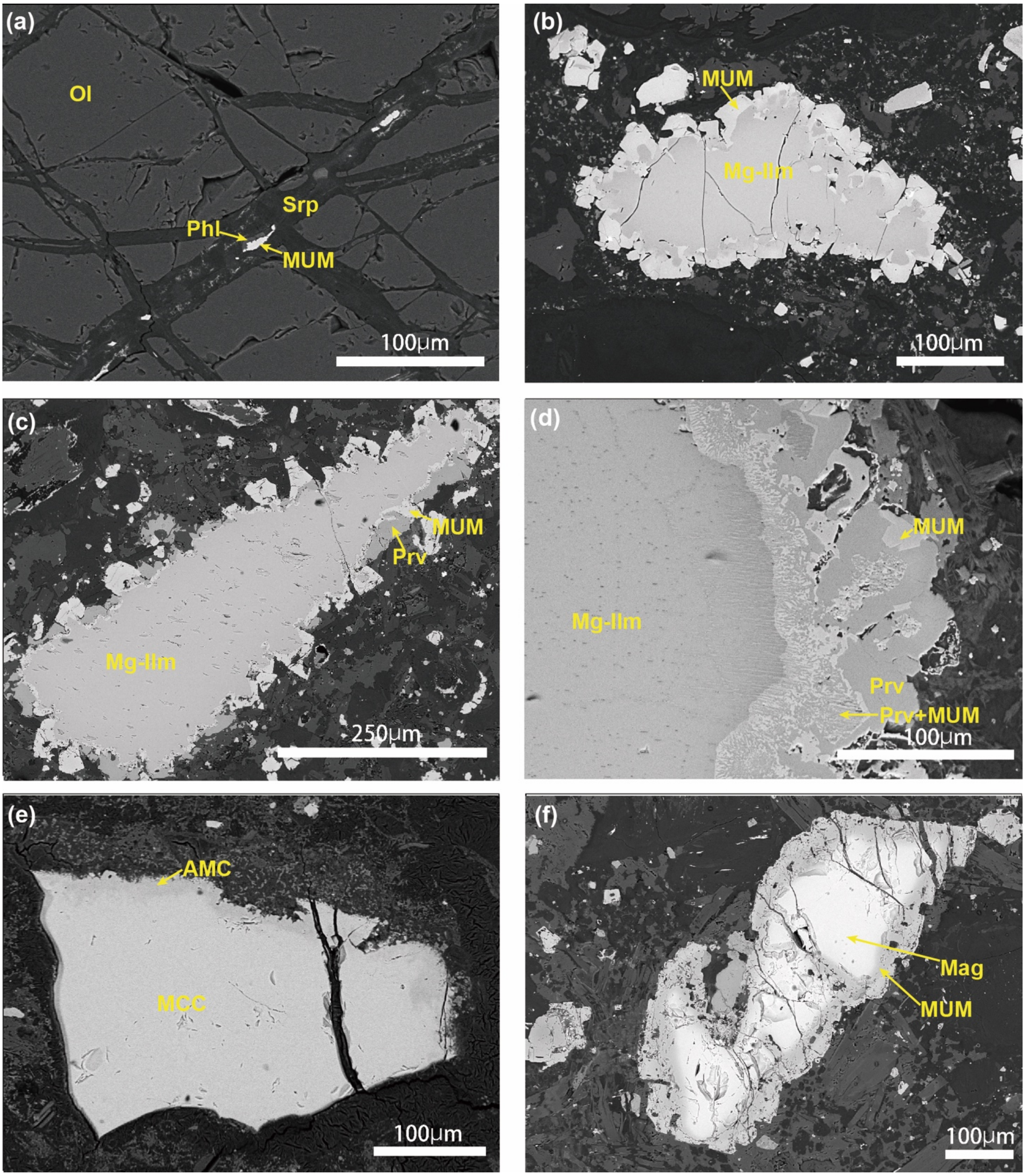

Fig. 5.3. Back-scattered electron (BSE) imagings of primary spinels. (a) MUM spinels in vein which crosscut olivine xenocryst together with phlogopite (Phl), DK1 Letlhakane kimberlite. (b) MUM spinels as rim mantle or replace Mg-rich ilmenite (Mg-Ilm) xenocryst, BK9 Damtshaa volcaniclastic kimberlite. (c) MUM spinels together with perovskite as rim mantle or replace Mg-rich ilmenite xenocryst, Kaalvallei lamproite. (d) Mg-rich ilmenite xenocryst is replaced by intergrowth of perovskite and MUM spinels (Prv+MUM), perovskite and MUM spinels, Monastery kimberlite. (e) MCC chromite xenocryst replaced by a reaction rim of AMC, AK1 Orapa volcaniclastic kimberlite. (f) Magnetite xenocryst replaced by rim of MUM spinels.

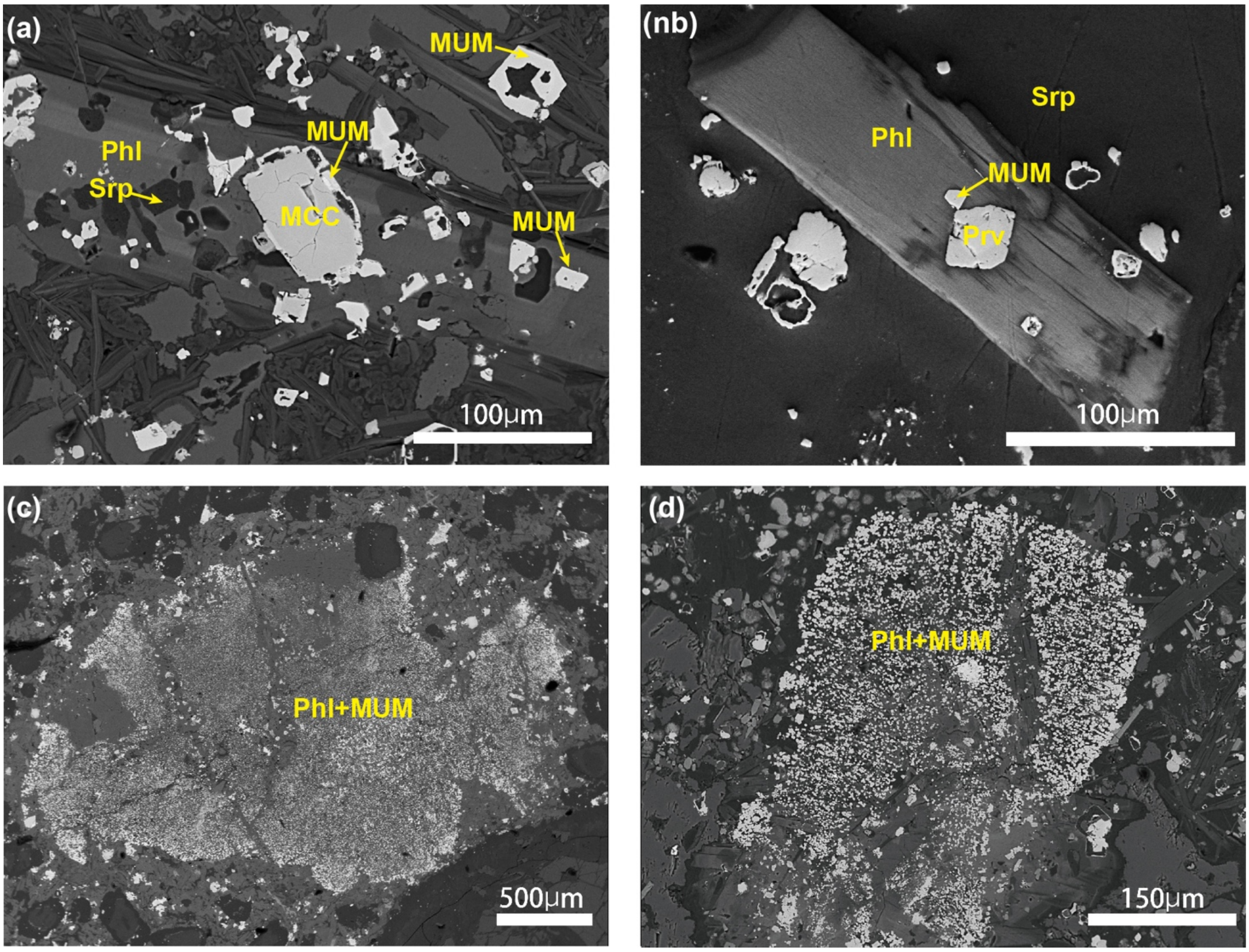

Fig. 5.4. Back-scattered electron (BSE) imagings of primary spinels. (a) Spinel (MCC core and MUM rim) included in groundmass phlogopite, Gate-Adah kimberlite. (b) MUM together with perovskite (Prv) included in groundmass phlogopite, Shengli kimberlite. (c) Spinel-phlogopite globular body (MUM+Phl), Banankoro kimberlite. (d) Spinel-phlogopite “globular body”, Bultfontein kimberlite.

5.4. CHEMICAL COMPOSITION OF PRIMARY SPINELS

Most kimberlite spinels have compositions within the eight-component system $MgCr_2O_4$ (magnesiochromite) - $FeCr_2O_4$ (chromite) - $MgAl_2O_4$ (spinel) - $FeAlO_4$ (hercynite) - Mg_2TiO_4 (magnesian ulvöspinel) - Fe_2TiO_4 (ulvöspinel) - $MgFe_2O_4$ (magnesioferrite) - Fe_3O_4 (magnetite). In spite the fact that the Mn_2TiO_4 (manganoan ulvöspinel) or $MnFeO_4$ (jacobsite) end members contents are usually insignificant, the composition between so many end members make it difficult to present the spinel composition in graphics. As indicated by Pasteris (1982), the use of classical binary spinel diagrams based on ratios of #Cr or #Fe are misleading because they neglect some of the main components in the spinel kimberlites, as Ti. Moreover, in the Ti spinels, the Fe^{2+}+Mg cannot be assumed as 1, but it should be equal to 1+Ti, thus introducing problems in the spinel end member calculations. Therefore, we are using different binary diagrams used by different authors, just trying to compare our results with those from the existing literature.

A classic method is the projection into two six-component spinel prisms, the reduced and the oxidized prisms (Irvine, 1965; Haggerty, 1975a; Mitchell, 1986). However, “reduced” spinel prism fails to illustrate the Fe_3O_4 and the $MgFe_2O_4$ component, while “oxidized” spine prism fails to represent the Mg_2TiO_4 and the Fe_2TiO_4 content. Moreover, the visualization and projection of large numbers of analyses is not easy within the 3D prisms (Roeder and Schulze, 2008). More commonly used projections include binary $Fe^{2+}_T/(Fe^{2+}_T+Mg)$ vs. Ti/(Ti+Cr+Al) (Mitchell, 1986), $Fe^{2+}/(Fe^{2+}+Mg)$ vs. Cr/(Cr+Al) and $Fe^{2+}/(Fe^{2+}+Mg)$ vs. $Fe^{3+}/(Fe^{3+}+Cr+Al)$ (Roeder and Schulze, 2008) diagrams and the ternary Al-Cr-Fe^{3+} program (Roeder and Schulze, 2008) which have used in this work to show primary spinel composition (Fig. 5.5). Different spinel compositional fields and evolutional trends have been determined for spinel from kimberlites in these diagrams (Mitchell, 1986; Roeder and Schulze, 2008).

The following compositional types are discriminated in the selected kimberlites: AMC, MCC, UM, Mag, Qan, Sp, UMS (Fig. 5.5). These compositional types have already been defined in the introductory part of this section 5.1. The distribution of AMC, MCC, MUM and Sp in the studied kimberlites is presented in Table 5.2. Representative primary spinel compositions given in Table 5.3, and end members are calculated between six component $MgAl_2O_4$ - Mg_2TiO_4 - $MnCr_2O_4$ - $MgCr_2O_4$ - $FeCr_2O_4$ - Fe_3O_4 because it is the most classically used in a large number of publications in the past and therefore use of this graphic makes easy for the comparison with the results from other authors.

5.4.1. Composition of groundmass euhedral spinel crystals

The groundmass euhedral crystals commonly have a chromite core (AMC and/or MCC, Table 5.2). Chromite is mantled by a MUM spinels rim (Table 5.2). However, in some of the studied samples, the chromite core is lacking, and groundmass spinel is only composed by MUM spinels (Table 5.2). For instance, this happens in coherent samples from Cacuilo, KL-4, south pipe from AK-6 Karowe, Helam, Kaalvallei, Menominee, CC-1 Chigicherla, KL-4 Kalyandurg and SK-2 Siddanpalli.

In other cases, MUM spinel rim is absent (Table 5.2) and groundmass spinel is only represented by chromite. For instance, in coherent samples from P-1 Wajrakarur, Wafangdian, Sloan and Roberts Victor.

In some rare cases, only two among the 79 studied samples (at Menominee and Lake Ellen), the qandilite component (extremely Mg-rich) is dominant.

Finally, in a unique case at Menominee, an Al- and Mg-rich spinel (spinel s.s., Sp) is found in groundmass assemblage (Table 5.1.3).

5.4.2. Composition of spinel inclusions in olivine microphenocrysts

Euhedral spinels inclusions in olivine microphenocrysts (Fig. 5.2e-f) are commonly chromite (both MCC or AMC). They have similar compositions to those found in spinels that occur at the core of groundmass spinel crystals (Table 5.3), and could indicate a simultaneous crystallization of the olivine (generally, the olivine rims) and the early generations of spinels.

5.4.3. Spinels in veinlets crosscutting xenocrysts

Spinels found in groundmass veinlets cutting xenocrysts are typically MUM-type spinels, and their compositions are similar to those found in the rims of the groundmass spinels. Hence, these spinels can be studied with the same generation as the rest of the groundmass. Contamination with the host minerals of the veins seems to be not significative.

5.4.4. Composition of spinel mantling other oxide macrocrysts

Spinels mantling or replacing other oxides are also MUM-type spinels. They have similar composition to that found in the rim of groundmass spinel, but can be enriched in some of the components of the replaced mineral. As the Mg enrichment in case of replacing geikielite.

5.4.5. Composition of spinel in inclusions in phlogopite

The studied euhedral to subhedral spinel inclusions in phlogopite microphenocrysts have similar composition to that of the groundmass spinel. Sometimes they are zoned with a chromite core and MUM rim, but in other cases they are only composed by MUM spinels.

5.4.6. Composition of spinel in spinel-phlogopite globular bodies

Spinels found in spinel-phlogopite globular bodies commonly have compositions similar to those of the groundmass spinels. For instance, those found in Banankoro have a composition intermediate between that of chromite core and that of MUM rim.

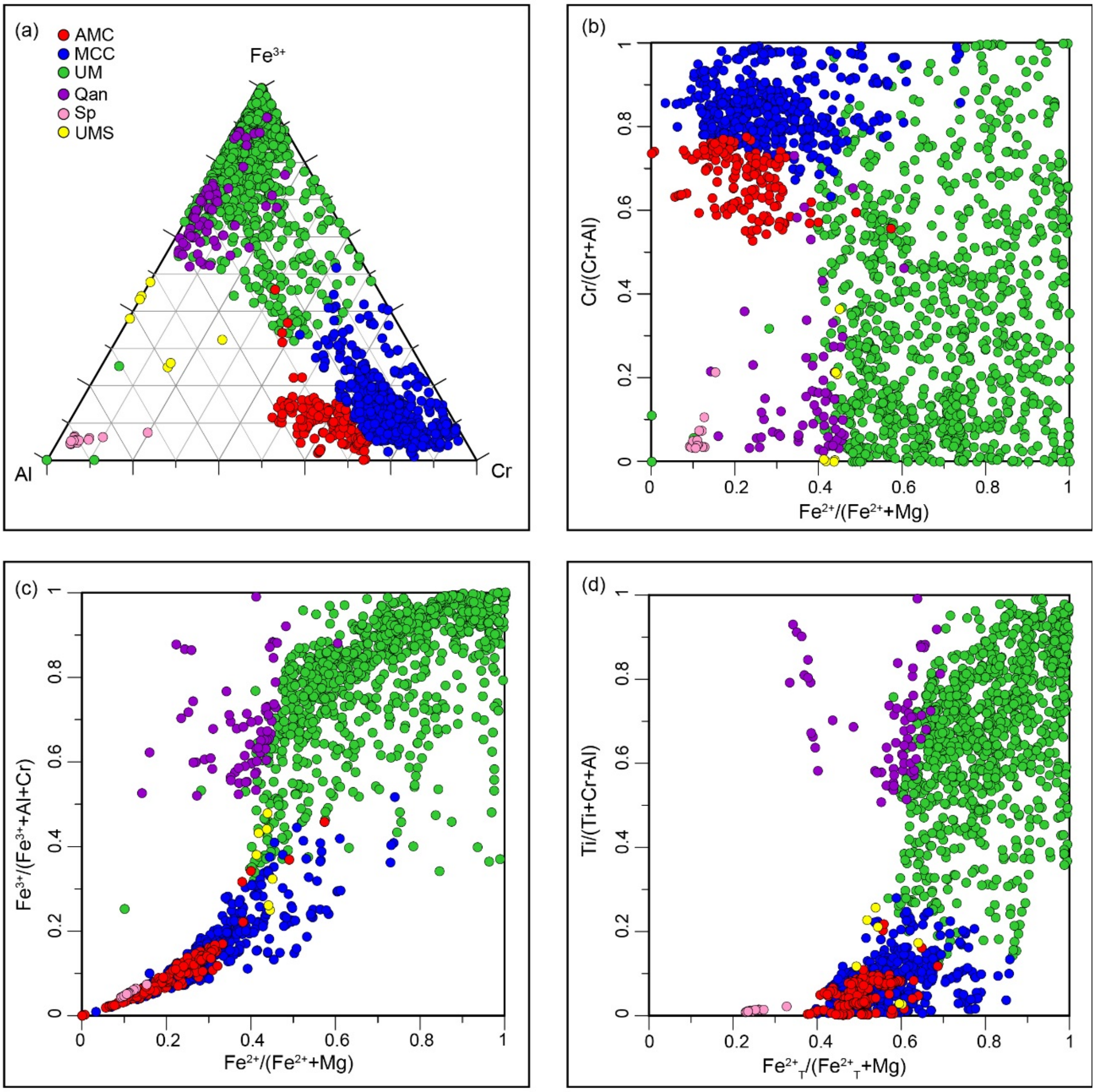

Fig. 5.5. Plot of the chemical compositions of all the primary spinel crystals of the studied spinel-bearing kimberlites and related rocks analysed in the present study. Compositional diagrams used are: (a) A-Cr-$Fe^{3+,}$ (b) $Fe^{2+}/(Fe^{2+}+Mg)$ vs. Cr/(Cr+Al) ratios, (c) $Fe^{2+}/(Fe^{2+}+Mg)$ vs. $Fe^{3+}/(Fe^{3+}+Cr+Al)$ ratios and (d) $Fe^{2+}{}_{T}/(Fe^{2+}{}_{T}+Mg)$ vs. Ti/(Ti+Cr+Al) ratios.

Table 5.2. Distribution and types of primary spinels present in the studied samples.

	Sample	Region	Location	Name	CK / VK / Orangeite / Lamproite / UML	AMC	MCC	Sp	MUM	Trend	Chromite #Cr>0.85
Angola	CU-79-70,5A, CU-79-113A		Cucumbi		VK						
Angola	TZ-G18-47, TZ-G18-252		Tchiuzo		VK	Y	Y		Y	A-B	
Botswana	10052	SD	Jwaneng	Centre pipe	VK		Y		Y	B	
Botswana	10053	SD	Jwaneng	North pipe	VK	Y	Y				
Botswana	10054	SD	Jwaneng	South pipe	VK		Y				
Botswana	10055	CD	Orapa	AK1, "A"	VK		Y		Y	B	
Botswana	10056	CD	Orapa	AK1, "B"	VK		Y				
Botswana	10057	CD	Orapa	AK1, "C"	VK		Y				
Botswana	10058	CD	Letlhakane	DK1	VK		Y		Y		
Botswana	10060	CD	Damtshaa	BK9, "A"	VK				Y		
Botswana	10061	CD	Damtshaa	BK9, "B"	VK		Y		Y		
Canada	7999	Quebec	Temiskaming	Ville-Marie	VK	Y	Y		Y	A-C	Y
Canada	9168	Ontario	Temiskaming	Seed	VK		Y		Y	(B)	
Canada	9359	NWT	SW Slave	Drybones Bay	VK		Y				Y
USA	8015	Michigan	Lake Ellen	Lake Ellen	VK				Y	G	
USA	9346	Utah	San Juan Co.	Alhambra Rock	VK				Y		
USA	9966	Tennessee	Tazewell	Norris metakimberlite	VK						
Venezuela	7544		Guaniamo		VK/CK				Y		
Russia	10077	NR	Lomonosovskaya		VK	Y	Y			A	Y
Russia	10079	NR	Pionerskaya		VK		Y				Y
Russia	9985	Yakutia	Pobeda ('Victory')		VK	Y	Y		Y	(C)	
Russia	9959	Yakutia	Leningrad		VK		Y			(A)-(H)	Y
Angola	CC-47-46		Cacuilo	K47	CK				Y		
Botswana	10049	CD	Karowe	AK6, South pipe	CK	Y	Y		Y	A-C	
Botswana	10050	CD	Karowe	AK6, Center pipe	CK				Y		
Botswana	10051	CD	Karowe	AK6, North pipe	CK				Y		
Botswana	10059	CD	Letlhakane	DK1	CK	Y			Y	E	
South Africa	7707	NCP		Riverton	CK	Y	Y		Y	C	Y
South Africa	9156	FSP		Bultfontein	CK		Y		Y		Y
South Africa	9311	NCP	Kimberley	Big Hole	CK		Y		Y		
South Africa	9351	NCP	Kimberley		CK		Y		Y	C	Y

Table 5.2. (continued 1)

	Sample	Region	Location	Name	CK / VK / Orangeite / Lamproite / UML	AMC	MCC	Sp	MUM	Trend	Chromite #Cr>0.85
South Africa	9364	NCP	Kimberly	DutoitSpan	CK		Y		Y		Y
South Africa	9725	FSP		Monastery	CK				Y		
South Africa	9630	FSP	Kaalvallei	"occurence A"	CK				Y		
Lesotho	9607			P200	CK	Y			Y	E	
Guinea	8870			Banakoro "A"	CK		Y		Y	(A)-C	Y
Guinea	8871			Banakoro "B"	CK		Y		Y	C-D	Y
Canada	9353, 9354	Québec	Temiskaming	Notre Dâme du Nord	CK	Y	Y		Y	A-C	Y
Canada	9577	Ontario	Bucke Township		CK		Y		Y		Y
Canada	6934	NWT	Somerset island		CK				Y	(B)	
Canada	7448	NWT	Diavik		CK		Y		Y	C	Y
Canada	7449	NWT	LDG Ekati	Point Lake	CK	Y	Y		Y	A-C	
Canada	9613	NWT	SW Slave	Snap Lake	CK		Y		Y	(A)	Y
Canada	7454	Alberta	Birch Mountains		CK		Y		Y	C	
Canada	9360	Nanavut	Baffin Island	Jackson inlet	CK		Y		Y	(A)-C,B-F	Y
USA	7314	Colorado	Larimer Co.	Chicken Park	CK	Y			Y	E	
USA	10070	Pennsylvania	Fayette Co.	Gate-Adah	CK	Y	Y		Y	A&B	
USA	9348	Colorado	Kelsey Lake		CK	Y	Y		Y	H-E	Y
USA	9345	Colorado	Laramie Co		CK		Y		Y	A-C	Y
USA	9352	Michigan	Menominee	Site 73	Ck			Y	Y,Qan	G	
USA	9576	Colorado	Larimer Co.	Sloan #2	CK	Y	Y			H	
Russia	10037	Yakutia	Udachnaya		CK		Y		Y		Y
Russia	10065	Yakutia	Obnazhonnaya		CK				Y		
Russia	4928	Yakutia	Mir		CK		Y		Y	C	
Russia	9611	Kola Peninsula	Emakowskaya		CK		Y		Y	C	Y
India	8021	RKF	Siddanpalli	SK-1	CK		Y		Y	C	Y
India	8044	RKF	Siddanpalli	SK-2	CK				Y		
India	8029	RKF	Siddanpalli	SK-3	CK		Y		Y	(H)-C	Y
India	8030, 8040, 8041	WKF	Chigicherla	CC-4	CK		Y		Y	C	Y
India	8022, 8023	WKF	Chigicherla	CC-5	CK	Y	Y		Y	E-D	
India	8036	WKF	Kalyandurg	KL-3	CK	Y	Y		Y	E	
India	8037, 8038	WKF	Kalyandurg	KL-4	CK				Y		
India	8027	WKF	Wajrakarur village	P-1	CK	Y	Y			A&(H)	Y
India	8043	WKF	Lattavaram village	P-3	CK		Y		Y		

Table 5.2. (continued 2)

	Sample	Region	Location	Name	CK / VK / Orangeite / Lamproite / UML	AMC	MCC	Sp	MUM	Trend	Chromite #Cr>0.85
China	9333	Shandong province	Mengyin	Red Flag #1	CK	Y	Y		Y	H-A	Y
China	9737,9738, 9740	Shandong province	Mengyin	Shengli	CK	Y	Y		Y	H-A-C	Y
China	9573, 9574	Liaoning province		Wafangdian	CK		Y				Y
South Africa	7881	NCP	Kimberley	Helam	Orangeite (Hammond and Mitchell, 2002)				Y		
South Africa	9375	FSP		Roberts Victor	Orangeite (Mitchell 1995)		Y				Y
South Africa	9952	NCP		Bellsbank	Orangeite (Mitchell 1995)		Y		Y	(A)-C	Y
South Africa	9602	FSP	Kaalvallei	"occurence B"	Lamproite (this work)				Y		
USA	9341	Colorado	Kelsey Lake		Lamproite (this work)		Y		Y	C	Y
USA	9340	Arkansas	Murfreesboro		Lamproite (McCandless et al. 1994)	Y			Y	E	
India	8024	WKF	Chigicherla cluster	CC-1	Lamproite (this work)		Y		Y	C	
India	8025	WKF	Wajrakarur village	P-2	Lamproite (Kaur and Mitchell 2013)		Y		Y	C	
India	8035	WKF	Lattavaram village	P-4	Lamproite (Shaikh et al., 2018)	Y	Y		Y	A-C	
India	8045	WKF	Mulligiripally	P-5	Lamproite (Kaur et al., 2013)	Y			Y	E	
Canada	10142	Quebec	Ugava Bay	Torngat	UML (Tappe et al., 2004)		Y		Y	A-C	Y

SD: Southern District; CD: Central District; NCP: Northern Cape Province; FSP: Free State Province; NR: Northern Region; RKF: Raichur kimberlite field; WKF: Wajrakarur kimberlite field. VK: volcaniclastic kimberlite; CK: coherent kimberlite; UML: ultramafic lamprophyres; Y: presence

Table 5.2. (continued 3)

	Sample	Region	Location	Name	CK / VK / Orangeite / Lamproite / UML	AMC	MCC	Sp	MUM	Trend	Chromite #Cr>0.85
China	9333	Shandong province	Mengyin	Red Flag #1	CK	Y	Y		Y	H-A	Y
China	9737,9738, 9740	Shandong province	Mengyin	Shengli	CK	Y	Y		Y	H-A-C	Y
China	9573, 9574	Liaoning province		Wafangdian	CK		Y				Y
South Africa	7881	NCP	Kimberley	Helam	Orangeite (Gurney et al. 2005)				Y		
South Africa	9375	FSP		Roberts Victor	Orangeite (Mitchell 1995)		Y				Y
South Africa	9952	NCP		Bellsbank	Orangeite (Mitchell 1995)		Y		Y	(A)-C	Y
South Africa	9602	FSP	Kaalvallei	"occurence B"	Lamproite (this work)				Y		
USA	9341	Colorado	Kelsey Lake		Lamproite (this work)		Y		Y	C	Y
USA	9340	Arkansas	Murfreesboro		Lamproite (McCandless et al. 1994)	Y			Y	E	
India	8024	WKF	Chigicherla cluster	CC-1	Lamproite (this work)		Y		Y	C	
India	8025	WKF	Wajrakarur village	P-2	Lamproite (Kaur&Mitchell 2013)		Y		Y	C	
India	8035	WKF	Lattavaram village	P-4	Lamproite (Shaikh et al., 2018)	Y	Y		Y	A-C	
India	8045	WKF	Mulligiripally	P-5	Lamproite (Kaur et al., 2013)	Y			Y	E	
Canada	10142	Quebec	Ugava Bay	Torngat	UML (Tappe et al., 2004)		Y		Y	A-C	Y

SD: Southern District; CD: Central District; NCP: Northern Cape Province; FSP: Free State Province; NR: Northern Region; RKF: Raichur kimberlite field; WKF: Wajrakarur kimberlite field. VK: volcaniclastic kimberlite; CK: coherent kimberlite; UML: ultramafic lamprophyres; Y: presence

Table 5.3. Representative compositions of primary groundmass spinels

No.	1	2	3	4	5	6	7	8	9	10	11
Sample	8035	8035	8035	8045	8045	8045	8022	8022	9352	9352	9352
Composition	AMC	MCC	MUM	AMC	MUM	MUM	AMC	MUM	Sp	Sp	Sp
(wt.%)											
TiO_2	2.80	3.28	7.37	0.88	9.29	12.89	6.06	17.53	1.18	1.19	1.20
Al_2O_3	12.54	8.79	0.38	18.17	4.73	0.70	11.39	5.73	55.10	52.33	57.00
Cr_2O_3	47.56	48.39	4.52	48.53	17.76	0.11	41.23	2.38	6.57	9.28	4.59
FeO*	23.23	28.02	78.74	16.20	57.17	79.83	26.64	62.19	13.53	14.13	13.04
MnO	0.80	1.05	0.93	0.30	0.76	1.58	0.30	1.53	0.08	0.09	0.07
MgO	11.58	9.41	4.53	13.52	6.86	0.07	12.16	5.05	21.19	21.09	21.58
SiO_2	0.17	0.12	0.06	bdl	0.14	0.07	0.15	0.05	0.09	0.15	0.11
ZnO	0.15	0.24	0.07	0.11	0.03	0.10	0.07	0.04	0.07	0.01	0.07
V_2O_3	0.16	0.14	0.16	0.24	0.08	0.17	0.25	0.17	0.23	0.22	0.20
Nb_2O_5	bdl	bdl	0.06	bdl	bdl	bdl	bdl	bdl	bdl	0.05	0.00
ZrO_2	bdl	bdl	bdl	bdl	bdl	bdl	bdl	0.05	bdl	bdl	bdl
NiO	0.14	0.10	0.23	0.11	0.13	0.09	0.23	0.16	0.19	0.16	0.16
CaO	0.05	0.06	0.14	0.01	0.04	0.18	0.02	0.15	0.02	0.08	0.16
Recalculated analyses											
FeO	17.78	20.81	30.61	14.01	29.46	41.20	19.96	38.09	8.70	8.73	8.34
Fe_2O_3	6.05	8.02	53.49	2.44	30.79	42.93	7.42	26.78	5.36	6.00	5.22
	99.79	100.41	102.54	98.31	100.08	100.09	99.24	97.72	98.79	99.38	98.70
Cations on basis of 4 O atoms (apfu)											
Ti	0.068	0.082	0.199	0.021	0.245	0.366	0.149	0.475	0.023	0.024	0.023
Al	0.480	0.345	0.016	0.678	0.195	0.031	0.439	0.244	1.702	1.626	1.745
Cr	1.220	1.275	0.128	1.214	0.492	0.003	1.065	0.068	0.136	0.193	0.094
Fe^{2+}	0.483	0.580	0.919	0.371	0.863	1.302	0.545	1.149	0.191	0.193	0.181
Fe^{3+}	0.148	0.201	1.445	0.058	0.812	1.221	0.182	0.727	0.106	0.119	0.102
Mn	0.022	0.030	0.028	0.008	0.023	0.051	0.008	0.047	0.002	0.002	0.002
Mg	0.560	0.467	0.242	0.638	0.358	0.004	0.592	0.271	0.827	0.828	0.835
Si	0.006	0.004	0.002	0.000	0.005	0.003	0.005	0.002	0.002	0.004	0.003
Zn	0.004	0.006	0.002	0.003	0.001	0.003	0.002	0.001	0.001	0.000	0.001
V	0.004	0.004	0.005	0.006	0.002	0.005	0.007	0.005	0.005	0.005	0.004
Nb	0.000	0.000	0.001	0.000	0.000	0.000	0.000	0.000	0.000	0.001	0.000
Zr	0.000	0.000	0.000	0.000	0.000	0.000	0.000	0.001	0.000	0.000	0.000
Ni	0.004	0.003	0.007	0.003	0.004	0.003	0.006	0.005	0.004	0.003	0.003
Ca	0.002	0.002	0.005	0.000	0.002	0.007	0.001	0.006	0.000	0.002	0.004
$Fe^{2+}/(Mg+Fe^{2+})$	0.463	0.554	0.791	0.368	0.707	0.997	0.480	0.809	0.187	0.189	0.178
#Cr	0.718	0.787	0.888	0.642	0.716	0.095	0.708	0.218	0.074	0.106	0.051
Mol % end member spinel molecules											
$MgAl_2O_4$	24.2	17.4	0.8	34.0	9.8	0.4	22.1	12.2	85.2	81.9	87.3
Fe_3O_4	7.4	10.1	72.7	2.9	40.8	62.1	9.2	36.5	5.4	6.0	5.3
Mg_2TiO_4	6.9	8.3	10.2	2.1	24.6	0.0	15.0	7.3	2.4	2.4	2.4
Mn_2TiO_4	-	-	1.2	-	-	2.5	-	2.3	0.0	0.0	0.0
Fe_2TiO_4	-	-	8.6	-	-	34.8	-	38.2	0.0	0.0	0.0
$FeCr_2O_4$	33.5	38.3	6.5	32.1	24.7	0.2	29.2	3.4	7.0	9.7	4.9
$MnCr_2O_4$	1.8	2.4	-	0.8	-	-	0.5	-	-	-	-
$MgCr_2O_4$	26.2	23.5	-	28.1	-	-	-	-	-	-	-

FeO*: total Fe as Fe^{2+}; bdl: below detection limit.

Table 5.3. (continued 1)

No.	12	13	14	15	16	17	18	19	20	21	22
Sample	9352	9352	9352	9352	9352	9352	9740	9740	9740	9740	9740
Composition	Sp	MUM	Qan	MUM	Qan	Qan	MCC	MCC	MCC	MUM	MUM
(wt.%)											
TiO_2	0.80	17.34	18.67	19.25	26.99	27.23	2.09	5.18	4.05	12.51	10.09
Al_2O_3	59.05	9.94	9.61	9.44	7.86	7.48	3.28	8.68	5.91	9.34	5.73
Cr_2O_3	3.52	0.43	0.51	0.73	1.32	1.49	63.11	49.60	56.34	16.95	0.99
FeO*	12.13	49.25	46.88	46.94	32.08	31.41	19.77	20.84	19.00	41.86	61.23
MnO	0.11	0.40	0.45	0.38	0.49	0.54	0.14	0.20	0.33	0.75	0.84
MgO	21.99	18.19	19.45	18.89	28.11	28.00	11.27	14.16	14.66	17.71	14.18
SiO_2	0.10	bdl	bdl	0.06	0.06	0.04	0.07	0.17	0.08	0.06	0.86
ZnO	0.04	0.00	0.04	0.02	0.00	0.03	0.08	0.05	0.04	0.07	0.02
V_2O_3	0.17	0.60	0.40	0.37	0.28	0.27	0.21	0.23	0.24	0.11	0.08
Nb_2O_5	bdl	bdl	0.09	0.05	0.11	0.12	bdl	bdl	bdl	bdl	0.09
ZrO_2	bdl	bdl	0.07	0.08	0.17	0.12	bdl	bdl	bdl	0.06	0.11
NiO	0.16	0.16	0.12	0.10	0.09	0.08	0.12	0.23	0.13	0.14	0.21
CaO	0.46	0.19	0.64	0.12	0.14	0.16	0.01	0.03	0.04	0.06	0.13
Recalculated analyses											
FeO	7.35	20.13	18.97	20.86	13.71	13.65	17.16	16.09	14.18	17.12	19.43
Fe_2O_3	5.31	32.36	31.01	28.99	20.42	19.74	2.90	5.28	5.36	27.49	46.45
	99.06	99.74	100.04	99.33	99.73	98.93	100.45	99.90	101.36	102.38	99.21
Cations on basis of 4 O atoms (apfu)											
Ti	0.015	0.414	0.441	0.459	0.607	0.617	0.053	0.126	0.098	0.293	0.254
Al	1.787	0.372	0.356	0.353	0.277	0.266	0.130	0.331	0.225	0.343	0.226
Cr	0.071	0.011	0.013	0.018	0.031	0.035	1.677	1.269	1.436	0.418	0.026
Fe^{2+}	0.158	0.534	0.498	0.553	0.343	0.344	0.483	0.436	0.382	0.446	0.545
Fe^{3+}	0.103	0.773	0.732	0.692	0.459	0.448	0.073	0.129	0.130	0.645	1.172
Mn	0.002	0.011	0.012	0.010	0.012	0.014	0.004	0.006	0.009	0.020	0.024
Mg	0.841	0.860	0.910	0.893	1.252	1.258	0.565	0.683	0.704	0.823	0.708
Si	0.003	0.000	0.000	0.002	0.002	0.001	0.002	0.006	0.003	0.002	0.029
Zn	0.001	0.000	0.001	0.000	0.000	0.001	0.002	0.001	0.001	0.002	0.001
V	0.004	0.015	0.010	0.009	0.007	0.007	0.006	0.006	0.006	0.003	0.002
Nb	0.000	0.000	0.000	0.001	0.001	0.002	0.000	0.000	0.000	0.000	0.001
Zr	0.000	0.000	0.000	0.001	0.002	0.002	0.000	0.001	0.000	0.001	0.002
Ni	0.003	0.004	0.003	0.002	0.002	0.002	0.003	0.006	0.003	0.004	0.006
Ca	0.013	0.006	0.022	0.004	0.004	0.005	0.000	0.001	0.001	0.002	0.005
$Fe^{2+}/(Mg+Fe^{2+})$	0.158	0.383	0.354	0.383	0.215	0.215	0.461	0.389	0.352	0.352	0.435
#Cr	0.038	0.028	0.034	0.049	0.101	0.118	0.928	0.793	0.865	0.549	0.104
Mol % end member spinel molecules											
$MgAl_2O_4$	89.1	18.8	17.9	17.8	14.0	13.4	6.5	16.7	11.3	17.2	11.7
Fe_3O_4	5.4	39.0	37.0	34.9	23.2	22.6	3.7	6.5	6.5	32.4	58.9
Mg_2TiO_4	1.6	33.8	37.2	35.6	55.1	55.6	5.3	12.7	9.9	29.4	26.3
Mn_2TiO_4	0.0	0.5	0.6	0.5	0.6	0.7	-	-	-	-	-
Fe_2TiO_4	0.0	7.4	6.7	10.3	5.6	5.9	-	-	-	-	-
$FeCr_2O_4$	3.8	0.5	0.6	0.9	1.6	1.8	39.7	26.6	25.0	21.0	1.4
$MnCr_2O_4$	-	-	-	-	-	-	0.4	0.4	0.7	-	-
$MgCr_2O_4$	-	-	-	-	-	-	44.4	37.1	46.6	-	-

FeO*: total Fe as Fe^{2+}; bdl: below detection limit.

Table 5.3. (continued 2)

No.	23	24	25	26	27	28	29	30	31	32	33
Sample	9740	9740	10059	10059	10059	9959	9959	9959	9360	9360	9360
Composition	AMC	MCC	AMC	MUM	AMC	MCC	MCC	MCC	MCC	MCC	MUM
(wt.%)											
TiO_2	4.65	4.25	5.42	9.14	4.85	5.97	2.49	4.98	3.26	2.95	22.35
Al_2O_3	10.97	9.42	12.78	0.68	12.59	2.83	8.63	3.86	7.58	4.04	3.63
Cr_2O_3	48.30	49.46	41.45	0.54	38.88	46.58	48.80	47.72	54.47	58.88	0.81
FeO*	19.70	19.44	26.53	77.32	26.73	32.77	27.14	31.35	19.51	21.27	53.97
MnO	0.15	0.12	0.57	0.75	0.29	0.30	0.25	0.29	0.16	0.27	0.71
MgO	14.09	14.28	11.39	4.23	12.36	9.01	10.18	8.54	12.98	11.11	14.23
SiO_2	0.11	0.19	0.11	0.04	0.68	0.05	0.07	bdl	0.15	0.05	0.05
ZnO	0.05	0.04	0.10	0.03	0.07	0.10	0.13	0.09	0.06	0.06	0.04
V_2O_3	0.28	0.23	0.32	0.16	0.26	0.18	0.25	0.25	0.19	0.11	0.07
Nb_2O_5	bdl	0.05	bdl	bdl	bdl	bdl	bdl	bdl	0.07	bdl	bdl
ZrO_2	bdl	bdl	bdl	bdl	bdl	0.06	bdl	bdl	bdl	bdl	0.05
NiO	0.30	0.25	0.23	0.11	0.25	0.09	0.17	0.14	0.18	0.12	0.13
CaO	0.01	0.03	0.05	0.19	0.05	0.04	0.07	0.09	0.03	0.03	0.12
Recalculated analyses											
FeO	15.75	14.77	20.55	31.58	18.94	23.22	19.14	22.85	15.84	17.69	29.29
Fe_2O_3	4.39	5.19	6.64	50.83	8.66	10.61	8.89	9.45	4.08	3.98	27.42
	99.04	98.28	99.62	98.28	97.88	99.04	99.07	98.24	99.05	99.29	98.92
Cations on basis of 4 O atoms (apfu)											
Ti	0.113	0.105	0.133	0.257	0.120	0.156	0.063	0.131	0.081	0.075	0.566
Al	0.418	0.363	0.490	0.030	0.487	0.116	0.342	0.159	0.295	0.162	0.144
Cr	1.234	1.279	1.066	0.016	1.008	1.282	1.296	1.320	1.423	1.579	0.022
Fe^{2+}	0.425	0.404	0.559	0.988	0.520	0.676	0.538	0.669	0.438	0.502	0.825
Fe^{3+}	0.107	0.128	0.162	1.431	0.214	0.278	0.225	0.249	0.101	0.101	0.695
Mn	0.004	0.003	0.016	0.024	0.008	0.009	0.007	0.009	0.004	0.008	0.020
Mg	0.678	0.696	0.552	0.236	0.604	0.468	0.510	0.445	0.639	0.562	0.714
Si	0.004	0.006	0.004	0.001	0.022	0.002	0.002	0.000	0.005	0.002	0.002
Zn	0.001	0.001	0.002	0.001	0.002	0.002	0.003	0.002	0.001	0.002	0.001
V	0.007	0.006	0.008	0.005	0.007	0.005	0.007	0.007	0.005	0.003	0.002
Nb	0.000	0.001	0.000	0.000	0.000	0.000	0.000	0.000	0.001	0.000	0.000
Zr	0.000	0.000	0.000	0.000	0.000	0.000	0.000	0.000	0.000	0.000	0.001
Ni	0.008	0.007	0.006	0.003	0.007	0.002	0.005	0.004	0.005	0.003	0.004
Ca	0.000	0.001	0.002	0.008	0.002	0.001	0.002	0.003	0.001	0.001	0.004
$Fe^{2+}/(Mg+Fe^{2+})$	0.385	0.367	0.503	0.807	0.462	0.591	0.513	0.600	0.406	0.472	0.536
#Cr	0.747	0.779	0.685	0.346	0.674	0.917	0.791	0.892	0.828	0.907	0.131
Mol % end member spinel molecules											
$MgAl_2O_4$	21.1	18.4	24.7	1.5	25.0	5.8	17.2	8.0	14.9	8.1	7.2
Fe_3O_4	5.4	6.5	8.2	71.9	11.0	14.0	11.3	12.5	5.1	5.1	34.9
Mg_2TiO_4	11.4	10.6	13.4	11.0	12.3	15.7	6.3	13.2	8.2	7.6	32.0
Mn_2TiO_4	-	-	-	1.2	-	-	-	-	-	-	1.0
Fe_2TiO_4	-	-	-	13.6	-	-	-	-	-	-	23.8
$FeCr_2O_4$	27.4	25.6	32.1	0.8	27.3	36.2	35.9	39.3	31.5	38.0	1.1
$MnCr_2O_4$	0.3	0.2	1.1	-	0.5	0.6	0.6	0.6	0.4	0.7	-
$MgCr_2O_4$	34.5	38.8	20.6	-	23.9	27.6	28.6	26.4	40.0	40.5	-

FeO*: total Fe as Fe^{2+}; bdl: below detection limit.

Table 5.3. (continued 3)

No.	34	35	36	37	38	39	40	41	42	43	44
Sample	9360	9360	9348	9348	9348	9348	9348	TZ-G18	TZ-G18	TZ-G18	TZ-G18
Composition	AUM	MCC	MCC	AMC	MUM	MUM	AMC	AMC	MCC	AMC	MCC
(wt.%)											
TiO_2	11.39	2.41	1.95	1.89	5.23	5.22	1.73	5.48	8.13	5.56	12.96
Al_2O_3	21.03	7.87	5.17	15.26	11.00	0.07	16.65	16.05	9.13	16.06	10.25
Cr_2O_3	0.12	54.29	57.58	43.35	19.41	1.19	41.32	38.50	37.90	38.79	19.67
FeO*	41.02	18.49	22.88	25.23	48.00	82.05	23.66	24.16	28.55	24.10	39.21
MnO	0.75	0.12	0.22	0.23	0.43	2.49	0.21	0.21	0.33	0.18	0.41
MgO	19.62	13.58	11.72	13.12	12.11	2.34	14.63	13.51	13.14	13.60	14.98
SiO_2	0.28	0.28	0.15	0.11	0.09	0.25	0.16	0.09	0.07	0.15	0.12
ZnO	0.04	0.04	0.08	0.07	0.07	0.19	0.10	0.06	0.05	0.07	0.11
V_2O_3	bdl	0.18	0.04	0.50	0.07	2.23	0.09	0.22	0.26	0.27	0.20
Nb_2O_5	bdl	bdl	bdl	0.04	bdl	bdl	0.05	0.30	bdl	bdl	bdl
ZrO_2	0.28	0.06	0.10	bdl	bdl	bdl	bdl	bdl	bdl	bdl	bdl
NiO	0.02	0.23	0.02	0.16	0.10	bdl	0.15	0.19	0.16	0.29	0.16
CaO	0.34	0.11	0.04	0.04	0.03	0.03	0.07	0.15	0.19	0.13	0.18
Recalculated analyses											
FeO	13.78	13.94	16.72	16.00	18.92	30.54	13.42	18.41	19.58	18.17	21.68
Fe_2O_3	30.27	5.06	6.85	10.26	32.31	57.24	11.38	6.39	9.97	6.59	19.49
	97.92	98.16	100.63	101.02	99.77	101.79	99.95	99.56	98.92	99.87	100.21
Cations on basis of 4 O atoms (apfu)											
Ti	0.261	0.060	0.049	0.045	0.130	0.145	0.041	0.130	0.201	0.132	0.312
Al	0.755	0.307	0.203	0.566	0.427	0.003	0.614	0.599	0.354	0.597	0.387
Cr	0.003	1.421	1.514	1.079	0.505	0.035	1.022	0.964	0.985	0.967	0.498
Fe^{2+}	0.351	0.386	0.465	0.421	0.521	0.941	0.351	0.487	0.538	0.479	0.581
Fe^{3+}	0.694	0.126	0.171	0.243	0.801	1.588	0.268	0.152	0.247	0.156	0.470
Mn	0.019	0.003	0.006	0.006	0.012	0.078	0.006	0.006	0.009	0.005	0.011
Mg	0.891	0.670	0.581	0.616	0.594	0.129	0.682	0.637	0.644	0.639	0.715
Si	0.009	0.009	0.005	0.003	0.003	0.009	0.005	0.003	0.002	0.005	0.004
Zn	0.001	0.001	0.002	0.002	0.002	0.005	0.002	0.001	0.001	0.002	0.003
V	0.000	0.005	0.001	0.013	0.002	0.066	0.002	0.005	0.007	0.007	0.005
Nb	0.000	0.000	0.000	0.001	0.000	0.000	0.001	0.004	0.000	0.000	0.000
Zr	0.004	0.001	0.002	0.000	0.000	0.000	0.000	0.000	0.000	0.000	0.000
Ni	0.001	0.006	0.001	0.004	0.003	0.000	0.004	0.005	0.004	0.007	0.004
Ca	0.011	0.004	0.001	0.001	0.001	0.001	0.002	0.005	0.007	0.005	0.006
$Fe^{2+}/(Mg+Fe^{2+})$	0.283	0.365	0.445	0.406	0.467	0.880	0.340	0.433	0.455	0.428	0.448
#Cr	0.004	0.822	0.882	0.656	0.542	0.922	0.625	0.617	0.736	0.618	0.563
Mol % end member spinel molecules											
$MgAl_2O_4$	38.3	15.6	10.2	28.6	21.4	0.2	30.9	30.3	17.8	30.1	19.6
Fe_3O_4	35.2	6.4	8.6	12.3	40.2	82.9	13.5	7.7	12.4	7.9	23.7
Mg_2TiO_4	25.3	6.1	4.9	4.5	13.0	5.5	4.1	13.2	20.2	13.3	18.7
Mn_2TiO_4	1.0	-	-	-	-	3.3	-	-	-	-	0.4
Fe_2TiO_4	0.2	-	-	-	-	6.3	-	-	-	-	12.4
$FeCr_2O_4$	0.1	27.6	33.4	25.6	6.0	1.8	18.7	26.6	23.1	26.2	25.2
$MnCr_2O_4$	-	0.3	0.5	0.5	0.6	-	0.5	0.4	0.5	0.3	-
$MgCr_2O_4$	-	44.1	42.3	28.4	18.8	-	32.3	21.8	26.0	22.2	-

FeO*: total Fe as Fe^{2+}; bdl: below detection limit.

5.5. COMPOSITIONAL TRENDS OF PRIMARY SPINELS

The typical patterns of the zoned groundmass spinels in most of the kimberlites and related rocks should be indicative of important changes in the composition of the parental magma, and define different compositional trends (Fig. 5.6). Therefore, a systematic study has been done in this memory on the zoning of the spinels in kimberlites and related rocks. Eight compositional trends (labelled as A, B, C, D, E, F, G and H) are found in the studied kimberlites and related rocks. The main characteristics of these trends are indicated in the following paragraphs.

Trend A

An AMC core evolves to MCC rim (Fig. 5.6 and 5.7). This evolution indicates a decrease of the Al content, commonly accompanied by increases of Cr and Fe contents and decrease of the Mg content. This trend is similar to one direction of the AMC trend described by Mitchell (1986).

Trend B

Spinel evolution is from MCC in the cores to MUM spinels at approximately constant $Fe^{2+}/(Fe^{2+}+Mg)$ ratio in the rims (Fig. 5.6 and 5.7). This trend is equivalent to the so-called ulvöspinel trend defined by (Mitchell, 1986) or magmatic trend 1 defined by Mitchell (1986) and Roeder and Schulze (2008).

Trend C

It is characterised by evolution from MCC in the cores to MUM or nearly pure Mag in the rim, accompanied with a rapid increase of the ratio $Fe^{2+}/(Fe^{2+}+Mg)$ (Fig. 5.6 and 5.7), in the rims. This trend is similar to the so-called titanomagnetite trend (Mitchell, 1986) or magmatic trend 2 (Mitchell, 1986; Roeder and Schulze, 2008).

Trend D

This trend evolves from MUM spinels in the cores towards pure magnetite component in the rims (Fig. 5.6 and 5.7).

Trend E

AMC cores evolve directly to MUM-Mag rims showing a rapid decrease of $Fe^{2+}/(Fe^{2+}+Mg)$ ratios (Fig. 5.6 and 5.7). This trend is similar to the trend C, but the spinels have a different initial composition. MCC is lacking.

Trend F

MUM cores evolve to UMS or Sp in the rims, thus increasing the Al content (Fig. 5.6 and 5.7). This trend is similar to trend 7 determined by (Roeder and Schulze, 2008) and to so-called pleonaste reaction trend by (Mitchell, 1986). It can be a continuum of trend B, C or E.

Trend G

UM spinel cores evolve to Qan rims, thus increasing the Mg content (Fig. 5.6 and 5.7).

Trend H

MCC cores evolve to AMC rims through an increase of the Al contents. This is a similar trend to described in A, but in a reverse direction (Fig. 5.6 and 5.7). This trend is similar to one direction of AMC trend described by Mitchell (1986).

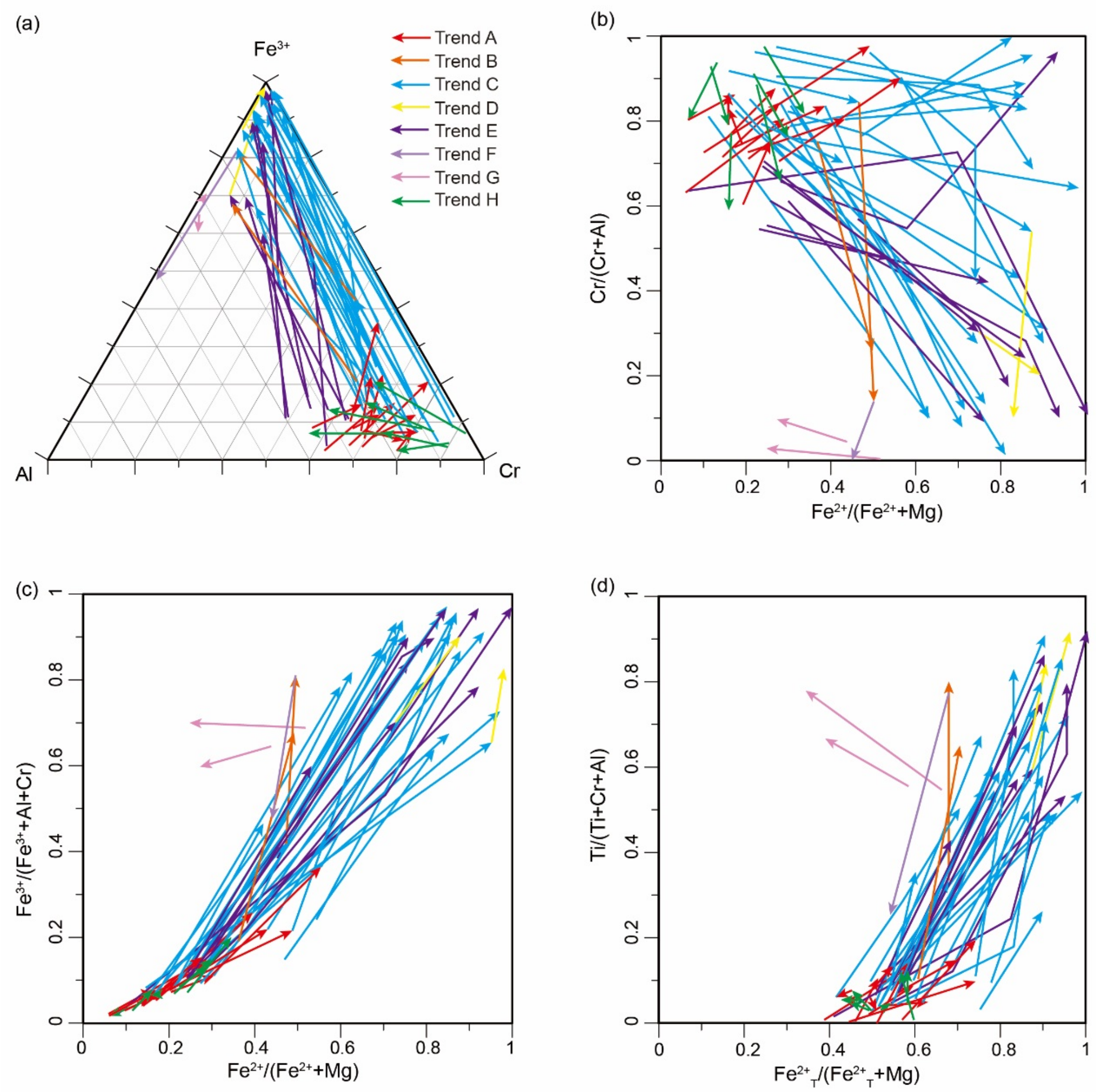

Fig. 5.6. Compositional trends of zoned groundmass spinel in kimberlites and related rocks obtained in the present study: (a) Al-Cr-Fe^{3+}, (b) $Fe^{2+}/(Fe^{2+}+Mg)$ vs. Cr/(Cr+Al), (c) $Fe^{2+}/(Fe^{2+}+Mg)$ vs. $Fe^{3+}/(Fe^{3+}+Cr+Al)$ and (d) $Fe^{2+}{}_{T}/(Fe^{2+}{}_{T}+Mg)$ vs. Ti/(Ti+Cr+Al).

These are the ideal evolutions of the spinels. However, not all of the studied samples present an evolutionary trend and some of them have unzoned groundmass spinels. Moreover, zoned groundmass spinel not present complete trend in many kimberlites are but. The zonings could present only one part (the start, end or medium) of a trend.

Many kimberlites present a combination of these trends. For instance, firstly they follow the trend A but then follow the trend C. Other combination of trends have also been found, for instance, A-C-B-F, A-H, A-B-D, C-D, H-C, E-D, H-A-C. Moreover, some spinel present compositions intermediate between the trends B and C or E. Finally, complex trends, evolving firstly following C, then changing to trend B, are also found.

Some compositions of some clearly zoned chromite cores vary within the MCC compositional field. Their evolutional trend is parallel to trend A or H. For instance relatively Al-rich MCC mantled by relatively Al-poor MCC, or contrast.

The trend B (trend 1) does not occur in any of those 11 samples which have been previously classified as lamproites, orangeites or ultramafic lamprophyres (UML). However, only 7 among the 68 studied kimberlites show a clear trend B, which is supposed to be characteristic of archetypical kimberlites (Mitchell, 1986, 1995).

In the 10 occurrences classified as lamproites (including in this category the rocks classically defined as orangeites or group II kimberlites), when the spinels show a clear zoning, they present trends C or E (trend 2). Some of them have a chromite core that evolves following the trend A.

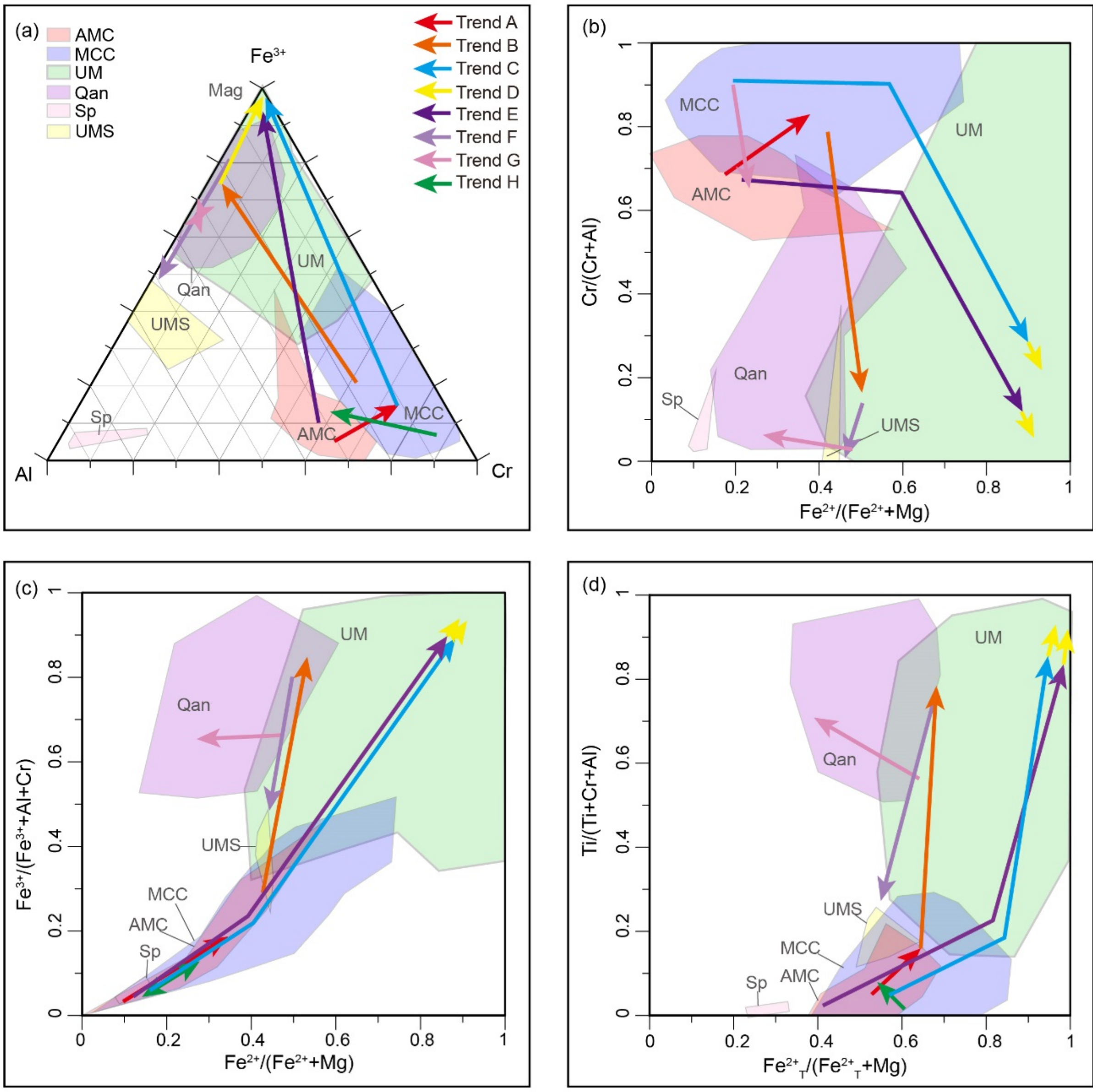

Fig. 5.7. Diagram showing the compositional fields of the groundmass spinel in kimberlites and the trends observed in the zoning, adapting dates from the present work: (a) diagram Al-Cr-Fe^{3+}, (b) diagram using $Fe^{2+}/(Fe^{2+}+Mg)$ vs. $Cr/(Cr+Al)$ ratios, (c) diagram using $Fe^{2+}/(Fe^{2+}+Mg)$ vs. $Fe^{3+}/(Fe^{3+}+Cr+Al)$ ratios and (d) diagram showing $Fe^{2+}{}_T/(Fe^{2+}{}_T+Mg)$ vs. $Ti/(Ti+Cr+Al)$ ratios.

5.6. EXAMPLES OF SPINELS WITHIN SINGLE KIMBERLITES AND RELATED ROCKS

Only a few examples from the 79 kimberlites studied in this thesis are presented in the following section. It should be tedious and repetitive to describe all of them, and only some representative examples were selected. The compositional projections from the present study are also compared with the previous commonly used fields and trends (Mitchell, 1986; Roeder and Schulze, 2008).

5.6.1. Lattavaram lamproite, India

Groundmass spinels from coherent P-4 Lattavaram lamproite has a complex zoning (Fig. 5.8a). They have an euhedral core of AMC enclosed by MCC following first a trend A, with a decrease of the Al content and a slight Cr enrichment (note a short trend which is distinct in the Fig 5.8b). The composition then evolves towards to rim of the crystal to MUM spinels following the trend C, thus showing a decrease of Cr and a Fe^{3+} increase (Fig. 5.8a-g), coupled with a rapid increase of the ratio $Fe^{2+}/(Fe^{2+}+Mg)$. This lamproite follows the classic T2 trend of Mitchell (1986), typical of orangeites and lamproites s.s., as can be seen in Fig. 5.8e.

The plots in the reduced and oxidized spinel prisms also allows to observe a relative increase in the Ti component in the reduced prism and Fe^{3+} in the oxidized prism along the trend C (Fig. 5.8f-g).

The same complex trend, starting with the trend A followed by the trend C is also found in the next kimberlites: Karowe, Laramie, Point Lake, Notre Dâme du Nord. It is also found in the Torngat ultramafic lamprophyre.

5.6.2. Mulligiripally lamproite, India

Groundmass spinels from the coherent P-5 Mulligiripally lamproite have a simple zoning with an euhedral core of AMC, corroded by MUM spinels (Fig. 5.9a). Hence, they follow the trend E and show a decrease of Cr coupled with a rapid increase of $Fe^{2+}/(Fe^{2+}+Mg)$ (Fig. 5.9b-d) and an increase of Ti at high Fe^{2+} (trend T2 typical of lamproites, Fig. 5.9e). This tendency can also be seen in the reduced spinel prism (Fig. 5.9f) and oxidized (Fig. 5.9g).

A similar simple trend E is also found in the Murfreesboro lamproites (Trend E). However, we have recorded a very similar trend in the next kimberlites: DK-1 Letlhakane, P200 Lesotho, KL-3 Lattavaram and Chicken Park.

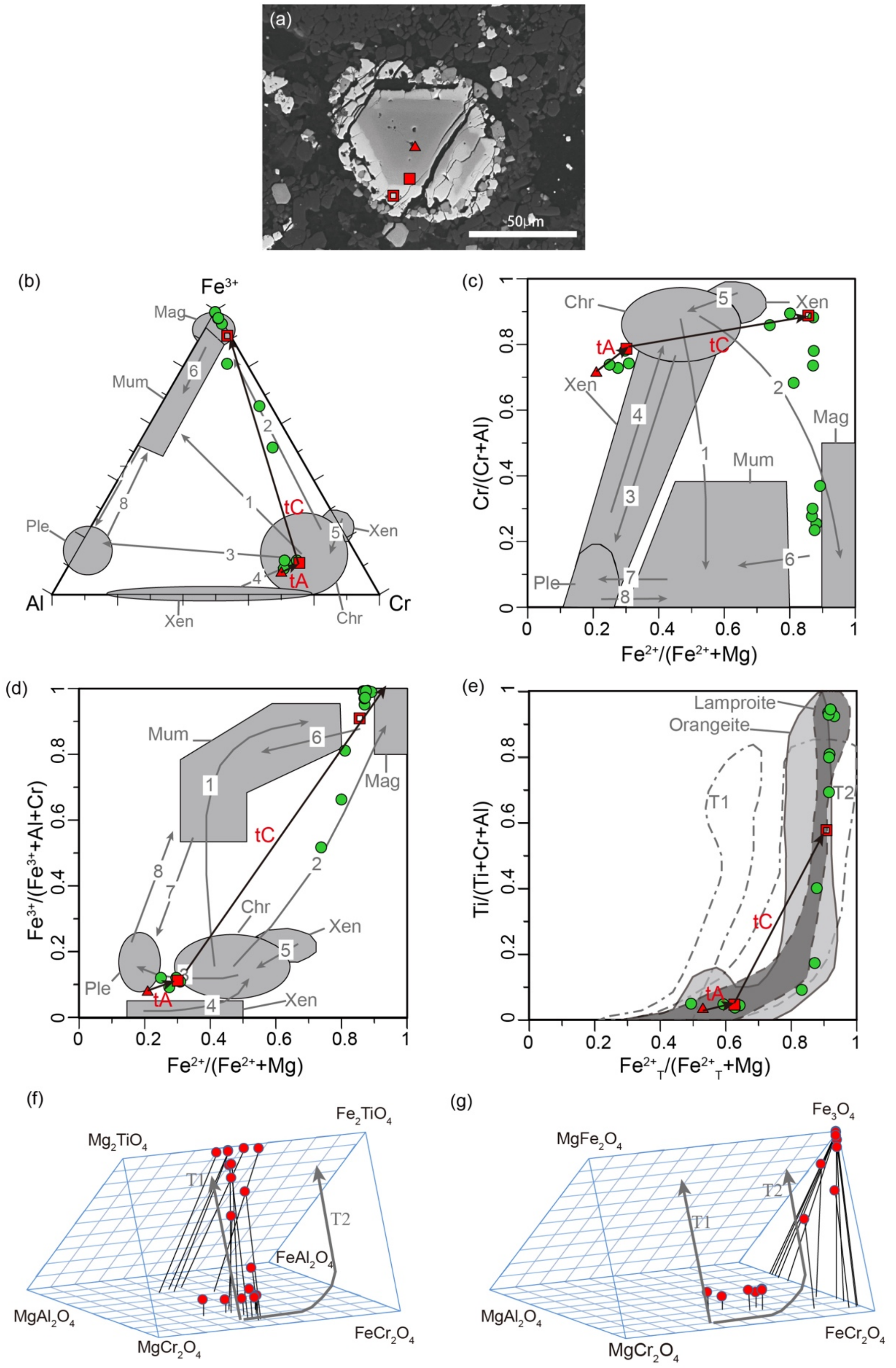

Fig. 5.8. (a) Example of groundmass spinel zoning with the situation of the points of analysis, BSE. Representation of compositions of primary spinels from P-4 Lattavaram lamproite in the following diagrams: (b) Al-Cr-Fe^{3+}, (c) $Fe^{2+}/(Fe^{2+}+Mg)$ vs. Cr/(Cr+Al), (d) $Fe^{2+}/(Fe^{2+}+Mg)$ vs. $Fe^{3+}/(Fe^{3+}+Cr+Al)$ and (e) $Fe^{2+}{}_T/(Fe^{2+}{}_T+Mg)$ vs. Ti/(Ti+Cr+Al). Red symbols in (b-e) correspond to the points in (a) and green circles are the rest of primary spinels analysed in this kimberlite; compositions of the spinels are also plotted in the reduced (f) and oxidized (g) spinel prisms. Compositional fields and trends from reference authors are indicated in grey colour, (b-d) from Roeder and Schulze (2008), (e-g) from Mitchell (1986, 1995).

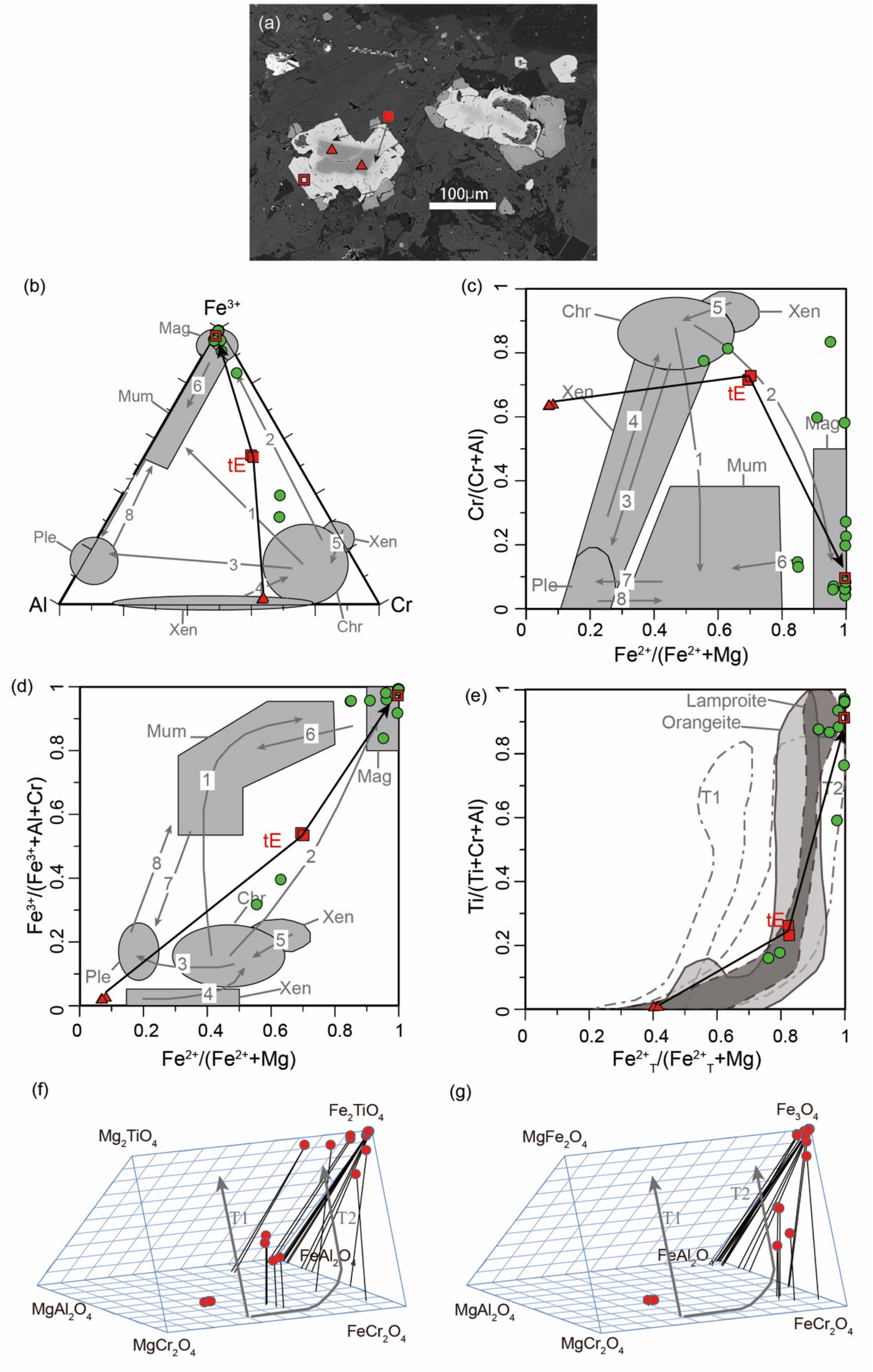

Fig. 5.9. (a) Example of zoned groundmass spinel showing the analysed points, BSE. Representation of compositions of primary spinels from P-5 Mulligiripally lamproite in the following diagrams: (b) Al-Cr-Fe^{3+}, (c) $Fe^{2+}/(Fe^{2+}+Mg)$ vs. Cr/(Cr+Al), (d) $Fe^{2+}/(Fe^{2+}+Mg)$ vs. $Fe^{3+}/(Fe^{3+}+Cr+Al)$ and (e) $Fe^{2+}{}_T/(Fe^{2+}{}_T+Mg)$ vs. Ti/(Ti+Cr+Al). Red symbols in (b-e) correspond to the points in (a) and green circles are the rest of primary spinels analysed in this kimberlite; compositions of the spinels are also plotted in the reduced (f) and oxidized (g) spinel prisms. Compositional fields and trends from previous works are indicated in grey colour, (b-d) from Roeder and Schulze (2008), (e-g) from Mitchell (1986, 1995).

5.6.3. Letlhakane kimberlite, Botswana

Groundmass spinels from coherent DK1 Letlhakane kimberlite have an euhedral core of AMC enclosed by MUM spinels (Fig. 5.10a). Euhedral, fine-grained chromite inclusions in rims of fresh olivine (Fig. 5.10b) are also of the AMC type, with compositions similar to those found in the cores of the groundmass spinel. Spinel in the olivine rims is interpreted as crystallizing with the groundmass chromite, and the core of the olivine grains is interpreted as xenocrystic.

The last rim is very rich in magnetite component, following the trend E and showing a decrease of Cr with a rapid increase of the ratio $Fe^{2+}/(Fe^{2+}+Mg)$, with slight increases in the proportions of Ti and strong in those of Fe^{3+} (Fig. 5.10c-h). MCC is absence.

5.6.4. Chigicherla, India

Groundmass spinels from coherent CC-5 Chigicherla kimberlite (Fig. 5.11a) have an euhedral core of AMC-MCC covered by MUM spinels following the trend E, this is, showing a decrease of Cr with a rapid increase of the ratio $Fe^{2+}/(Fe^{2+}+Mg)$; latter, this rim evolve to nearly pure magnetite following the trend D (Fig. 5.11-g).

The spinel follows the trend T2, claimed as typical of lamproites and orangeites (Mitchell, 1986, 1995); however, it should be noticed that there are many values intermediate between trends T1 and T2 (Fig. 5.11e)

5.6.5. Kelsey Lake kimberlite, USA

Groundmass spinels from a sample from the Kelsey Lake kimberlite have a complex zoning, with up to four zones of different composition (Fig. 5.12a). The spinels enclosed in olivine microphenocrysts (Fig. 5.12b) are euhedral and are similar in composition to the two first chromites, MCC and AMC.

The core of the groundmass spinel, consisting of an euhedral to subhedral MCC-type spinel, is slightly rounded suggesting processes of resorption and evolves to AMC following the trend H; on its turn, the AMC unit is overgrown and partly replaced by MUM spinels following the trend E. Finally, the spinel evolves to nearly pure magnetite, which makes a thin skeletal rim over the crystals (Fig. 5.12c-h).

5.6.6. Leningrad volcaniclastic kimberlite, Russia

Groundmass spinels from the Leningrad volcaniclastic kimberlite (Fig. 5.13a) have a complex zoning, although its composition varies within the MCC field. They evolve from relative Al-rich MCC to relatively Al-poor MCC, thus decreasing the Al contents following a trend parallel to the trend A. Finally, the spinel composition evolves back to a relatively Al-rich MCC by increasing the Al content, thus following a reverse trend parallel to the trend H. Therefore, this could be defined as an oscillatory trend A-H (Fig. 5.13b-g). MUM spinels have not been developed in this kimberlite.

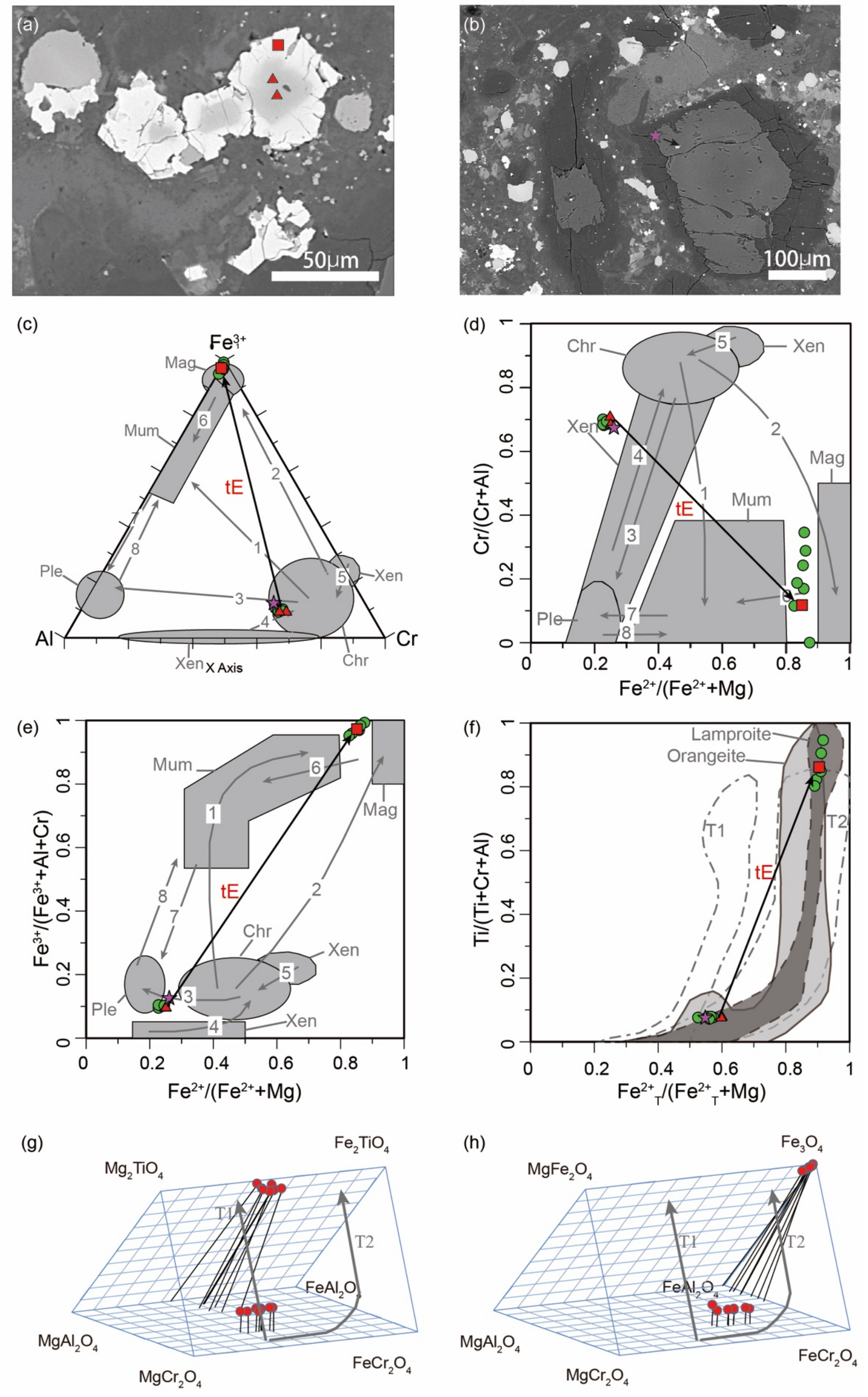

Fig. 5.10. (a-b) Examples of groundmass spinel zoning, with situation of the analysed points, BSE. Representation of compositions of primary spinels from DK1 Letlhakane kimberlite in the next diagrams: (c) Al-Cr-Fe^{3+}, (d) $Fe^{2+}/(Fe^{2+}+Mg)$ vs. Cr/(Cr+Al), (e) $Fe^{2+}/(Fe^{2+}+Mg)$ vs. $Fe^{3+}/(Fe^{3+}+Cr+Al)$ and (f) $Fe^{2+}{}_T/(Fe^{2+}{}_T+Mg)$ vs. Ti/(Ti+Cr+Al). Red symbols in (c-f) correspond to the points in (a,b) and green circles are the rest of primary spinels analysed in this kimberlite. Compositions of the spinels are also plotted in the reduced (g) and oxidized (h) spinel prisms. Compositional fields and trends from previous works are indicated in grey colour, (c-e) from Roeder and Schulze (2008), (f-h) from Mitchell (1986, 1995).

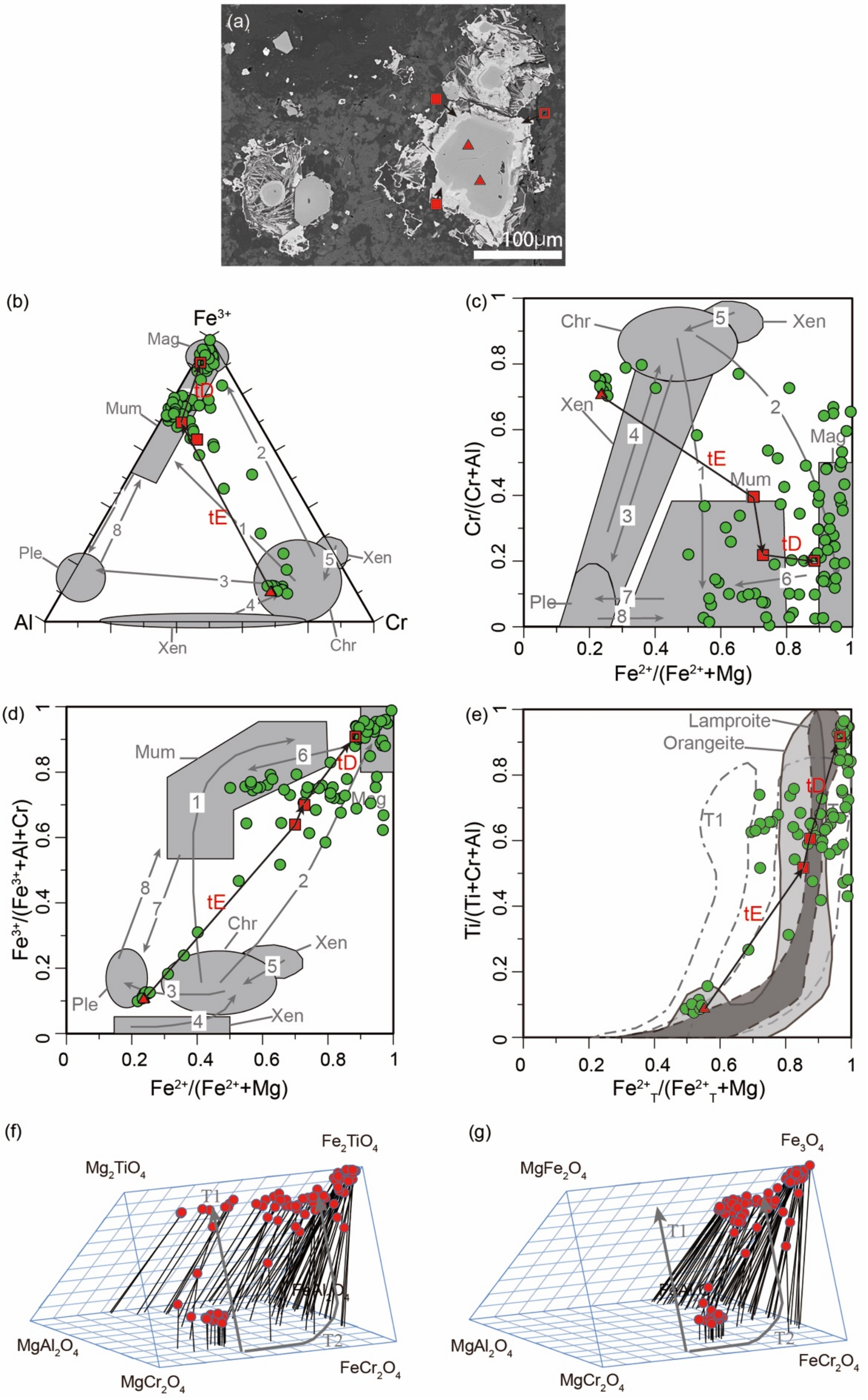

Fig. 5.11. (a) Examples of groundmass spinel zoning, with situation of the analysed points, in BSE. Representation of compositions of primary spinels from the CC-5 Chigicherla kimberlite in the following diagrams: (b) Al-Cr-Fe^{3+}, (c) $Fe^{2+}/(Fe^{2+}+Mg)$ vs. Cr/(Cr+Al), (d) $Fe^{2+}/(Fe^{2+}+Mg)$ vs. $Fe^{3+}/(Fe^{3+}+Cr+Al)$ and (e) $Fe^{2+}_T/(Fe^{2+}_T+Mg)$ vs. Ti/(Ti+Cr+Al). Red symbols in (b-e) correspond to the points in (a) and green circles are the rest of primary spinels analysed in this kimberlite. Compositions of the spinels are also plotted in the reduced (f) and oxidized (g) spinel prisms. Compositional fields and trends from previous works in grey colour, (b-d) from Roeder and Schulze (2008), (e-g) from Mitchell (1986, 1995).

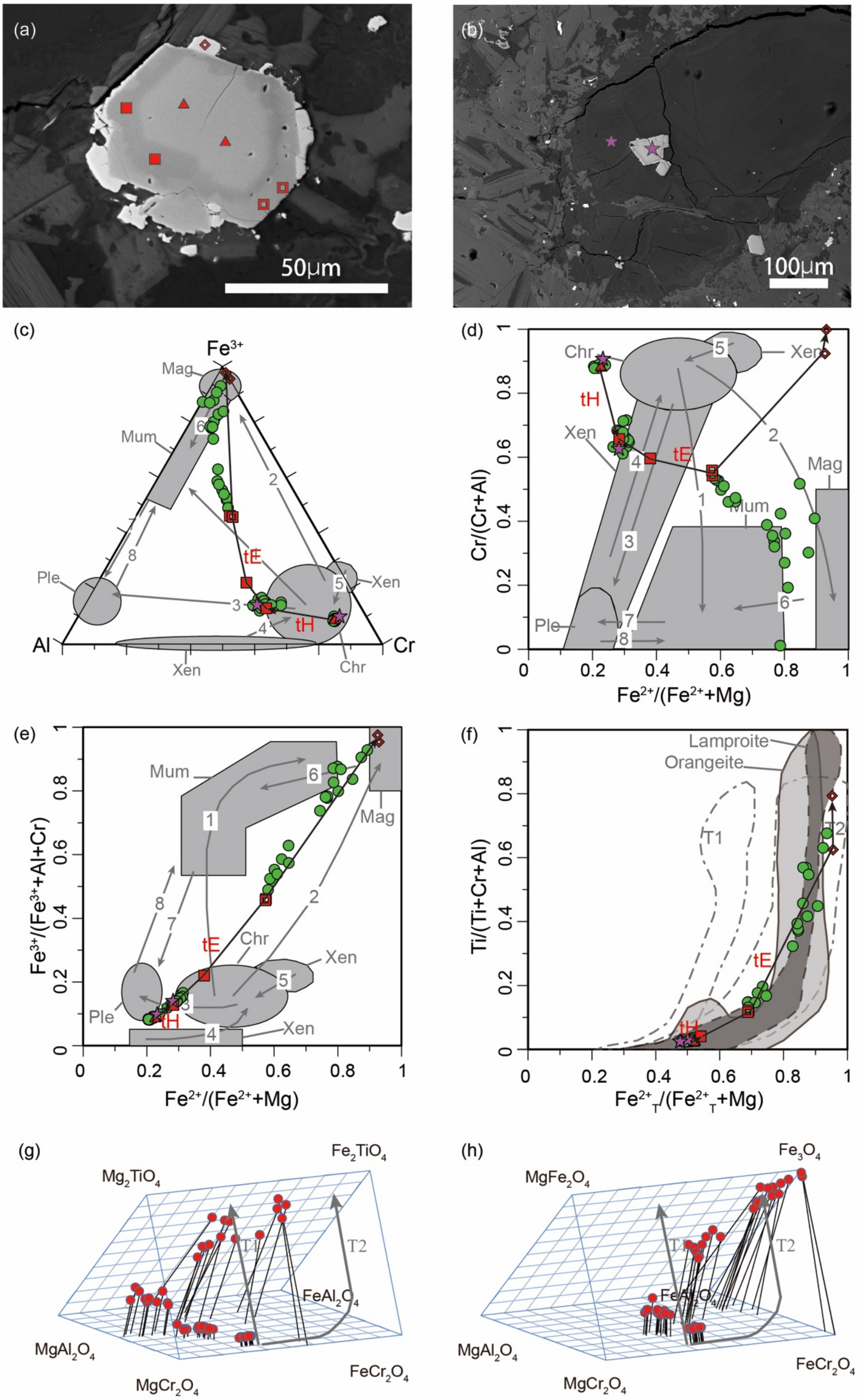

Fig. 5.12. (a-b) Examples of groundmass spinel zoning in BSE, with situation of the analysed points, from Kelsey Lake kimberlite. Representation of compositions of primary spinels from Kelsey Lake kimberlite in the following diagrams: (c) Al-Cr-Fe^{3+}, (d) $Fe^{2+}/(Fe^{2+}+Mg)$ vs. Cr/(Cr+Al), (e) $Fe^{2+}/(Fe^{2+}+Mg)$ vs. $Fe^{3+}/(Fe^{3+}+Cr+Al)$ and (f) $Fe^{2+}{}_T/(Fe^{2+}{}_T+Mg)$ vs. Ti/(Ti+Cr+Al). Red symbols in (c-f) correspond to the points in (a,b) and green circles are the rest of primary spinels analysed in this kimberlite; compositions of the spinels are also plotted in the reduced (g) and oxidized (h) spinel prisms. Compositional fields and trends from previous works are shaded in grey colour, (c-e) from Roeder and Schulze (2008), (f-h) from Mitchell (1986, 1995).

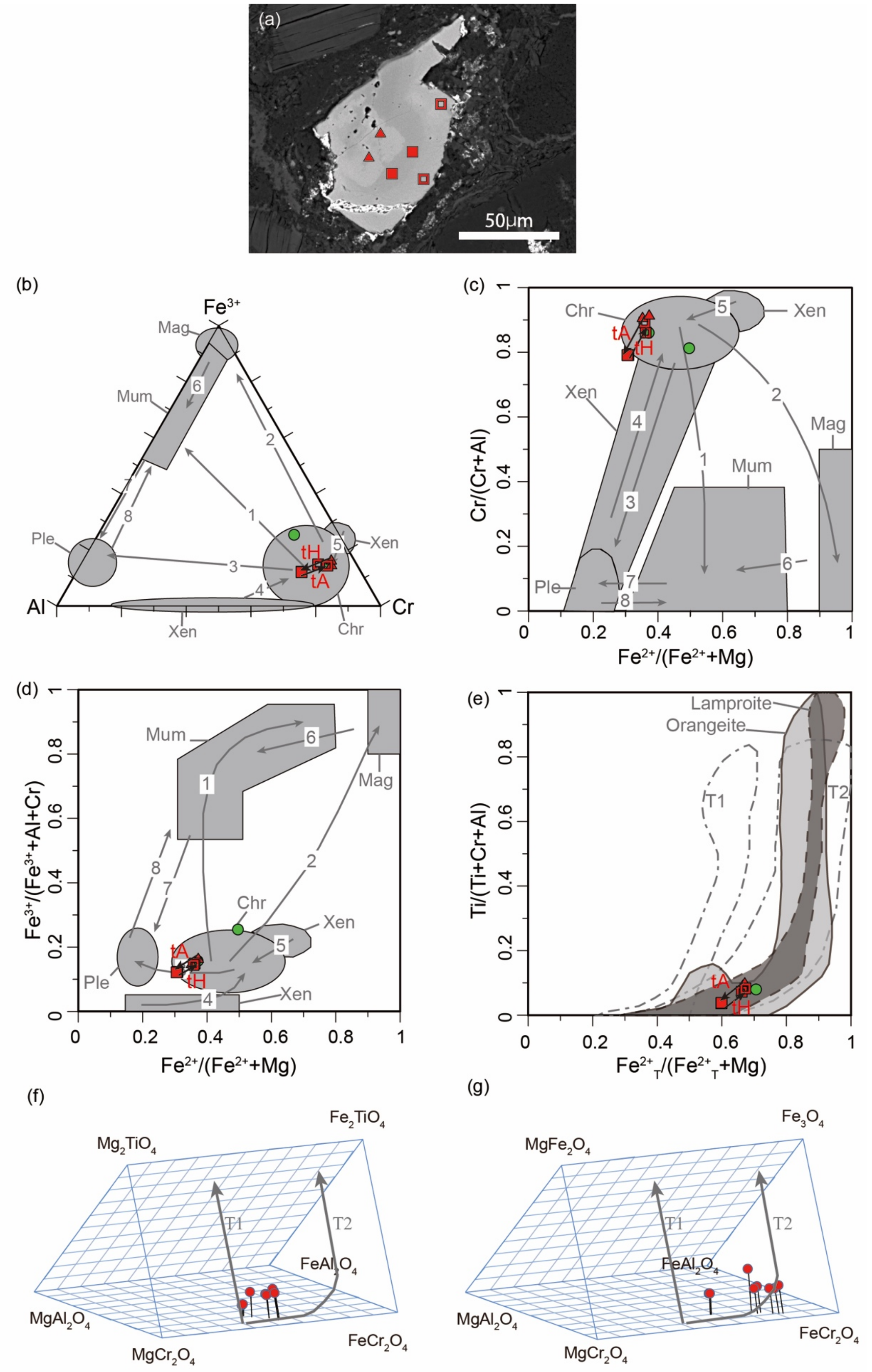

Fig. 5.13. (a) Examples of groundmass spinel zoning, with situation of the analysed points, in BSE. Representation of compositions of primary spinels from Leningrad volcaniclastic kimberlite in the next diagrams: (b) Al-Cr-Fe^{3+}, (c) Fe^{2+}/(Fe^{2+}+Mg) vs. Cr/(Cr+Al), (d) Fe^{2+}/(Fe^{2+}+Mg) vs. Fe^{3+}/(Fe^{3+}+Cr+Al) and (e) Fe$^{2+}_{T}$/(Fe$^{2+}_{T}$+Mg) vs. Ti/(Ti+Cr+Al). Red symbols in (b-e) correspond to the points in (a) and green circles are the rest of primary spinels analysed in this kimberlite; compositions of the spinels are also plotted in the reduced (f) and oxidized (g) spinel prisms. Compositional fields and trends from previous works are shadowed in grey colour, (b-d) from Roeder and Schulze (2008), (e-g) from Mitchell (1986, 1995).

5.6.7. Tchiuzo volcaniclastic kimberlite, Angola

Groundmass spinels studied in *Tchiuzo* volcaniclastic kimberlite are found as single euhedral crystals scattered in the groundmass, with an atoll texture (Fig. 5.14a-b) or as euhedral crystals included in altered olivine microphenocrysts (Fig. 5.14c).

Groundmass spinels have an euhedral core of AMC-type spinel mantled by MCC spinel, thus following the trend A, by decreasing the Al content. MCC then evolves to MUM spinels following the trend B, by showing an increasing of Ti at nearly constant $Fe^{2+}/(Fe^{2+}+Mg)$ ratios. Finally, they present a slight increase of Fe^{3+} at high Ti (trend D) (Fig. 5.14d-i).

Compositions of the chromite inclusions in altered olivine plot close to those from the core of groundmass crystals, i.e., AMC-type. In addition, they also display the trend B, which is clearly distinguishable in the reduced prism and in the $Fe^{2+}{}_T/(Fe^{2+}{}_T+Mg)$ vs. Ti/(Ti+Cr+Al) diagram.

5.6.8. Jackson Inlet kimberlite, Canada

Groundmass spinels from *Jackson Inlet* kimberlite (Fig. 5.15a-h) have also a complex zoning. A core of relatively Al-rich euhedral MCC evolves to Al-poor euhedral MCC parallel to trend A.

Chromite inclusions in fresh olivine (Fig. 5.15b) have similar composition to the MCC core of the groundmass spinel.

The MCC zones are on its turn mantled (without replacement) by a zoned rim of euhedral MUM spinels (Fig. 5.15a) following firstly a trend parallel to the trend C and then changing to be parallel to the trend B. Finally, MUM spinels are mantled by a rim of of the UMS spinel which implies an increasing of Al content following the trend F.

The most of crystals from this chromite suite follow the T1 kimberlitic trend (Fig. 5.15f-h) in the classical diagram $Fe^{2+}{}_T/(Fe^{2+}{}_T+Mg)$ vs. Ti/(Ti+Cr+Al) (Mitchell, 1986).

5.6.9. Shengli kimberlite, China

Groundmass spinels from Shengli kimberlite (Fig. 5.16) have a complex zoning. An euhedral core, made up of MCC, is surrounded by AMC-MCC, thus revealing an increasing Al content following trend H. The AMC-MCC unit evolves later back to MCC by decreasing Al content, following the A trend. Finally, this zoned chromite core is mantled by MUM spinels following trend C.

Chromite inclusions in altered olivine have the same compositions of AMC and MCC found in the groundmass chromite.

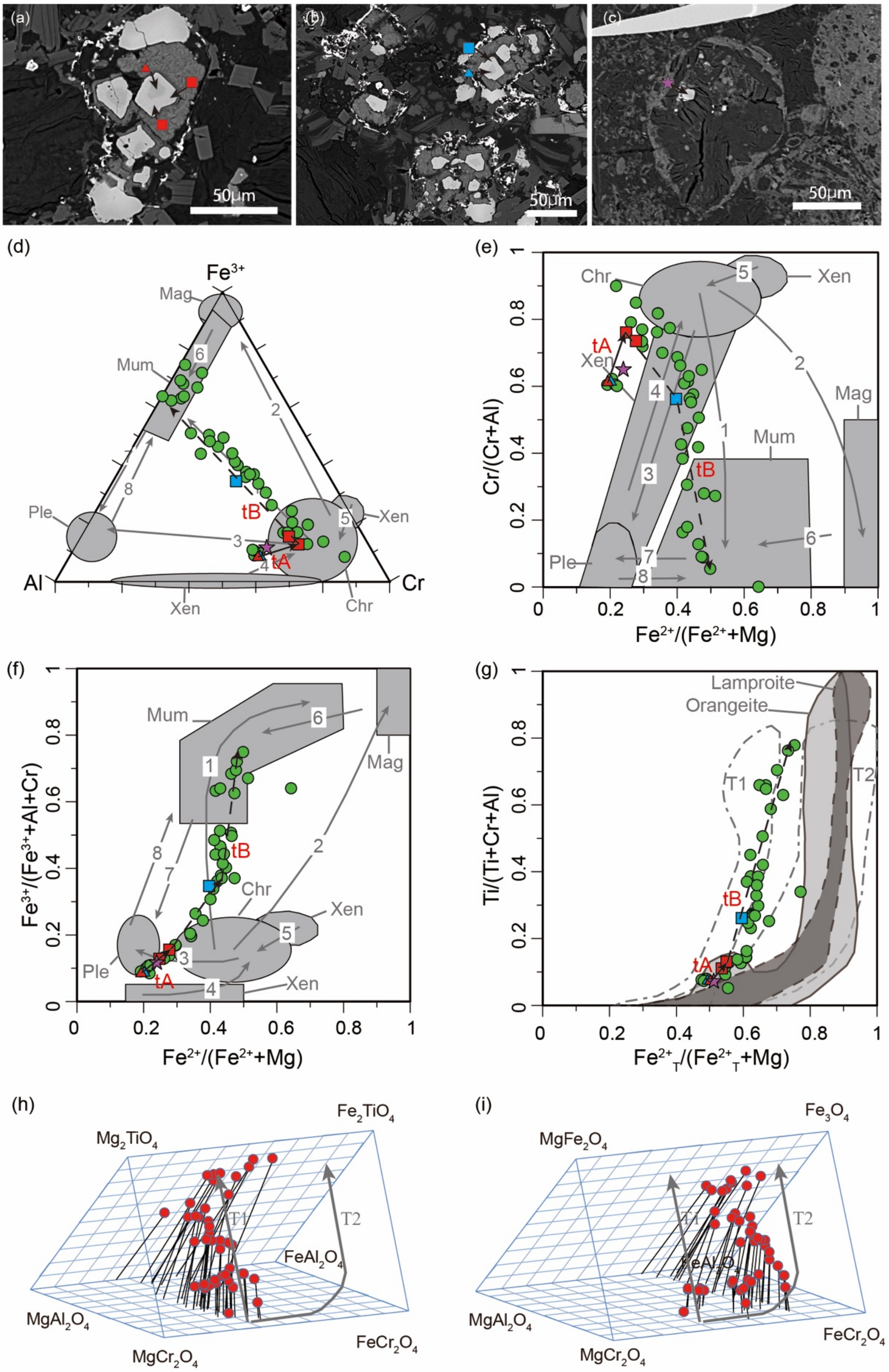

Fig. 5.14. (a-c) Examples of groundmass spinel zoning, with situation of the analysed points, BSE. Representation of compositions of primary spinels from Tchiuzo volcaniclastic kimberlite in (d) Al-Cr-Fe^{3+}, (e) $Fe^{2+}/(Fe^{2+}+Mg)$ vs. $Cr/(Cr+Al)$, (f) $Fe^{2+}/(Fe^{2+}+Mg)$ vs. $Fe^{3+}/(Fe^{3+}+Cr+Al)$ and (g) $Fe^{2+}{}_T/(Fe^{2+}{}_T+Mg)$ vs. $Ti/(Ti+Cr+Al)$. Red and blue symbols in (d-g) correspond to the points in (a-c) and green circles are the rest of primary spinels analysed in this kimberlite; compositions of the spinels are also plotted in the reduced (h) and oxidized (i) spinel prisms. Compositional fields and trends from previous works in grey colour, (d-g) from Roeder and Schulze (2008), (g-i) from Mitchell (1986, 1995).

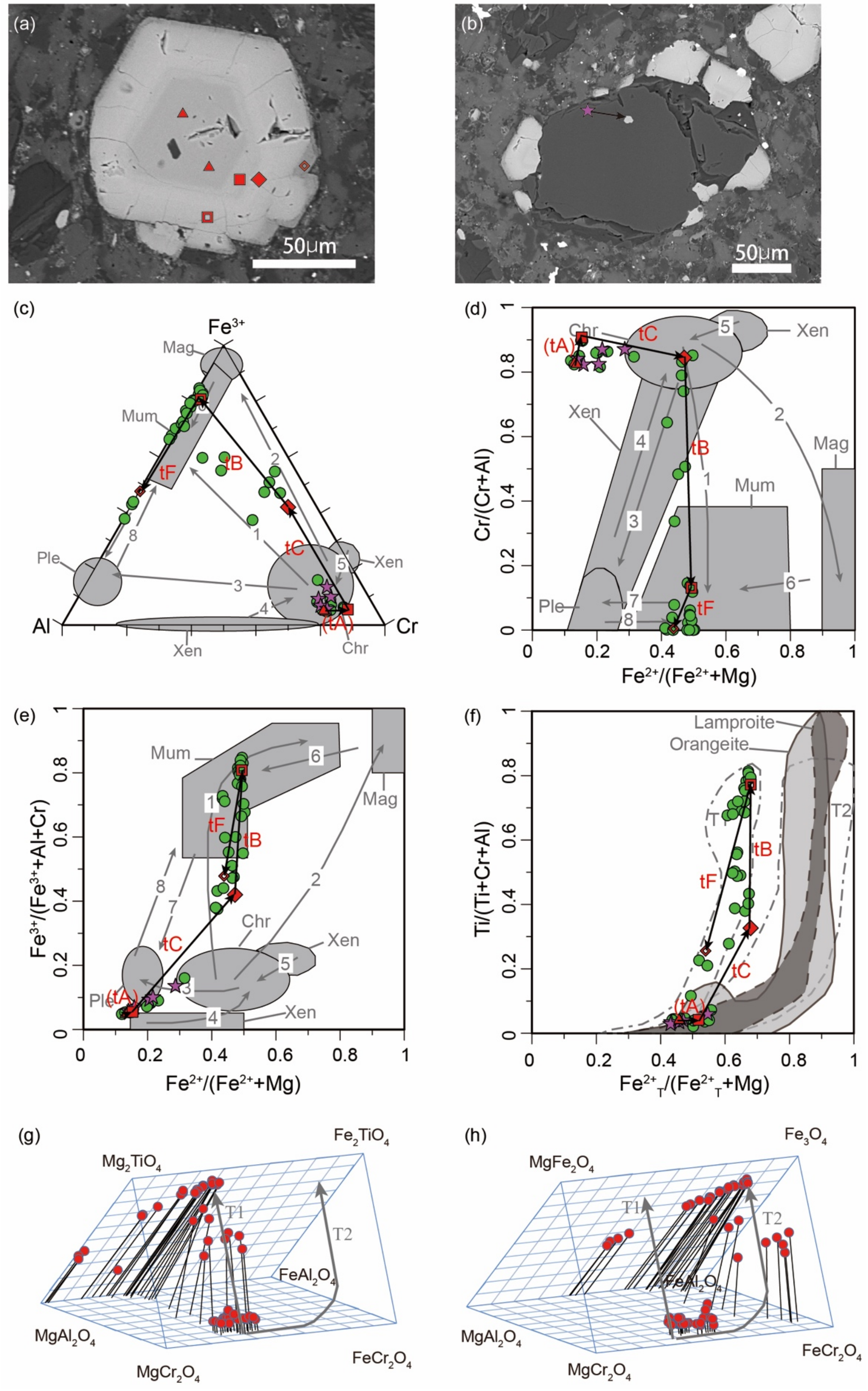

Fig. 5.15. (a-b) Examples of groundmass spinel zoning, with situation of the analysed points, in BSE. Representation of compositions of the primary spinels from Jackson Inlet kimberlite in the next diagrams: (c) Al-Cr-Fe^{3+}, (d) $Fe^{2+}/(Fe^{2+}+Mg)$ vs. Cr/(Cr+Al), (e) $Fe^{2+}/(Fe^{2+}+Mg)$ vs. $Fe^{3+}/(Fe^{3+}+Cr+Al)$ and (f) $Fe^{2+}{}_T/(Fe^{2+}{}_T+Mg)$ vs. Ti/(Ti+Cr+Al). Red symbols in(c-f) correspond to the points in (a-b) and green circles are the rest of primary spinels analysed in this kimberlite; compositions of the spinels are also plotted in the reduced (g) and oxidized (h) spinel prisms. Compositional fields and trends from previous works are shadowed in grey colour, (c-e) from Roeder and Schulze (2008) (f-h) from Mitchell (1986, 1995).

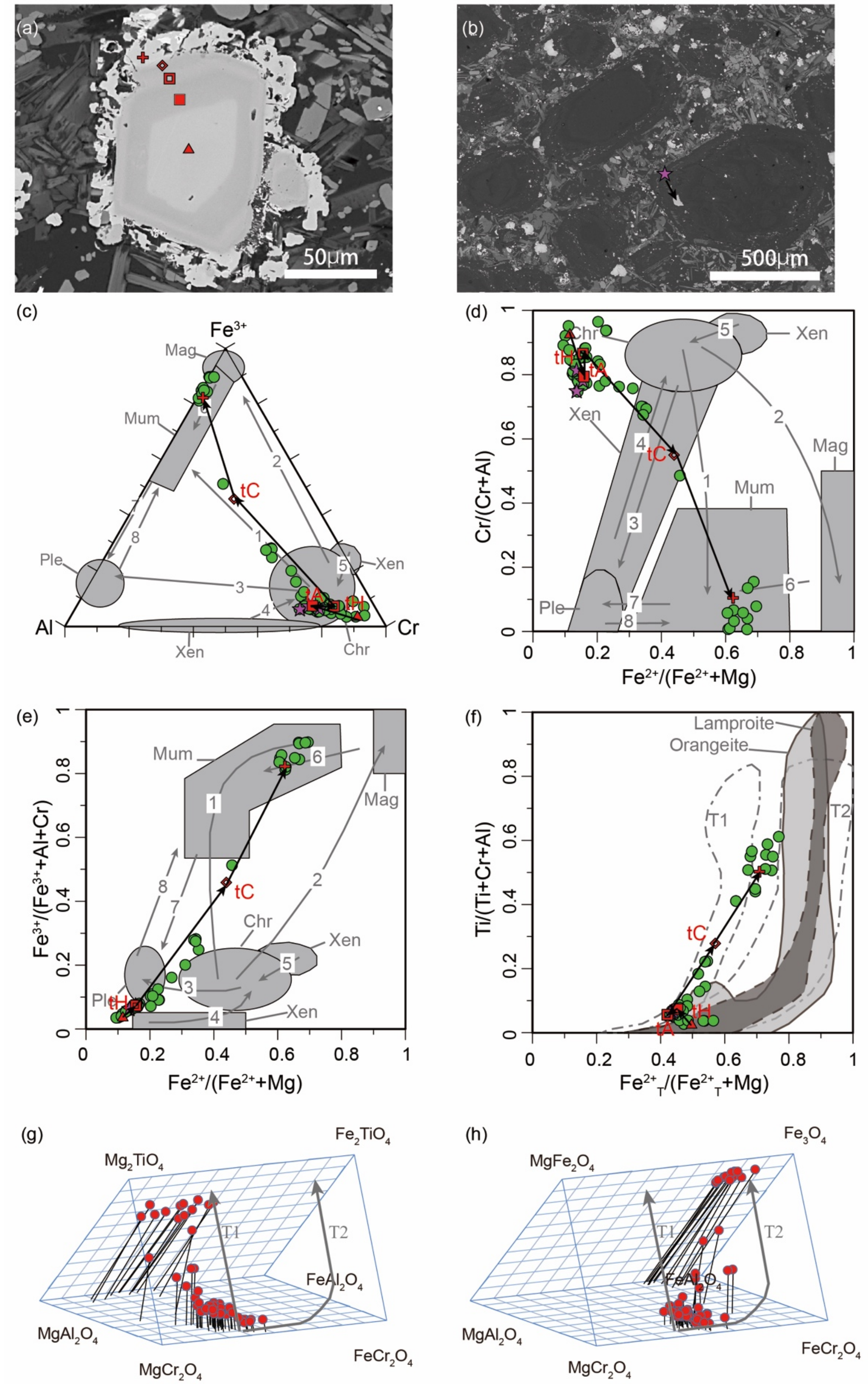

Fig. 5.16. (a-b) Examples of groundmass spinel zoning, with situation of the analysed points, in BSE. Representation of compositions of primary spinels from Shengli kimberlite in (c) Al-Cr-Fe^{3+}, (d) $Fe^{2+}/(Fe^{2+}+Mg)$ vs. Cr/(Cr+Al), (e) $Fe^{2+}/(Fe^{2+}+Mg)$ vs. $Fe^{3+}/(Fe^{3+}+Cr+Al)$ and (f) $Fe^{2+}{}_T/(Fe^{2+}{}_T+Mg)$ vs. Ti/(Ti+Cr+Al). Red symbols in (c-f) correspond to the points in (a,b) and green circles are the rest of primary spinels analysed in this kimberlite; compositions of the spinels are also plotted in the reduced (g) and oxidized (h) spinel prisms. Compositional fields and trends from previous works in grey colour, (c-e) from Roeder and Schulze (2008), (f-h) from Mitchell (1986, 1995).

5.6.10. Menominee kimberlite, USA

The spinel-group minerals of the Menominee kimberlite are very different when compared to the rest of studied kimberlites. Two different groundmass spinels occur in the Menominee coherent kimberlite (Fig. 5.17), with compositions of spinel sensu strictu (Sp) and qandilite (Qan). Both spinels occur in similar proportions and are very abundant in the groundmass. These spinels do not show overgrowths of one by the other, and the textural patterns suggest that they crystallized simultaneously.

The Al-Mg-rich spinel (Sp) may be found commonly as euhedral to subhedral groundmass mineral (Fig. 5.17a-b), but it is also found as small inclusions in fresh olivine, together with geikielite (Fig. 5.17c), thus indicating that it is a groundmass mineral. It is pseudomorphized by fine-grained meixnerite aggregates ($Mg_6Al_2(OH)_{18}\cdot4H_2O$) at the crystal rims.

Another groundmass spinel is euhedral MUM spinel. It can be found as euhedral crystals scattered across the groundmass or replacing geikielite xenocrysts; in the last case, the spinel is enriched in Mg and approaches towards the qandilite component (Mg up to 1.26 apfu) following the trend G. This trend G has been found only in the Lake Ellen and in the Menominee kimberlite. In the case of the euhedral MUM in the groundmass, they increases its Mg content towards the border of the crystal, but the most external Mg-rich MUM is too thin to allow obtaining accurate microprobe analysis.

The simultaneous occurrence of two types of spinels suggests the existence of two separate magmas (magma mingling) in this kimberlite.

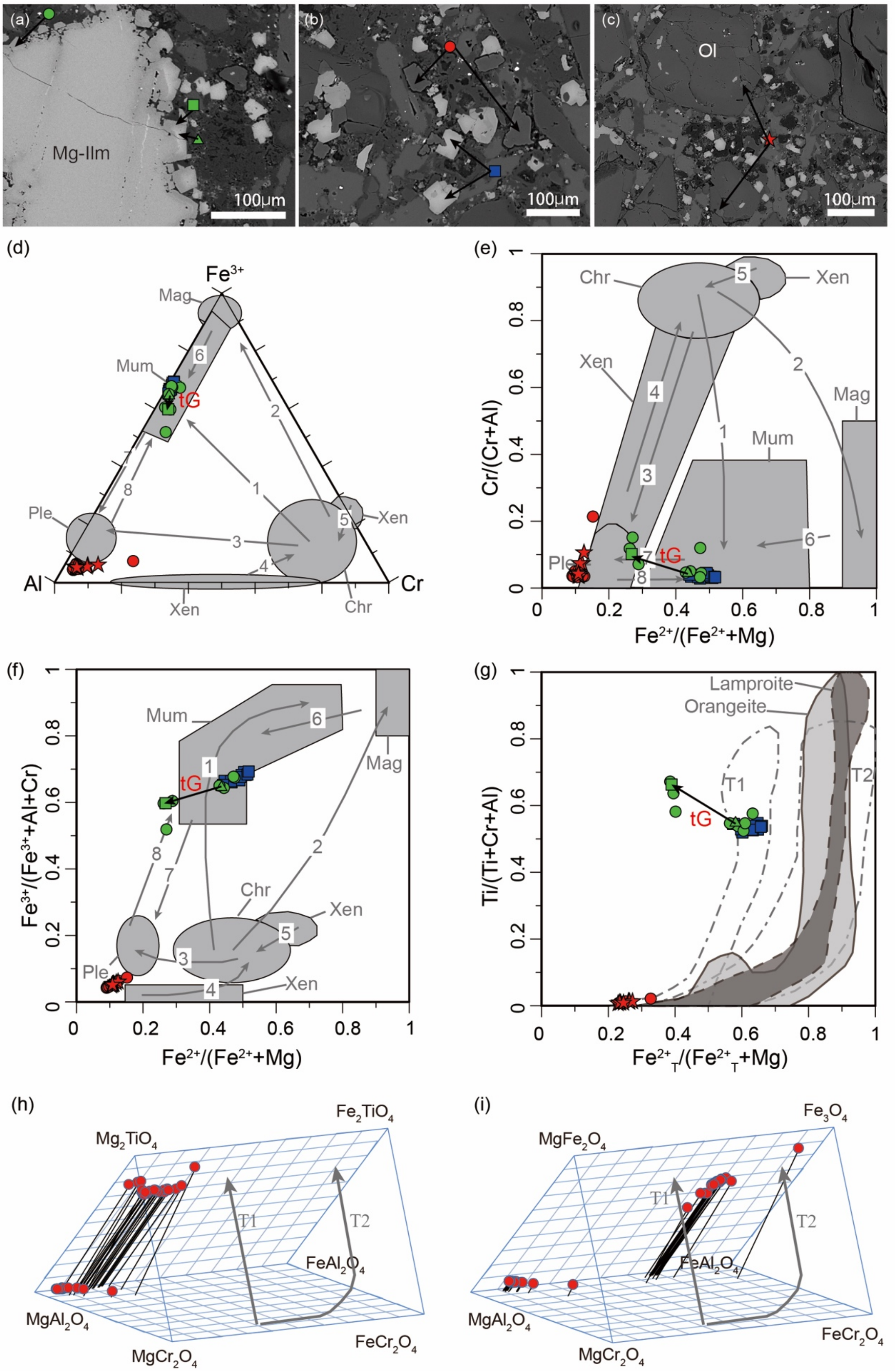

Fig.5.17. (a-c) Examples of groundmass spinel zoning, with the situation of the analysed points, in BSE. Representation of compositions of primary spinels from Menominee in the following diagrams: (d) Al-Cr-Fe^{3+}, (e) $Fe^{2+}/(Fe^{2+}+Mg)$ vs. Cr/(Cr+Al), (f) $Fe^{2+}/(Fe^{2+}+Mg)$ vs. $Fe^{3+}/(Fe^{3+}+Cr+Al)$ and (g) $Fe^{2+}{}_T/(Fe^{2+}{}_T+Mg)$ vs. Ti/(Ti+Cr+Al). Red symbols in (d-g) correspond to the points in (a-c) and green circles are the rest of primary spinels analysed in this kimberlite; compositions of the spinels are also plotted in the reduced (h) and oxidized (i) spinel prisms. Compositional fields and trends from previous works are shaded in grey colour, (d-f) from Roeder and Schulze (2008), (g-i) from Mitchell (1986, 1995).

5.7. SPINEL GEOTHERMOMETER

Composition of the spinels found as inclusions in fresh olivine, combined with the composition of host olivine, could be used as a geothermometer (Table 5.4). The majority of temperatures calculated for spinel inclusions in olivine by using the olivine-spinel geothermometer method of (Roeder *et al.*, 1979) are between 650 and 1000ºC (Table 5.4). Anomalously high temperatures are obtained in Jackson inlet and Menominee when compared with those obtained with the olivine-ilmenite pair. Good consistent temperatures are calculated in the Ak6 Karowe kimberlite by using the olivine-spinel and olivine-ilmenite geothermometers, returning values about 830ºC. Moreover, temperatures calculated by spinel and ilmenite are not consistent in Menominee kimberlite where spinel and ilmenite are in contact together as inclusion in olivine.

Table 5.4: Temperature calculated for spinel inclusion in olivine using the olivine-spinel geothermometer method of Roeder *et al.* (1979). Temperature calculated by using the olivine-ilmenite pair is explained in chapter 6.

			Spinel					Olivine		TºC	TºC by Olivine-Ilmenite
No.			XCr	XAl	XFe^{3+}	XMg	XFe	XMg	XFe		
1	8025	P2 lamproite, India	0.239	0.256	0.505	0.523	0.477	0.912	0.088	729	
2	9352	Menominee,USA	0.045	0.906	0.050	0.805	0.195	0.904	0.096	1118	800
3	9352	Menominee,USA	0.035	0.911	0.055	0.852	0.148	0.904	0.096	1638	800
4	9353	Notre Dâme du Nord, Canada	0.675	0.284	0.041	0.521	0.479	0.904	0.096	734	800
5	10049	South pipe of AK6 Karowe, Botswana	0.580	0.310	0.110	0.526	0.474	0.918	0.082	658	830
6	10049	South pipe of AK6 Karowe, Botswana	0.570	0.322	0.107	0.525	0.475	0.883	0.117	827	830
7	9607	P200, Lesotho	0.590	0.285	0.125	0.538	0.462	0.899	0.101	795	817
8	9607	P201, Lesotho	0.485	0.360	0.155	0.526	0.474	0.873	0.127	864	
9	9607	P202, Lesotho	0.489	0.364	0.148	0.507	0.493	0.872	0.128	822	
10	9607	P203, Lesotho	0.487	0.343	0.170	0.532	0.468	0.860	0.140	975	
11	9607	P204, Lesotho	0.467	0.375	0.158	0.543	0.457	0.856	0.144	1000	
12	9607	P205, Lesotho	0.481	0.375	0.145	0.513	0.487	0.868	0.132	850	
13	9360	Jackson inlet, Canada	0.766	0.166	0.068	0.635	0.365	0.864	0.136	1414	

$XCr=Cr/(Cr+Al+Fe^{3+})$; $Xal=Al/(Al+Fe^{3+}+Cr)$;$XFe^{3+}=Fe^{3+}/(Fe^{3+}+Cr+Al)$; $XMg=(Mg/(Mg+Fe^{2+})$;$XFe=Fe^{2+}/(Fe^{2+}+Mg)$

5.8. SPINEL IN XENOLITHS

Use of spinel from xenoliths in diamond exploration is a well-proven common technique.

Spinels in basaltic xenoliths have compositions in the UM domain but close to magnetite (Fig. 5.18), whereas spinels in granitic xenoliths are nearly purely magnetite.

The compositions of spinels in the studied MARID xenoliths are mainly MCC and have minor molecular proportion of AMC (Fig. 5.18).

Spinels in the studied peridotitic xenoliths correspond mainly to AMC and spinel s.s.. In comparison, generally, spinels from MARID xenoliths have higher Cr/(Cr+Al) values, while in peridotitic xenoliths spinels have higher Al contents, higher $Fe^{2+}/(Fe^{2+}+Mg)$ ratios and higher $Fe^{3+}/(Fe^{3+}+Al+Cr)$ values (Fig. 5.18). The highest Cr contents of spinel are found in MARID xenoliths (up to 1.7 apfu Cr), while the highest Al contents (0.5-1.4 apfu Al) are found in peridotitic xenoliths.

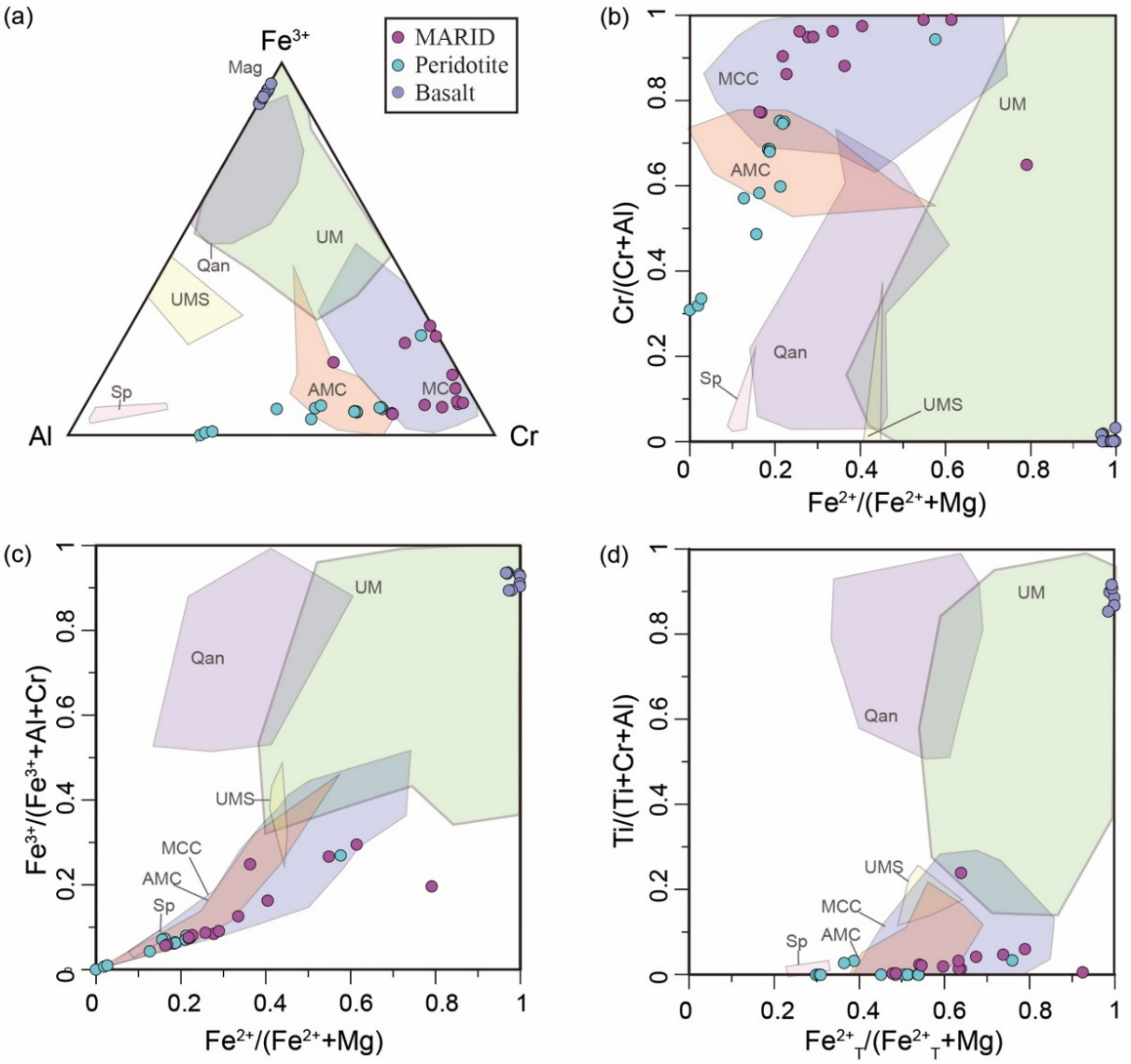

Fig. 5.18. Compositions of spinels in xenoliths of MARID, peridotites and basalts in (a) A-Cr-Fe^{3+}, (b) $Fe^{2+}/(Fe^{2+}+Mg)$ vs. $Cr/(Cr+Al)$, (c) $Fe^{2+}/(Fe^{2+}+Mg)$ vs. $Fe^{3+}/(Fe^{3+}+Cr+Al)$ and (d) $Fe^{2+}{}_T/(Fe^{2+}{}_T+Mg)$ vs. $Ti/(Ti+Cr+Al)$ plot.

5.9. DISCUSSION

Spinel is commonly one of the principal kimberlite groundmass constituents and its composition and evolution is proposed as a key for the rock classification between kimberlite and related rocks (Mitchell, 1995; Tappe *et al.*, 2005). Moreover, the different compositions of primary spinel could provide information on the different melt compositions. In addition, the compositional evolution of spinel may be useful to understand the kimberlite evolution, and even possibly to reveal the conditions that influence the diamond preservation (Roeder and Schulze, 2008).

However, spinels do not occur in all the studied kimberlite samples. At least in Cucumbi field (Angola) and Tassewell (Tennessee, USA) the studied kimberlite samples do not contain spinels. However, these samples correspond to volcaniclastic kimberlites and a possible explanation can be that these samples are too much contaminated with crustal components, or perhaps that the spinels become weathered.

Normally, primary spinels crystallize in two general different stages. The first spinel crystallized from magma occurs as small (25-100μm) euhedral octahedral crystals, in many cases as chromite (but not in all of the cases), and could be crystallized between the source of kimberlite and the Earth surface (Roeder and Schulze, 2008). These spinels are found as core of groundmass spinel and also as inclusions in olivine. Hence, these spinels are one of the early crystallized minerals in kimberlite and are contemporary to olivine microphenocrysts.

Rim of groundmass spinels mantles the spinel cores, and is MUM in majority cases. However, MUM spinels can also be found as cores. MUM spinels may be found as a rim in groundmass spinels, but also together with perovskite as a rim replacing other oxides (eg. chromite and ilmenite). MUM spinels crystallize in a later stage, contemporary to perovskite, but before the groundmass phlogopite.

Morphological and compositional variations in the primary spinel in a single kimberlite could be result of a rapid thermal and pressure change (Roeder and Schulze, 2008). The existing different trends have been attributed to differences in cooling rate and combination of factors such as immiscibility, rapid growth, different melt composition and local nucleation of other phases (Roeder and Schulze, 2008).

The large problem when studying the evolution of the spinel compositions is that the available diagrams do not show all the possible components, and this can lead to misinterpretations. Therefore, we intended to construct a diagram in which end members of the spinel group could plot in different positions. Following the criteria of Pasteris (1984), in the X axis we did not use ratios, although the use of ratios was imperative in the axis Y to show the variations of Mg and Fe^{2+}. The results are presented in the Fig. 5.19.

5.9.1. Spinel core

Spinel core in the groundmass of the studied rocks is found as chromite (AMC or MCC), UM, qandilite-rich spinel or spinel s.s. The first spinel, as AMC or MCC, may indicate that the early melt had different composition, which should be relatively Al-rich or Al-poor respectively. In fact, some kimberlites may have spinel s.s. as the early phase, as in Menominee, although that this is very rare. We will discuss the meaning of each type of spinel. We have used to represent these compositions (Fig. 5.20) in the same diagram of Fig. 5.19.

Chromite

Chromite has been considered as an important petrogenetic indicator in ultramafic to mafic rocks (i.e, the classical publications from Irvine 1965, 1967). Chromite may be found as inclusions in diamonds, and these chromites are strongly enriched in Cr (Barnes and Roeder, 2001). However, the attempting to relate the compositions of the groundmass chromite with the diamond content is failed (ie., Barnes and Roeder, 2001).

Chromite is one of the first crystallized groundmass mineral (contemporaneous with olivine) in many kimberlites, but not in all of them. In spite Griffin *et al.* (1994) propose that both groups AMC and MCC are primary, Minin *et al.* (2011) suggest that the spinels of AMC composition can be restitic (xenocrystic) and those of MCC primary. But they do not provide textural evidences because they use concentrates obtained by crushing the rock. However, we found both types of spinels as inclusions in olivine rims, and olivine rims may also contain spinel s.s. inclusions. Moreover, they tend to be euhedral. Therefore, we suggest them as primary.

The early chromite core of groundmass spinel has two distinct compositions based on their Al content: AMC (Al-rich) and MCC (Al-poor). There are three different possibilities (Table 5.2). MCC is the unique chromite in most of the studied kimberlites or orangeites, lamproites and ultramafic lamprophyres. However, AMC may be the only early spinel in many kimberlites, as in Lethakane (CK, Botswana), Chicken Park Colorado, USA), Murfreesboro (a lamproite, Arkansas, USA), or Mulligripally (India). In other cases, both types of chromites are found, as in Tchiuzo, (VK, Angola), Jwaneng (VK, Botswana), Karowe (CK, Botswana), Riverton (CK, South Africa), Ville-Marie (VK, Quebec, Canada), Pointe Lake (CK, Canada), Sloan 2 (CK, Colorado, USA), Kelsey Lake (CK, Colorado, USA), Gate Adah (CK, Pennsylvania, USA), Lomonosovskaya (CK, NR, Russia) and Pobeda (CK, Yakutia, Russia). When existing jointly both chromites, the Z contrast in back-scattered electron (BSE) imaging is suitable to enhance the differences of zoning between AMC and MCC (Fig. 5.11a, 5.13a-b, 5.15a).

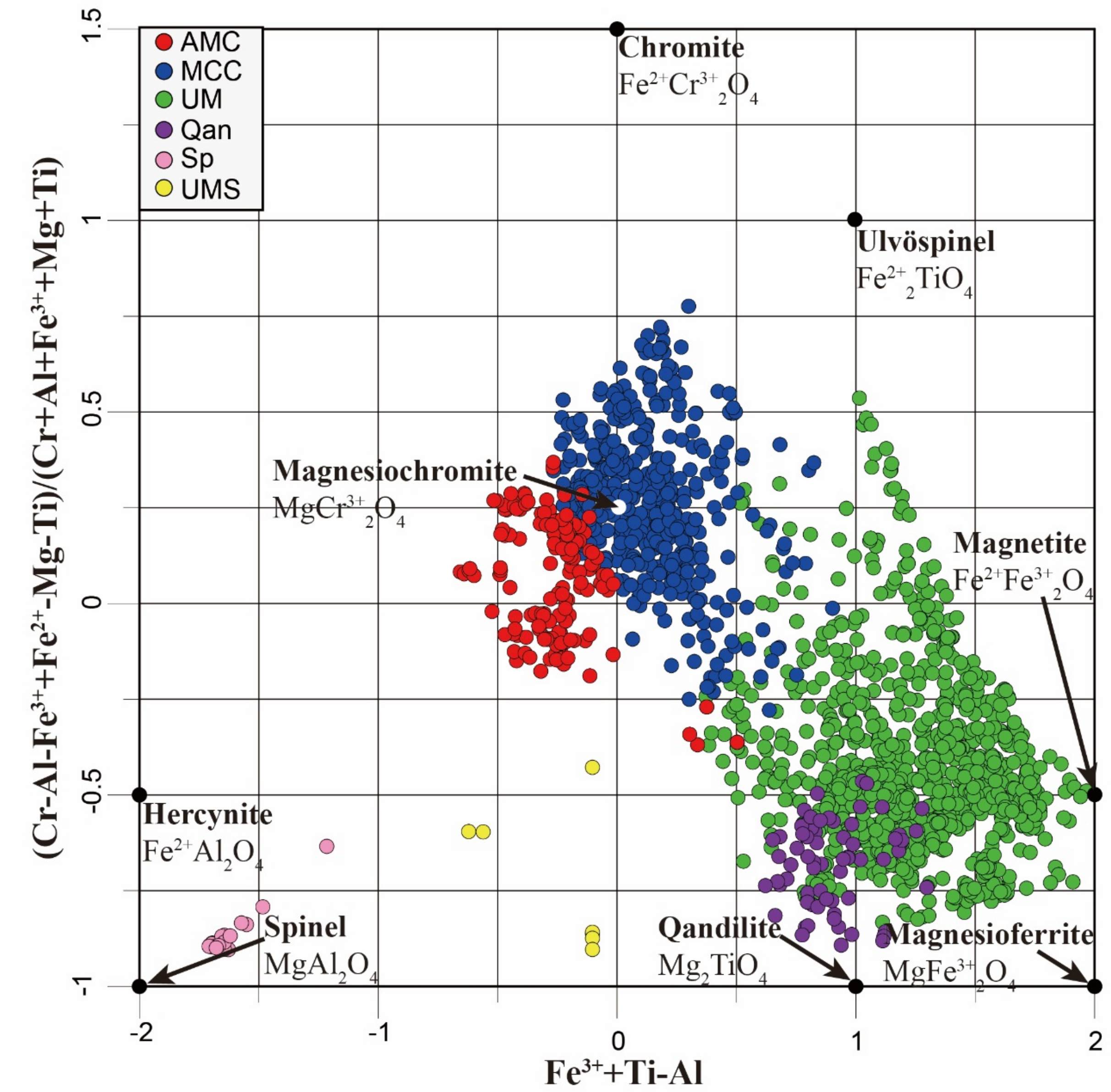

Fig. 5.19. Representation of the compositions of the analysed spinels from the studied kimberlites in the graphic (Fe^{3+}+Ti-Al) vs (Cr-Al-Fe^{3+}-Mg-Ti+Fe^{2+})/(Cr+Al+Fe^{3+}+Ti+Mg). The position of the end members is also indicated.

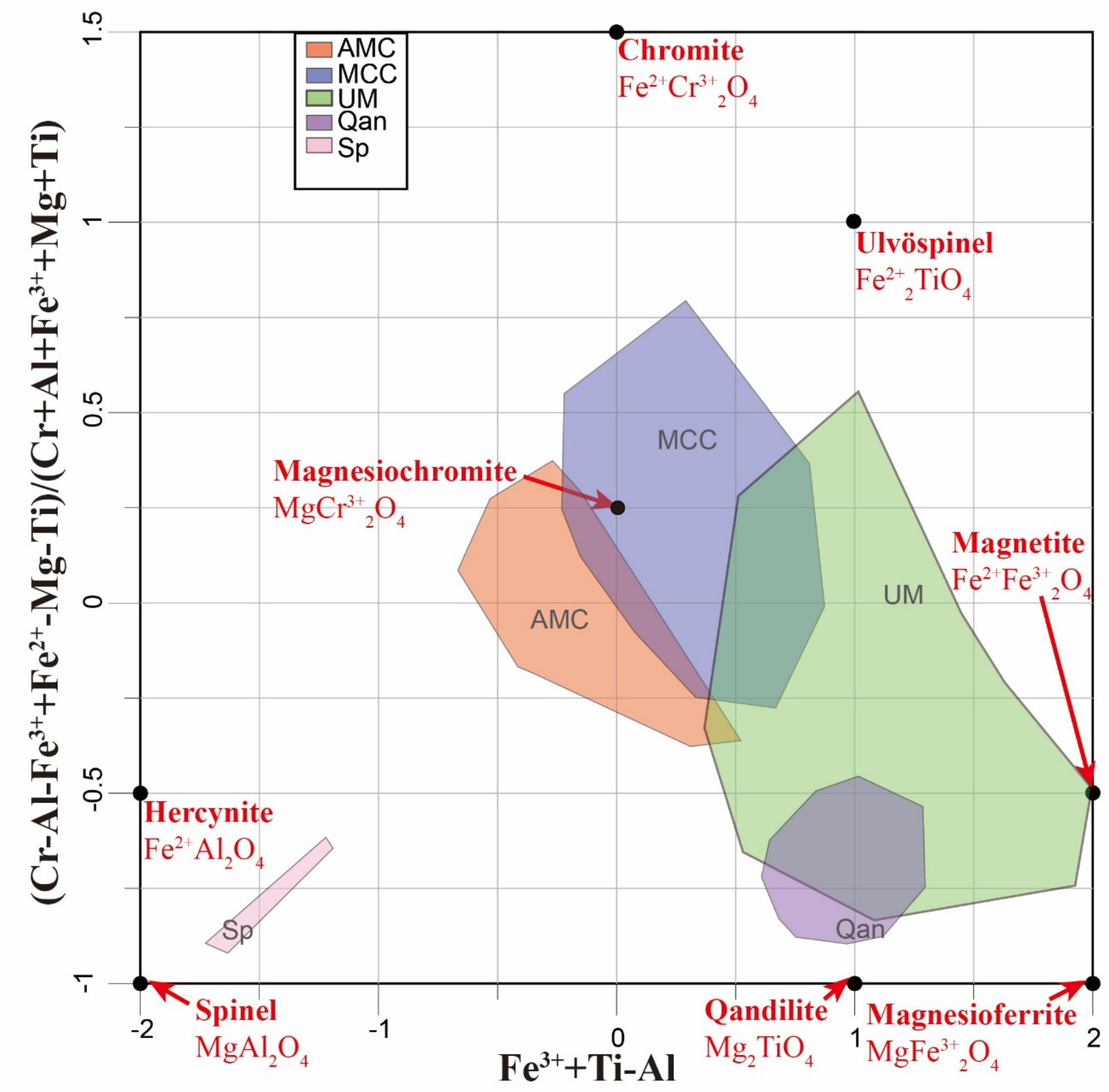

Fig. 5.20. Representation of the compositional domains of the analysed primary spinels (cores) from the 79 studied kimberlites in the graphic (Fe^{3+}+Ti-Al) vs (Cr-Al-Fe^{3+}-Mg-Ti+Fe^{2+})/(Cr+Al+Fe^{3+}+Ti+Mg). The position of the end members is also indicated.

Therefore, respect to the six spinel composition field proposed by Roeder and Schulze (2008), a primary groundmass chromite core AMC field, which is Al-rich chromite (Al > 0.4 apfu) has been added in this work (Fig. 5.5-5.7). AMC fall out of the primary chromite field determined by Roeder and Schulze (2008). AMC is found commonly as small euhedral octahedra crystal as the core of groundmass spinel. This AMC is, in many cases (eg. Tchiuzo), the first chromite crystallized from the kimberlite magma. Moreover, many of our MCC data plot out of the compositional field determined by Roeder and Schulze (2008) in the binary diagram $Fe^{2+}/(Fe^{2+}+Mg)$ vs.Cr/(Cr+Al) to define the domain of groundmass chromite (eg. Fig. 5.8, 5.12, 5.14 and 5.16). Therefore, MCC chromite field has been redrawn accordingly to our data (Fig. 5.1.7).

The lack of chromite core in some kimberlites is an interesting problem. It can be explained by several possibilities: a) redissolution of the early formed chromite before the precipitation of other spinels; b) non-precipitation because the melt was impoverished in Cr. Other authors believe that the chromite core may be present, but should be too small and hard to be observed (Nielsen *et al.*, 2009). However, we can rule out this possibility, because in our study we used SEM images working at high magnification and contrast, and under these conditions chromite is easily distinguished from other spinels. The possibility of dissolution of chromite could be feasible, and experimental data could give support to this hypothesis (Fedortchouk and McIsaac, 2013), but there are no evidences of redistribution of the Cr between the following minerals in the sequence. Therefore, we considered that the composition of the early spinel is in all the cases controlled by the composition of the magma.

MUM

On the other hand, as indicated, chromite or spinel s.s. are lacking in many kimberlites, and many of them are important diamond-producing mines. Groundmass spinel is consist of only MUM (lake of chromite core) is found in many kimberlites and related rocks, as Cacuilo (CK, in Angola), Damtshaa (VK, in Botswana), Karowe (CK, in Botswana), Helam (coherent, an orangeite after Hammond and Mitchell, 2002, in Kimberley, South Africa), Monastery (CK, South Africa), Kaalvallei (coherent, lamproite, South Africa), Somerset island (CK, NWT, Canada), Lake Ellen (VK, Michigan), Alhambra (VK, Colorado, USA), Guaniamo (CK, Venezuela), Obnazonnaya (VK, Yakutia, Russia), Siddanpalli SK2 (CK, India), Kalyandur KL4 (CK, India). These representing about the 16% of the studied occurrences. Many of these rocks are coherent, and in many cases the lack of chromite cannot be attributed to a subsolidus alteration, because the rock is reasonably fresh.

One must take into account, however, that chromite can be present in other nearby kimberlites of the same district, and therefore the composition of the spinel is not a criteria to distinguish districts. Hence, the question is how to explain the composition of spinel changes in kimberlites that can be formed in the same geodynamic context and form part of the same suite of magmas. The absence of groundmass chromite (coupled with the alternative occurrence of MUM spinels) has been explained as due to an extreme development of the T1 trend in highly evolved calcite kimberlites (Mitchell, 1986). An alternative explanation could be that the chromite has a fine-grained size compared with that of MUM spinel, which should be a growth feature and not a result of resorption of the chromite (Roeder and Schulze, 2008). However, there is no other groundmass mineral that could be another host for Cr: phlogopite uses to be Cr-poor, perovskite does not contains Cr and this element is lacking in the late ilmenites. Therefore, the presence or absence of chromite in groundmass should indicate different magma compositions, which could be relatively Cr-rich or Cr-poor respectively.

Conversely, the absence of MUM spinels and the existence of chromite as the unique spinels could be due to different bulk composition of magma, or rapid complete crystallization of the kimberlite before the MUM nucleation, or MUM resorption by the groundmass once having formed (Mitchell, 1986). Resorption of early formed spinels could be feasible in some cases, but in many other cases this possibility must be ruled out because the crystals formed in the early stages have systematically net, uncorroded euhedral facets. The assume of a crystallization of the kimberlite before the formation of MUM would suppose the formation of volcanic glass (which has never been described in kimberlite and it is not the case in the studied kimberlites) or the incorporation of titanium to other phases. However, other possible carriers of Ti, as perovskite, may occur both in rocks having MUM or where MUM is lacking. Therefore, we suggest that spinel differences in composition may reflect the composition of three main groups of magma: Al-rich, Cr-rich and Ti-rich.

MUM-type spinels can be present in some carbonatites and phoscorites (i.e., Milani *et al.* (2017) and therefore a carbonatitic influence could be considered. Compositions in terms of minor elements seem not to be relevant: some of the analysed spinels in carbonatites worldwide can be V-rich (0.5-2 wt % V_2O_3), as those in Bailundo, Angola (Castellano, com. Pers.), but many others are V-poor, as some examples in Sokli, Finland (Lee *et al.*, 2005) or some magnetite cumulates in India with less than 0.5 wt % V_2O_3 (Hoda and Krishnamurthy, 2014). The analysed groundmass spinels in kimberlites and related rocks are in all the cases V-poor.

Qandilite-rich spinel

Qandilite-rich spinel may occur in the groundmass of some kimberlites, as in the Michigan area (Menominee and Lake Ellen). In these cases, qandilite-rich spinel occur as discrete euhedral spinel crystals in the groundmass, although the crystals have variable compositions (30-50 % of the qandilite component) and the highest qandilite compositions (up to 60% of the qandilite component) are found in the vicinity of magnesian ilmenite inclusions; qandilite-richest compositions (up to 80% of qandilite component) are found when the spinel replacing geikielite.

However, the geikielite is replaced by spinel in many kimberlites, without arriving to produce qandilite. Therefore, the occurrence of groundmass qandilite-rich spinels could indicate at least the existence of a high activity of Mg in the magma:

$MgTiO_3 + MgO \rightarrow Mg_2TiO_4$

Spinel s.s.

Spinel s.s. cores in groundmass kimberlite are very rare. Spinel s.s. (some authors prefer to use the old term of pleonast instead of the IMA rules) has been described before in a few kimberlites, such as Igwisi (Reid *et al.*, 1975; Roeder and Schulze, 2008) and Tli Kwi Cho (Roeder and Schulze, 2008). The early crystallization of aluminium spinels in kimberlite groundmass has been explained as a result of the absence of phlogopite crystallization (Pasteris, 1983; Roeder and Schulze, 2008).

Spinel s.s. is a component of the cores of some lamprophyres, as is the case of the polzenites and melilitolites of the Ploucnice river region, Czechoslovakia (Ulrych *et al.*, 1986). These spinels have also a Cr component (pleonast), and could be similar to the aluminium spinels found in the Menominee kimberlites. However, the Czech spinels are zoned and have a Ti-rich rim of MUM type. In this case, a higher Al content of the magma can explain the occurrence of these spinels.

In the case of Menominee, the crystallization of djerfisherite, a K-rich sulfide, could produce the depletion of K in the magma and therefore favour the crystallization of spinel. However, djerfisherite is a very late phase in this pipe, whereas spinel formed in the early stages. Djerfisherite occurrences in worldwide kimberlites has also been described as a very late product, being usually produced by replacement of early-formed sulfides (Abersteiner *et al.*, 2019a). By the contrary, the early crystallization of spinel could produce the depletion of Al in the magma and therefore favour the crystallization of K sulfides.

Jaques and Foley (1985) and Mitchell and Bergman (1991) described the occurrence of pleonast in the West kimberly lamproites as inclusions in leucite, and proposed that these crystals could be formed by exsolution from a non-stoichiometric leucite containing Mg, Fe and Ti in solid solution. These authors argued that there is a certain grade of solution of these elements in the leucite structure, and the exsolution could be favoured by undercooling. However, it can be argued that the undercooling would favour exactly the contrary, the preservation of metastable high-T phases. However, exsolution hypothesis must be ruled out in the studied rocks, because the spinels are clearly groundmass material and can also be found in some cases in the olivine rims.

Peraluminic minerals may also be present in some peraluminic xenoliths, in the form of associations with garnet+spinel (alkremite), corundum+garnet (corganite) or corundum+garnet+spinel (corgaspinite), as those found in the Jagersfontein kimberlite pipe (Mazzone and Haggerty, 1986). These authors also suggest that a possibility to have these unusual contents in Al in the mantle may be by subduction of oceanic pelitic sediments (Mazzone and Stephen E, 1989). Other types of peraluminic xenoliths in kimberlites with a similar origin include the grospydites (associations of garnet + clinopyroxene + kyanite ±corundum, Sobolev *et al.*, 1968; Lappin, 1978, sometimes with quartz and coesite; Smyth and Hatton, 1977) and the corundum eclogites (Smyth *et al.*, 1984). An origin as restites produced by partial melting of oceanic lithosphere has been suggested by several authors as in Wyoming (Kuehner and Irving, 1998) or in South Africa (Viljoen *et al.*, 2005). The origin of these peraluminic associations is important, because some diamonds contain ruby corundum inclusions, as in Sao Luiz, Brazil (Hall *et al.*, 1994). Moreover, all the highly peraluminous xenoliths contain diamonds, as Spetsius (2004) describes in the Siberian kimberlites and as we observed in Catoca (Angola) and the Roberts Victor kimberlite in South Africa. In addition, the occurrence of sapphire corundum may be enough important in some lamproites that the rock can be commercially exploited for gemmy corundum, as in Yogo, Montana (USA; Meyer and Mitchell, 1988); for these authors, corundum is xenocrystic. Palke *et al.* (2016) analysed the melt inclusions in these crystals and conclude that corundum may be produced by peritectic melting of kyanite, perhaps at the basis of the continental crust.

5.9.2. Evolutionary trends

Zoning in spinels may be explained by a diversity of factors, including changes in the magma composition, disequilibria, or to solid-silquid or solid gas reactions, as proposed in the case of the Czec lamprophyres (Ulrych *et al.*, 1986).

The evolutionary trends in the analysed spinels can be schematized in the accompanying diagram (Fig. 5.21).

Trend A

AMC cores are sometimes mantled by MCC, thus indicating a decrease of Al content and Cr enrichment (trend A). However, the zoning involving both spinel types is sometimes reverse (MCC to AMC, trend H). The trend A and H are similar to so-called macrocrystal trend (or AMC trend) described by (Mitchell, 1986). However, hypothesis to explain the origin of these sequences have not been proposed in this classical synthesis. These trends have been neglected again in the recent synthesis of (Roeder and Schulze, 2008). However, the trends A and/or H are common in groundmass kimberlites and related rocks, and have been found in 21 samples among the 79 studied localities. Therefore, trends A and H are important for our synthesis.

AMC spinels are also found as primary magmatic phases in diverse mafic and ultramafic rocks, as in midocean ridge basalts, meimechites, komatiites, podiform chromitites and layered basic intrusions (Mitchell, 1986). In these environments, the existence of chromite liquidus and the ratios Al/Cr in the spinel are explained in many cases by interaction of peridotite with percolating magma at different fO_2 (i.e., Proenza *et al.*, 1999), or by reaction of magma with silica richer rocks.

These evolutionary Al variations in spinels have been considered to be controlled by the crystallization of phlogopite macrocrysts who could extract Al from the magma and therefore force the crystallization of Al-poor spinel (Pasteris, 1983; Mitchell, 1986; Roeder and Schulze, 2008). In addition, not all the studied samples which contain AMC have phlogopite macrocrysts, and in fact, according with our textural observations most of macrocryst phlogopite crystals have been interpreted as xenocrysts in this memory. Contrastingly, in our observations, we find that Al- and Cr-poor MUM spinel is formed in some cases after the crystallization of scarce corroded phlogopite macrocrysts, simultaneously with the crystallization of groundmass phlogopite. Therefore, this type of zoning can be connected with the exhaustion of Al during crystallization of groundmass phlogopite.

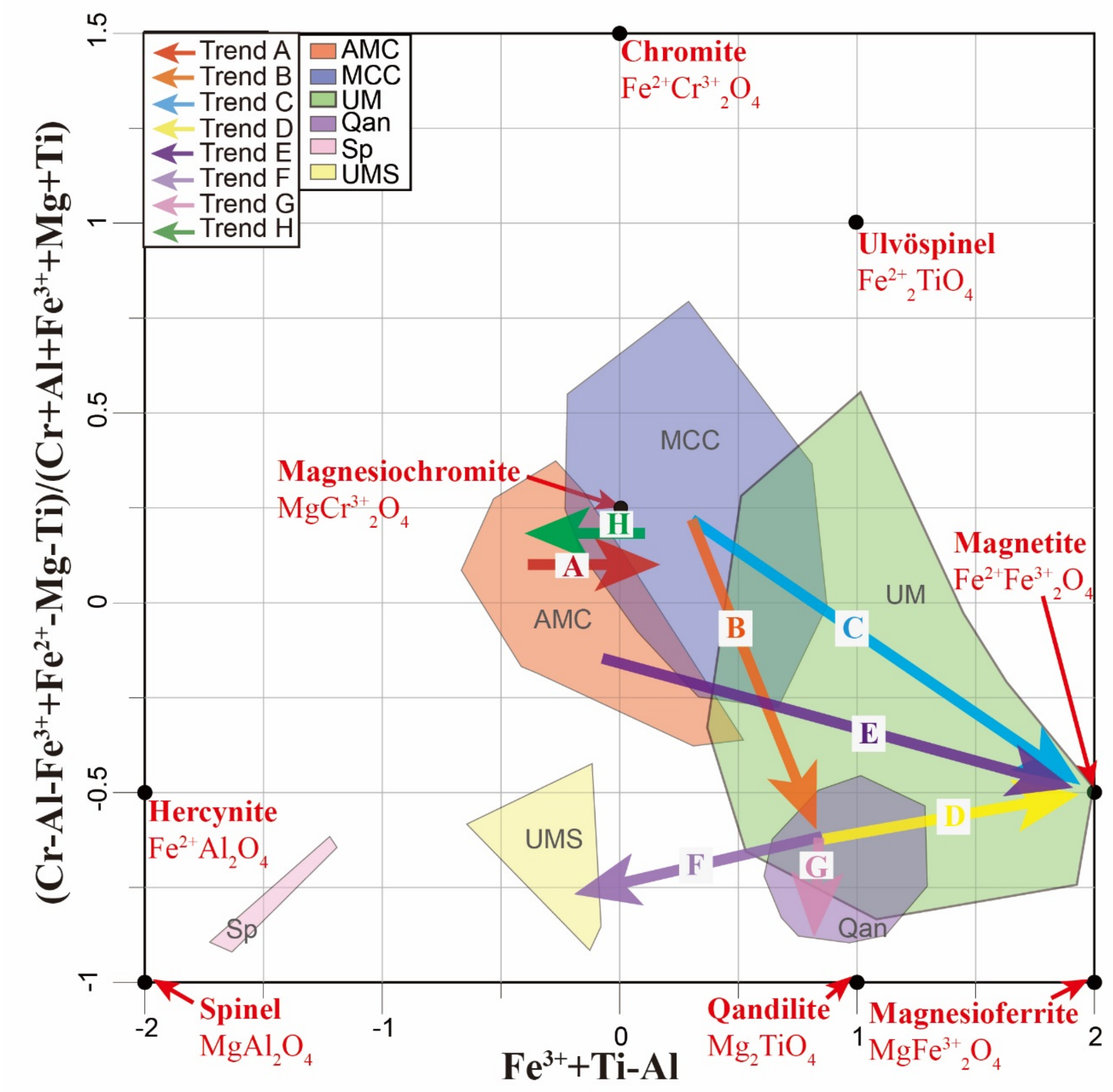

Fig. 5.21. Representation of the compositional trends of the analysed primary spinels from the studied kimberlites in the diagram (Fe^{3+}+Ti-Al) vs (Cr-Al-Fe^{3+}-Mg-Ti+Fe^{2+})/(Cr+Al+Fe^{3+}+Ti+Mg). The position of the end members is also indicated. AMC, MCC, UM, Qan, Sp and UMS fields are determined by composition of primary groudmass spinel from this work.

Trend B

The trend B evolve from MCC to MUM spinel at constant Fe^{2+}/(Fe^{2+}+Mg). Trend B commonly called as trend 1 (Mitchell, 1986; Roeder and Schulze, 2008), magnesian ulvöspinel trend (Mitchell, 1986; Tappe *et al.*, 2005) or kimberlite trend (Barnes and Roeder, 2001) in previous works. It may be found in archetypical kimberlites, as in the diamondiferous pyroclastic rocks from the Fort à la Corne kimberlite field (Chalapathi Rao *et al.*, 2017).

It is suggested that this trend is due to high carbonate content of kimberlite which lead a high magnesian activity (Roeder and Schulze, 2008). Trend B does not show in any of those 11 studied samples which have been previously classified as lamproite, orangeite or UML (Table 5.2). This is consistent to which have been suggested by (Mitchell, 1986; Tappe *et al.*, 2005) that trend B is unique to kimberlite. Although trend B has also been suggested as unique to kimberlite, and also to carbonatite and lamprophyres by (Roeder and Schulze, 2008). However, Kressall *et al.*, (2015) proposed that the replacement of early phases by MUM is produced by an increasing in the fO_2.

Trend C

Trend C evolve from MCC to MUM-magnetite with a rapid increase of $Fe^{2+}/(Fe^{2+}+Mg)$. Trend C is commonly called trend 2 (Mitchell, 1986; Roeder and Schulze, 2008), titanomagnetite trend (Mitchell, 1986; Tappe *et al.*, 2005) or Fe-Ti trend (Barnes and Roeder, 2001) in previous works. Trend C is found in a wide variety of rocks, such as basalt, alnoites, melilitites, lamproites and lamprophyres (Mitchell, 1995). It has been used as one of the conditions for the classification between orangeite, aillikite and kimberlite (Tappe *et al.*, 2005).

It is suggested that trend C is due to the crystallization of abundant phlogopite prior to groundmass spinel that cause the rapid depletion of Mg (Mitchell, 1995). Trend C has also been interpreted as due to co-crystallization of Mg- and Al-rich silicate such as olivine and phlogopite (Roeder and Schulze, 2008). However, in our study phlogopite macrocrysts do not occur in all of the samples which have spinels following the trend C. Moreover, abundant olivine phenocrysts occur not only in samples having spinels of trend C, but also in kimberlites that have spinel of trend B.

Trend D

Trend D evolve from MUM spinels towards the magnetite endmember. It could be the continuation of the trends B, C or E. The existence of an outer rim of magnetite is common in many igneous rocks and has been related with a progressive oxidation of the magma. This could be related with the exsolution of the magmatic fluids, or could be due to entrance of external fluids into the system, probably from the host rock

Trend E

Trend E is similar to trend C that show a rapid depletion of Mg. It differ with the trend C by its early composition of chromite. Trend E starts from AMC, while trend C starts from MCC. Thereby, trend E could be influenced by the same factor as trend C, but have a slightly higher Al content in the early melt.

Many kimberlite have spinel evolve follow trend 2 in nearly all diagrams (equivalent to trend C and trend E), but exceptionally follow trend 1 in reduced prism (Fig. 5.8, 5.10.

Trend F

Trend F evolve from MUM to UMS or Sp increasing Al content. This trend is similar to trend 7 determined by (Roeder and Schulze, 2008) and to the so-called pleonaste reaction trend by (Mitchell, 1986). Pleonast is found, among others, in the external rim of titanomagnetite in the De Beers kimberlite in South Africa (Pasteris, 1983), or in the Orapa Kimberlite (Milligan, 2014) and in the Benfontein kimberlite sill complex (Kimberley, South Africa; Abersteiner *et al.*, 2019). Pasteris (1983) explains this trend as being controlled by the cessation of the crystallization of phlogopite who retained Al, thus leading the remaining Al and Mg to form Sp (Mitchell, 1986) by the next reaction:

$4KMg_3AlSi_3O_{10}(OH)_2$ - $5Mg_2SiO_4$ + $2MgAl_2O_4$ + $(2K_2O$+ $4H_2O$+$7SiO_2)$

phlogopite forsterite spinel melt

An extreme Al enrichment can also be observed when the precipitation of spinel s.s. occurs as a very late product in the outermost rim of the spinel. This rim has been rarely observed, as in kimberlites from the Igwisi hills in Tanzania (Reid *et al.*, 1975). (Mitchell, 1986) also suggested that the Al-rich spinels have a multiplicity of origins and may be different in each occurrences, but does not explain the causes. However, the different occurrences have been explained by different processes. For instance, in the case of the Dutoitspan kimberlite (Snowden, 1981) in South Africa suggest that Al enrichment comes through garnet breakdown in spite there are no evidences of such decomposition. Masun (1999) found this trend in hypabyssal kimberlite facies from the Lac de Gras field, and explained the Al enrichment by contamination from the host rocks. However, this explanation must be ruled out, because an extensive crustal assimilation would produce in a first instance the destruction of olivine and the extensive formation of clinopyroxene, which is not present in these hypabyssal kimberlites. Kressall *et al.* (2015) proposed that it can be a result of a rapid emplacement, but this proposition is not argued.

We have found this trend only in the Jackson inlet kimberlite in Canada, as thin and discontinuous rims on MUM in a complex zoned crystals. However, the zoning seems to be progressive and continuous in this case, and could be a consequence of fractionation processes during the crystallization of the magma. Hence, the hypothesis of the cessation of crystallization of phlogopite (Pasteris, 1983) could be possibly applied in this case.

Trend G

Trend G follows an evolution from UM towards Qan. This trend is very rare, and has been found in few kimberlites only when the spinels replace Mg-ilmenite and/or geikielite. Hence, it is considered that trend G is due to the interaction with Mg-rich ilmenites causing the increasing of Mg to form Qan. Therefore, it may be considered as a reaction trend. The increase or high Mg spinels have been considered to be related to carbonate (Roeder and Schulze, 2008)). Moreover, the replacement (or overgrowth) of ilmenite and geikielite by spinel is very commonly found in many kimberlites and related rocks, but Qan is only found in two of the 79 studied samples (Lake Ellen and Menominee). Thereby, the presence of Qan also could indicate a high Mg melt composition.

Some kimberlites evolve from AMC directly to MUM-Mag following trend E, but some kimberlites evolve firstly from AMC to MCC, then to MUM-magnetite, (trend A to C). This could due to different crystallization rate that trend E crystallized faster than those follow trend A to C.

Many kimberlites show the common trend C but at different position in the composition diagrams (as trends parallel to trend C). These parallel evolutionary trend could derive from parental magmas that have slightly different bulk composition, formed by mixing of batches of magmas at different stages of differentiation in the source region at depth (Mitchell, 1986).

We agree with Roeder and Schulze (2008) that atoll spinel is a growth feature and not as a result of resorption as described by (Mitchell and Clarke, 1976).

Trend H

Roeder and Schulze (2008) suggest that the trend from chromite to aluminum spinel results from a rapid growth at a high degree of supersaturation of spinel, and at near constant $Fe^{2+}/(Fe^{2+}+Mg)$ ratio in the magma, based on similarities with the spinels grown from MORB melts. This could also explain the oscillatory zoning that may appear in some of the studied kimberlites, with some reverse zoning with the trend A-H.

Trends T1 and T2

Finally, it is important to mention that trends named T1 and T2 have been used to discriminate between kimberlites and other related rocks. Roeder and Schulze (2008) explained the trend T1 in spinels, at essentially constant and relatively low ratio $Fe^{2+}/(Fe^{2+}+Mg)$, by spinel growth in kimberlites in which carbonate played a major role, thus favoring high magnesium activities under relatively oxidizing conditions. These authors mention a high magnesioferrite component content in spinels associated with carbonatites and lamproites. However, this is a mistake; in fact, the authors mentioned as references for carbonatites and other in addition (Mariano and Roeder, 1983; Gaspar and Wyllie, 1984; Treiman and Essene, 1985; Barnes and Roeder, 2001; Armstrong *et al.*, 2004a; Melgarejo *et al.*, 2012; Campeny *et al.*, 2017) or lamprophyres (Rock, 1986; Ulrych *et al.*, 1986; Tappe *et al.*, 2006; Campeny *et al.*, 2017) indicates that spinels in carbonatites and lamprophyres are magnetite or titanomagnetite. Moreover, aillikite spinels follow intermediate trends between T1 and T2 whereas spinel carbonatites have a net trend T2, as in Tikiusaaq in Western Greenland (Tappe *et al.*, 2009) or in Catanda, Angola (Campeny *et al.*, 2015).

5.9.3. Coexistence of two groundmass spinels

The coexistence of two spinels in the same groundmass, as in the Menominee pipe in USA (Fig. 5.22), is a strange phenomenon in kimberlites. It is also a rare phenomenon in other types of rocks. A possibility to explain such phenomenon could be the crystallization subsolvus of two spinels, taking into account that there is a miscibility gap of qandilite and spinel s.s. below 1300ºC, which expands below 1000ºC to practically restrict he solutions between qandilite and spinel s.s. to the pure end members (Muan *et al.*, 1972). In other cases, their occurrence in basalts has been suggested as due to magmatic mingling phenomenon related to the coexistence of two immiscible magmas (i.e. Reubi *et al.*, 2003), based on the experiments showing that at least the Al and Ti contents of Cr-spinel are essentially controlled by the melt composition (McMahon and Haggerty, 1979; Roeder and Reynolds, 1991; Arai, 1992; Kamenetsky *et al.*, 2001). This process has also been described in mixing of undersaturated and saturated magmas, as in el Hierro island; in this case, Sigmarsson *et al.*, (2013) described the coexistence of small scale domains of different magmas, each with the corresponding spinel.

In the case of the Menominee kimberlite, the subsolvus crystallization can be ruled out because only the spinel s.s. occurs as inclusions in olivine rims, whereas qandilite-rich spinel occurs in the groundmass, along with spinel s.s.. Therefore, the crystallization of spinel started a little before than that of the qandilite. Therefore, this texture could be the result of intimate mingling of two immiscible magmas, probably favoured by the rapid ascent of magma and the high temperature of the liquids. Accepting that the nearby simultaneous growth of spinels is produced by the crystallization of two magmas, the question is the nature and source of these magmas.

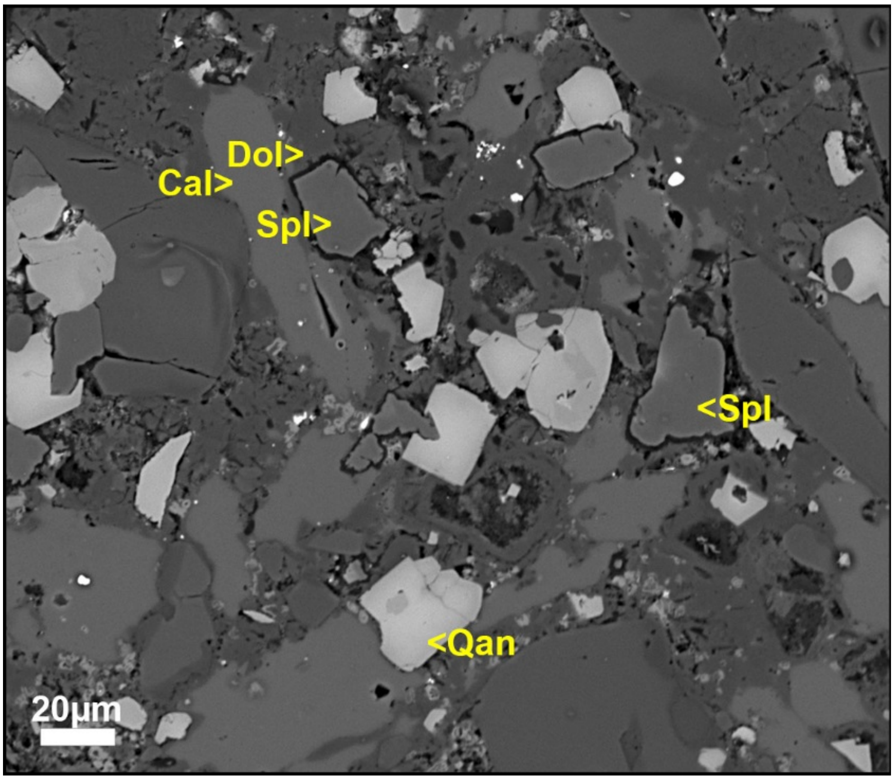

Fig. 5.22. Qandilite (Qan) and spinel (Spl) coexisting in the groundmass of the Menominee pipe. Note that spinel is partly altered to dark meixnerite, and is partly corroded; qandilite may mantle partially the spinel corners indicating its slightly later formation. Qandilite is associated with calcite (Cal), and spinel with the dark groundmass, enriched in forsterite and dolomite (Dol). Dolomite replaces calcite.

In fact, the spinels at Menominee seem to had been formed in different domains: Al-Mg- rich spinel occurs in association with a more magnesian groundmass with olivine, dolomite and serpentine; Ti-Mg-rich spinel is associated with a calcite-rich groundmass (Fig. 5.20).

The coexistence of these types of spinels has not been described in more kimberlites, but van Straaten *et al.* (2008) demonstrated that the changes in diamond content in the Victor North pyroclastic kimberlite are related to the existence of two magmatic pulses, one rich in diamond and another with lower tenors, and that both magmas had different spinels. In this case, one of the spinels is atoll type and has an Ti-rich AMC core with a magnetite rim which is never in direct contact with chromite, and the other has not atolls and has a magnetite rim directly in contact with a Ti-poor MCC core.

On the other hand, Keshav and Sen (2003) describe the simultaneous growth of garnet, spinel s.s. and spinels with a MUM affinity as a metasomatic product of kimberlite affecting a peridotite mantle xenolith. They propose that both crystals can be explained by percolation of two successive magmas, one more fractionated which could be the responsible of the precipitation of Ti-rich spinel. In our case the crystallization could be explained by the intrusion of a carbonate-rich magma (responsible of the Ti-rich spinel) into an Mg-richer magma (responsible of the precipitation of Al-Mg spinel).

Occurrence of two spinels in lamproite groundmass is described in Western Australia, because in addition with the above-mentioned occurrence (Jaques and Foley, 1985; Mitchell and Bergman, 1991) as spinel inclusions in leucite interpreted as exsolutions, the groundmass also contains chromite. Although these authors mention the two interpretations to explain the occurrence of spinel, by exsolution process and by crystallization of spinels from two magmas, they only discuss the first possibility, and in our opinion the second cannot be ruled out, because the exsolution processes are not favoured by undercooling of a melt.

5.9.4. Spinels and the globular bodies problem

The composition of the globular bodies can be different of that of the groundmass, as in the Letšeng diamond mine, Lesotho (Hetman *et al.*, 2018). However, most of the studies developed in the recent years have not focussed on the possible differences between the minerals in these bodies and the rest of the groundmass (i.e., Gaudet *et al.*, 2018; Muntener and Gaudet, 2018; Rapopo and Sobie, 2018).

Our studies suggest that spinels from the globular bodies can be different of those of the rest of the groundmass, as in the Banankoro pipe, thus suggesting significative differences in the magma compositions. Therefore, this is another strong argument for magma mixing, probably in many of the kimberlites.

5.9.5. Considerations for using spinels in classification of kimberlite-related rocks

Groundmass spinel composition is one of the key criteria used to distinguish between kimberlite and related rocks, as proposed in the standard petrological nomenclature of the IUGS (Tappe *et al.*, 2005). This classification has been used in different places to distinguish different groups of rocks (i.e., in Greenland, Nielsen *et al.*, 2009). However, we consider that it not suitable the use of the rules defined by these authors for the classification of these groups of rocks. In fact, compositional trend B (trend 1) is unique for kimberlite, but kimberlite could have spinels following trends B, C or E. Only 7 among the 68 studied kimberlites (which have not been classified as other rocks by far) show a clear trend B in the spinels, which is mentioned classically as characteristic of spinel kimberlite. In fact, the majority of kimberlite spinels show the trend C. Most of kimberlites and related rocks show trends C or E (trend 2) that could be kimberlite, lamproite (including orangeite), basalts, alnoites, melilitoide, minnette and other lamprophyres (Mitchell, 1986).

For those spinels presenting trends C or E (trend 2) discriminations based on #Cr (#Cr = Cr/(Cr+Al)) has been provided. #Cr > 0.85 is indicative for kimberlite containing macrocryst and lamproite (including orangeite, Mitchell, 1995). Whether #Cr > 0.85 could be spinels from aillikite (Tappe *et al.*, 2005) or basaltoid, melilitoide (including alnoite and polzenite) and minette (Mitchell, 1995). However, aillikite from Torngat dykes have spinel with #Cr > 0.85 (Tappe *et al.*, 2004b) showing the classification doesn't always work. Moreover, chromite with #Cr > 0.85 have not been found in five studied samples which are previously classified as orangeite or lamproite (Table 5.2). Exact classification can only be made in conjunction with other mineralogical and geochemical data (Mitchell, 1986).

Mitchell (1986) proposed to use the diagram $Fe^{3+}/(Fe^{3+}+Al+Cr)$ *vs* $Fe^{2+}/((Fe^{2+}+Mg)$ as a possible tool to distinguish the trends of the kimberlite spinels from the trends of lamproites. This diagram could be therefore suitable to help distinguish altered rocks of kimberlitic affinity from rocks of lamproitic tendency, and has been used in many publications. However, Mitchell (1986) also detailed a number of exceptions, and in our review we found many cases of kimberlites with the trend T2, which should be typical of lamproites and aillikites. Spinels following intermediate trends are also common. Therefore, we believe that these diagrams no not provide meaningful information.

Since spinel is one of the earliest mineral crystallized in the groundmass of kimberlites and related rocks, the composition of spinel could reflect the composition of the magma. Moreover, there are no evidences suggesting that the kimberlite composition of the magma could change by formation of cumulates. The ascent of the magmas are supersonic up to the surface and the crystallization took place under volcanic conditions, therefore we cannot expect diffusion of most of the components. Moreover, in the case of the spinel included into olivine, there are not good facilities for diffusion of Cr, Al and Ti in the structure of the hosting olivine (Kamenetsky *et al.*, 2001), thus helping to preserve the composition of the trapped spinel. Kamenetsky *et al.* (2001) also studied the variations in composition of the volcanic chromites compared with the inclusions of trapped melts. They conclude that the Al_2O_3 of the spinel is a function of the Al_2O_3 content in the melt, and therefore it can be used to discriminate between different magma types. In addition, there are no other Cr-rich minerals in the groundmass of kimberlites and related rocks. Therefore, at the least the occurrence of high chromite contents in the groundmass is criteria to indicate that the crystallizing magma had a distinct high Cr content, independently of the conditions of crystallization.

5.9.6. Considerations about using groundmass spinel as diamond potential indicator

Shape of xenocrystic chromites in detrital rocks and sediments can be used as a KIM, despite the compositions of spinels from kimberlites and related rocks are similar to those found in most of the other spinel-bearing rocks, as many volcanic rocks and ophiolites (i.e., Arai, 1992). Lee *et al.* (2004) proposed to use the elongate and distorted shapes of the kimberlite xenocrystic chromites as a difference; Fedortchouk and McIsaac (2013) proposed to use the different patterns of dissolution experimented by kimberlite xenocrystic chromites when compared to those from other environments of formation. Such textures were obtained during experimental work on chromite grains affected by fluid attack at high pressures and temperatures and different ratios of H_2O and CO_2. However, all these authors work with grain concentrates and therefore they do not distinguish among the different chromite populations. Moreover, these are only surficial features and therefore are hardly revealed on thin polished section. Our studies failed to find these textures in the chromites from the analysed kimberlites and related rocks. In fact, chromite groundmass is generally euhedral and not corroded; moreover, most of the chromite xenocrysts are mantled by other Fe-Ti oxides.

Different authors propose to use the composition of xenocrystic chromite as a direct diamond indicator, because they consider that chromite composition is influence during the redox metasomatic processes leading to diamond formation (Malkovets *et al.*, 2007). The higher the content of Cr is, the higher the content of diamond; inversely, higher contents of Al component correlate with barren kimberlites, because the Cr-rich chromite should be formed in deeper sections of the mantle than the Al-rich chromite. These criteria have been applied in the study of prospective kimberlites in China (Xiaoying and Posukhova, 2010) and Western Australia (Hutchison, 2018). It is important to note that some of these studies have been done on concentrates, and this drives a problem because many of the analysed groundmass chromites may plot in the same compositional fields. Therefore, we find that it is necessary to proceed with a detailed petrographic study in order to avoid misinterpretations.

In addition, the composition and evolution of groundmass spinel has been proposed as indicative of the evolution of the oxygen fugacity in the kimberlite and, therefore, as an indicative of the capacity of the magma to preserve or destroy the diamond xenocrysts. In fact, diverse authors propose that the kimberlite and related magmas are environments were diamond can be easily destroyed. This idea is based in the evolution of spinels, resulting lately in the crystallization of magnetite which would indicate a more oxidizing environment that could be responsible of diamond oxidation (Nixon, 1995; McCammon, 2001; Malkovets *et al.*, 2007). Conversely, the environments with reduced spinels as spinel s.s., chromite, ulvöspinel or qandilite could be more favourable for the diamond preservation. However, a quantitative approach to reveal the stability in diamond in kimberlite magmas can be done when chromite is enclosed in olivine, as happens in many cases. In these cases, the olivine is clearly zoned, with a core and a rim that hosts the spinels. This means that the core corresponds to olivine mantle xenocrysts, and the rim a crystallization from the magma, before or simultaneously to the groundmass crystallization. The use of the available data obtained in different kimberlites in Canada suggest that diamond is far of the equilibria in the kimberlite and related magmas, thus producing resorption (Fedortchouk and Canil, 2004).

However, some authors propose the use of the groundmass spinel to determine the diamond grade, although they use empiric arguments. Bovkun *et al.*, (2001), after studying the mineral associations in 30 kimberlites from 9 fields in Yakutia (Russia), proposed that the composition of groundmass spinel could be easily used to evaluate the diamond grade of kimberlites (Table 5.4). They conclude that the higher is the Cr_2O_3 content in groundmass spinel, the higher is the diamond grade; conversely, an increase in the ulvöspinel content is accompanied by a decrease in the diamond grade. The occurrence of groundmass picroilmenite and perovskite is also correlated with a decrease of diamond grade (Table 5.4).

Table 5.4. Correlation of the diamond grade of Yakutian kimberlites with the groundmass spinel composition and kimberlite mineral associations (Bovkun *et al.*, 2001).

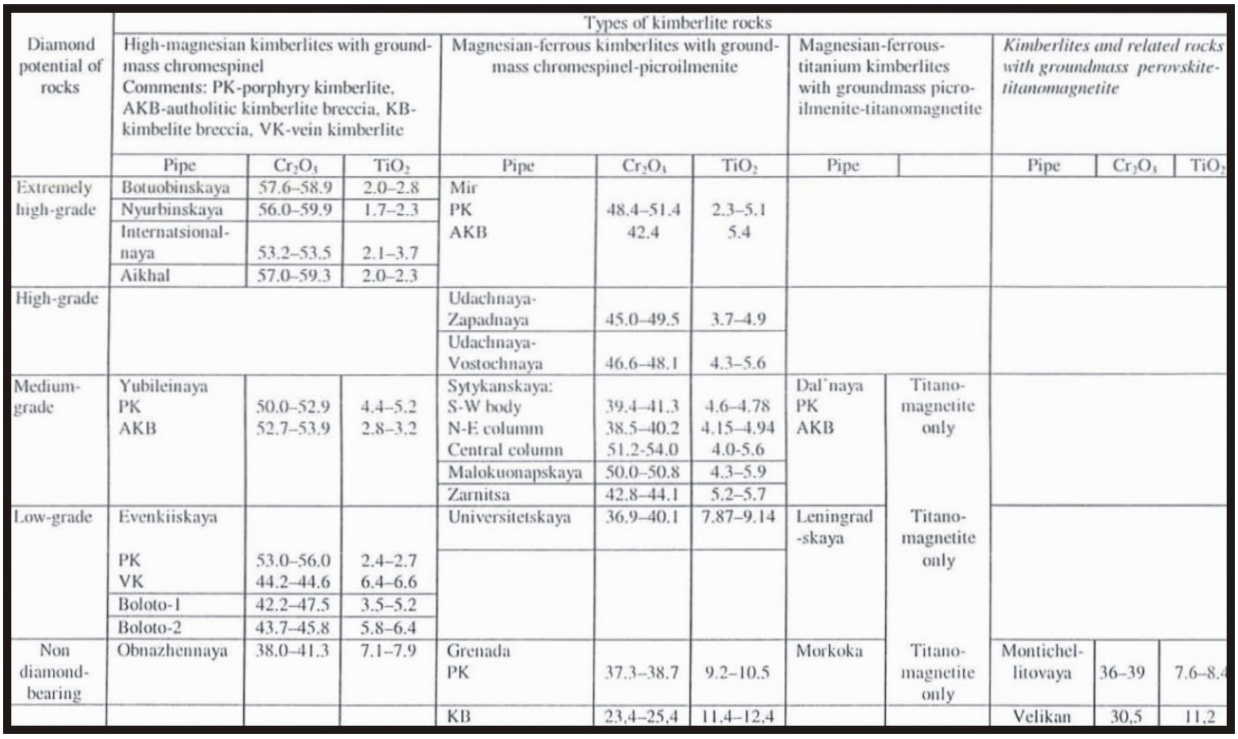

Diamond potential of rocks	Types of kimberlite rocks										
	High-magnesian kimberlites with ground-mass chromespinel Comments: PK-porphyry kimberlite, AKB-autholitic kimberlite breccia, KB-kimbelite breccia, VK-vein kimberlite			Magnesian-ferrous kimberlites with ground-mass chromespinel-picroilmenite			Magnesian-ferrous-titanium kimberlites with groundmass picro-ilmenite-titanomagnetite		*Kimberlites and related rocks with groundmass perovskite-titanomagnetite*		
	Pipe	Cr_2O_3	TiO_2	Pipe	Cr_2O_3	TiO_2	Pipe		Pipe	Cr_2O_3	TiO_2
Extremely high-grade	Botuobinskaya	57.6–58.9	2.0–2.8	Mir PK AKB	48.4–51.4 42.4	2.3–5.1 5.4					
	Nyurbinskaya	56.0–59.9	1.7–2.3								
	Internatsional-naya	53.2–53.5	2.1–3.7								
	Aikhal	57.0–59.3	2.0–2.3								
High-grade				Udachnaya-Zapadnaya	45.0–49.5	3.7–4.9					
				Udachnaya-Vostochnaya	46.6–48.1	4.3–5.6					
Medium-grade	Yubileinaya PK AKB	50.0–52.9 52.7–53.9	4.4–5.2 2.8–3.2	Sytykanskaya: S-W body N-E column Central column	39.4–41.3 38.5–40.2 51.2-54.0	4.6–4.78 4.15–4.94 4.0-5.6	Dal'naya PK AKB	Titano-magnetite only			
				Malokuonapskaya	50.0–50.8	4.3–5.9					
				Zarnitsa	42.8–44.1	5.2–5.7					
Low-grade	Evenkiiskaya PK VK	53.0–56.0 44.2–44.6	2.4–2.7 6.4–6.6	Universitetskaya	36.9–40.1	7.87–9.14	Leningrad-skaya	Titano-magnetite only			
	Boloto-1	42.2–47.5	3.5–5.2								
	Boloto-2	43.7–45.8	5.8–6.4								
Non diamond-bearing	Obnazhennaya	38.0–41.3	7.1–7.9	Grenada PK	37.3–38.7	9.2–10.5	Morkoka	Titano-magnetite only	Montichel-litovaya	36–39	7.6–8.4
				KB	23,4–25,4	11,4–12,4			Velikan	30,5	11,2

In fact, some authors correlate high Ti amounts in whole rock analysis with low grade in the kimberlites (Bogatikov *et al.*, 2009) and this could be related with the Ti content in spinel. However, a significative part of this Ti may be in the structure of xenocrystic ilmenite and other minerals as perovskite, rutile or phlogopite. As seen, many kimberlites are rich in ilmenite, as Catoca, and they are diamond-rich. Therefore, this is an interesting possibility to be analysed in future, but in our opinion it must be contrasted with the petrographic data.

Moreover, the diagram created in this work (Fig. 5.19) could be also used to show the composition of xenolithic and xenocrystic spinels (Fig.5.22). The composition of spinels from mantle xenoliths and crustal xenoliths are quite well separated , as well as spinels from peridotitic xenoliths and from MARID xenoliths. Spine in basaltic crustal xenoliths are UM. Spinels in peridotitic xenoliths are AMC to spinel s.s.. Spinels in MARID are MCC which is quite Cr-rich than spinel from peridotite xenoliths. However, the majority composition of spinels from xenolith overlap with composition of primary groundmass spinel in this new diagram as well as those classic diagram (Fig. 5.18 and 5.23). Therefore, studies based on composition of concentrate spinel could lead misinterpretation as they do not distinguish between xenocrystic and primary chromite.

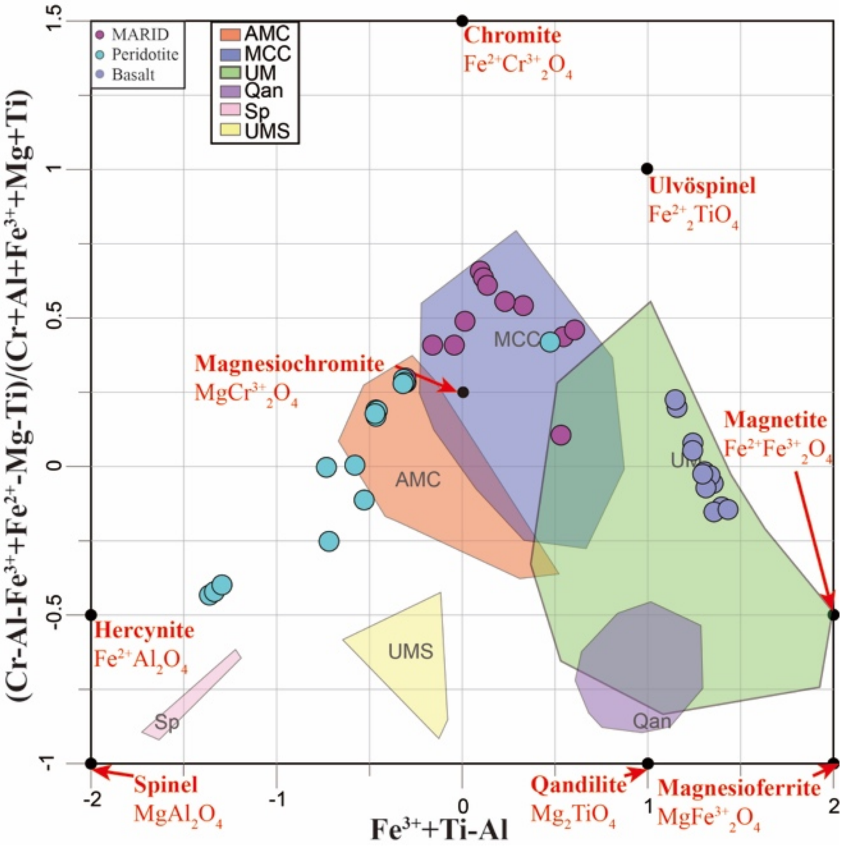

Fig. 5.23. Compositions of spinels in xenoliths of MARID, peridotites and basalt in the (Fe^{3+}+Ti-Al) vs. (Cr-Al-Fe^{3+}+Fe^{2+}-Mg-Ti)/(Cr+Al+Fe^{3+}+Mg+Ti) diagram. AMC, MCC, UM, Qan, Sp and UMS fields are determined by compositions of primary groudmass spinels from this work.

CHAPTER 6

ILMENITE GROUP

6. ILMENITE GROUP

6.1. INTRODUCTION

The minerals of the ilmenite group are rhombohedric (*R*-3) double oxides, with an ordered structure derived from that of corundum, with each of the cations arranged in a six-fold coordination with oxygen; one of three of the octahedral positions remains vacant (Fig. 6.1).

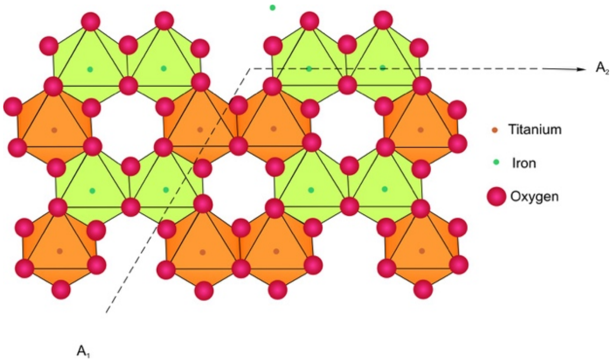

Fig. 6.1. Structure of ilmenite.

The isostructural members of the group are ilmenite ($Fe^{2+}TiO_3$), geikielite ($MgTiO_3$), pyrophanite ($Mn^{2+}TiO_3$), ecandrewsite ($(Zn,Fe^{2+},Mn^{2+})TiO_3$), hemleyite ($(Fe^{2+}_{0.48}Mg_{0.37}Ca_{0.04}Na_{0.04}Mn^{2+}_{0.03}Al_{0.03}Cr^{3+}_{0.01})_{1.00}Si_{1.00}O_3$) and akimotoite ($(Mg,Fe^{2+})SiO_3$). Among these minerals, only geikielite, pyrophanite and ilmenite have been described in kimberlites and related rocks. Ecandrewsite is very rare, and the last two minerals are high-pressure minerals that have been described only in meteorites, although they could appear in deep mantle associations (Bindi *et al.*, 2017)(Bindi et al., 2016).

Ilmenite, pyrophanite and geikielite have complete solid solutions among them, and they also present partial solid solutions with hematite (Fe_2O_3).

A total of 1473 EMPA analyses of ilmenite group minerals from 79 kimberlites have been carried out in this work. Part of the results of ilmenites from India and Guinea that will be presented in this memory have been already published (Xu *et al.*, 2018a; b).

Minerals of the ilmenite group are common accessory minerals in many kimberlites and related rocks. In adition, minerals of the ilmenite group are considered as mantle-derived kimberlite indicator minerals (KIM) and have been used in kimberlite exploration. Moreover, kimberlites containing magnesian ilmenite are believed to be produced by a reduced magma, thus indicating an environment that preserves diamond, while the presence of Fe^{3+}-rich ilmenite could indicate an oxidizing environment that could destroy diamond (Gurney *et al.*, 1993; Gurney and Zweistra, 1995; Kostrovitsky *et al.*, 2004, 2006; van Straaten *et al.*, 2008). However, incorrect link of oxidized ilmenite with the diamond resorption has also been indicated (Schulze *et al.*, 1995). Robles-Cruz *et al.* (2009) demonstrated that the presence of dominant Fe^{3+}-rich ilmenite is not a convincing argument to exclude the occurrence of economic diamond deposits, and indicated that compositional attributes must be evaluated alongside textural studies. These authors also demonstrated the existence of many different generations of ilmenite in the same pipe. Therefore, it is important to carry out a systematic study of the ilmenite occurrences in worldwide kimberlites, in particular, of the variation of their chemical composition in their different generations.

The compositions of the minerals from the ilmenite group should be defined as a combination of the 4 main endmembers, this is, ilmenite s.s. ($FeTiO_3$), pyrophanite ($MnTiO_3$), geikielite, ($MgTiO_3$) and hematite (Fe_2O_3). The use of every name, as ilmenite or geikielite or pyrophanite should be based on the dominant component among ilmenite-geikielite-pyrophanite-hematite endmember system (50% rule; Nickel, 1992, 1995). However, the term ilmenite s.s. will be used here to describe the minerals with ilmenite endmember dominant when they are very impoverished in Fe^{3+}, Mg or Mn. The term "ilmenites" will be used as an equivalent to "members of the ilmenite group", in general.

6.2. GENERATIONAL VARIETIES

The ilmenite-group minerals in kimberlite and related rocks are not formed in a single process, and many ilmenite generations can be distinguished in the different rocks on the basis of textural and chemical differences among them. These different generations can occur in the same pipe and therefore are a good recorder of the evolution of these magmas from the mantle to the surface and reflect also the subsolidus evolution of the rock. Hence, it is very important to describe accurately the textures of these minerals in order to carry out a petrogenetic and economic study.

The summary of textural-compositional varieties of the ilmenite-group minerals found in the selected kimberlites and related rocks, based on petrographic and compositional characteristics, is presented in Table 6.1. Two main categories could be established, because the textural criteria allow establish if ilmenite was formed in pre-existing rocks or during the intrusive processes. Moreover, the textural and chemical criteria can also help to distinguish several categories among those formed during the intrusive processes. Therefore, the distinguished generations are the following:

A) ilmenites within xenoliths;

B) xenocrystic ilmenites;

C) ilmenites of the intrusive stage 1 (interpreted as early magmatic primary ilmenites);

D) ilmenites of the intrusive stage 2 (interpreted as late magmatic ilmenites, formed before perovskite and ulvöspinel and replaced by them);

E) ilmenites of the intrusive stage 3 (interpreted as hydrothermal late-post magmatic ilmenites).

These textural and chemical varieties of ilmenites are not found simultaneously in all of the sampled kimberlites and related rocks; their distribution in the different intrusions studied in this work is indicated in the Table 6.2

Table 6.1. Compositional-textural types of ilmenite group minerals discriminated in this work, based on their texture and composition.

Texture-compositional types of ilmenite group minerals			Fe^{3+}-rich Ilm	Fe^{3+}- and Mg-rich Ilm	Mg-rich Ilm	Fe^{3+}-rich Gk	Gk	Ilm s.s.	Fe^{3+}- and Mn-rich Ilm	Mg- and Mn-rich Ilm	Mn-rich Ilm	Pph
A Within xenolith	1 Peridotitic xenolith		A1-1		A1-2			A1-3				
	2 MARID/PIC xenolith		A2-1	A2-2	A2-3			A2-4				
	3 Basaltic xenolith		A3-1					A3-2			A3-3	
	4 Granitic xenolith							A4-1			A4-2	A4-3
	5 Inclusion in Phl macrocryst		A5-1	A5-2								
	6 Inclusion in Ol macrocryst			A6-1								
B Xenocryst			B-1	B-2	B-3			B-4			B-5	B-6
C Kimberlitic stage 1 (Magmatic primary early)	1 Inclusion in Ol microphenocryst				C1-1	C1-2	C1-3					
	2 Groundmass				C2-1	C2-2	C2-3					
	3 In vein cut Ol						C3-1					
	4 Replacement	a Replace Fe^{3+}-rich Ilm		C4a-1	C4a-2	C4a-3	C4a-4					
		b Replace Fe^{3+}- and Mg-rich Ilm			C4b-1	C4b-2	C4b-3					
		c Replace Mg-rich Ilm				C4c-1	C4c-2					
		d Replace Ilm s.s.			C4d-1		C4d-2					
		e Replace Rt xenocryst			C4e-1		C4e-2					
		f Replace Cct xenocryst			C4f-1		C4f-2					
		g Replace Chr xenocryst					C4g-1					
		h Replace Usp-Mag xenocryst		C4h-1	C4h-2		C4h-3					
		i Totally replaced				C4i-1	C4i-2					
D Kimberlitic stage 2 (Magmagtic late, before and replaced by Prv and Usp)	1 Replacement	a Replace Fe^{3+}-rich Ilm							D1a-1			
		b Replace Fe^{3+}- and Mg-rich Ilm						D1b-1				
		c Replace Mg-rich Ilm							D1c-1		D1c-2	
		d Replace Gk								D1d-1	D1d-2	
		e Replace Rt									D1e-1	
		f Totally replaced								D1f-1		
E Stage 3 (Hydrothermal late-post magmatic)	1 Tabular euhedral				E1-1		E1-2				E1-3	E1-4
	2 Replacement	a Replace Fe^{3+} rich Ilm									E2a-1	
		b Replace Fe^{3+}- and Mg-rich Ilm						E2b-1				
		c Replace Mg-rich Ilm						E2c-1			E2c-2	
		d Replace Gk									E2d-1	
		e Replace Prv						E2e-1			E2e-2	
		f Replace Usp-Mag xenocryst						E2f-1			E2f-2	E2f-3
		g Replace Mag xenocryst	E2g-1								E2g-2	
		h Totally replaced									E2h-1	

Ilm=ilmenite; Pph=pyrophanite; Gk=Geikielite; Ol=olivine; Phl=phlogopite; Rt=rutile; Mag=magnetite; Usp=ulvöspinel; Prv=perovskite; Cct=crichtonite group minerals; Chr=chromite

Table 6.2. Types of ilmenite-group minerals observed in different kimberlite studied in this work.

	Sample	Region	Location	Name	Rock	A. Xenolith	B. Xenocryst	C. Intrusive stage 1	D. Intrusive stage 2	E. Intrusive stage 3
Angola	CU-79-70,5A, CU-79-113A		Cucumbi		VK	A2-1	B-1; B-2; B-3; B-4	C1-1		
Angola	TZ-G18-47, TZ-G18-252		Tchiuzo		VK	A4-2; A4-3	B-1; B-2; B-3; B-4; B-6	C1-3; C2-3; C4a-4; C4c-2; C4i-2	D1d-1; D1d-2; D1f-1	E2d-1; E2h-1
Botswana	10052	SD	Jwaneng	Centre pipe	VK		B-3; B-4; B-5	C2-3; C4i-2		E2g-2
Botswana	10053	SD	Jwaneng	North pipe	VK		B-3; B-4	C4c-2; C4i-2		E1-3; E2c-2; E2d-1
Botswana	10054	SD	Jwaneng	South pipe	VK		B-3; B-4; B-5	C4c-2; C4i-2		E1-3
Botswana	10055	CD	Orapa	AK1, "A"	VK	A3-2	B-2; B-3; B-4	C4c-2; C4i-2		
Botswana	10056	CD	Orapa	AK1, "B"	VK					
Botswana	10057	CD	Orapa	AK1, "C"	VK	A3-2; A4-2	B-3; B-4			
Botswana	10058	CD	Letlhakane	DK1	VK	A2-1; A3-2; A3-3	B-3; B-4	C4c-2		
Botswana	10060	CD	Damtshaa	BK9, "A"	VK	A1-1; A1-2; A1-3; A3-2	B-3; B-4	C2-2; C2-3; C4d-1; C4i-2		
Botswana	10061	CD	Damtshaa	BK9, "B"	VK	A1-2; A1-3; A2-1; A3-1; A3-2; A5-2	B-1; B-2; B-3; B-4	C2-3; C4a-2; C4c-2		
Venezuela	7544		Guaniamo		VK/CK					
Russia	10077	NR	Lomonosovskaya		VK					
Russia	10079	NR	Pionerskaya		VK					
Russia	9985	Yakutia	Pobeda ('Victory')		VK	A4-1	B-1; B-4			
Canada	7999	Quebec	Temiskaming	Ville-Marie	VK	A3-2; A3-3	B-3	C1-3		
Canada	9168	Ontario	Temiskaming	Seed	VK	A3-2; A4-2	B-3	C4c-2; C4i-2		
Canada	9359	NWT	SW Slave	Drybones Bay	VK	A5-1	B-1; B-2	C1-1; C4a-2; C4a-4; C4b-1; C4b-2; C4b-3		
USA	8015	Michigan	Lake Ellen	Lake Ellen	VK	A4-1	B-3; B-4	C1-3; C2-3; C4c-2; C4e-2; C4g-1; C4i-2		
USA	9346	Utah	San Juan Co.	Alhambra Rock	VK					
USA	9966	Tennessee	Tazewell	Norris metakimberlite	VK		B-1; B-2; B-3	C4a-1; C4a-2; C4b-1; C4i-1; C4i-2		E1-3; E2a-1; E2c-2; E2d-1
Russia	9959	Yakutia	Leningrad		VK		B-1; B-2	C4h-1; C4h-2		

Table 6.2. (continued 1)

	Sample	Region	Location	Name	Rock	A. Xenolith	B. Xenocryst	C. Intrusive stage 1	D. Intrusive stage 2	E. Intrusive stage 3
Angola	CC-47-46		Cacuilo	K47	CK	A2-1; A2-2; A2-3; A2-4	B-2; B-3	C4c-2		
Botswana	10049	CD	Karowe	AK6, South pipe	CK		B-3	C1-1; C1-3; C4i-2		
Botswana	10050	CD	Karowe	AK6, Center pipe	CK		B-1; B-2; B-3; B-4	C1-3; C4a-1; C4a-3; C4c-2; C4i-1; C4i-2		
Botswana	10051	CD	Karowe	AK6, North pipe	CK		B-1; B-2; B-3; B-4	C1-1; C1-3; C2-3; C4a-2; C4b-3; C4h-2	D1c-1	E2f-1; E2g-1
Botswana	10059	CD	Letlhakane	DK1	CK	A6-1				
South Africa	7707	NCP		Riverton	CK		B-2	C2-3; C4c-2		E2e-2
South Africa	9156	FSP		Bultfontein	CK		B-1; B-2; B-3	C1-1; C1-3; C2-3; C4a-1; C4b-1; C4b-2; C4c-2; C4i-1	D1a-1; D1c-2; D1d-2	E2b-1
South Africa	9311	NCP	Kimberley	Big Hole	CK	A3-2	B-2; B-4	C1-3; C4b-3; C4e-1		
South Africa	9351	NCP	Kimberley		CK					
South Africa	9364	NCP	Kimberly	DutoitSpan	CK		B-1; B-3	C1-1; C1-2; C1-3; C4a-1; C4e-2; C4f-1; C4f-2		E1-3
South Africa	9725	FSP		Monastery	CK		B-2; B-3; B-4	C4d-2; C4i-2		
South Africa	9630	FSP	Kaalvallei	"occurence A"	CK		B-1; B-2; B-3; B-4	C1-1; C1-2		
Lesotho	9607			P200	CK			C1-3		
Guinea	8870			Banakoro	CK					
Guinea	8871			Banakoro	CK			C2-3; C3-1		E1-1; E2c-1; E2c-2; E2e-2
Canada	9353, 9354	Québec	Temiskaming	Notre Dâme du Nord	CK		B-3	C1-1; C1-3; C4c-2; C4e-1		E2c-2
Canada	9577	Ontario	Bucke Township		CK		B-3	C4i-2		
Canada	6934	NWT	Somerset island		CK		B-3	C1-3; C4e-2; C4g-1; C4i-2		
Canada	7448	NWT	Diavik		CK					E2f-3
Canada	7449	NWT	LDG Ekati	Point Lake	CK		B-3	C4c-2		

Table 6.2. (continued 2)

	Sample	Region	Location	Name	Rock	A. Xenolith	B. Xenocryst	C. Intrusive stage 1	D. Intrusive stage 2	E. Intrusive stage 3
Canada	9613	NWT	SW Slave	Snap Lake	CK					
Canada	7454	Alberta	Birch Mountains		CK					
Canada	9360	Nanavut	Baffin Island	Jackson inlet	CK					
USA	7314	Colorado	Larimer Co.	Chicken Park	CK			C1-3; C4h-3; C4i-2		E1-3; E2d-1; E2g-2
USA	10070	Pennsylvania	Fayette Co.	Gate-Adah	CK		B-2	C2-2; C2-3		
USA	9348	Colorado	Kelsey Lake		CK					
USA	9345	Colorado	Laramie Co		CK					E2f-3
USA	9352	Michigan	Menominee	Site 73	Ck		B-3	C1-3; C2-3; C4c-2; C4i-2; C4e-2		
USA	9576	Colorado	Larimer Co.	Sloan #2	CK		B-2; B-3	C4c-2; C4i-2		
Russia	10037	Yakutia	Udachnaya		CK		B-1; B-3; B-4	C1-1; C1-3; C4d-1		
Russia	10065	Yakutia	Obnazhonnaya		CK		B-2; B-3	C1-3; C2-3; C4c-2; C4g-1; C4i-1; C4i-2		
Russia	4928	Yakutia	Mir		CK		B-1; B-3	C2-2; C2-3; C4c-2		E2f-2
Russia	9611	Kola Peninsula	Emakowskaya		CK					E2f-3
India	8021	RKF	Siddanpalli cluster	SK-1	CK			C1-1; C1-3; C2-3; C4f-2; C4g-1		
India	8044	RKF	Siddanpalli cluster	SK-2	CK		B-3	C4f-1; C4f-2	D1e-1;	E2e-2
India	8029	RKF	Siddanpalli cluster	SK-3	CK			C4i-2	D1d-2; D1f-1	E2f-2
India	8030, 8040, 8041	WKF	Chigicherla cluster	CC-4	CK		B-3	C4c-2; C4i-2	D1d-2	E2e-2; E2f-2
India	8022, 8023	WKF	Chigicherla cluster	CC-5	CK					E2e-2; E2f-2
India	8036	WKF	Kalyandurg	KL-3	CK		B-3			E2c-2; E2e-2
India	8037, 8038	WKF	Kalyandurg	KL-4	CK		B-1; B-2; B-3	C4a-1; C4b-1; C4b-2; C4b-3; C4c-1; C4c-2; C4g-1; C4i-1; C4i-2;		
India	8027	WKF	Wajrakarur village	P-1	CK					E1-3

Table 6.2. (continued 3)

	Sample	Region	Location	Name	Rock	A. Xenolith	B. Xenocryst	C. Intrusive stage 1	D. Intrusive stage 2	E. Intrusive stage 3
India	8043	WKF	Lattavaram village	P-3	CK		B-1; B-3; B-4	C2-3; C4a-1; C4c-2; C4d-1; C4i-2		
China	9333	Shandong province	Mengyin	Red Flag #1	CK			C2-3		E1-3
China	9737,9738, 9740	Shandong province	Mengyin	Shengli	CK					E1-4; E2e-1; E2f-2; E2f-2
China	9573, 9574	Liaoning province		Wafangdian	CK		B-5			E2e-2
South Africa	7881	NCP	Kimberley	Helam	Orangeite (Hammond and Mitchell 2002)		B-1; B-2	C1-1; C2-3; C4a-1; C4b-1; C4b-2; C4i-1; C4i-2		
South Africa	9375	FSP		Roberts Victor	Orangeite (Mitchell 1995)					E1-4
South Africa	9952	NCP		Bellsbank	Orangeite (Mitchell 1995)					
South Africa	9602	FSP	Kaalvallei	"occurence B"	Lamproite (this work)		B-1; B-2; B-3	C1-1; C4a-1	D1b-1	E1-4; E2c-1
USA	9341	Colorado	Kelsey Lake		Lamproite (this work)					
USA	9340	Arkansas	Murfreesboro		Lamproite (McCandless et al. 1994)		B-3			E2e-2
India	8024	WKF	Chigicherla cluster	CC-1	Lamproite (this work)					
India	8025	WKF	Wajrakarur village	P-2	Lamproite (Kaur&Mitchell 2013)					
India	8035	WKF	Lattavaram village	P-4	Lamproite (Shaikh et al., 2018)					
India	8045	WKF	Mulligiripally	P-5	Lamproite (Kaur et al., 2013)					E2e-2
Canada	10142	Quebec	Ugava Bay	Torngat	UML (Tappe et al., 2004)			C1-1; C2-1		E2c-2; E2e-2

SD: Southern District; CD:Central District; NCP:Northern Cape Province; FSP:Free State Province; NR:Northern Region; RKF: Raichur kimberlite field; WKF: Wajrakarur kimberlite field. VK: volcaniclastic kimberlite; CK: coherent kimberlite; UML: ultramafic lamprophyres; Ba: highest Ba content zone. Ilmenite types are listed in Table 6.1

6.2.1. Ilmenites within xenoliths (paragenesis A)

Ilmenite group minerals are found in different xenoliths including mantle xenoliths and crustal xenoliths. Following types of xenoliths were found in this study as containing ilmenites: A1) peridotitic xenoliths; A2) MARID (Mica-Amphibole-Rutile-Ilmenites-Diopside) and PIC (Phlogopite-Ilmenites-Clinopyroxene) xenoliths; A3) basaltic xenoliths; A4) granitic xenoliths; A5) ilmenites found as inclusion in phlogopite macrocrysts; A6) as inclusion in olivine macrocrysts.

Metasomatized peridotitic xenoliths

Peridotitic xenoliths (Fig. 6.3)studied in the present work present the following mineral associations: olivine + phlogopite + ilmenites; olivine + clinopyroxene + orthopyroxene + phlogopite + ilmenites; clinopyroxene + orthoyroxene + ilmenites. These mineral associations exhibit evidences of replacement. Ilmenites found in these xenoliths use to be anhedral, and they are clearly metasomatic because they replace olivine and enstatite, in association with clinopyroxene (Fig. 6.3a). Ilmenites within peridotitic xenolith are subdivided based on its composition into the following varieties: A1-1) Fe^{3+}-rich ilmenite; A1-2) Mg-rich ilmenite; A1-3) ilmenite s.s..

MARID/PIC xenoliths

MARID/PIC xenoliths (Fig. 6.3b) studied here occur in the following mineral associations: phlogopite + diopside + ilmenites; phlogopite + ilmenites; phlogopite + ilmenites + rutile + diopside. Ilmenites found in these xenoliths are normally anhedral, and grain size is variable, in many cases is less than 1 mm, but it can be coarse, up to several centimetres in diameter. Ilmenites may replace rutile and occur in an interstitial position between the silicates (including phlogopite; Fig. 6.3b), thus indicating that they formed lately in the paragenetic sequence. Ilmenites within MARID/PIC xenoliths found in the present study have similar composition as those from peridotitic xenoliths: A2-1) Fe^{3+}-rich ilmenite; A2-2) Fe^{3+}-rich and Mg-rich ilmenite; A2-3) Mg-rich ilmenite; A2-4) ilmenite ss.

Basaltic xenoliths

Basaltic xenoliths (Fig. 6.3c) found in this study contain augite-diopside, ilmenite and altered mineral or minerals, being difficult in these cases to identify the original mineral phase. Some of these xenoliths also contain ulvöspinel-magnetite and apatite. The ilmenites found in these rocks may be primary, because they are normally euhedral to subhedral, with tabular habit, and are fine-grained. Ilmenite within basaltic xenolith is subdivided based on its composition to following varieties: A3-1) Fe^{3+}-rich ilmenite; A3-2) ilmenite s.s.; A3-3) Mn-rich ilmenite. The two first can be primary, and the last can be a metasomatic product.

Granitic xenoliths

Granitic xenoliths (Fig. 6.3d) studied in the present work normally present part of the following mineral associations: quartz, plagioclase, potassic feldspar, annite, muscovite and magnetite.

Ilmenites found in these xenoliths are normally anhedral and may be primary, and the following varieties cab be distinguished on the compositional basis: A4-1) ilmenite s.s.; A4-2) Mn-rich ilmenite; A4-3) pyrophanite. The first can be primary, and the last can be a metasomatic product.

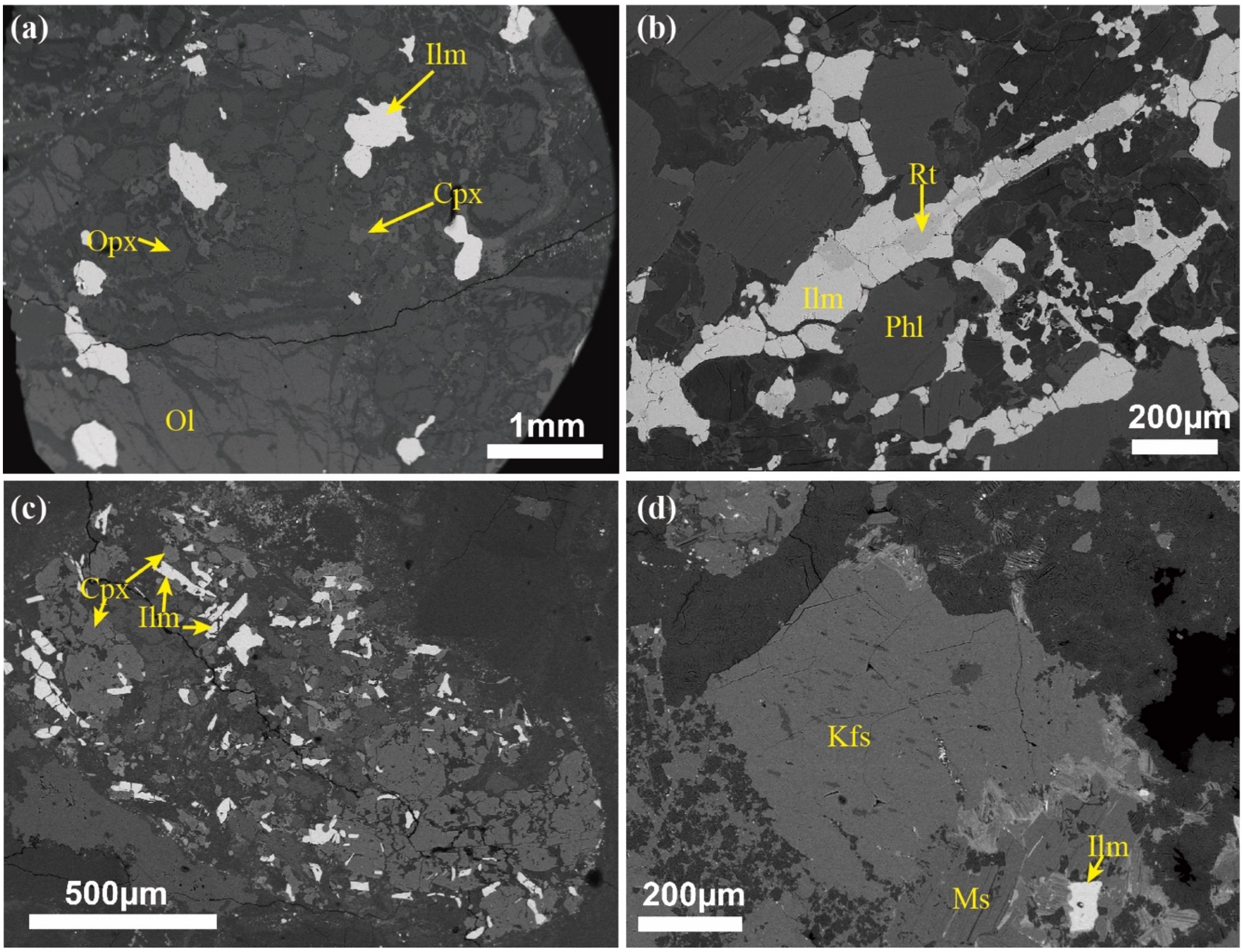

Fig. 6.3. Back-scattered electron (BSE) imagings of ilmenite of paragenesis A, in xenoliths (a) Ilmenite (Ilm) in peridotitic xenolith with replacing olivine (Ol) and orthopyroxene (Opx), along with clinopyroxene (Cpx) in the Damtshaa BK9 “A” volcaniclastic kimberlite. (b) Ilmenite in MARID xenolith replacing phlogopite (Phl) and rutile (Rt) in the Letlhakane DK1 volcaniclastic kimberlite. (c) Ilmenite in basaltic xenolith with clinopyroxene in the Damtshaa BK9 “B” volcaniclastic kimberlite. (d) Ilmenite in granitic xenolith with K-feldspar (Kfs) and muscovite (Ms) in the Tchiuzo volcaniclastic kimberlite.

Inclusions in phlogopite microcrysts

Ilmenites also occur as inclusions in phlogopite microcrysts (Fig. 6.4a) which are more probably xenocrystic. These ilmenites correspond to Fe^{3+}-rich ilmenite (A5-1) and Fe^{3+}-rich and Mg-rich ilmenite (A5-2).

Inclusions in olivine macrocrysts

Ilmenites were also determined as inclusions in olivine macrocrysts (Fig. 6.4b) which are more probably xenocrystic. These ilmenites are Fe^{3+}- and Mg-rich ilmenite (A6-1).

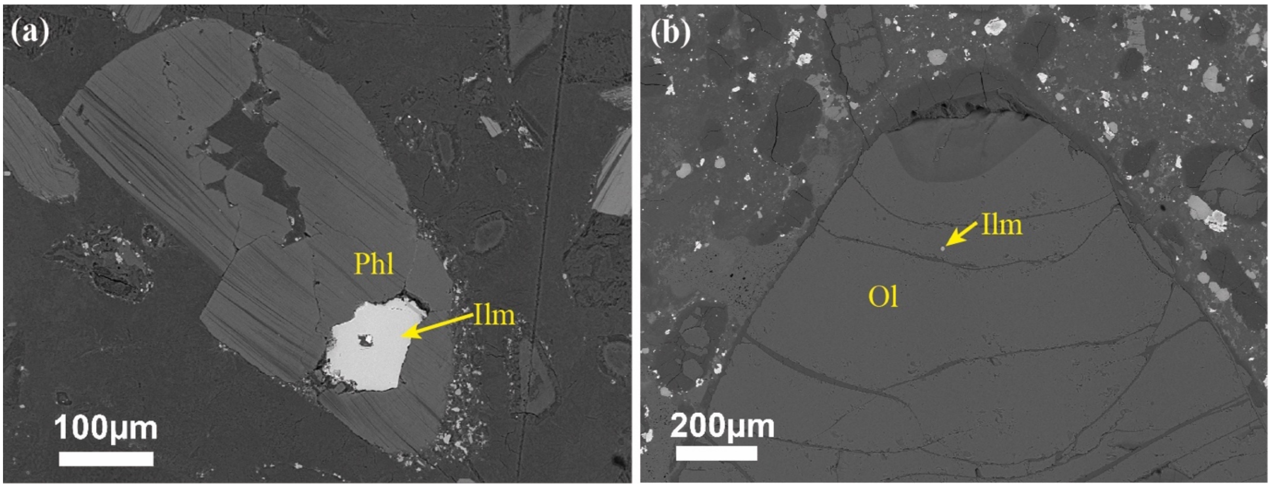

Fig. 6.4. Back-scattered electron (BSE) imagings of ilmenite of paragenesis A: (a) Ilmenite as inclusion in phlogopite xenoccryst from the Drybones Bay volcaniclastic kimberlite. (b) Ilmenite as inclusion in olivine xenocryst from the Letlhakane DK1 coherent kimberlite.

6.2.2. Ilmenites as xenocrysts (paragenesis B)

Depending on the texture, two subtypes are defined in this type of ilmenites: the first subtype is found as clasts formed by monomineralogic polycrystalline aggregates of ilmenite and the second one occurs as single grains of rounded megacrysts or macrocrysts.

Monomineralogic polycrystalline aggregates of ilmenites have a rounded (“nodular”) shape and can achieve 5 cm in diameter. These ilmenites have a granoblastic polygonal texture suggesting textural equilibria (triple junctions at about 120°, curved boundaries); the size of these individual grains is about 300 μm (Fig. 6.4a). Some serpentine minerals occur along the grain boundaries, thus suggesting that these xenoliths were infiltrated by kimberlite fluids or melts along the grain boundaries. This ilmenite generation is usually replaced by a sequence involving ilmenites of higher Mg content, then ulvöspinel and perovskite. In most cases, this replacement is along the borders of the grains, but it may also occur along tiny cracks.

Rounded anhedral grains of ilmenites (Fig. 6.4b) are found in many kimberlites. Their grain size is very variable, from microcryst (<1mm) to macrocrysts (>1mm). They are roughly rounded. As in the case of the polycrystalline ilmenite, these isolated ilmenite grains are commonly replaced by ilmenites of higher Mg content, followed by ulvöspinel and perovskite. This replacement is present along grain boundaries or small cracks.

In some occasions, xenocrystic ilmenite may present exsolutions of Al-spinel which normally show as extremely small dots within ilmenite xenocryst (Fig. 6.4c). Exsolution of ulvöspinel-titanomagnetite in ilmenite xenocryst is also observed (Fig. 6.4d), although in some cases it is hard to distinguish between exsolution or replacement following cleavage plans. Although they display exsolution textures, their composition is identical to those that does not show exsolution textures, thereby, ilmenite containing exsolution of spinel s.s. or ulvöspinel-magnetite exsolutions are included in this catalogue of ilmenite xenocrysts.

Ilmenite xenocrysts (paragenesis B) are subdivided based on their compositions into the following subtypes: B-1) Fe^{3+}-rich ilmenite; B-2) Fe^{3+}-rich and Mg-rich ilmenite; B-3) Mg-rich ilmenite; B-4) ilmenite s.s.; B-5) Mn-rich ilmenite; B-6) Pyrophanite.

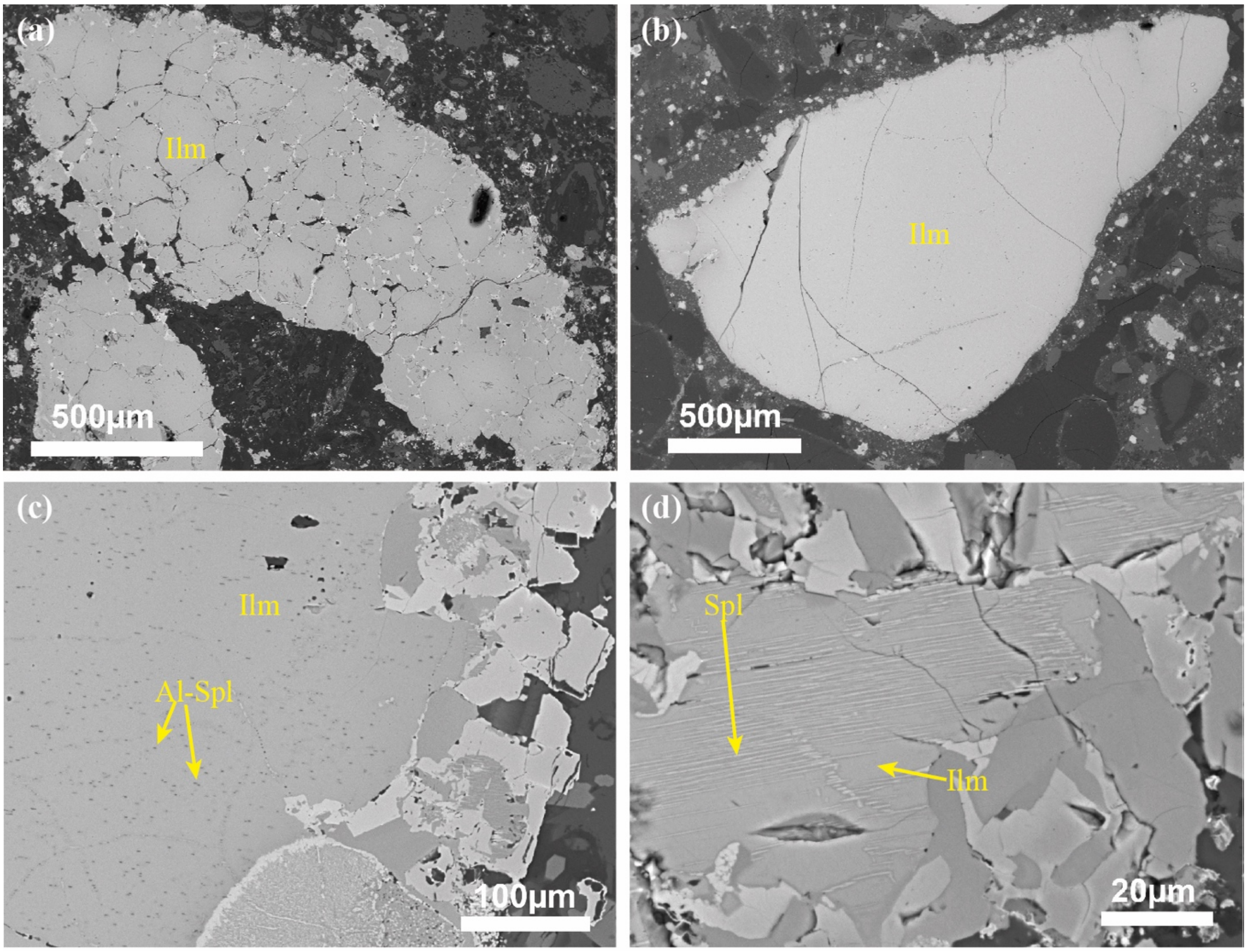

Fig. 6.4. Back-scattered electron (BSE) imagings of ilmenite-group minerals as xenocrysts of the paragenesis B. (a) Polycrystalline ilmenites (Ilm) in the Kalyandurg KL-4 coherent kimberlite. (b) Anhedral xenocrystic ilmenites in north pipe of the Karowe AK6 coherent kimberlite. (c) Xenocrystic ilmenites with exsolution of Al-spinel (Al-Spl) in the Helam orangeite. (d) Ilmenites with exsolution of ulvöspinel-titanomagnetite of spinel (Spl) group in the Kalyandurg KL-4 coherent kimberlite.

6.2.3. Ilmenites of the intrusive stage 1 (early magmatic primary ilmenites (paragenesis C)

Ilmenites usally crystallize in the early stages of the kimberlitic magma, they are found in the next textural occurrences: C1) inclusions in olivine microphenocrysts; C2) groundmass; C3) ilmenite in veins crosscutting olivine xenocrysts; C4) replacing xenocrysts.

Inclusions in olivine microphenocrysts

Ilmenites found as inclusions in olivine microphenocrysts are euhedral (Fig. 6.5a) to anhedral bleb-like (Fig. 6.5b). In unaltered or only slightly altered samples ilmenites are found in fresh olivine microphenocrysts, while ilmenites of the same aspect are found in olivine totally pseudomorphosed to serpentine in moderate to highly altered samples. Ilmenite-group inclusions in olivine (C1) are subdivided based on their composition into the following compositional domains: C1-1) Mg-rich ilmenite; C1-2) Fe^{3+}-rich geikielite; C1-3) geikielite.

Primary groundmass

Primary groundmass ilmenites (C-2) are normally found as anhedral and fine-grained crystals (< 0.05 mm, Fig. 6.5c). However, the distinction between groundmass ilmenites which crystallised directly from kimberlite magma (C-2) and xenocrystic ilmenites (B) or even xenocrystic ilmenites totally replaced by metasomatism process by kimberlite magma (C-3i) is normally ambiguous. Fragmentation of macrocrystic (xenocrystic) ilmenites can also produce similar small sized grains similar to primary groundmass ilmenites. Moreover, both primary and xenocrystic ilmenites could be mantled by primary spinels and perovskite. Primary groundmass ilmenites are subdivided based on their composition intothe following compositional domains: C2-1) Mg-rich ilmenite; C2-2) Fe^{3+}-rich geikielite; C2-3) geikielite.

In veins crosscutting olivine xenocrysts

Ilmenite is also in veins crosscutting olivine xenocrysts (C3), commonly together with other groundmass minerals such as minerals of the spinel group (Fig. 6.5d), perovskite and phlogopite. Their composition is into the geikielite domain (C3-1).

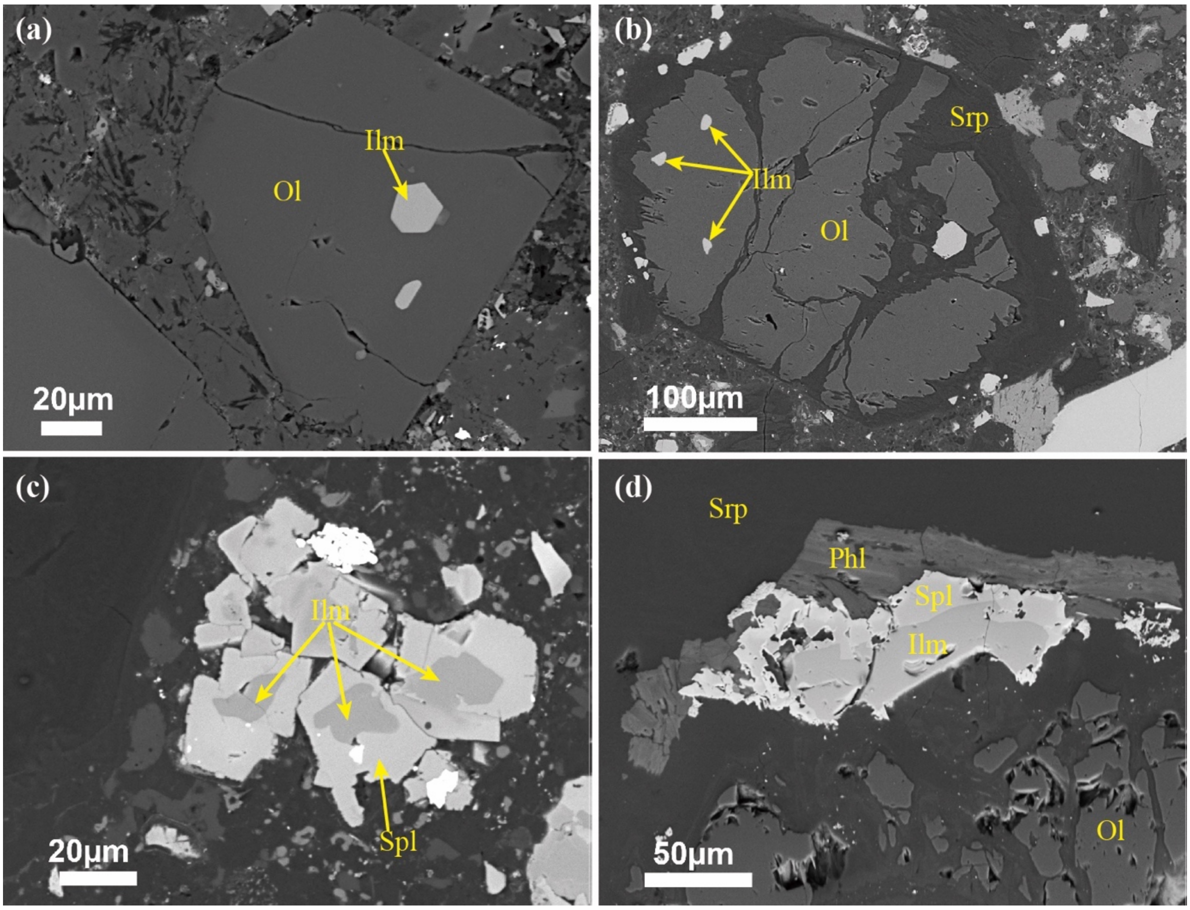

Fig. 6.5. Back-scattered electron (BSE) imagings of magmatic primary early ilmenites (paragenesis C). (a) Euhedral ilmenites (Ilm) as inclusions in fresh olivine (Ol) in the Menominee coherent kimberlite. (b) Anhedral ilmenites as inclusions in olivine partially altered to serpentine (Srp) in the north pipe of Karowe AK6 coherent kimberlite. (c) Groundmass ilmenites included in groundmass ulvöspinel-magnetite (Spl) in the Damtshaa BK9 “A” volcaniclastic kimberlite. (d) Ilmenites in vein crosscutting. olivine xenocrysts together with ulvöspinel-titanomagnetite (Spl) and phlogopite in the Banankoro “B” coherent kimberlite.

Replacement of xenocrystic Ti-bearing minerals

Different textural generations of ilmenite-group minerals are found as a replacement product of ilmenite xenocrysts (C4), as well as other Ti-rich xenocrysts, such as Ti-bearing chromite and Cr-rich mathiasite. Replacement of xenocrystic Ti-rich minerals by ilmenites (C4) is developed along discontinuities as grain boundaries, small cracks and the cleavages of the replaced minerals. The contacts between the different ilmenite generations are extremely irregular and, in most of the cases, diffuse. This fact may account by the progressive changes in compositions between boundaries of the different generations of ilmenite-group minerals.

Depending on the replaced mineral, nine compositional subtypes are defined (Table 6.3): C4a) replacing Fe^{3+}-rich ilmenites; C4b) replacing Fe^{3+}-rich and Mg-rich ilmenites; C4c) replacing Mg-rich ilmenites (Fig. 6.6a-b); C4d) Replacing ilmenite s.s.; C4e) replacing rutile (Fig. 6.6c); C4f) replacing xenocrysts of minerals belonging to the crichtonite group (Fig. 6.6d); C4g) replacing chromite xenocrysts (Fig. 6.6e); C4h) replacing ulvöspinel-magnetite xenocrysts (Fig. 6.6f) C4i) the xenocryst is totally replaced.

Table 6.3. Textural types and dominant composition of early magmatic ilmenites produced by replacement, established depending on the composition of the replaced mineral and the composition of the replacing member of the ilmenite group.

replaced subtype	partly replaced mineral	replacing subtype	resulting mineral of the ilmenite group
C4a	Fe^{3+} ilmenite	C4a-1	Fe^{3+}- and Mg-rich ilmenite
		C4a-2	Mg-rich ilmenite
		C4a-2	Fe^{3+}-rich geikielite
		C4a-4	Geikielite
C4b	Fe^{3+}- and Mg-rich ilmenite	C4b-1	Mg-rich ilmenite
		C4b-2	Fe^{3+}-rich geikielite
		C4b-3	Geikielite
C4c	Mg-rich ilmenite	C4c-1	Fe^{3+}-rich geikielite
		C4c-2	Geikielite
C4d	Ilmenite	C4d-1	Mg-rich ilmenite
		C4d-2	Geikielite
Other minerals	Rutile	C4e-1	Mg-rich ilmenite
		C4e-2	Geikielite
	Crichtonite	C4f-1	Mg-rich ilmenite
		C4f-2	Geikielite
	Chromite	C4g-1	Geikielite

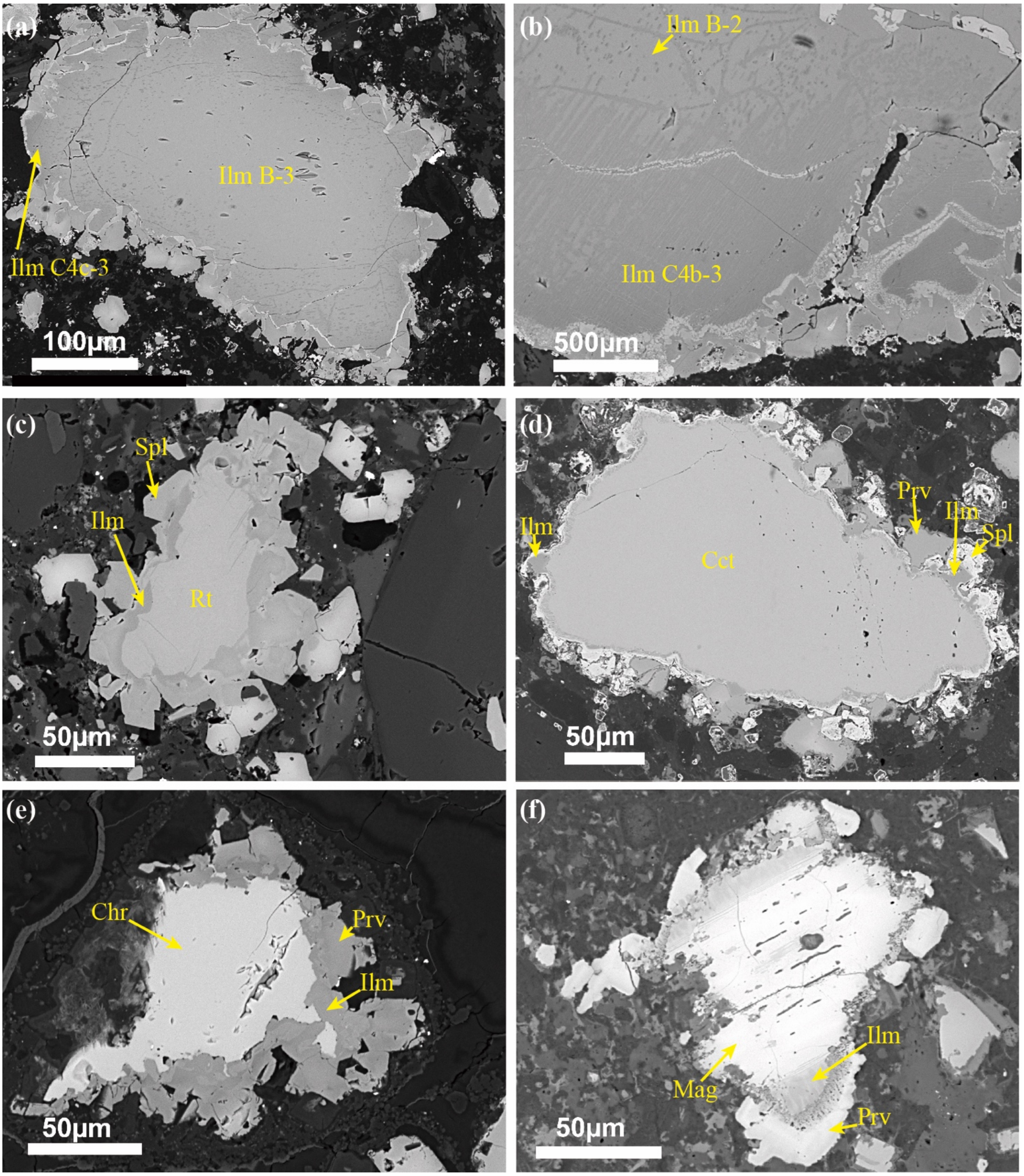

Fig. 6.6. Back-scattered electron (BSE) imagings of magmatic primary early ilmenites formed by replacement (paragenesis C-4). (a) Geikielite (Ilm C4c-3) replacing Mg-rich ilmenite xenocryst (Ilm B-3) in the Kalyandurg coherent KL-4 kimberlite. (b) Geikielite (Ilm C4b-3) replacing Fe^{3+}- and Mg-rich ilmenite (B-2) in the Kalyandurg KL-4 coherent kimberlite. (c) Geikielite (Ilm) replaces rutile (Rt) and the ensemble is mantled by ulvöspinel-titanomagnetite (Spl) in the Menominee coherent kimberlite. (d) Ilmenite replacing mathiasite (of the crichtonite group, Cct) being mantled by ulvöspinel-titanomagnetite (Spl) and perovskite (Prv) in the Siddanpalli SK-1 coherent kimberlite. (e) Ilmenite replacing chromite (Chr) in the Lake Ellen volcaniclastic kimberlite. (f) Ilmenite replacing magnetite (Mag) mantled by perovskite in the north pipe of the Karowe AK6 coherent kimberlite.

6.2.4. Ilmenites of the intrusive stage 2 (late magmatic ilmenites, formed before than primary perovskite and spinels and replaced by these minerals, paragenesis D)

Late magmatic ilmenite generations occur replacing (D1) early formed or xenocrystic ilmenites and other minerals. They are replaced by primary spinel-group minerals and perovskite. Depending on the replaced mineral, six subtypes have been defined (Table 6.4): D1a) partly replacing Fe^{3+}-rich ilmenite; D1b) partly replacing Fe^{3+}-rich and Mg-rich ilmenite; D1c) partly replacing Mg-rich ilmenite; D1d) partly replacing geikielite (Fig. 6.7a); D1e) partly replacing rutile (Fig. 6.7b); D1f) complete replacement of the above minerals.

Table 6.4. Textural types and dominant composition of late magmatic ilmenites produced by replacement, established depending on the composition of the replaced mineral and the composition of the replacing member of the ilmenite group.

replaced subtype	partly replaced mineral	replacing subtype	resulting mineral of the ilmenite group
D1a	Fe^{3+} ilmenite	D1a-1	Fe^{3+}- and Mn-rich ilmenite
D1b	Fe^{3+}- and Mg-rich ilmenite	D1b-1	Ilmenite s.s.
D1c	Mg-rich ilmenite	D1c-1	Fe^{3+}-rich and Mn-geikielite
		D1c-2	Mn-rich ilmenite
D1d	Geikielite	D1d-1	Mg-and Mn-rich ilmenite
		D1d-2	Mn-rich ilmenite
	Rutile	D1e-1	Mn-rich ilmenite
	Full replacement	D1f-1	Mg-and Mn-rich ilmenite

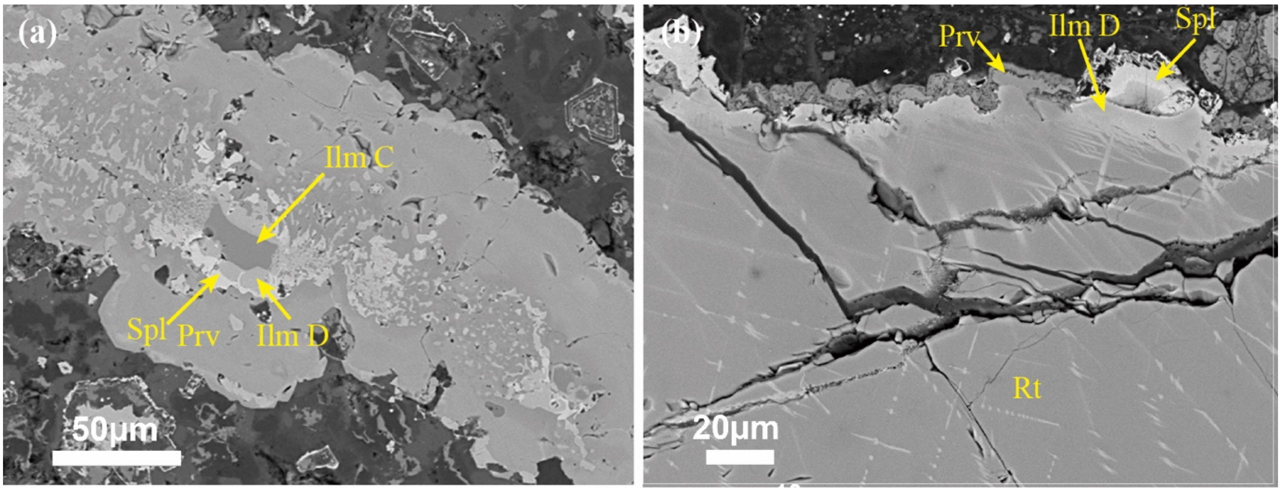

Fig. 6.7. Back-scattered electron (BSE) imagings of late magmatic primary ilmenite formed by replacement (paragenesis C-4). (a) Mn-rich ilmenite of paragenesis D (Ilm D) replacing geikielite of paragenesis C (Ilm C), replaced by ulvöspinel-titanomagnetite (Spl) and perovskite (Prv), in the Chigicherla CC-4 coherent kimberlite. (b) Mn-rich ilmenite (Ilm D) replacing rutile (Rt), replaced by ulvöspinel-titanomagnetite and perovskite in the Siddanpalli SK-3 coherent kimberlite.

6.2.5. Ilmenites of the intrusive stage 3 (hydrothermal late-post magmatic ilmenites; paragenesis E)

They are relatively common in many kimberlites that have experienced different grades of hydrothermal alteration ranging from moderate to high. They are identified as euhedral crystals with tabular habit, ribbon-like (E1) or replacing all the above minerals (E2) following grain borders, small cracks, zoning, cleavages or other small discontinuities. These secondary ilmenites have a large diversity of chemical compositions, and are associated with fine-grained serpentine minerals, chlorite and calcite. Fine-grained galena and pentlandite may also be present in association with them.

Euhedral tabular crystals

Euhedral to subhedral crystals of minerals of the ilmenite group (E-1) occur as the next types based on the chemical composition of these minerals: E1-1) Mg-rich ilmenite groundmass-like (only in the Banankoro “B” kimberlite, Fig. 6.8a); E1-2) geikielite (only in the Banankoro kimberlites); E1-3) Mn-rich (Fig. 6.8b); E-1-4) pyrophanite. Grain size varies from <0.1mm to 0.5mm.

Replacement

Minerals of the ilmenite group may occur as a late product of replacement of Ti-bearing pre-existing minerals (E2); depending on the replaced mineral, the following compositional and textural subtypes are defined: E2a) partly replacing Fe^{3+} rich ilmenite; E2b) partly replacing Fe^{3+}-rich and Mg-rich ilmenite; E2c) partly replacing Mg-rich ilmenite; E2d) partly replacing geikielite (Fig. 6.8c); E2e) replace partly replacing perovskite (Fig. 6.8d); E2f) partly replacing ulvöspinel-magnetite (Fig. 6.8e-f); E2g) partly replacing magnetite xenocrysts; E2h-1) fully replacing other Ti-minerals. The resulting compositions are very diverse, including within the same type of replaced mineral, and a given mineral may be replaced by several types of minerals of the ilmenite group. Some of these types exhibit similarities in the composition of major elements, but they could have differences in the trace elements and therefore we preferred to retain this classification. The compositions of the subtypes are indicated in the Table. 6.5.

Table 6.5. Classification of the different types of the intrusive stage 3 (hydrothermal-post magmatic) replacing ilmenites depending on the composition of the above-existing Ti-rich minerals. The chemical composition of the replacing ilmenites is also indicated.

replaced subtype	partly replaced mineral	replacing subtype	resulting mineral of the ilmenite group
E2a	Fe^{3+}-rich ilmenite	E2a-1	Mn-rich ilmenite
E2b	Fe^{3+} and Mg-rich ilmenite	E2b-1	Ilmenite s.s.
E2c	Mg-rich ilmenite	E2c-1	Ilmenite s.s.
		E2c-2	Mn-rich ilmenite
E2d	Geikielite	E2d-1	Mn-rich ilmenite
	Perovskite	E2e-1	Ilmenite s.s.
		E2e-2	Mn-rich ilmenite
	Ulvöspinel-magnetite	E2f-1	Ilmenite s.s.
		E2f-2	Mn-rich ilmenite
		E2f-3	Pyrophanite
	magnetite	E2g-1	Fe^{3+}-rich ilmenite
		E2g-2	Mn-rich ilmenite
E2h	Full replacement	E2h	Mn-rich ilmenite

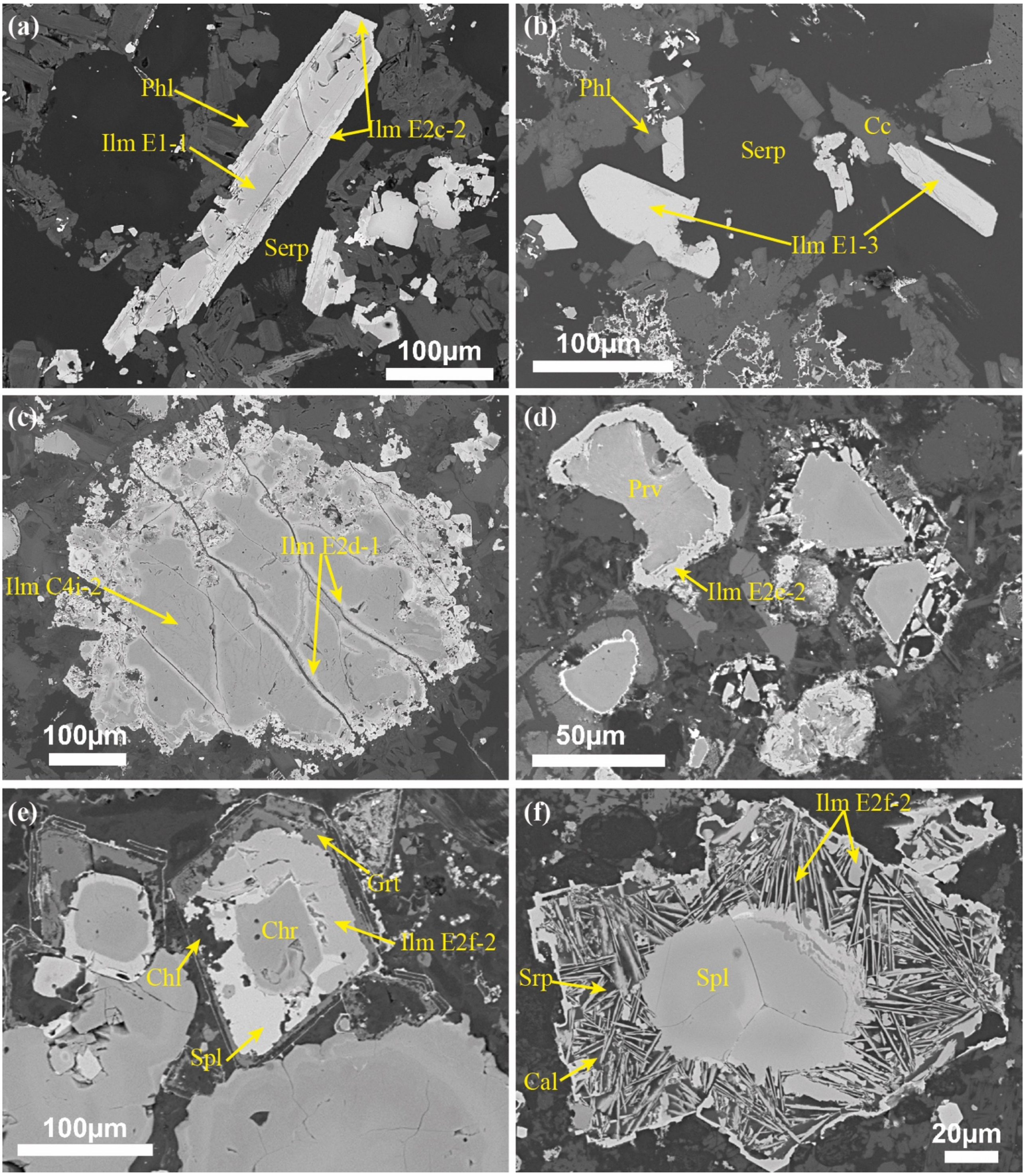

Fig. 6.8. Back-scattered electron (BSE) imagings of hydrothermal ilmenite of paragenesis E. (a) Hydrothermal tabular Mg-rich ilmenite (Ilm E1-1) overgrowing on phlogopite (Phl) and associated with serpentine (Srp); this first ilmenite is replaced by Mn-rich ilmenite (Ilm E2c-2), in the Banankoro "B" coherent kimberlite. (b) Mn-rich tabular ilmenite (Ilm E1-3) overgrowth on phlogopite and calcite (Cc) and associated with serpentine, in the Chicken Park coherent kimberlite. (c) Mn-rich ilmenite (Ilm E2d-1) replacing geikielite (Ilm C4i-2) along cracks, in the Chicken Park coherent kimberlite. (d) Mn-rich ilmenite (Ilm E2e-2) replacing perovskite (Prv), in the Shengli coherent kimberlite. (e) Mn-rich ilmenite (Ilm E2f-2) replacing ulvöspinel-titanomagnetite (Spl), associated with chlorite (Chl) and hydrogarnet (Grt), in the Chigicherla CC-4 coherent kimberlite. (f) Tabular Mn-rich ilmenite (Ilm E2f-2) replacing ulvöspinel-titanomagnetite (Spl), associated with serpentine and calcite, from the Chigicherla cluster CC-5 coherent kimberlite. Chr: chromite.

6.3. CHEMICAL COMPOSITION

Ilmenite group minerals found in kimberlite and related rocks are essentially solid solutions between ilmenite ($Fe^{2+}TiO_3$), geikielite ($MgTiO_3$), pyrophanite ($Mn^{2+}TiO_3$) and hematite (Fe_2O_3). Different paragenesis types fall in the ilmenite dominant field, but there are others that fall into the geikielite and pyrophanite dominant fields.

6.3.1. Ilmenites within xenolith (paragenesis A)

As explained in the introduction to the classification of ilmenites, ilmenites found in peridotitic xenoliths are Fe^{3+}-rich ilmenite (A1-1), Mg-rich ilmenite (A1-2) and ilmenite s.s. (A1-3). Ilmenites in MARID/PIC xenoliths are Fe^{3+}-rich ilmenite (A2-1), Fe^{3+}-rich and Mg-rich ilmenite (A2-2), Mg-rich ilmenite (A2-3) and ilmenite ss. (A2-4). Ilmenites in basaltic xenoliths are Fe^{3+}-rich ilmenite (A3-1); ilmenite s.s. (A3-2) and Mn-rich ilmenite (A3-3). Ilmenites in granitic xenoliths are ilmenite s.s. (A4-1), Mn-rich ilmenite (A4-2) and pyrophanite (A4-3). Ilmenite inclusions in phlogopite xenocrysts is Fe^{3+}-rich (A5-1) and Mg-rich ilmenite (A5-2).

The classification of the ilmenite types, in terms of the proportions of the end members of the ilmenite-hematite-geikielite-pyrophanite series, shows that most crystals fall within the ilmenite field, except that of pyrophanite (91 mol% pyrophanite) found in granitic xenoliths (Fig. 6.9). No geikielite dominant ilmenites were found in xenoliths. The hematite component remains below 16 mol%. The pyrophanite component is low in the most of crystals except in the crystal of pyrophanite, while a slight Mn-enrichment is found in some crystals in basaltic and granitic xenoliths. The compositional ranges of ilmenites in mantle xenoliths including peridotitic xenoliths, MARID xenoliths and ilmenites as inclusion in phlogopite and olivine macrocrysts are very similar, while ilmenite in crustal xenoliths including basaltic xenoliths and granitic xenoliths are very similar (Fig. 6.9-6.11).

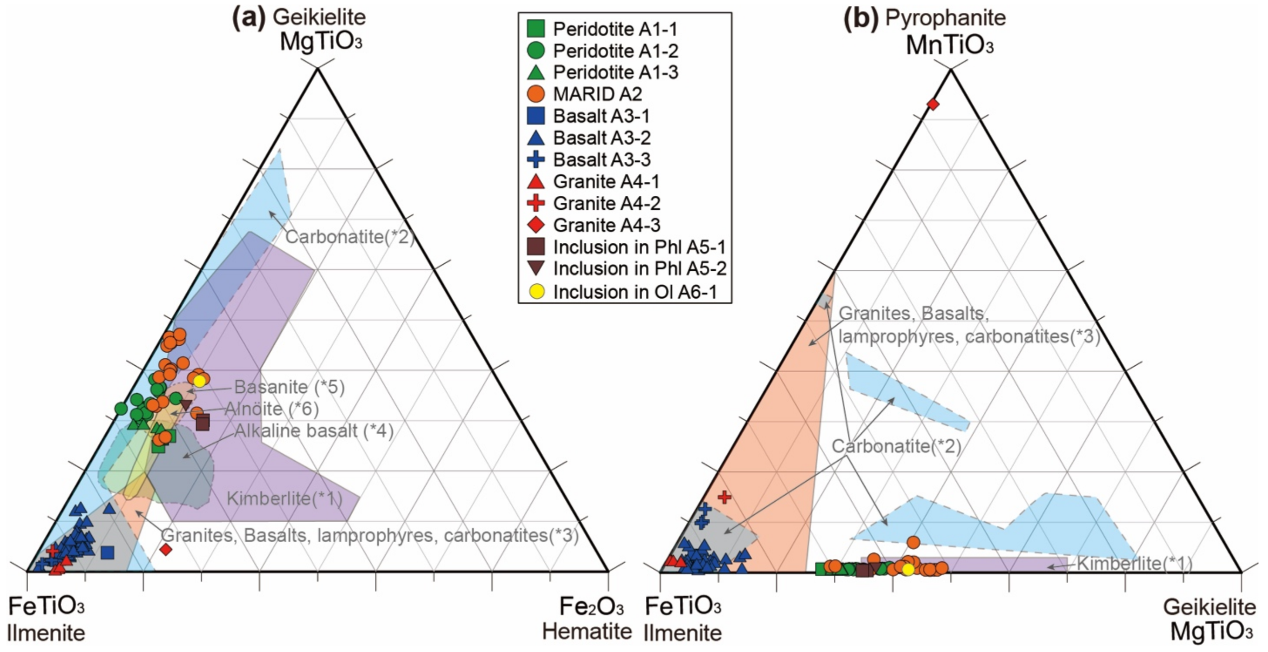

Fig. 6.9. Composition of ilmenite in xenoliths in the system (a) $MgTiO_3$-$FeTiO_3$-Fe_2O_3 and (b) $MnTiO_3$-$FeTiO_3$- $MgTiO_3$, compared with those of kimberlites (*1=Mitchell, 1986), carbonatites (*2=Mitchell, 1978; Gaspar and Wyllie, 1983), granites and basalts (*3=Mitchell, 1978), alkaline basalts (*4=Parfenoff, 1982), basanites (*5=Leblanc et al., 1982) and alnöites (*6=Nixon and Boyd, 1979).

Ilmenites from mantle xenoliths (in peridotitic and MARID xenoliths and in inclusions in phlogopite) have higher MgO content (6.7-10.5 wt% MgO in peridotitic xenoliths, 7.3-13.2 wt% MgO in MARID xenoliths and 7.2-9.0 wt% MgO in inclusions in phlogopite). They fall into the field of kimberlitic ilmenites (Wyatt *et al.*, 2004) and most of them fall into the MARID field (Fitzpayne *et al.*, 2018, Fig. 6.10a).

Ilmenites from crustal xenoliths have lower MgO content (0.3-3.3 wt% MgO in basaltic xenoliths and 0.1-0.9 wt% MgO in granitic xenoliths). They fall out of the field of kimberlitic ilmenites (Wyatt *et al.*, 2004, , Fig. 6.10a). However, magnesian ilmenite, (<30 mol% geikielite) in addition to its occurrence in some peridotitic xenoliths (A1-3) may also be found in basaltic (A3-2) and granitic (A4-1) xenoliths, but showing quite different compositions. Ilmenite in peridotitic xenoliths has higher Mg content (26.2-29.2 mol% geikielite, 7.1-8.1 wt% MgO) than in crustal xenoliths (1.1-12.5 mol% geikielite, 0.2-3.3 wt% MgO).

Ilmenite in mantle xenoliths is enriched in Cr (1.3-2.4 wt% Cr_2O_3 in peridotitic xenoliths; 0-4.1wt% Cr_2O_3 in MARID xenoliths, and 1.6-10 wt% Cr_2O_3 in ilmenite inclusions in phlogopites), while ilmenite from crustal xenoliths is Cr-free (< 0.2 wt% Cr_2O_3, Fig. 6.10b). Ilmenite in peridotitic xenoliths fall into the ilmenite megacryst parabola (Haggerty, 1991, 1995) while ilmenite in MARID xenoliths fall out of the parabola. Extremely high Cr contents are found in Fe^{3+}-rich ilmenite inclusions in phlogopite (9.3-9.9 wt% Cr_2O_3). There is no correlation between Ti and Cr, although the highest Cr contents of ilmenite in phlogopite are accompanied by the lowest Ti contents (Fig. 6.11a).

There is no correlation between Mn and Nb (Fig. 6.11b). Nb content is generally low in crustal xenoliths (< 0.2 wt% Nb_2O_5) except in one crystal, while part of ilmenite in mantle xenoliths is relatively Nb-enriched, the highest Nb content being found in Mg-rich ilmenite in MARID xenolith (up to 1.85 wt% Nb_2O_5, Fig 6.11c).

The Fe_2O_3 contents in ilmenite are similar in crustal and mantle xenoliths, while the highest Fe_2O_3 tenors are found in ilmenite inclusions in phlogopite and in ilmenite from MARID xenoliths (Fig. 6.10d). As expected, there is a good negative correlation between Ti and Fe^{3+} and ilmenite compositions are similar in terms of Fe^{3+}-Ti relation in mantle xenoliths and crustal xenoliths (Fig. 6.11c). The highest Fe^{3+} values are found in Fe^{3+}-rich ilmenite inclusions in phlogopite.

Finally, a slight enrichment in Zr may occur in some ilmenite s.s. crystals in basaltic xenoliths (Fig. 6.11-12), achieving about 1.8 wt% Zr.

All the compositions of ilmenite in xenoliths plot far from the ilmenite inclusions in diamond reported by (Sobolev *et al.*, 1997, Fig. 6.12a-c). The Mg-rich ilmenite in MARID xenoliths having relatively higher Nb content have relatively low Zr, Ni and Cr content (Fig. 6.12a-c).

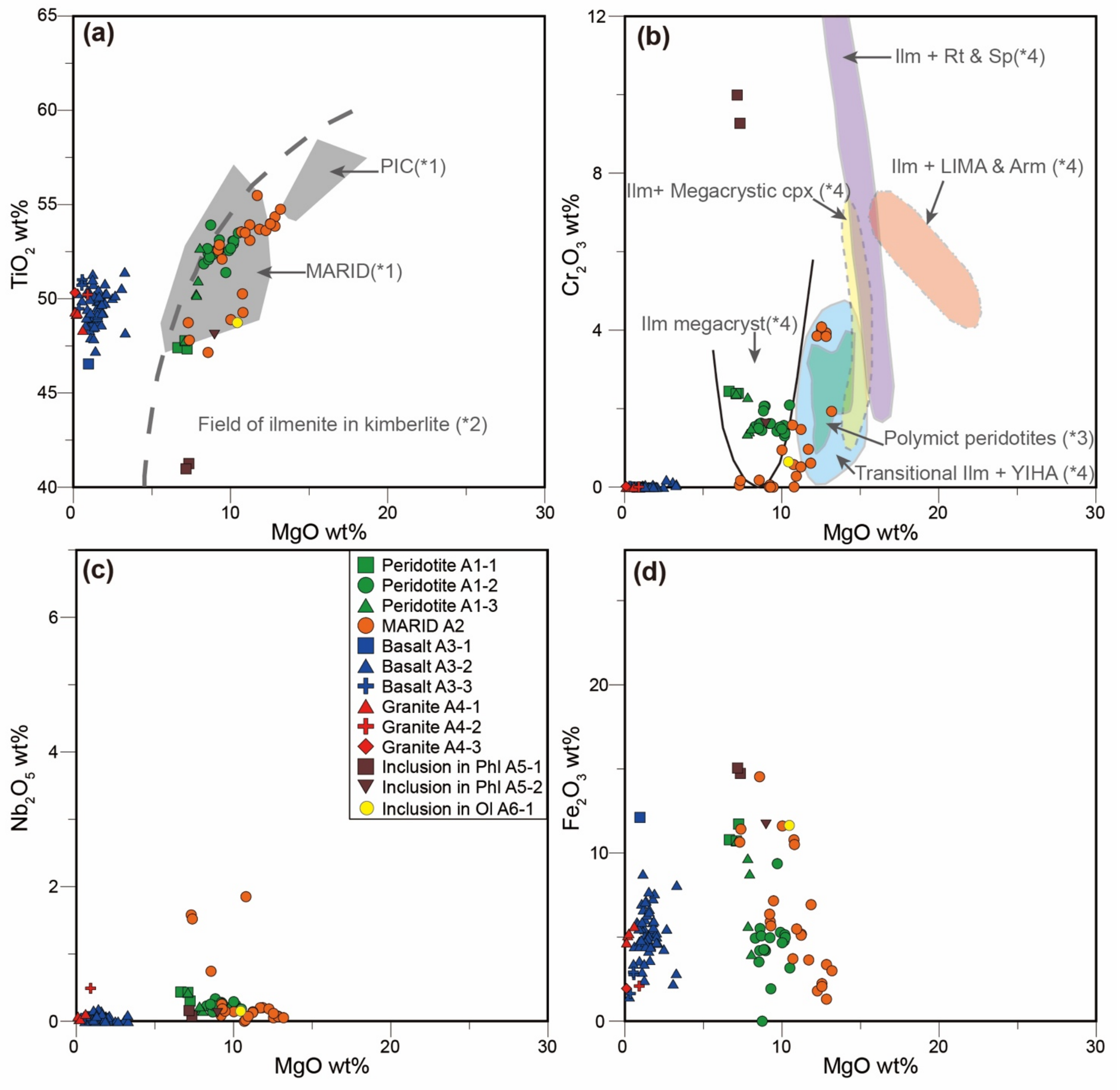

Fig. 6.10. Compositional diagrams of ilmenite in xenoliths:. (a) MgO wt% vs. TiO_2 wt%; (b) MgO wt% vs. Cr_2O_3 wt%; (c) MgO wt% vs. Nb_2O_5 wt%; (d) MgO wt% vs. Fe_2O_3 wt% projection. MARID and PIC fields (*1) from Fitzpayne et al. (2018). Field of ilmenite in kimberlites (*2) from (Wyatt et al., 2004). Ilmenite field in polymict peridotites (*3) from Zhang et al. (2001). Metasomatic ilmenites (Ilm) in association with LIMA and armalcolite (Arm), with rutile (Rt) and spinel (Sp), and with megacrystic clinopyroxene (Cpx), with YIHA (yimengite and hawthorneite) respectively (*4=Haggerty, 1991, 1995). Megacrystic ilmenite (*4) from Haggerty (1991, 1995).

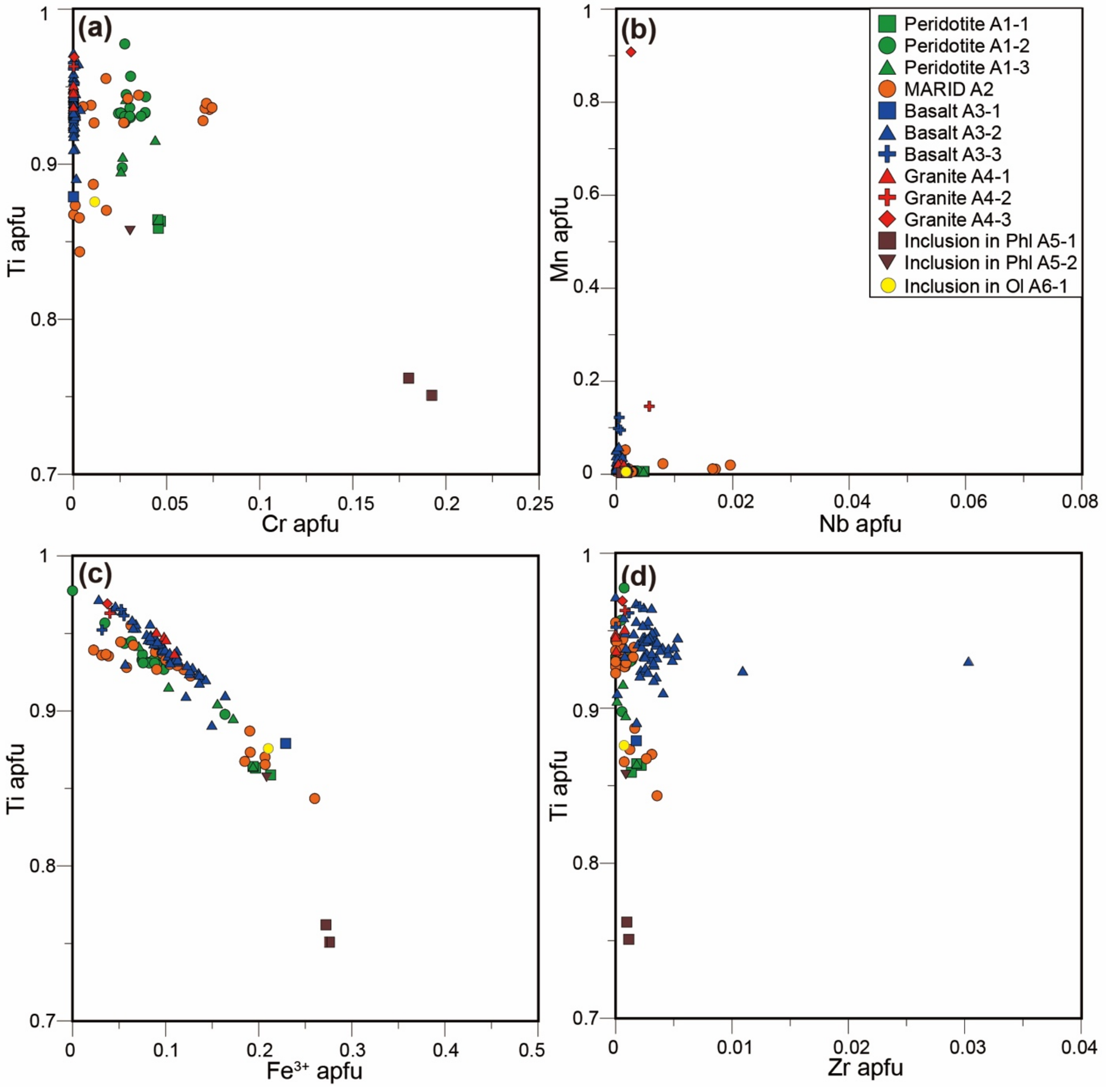

Fig. 6.11. Composition of ilmenite in xenoliths in (a) Cr apfu vs. Ti apfu; (b) Nb apfu vs. Mn apfu ; (c) Fe^{3+} apfu vs. Ti apfu; (d) Zr apfu vs. Ti apfu.

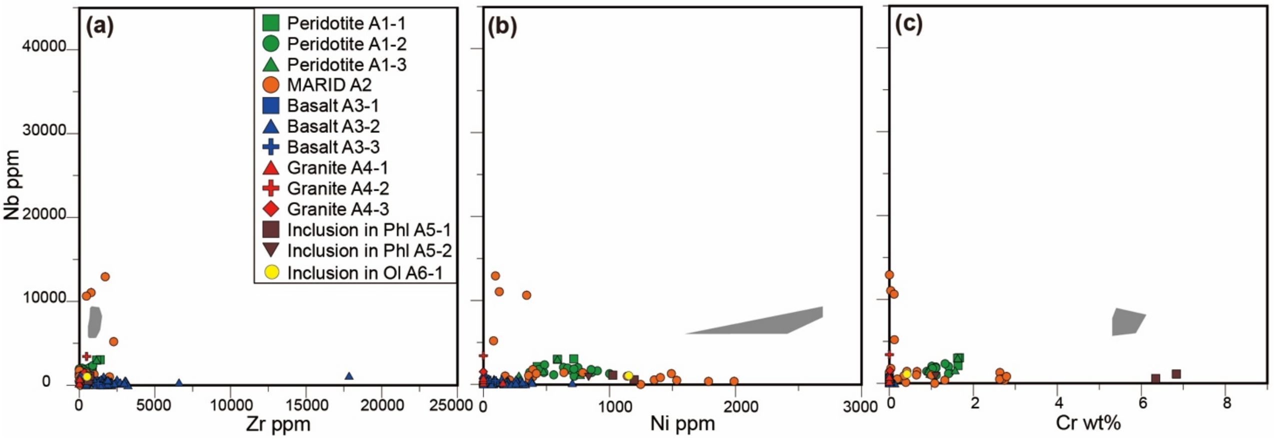

Fig. 6.12. Composition of ilmenite in xenoliths in (a) Zr ppm vs. Nb ppm; (b) Ni ppm vs. Nb ppm; (c) Cr wt% vs. Nb ppm projections. Grey area corresponds to compositions of ilmenite inclusions in diamond from the Sputnik kimberlite (Sobolev et al., 1997).

6.3.2. Ilmenite xenocrysts (paragenesis B)

As explained in the classification of the ilmenites, ilmenite-group xenocrysts have many possible compositions: Fe^{3+}-rich ilmenite (B-1); Fe^{3+}-rich and Mg-rich ilmenite (B-2), Mg-rich ilmenite (B-3), ilmenite s.s. (B-4), Mn-rich ilmenite (B-5) and pyrophanite (B-6). The classification of the these types, in terms of the proportions of the end members of the ilmenite-hematite-geikielite-pyrophanite series, shows that most crystals fall within the ilmenite field, with the exception of the B-4 pyrophanite (51.3-82.4 mol% pyrophanite) which is similar to that found in some crystals in granitic xenoliths (Fig. 6.13).

Since geikielite has not been found as a component of the xenoliths, we assume that geikielite isolated anhedral crystals in the groundmass cannot be considered as reflecting the primary compositions of xenocrysts and are considered as groundmass ilmenite or as xenocrysts totally replaced by geikielite.

The hematite component is relatively enriched in Fe^{3+}-rich ilmenite (B-1, 10.0-24.6 mol% hematite); Fe^{3+}-rich and Mg-rich ilmenite has similar contents (B-2, 10.1-20.4 mol% hematite). The pyrophanite component is low most of the crystals, except in the crystals of Mn-rich ilmenite and pyrophanite.

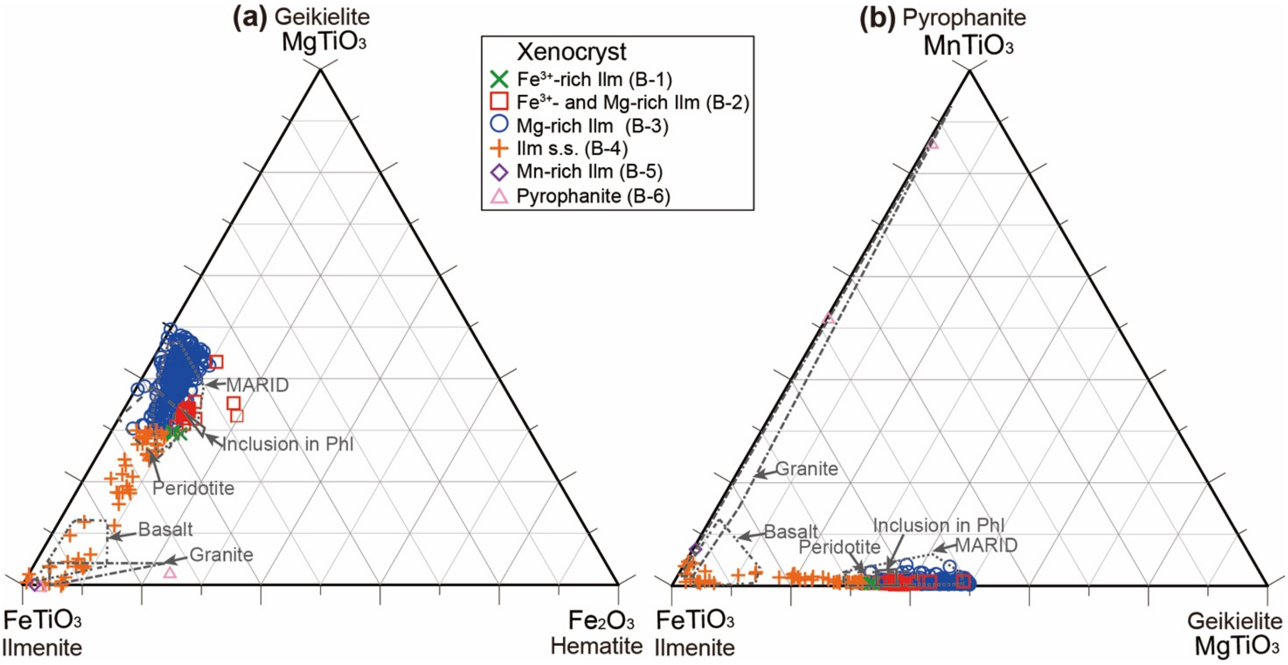

Fig. 6.13. Composition of ilmenite-group minerals in xenocrysts in the system (a) $MgTiO_3$-$FeTiO_3$-Fe_2O_3 and (b) $MnTiO_3$-$FeTiO_3$-$MgTiO_3$, compared with the compositions of ilmenites from different xenoliths studied in this work.

The compositional ranges of Fe^{3+}-rich ilmenite (B-1), Fe^{3+}-rich and Mg-rich ilmenite (B-2), Mg-rich ilmenite (B-3) found in xenocrysts are similar to that of the ilmenite found in mantle xenoliths, including peridotitic xenoliths, MARID xenoliths and ilmenite as inclusion in phlogopite macrocrysts. Similarly, Mn-rich ilmenite (B-5) and pyrophanite (B-6) have similar compositions to the ilmenite-group minerals found in basaltic or granitic crustal xenoliths (Fig. 6.13-6.14).

Fe^{3+}-rich ilmenite (B-1), Fe^{3+}-rich and Mg-rich ilmenite (B-2) and Mg-rich ilmenite (B-3) are enriched in Cr (0-4.16 wt% Cr_2O_3 in Fe^{3+}-rich ilmenite; 0-5.9 wt% Cr_2O_3 in Fe^{3+}- and Mg-rich ilmenite, and 0-4.81 wt% Cr_2O_3 in Mg-rich ilmenite).

Contrastingly, Mn-rich ilmenite (B-5) and pyrophanite (B-6) have low Cr (< 0.4 wt% Cr_2O_3, Fig.

6.14b). Ilmenite s.s. has Cr contents varying from 0 to 2.9 wt% Cr_2O_3. The highest Cr content is found in Fe^{3+}-rich and Mg-rich ilmenite. There is no clear correlation between Ti and Cr, although the highest Cr contents in ilmenite corresponds with relatively low Ti content (Fig. 6.15a).

There is no correlation between Mn and Nb (Fig. 6.15b). Nb content is generally low (< 1 wt% Nb_2O_5). Relatively high Nb contents are found in ilmenite s.s. (up to 4.7 wt% Nb_2O_5) and pyrophanite (up to 2.6 wt% Nb_2O_5, Fig 6.14c).

The Fe_2O_3 content is similar in ilmenite s.s. and Mg-rich ilmenite (Fig. 6.14d). The Fe^{3+}- and Mg-rich ilmenite may have up to 0.4 apfu Fe^{3+}. Mn-rich ilmenite and pyrophanite have low Fe^{3+} content. As expected, there is a good negative correlation between Ti and Fe^{3+} (Fig. 6.15c).

Finally, Zr content remains relatively low (Fig. 6.15-16). The highest Zr content is 12453 ppm.

All ilmenite xenocrysts plot far from those ilmenite inclusions in diamond reported by (Sobolev *et al.*, 1997, Fig. 6.16a-c). Ilmenite s.s. having relatively higher Nb content has relatively low Zr, Ni and Cr content (Fig. 6. 16a-c). Mg-rich ilmenite which has relatively high Ni and Cr content has low Nb content.

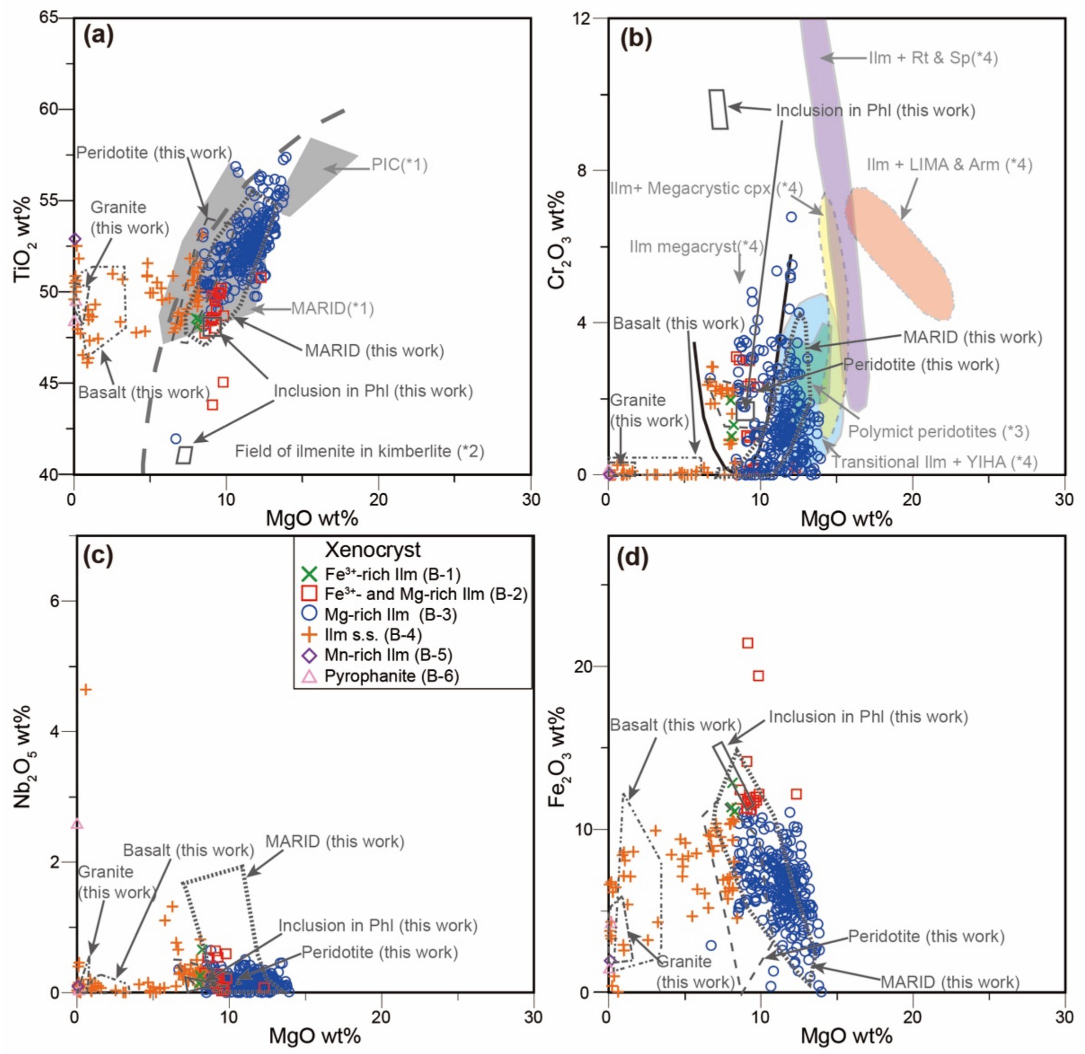

Fig. 6.14. Composition of ilmenite xenocrysts in (a) MgO wt% vs. TiO_2 wt%; (b) MgO wt% vs. Cr_2O_3 wt%; (c) MgO wt% vs. Nb_2O_5 wt%; (d) MgO wt% vs. Fe_2O_3 wt% projection. MARID and PIC fields (*1) from Fitzpayne et al. (2018). Field of ilmenite in kimberlite (*2) from (Wyatt et al., 2004). Ilmenite field in polymict peridotite (*3) from Zhang et al. (2001). Metasomatic ilmenites (Ilm) in association with LIMA and armalcolite (Arm), with rutile (Rt) and spinel (Sp), and with megacrystic clinopyroxene (Cpx), with YIHA (yimengite and hawthorneite) respectively (*4=Haggerty, 1991, 1995). Megacrystic ilmenite (*4) from Haggerty (1991, 1995).

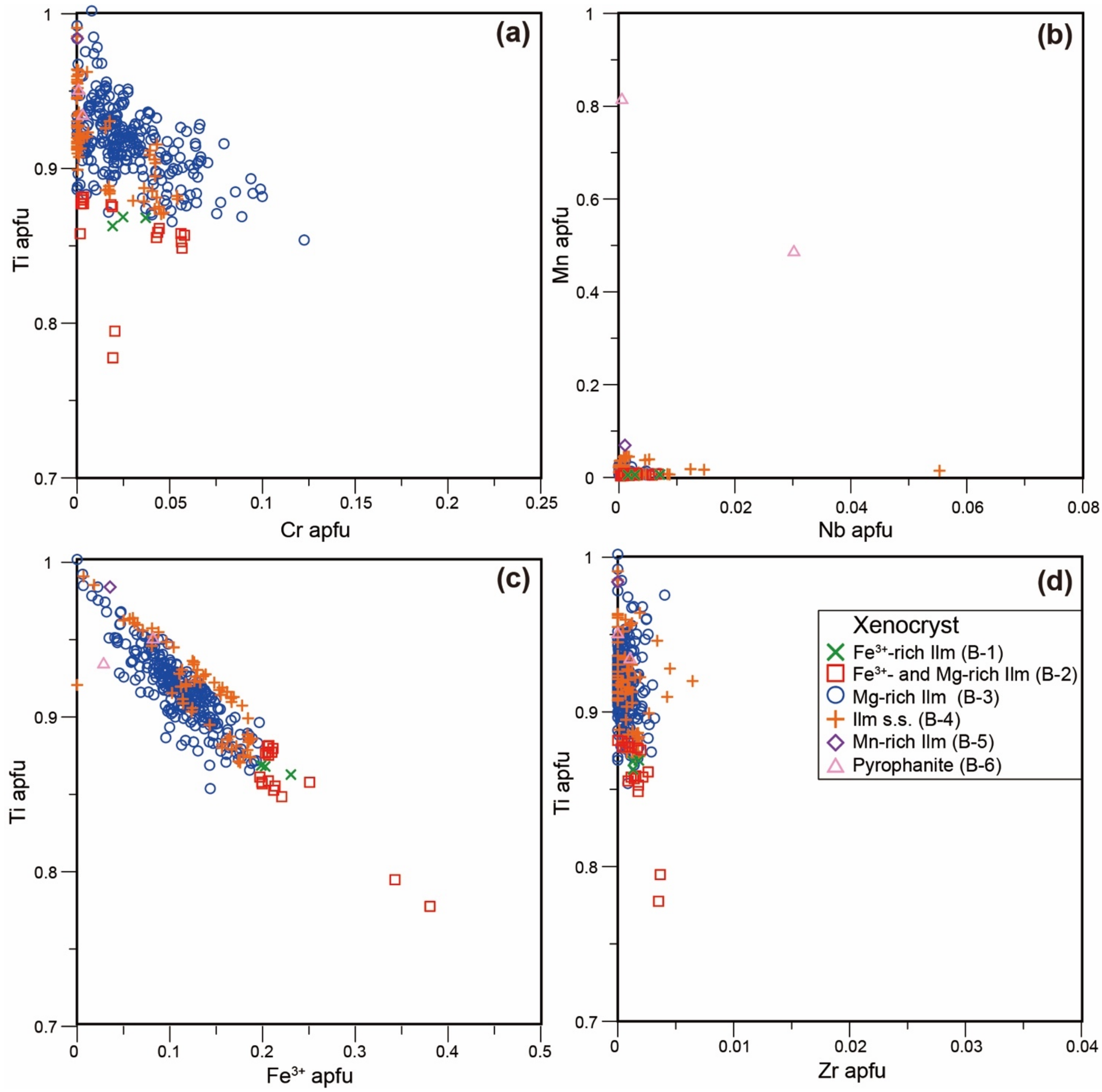

Fig. 6.15. Composition of ilmenite xenocrysts: (a) Cr apfu vs. Ti apfu; (b) Nb apfu vs. Mn apfu; (c) Fe^{3+} apfu vs. Ti apfu; (d) Zr apfu vs. Ti apfu.

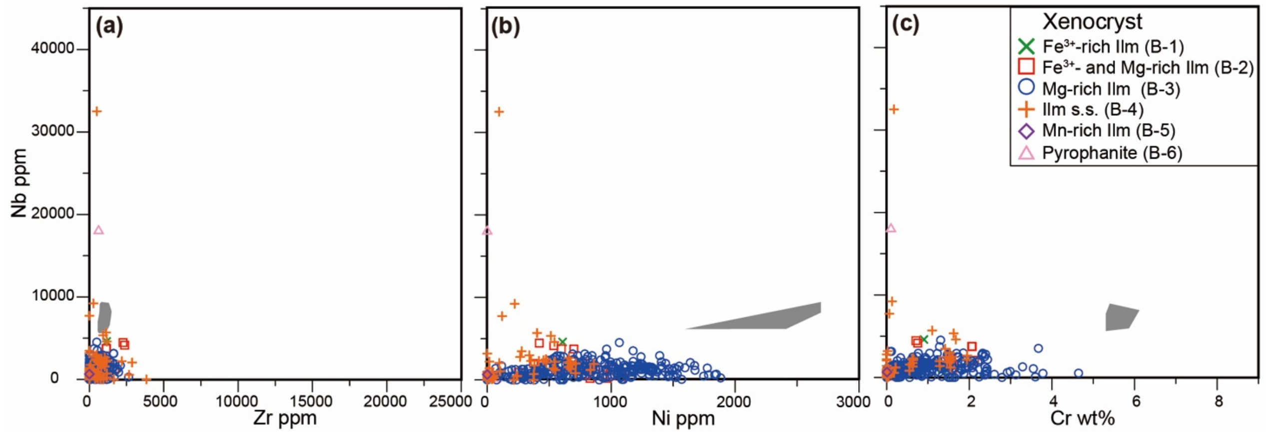

Fig. 6.16. Composition of ilmenite xenocrysts: (a) Zr ppm vs. Nb ppm; (b) Ni ppm vs. Nb ppm; (c) Cr wt% vs. Nb ppm projections. Grey area is ilmenite inclusions in diamond from the Sputnik kimberlite (Sobolev et al., 1997).

6.3.3. Ilmenites of the intrusive stage 1 (early magmatic primary ilmenite; paragenesis C)

Ilmenite found as inclusion in fresh or pseudomorphosed olivine (C1), groundmass ilmenite (C2), and ilmenite found in veins crosscutting olivine macrocrysts (C3) have similar chemical compositions (Fig. 6.17). In the case of the ilmenites found as inclusions in olivine, those found in both fresh olivine and pseudomorphosed olivine have similar compositions, and therefore the serpentinization process does not produce significative modifications.

Ilmenites found as inclusions in olivine phenocrysts in kimberlites are highly magnesian, having compositions ranging from Mg-rich ilmenite (C1-1), to Fe^{3+}-rich geikielite (C1-2) and to geikielite (C1-3). The same three compositional types of ilmenite are also found in groundmass ilmenite in kimberlite. The majority of C1-C3 ilmenite in kimberlites have more than 40 mol% of geikielite component, and less than 10 mol% of the hematite component (Fig. 6.17). Groundmass ilmenite reaches the highest geikielite contents (up to 74.4 mol% geikielite). Nearly all C1 to C3 ilmenite are almost devoid of pyrophanite component (< 6 mol% pyrophanite, and in most of the cases well below 5 mol% pyrophanite).

Contrastingly, the equivalent magmatic ilmenites found in lamproites, orangeites and UMLs as inclusions in olivine and as groundmass have relatively lower Mg contents than those of the majority of ilmenite in kimberlites. The C1-C2 ilmenites in lamproites, orangeites and UMLs are Mg-rich ilmenite, but geikielite is not found in these rocks. Altred

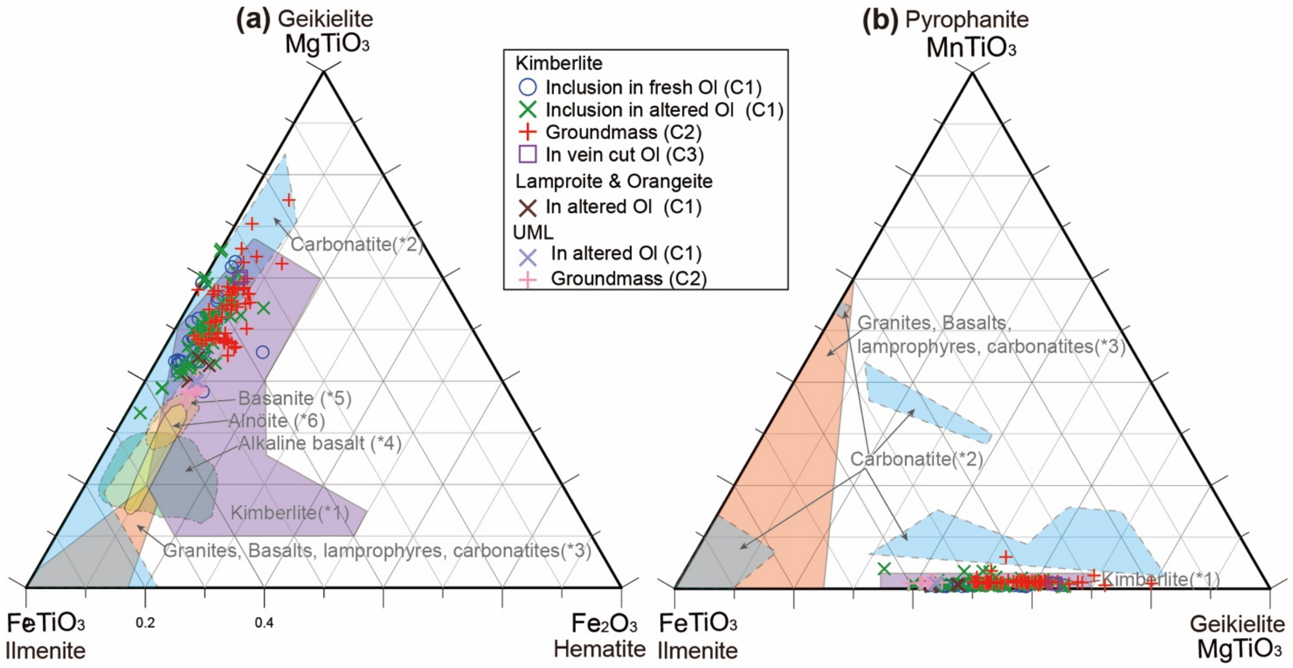

Fig. 6.17. Composition of primary magmatic early ilmenites as inclusions in olivine (C1), as groundmass (C2) and filling veinlets crosscutting olivine (C3) in the system (a) $MgTiO_3$-$FeTiO_3$-Fe_2O_3 and (b) $MnTiO_3$-$FeTiO_3$-$MgTiO_3$. For comparison, there are the fields of next rocks: "kimberlites" (*1=Mitchell, 1986), carbonatites (*2=Mitchell, 1978; Gaspar and Wyllie, 1983), granites and basalts (*3=Mitchell, 1978), alkaline basalts (*4=Parfenoff, 1982), basanites (*5=Leblanc et al., 1982) and alnöites (*6=Nixon and Boyd, 1979).

Nearly all of the analysed C1-C3 ilmenites fall into or in the vicinity of the field of kimberlitic ilmenites as defined by Wyatt *et al.* (2004, Fig. 6.18a), including primary ilmenite in lamproites, orangeites and UML. MgO content vary from 8.8 to 22.0 wt% in C1-C3 ilmenite from kimberlites, while ranges 10.7-12.6 wt% MgO in lamproites and orangeites, and 10-11.4 wt % MgO in UML.

The majority of C1-C3 ilmenites fall out of the megacrystic ilmenite field as defined by (Haggerty, 1991, 1995, Fig. 6.18b) but overlap with the compositional field of ilmenites from polymictic peridotites from (Zhang *et al.*, 2001, Fig. 6.18b), and with the transitional ilmenite + YIHA suite, megacrystic ilmenite – clinopyroxene suite and ilmenite + rutile + spinel suite from (Haggerty, 1991, 1995, Fig. 6.18b). Cr contents vary from 0 to 6.7 wt% Cr_2O_3 in C1-C3 ilmenites in kimberlites. The highest Cr content is found in inclusion of ilmenite in fresh olivine in Notre Dâme du Nord (Canada) kimberlite (6.7 wt % Cr_2O_3), while primary ilmenite in lamproite and orangeite has up to 4.0 wt% Cr_2O_3, and up to 1.6 wt% Cr_2O_3 in UML. There is no clear correlation between Ti and Cr, although the highest Cr content ilmenite has relatively low Ti content (Fig. 6.19a).

Nb content is generally low in C1-C3 primary ilmenite (Fig. 6.18c). A slight Nb enrichment is found in ilmenite inclusion in altered olivine in kimberlite (up to 1.2 wt% Nb_2O_5). There is no correlation between Mn and Nb (Fig. 6.19b).

Calculated Fe_2O_3 in C1-C3 ilmenites in kimberlites shows a wide range, varying from 0 to 18.4 wt% (0.3 apfu, Fig. 6.18d), while their values are more restricted in ilmenites from lamproites and orangeites (7.3-10.1 wt% Fe_2O_3) and UML (8.8-11.1wt% Fe_2O_3). As expected, there is a good negative correlation between Ti and Fe^{3+} (Fig. 6.19c).

Finally, Zr content remains low (Fig. 6.19 and 6.20). The highest Zr content is 4258 ppm.

The compositions of the majority of C1-C3 ilmenites plot far from those of the ilmenite inclusions in diamond reported by (Sobolev *et al.*, 1997, Fig. 6.20a-c). No correlation between Nb and Zr, Ni, Cr is observed (Fig. 6.20a-c).

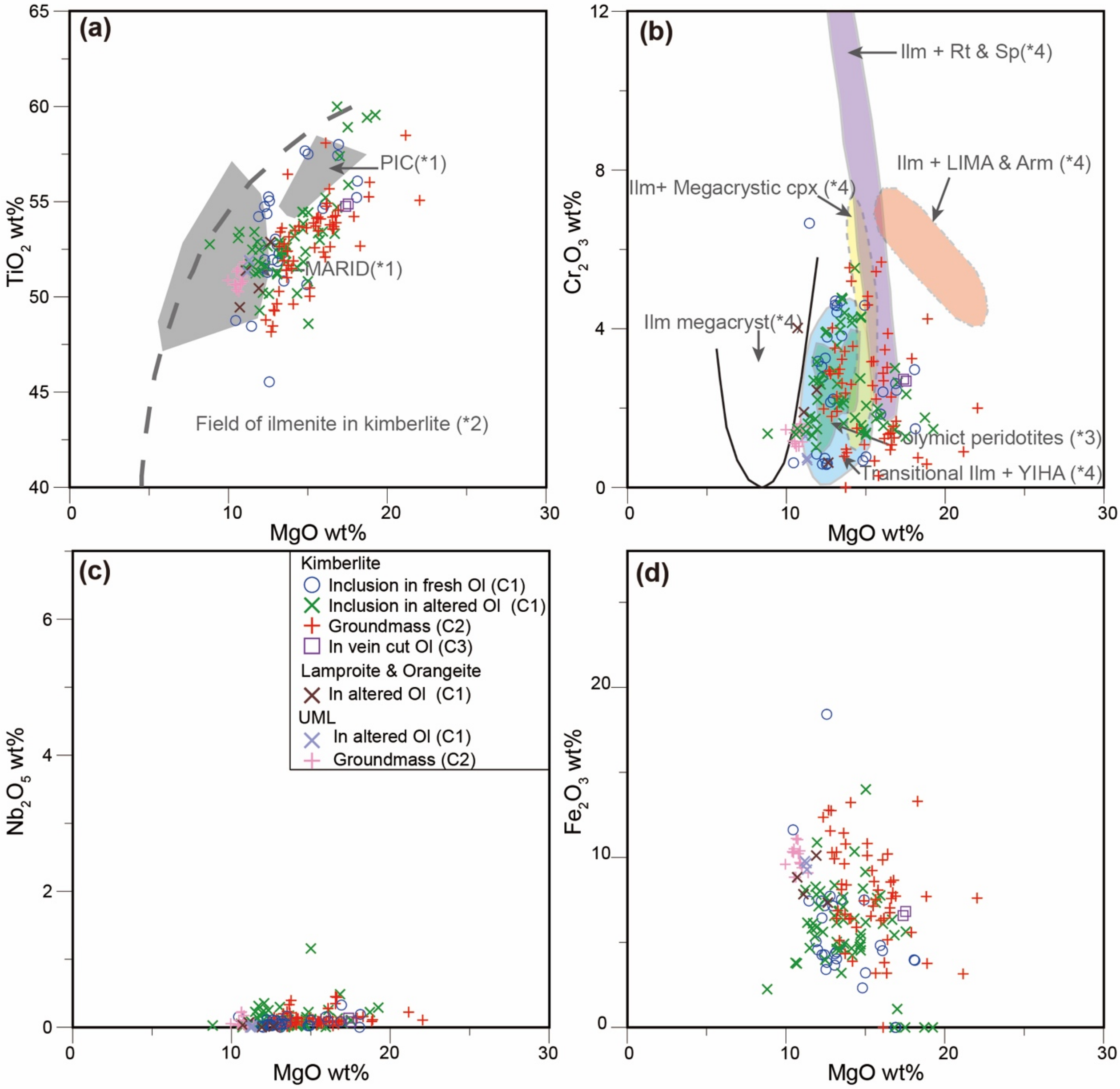

Fig. 6.18. Composition of primary magmatic early ilmenites found as inclusions in olivine (C1), as groundmass (C2) and infilling veinlets cutting olivine (C3), in terms of the following components: (a) MgO wt% vs. TiO_2 wt%; (b) MgO wt% vs. Cr_2O_3 wt%; (c) MgO wt% vs. Nb_2O_5 wt%; (d) MgO wt% vs. Fe_2O_3 wt% projection. MARID and PIC field (*1) from Fitzpayne et al. (2018). Field of ilmenite in kimberlites (*2) from (Wyatt et al., 2004). Ilmenite field in polymict peridotite (*3) from Zhang et al. (2001). Metasomatic ilmenites (Ilm) in association with LIMA and armalcolite (Arm), with rutile (Rt) and spinel (Sp), and with megacrystic clinopyroxene (Cpx), with YIHA (yimengite and hawthorneite) respectively (*4=Haggerty, 1991, 1995). Megacrystic ilmenite (*4) from Haggerty (1991, 1995).

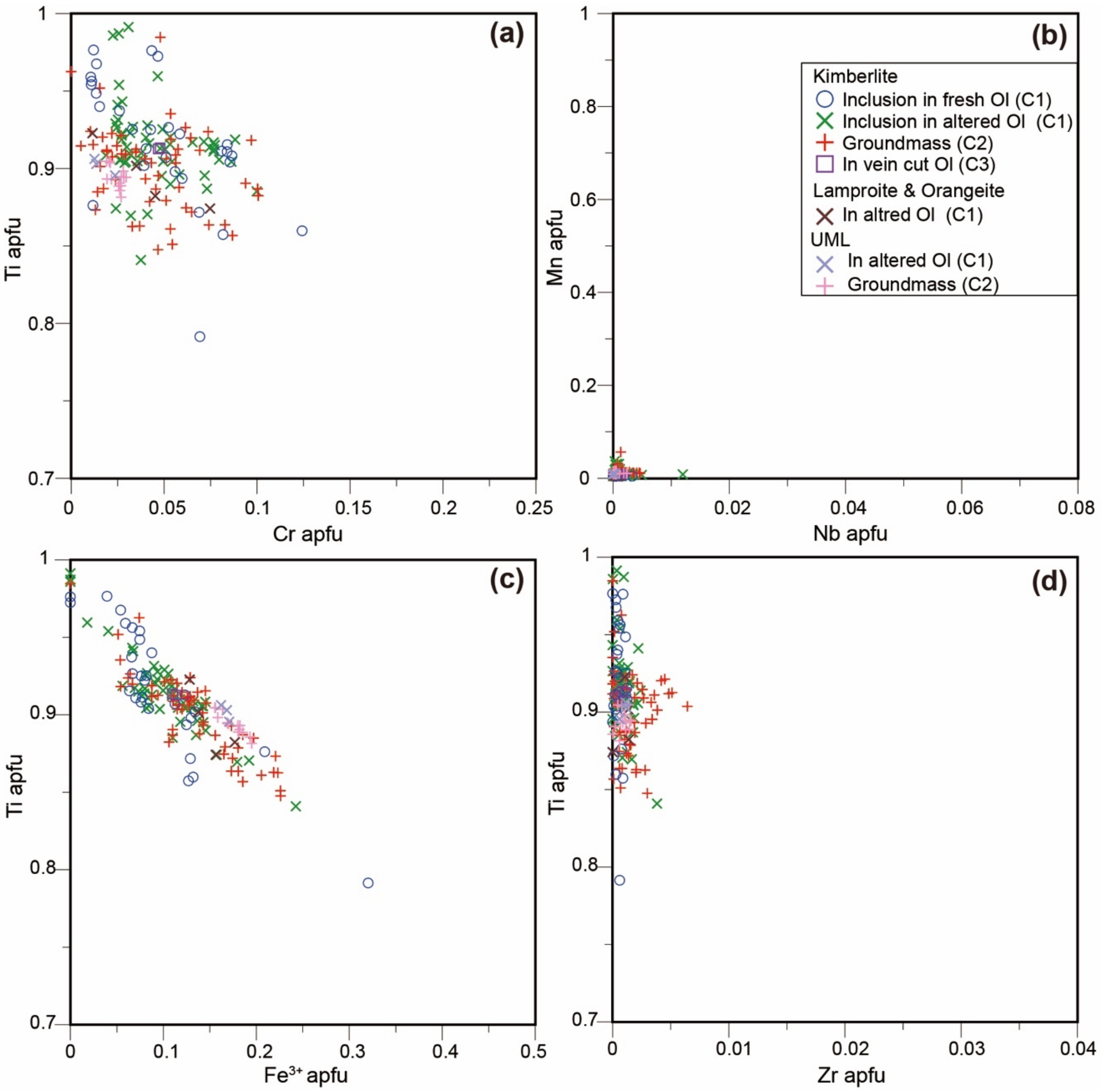

Fig. 6.19. Composition of primary magmatic early ilmenites found as inclusions in olivine (C1), as groundmass (C2) and filling veinlets cutting olivine (C3) in terms of the following components: (a) Cr apfu vs. Ti apfu; (b) Nb apfu vs. Mn apfu; (c) Fe^{3+} apfu vs. Ti apfu; (d) Zr apfu vs. Ti apfu projections.

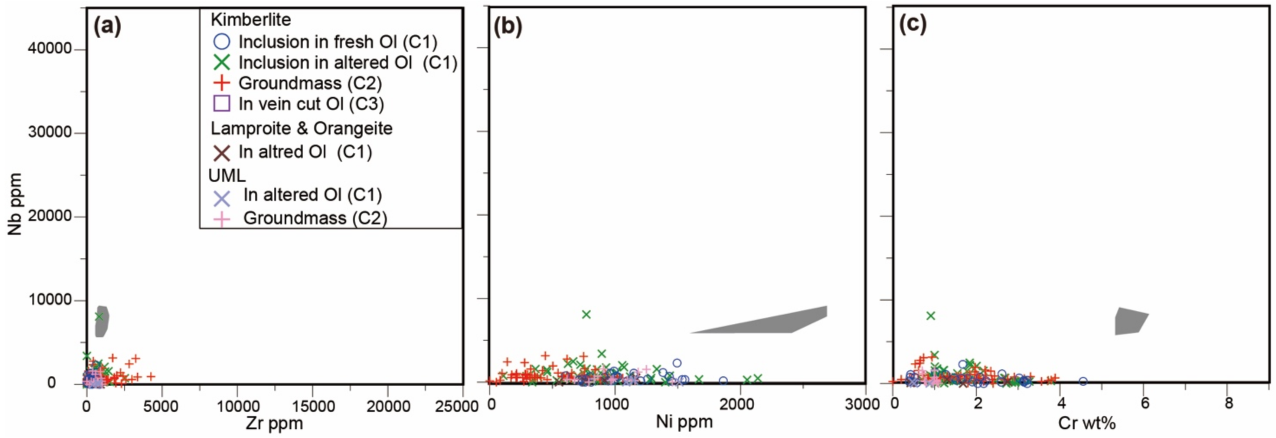

Fig. 6.20. Composition of primary magmatic early ilmenites as inclusion in olivine (C1), as groundmass (C2) and as found in vein cut olivine (C3) in terms of the following components: (a) Zr ppm vs. Nb ppm; (b) Ni ppm vs. Nb ppm; (c) Cr wt% vs. Nb ppm projections. Grey area corresponds to compositions of ilmenite inclusions in diamond from the Sputnik kimberlite (Sobolev et al., 1997).

Replacement of xenocrystic ilmenites and Ti-bearing minerals

As indicated before, the replacement can be produced via diffusion across grain boundaries, small cracks and other discontinuities. Therefore, the variation in composition is strongly dependent of the composition of the replaced mineral, but also of the grade of replacement, thus resulting in a large span of mineral compositions.

The most distinctive property of ilmenites replacing other pre-existing generations of ilmenite or Ti-minerals is that they have a very high geikielite component, varying from 30.2 to 85.3 mol%. The highest content of geikielite component is found in geikielite replacing rutile (C4e-1) in the Menominee kimberlite (Fig. 6.21). In the meantime, the hematite component remains low: the highest value is found in ferrian magnesian ilmenite found partly replacing a Fe^{3+}-rich ilmenite (C4a-1, up to 19.8 mol% hematite) in the Bultfontein kimberlite. The majority of C4 ilmenites are free of pyrophanite component, although some slightly pyrophanite-enriched ilmenites were found in geikielite replacing Mg-rich ilmenite (C4c-2, up to 11.9 mol% pyrophanite) in the Tchiuzo volcaniclastic kimberlite.

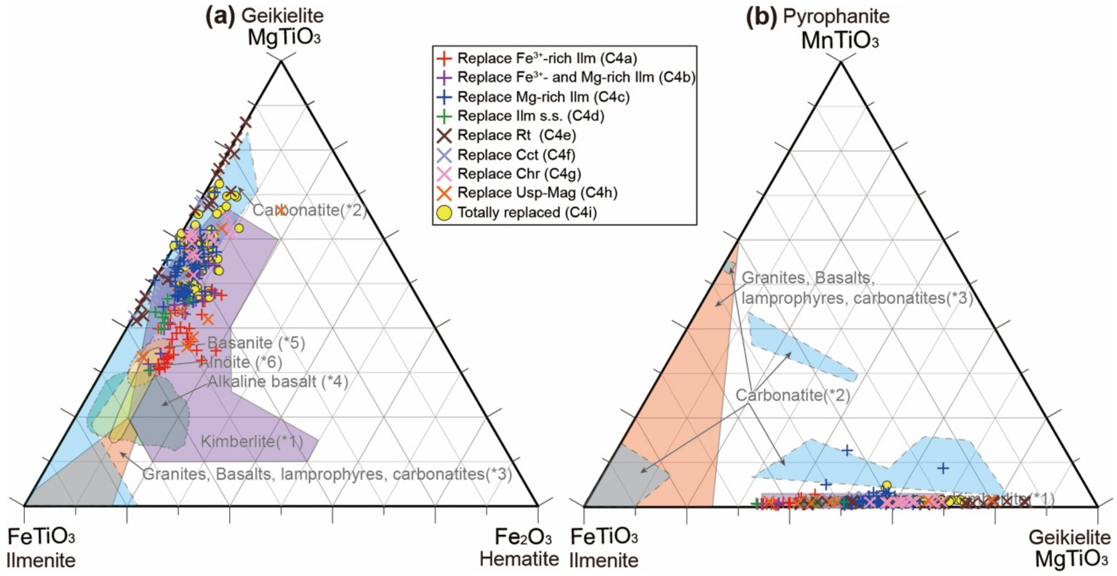

Fig. 6.21. Composition of primary magmatic early ilmenites replacing other ilmenites or Ti-rich minerals in the following diagrams: (a) $MgTiO_3$-$FeTiO_3$-Fe_2O_3 and (b) $MnTiO_3$-$FeTiO_3$- $MgTiO_3$. These results can be compared with the fields defined by other authors: kimberlites (*1=Mitchell, 1986), carbonatites (*2=Mitchell, 1978; Gaspar and Wyllie, 1983), granites and basalts (*3=Mitchell, 1978), alkaline basalts (*4=Parfenoff, 1982), basanites (*5=Leblanc et al., 1982) and alnöites (*6=Nixon and Boyd, 1979).

Nearly all of the analysed C4 ilmenites fall into the field of kimberlitic ilmenites defined by Wyatt *et al.* (2004, Fig. 6.22a). MgO contents vary from 8.3-26.0 wt%.

The majority of the C1-C3 ilmenites fall out of the megacrystic ilmenite field determined by (Haggerty, 1991, 1995, Fig. 6.22b), but overlap with the compositional field of ilmenite from polymictic peridotites from (Zhang *et al.*, 2001, Fig. 6.22b), from transitional ilmenite + YIHA suites, megacrystic ilmenite – clinopyroxene suite and ilmenite + rutile + spinel suites from (Haggerty, 1991, 1995, Fig. 6.22b).

Cr contents are independent of the Mg content, varying from 0 to 9.0 wt% Cr_2O_3. The highest Cr content is found in geikielite replacing crichtonite-group minerals (C4f-2) in the Siddanpalli SK-1 kimberlite (Fig. 6.22b and 6.23a).

Nb tenors are generally low (Fig. 6.22c and 6.23b), while the highest Nb content (up to 1.3 wt%

Nb_2O_5) is found in Mg-rich ilmenite replacing niobian rutile. There is no correlation between Mn and Nb as indicated in the Catoca kimberlite by Robles-Cruz *et al.* (2009), and the highest Nb content is found in ilmenite with low Mn content (Fig. 6.23b).

Calculated Fe_2O_3 in C4 ilmenite in kimberlites show a wide range varying from 0 to 21.2 wt% (0.4 apfu, Fig. 6.22d). Higher Fe^{3+} content is found in ilmenite replacing Fe^{3+}-rich ilmenite (C4a) and replacing ulvöspinel-magnetite (C4h). As expected, there is a good negative correlation between Ti and Fe^{3+} (Fig. 6.23c). Finally, the majority of C4 ilmenite have low Zr contents (Fig. 6.22d and 6.23c). A slight enrichment of Zr is found in ilmenite replacing Zr-rich crichtonite-group minerals (C4f) and replacing Mg-rich ilmenite (C4c). The highest Zr content is 10290 ppm.

The majority of the compositional range of C4 ilmenites plot far from the compositions of ilmenite inclusions in diamond reported by (Sobolev *et al.*, 1997, Fig. 6.24a-c). No correlation between Nb and Zr, Ni, Cr is observed (Fig. 6.24a-c).

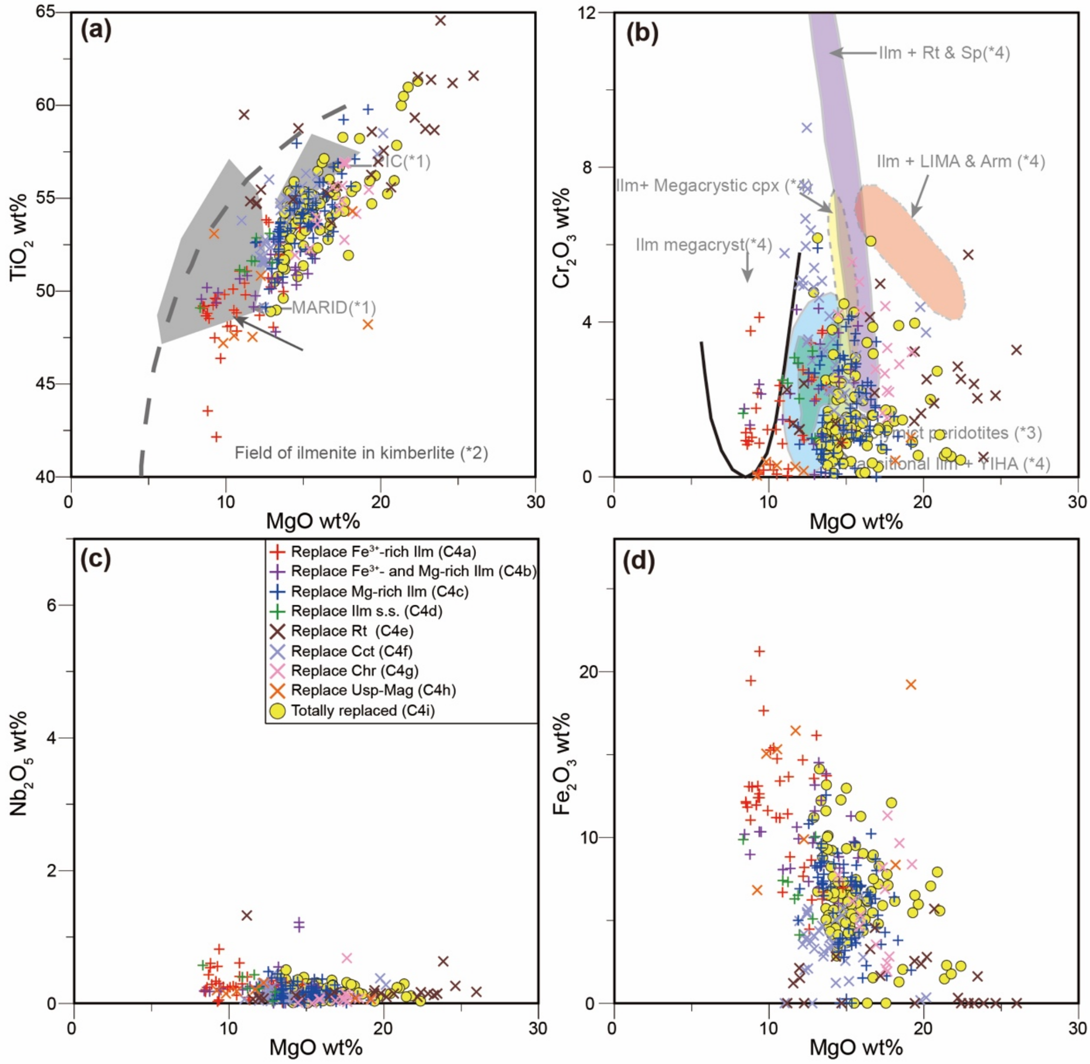

Fig. 6.22. Composition of primary magmatic early ilmenites replacing other ilmenites or Ti-rich minerals in terms of the following parameters: (a) MgO wt% vs. TiO_2 wt%; (b) MgO wt% vs. Cr_2O_3 wt%; (c) MgO wt% vs. Nb_2O_5 wt%; (d) MgO wt% vs. Fe_2O_3 wt% projection. MARID and PIC field (*1) from Fitzpayne et al. (2018). Field of ilmenite in kimberlite (*2) from (Wyatt et al., 2004). Ilmenite field in polymict peridotites (*3) from Zhang et al. (2001). Metasomatic ilmenites (Ilm) in association with LIMA and armalcolite (Arm), with rutile (Rt) and spinel (Sp), and with megacrystic clinopyroxene (Cpx), with YIHA (yimengite and hawthorneite) respectively (*4=Haggerty, 1991, 1995). Megacrystic ilmenite (*4) from Haggerty (1991, 1995).

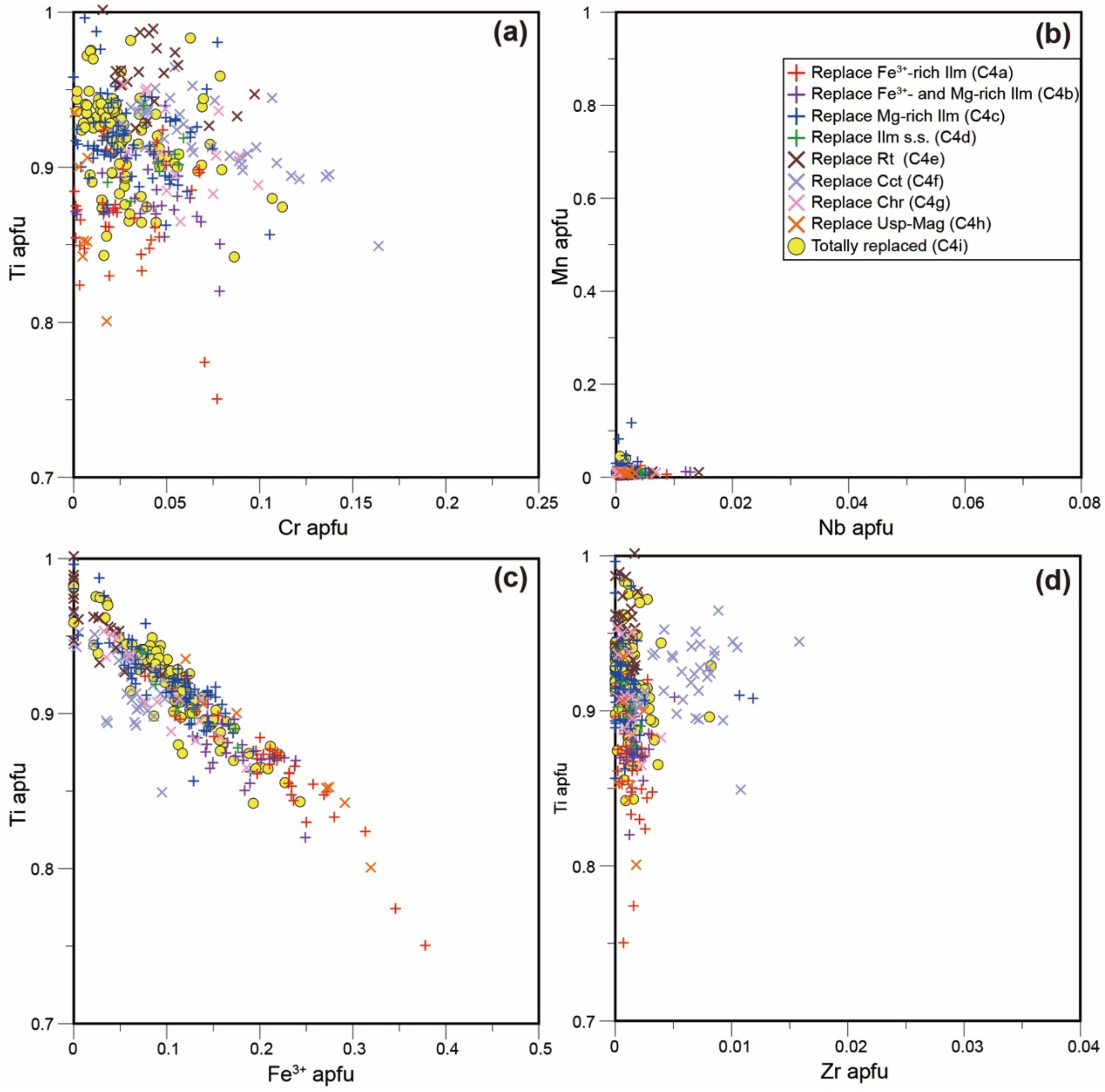

Fig. 6.23. Composition of primary magmatic early ilmenites replacing other ilmenites or Ti-rich minerals expressed in terms of the following parameters: (a) Cr apfu vs. Ti apfu; (b) Nb apfu vs. Mn apfu; (c) Fe^{3+} apfu vs. Ti apfu; (d) Zr apfu vs. Ti apfu projections.

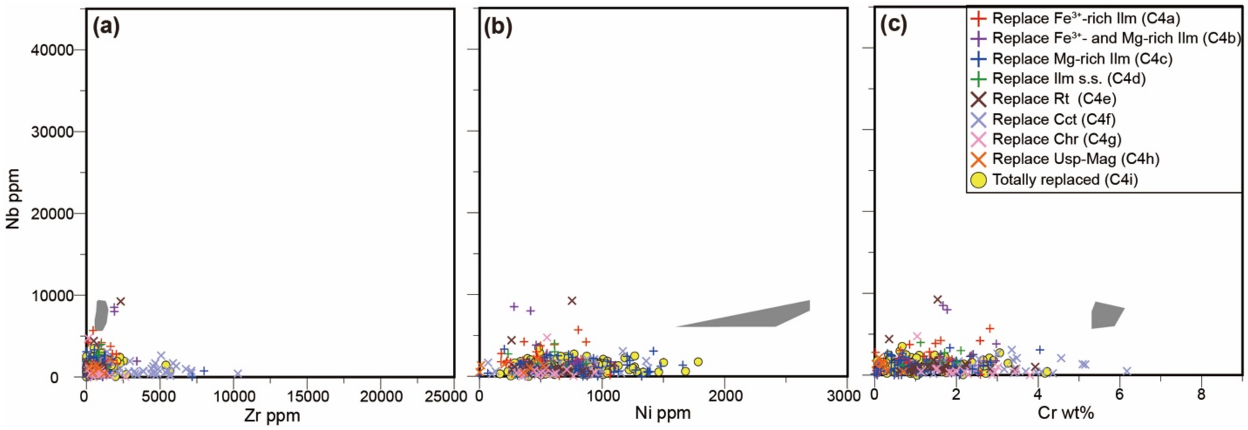

Fig. 6.24. Composition of primary magmatic early ilmenites replacing other ilmenites or Ti-rich minerals in terms of the following parameters: (a) Zr ppm vs. Nb ppm; (b) Ni ppm vs. Nb ppm; (c) Cr wt% vs. Nb ppm projections. Grey area represents compositional field of ilmenite inclusions in diamond from the Sputnik kimberlite (Sobolev et al., 1997).

6.3.4. Ilmenites of the intrusive stage 2 (late magmatic ilmenite, formed before primary perovskite and ulvöspinel and replaced by them, paragenesis D)

Ilmenites from these paragenesis fall into the ilmenite-dominant field, and neither geikielite nor pyrophanite are found (Fig. 6.25). However, some ilmenites replacing geikielite (D1d) or Mg-rich ilmenite (D1c) may be relatively enriched in geikielite component (up to 41.9 mol% geikielite). Those replacing Fe^{3+}-rich ilmenite (D1a) are relatively enriched in hematite component (up to 15.3 mol% hematite). Pyrophanite component is enriched (up to 40.3 mol% pyrophanite) in ilmenite replacing Mg-rich ilmenite (D1c) as well as those replacing Fe^{3+} ilmenite (D1a) and geikielite (D1d).

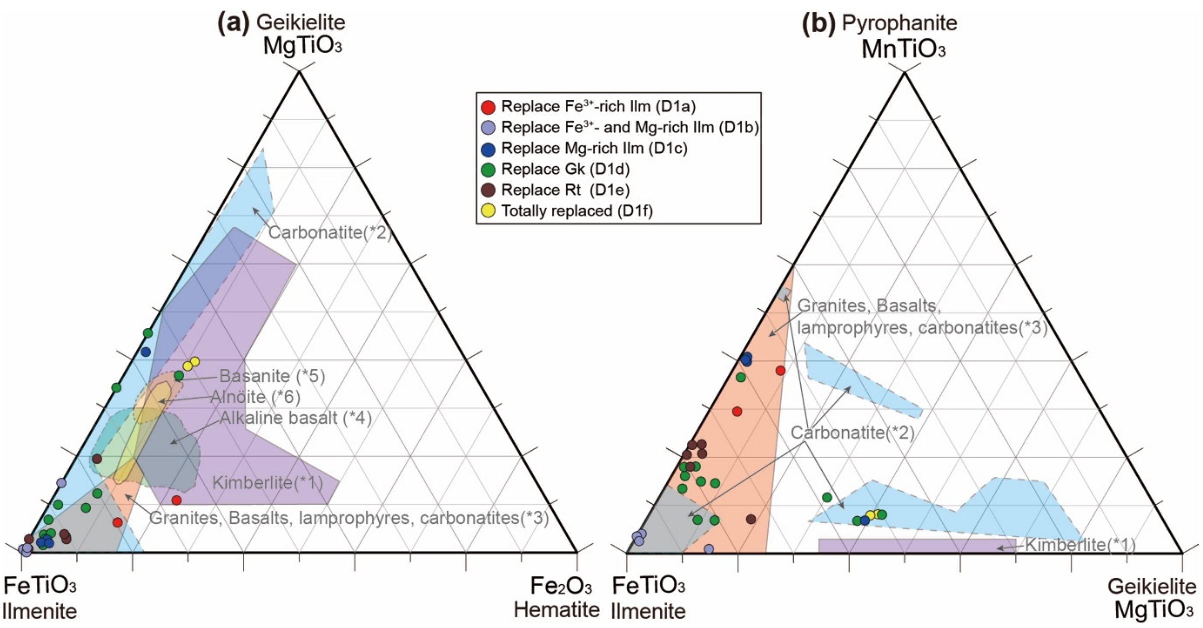

Fig. 6.25. Composition of primary magmatic late ilmenites replacing other ilmenites or Ti-rich minerals in terms of the following parameters: (a) $MgTiO_3$-$FeTiO_3$-Fe_2O_3 and (b) $MnTiO_3$-$FeTiO_3$- $MgTiO_3$. By comparison, there are represented the compositional fields defined by above authors: kimberlites (*1=Mitchell, 1986), carbonatites (*2=Mitchell, 1978; Gaspar and Wyllie, 1983), granites and basalts (*3=Mitchell, 1978), alkaline basalts (*4=Parfenoff, 1982), basanites (*5=Leblanc et al., 1982) and alnöites (*6=Nixon and Boyd, 1979).

Therefore, Mg content is relatively lower than in the case of early magmatic primary ilmenite (paragenesis C). MgO contents vary from 0 to 11wt%. The majority of these ilmenites fall out of the field of kimberlitic ilmenite defined by (Wyatt *et al.*, 2004, Fig. 6.26a).

Most of the D ilmenites fall out of the megacrystic ilmenite field determined by (Haggerty, 1991, 1995, Fig. 6.26b), out of the compositional field of ilmenites from polymictic peridotites from (Zhang *et al.*, 2001, Fig. 6.26b) and other mantle metasomatic fields from (Haggerty, 1991, 1995, Fig. 6.26b). Cr content is independent of the Mg content,and vary from 0 to 3.4 wt% Cr_2O_3. The relatively highest Cr contents are found in ilmenites replacing geikielite (D1d) and replacing Cr-rich rutile (D1e, Fig. 6.22b and 6.23b).

Nb contents are generally low (Fig. 6.26c and 6.27b) except when is enriched in Mn-rich ilmenite (0.9-3.1 wt% Nb_2O_5) replacing Nb-rich rutile. There is no correlation between Mn and Nb, and the highest Nb content is found in ilmenite with medium Mn content, about 0.2 apfu (Fig. 6.27b).

Calculated Fe_2O_3 in D ilmenites in kimberlites show a wide range, varying from 0 to 15.5 wt% (0.3 apfu, Fig. 6.26d). Higher Fe^{3+} content is found in ilmenites replacing Fe^{3+}-rich ilmenite (D1a). There is a good negative correlation between Ti and Fe^{3+} (Fig. 6.27c).

The majority of D ilmenite crystals have low Zr contents (Fig. 6.24d and 25c). Zr enrichment is found in ilmenite replacing Fe^{3+}- and Mg-rich ilmenite (D1b) and replacing geikielite (D1d, up to 15621ppm).

The majority of D ilmenite plots far from the ilmenite found as inclusions in diamond reported by (Sobolev *et al.*, 1997, Fig. 6.28a-c). No correlation between Nb and Zr, Ni, Cr is observed (Fig. 6.28a-c).

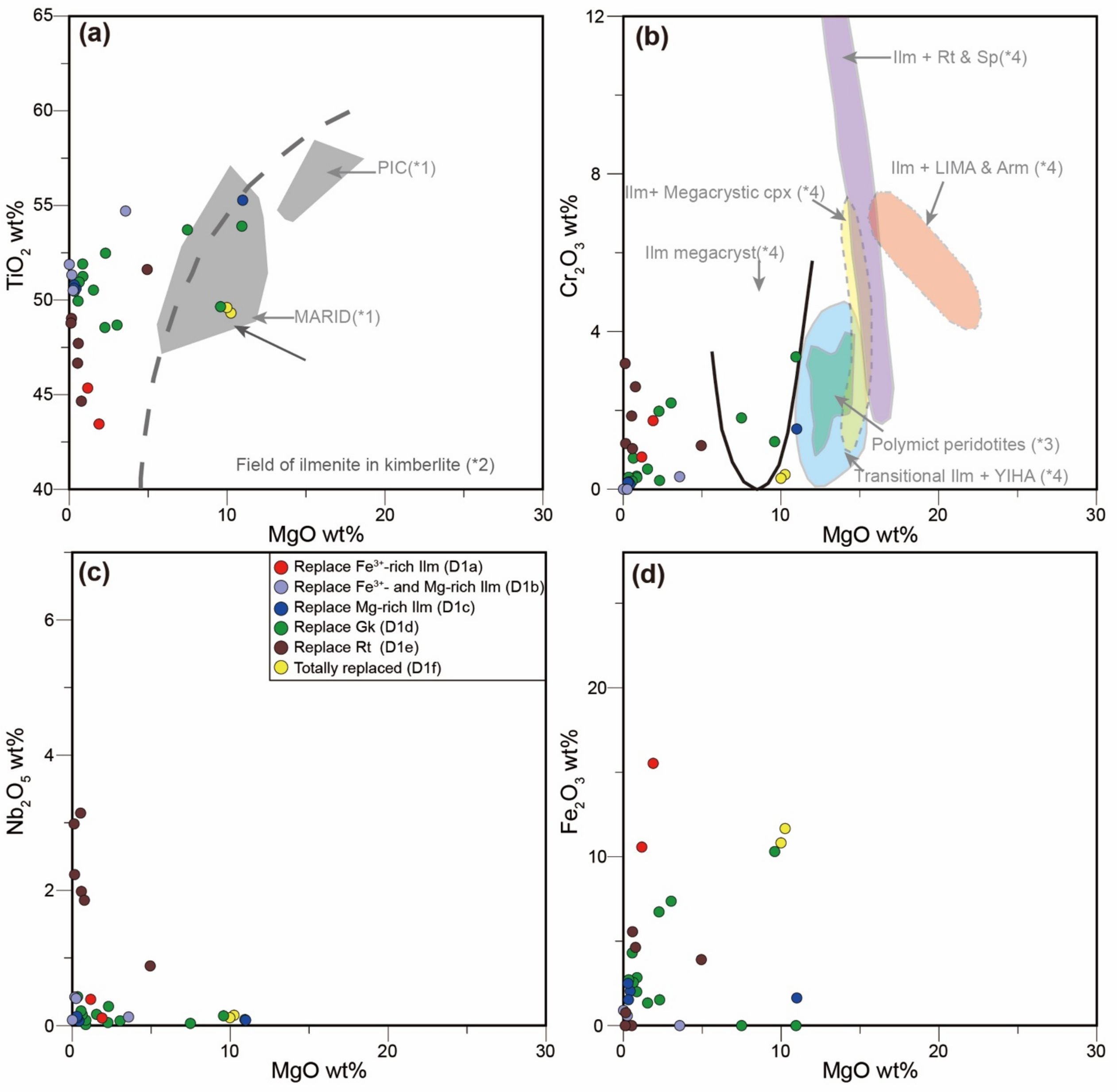

Fig. 6.26. Composition of primary magmatic late ilmenites replacing other ilmenites or Ti-rich minerals: (a) MgO wt% vs. TiO_2 wt%; (b) MgO wt% vs. Cr_2O_3 wt%; (c) MgO wt% vs. Nb_2O_5 wt%; (d) MgO wt% vs. Fe_2O_3 wt% projection. MARID and PIC fields (*1) from Fitzpayne et al. (2018). Field of ilmenite in kimberlites (*2) from (Wyatt et al., 2004). Ilmenite field in polymict peridotites (*3) from Zhang et al. (2001). Metasomatic ilmenites (Ilm) in association with LIMA and armalcolite (Arm), with rutile (Rt) and spinel (Sp), and with megacrystic clinopyroxene (Cpx), with YIHA (yimengite and hawthorneite) respectively (*4=Haggerty, 1991, 1995). Megacrystic ilmenite (*4) from Haggerty (1991, 1995).

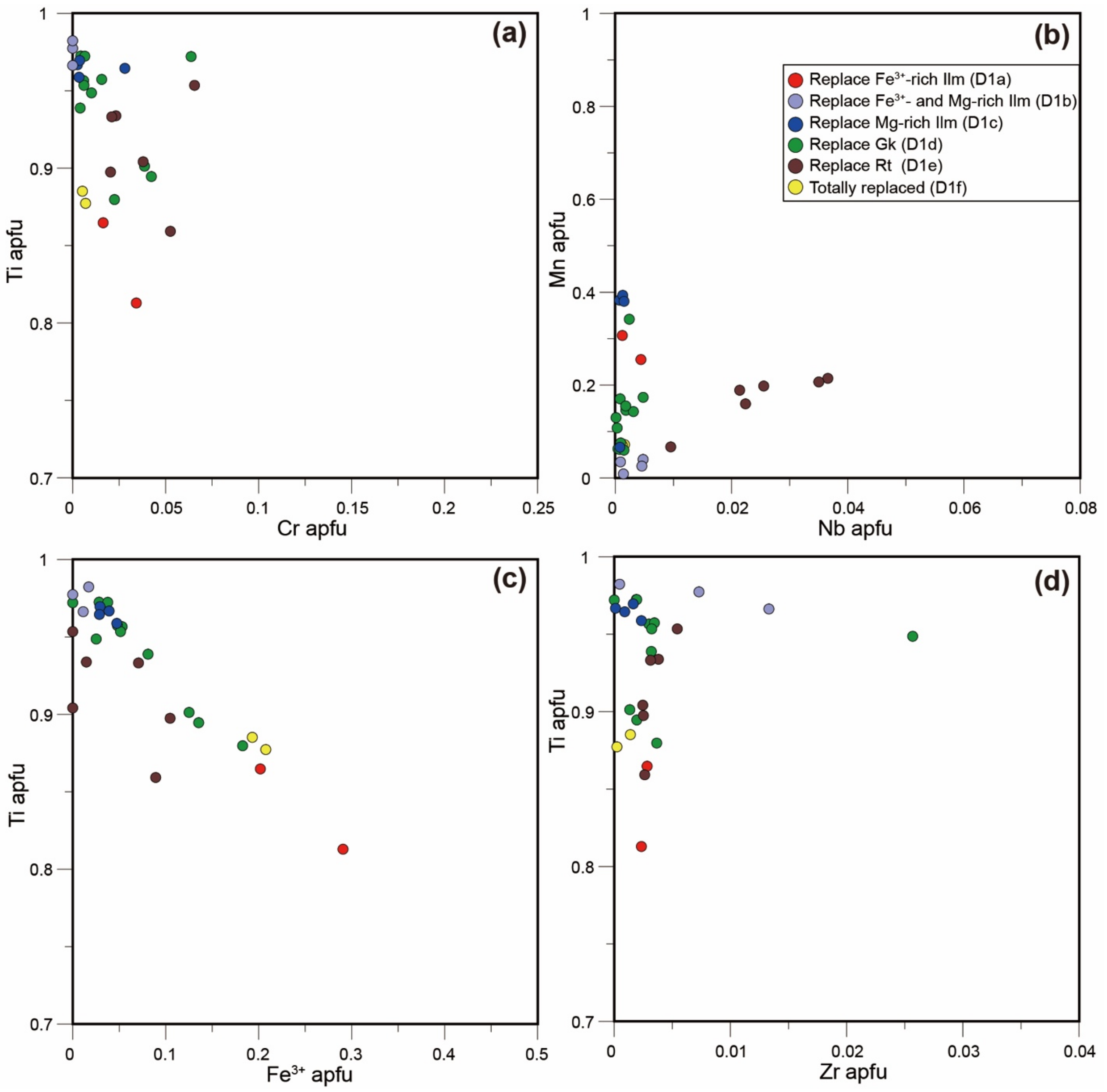

Fig. 6.27. Composition (apfu) of primary magmatic late ilmenites replacing other ilmenite or Ti-rich minerals: (a) Cr vs. Ti; (b) Nb vs. Mn; (c) Fe^{3+} vs. Ti; (d) Zr vs. Ti.

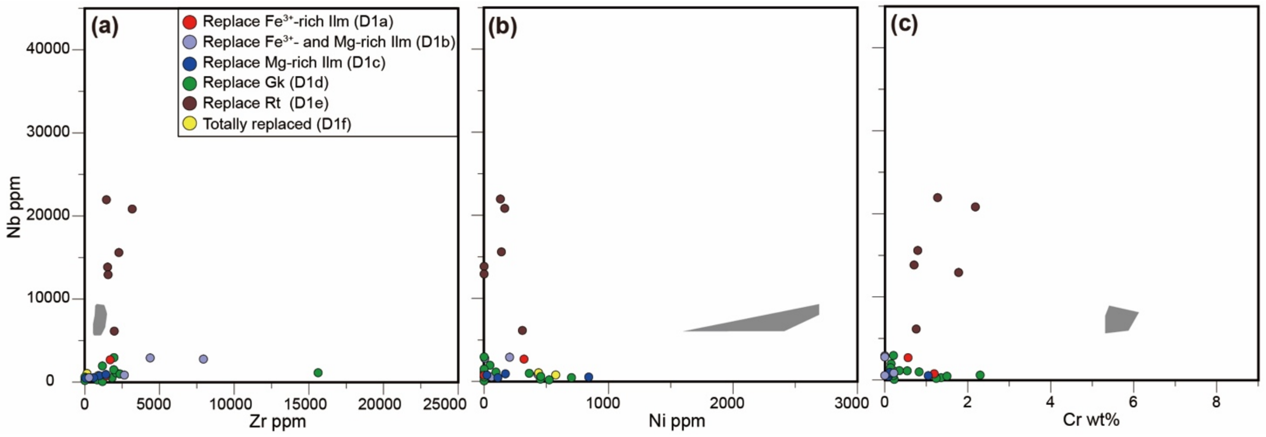

Fig. 6.28. Composition of primary magmatic late ilmenites replacing other ilmenite or Ti-rich minerals in the following projections: (a) Zr ppm vs. Nb ppm; (b) Ni ppm vs. Nb ppm; (c) Cr wt% vs. Nb ppm. Grey area represents the compositional domain of ilmenite inclusions in diamond from the Sputnik kimberlite (Sobolev et al., 1997).

6.3.5. Ilmenites of the intrusive stage 3 (hydrothermal late-post magmatic ilmenite; paragenesis E)

Ilmenites from this paragenesis have compositions into the ilmenite-dominant field, or in the pyrophanite-dominant field. However, two analyses of tabular ilmenite just fall into the geikielite dominant field (Fig. 6.29) and show the highest geikielite component of the paragenesis E (up to 48.8 mol% geikielite). Although some ilmenites replacing geikielite fall into the geikielite dominant field in Fig. 6.29., this is due to an artefact because the pyrophanite endmember is not represented in this ternary projection.

Hematite component is enriched in some ilmenites replacing magnetite (E2g, 3.3-16.0 mol% hematite) and replacing ulvöspinel-magnetite (E2f, 0-6.4 mol% hematite).

Pyrophanite component is enriched in tabular ilmenites (E1, up to 48.7 mol% pyrophanite) and ilmenites replacing geikielite (E2d, up to 51.9 mol% pyrophanite) and ulvöspinel-magnetite (E2f, up to 96.1 mol% pyrophanite).

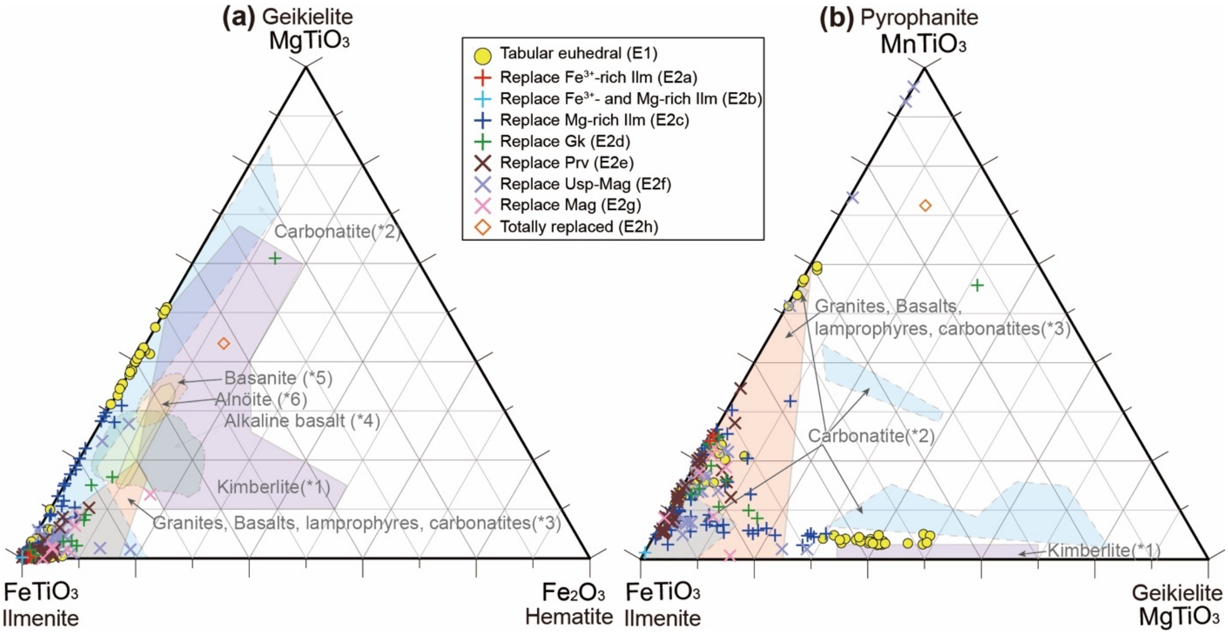

Fig. 6.29. Composition of hydrothermal ilmenites replacing other ilmenites or Ti-rich minerals in the following diagrams:(a) $MgTiO_3$-$FeTiO_3$-Fe_2O_3 and (b) $MnTiO_3$-$FeTiO_3$-$MgTiO_3$. These compositions are compared with those defined by other authors in kimberlites (*1=Mitchell, 1986), carbonatites (*2=Mitchell, 1978; Gaspar and Wyllie, 1983), granites and basalts (*3=Mitchell, 1978), alkaline basalts (*4=Parfenoff, 1982), basanites (*5=Leblanc et al., 1982) and alnöites (*6=Nixon and Boyd, 1979).

Mg content is relatively low in hydrothermal ilmenites (Fig. 6.30a). MgO content varies from 0 to 14.2 wt%. Although relatively higher MgO content is found in tabular ilmenite (E1a) from the Banankoro A kimberlite, the majority of ilmenite is represented out of the field of ilmenites in kimberlites as defined by Wyatt *et al.* (2004, Fig. 6.30a), except some tabular ilmenites.

The majority of the E ilmenites fall out of the megacrystic ilmenite field defined by (Haggerty, 1991, 1995, Fig. 6.30b), out of the compositional field of ilmenites from polymictic peridotites proposed by Zhang *et al.* (2001, Fig. 6.30b) and other mantle metasomatic fields from Haggerty (1991, 1995, Fig. 6.30b).

Cr content is commonly low in the majority of E imenite, independent of the Mg content, varying from 0 to 1.1 wt% Cr_2O_3, except one relatively high Cr content found in one totally replaced pyrophanite (Fig. 6.30b and 6.31a).

Nb content is generally between 0 and 2.76 wt% Nb_2O_5 (Fig. 6.30c and 6.31b), except a strong Nb enrichment found in a Mn-rich ilmenite (E2c-2, 6.4 wt% Nb_2O_5). However, there is no correlation between Mn and Nb, the highest Nb content is found in ilmenite with medium Mn contents, about 0.2 apfu (Fig. 6.31b).

Calculated Fe_2O_3 in C4 ilmenite in kimberlite shows a wide range, between 0 to 7.6 wt% (0.3 apfu, Fig. 6.30d), except a Fe^{3+}-rich ilmenite replacing magnetite (E2g) having higher Fe^{3+} contents (17.2 wt% Fe_2O_3). There is a good negative correlation between Ti and Fe^{3+} (Fig. 6.31c).

Zr enrichment is found in some tabular Mn-rich ilmenite (E1-3, up to 11327ppm) and pyrophanite (E1-4, up to 23320 ppm). No correlation between Nb and Zr, Ni, Cr is observed (Fig. 6.32a-c).

The majority of compositions of D ilmenites plots far from those found in the ilmenite inclusions in diamond reported by (Sobolev *et al.*, 1997, Fig. 6.32a-c).

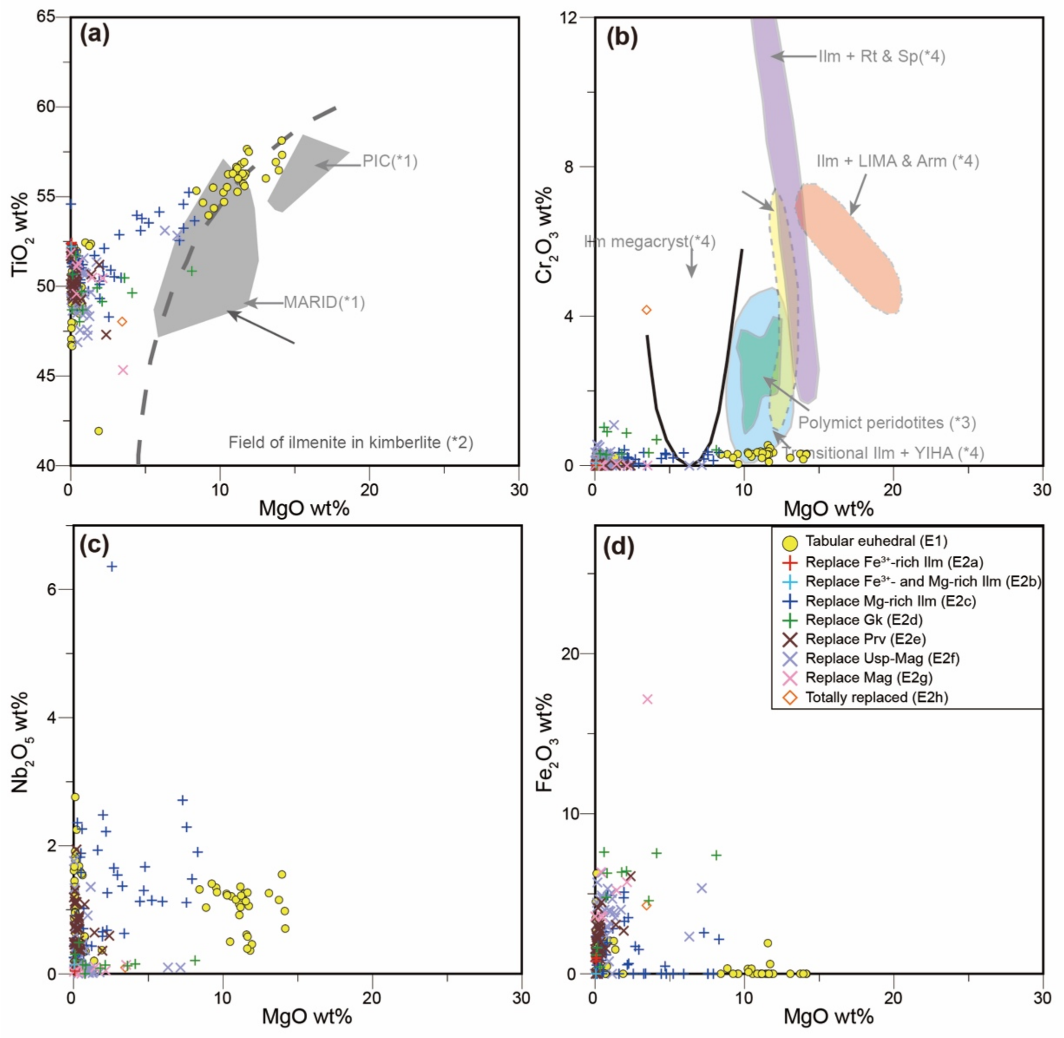

Fig. 6.30. Composition of hydrothermal ilmenites replacing other ilmenites or Ti-rich minerals in the next projections: (a) MgO wt% vs. TiO_2 wt%; (b) MgO wt% vs. Cr_2O_3 wt%; (c) MgO wt% vs. Nb_2O_5 wt%; (d) MgO wt% vs. Fe_2O_3 wt%. MARID and PIC field (*1) from Fitzpayne et al. (2018). Field of ilmenite in kimberlites (*2) from (Wyatt et al., 2004). Ilmenite field in polymict peridotites (*3) from Zhang et al. (2001). Metasomatic ilmenites (Ilm) in association with LIMA and armalcolite (Arm), with rutile (Rt) and spinel (Sp), and with megacrystic clinopyroxene (Cpx), with YIHA (yimengite and hawthorneite) respectively (*4=Haggerty, 1991, 1995). Megacrystic ilmenite (*4) from Haggerty (1991, 1995).

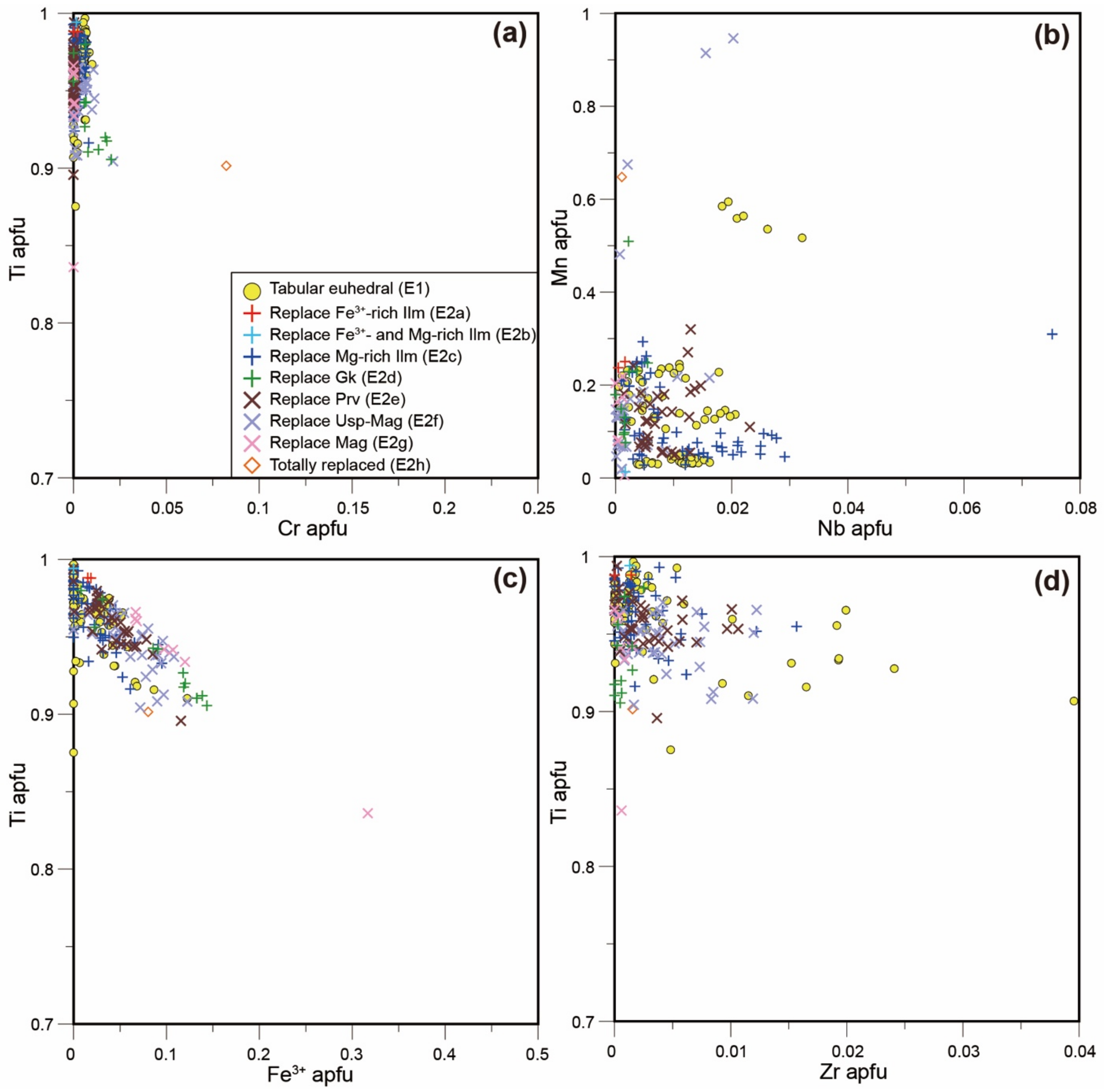

Fig. 6.31. Composition of hydrothermal ilmenites replacing other ilmenite or Ti-bearing minerals in the following projections: (a) Cr apfu vs. Ti apfu; (b) Nb apfu vs. Mn apfu; (c) Fe^{3+} apfu vs. Ti apfu; (d) Zr apfu vs. Ti apfu.

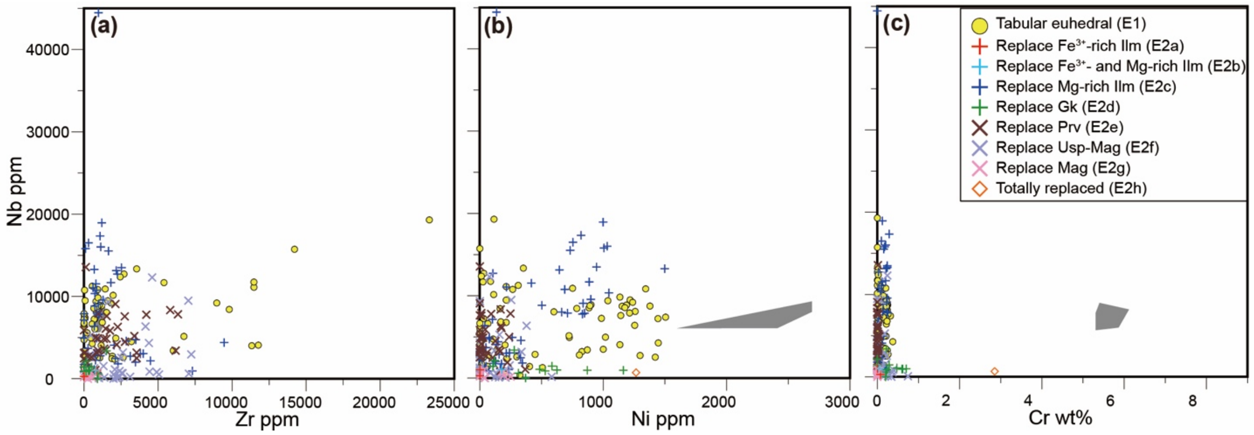

Fig. 6.32. Composition of hydrothermal ilmenites replacing other ilmenites or Ti-bearing minerals in the following projections: (a) Zr ppm vs. Nb ppm; (b) Ni ppm vs. Nb ppm; (c) Cr wt% vs. Nb ppm. Grey area represents the compositional domain of the ilmenite inclusions in diamond from the Sputnik kimberlite (Sobolev et al., 1997).

6.3.6. lmenite-olivine geothermometer

Ilmenite inclusion in fresh olivine could be used as geothermometer. Calculated temperature based on Fe-Mg equilibria between olivine microphenocrysts and their ilmenite inclusions, using the ilmenite-olivine geothermometer of Andersen and Lindsley (1979) is provided in Table 6.6. The obtained temperature varies from 800 to 833 ºC in seven studied kimberlite samples, although the estimated temperature obtained in other kimberlites is higher, 965ºC for the Elliott County (Kentucky) kimberlite (Agee *et al.*, 1982a).

Table 6.6. Calculated temperature based on Fe-Mg equilibria between olivine microphenocryst and its ilmenite inclusions, using the geothermometer of Andersen and Lindsley (1979).

No.	Sample	Locality	$X(_{Fo})$	$X_{(Fa)}$	$X_{(Il)}$	$X_{(Gk)}$	$X_{(Hem)}$	T ºC (P=1kbar)	TºC (P=50kbar)
1	9352	Menominee,USA	90.4	9.6	38.2	54.1	7.7	800.1	800.0
2	9353	Notre Dâme du Nord, Canada	89.5	10.5	45.8	40.8	13.4	817.4	817.4
3	9353	Notre Dâme du Nord, Canada	89.5	10.5	42.2	45.1	12.7	812.6	812.6
4	9630	Kaalvallei "A", South Africa	86.0	14.0	32.1	39.0	28.9	805.8	805.8
5	9630	Kaalvallei "A", South Africa	86.0	14.0	50.5	42.2	7.3	827.9	827.9
6	9630	Kaalvallei "A", South Africa	86.0	14.0	51.3	40.1	8.6	829.4	829.4
7	9630	Kaalvallei "A", South Africa	85.0	15.0	51.6	42.6	5.9	832.8	832.8
8	9364	Dutoit Span, South Africa	90.8	9.2	37.5	49.8	12.6	807.2	807.2
9	9364	Dutoit Span, South Africa	89.2	10.8	45.7	46.4	7.9	815.9	815.9
10	9364	Dutoit Span, South Africa	89.2	10.8	47.2	46.3	6.5	818.6	818.6
11	9364	Dutoit Span, South Africa	88.9	11.1	46.1	46.7	7.2	816.2	816.2
12	9364	Dutoit Span, South Africa	88.6	11.4	45.9	46.3	7.7	816.2	816.2
13	10049	South pipe of AK6 Karowe, Botswana	87.2	12.8	51.0	41.7	7.3	829.5	829.5
14	10049	South pipe of AK6 Karowe, Botswana	87.2	12.8	50.8	42.7	6.6	829.4	829.4
15	10051	North pipe of AK6 Karowe, Botswana	87.8	12.2	47.1	41.8	11.1	819.6	819.6
16	10051	North pipe of AK6 Karowe, Botswana	87.8	12.2	44.3	42.7	13.0	815.4	815.4
17	10051	North pipe of AK6 Karowe, Botswana	87.8	12.2	44.8	43.2	12.0	816.0	816.0
18	10051	North pipe of AK6 Karowe, Botswana	88.4	11.6	46.1	41.2	12.7	818.0	818.0
19	10059	DK1 Letlhakane, Botswana	86.5	13.5	46.4	34.3	19.3	816.5	816.5

6.4. DISCUSSION

Ilmenites found in kimberlites and related rocks have a large potential as recorders of processes from mantle to surface. The kimberlites and related rocks studied here host diverse ilmenite types defined by distinct compositions and textural features, reflecting their conditions of formation in different stages, before the intrusion and during the intrusion (Table 6.2). Ilmenites can be present in most of kimberlites, lamproites, orangeites and ultramafic lamprophyres, but ilmenites (particularly, primary magmatic ilmenites) may be absent in many of these rocks (Table 6.3).

The minerals of the ilmenite group form extensive solid solutions and from the economic and petrogenetic interpretation it is important to consider the different compositional varieties. Therefore, the magnesium-rich ilmenites (also named as “picroilmenites”) have been described classically as typical from kimberlites, being used as an exploration criterion. However, these terms are imprecise and the compositional domains of these varieties have never been defined.

Therefore, in order to facility the description, the original domains of geikielite, the next compositional varieties have been discriminated in the ilmenite-group minerals in case of solid solutions between two main endmembers, with entrance of more than 10 mol% of another end-member : ilmenite *sensu strictu* (s.s.), Fe^{3+}-rich ilmenite (or ferrian ilmenite), Mg-rich ilmenite (or magnesian ilmenite), Mn-rich ilmenite (or manganoan ilmenite), geikielite *sensu strictu* s.s., Fe^{3+}-rich geikielite (or ferrian geikielite), Fe^{2+}-rich geikielite (or ferroan geikielite), Mn-rich geikielite (or manganoan geikielite), pyrophanite s.s., Fe^{2+}-rich pyrophanite (or ferroan pyrophanite), Fe^{3+}-rich pyrophanite (or ferrian pyrophanite), Mg-rich pyrophanite (or magnesian pyrophanite) and hematite (the diverse varieties of hematite have no sense).

When there are proportions of more than 2 endmembers, the nomenclature has more complexity and the two additional components are ordered in the prefixes following their abundance. This means that each variety is defined by using three terms, i.e. Mg- and Mn-rich ilmenite (or magnesian manganoan ilmenite) should be a variety of ilmenite with more than 10 mol % of geikielite and pyrophanite, being the geikielite component dominant over that of pyrophanite. In most of the cases, the mineral composition can be expressed in terms of two or three end-members, being extremely rare the compositions that should be described with more than three endmembers. Therefore, the compositions of the minerals of the ilmenite group in kimberlites can be represented with a ternary diagram (Fig. 6.33).

As indicated by the five paragenetic groups established in this work, ilmenite group minerals formed in different moments in the history of the kimberlites and related rocks, giving origin to the different kimberlite generations. We will discuss in this section the meaning of the different ilmenite generations and their possible application to diamond exploration.

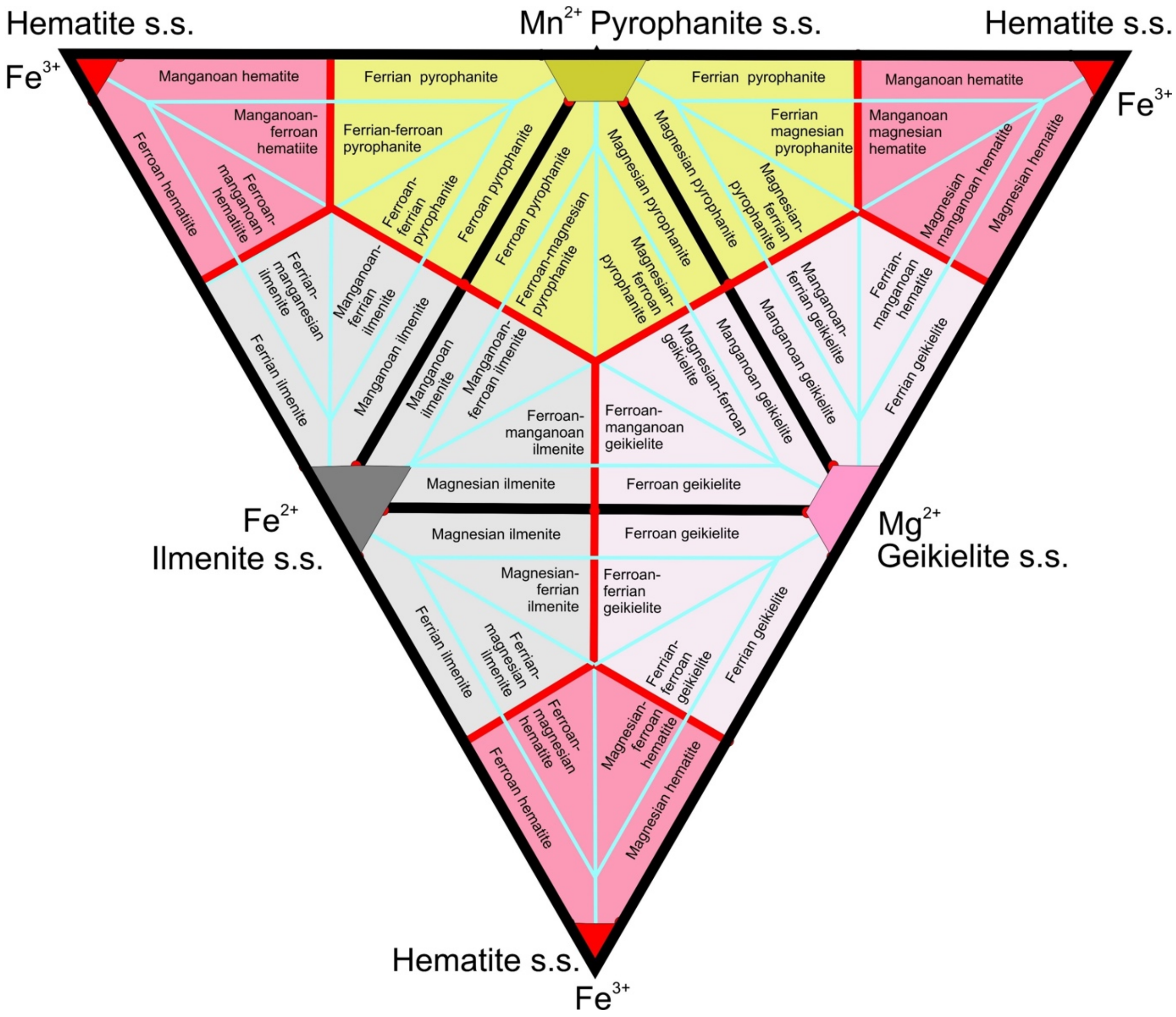

Fig. 6.33. Nomenclature of the minerals of the ilmenite group and their compositional varieties.

6.4.1. Xenoliths and xenocrysts (Paragenesis A and B)

Xenocrysts are derived from the disaggregation of xenoliths. The composition of ilmenites from mantle xenoliths (peridotitic and MARID/PIC xenolith) are quite different than those of ilmenite from crustal xenoliths (basaltic and granitic xenoliths, Fig. 6.3). The main difference is that mantle ilmenite has higher Mg content (geikielite component) or Fe^{3+} (hematite component; Robles-Cruz *et al.*, 2009) than ilmenite in crustal xenoliths. Moreover, ilmenite in mantle xenoliths could have higher Cr, Nb, and Ni content (Fig. 6.9-6.12). Probably, part of the Nb content may be produced because ilmenites formed during mantle metasomatic processes can replace rutile in these xenoliths, well before the intrusions of kimberlites and related rocks.

One of the remarkable textures in the xenocrystic and xenolithic ilmenite is the occurrence of spinel s.s. lamellae crystallographically oriented. This texture is very common in many mantle ilmenites and has been attributed to subsolidus equilibration under reducing conditions (i.e., Haggerty, 1991). However, the Al content of ilmenite increases with the pressure (Green and Sobolev, 1975). In fact, the existence of a high pressure polymorph of the spinels can favour the solution with ilmenite and the stabilization of high-aluminous ilmenite in lower mantle (Akaogi, 2007). Russell *et al.* (2004) also mention the occurrence of aluminous ilmenite in meteorites, and Danchin and D'Orey (1972) also remarked the similarity of spinel exsolutions in the Premier kimberlite with those of lunar regolith. Therefore, these ilmenites could form under ultrahigh pressure and therefore they have potential to be a diamond indicator.

Anhedral isolated single ilmenite xenocrysts (paragenesis B) could be derived from both mantle xenoliths and crustal xenoliths. Comparison of compositions of ilmenite from xenoliths and that of ilmenite xenocrysts indicates that Fe^{3+}-rich ilmenite (B-1), Fe^{3+}-Mg-rich ilmenite (B-2) and Mg-rich ilmenite (B-3) xenocrysts are derived from mantle xenoliths, while Mn-rich ilmenite and pyrophanitic xenocrysts are derived from crustal xenoliths, although it is not clear if this enrichment can be produced by the metasomatism of the intrusive stage 3 (Fig. 6.13-6.16).

Xenocrystic ilmenites are older and they have been systematically replaced by the other ilmenite types. The macrocrystic ilmenites in kimberlite have been interpreted either as produced by primary magmatic crystallization (Moore, 1987) or as xenocrysts (Armstrong *et al.*, 2004b; Hearn Jr., 2004). Since ilmenite macrocryst and monomineralogic polycrystalline ilmenite have exactly same compositions, ilmenite macrocrysts can be interpreted as produced by disaggregation of the polycrystalline aggregates. The same conclusions were established by Robles-Cruz *et al.* (2009) for the older ilmenite generations from the Catoca pipe (Angola). Those authors also demonstrated that polycrystalline ilmenite also occurs in metasomatized mantle xenoliths.

Magnesian ilmenite is found in metasomatized lherzolites and eclogites and MARID xenoliths (Mitchell, 1986). These macrocrystic ilmenite generations are often relatively rich in Fe^{3+}. This ferric character occurs in Catoca (up to 27 mol% hematite, Robles-Cruz *et al.*, 2009), in Mir (4.5-21.0 mol% hematite, Mitchell, 1986) and in many kimberlites studied here. Similar ilmenite generations were described in many metasomatized peridotite xenoliths and in glimmerites (Kaminsky *et al.*, 2002; Robles-Cruz *et al.*, 2009). Some of them comprise the MARID (Mica-Amphibole-Rutile-Ilmenite-Diopside) and PIC (Phlogopite-Ilmenite-clinopyroxene) xenoliths (Dawson and Smith, 1977; Grégoire *et al.*, 2002). In polymictic xenoliths, ilmenites have been proposed to be formed by mantle pegmatitic and/or metasomatic processes by the action of an H_2O-TiO_2-K_2O fluid (Wyatt and Lawless, 1984) or a Fe-Ti-Cr-rich melt (Zhang *et al.*, 2001), or could be crystallised from a S-bearing Ti-Fe-K-rich ultramafic silicate melt derived from an ascending proto-kimberlite melt (Giuliani *et al.*, 2013). Hence, Fe^{3+}-rich ilmenite, Fe^{3+}-Mg-rich ilmenite, Mg-rich ilmenite and relatively Mg enriched ilmenite s.s. xenocrysts are interpreted as produced by mantle metasomatic processes which were strongly controlled by redox reactions.

A primary origin for magnesium-rich ilmenite was early suggested by (Mitchell, 1973) as crystallizing from Ti and Mg rich melt (protokimberlite) formed by low partial melting of lherzolite. High MgO, intermediate Fe_2O_3 and presence of Cr_2O_3 are characteristic of kimberlitic ilmenites (Haggerty, 1975a). Ilmenite crystallized during kimberlite ascent should be Cr-rich due to lack of Cr-depleting because of the crystallization of olivine instead of garnet and pyroxene, that could accept Cr in their structures (Moore, 1987). Ilmenite mega and macrocryst suites have been suggested as a product of late fractionated crystallization of a mafic magma at depth, being Nb content an index of the degree of fractionated crystallization (Griffin *et al.*, 1997). Constant Zr with increasing Nb may be derived from metasomatized peridotite, while another type show a positive correlation between Nb and Zr that could be indicative of crystallization from a single batch of magma (Griffin *et al.*, 1997).

The minor element contents of xenocrystic ilmenite varies with respect to Cr in particular. They show wide range of Cr_2O_3 contents that are independent of the MgO content. Some have a similar low content, whereas others have slightly higher values (Fig. 6.14). This Cr variability could either reflect different metasomatic processes in the mantle or be related to similar processes occurring at different depths. Cr-poor ilmenite macrocrysts may be related to a mantle fractional crystallization origin (Schulze *et al.*, 1995). High-Cr ilmenite is also found as veins in polymict xenoliths, being the Cr_2O_3 content higher (>5 wt%) at the edges of the vein, which is interpreted as earlier crystallisation or “chilling” of high temperature ilmenite during fractional crystallisation (Wyatt and Lawless, 1984). However, as demonstrated in our work, Cr-rich ilmenites can be produced by replacement of mantle xenocrysts of Cr-rich minerals, as chromite, garnet or minerals of the crichtonite group during the intrusion processes.

6.4.2. Ilmenites of the intrusive stage 1 (Paragenesis C)

Euhedral or anhedral inclusions of ilmenites could indicate the existence of primary groundmass ilmenite. Primary early ilmenites that occur as inclusions in olivine microphenocrysts, replacing xenocrystic ilmenite and as primary groundmass ilmenite have similar compositions between them and all are Mg-enriched. Ilmenites found as inclusions in fresh olivine contain 37.8-62.7 mol% geikielite (10.5-18.2 wt% MgO). Mg content in ilmenite of groundmass achieves higher values (44.5-74.4 mol% geikielite, 12.4-22.0 wt% MgO). Ilmenites produced by replacement have a wider range of composition (30.2 to 85.3 mol% geikielite, 8.3-26 wt% MgO), because their compositions are influenced by the compositions of the original replaced xenocrysts and by the xenocryst-melt interaction degree. The composition of the ilmenites found as inclusions in olivine overlap the composition of replacement ilmenites and groundmass ilmenites at the relatively lower part of the Mg contents, thus indicating possible simultaneous crystallization of these three types of ilmenite, although the crystallization period of the replacement and groundmass ilmenites should prolong until a relatively later stage when compared with the olivine-included ilmenites. These primary ilmenites crystallized in early stages of magma crystallization, along with olivine microphenocryst and chromite and before the crystallization of groundmass spinel and perovskite.

Groundmass ilmenites are also reported in previous works (i.e., Pasteris, 1981; Mitchell, 1986). Kimberlite groundmass ilmenites are typically geikielite (50-90 mol% $MgTiO_3$, Mitchell, 1995). Magnesian enrichment trend is described as an overgrowth rather than continuous zoning formed by fractional crystallization (Mitchell, 1986). However, the textural patterns observed in this study, with Mg enrichment following margins, fractures and cleavage planes indicate that it is rather a replacement process than an overgrowth. The magnesium enrichment is towards composition of groundmass ilmenite, thus indicating interaction of xenocryst and host magma to attempt to achieve equilibrium (Agee *et al.*, 1982a)..

Mg-rich ilmenites are found in most of the cases as replacement products of pre-existing ilmenite xenocrysts (i.e., Robles-Cruz *et al.*, 2009; Castillo-Oliver *et al.*, 2017). The origin of ilmenite replacing other ilmenites or other minerals is clearly metasomatic because it replaces ilmenite xenocryst of paragenesis B, starting along grain boundaries and following cleavages, fractures or twin planes (Fig. 6.6a-b). Haggerty *et al.* (1979) noted that the kimberlitic ilmenite shows a magnesium-enrichment trend along grain rims (i.e. the kimberlite magmatic trend),and proposed that this Mg enrichment is related to a decrease in fO_2. Similar Mg enrichments have been subsequently reported in many kimberlites worldwide, despite in some cases an inverse trend is evident (e.g., Golubkova *et al.*, 2013). Mg enrichment is also suggested to be related to the assimilation of magnesite during the magma ascent (Schulze *et al.*, 1995).

In many cases, this process can strongly affect ilmenite xenocrysts, and they may be completely replaced by primary magmatic ilmenite of paragenesis C. Ilmenite xenocrysts (for instance, Fe^{3+}-rich ilmenite, Mg-rich ilmenite) interact with kimberlite melt producing replacement by higher Mg content ilmenite (Mg-rich ilmenite, Fe^{3+} and Mg-rich ilmenite, geikielite). This replacement is a continue process which is more congruent with a diffusion process. Different replacement mechanisms have been identified. In some cases, the replacement is along grain boundaries, whereas in others it progressed along small cracks, cleavages and twin planes (Fig. 6.6b). The replacement along small cracks suggests that it was not produced in the mantle. Moreover, the replacement of minerals along thin microsurfaces could be explained as produced by a fluid exsolved from the kimberlite magma near the Earth surface (Sparks *et al.*, 2006, 2009) or by interaction with a low-viscosity magma. However, C-4 ilmenite is replaced by typical groundmass minerals as perovskite and Ti-rich spinels, and therefore it must be produced during the magmatic stages. Moreover, the kimberlite magma has a very low viscosity during its emplacement (~ 10 Pa·s; Persikov *et al.*, 2015) thus favoring the infiltration of the magma into small cracks. In addition, Robles-Cruz *et al.* (2009) demonstrated, based on textural evidence, that the replacement of ilmenite macrocrysts by Mg-rich ilmenite and geikielite took place before the explosive processes of the near surface kimberlite emplacement, which is consistent to our observation in this work. Therefore, C-4 ilmenite could be produced by a low-viscosity magma near the Earth's surface. Likewise, the degree of replacement of the primary ilmenite can be an indicator of the degree of the magma/xenocryst interaction.

It is likely that magnesian xenocrystic ilmenites have a very wide compositional range, even within a hand specimen (Wyatt *et al.*, 2004). This could be attributed to random mixing of fragmented zoned ilmenite cumulates (Mitchell, 1986). However, it is possible that many studied magnesian xenocrystal ilmenite have interacted with kimberlite magma and their compositions have already changed. In our opinion, the replacement of ilmenite xenocrysts produced by interaction with kimberlite magma seems to be a diffusive process, from the contact with kimberlite melt towards the interior of the grains. The different interaction degree with the kimberlite melt could give ilmenites of different compositions.

Ilmenites of paragenesis C show a wide range of Cr_2O_3 contents, which are independent of the MgO contents. The composition of the replacing ilmenite (C-4) strongly depends on the composition of the replaced mineral. If it replaces Cr-rich minerals, such as mathiasite of crichtonite group and chromite, it could become strongly enriched in Cr (Fig. 6.22b). However, this enrichment is not present in all the cases, as it is also dependent of the interaction degree with the Cr-bearing crystal. Therefore, caution should be taken when trying to distinguish the primary suites of Cr-rich and Cr-poor ilmenite (Moore and Belousova, 2005; Ashchepkov *et al.*, 2014). As shown in our study, variations in the Cr contents can result from different compositions of the Ti-rich replaced substratum and thus they might not reflect different primary magmatic sources.

The same influence is also observed in the Nb and Zr content of some replacing ilmenites (Fig. 6.22-6.24). Ilmenites from carbonatites typically contain more than 1wt% Nb_2O_5 (Gaspar and Wyllie, 1983) and therefore a carbonatitic influence was suggested for these ilmenites. However, Nb enrichment is also found in ilmenites replacing Nb-bearing rutile (Fig. 6.22-6.24). Finally, Zr contents are generally high in ilmenites replacing Zr-bearing minerals of the crichtonite group (Fig. 6.22-6.24). Again, we suggest that the trace element composition in ilmenite can be a local process related with local replacement of grains of minerals of the ilmenite group.

6.4.3. Ilmenites of the intrusive stage 2 (Paragenesis D)

It is necessary to note that the above ilmenite generations (paragenesis B and C) are mantled by a succession of Ti-rich minerals, including ilmenites of paragenesis D, ulvöspinel, perovskite, Ti-rich magnetite and, finally, ilmenites of the paragenesis E. Ilmenites of paragenesis D are normally Mn-rich ilmenite crystallised after previously formed ilmenites of the intrusive stage 1 and replace them and the xenocrysts. However, ilmenites D crystallised before than ulvöspinel and perovskite of the groundmass and are replaced by these minerals. Ulvöspinel, perovskite and Ti-rich magnetite are common in the kimberlite groundmass. Therefore, the sequence of replacement from type D ilmenite to Ti-rich magnetite suggests an interaction between the kimberlite magma and the pre-existing ilmenite generations during the crystallization of the kimberlite magma. Similar reactions have been noted in many kimberlites worldwide (i.e. Golubkova *et al.*, 2013). Haggerty *et al.* (1979) proposed the existence of a distinct manganese-enrichment trend on the rims of some macrocrystic Mg-rich ilmenite and suggested its formation by carbonate immiscibility during the late stages of crystallization of kimberlite magma, associated with a strong decrease in fO_2.

6.4.4. Hydrothermal late-post magmatic ilmenite (Paragenesis E)

Euhedral tabular geodic ilmenites of the (E-1) type show variable compositions evolving from Mg-rich ilmenite to geikielite, to Mn-rich ilmenite and finally pyrophanite. Ilmenites formed by hydrothermal replacement of pre-existing ilmenites (E-2) evolve from ilmenite s.s. to Mn-rich ilmenite and finally to pyrophanite. Some Mg-rich euhedral tabular ilmenite looks like primary groundmass mineral (eg. Banankoro “B” kimberlite). However, they are associated with serpentine and calcite indicating that they formed during late hydrothermal processes. Therefore, not all Mg-rich ilmenite and geikielite are mantle xenocrystic or primary kimberlitic and they can be of secondary origin.

As indicated above, Mg-rich ilmenite is commonly found as macro- and megacrysts in kimberlites, which are interpreted either as produced by primary kimberlitic magma crystallization (Mitchell, 1973; Moore, 1987; Golubkova *et al.*, 2013; Xu *et al.*, 2018a) or as xenocrysts (Wyatt and Lawless, 1984; Armstrong *et al.*, 2004b; Hearn Jr., 2004). However, for instance, in the Banankoro “B” kimberlite, the primary early geikielite (C3-1) found in veins crosscuting olivine plots far from the hydrothermal “groundmass-like” tabular Mg-ilmenite to geikielite (E1-1 and E1-2) in compositional diagrams (Xu *et al.*, 2018b), thus suggesting very different conditions of formation between primary early ilmenite and hydrothermal tabular ilmenite. Mg-rich euhedral ilmenite crystals could resemble groundmass in a first examination, but ilmenite phenocrysts are extremely rare in kimberlite and orangeite (Mitchell, 1995). However, E1-1 and E1-2 tabular Mg-rich ilmenite and geikielite mantles groundmass minerals and it is found filling vuggy porosities. Hence, the textural relations with the associated minerals suggest that, at the least in Banankoro, these ilmenites formed as a late product after the crystallization of the kimberlite groundmass. They crystallised contemporaneously with the serpophitic non-pseudomorphic late serpentine, and therefore could be formed during low temperature hydrothermal processes (Mitchell, 2013). Moreover, its composition (26.3-48.2 mol % geikielite) is different of that of the primary groundmass ilmenites from kimberlites (59-90 mol % geikielite) or orangeites (<11.1% mol geikielite). E1-1 and E1-2 Mg-rich euhedral tabular ilmenites and geikielite could be similar to those found in kimberlite groundmass from Lepelaneng (Haggerty, 1975b) and Loqhobong (few crystals, Boctor and Boyd, 1980). However, the Banankoro “A” E1-1 and E1-2 ilmenites are slightly enriched in Mn and Nb when compared to the groundmass ilmenite in these localities. These Mn-rich compositions can be produced after replacement of Mn-bearing late magmatic ilmenites of the paragenesis C.

Wyatt (1979) suggested that Mn rich ilmenite is formed by non-magmatic process related to groundwater circulation, while (Gaspar and Wyllie, 1984) believe that Mn-rich ilmenite in carbonate dikes in Premier are primary liquidus phases and represent reaction trend. Our results indicate that the two possibilities can be valid in the same pipe.

Mitchell (1995) proposed that Mn-rich ilmenites are commonly found in carbonatites more than associated with kimberlites or lamproites. Primary ilmenite from carbonatites could be distinguished from ilmenite from kimberlites on basis of higher Mn, Nb and lower Cr contents in carbonatites (Gaspar and Wyllie, 1983; Mitchell, 1986). In the studied examples, however, there are no significative compositional differences.

Hydrothermal late-post magmatic ilmenite of paragenesis E frecuently occurs as a late replacement product of Ti-rich minerals. It is also found as a replacement product of Ti-rich minerals in the kimberlite groundmass, in association with calcite and hydrous minerals as serpentine and chlorite. The textural patterns also suggest that these Mn-rich ilmenite generations can result from the reaction with a late fluid.

The problem is the nature of this fluid and its stage of formation. A supergene process must be discarded because these ilmenites are formed along with minerals formed by hydrothermal fluids, as serpentines and chlorite. Therefore, the problem becomes associated with the question about the origin of serpentine in kimberlites: deuteric (Mitchell, 2013) or produced by convective circulation of external fluids (Wyatt *et al.*, 2004; Sparks, 2013; Afanasyev *et al.*, 2014), or a combination of these phenomena during the decrease of the temperature, as suggested by the occurrence of different generations of serpentine (Giuliani *et al.*, 2017). We suggest that at least pyrophanite of the paragenesis E is produced by late reaction with heated groundwater, that could supply at least part of the Mn. Hence, the differences in the Mn content in ilmenites of paragenesis E from different kimberlites can be related to different grades of fluid-rock interaction. Other differences on the composition of ilmenite of parageneses D and E are reflective of the composition of the replaced mineral. Mn-rich ilmenite becomes enriched in Nb when it replaces Nb-rich minerals such as Nb-bearing rutile (Fig. 6.26c). Hence, the composition of Mn-rich ilmenite cannot be used as an exploration criteria for diamond as previously proposed (i.e. Kaminsky and Belousova, 2009) and is not related with a carbonatitic influence.

Despite Mn-rich ilmenites replace type E1-1 and E1-2 ilmenite in Banankoro, in other places Mn- and Nb-rich ilmenite grew apparently without the existence of a precursor ilmenite, as in Angolan kimberlites (Robles-Cruz *et al.*, 2009; Castillo-Oliver *et al.*, 2017). Mn-rich ilmenites have also been described as produced during a late replacement of perovskite in kimberlites from India (Xu *et al.*, 2018c; a). However, its origin is not clear. The possibilities include late crystallisation from a evolved fraction of the kimberlitic melt (e.g. Tompkins & Haggerty, 1985), interaction of kimberlite groundmass with a CO_2–rich fluid or a carbonatite-like magma (Gaspar and Wyllie, 1984;

Robles-Cruz *et al.*, 2009) and even late hydrothermal activity related to serpentinisation (Castillo-Oliver et al. 2017). Magmatic formation of these Mn-rich ilmenites must be ruled out because this ilmenite generation formed contemporaneously or after the serpentines.

A classical argument favouring a carbonatite influence is the high Nb content in Mn-rich ilmenite. However, late ilmenites may incorporate Nb by replacement of Nb-rich perovskite. Finally, Mn-rich ilmenite has been described as a product of late high-temperature hydrothermal replacement in other similar olivine-rich environments, as in many podiform chromite deposits (Melcher *et al.*, 1997; Saleh, 2006) or other ultramafic rocks (i.e., Abzalov, 1998), associated with serpentine and chlorite and replacing chromite. Hence, we suggest that the Mn-rich ilmenite can be produced by late hydrothermal processes during the serpentinization of the kimberlite.

6.4.5. Synthesis: a model for ilmenite evolution in kimberlites

First, kimberlites and related rocks carry xenoliths encountered and trapped by the magma during their ascent towards the surface (paragenesis A). Kimberlites and similar magmas can be formed at superdeep conditions, and therefore the xenoliths found in these intrusions may come from the deep or upper mantle, or crustal environments. Hence, kimberlites are windows to the composition of the mantle and the study of the xenoliths is equivalent to that would be obtained with a deep drill. Xenocrystic material from granites tends to have a composition close to the ilmenite end-member, with only slight enrichments in Mg (Mitchell, 1978). A moderate magnesian enrichment is reported in the case of the alkaline basalts (Parfenoff, 1982) and basanites (Leblanc *et al.*, 1982), although in this case all the registered values for ilmenites from these rocks are well close to the ilmenite end-member. Metasomatized peridotites and MARID usually have a composition in the fields of the magnesian to ferrian ilmenite (Mitchell, 1986; Robles-Cruz *et al.*, 2009). Some ilmenites from these associations can have textures suggesting a very deep origin, that will be described with more detail later.

Xenocrysts (paragenesis B) are produced by disaggregation of xenoliths, because in most of the cases they have textural or chemical similarities.

Xenolithic and xenocrystic minerals of the ilmenite group have a large textural diversity, reflecting probably differences in the original environments of the trapped rock. Therefore, when ilmenite is coming from the deep mantle, it has a good potential as DIM, which is underexplored yet.

Ilmenites from the intrusive stage 1 (paragenesis C) are widespread in most of the studied characterized by having a geikielite component dominant over pyrophanite and hematite. They can be easily interpreted as primary magmatic early ilmenites, because they are contemporary with the crystallization of olivine microphenocrysts and chromite. This simultaneous crystallization is demonstrated because ilmenite C occurs as inclusions in the external rims of olivine microphenocrysts, as early groundmass mineral and infilling veins in xenocrysts along with other magmatic minerals as olivine and phlogopite, with compositions identical to those of the groundmass. Ilmenites of this generation have important variations in their chemical composition, that can be explained taking into account that they are produced in many of the cases by uncomplete reaction with xenocrystic ilmenites or, less commonly, with ilmenite from the xenoliths. The replacing magma tends to produce a diffusive replacement on the replaced grain, and therefore the reaction is progressive and discontinuous. Therefore, it is easy to find in the same grain compositions from nearby geikielite to ferrian ilmenite, produced by partial replacement of the mantle xenocrysts; or compositions from geikielite to ilmenite, when the grain replaced has a crustal origin. Therefore, the main composition of the resulting ilmenite reflects the original composition of the grain and the grade of magma/xenocryst interaction. Therefore, we can assume that in this stage there is a magmatic reaction trend characterized by an extreme enrichment in Mg in the crystallizing or replacing ilmenite, at Mn close to 0 (Fig. 6.34).

Ilmenites from the intrusive stage 2 (characterized by having pyrophanite component dominant over geikielite and hematite, paragenesis D) crystallized after all the above paragenesis and mantle the above generations of ilmenites (A, B, C). They crystallized before the crystallization of other groundmass minerals, such as perovskite and ulvöspinel, and are replaced by these minerals. Therefore, these Mn-rich ilmenites must also be considered as primary and late magmatic. These ilmenites can have an extreme pyrophanitic composition, although they may be also produced by diffusive replacement on the preexisting ilmenites, thus producing a large diversity of mineral compositions, because they replace usually ilmenites of very different composition (trends type 2, convergint on the pyrophanite endmember, Fig. 6.34).

Ilmenites from the intrusive stage 3 (paragenesis E) have similar compositions than those of the above stages, but they formed very late in the crystallization sequence, well after all previously formed minerals of the groundmass, including perovskite and ulvöspinel and the earlier formed ilmenites. The genetic mechanism of this association is not so clear as in the above cases. These ilmenites use to occupy geodic porosity and are accompanied by calcite and minerals of the serpentine group. Therefore, they could be late products derived by deuteric alteration of kimberlite glass or could precipitate directly from residual fluids. It is interesting to note that they have similar sequences that in the case of primary magmatic ilmenite, this is, Mg-rich members of the ilmenite group crystallize are the first to crystallize in this stage, followed by late Mn-rich minerals of the ilmenite group.

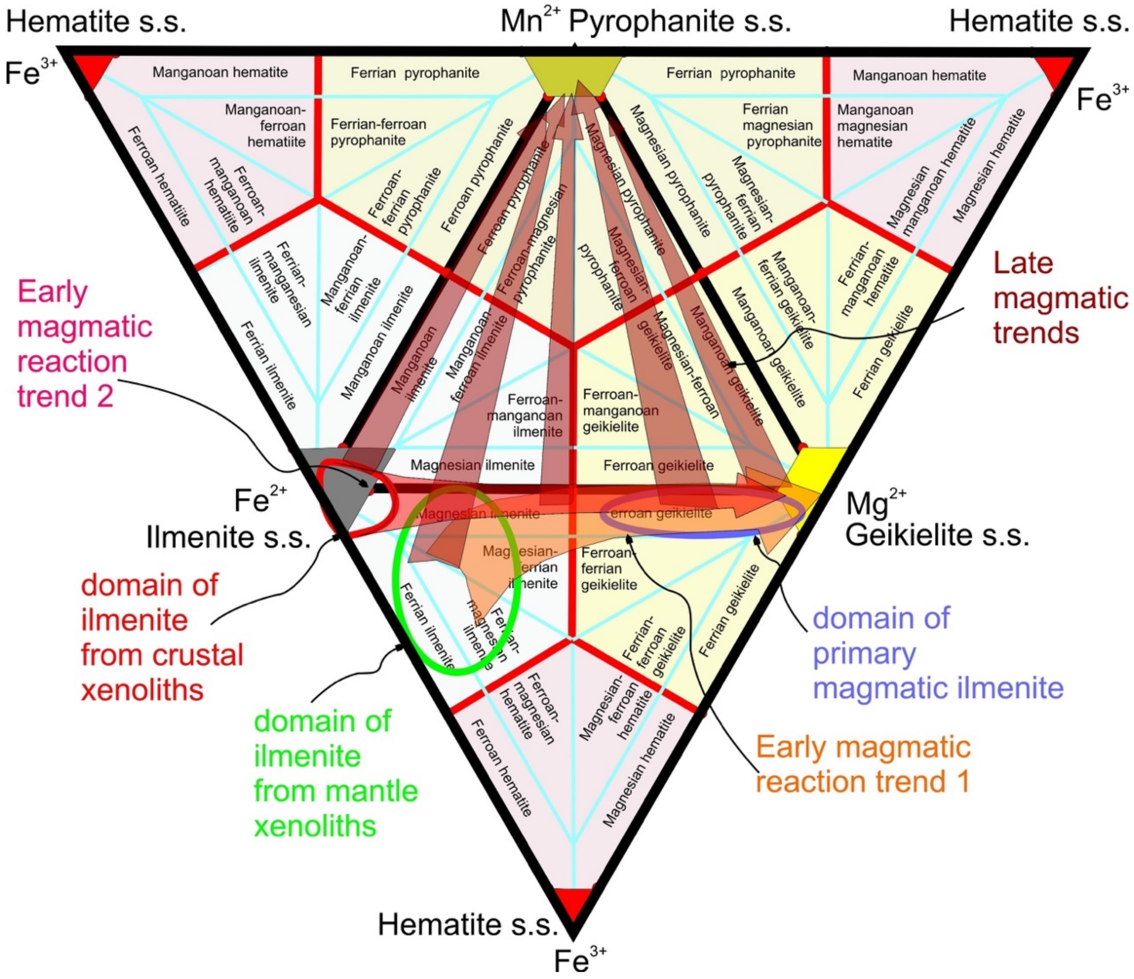

Fig. 6.34. Trends produced by reaction of the kimberlitic and related magmas with xenocrystic ilmenites.

6.4.6. Ilmenites in lamproites, orangeites and UMLs

Primary minerals of the ilmenite group are Mg-rich ilmenites (10.5-11.4 wt% MgO, 35.4-39.0 mol% geikielite) in the studied UMLs, lamproites and orangeites. Therefore, they are poorer in Mg than the primary ilmenites in kimberlites. No geikielite is found in UMLs, lamproites and orangeites, and this is a neat difference with primary ilmenites from kimberlites, which generally have higher Mg content (Fig. 6.17-18). However, other studies report ilmenites with geikielite-dominant component in UML (i.e., Tappe *et al.*, 2014).

Moreover, the preliminary data from this study suggest that primary ilmenites in UMLs, lamproites and orangeites have relatively low Cr and Nb contents and intermediate Ni contents relative to primary ilmenites from kimberlites.

6.4.7. Use of ilmenite as kimberlite indicator mineral (KIM) and diamond indicator mineral (DIM)

The relationship between ilmenite and diamond preservation potential has been discussed in several works. Mg enrichment is related to decreasing fO_2 (Mitchell, 1986), whereas high Fe^{3+} and low Mg content should indicate low diamond preservation (Gurney and Zweistra, 1995). The Fe_2O_3 content in ilmenite was suggested as a good indicator for environments producing diamond resorption and, following this argument, the Fe^{3+}- bearing ilmenites should be indicative of pipes with low diamond preservation (Schulze *et al.*, 1995). However, in the Catoca pipe in Angola the dominant ilmenite megacryst is highly Fe^{3+}-rich ilmenite, and the kimberlite has well-preserved diamonds and is one of the richest pipes in the world (Robles-Cruz *et al.*, 2009). However, as described in this work, Mg-rich ilmenite can be formed by many processes, partly developed in the mantle, but being mainly developed during the intrusive stages, from the early magmatic crystallization to the deuteric stage. Therefore, Mg-rich ilmenite cannot be considered as a diamond indicator mineral, because most of the grains are absolutely unrelated with the diamond formation and could perhaps be an indicator of good preservation.

There is also an empirical rule indicating that the best preservations of diamond are achieved in kimberlites with ilmenites enriched in Mg and Cr (i.e., Fig. 6.35, Semytkivska, 2010). For a long time Mg-rich ilmenite has been believed to be produced either by a Mg-rich metasomatic fluid (Boctor and Boyd, 1980), or by a reduced magma, thus stimulating the diamond preservation (Gurney *et al.*, 1993; Gurney and Zweistra, 1995; Kostrovitsky *et al.*, 2004, 2006; van Straaten *et al.*, 2008). However, we must remember here that a part of the magnesian ilmenites can be of duteric origin (Xu *et al.*, 2018b). Moreover, as observed in our study, the enrichment in Cr in ilmenite can be due to the replacement of Cr-rich minerals, as chromite xenocrysts or minerals of the crichtonite group. Therefore, this criterion could perhaps be retained, but only with many cautions by taking into account the possibility that the Cr enrichment is not produced by replacement during the kimberlite intrusion. Therefore, this method should not be very valid for ilmenite in stream concentrates but could work on thin section.

The paragenetic association of mantle ilmenites with diamond is another problem. Despite ilmenites are rarely found as inclusions in diamond, the Sputnik diamonds contain two types of ilmenites: a) certain types of high-Cr “peridotitic ilmenite” b) low-Cr ilmenites from eclogitic origin (Sobolev *et al.*, 1997). These high-Cr ilmenite inclusions have been suggested to reflect metasomatic episodes in the mantle before or during the diamond formation (Sobolev *et al.*, 1997). Ilmenite grains included in diamond are strongly enriched in Cr and Ni, as well as in Nb, but all the compositions of the early ilmenites studied in this work plot out of the compositional domain of the ilmenites found in diamond inclusions (Fig. 6.16). Moreover, it should be noted that in this study we had seen evidences of Nb-bearing rutile replaced in the mantle by ilmenite. Therefore, Nb enrichment in ilmenite could also be produced due to replacing rutile. Finally, there is no obvious correlation between the diamond grade and the composition of the primary ilmenite analysed in this study. Therefore, xenocrystic ilmenite is likely produced by mantle metasomatic processes unrelated to those that led to diamond formation.

Minerals of the ilmenite group are classic indicator minerals of kimberlite (KIMs) and have been used as a guide for kimberlite exploration. Magnesian ilmenite is a characteristic mineral in kimberlites and related rocks and is important for exploration because it is resistant to physical and chemical alteration and is easy to be located and concentrated (i.e., Muggeridge, 1995; Nowicki *et al.*, 2007). However, as indicated, Mg-rich ilmenite is formed in diverse stages by concurrent mechanisms, and the monomineralic grains cannot give information about the stage of formation: Mg-rich ilmenite found in concentrates can came from macrocrysts with xenocrystic origin (Armstrong *et al.*, 2004b; Hearn Jr., 2004) or can be produced by kimberlitic magma crystallization (Moore, 1987; Golubkova *et al.*, 2013), or by hydrothermal fluids (Xu *et al.*, 2018b). However, the modal proportions of ilmenites are variable between all the worldwide kimberlites, and Mg-ilmenite (to geikielite) is rarely documented as a euhedral crystal component of the kimberlite groundmass (Haggerty, 1975b; Boctor and Boyd, 1980). The discovery of euhedral Mg-ilmenite (to geikielite) crystals as groundmass-like crystal in an intrusion in the Banankoro area cluster (Guinea Conakry) suggests a late hydrothermal late-post magmatic origin (Xu et al., 2018b). Therefore, the majority of Mg-rich ilmenite is mantle-derived and geikielite is a common mineral produced in early stages of crystallization of kimberlitic and related magmas, but Mg-rich (to geikielite) euhedral tabular ilmenite has a late hydrothermal origin and cannot be used as neither KIM nor DIM. Moreover, a late hydrothermal enrichment in Mg can alter the original chemistry of ilmenite. Perhaps a remarkable difference between both ilmenite generation is that hydrothermal Mg-rich ilmenites could inherit its Mn content from late magmatic Mn-rich ilmenite, which is practically never present in magmatic Mg ilmenites, as demonstrated in our study.

Mn-rich ilmenite has also been proposed as a guide for diamond exploration (Kaminsky and Belousova, 2009), after the studies developed in the West African craton (Tompkins and Haggerty, 1985) and Brazil, based on the discovery of Mg-poor, Mn-rich ilmenite apparently included in diamonds (Meyer and McCallum, 1986; Sobolev *et al.*, 1999; Kaminsky *et al.*, 2000, 2001, 2006). However, Meyer and McCallum (1986) described in detail mineral inclusions in diamond from Colorado and demonstrated that the Mn-rich ilmenite found into these diamonds is epigenetic, and connected by small cracks with the surface. Moreover, the textures of detrital Mn-rich ilmenite observed in the Brazilian samples suggest that at least a part of these ilmenites replace other minerals, as is observed by us in this study. Mn-ilmenite is observed as intrusion-related mineral and can also be found in some crustal xenoliths. Hence, Mn-rich ilmenite is clearly a late product and its formation is connected in most cases with the serpentinization processes, thus unrelated with the diamond formation or preservation.

Finally, Carmody *et al.* (2014) suggests that the Zr/Nb ratio of ilmenite reflects the diamond potential in kimberlites and that ilmenite with Zr/Nb>0.37 should be DIM. Again, it is necessary to take into account that, as demonstrated in our study, Nb- and Zr-rich ilmenites can be produced by replacement of xenocrysts of Nb- and Zr-bearing mantle minerals, as rutile and members of the crichtonite group.

Therefore, Mg-rich and Mn-rich ilmenite cannot be used as a KIM or DIM mineral unless significant petrographic information could argue for a primary origin in depth.

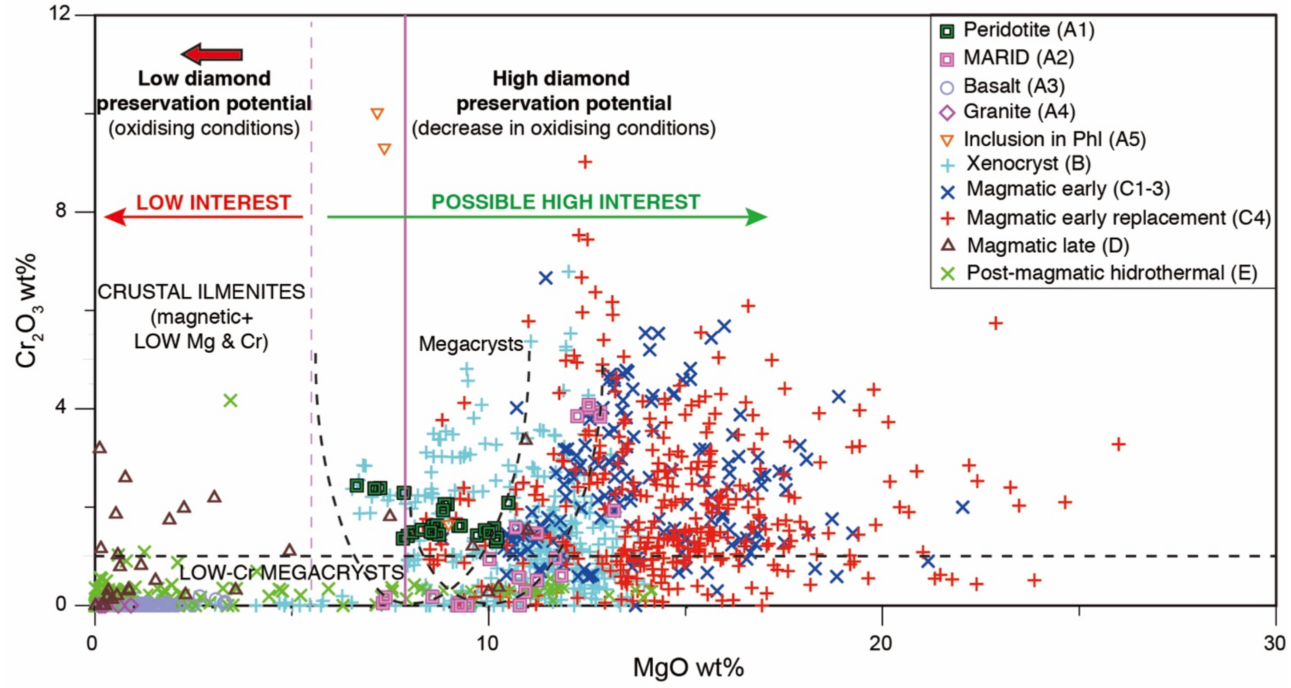

Fig. 6.35. Representation of compositions of ilmenite from this work on the Cr_2O_3 vs MgO (wt%) diagram with schematic correlation between oxidation state and Cr content of ilmenites and the diamond grade (from Semytkivska, 2010).

CHAPTER 7

RUTILE

7. RUTILE

7.1. INTRODUCTION

Rutile is a tetragonal polymorph of the titanium oxide, with general structural formula TiO_2. It is a mineral that can occur commonly in many crustal and mantle parageneses, and its relative stability and harness in the supergene environments, along with it density and bad cleavages, allows this mineral be found commonly in placer sediments, thus favouring its use in the exploration of the mineral deposits containing this mineral.

The structure of rutile allows common substitutions of Ti atoms by other elements, in particular, transition metals. These substitutions are common in the crustal occurrences of rutile. Rutile crystals from mantle paragenesis and kimberlites and related rocks have also complex substitutions of Ti by other metals, containing variable proportions of Fe, Al, Cr, V and HFSE as Ta, Nb, Zr and Sn (i.e., Sobolev and Yefimova, 2000). In this sense, a difference with the typical occurrences of Nb- and Ta-rich rutile in crustal paragenesis is the simultaneous enrichment in HFSE and Cr.

The TiO_2 structure is tetragonal $P4_2/mnm$ but it has many polymorphs (Zhu and Gao, 2014). The structure of rutile is a tetragonal arrangement of TiO_6 octahedrons with shared vertices (Fig. 7.1a). Other common rutile polymorphs are tetragonal anatase ($I4_1/amd$; Fig. 7.1b) and orthorhombic brookite (Pbca; Fig. 7.1c); these minerals are typically formed in hydrothermal or metamorphic crustal environments. In addition, there are several dense ultrahigh-pressure polymorphs as TiO_2 II (columbite-type structure, orthorhombic Pbcn; Fig.7.1d) and akaogiite (baddeleyite-type structure, monoclinic P21/c; Fig. 7.1e). Other synthetic phases, not described in natural occurrences yet, include a cotunnite-like structure (orthorhombic, Pnma; Fig.7.1f), a pyrite-type structure (cubic, Pa-3; Fig. 7.1g), fluorite-type structure (cubic, Fm-3m, Fig. 7.1h) and a tridymite-like structure /hexagonal, $P6_3/mmc$; Fig. 7.1 i). Moreover, an also dense monoclinic P2/b polymorph, riesite, has been found in impact structures, being produced by retrogression of akaogiite (Tschauner *et al.*, 2017). There are no descriptions of mantle occurrences of this mineral.

Rutile has been found as inclusions in diamond or equilibrated with this mineral in mantle ultramafic and eclogitic xenoliths, along with pyrope, minerals of the crichtonite group and others (Malkovets et al., 2016); therefore, it is considered as another powerful tool for diamond exploration (Sobolev and Yefimova, 2000). When available in kimberlites, rutile is also commonly used to determine their U-Pb age (eg. Cooper et al., 2008; Tappe et al., 2014). Therefore, rutile is a mineral of petrogenetic and economic interest and has been studied in the selected kimberlites and related rocks, although it is not found in all of them, and in fact is a relatively uncommon mineral in these geological environments.

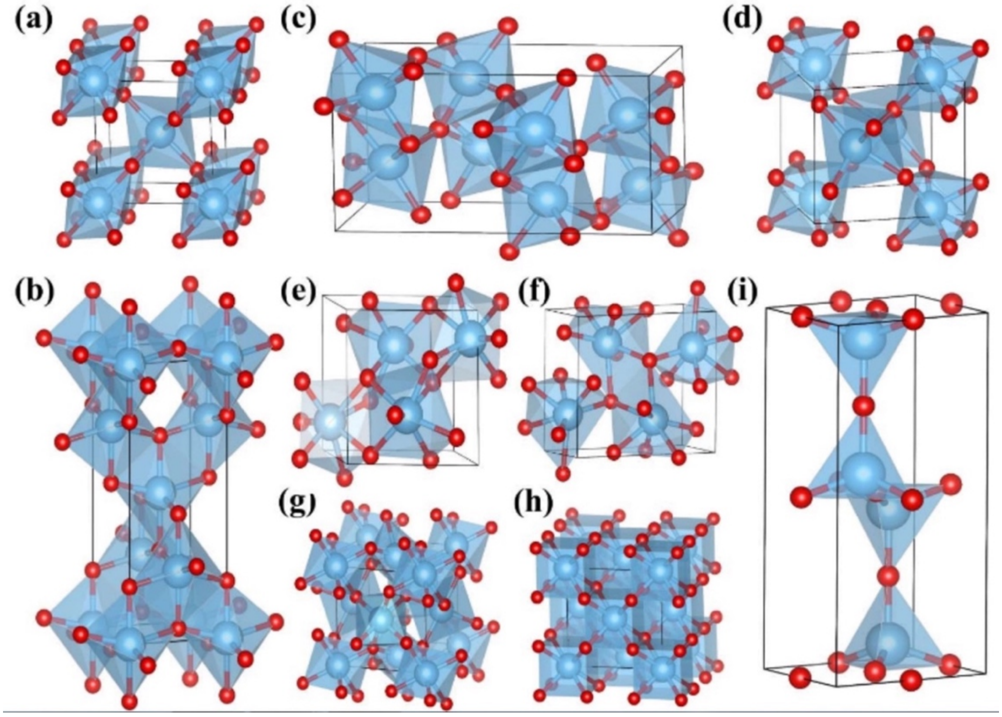

Fig. 7.1. Polyhedral structures for the main TiO_2 polymorphs, natural or synthetic: (a) rutile, (b) anatase, (c) brookite, (d) columbite-like structure (TiO_2-II), (e) baddeleyite-like structure (akaogiite), (f) cotunnite-like structure, (g) pyrite-like structure, (h) fluorite-like structure, and (i) tridymite-like structure. Ti and O atoms are represented by big blue and small red spheres respectively. Adapted from Zhu and Gao (2014).

7.2. TEXTURAL PATTERNS

Rutile in the studied kimberlite samples is found as the following different textural types:

1) Rutile within xenoliths;
2) Rutile xenocrysts;
3) Primary rutile as inclusions in olivine microphenocrysts;
4) Primary rutile anhedral microcrysts replaced by primary ilmenite (geikielite);
5) Primary rutile replacing ilmenite and other xenocrysts

Textural types 1 and 2 are xenolitic rutile, types 3 to 5 are considered as primary magmatic. The distribution of these rutile types found in the studied samples is listed in Table 7.1.

Moreover, titanium oxide is also commonly found as a secondary post magmatic hydrothermal mineral replacing titanium oxide in kimberlite. However, rutile cannot be distinguished from its other polymorphs (for instance, anatase) only based on its chemical composition, and optical characterization can be difficult because of the fine-grained sizing of these minerals. Hence, other analytical techniques, such as microRaman, must be used to distinguish among these polymorphs of TiO_2. Therefore, secondary rutile has not been described in this work as Raman study has not been done in all studied samples; however, anatase has been found in some of the analysed samples.

Other parageneses of rutile were mentioned in other studies, but they have not been described in this work. Among them, rutile reaction mantles upon perovskite were considered to be a primary phase in (Mitchell, 1986), while it was considered to be perovskite replaced by anatase (Pasteris, 1980); in this work, as described in the chapter 8 (perovksite) is also considered as secondary. Other paragenetic types such as rutile-silicate intergrowth and rutile-ilmenite intergrowth were considered to a be part of the megacrystic suite or as being derived from metasomatized mantle xenoliths (Mitchell, 1986), but they were not found in our study.

Table 7.1. Textural types of rutile found in the studied samples in this work.

								Primary		
	Sample	Region	Location	Name	Rock	1. Xenolith	2. Xenocryst	3. Inclusion in olivine	4. Microcrystal	5. Replacement
Angola	TZ-G18-47, TZ-G18-252		Tchiuzo		VK		2b			
Botswana	10052	SD	Jwaneng	Centre pipe	VK			3		
Botswana	10054	SD	Jwaneng	South pipe	VK		2b	3		
Botswana	10057	CD	Orapa	AK1, "C"	VK		2b			
Botswana	10058	CD	Letlhakane	DK1	VK	1				
South Africa	7707	NCP		Riverton	CK		2b			
South Africa	9311	NCP	Kimberley	Big Hole	CK			3		
South Africa	9364	NCP	Kimberly	DutoitSpan	CK			3	4	
South Africa	9375	FSP		Roberts Victor	Orangeite (Mitchell 1995)		2b			
Canada	9359	NWT	SW Slave	Drybones Bay	VK			3		
Canada	6934	NWT	Somerset island		CK			3		
USA	8015	Michigan	Lake Ellen	Lake Ellen	VK			3	4	5
USA	9352	Michigan	Menominee	Site 73	Ck			3	4	5
Russia	10079	NR	Pionerskaya		VK		2b			
Russia	10037	Yakutia	Udachnaya		CK			3	4	5
Russia	9611	Kola Peninsula	Emakowskaya		CK				4	
India	8044	RKF	Siddanpalli cluster	SK-2	CK		2a			
India	8029	RKF	Siddanpalli cluster	SK-3	CK		2a			

SD: Southern District; CD:Central District; NCP:Northern Cape Province; FSP:Free State Province; NR:Northern Region; RKF: Raichur kimberlite field. VK: volcaniclastic kimberlite; CK: coherent kimberlite

7.2.1. Xenolitic /xenocrystic rutile (types 2a and 2b)

Rutile is found in MARID xenoliths (type 1) in the Letlhakane DK1 volcaniclastic kimberlite (Fig. 7.2a). This MARID xenolith is composed by phlogopite, ilmenite and rutile. Rutile is commonly mantled by ilmenite.

Anhedral single crystals of rutile may occur in many kimberlites. Some large anhedral single crystals are clearly xenocrysts. These often show exsolutions of ilmenite (type 2a, Fig. 7.2b-c), and commonly are mantled by groundmass minerals such as perovskite and spinel. However, in many occurrences, small (<100 µm) anhedral single crystals of rutile occur (type 2b, Fig. 7.2d). In these cases, it is ambiguous whether it is primary or xenocrystic. Single anhedral rutile is only considered as primary in this work when there are textural evidences, including those found as inclusions in olivine and those replacing ilmenite xenocrysts and replaced by primary geikielite.

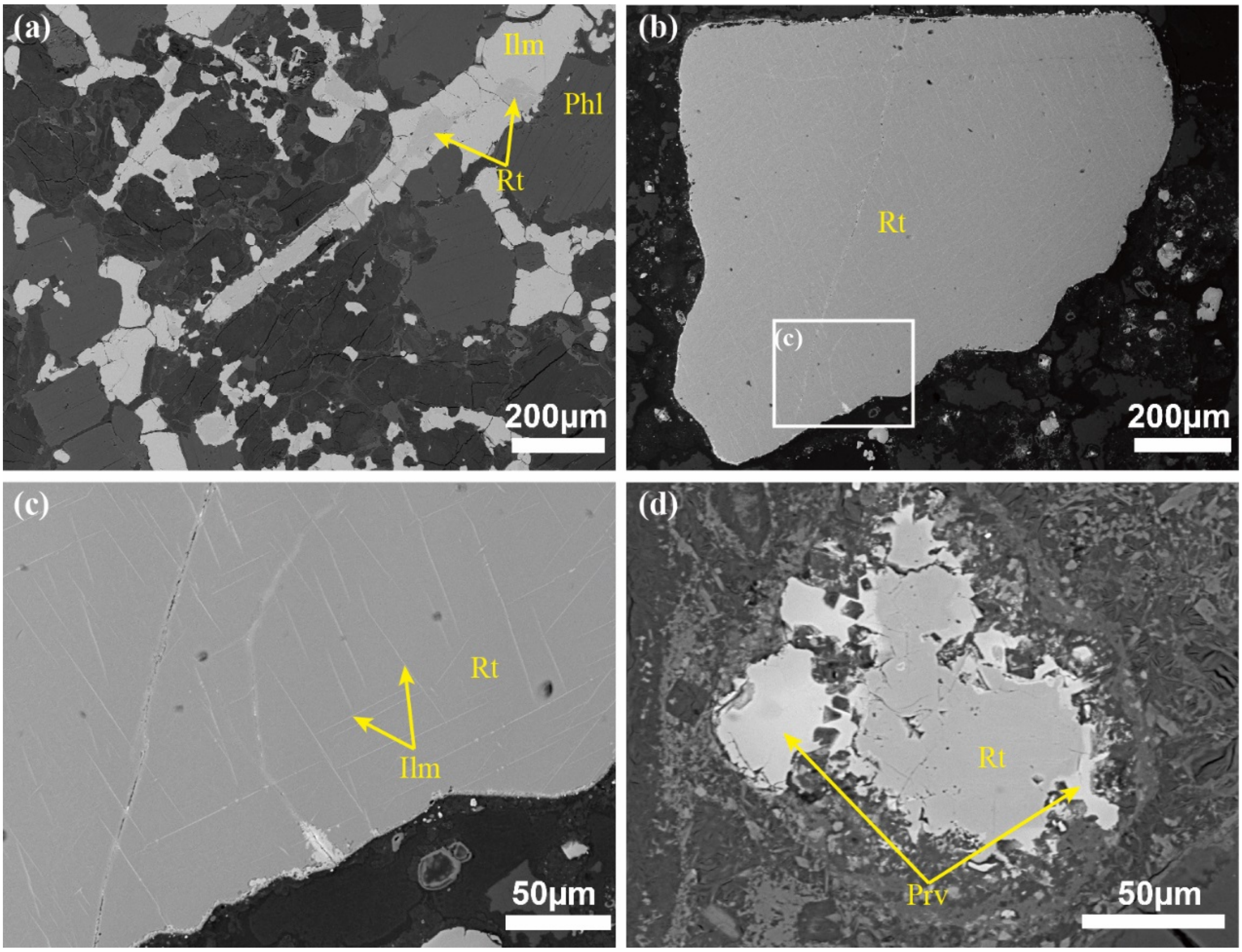

Fig. 7.2. Back-scattered electron (BSE) imagings of rutile. (a) Rutile (Rt) in MARID xenolith being replaced by ilmenite (Ilm) and phlogopite (Phl), in the Letlhakane DK1 volcaniclastic kimberlite. (b) Large type 2b rutile xenocryst displaying ilmenite exsolutions, in the Siddanpalli SK-2 coherent kimberlite. (c) Zoom of figure b, showing in detail the ilmenite exsolutions in rutile, in the Siddanpalli SK-2 coherent kimberlite. (d) Small anhedral type 2a rutile mantled by perovskite (Prv), in the Orapa AK1 "C" volcaniclastic kimberlite.

7.2.2. Primary rutile (types 3, 4 and 5)

Primary rutile is found as inclusions in olivine microphenocrysts (type 3). These rutile crystals are often small and show tabular or needle-like habits (Fig. 7.1.3a-b). In some cases, the hosting olivine is partially or totally pseudomorphised by serpentine (Fig. 7.1.3c-d).

However, in many cases rutile occurs as anhedral single microcrysts and then is difficult to determine its origin, whether it is xenocrystic or primary. In some samples, rutile occurs both as inclusions in olivine and as anhedral single microcryst in the same sample, showing the same chemical composition. In these cases, such discrete single crystals of rutile can be interpreted as primary, and their crystallization would take place during all the process of groundmass crystallization (type 4, Fig.7.4a).

Primary rutile is also found as a replacement product of xenocrysts of Ti-rich minerals, such as Mg-rich ilmenite (Fig. 7.4b-c) or Ti-rich chromite (Fig. 7.4d). This type of rutile is sometimes replaced by primary ilmenite (geikielite).

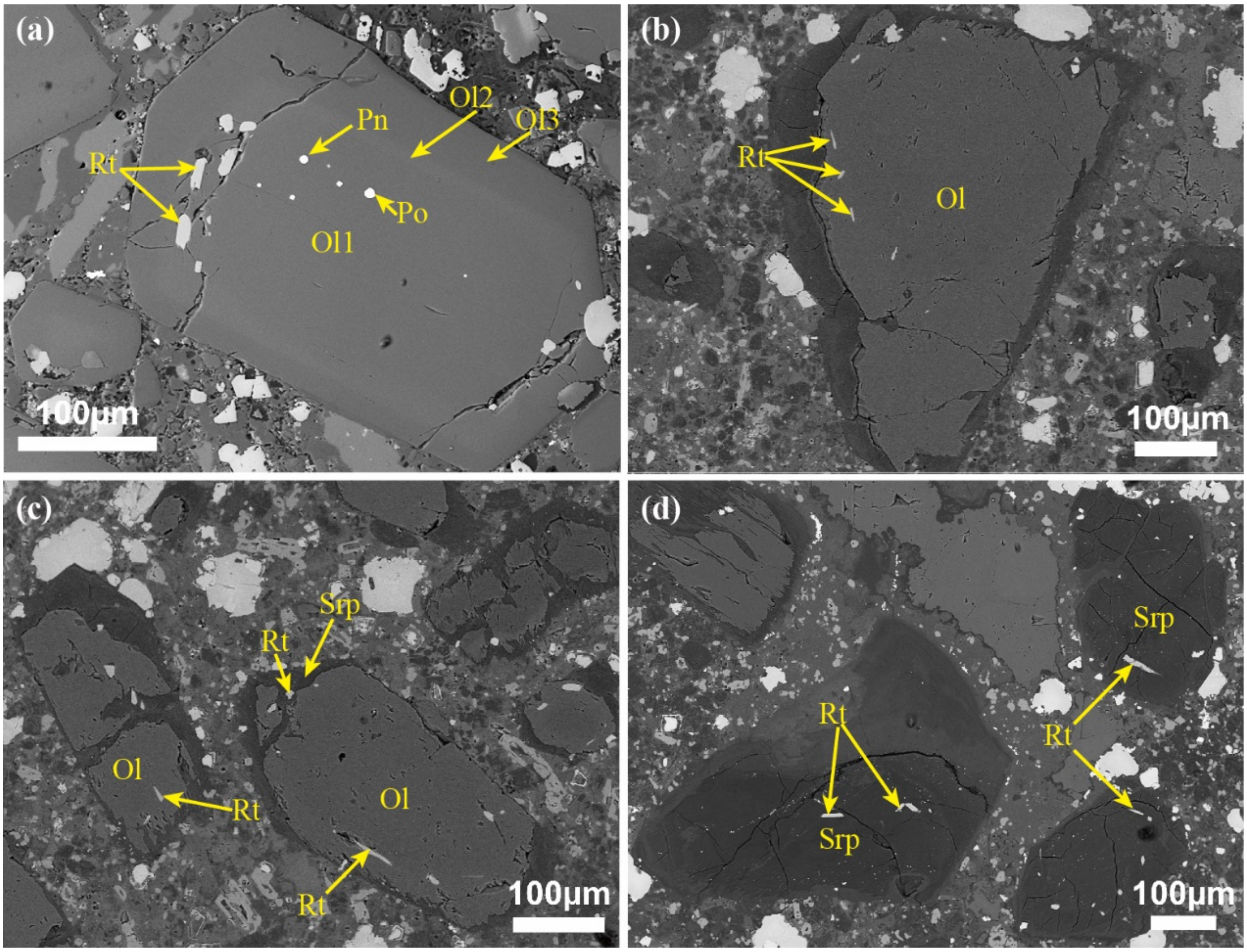

Fig. 7.3. Back-scattered electron (BSE) imagings of rutile. (a) Fresh zoned olivine (Ol1 to Ol3) containing inclusions of pyrrhotite (Po), pentlandite (Pn) and rutile (Rt), in the Menominee coherent kimberlite. (b) Fresh olivine containing inclusions of needle-like rutile, in the Dutoit Span coherent kimberlite. (c) Olivine partially altered to serpentine (Srp) containing inclusions of rutile, in the Dutoit Span coherent kimberlite. (d) Olivine, totally altered to serpentine, containing inclusions of rutile, in the Dutoit Span coherent kimberlite.

An example found in a relatively fresh kimberlite, from Menominee in USA, allowed develop a detailed study of primary rutile. In the Menominee kimberlite, rutile is found as the next textural types: 1) euhedral rutile as inclusions in olivine microphenocrysts, at the contact between the olivine core and the first rim (Fig. 7.3a); 2) rutile microphenocrysts (about 200 µm) which are replaced by geikielite (Fig. 7.4a) along their crystal edges and fractures, and then by qandilite-rich spinel (Spl); 3) rutile replacing Mg-rich ilmenite xenocrysts (Ilm 1), which is on its turn is replaced by primary geikielite (Ilm2, Fig. 7.4c).

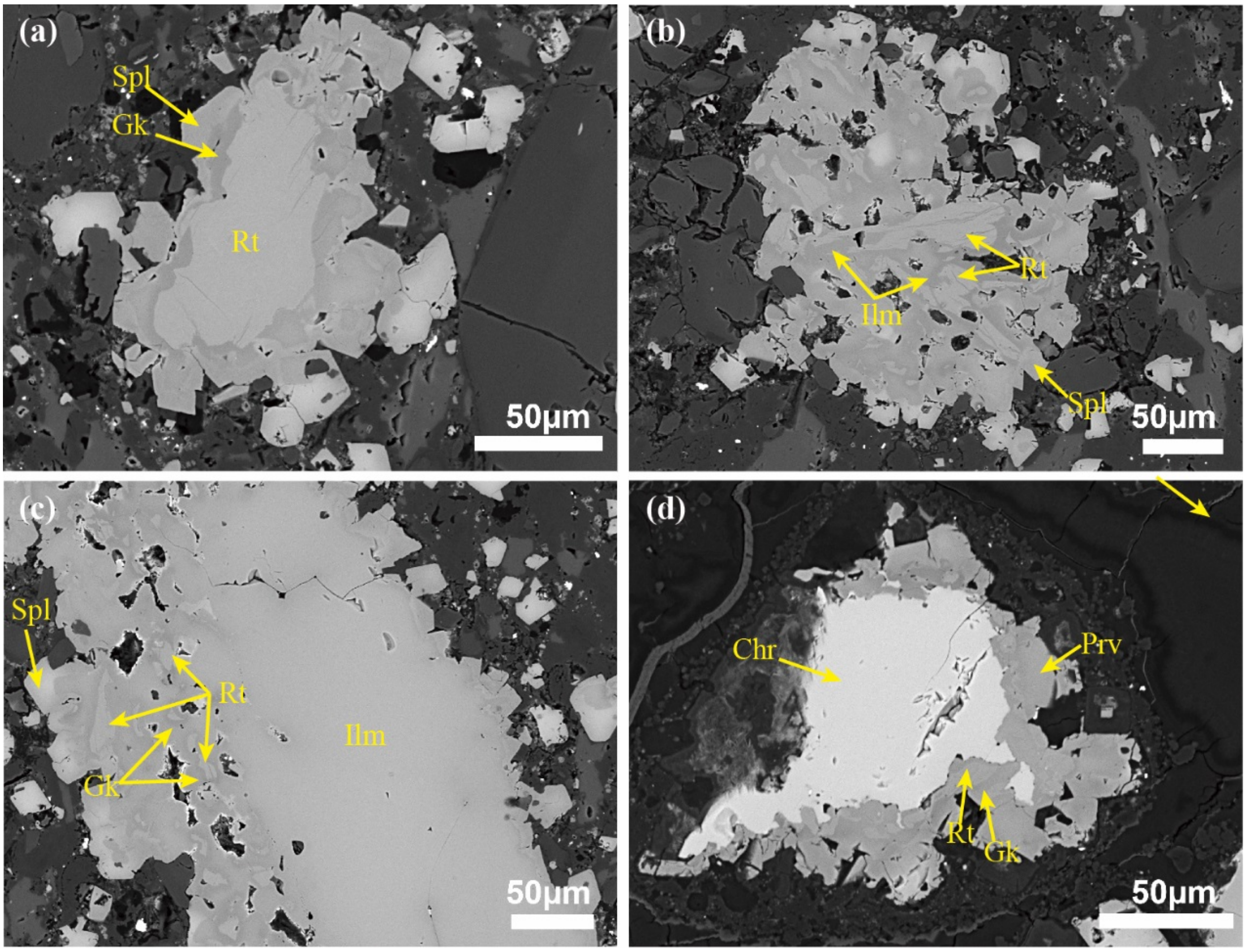

Fig. 7.4. Back-scattered electron (BSE) imagings of rutile. (a) Primary microphenocryst rutile replaced by geikielite (Gk, ilmenite group) which is mantled by qandilite (spinel group, Spl), in the Menominee coherent kimberlite. (b) Primary rutile replaced by geikielite which is on its turn mantled by qandilite, in the Menominee coherent kimberlite. (c) Primary rutile replacing Mg-rich ilmenite xenocryst (Ilm); the ensemble is replaced by primary geikielite (ilmenite group) and then by qandilite (spinel group), also in the Menominee coherent kimberlite. (d) Chromite xenocryst (Chr) replaced by primary rutile; the ensemble is replaced by primary geikielite (ilmenite group) and then by perovskite, in the Lake Ellen volcaniclastic kimberlite.

7.3. MINERAL CHEMISTRY

Rutile grains from the MARID xenoliths in the studied samples have relatively high Cr, Nb and V contents (2.7-3.6 wt% Cr_2O_3, 1.7-1.9 wt% Nb_2O_5 and 0.7-0.8 wt% V_2O_3) and relatively low Fe content (0.5-0.8 wt% Fe_2O_3, Fig. 7.5). Xenolitic and xenocrystic rutile have wide compositional range (0-7-3 wt% Cr_2O_3, 0.1-7.2 wt% Nb_2O_5 and 0-2.4 wt% V_2O_3 and 02-7.2 wt% Fe_2O_3, Fig. 7.5). However, there are neat differences in composition between the type 2a rutile and the type 2b rutile, especially in their Cr and Nb contents. Rutile 2a occur as large crystals with exsolutions of ilmenite and has higher Cr and Nb contents (3.0-7.3 wt% Cr_2O_3, 4.1-7.2 wt% Nb_2O_5) than the type 2b rutile (0-2.0 wt% Cr_2O_3, 0.1-2.7 wt% Nb_2O_5) which are relatively small crystals without exsolutions (Fig. 7.5). Zr is also enriched in type 2a xenocrysts (5958-8313 ppm, Fig. 7.6).

Types 3, 4 and 5 of primary rutile have similar compositional range (Fig. 7.6). Cr_2O_3 concentrations vary in the range 0-4.5 wt% and those of V_2O_3 between 0 to 0.9 wt%; whereas Nb_2O_5

values are in the range 0.3-6.4 wt% and those of Fe_2O_3 vary from 0.2 to 11.4 wt%. Some of them are enriched in Zr (up to 17027 ppm Zr, Fig. 7.6)

7.4. DISCUSSION

MARID and other xenolith containing rutile are sampled by deep-generated magmas. Disaggregation of these xenoliths give anhedral xenocrysts of rutile. Subhedral rutile co-crystallized in the early stages of magma crystallization with the first forsterite rim, a bit before the crystallization of primary ilmenite.

7.4.1. Xenolitic and xenocrystic rutile

The observed rutile paragenesis in kimberlites and related rocks can be commonly interpreted as xenocrystic, derived from the disaggregation of a wide variety of rocks either of crustal or mantle origin (eclogites, MARID, pyroxenites, metasomatized peridotites, as diverse authors indicated before (Haggerty, 1991; Meinhold, 2010). On the other hand, rutile has been also described as inclusions within diamond and/or intergrown with this mineral (Haggerty, 1991; Meinhold, 2010). Its composition is broadly used to constrain its source rock. Cr-poor rutile has been interpreted to derive from both crustal and off-cratonic or cratonic mantle rocks; Cr-rich rutile (>1.7 wt% Cr_2O_3) is currently thought to be exclusively related to cratonic mantle (Malkovets et al., 2016). Rutile derived from metasomatized mantle xenoliths may have Cr_2O_3 concentrations up to 9.75 wt% (Haggerty, 1991; Rezvukhin *et al.*, 2016a) and 7-13 wt% Nb_2O_5 (Haggerty, 1983).

In the TiO_2- Cr_2O_3 plot (Fig. 7.5a), most of the studied rutile crystals plot in the domain of rutile from cratonic deep-seated magmatic rocks, as delimited by Malkovets et al. (2016). Following the same reference, both types 2a rutile and rutile in MARID xenoliths plot in the domain of rutile from cratonic deep-seated magmatic rocks and above the limit of rutile from cratonic mantle (Fig. 7.5), while type 2b xenocrystic plot below this limit due to its relatively low Cr content. The majority of primary rutile plots within the domain of groundmass rutile field, but some rutile crystals found as inclusions in olivine could arrive to return higher Cr values than those of the field limit.

In th Cr_2O_3-Nb_2O_5 plot (Fig. 7.5b), there is a large overlap of different compositional fields with those determined by previous works. Analyses of type 1 rutile from MARID xenoliths plot in the field of xenogenic material (Haggerty, 1991), or that of inclusions in pyrope (Wang et al., 1999; Rezvukhin et al., 2016), or rutile in polymict breccia (Zhang et al., 2001; Giuliani et al., 2013). Type 2a xenocrysts plot in the field of xenogenic material (Haggerty, 1991), metasomatic nodules (Haggerty, 1991) and inclusions in pyrope (Rezvukhin *et al.*, 2016a). Type 2b xenocrysts plot in the field of inclusions in pyrope (Rezvukhin *et al.*, 2016a) or out of all these fields. Primary rutile plot in the field of xenogenic material, that of inclusions in pyrope from (Wang et al., 1999; Rezvukhin et al., 2016) and polymict breccias (Zhang et al., 2001; Giuliani et al., 2013). Therefore, one must conclude that use of these graphics can create confusion, because typical compositions of primary rutile formed during the emplacement should be attributed to get mantle values.

Nearly all xenolitic and xenocrystic rutile plot out of the field of rutile from eclogites (Fig. 7.6a-b). They also plot out of the field of rutile found as inclusions in diamonds on field. However, again, some primary rutile could have similar Zr, Nb and Fe contents as those from rutile from eclogites and diamond inclusions (Fig. 7.6a-b). Therefore, we found these graphics as inadequate.

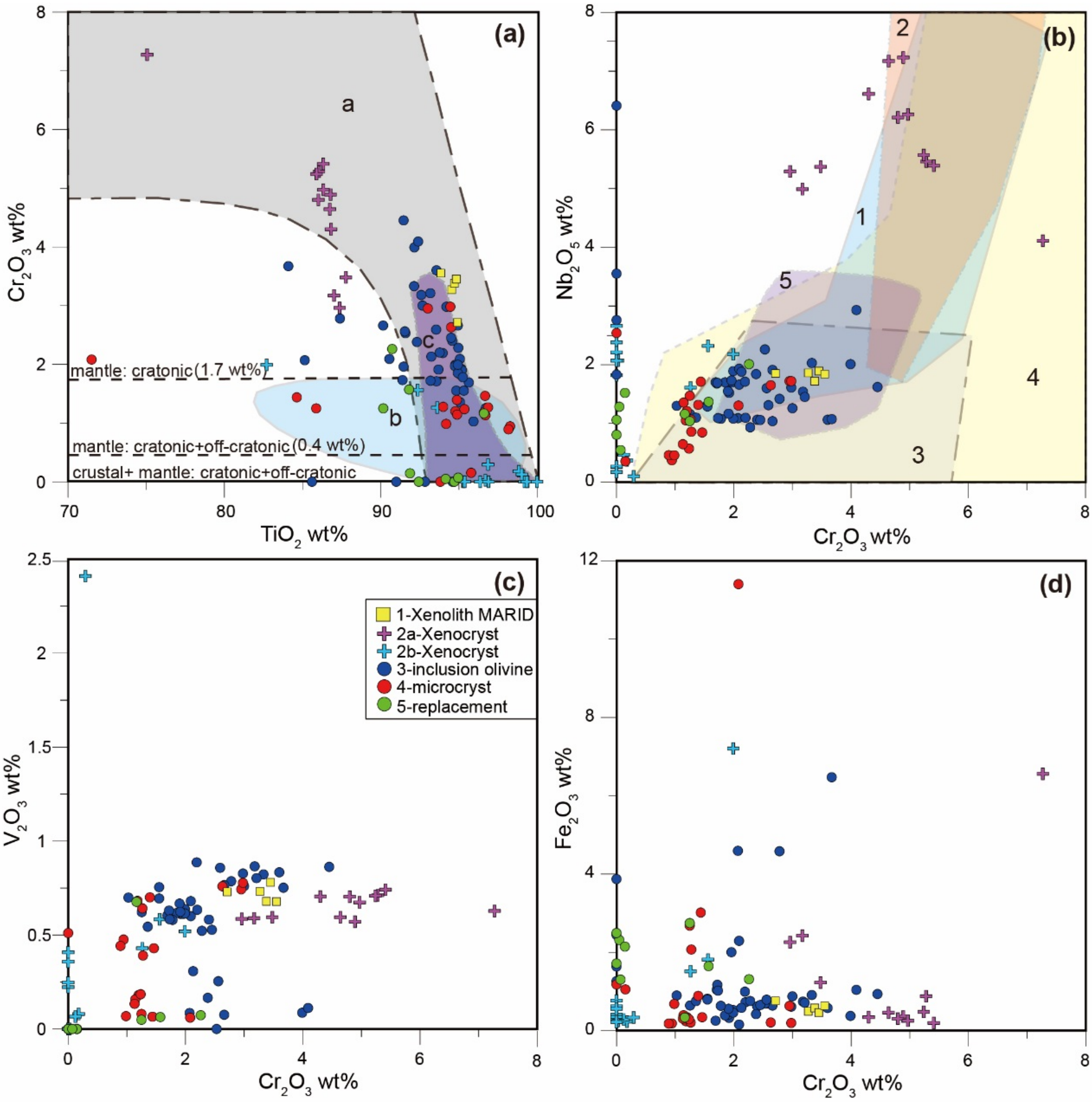

Fig. 7.5. Chemical composition of the rutile crystals in terms of dominant components. (a) TiO_2-Cr_2O_3 plot. Outlined field (after Malkovets et al., 2016) labeled as “a” corresponds to rutile from cratonic deep-seated magmatic rocks, field “b” to rutile from off-craton alkali basalts, field “c” to groundmass rutile from kimberlites. Subdivision of rutile from cratonic mantle, cratonic and off-cratonic mantle and from crustal and mantle is based on Malkovets et al. (2016). (b) Cr_2O_3-Nb_2O_5 plot. Domain labeled 1 corresponds to rutile from xenogenic material of kimberlites of South Africa (Haggerty, 1991), domain 2 to rutile in metasomatic nodules from kimberlites of the Orapa pipe, Botswana (Haggerty, 1991), domain 3 to rutile inclusions in pyrope from Garnet Ridge (Wang et al., 1999), domain 4 to rutile inclusions in pyrope from the Internatsionalnaya pipe (Rezvukhin et al., 2016a), domain 5 to rutile in polymict breccia (Zhang et al., 2001; Giuliani et al., 2013). (c) Cr_2O_3-V_2O_3 plot. (d) Cr_2O_3-Fe_2O_3 plot.

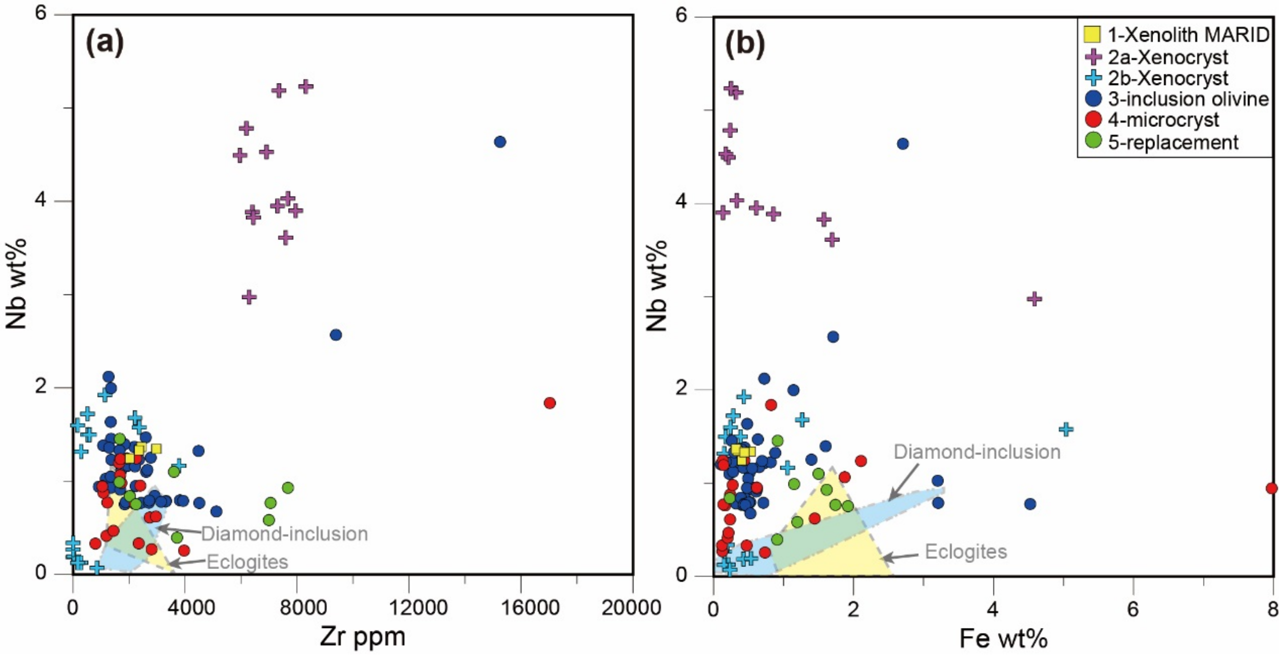

Fig. 7.6. Chemical composition of rutile in the selected kimberlites and related rocks in this study. (a) Zr (ppm) vs. Nb (wt%) plot. (b) Fe (wt%) vs. Nb (wt%) plot. Outlined fields of rutile as diamond inclusion and rutile in eclogites after Sobolev et al. (1997).

These determinations and the potential for U-Pb dating have categorized mantle rutile as a diamond indicator mineral (e.g., Malkovets et al., 2016). Rutile with ilmenite in “polymict breccias” is proposed to be precipitated from a Fe–Ti–Cr oxide immiscible melt that separated from an originally homogenous ultramafic silicate melt (Zhang et al., 2001). Crystallisation of rutile in polymict breccias (probably proto-kimberlitic melts) is also suggested to be due to a Ca-poor Ti–Fe–K-rich ultramafic silicate melt (Giuliani et al., 2013). It is suggested that the ultramafic silicate melt that crystallised rutile in polymict breccia was also carbonate-rich and originated from a silicate-carbonate melt whose composition was modified by processes such as differentiation and wall rock assimilation during ascent in the mantle (Giuliani et al., 2013).

7.4.2. HFSE content and the problem of exsolutions in rutile

Rutile-ilmenite intergrowths in kimberlite and related rocks were initially attributed to the breakdown of armalcolite ($(Fe,Mg)Ti_2O_5$, Haggerty, 1975). However, a large volume of experimental data (i.e., Friel *et al.*, 1977), as well as thermodynamic calculations (Anovitz *et al.*, 1985) demonstrated that that armalcolite should be stable only at crustal conditions. In fact, armalcolite is a mineral that use to be found in terrestrial or lunar volcanic rocks and it is not stable at more than 14 Kbar (Friel *et al.*, 1977). A mechanism of exsolution of the small amounts of FeO and MgO in solid solution (Agee *et al.*, 1982b) can also be refused because rutile used to have large amounts of Fe and never produces exsolutions.

Another possibility is the exsolution from high-pressure phases. In fact, the recent knowledge of the high-pressure polymorphs of TiO_2 can give a more interesting explanation. Ilmenite lamellae on rutile {010} planes were described in UHP metamorphosed eclogites and were interpreted in terms of exsolution from TiO_2-II polymorph (Brenan *et al.*, 1994; Rudnick, 2000). Liu *et al.* (2004) described the occurrence of ilmenite exsolutions in rutile from eclogite from Altyn Tagh in China and demonstrated that their abundance could be compatible with a high Fe^{3+} content in a TiO_2-II precursor, stable at more than 7-8 Gpa, well below the limit graphite/diamond. However, Tollo and Haggerty (1987) found rutile with similar exsolutions as xenocrysts in the Orapa kimberlite, and also proposed an origin by exsolution of TiO_2-II based on the high tenors of Nb. Haggerty (1991) differentiated a field of kimberlitic rutile, which has a wide compositional range, from relatively poor compositions to rutile crystals with up to 20 at% Nb+Ta+Cr (Fig. 7.7).

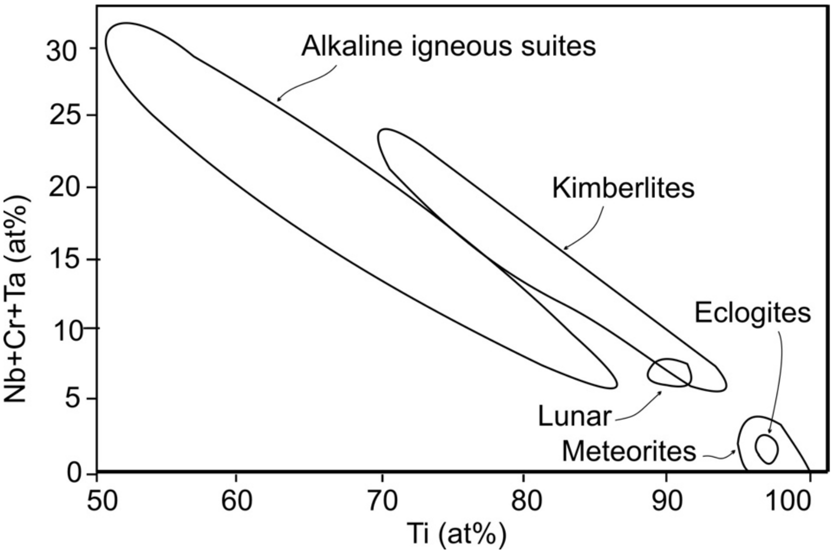

Fig. 7.7. Compositional variations in rutile depending on the mode of occurrence as defined by Haggerty (1991).

In our study, we have differentiated between different textural “kimberlitic” rutile, and we have represented these data in a diagram similar to that proposed by Haggerty (1991) but using only Nb and Cr (Fig. 7.8a). As shown in these graphics, the compositions of the rutile euhedral crystals considered as primary and included into the olivine phenocrysts are relatively poor in Nb, Ta and Cr, with less than 7 at%. This is congruent with a crystallization of these rutile crystals (and the mantling olivine) in crustal conditions, probably during the kimberlite emplacement. Similar results are obtained in the groundmass rutile and the replacing rutile. By the contrast, the rutile found in xenoliths may be strongly enriched in HFSE and Cr, thus indicating a very deep origin of these crystals. However, as indicated, there are large differences among rutile xenocrysts. Those having exsolutions (type 2a) are, in fact, those enriched in HFSE and Cr, whereas those without exsolutions (type 2b) do not have these enrichments.

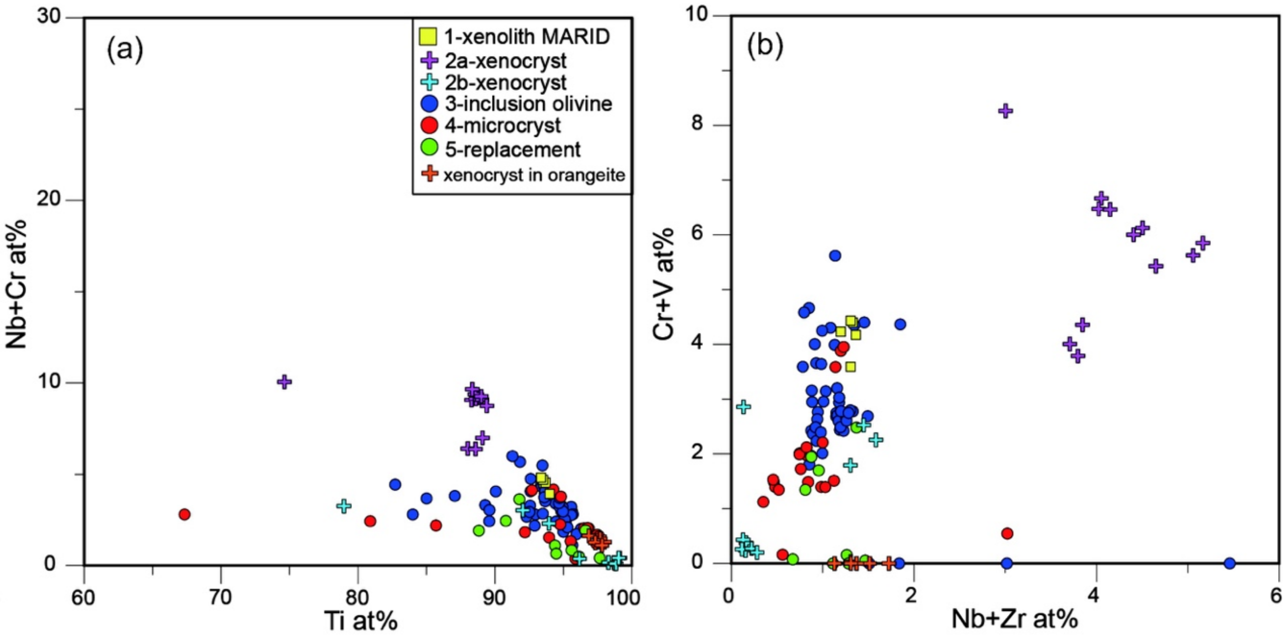

Fig. 7.8. Compositional variations in rutile based on the variations of Nb+Cr vs. Ti (a) and based on the variations of Cr+V vs. Nb+Zr (b).

Rutile xenocrysts in orangeites are among the most impoverished in HFSE and Cr, with rutile compositions close to the theoretical end-member.

Fig. 7.8b shows the correlation between the relatively compatible mantle elements Cr and V and the more incompatible HFSE as Nb and Zr. There is a relatively good correlation in most of the cases between these elements, thus indicating that the most possible mechanism for the incorporation of these elements into the rutile structure is the substitution $Nb^{5+}+Cr^{3+}=2Ti^{4+}$. A problem is to ensure the oxidation state of Nb and Ta, because it could be 3+. However, Burnham *et al.* (2012) demonstrated that, at the least in the upper mantle conditions, these elements are found with 5+ valence. Therefore, it is a valid mode of substitution in the structure, that can be favoured because at high pressure the structure of TiO_2 is identical to that of columbite.

However, there are important differences: rutile xenocrysts from orangeites is extremely impoverished in Cr and V, but slightly enriched in Zr and Nb. Some of the groundmass ilmenite from kimberlites may also follow this trend (Fig. 7.8b).

Hence, this is again a strong argument to argue for a deep origin of the type 2A rutile crystals, above the transit rutile-TiO_2-II, whereas the 2B type could be trapped below this limit (Fig. 7.9). Therefore, the Ti metasomatism can be produced at different depths in the mantle, thus producing different polymorphs. The existence of these polymorphs can be assessed by the appearance of ilmenite exsolutions.

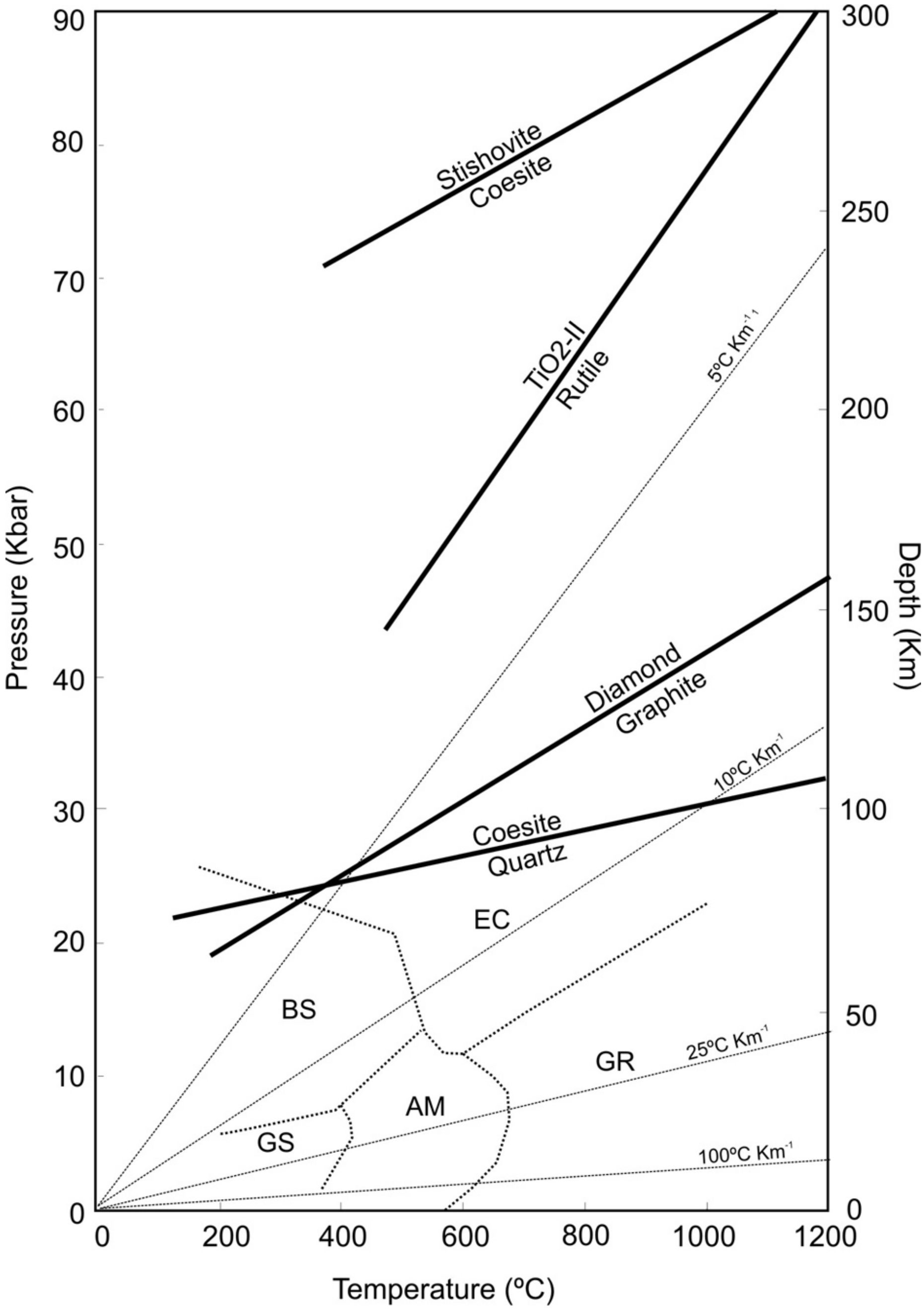

Fig. 7.9.. Pressure–temperature diagram (after Baldwin et al., 2004; Okamoto and Maruyama, 2004; Meinhold, 2010). Phase transition line for rutile and TiO_2(II) is based on experimental data (after Withers et al., 2003). A range of geotherms and other mineral transitions boundaries are also indicated. Abbreviations: GS, greenschist facies; AM, amphibolite facies; GR, granulite facies; BS, blueschist facies; EC, eclogite facies.

7.4.3. Primary magmatic rutile

Rutile was proposed as a primary phase precipitated from the kimberlite liquid (Agee *et al.*, 1982b). In our textural study we demonstrated that primary magmatic rutile occurs in many kimberlites (types 3, 4 and 5). However, their compositions plot in the "cratonic mantle field" as established by different authors. Hence, it should be important to plot separately the different textural generations of rutile. Moreover, the rutile inclusions in fresh olivine, the rutile replacing Mg-ilmenite xenocrysts and the rutile microphenocrysts which are replaced by primary magmatic ilmenite, all have similar chemical composition in the Menominee kimberlite. Hence, we suggest that all these rutile crystals formed during the early stages of magma crystallization, immediately followed by the crystallization of primary ilmenite, prior to the crystallization of the first olivine rim. As a consequence, the occurrence of phenocrystic rutile in Menominee precludes the use of the aforementioned rutile-based diagrams unless previous accurate petrographic study ensure that the rutile crystals are xenocrysts. In any case, all the rutile types tend to be replaced by primary ilmenite, which also replaces the ilmenite xenocrystic generations. Rutile not preserved in olivine may have been resorbed into the melt (Mitchell, 1986).

7.4.4. Rutile in lamproites, orangeites and UML

Rutile is also found as groundmass mineral in orangeites (Mitchell, 1995). However, primary rutile was not found in any orangeite, lamproite or UML in this study. Only xenocrystic rutile was found in Roberts Victor orangeite (Table 7.1). Rutile from xenoliths in orangeites is distinguished from rutile in kimberlites by its very low Cr independently of its high Nb content (Fig. 7.8). Mitchell (1995) found similar differences. Rutile is not a common mineral in lamproite (Mitchell, 1995).

7.4.5. Use of rutile as kimberlite indicator mineral (KIM) and diamond indicator mineral (DIM)

Rutile may be a good KIM because most of the rutile generations are simultaneously enriched in Nb+Ta+Zr and Cr; however, one must take into account that orangeites are impoverished in Cr.

The occurrence of rutile is not an indicator of the possible existence of diamond, but a high tenor in HFSE and Cr can indicate a deep sampling by the kimberlite magma. In particular, the existence of ilmenite exsolutions coupled with high tenors in both mantle incompatible elements as HFSE (Nb, Ta, Zr) and mantle compatible elements as Cr and V can be a good criterion because it indicates an ultra-high pressure environment for the association.

CHAPTER 8

PEROVSKITE

8. PEROVSKITE

8.1. INTRODUCTION

The name perovskite is used in different senses. In a more generic sense, perovskite is a structural type of the general composition ABX_3 characterized by a cubic structure, with large A cations as Ba or Sr in 12-coordination and B cations in 6-coordination, and X as anion. This structure is common to tens of minerals of different classes, including oxides, silicates, arsenides and others. However, there are many structural variations owing to the entrance of different cations with different ionic radius or ionic strength, thus producing tilting and distortion of the BX_6 octahedra, ordering of A- and B-site cations and formation of A-, B- or X-site vacancies. These disturbances result in the appearance of different structures and, hence, different subgroups (Nickel and McAdam, 1963; Mitchell *et al.*, 2017).

Hence, the perovskite subgroup is characterized by tilting of the octahedrons, thus resulting in a more reduced coordination of the A position (VIII), the entrance of medium-sized cations as Ca and a lower symmetry, typically orthorhombic Pbna (Fig. 8.1). However, the shape of the crystals is pseudocubic and the anisotropy is low.

The mineral species perovskite (with an ideal formula $CaTiO_3$) belongs to the perovskite subgroup. Although the essential composition of perovskite is $CaTiO_3$, most of natural perovskite crystals from different occurrences have substitution of REE, Sr and Na for Ca and Nb or Ta for Ti (Deer *et al.*, 1992, Table 8.1).

Perovskite is a common mineral in the groundmass of many kimberlites and related rocks, where it crystallizes directly from the kimberlite magma (Mitchell, 1986). Therefore, taking into account the common occurrence of traces of U in the A position, perovskite could also be used to determine the kimberlite emplacement age (Batumike et al., 2008; Castillo-Oliver et al., 2016). However, in many cases these minerals are underwent complex alteration processes during the hydrothermal or supergene late stages of the kimberlite crystallization sequence that could disturb the petrogenetic interpretations based on geochemical data. Hence, our petrographic study was carried out with the objective of valuate the limitations of the dating of perovskite.

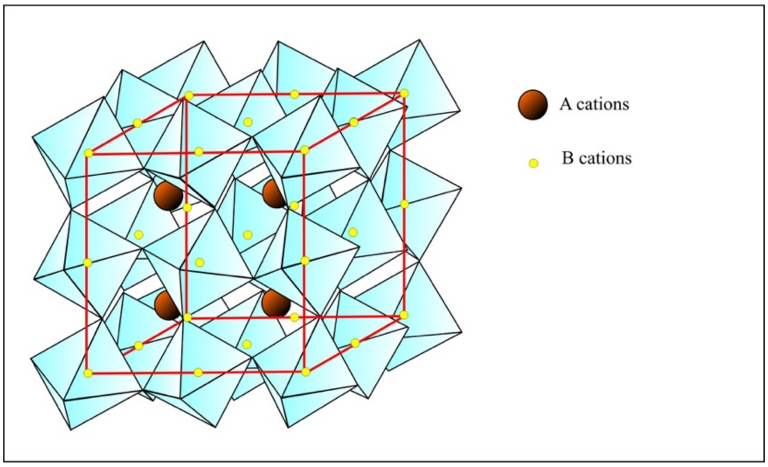

Fig. 8.1. Structure of perovskite subgroup (Mitchell et al., 2017).

Table 8.1. Members of the perovskite subgroup (Mitchell et al., 2017).

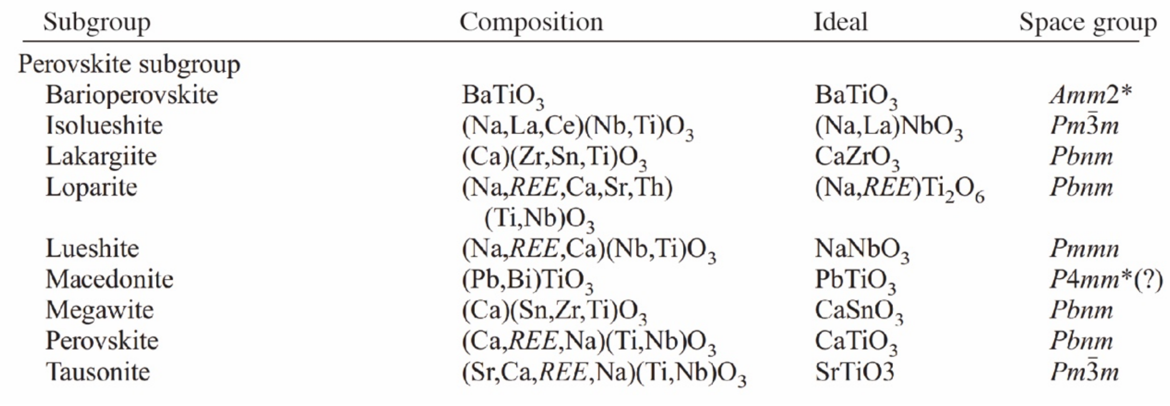

Subgroup	Composition	Ideal	Space group
Perovskite subgroup			
Barioperovskite	$BaTiO_3$	$BaTiO_3$	*Amm*2*
Isolueshite	$(Na,La,Ce)(Nb,Ti)O_3$	$(Na,La)NbO_3$	$Pm\bar{3}m$
Lakargiite	$(Ca)(Zr,Sn,Ti)O_3$	$CaZrO_3$	*Pbnm*
Loparite	$(Na,REE,Ca,Sr,Th)(Ti,Nb)O_3$	$(Na,REE)Ti_2O_6$	*Pbnm*
Lueshite	$(Na,REE,Ca)(Nb,Ti)O_3$	$NaNbO_3$	*Pmmn*
Macedonite	$(Pb,Bi)TiO_3$	$PbTiO_3$	*P*4*mm**(?)
Megawite	$(Ca)(Sn,Zr,Ti)O_3$	$CaSnO_3$	*Pbnm*
Perovskite	$(Ca,REE,Na)(Ti,Nb)O_3$	$CaTiO_3$	*Pbnm*
Tausonite	$(Sr,Ca,REE,Na)(Ti,Nb)O_3$	SrTiO3	$Pm\bar{3}m$

8.2. PRIMARY AND SECONDARY PEROVSKITE

8.2.1. Textural patterns

Perovskite is not found in all but in majority kimberlites, where it is one of the most common groundmass minerals. It also commonly found in lamproites as well as orangeites and UML In this work, two different perovskite parageneses have been found:

1) Primary magmatic perovskite;
2) Secondary hydrothermal perovskite.

Primary perovskite

Primary perovskite occurs as:

a) Primary perovskite crystals scattered in the groundmass;
b) Perovskite replacing and/or overgrowing previously formed Ti-oxides.

Primary groundmass perovskite occurs as euhedral to anhedral groundmass crystals with a variable size, generally around 10-200µm (Fig. 8.2a). Sometimes it is found as very fine-grained aggregates (Fig. 8.2b). It is also found cocrystallised with groundmass ulvöspinel (Fig. 8.2c). Groundmass perovskite is frequently zoned, although not in all of the cases. Zoning patterns correspond mostly to changes in the REE and Nb contents; in a few cases zoning can be produced by differences in the Fe contents. Different zoning patterns can be identified, as the next: i) frequently, with higher REE and/or Nb contents in the crystal core (Fig. 8.2d); ii) less frequently, higher REE and Nb contents in the crystal rims (Fig. 8.2e); iii) oscillatory zoning (Fig. 8.2f).

Primary perovskite is also found replacing and/or overgrowing previously formed Ti-oxides, such as ilmenite, frequently together with ulvöspinel-titanomagnetite forming a rim around ilmenite xenocrysts. Sometimes perovskite is also found mantling ulvöspinel-titanomagnetite,being formed just later than these minerals (Fig. 8.3a-b), sometimes it is intergrown with them (Fig. 8. 3c-d).

Representative examples of primary perovskite can be provided by the SK-1 and SK-2 kimberlite. Groundmass perovskites (type 1 perovskite) in SK-1 kimberlite are euhedral crystals around 60µm in diameter (Fig. 8. 4a). These crystals are slightly replaced by anatase along the grain borders and following small cracks Groundmass perovskite (type 1 perovskite) in SK-2 occurs as subhedral crystals around 60µm (Fig. 8. 4b) that may show oscillatory zoning. Perovskite is partially replaced by fine-grained aggregates of mixtures of kassite and aeschynite-(Ce). Alteration of perovskite from SK-1 and Sk-2 kimberlite is explained in section 8.2.2.

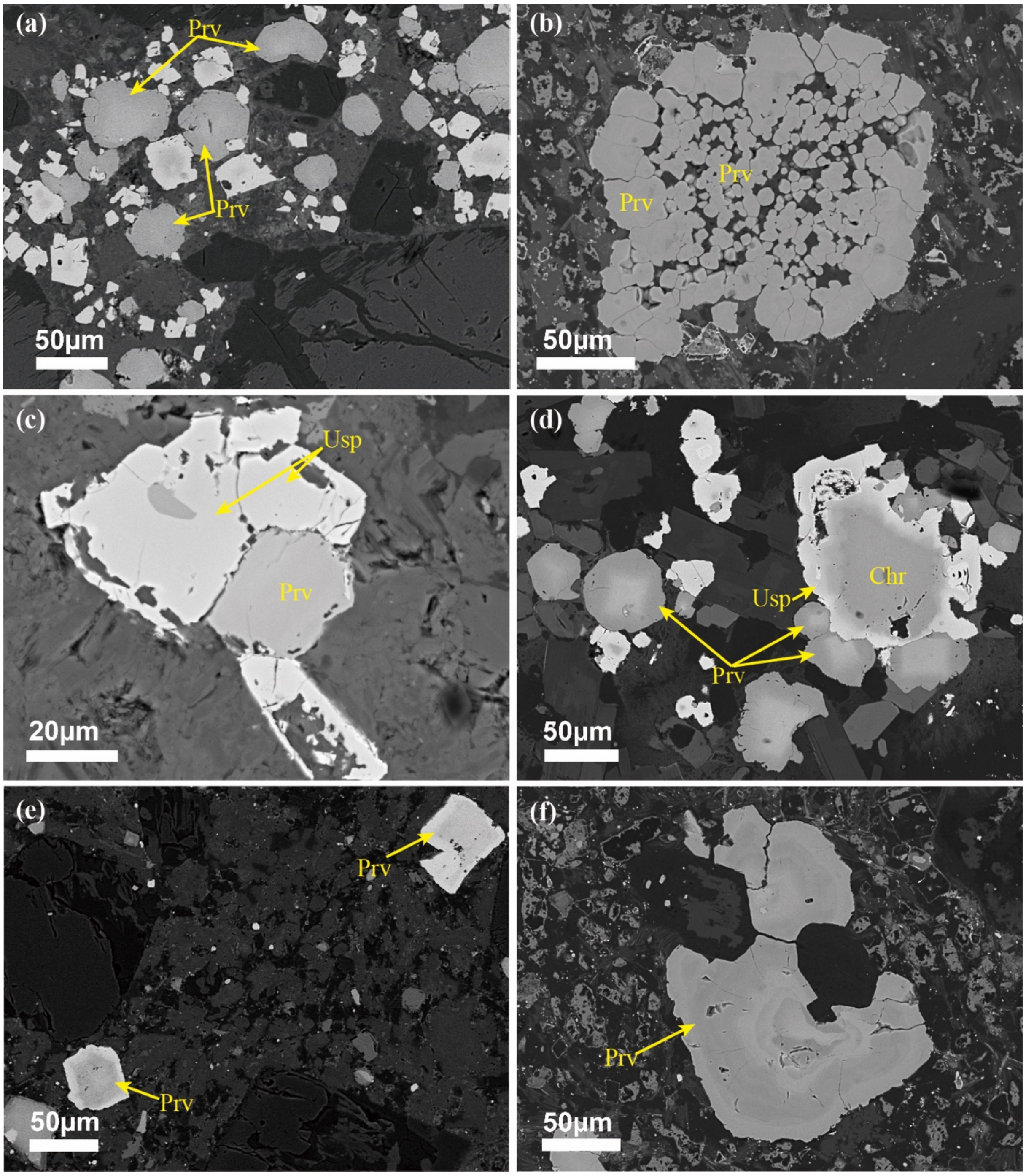

Fig 8.2. Representative SEM (BSE) images of the primary groundmass (type 1) perovskite. (a) Anhedral rounded groundmass perovskite (Prv1), from South pipe of Karowe AK6 kimberlite. (b) Very fine grained perovskite aggregate mantled by coarse perovskite, from Chigicherla CC-4 kimberlite. (c) Groundmass perovskite cocrystallised in equilibrium with groundmass ulvöspinel, from the Banankoro "B" kimberlite. (d) Zoned groundmass perovskite with higher REE and/or Nb content in core, in contact with groundmass spinel formed by chromite (Chr) cores and ulvöspinel rims, from the Banankoro "A" kimberlite. (e) Zoned groundmass perovskite with higher REE and/or Nb content in rim, from the Jackson inlet kimberlite. (f) Zoned groundmass perovskite showing oscillatory zoning, from the Chigicherla CC-4 kimberlite.

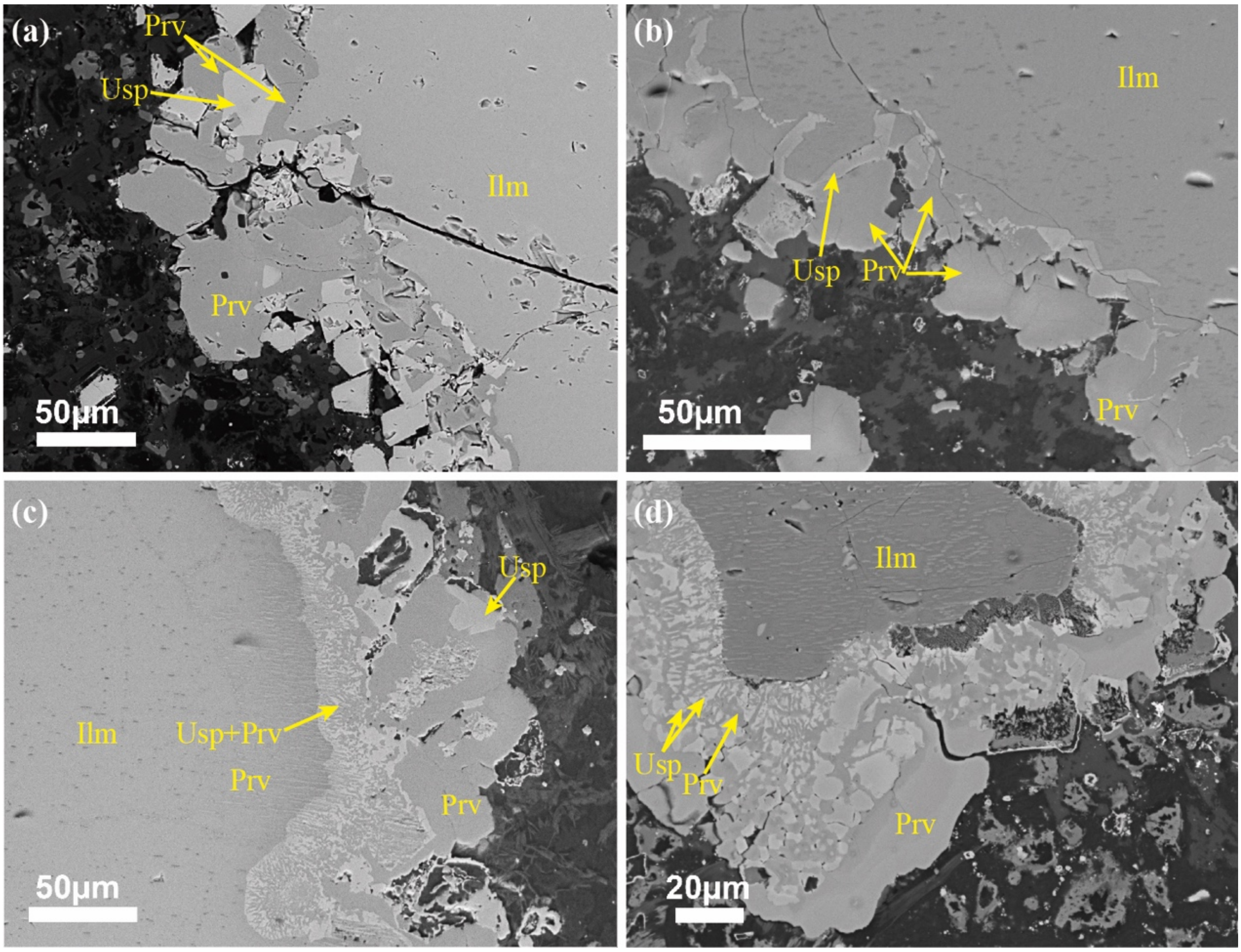

Fig 8.3. Representative SEM (BSE) images of primary groundmass (type 1) perovskite. (a) Perovskite (Prv) replaces ilmenite (Ilm) xenocryst together with ulvöspinel (Usp), from the Dutoit Span kimberlites. (b) Perovskite (Prv) mantling ulvöspinel, mantling ilmenite, from the Kalyandurg KL-4 kimberlite. (c) Ulvöspinel-perovskite intergrowth (Usp+Prv) replacing ilmenite, from the Monastery kimberlite. (d) Ulvöspinel-perovskite intergrowth replacing ilmenite, from the Banankoro “B” kimberlite.

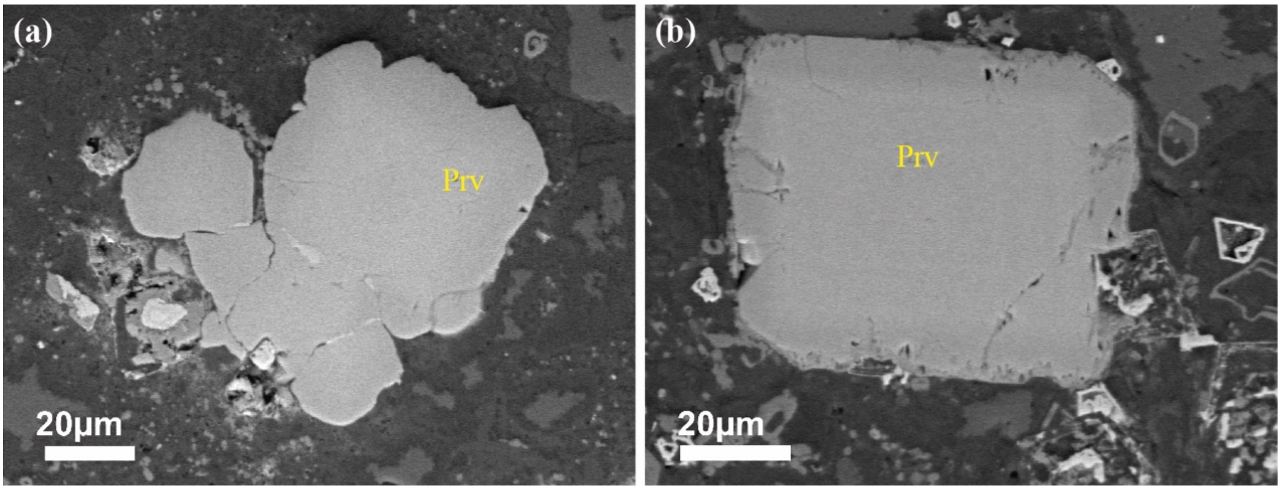

Fig 8.4. Representative SEM (BSE) images of the primary groundmass (type 1) perovskite from (a) Sk-1 kimberlite and (b) Sk-2 kimberlite.

Secondary perovskite

Another generation of perovskite, which corresponds to secondary hydrothermal perovskite (type 2 perovskite, euhedral to anhedral) is found replacing groundmass atoll spinels in SK-2 kimberlite (Fig. 8.5a-b), along with Ti-rich hydrogarnets, calcite and serpentine (Fig. 8.5a-d). Type 2 perovskite often shows a geode-like texture into the pseudomorphized atoll spinel (Fig. 8.5). Ilmenite and magnetite xenocrysts from SK-2 may also be replaced by a sequence of typical groundmass minerals and sometimes by type 2 perovskite.

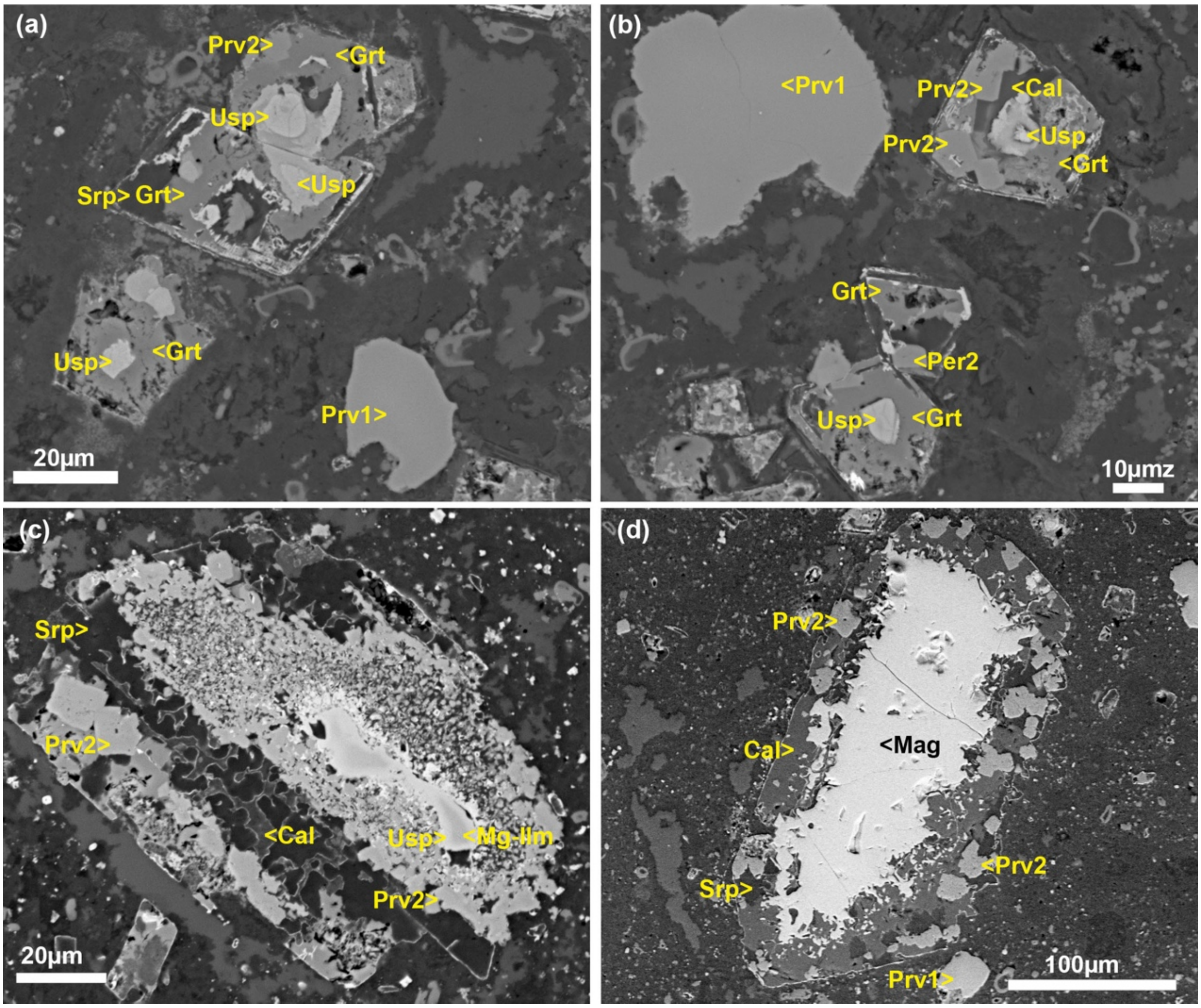

Fig 8.5. Representative SEM (BSE) images of the perovskite generations from SK-2 kimberlites. (a) Groundmass atoll spinel altered to type 2 perovskite (Prv2), Ti-rich garnets (Grt) and serpentine (Srp), showing ulvöspinel (Usp) relicts; primary groundmass type 1 perovskite (Prv 1) is also present. (b) Atoll groundmass spinel altered to type 2 euhedral perovskite, Ti-rich garnets and calcite (Cal), showing relicts of ulvöspinel and type 1 perovskite. (c) Mg-rich ilmenite (Mg-ilm), replaced by ulvöspinel, which on its turn is replaced by type 2 perovskite, calcite and serpentine. (d) Magnetite (Mag), replaced by type 2 euhedral perovskite, serpentine and calcite.

8.2.2. MicroRaman Study

The microRaman study also confirmed the identification of the second generation of perovskite (type 2) by comparison with the spectrum of the magmatic perovskite (type 1; Fig. 8.6). Minor differences in the position and intensity of the bands can also be related to changes in the chemical composition and/or to different orientation.

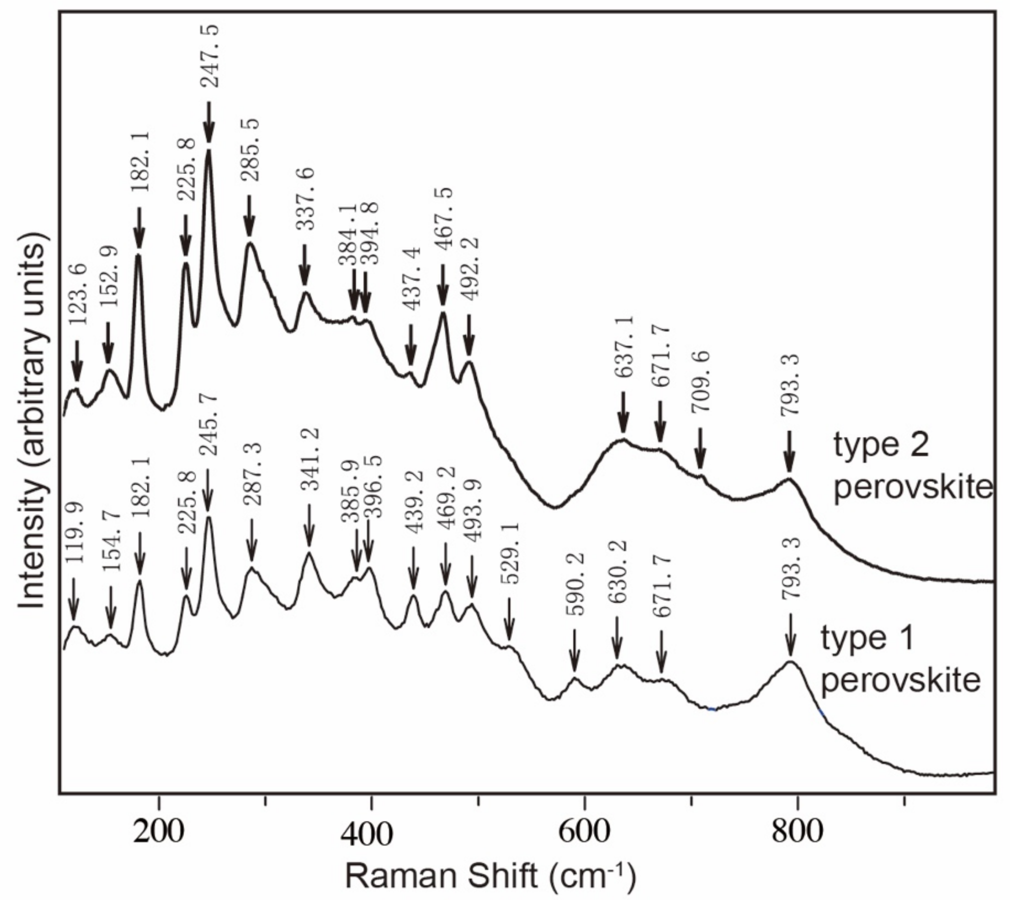

Fig. 8.6. Representative Raman spectrum analysed in type 2 perovskite replacing spinel and type 1 groundmass perovskite from SK-2 kimberlite (this work).

8.2.3. Chemical composition

Primary perovskite

Around 435 chemical composition analyses have been carried out in primary perovskite from 14 localities, including 4 lamproites and 10 kimberlites. Studied lamproites are Wajrakarur P2, Lattavaram P4, Mulligiripally P5 and Murfreesboro lamproite. Kimberlites include Siddanpalli SK-1, Siddanpalli SK-2, Siddanpalli SK-3, Chigicherla CC-4, Chigicherla CC-5, Wajrakarur P1, Kalyandurg KL-4, Banankoro “A”, Banankoro “B” and Shengli. Some representative compositions of primary perovskite is shown in Table 8.2.

All the analysed primary perovskite crystals from lamproites and kimberlites correspond with perovskite and ceroan perovskite (Fig. 8.7) in the ternary systems perovskite – loparite – lueshite ($CaTiO_3$ – Na*REE*Ti_2O_6 – $NaNbO_3$) and perovskite – loparite – tausonite ($CaTiO_3$ – Na*REE*Ti_2O_6 – $SrTiO_3$). Perovskite member is 83.6-99.8 mol%, loparite member is 0-12.7 mol%, while lueshite and tausonite member only are 0-2.8 mol% and 0-1.9 mol% respectively. Lamproite and kimberlite perovskite show similar range, although groundmass perovskite in lamproite has lower loparite component than groundmass perovskite in kimberlite.

Table 8.2. Representative electron microprobe (EMPA) analysis of type 1 perovskite from SK-1 and SK-2 kimberlites, type 2 perovskite, kassite and aeschynite-(Ce) from SK-2 kimberlite.

Mineral	Type 1 perovskite								Type 2 perovskite		Aeschynite-(Ce)		Kassite		
	SK-1				SK-2				SK-2	SK-2	SK-2	SK-2	SK-2	SK-2	SK-2
	centre	center	border	border	centre	center	border	border							
(wt%)															
SrO	0.34	0.18	0.23	0.25	0.20	0.19	0.20	0.24	bdl	bdl	0.13	bdl	bdl	bdl	bdl
ZrO_2	0.10	0.21	0.23	0.38	0.08	0.14	0.19	0.28	0.09	0.46	0.74	0.25	0.43	0.40	0.08
Nb_2O_5	0.60	0.98	0.73	0.61	0.54	0.63	0.44	0.50	0.10	bdl	3.10	0.99	0.63	0.46	0.62
CaO	34.68	34.64	37.11	37.63	35.36	35.27	38.06	38.19	39.95	38.20	7.24	8.00	22.49	22.12	21.32
ThO_2	-	-	-	-	-	-	-	-	-	-	0.37	bdl	-	-	-
Na_2O	0.57	0.57	0.35	0.22	36.53	0.60	0.28	0.22	bdl	bdl	bdl	bdl	bdl	bdl	bdl
MgO	0.06	bdl	0.05	0.09	0.08	bdl	0.05	0.05	0.14	0.08	0.04	0.05	0.26	0.05	bdl
Al_2O_3	0.33	0.30	0.24	0.31	0.25	0.29	0.23	0.28	bdl	bdl	bdl	bdl	bdl	0.03	bdl
SiO_2	bdl	bdl	bdl	0.04	bdl	bdl	bdl	bdl	0.61	0.60	0.38	bdl	0.05	0.06	0.07
BaO	0.19	0.12	-	0.08	-	0.13	0.18	0.12	-	-	0.46	0.15	-	-	-
TiO_2	54.36	54.26	54.13	56.30	54.99	54.75	57.10	56.67	55.49	53.48	48.61	52.20	62.42	64.74	65.26
La_2O_3	0.97	1.02	0.67	0.50	0.60	0.84	0.62	0.53	bdl	bdl	7.79	11.11	bdl	bdl	0.15
Ce_2O_3	3.07	3.03	1.79	0.88	2.18	2.84	0.89	0.89	bdl	bdl	18.34	17.99	0.23	0.48	0.58
Nd_2O_3	1.56	1.50	1.08	0.35	1.18	1.50	0.34	0.41	bdl	bdl	6.88	3.99	0.24	0.22	0.28
Cr_2O_3	-	-	-	-	-	-	-	-	-	-	bdl	0.05	-	-	-
Pr_2O_3	0.45	0.43	0.17	0.19	0.08	0.36	0.19	0.17	bdl	bdl	1.97	1.45	0.12	0.08	bdl
MnO	0.02	0.05	0.04	bdl	0.03	bdl	0.02	0.05	bdl	0.03	bdl	0.19	0.15	0.37	1.28
Sm_2O_3	-	-	-	-	-	-	-	-	-	-	0.51	0.19	-	-	-
Fe_2O_3	1.28	1.36	1.74	1.31	0.99	1.29	1.16	1.01	2.00	4.03	0.59	0.66	1.29	0.93	0.51
Gd_2O_3	-	-	-	-	-	-	-	-	-	-	0.24	0.13	-	-	-
HfO_2	-	-	-	-	-	-	-	-	-	-	0.11	bdl	-	-	-
Ta_2O_5	bdl	bdl	bdl	bdl	bdl	bdl	bdl	bdl	0.07	bdl	0.06	0.11	bdl	0.04	bdl
K_2O	0.04	0.03	0.02	0.00	0.03	0.03	0.02	0.02	0.00	0.02	-	-	bdl	0.01	bdl
Total	98.63	98.74	98.57	99.16	98.25	98.92	99.99	99.65	98.80	97.19	97.53	97.79	88.37	90.05	90.19
$\Sigma LREE_2O_3$	6.04	5.98	3.70	1.93	4.04	5.54	2.04	1.99	0.14	0.15	35.49	34.73	0.59	0.81	1.03
(apfu)	O=3								O=3		Σcations=3		Σcations=3		
Sr	0.005	0.003	0.003	0.003	0.003	0.003	0.003	0.003	0.000	0.000	0.004	0.000	0.000	0.000	0.000
Y	-	-	-	-	-	-	-	-	-	-	0.000	0.000	-	-	-
Zr	0.001	0.002	0.003	0.004	0.001	0.002	0.002	0.003	0.001	0.005	0.018	0.006	0.001	0.001	0.001
Nb	0.006	0.011	0.008	0.006	0.006	0.007	0.005	0.005	0.001	0.000	0.070	0.022	0.012	0.008	0.011
Ca	0.885	0.883	0.938	0.932	0.924	0.894	0.936	0.942	0.985	0.960	0.387	0.417	0.986	0.957	0.926
Th	-	-	-	-	-	-	-	-	-	-	0.004	0.000	-	-	-
Na	0.026	0.026	0.016	0.010	0.022	0.027	0.012	0.010	0.000	0.001	0.000	0.000	0.000	0.000	0.000
Mg	0.002	0.001	0.002	0.003	0.003	0.000	0.002	0.002	0.005	0.003	0.003	0.004	0.016	0.003	0.000
Al	0.009	0.008	0.007	0.008	0.007	0.008	0.006	0.008	0.000	0.000	0.000	0.000	0.000	0.001	0.000
Si	0.000	0.000	0.000	0.001	0.000	0.000	0.000	0.000	0.014	0.014	0.019	0.000	0.002	0.002	0.003
Ba	0.002	0.001	0.000	0.001	0.000	0.001	0.002	0.001	-	-	0.009	0.003	-	-	-
Ti	0.974	0.970	0.960	0.979	0.977	0.974	0.985	0.981	0.960	0.943	1.823	1.908	1.922	1.967	1.990
La	0.008	0.008	0.005	0.004	0.005	0.007	0.005	0.004	0.000	0.000	0.132	0.184	0.000	0.000	0.002
Ce	0.027	0.026	0.015	0.007	0.019	0.025	0.007	0.007	0.000	0.000	0.335	0.320	0.004	0.007	0.009
Nd	0.013	0.013	0.009	0.003	0.010	0.013	0.003	0.003	0.000	0.000	0.123	0.069	0.003	0.003	0.004
Cr	-	-	-	-	-	-	-	-	-	-	0.000	0.002	-	-	-
Pr	0.004	0.004	0.001	0.002	0.001	0.003	0.002	0.001	0.000	0.000	0.036	0.026	0.002	0.001	0.000
Mn	0.000	0.001	0.001	0.000	0.000	0.000	0.000	0.001	0.000	0.000	0.000	0.006	0.004	0.010	0.036
Sm	-	-	-	-	-	-	-	-	-	-	0.009	0.003	-	-	-
Fe	0.023	0.024	0.031	0.023	0.018	0.023	0.020	0.017	0.035	0.071	0.022	0.024	0.040	0.028	0.016
Gd	-	-	-	-	-	-	-	-	-	-	0.004	0.002	-	-	-
Hf	-	-	-	-	-	-	-	-	-	-	0.002	0.000	-	-	-
Ta	0.000	0.000	0.000	0.000	0.000	0.000	0.000	0.000	0.000	0.000	0.001	0.001	0.000	0.000	0.000
K	0.001	0.001	0.001	0.000	0.001	0.001	0.001	0.001	0.000	0.000	-	-	0.000	0.000	0.000
ΣLREE	0.052	0.051	0.031	0.016	0.034	0.047	0.017	0.016	0.001	0.001	0.512	0.533	0.009	0.012	0.015

"bdl": below detection limit; "-": no analyzed

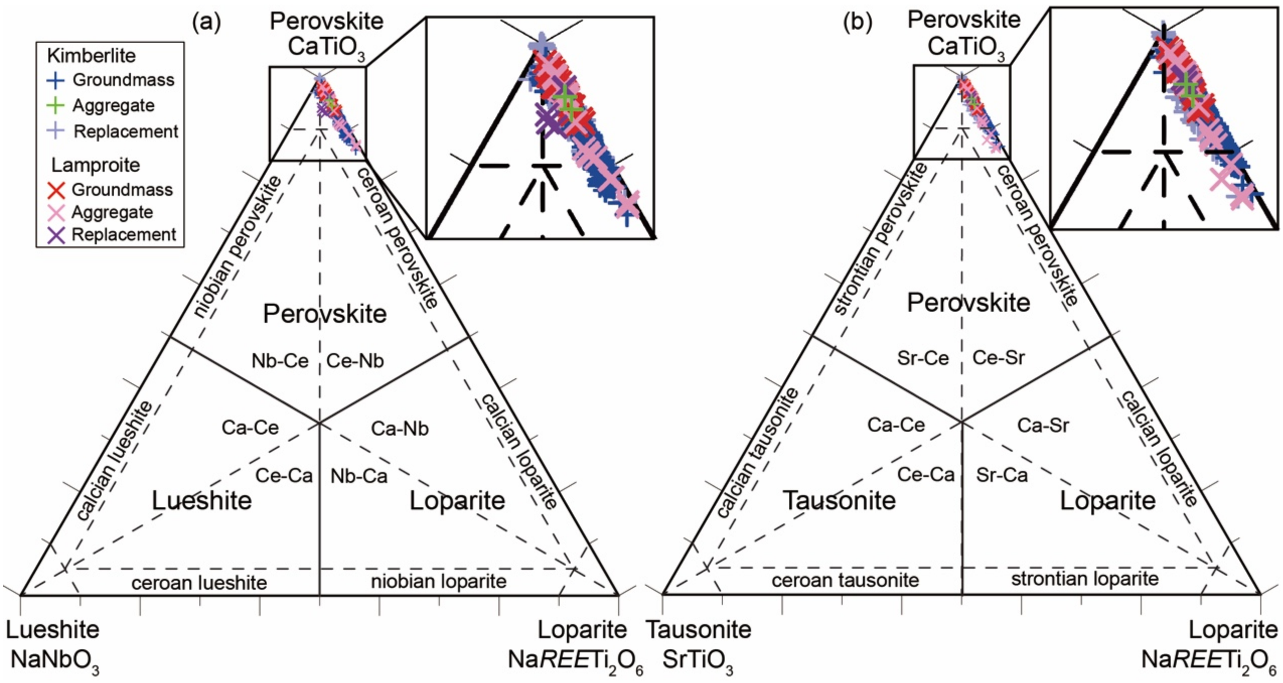

Fig. 8.7. Composition of primary perovskite in the ternary system (a) perovskite – loparite – lueshite ($CaTiO_3$ – $NaREETi_2O_6$ – $NaNbO_3$); (b) perovskite – loparite – tausonite ($CaTiO_3$ – $NaREETi_2O_6$ – $SrTiO_3$). Classification according to Mitchell (2002).

Groundmass crystals and aggregates of perovskite have 0.1-1.0 wt% Na_2O, 0.3-2.1 wt% Nb_2O_5 in kimberlites and 0.1-1.3 wt% Na_2O, 0.3-1.2 wt% Nb_2O_5 in lamproites. Negative correlations are shown in the Na_2O-CaO and Nb_2O_5-CaO diagrams, because there is a coupled substitution of Ca by Na and Ti by Nb, but the Na_2O -Nb_2O_5 relation does not show very clear correlation (Fig. 8.8a-c). Groundmass crystals and aggregates of perovskite have 1.0-2.5 wt% Fe_2O_3 in kimberlites and 0.4-2.3 wt% Fe_2O_3 in lamproites (Fig. 8.8d). Good negative correlation is shown in the $LREE_2O_3$-CaO diagram; groundmass perovskite in kimberlites should have higher LREE contents than those in lamproites (0.9-7.7 wt% $LREE_2O_3$ in kimberlites and 0-2-9 wt% $LREE_2O_3$ in lamproites, Fig. 8.8e). TiO_2 and CaO are slightly positively correlated (Fig. 8.8f).

Groundmass and aggregate perovskite have 0.4-4.0 wt% Ce_2O_3, 0-1.7 wt% La_2O_3, 0-0.5 wt% Pr_2O_3 and 0-1.8 wt% Nd_2O_3 in kimberlite, while 0.4-2.1 wt% Ce_2O_3, 0-0.6 wt% La_2O_3, 0-0.3 wt% Pr_2O_3 and 0-0.8 wt% Nd_2O_3 in lamproite (Fig. 8.9a-d). In general, LREE contents in groundmass perovskite are higher in kimberlites than in lamproites. No correlation is observed between LREE and Nb (Fig. 8.9e). Most perovskite compositions from lamproites plot in the kimberlite and alnoite fields of Mitchell (1995) and part of perovskites show higher Sr content than those from the kimberlite field (Fig. 8.9f). The majority of perovskites have SrO lower than 0.4 wt%, while some perovskites formed during replacement processes in kimberlite and those in groundmass aggregates in lamproite show a Sr enrichment (Fig. 8.9f).

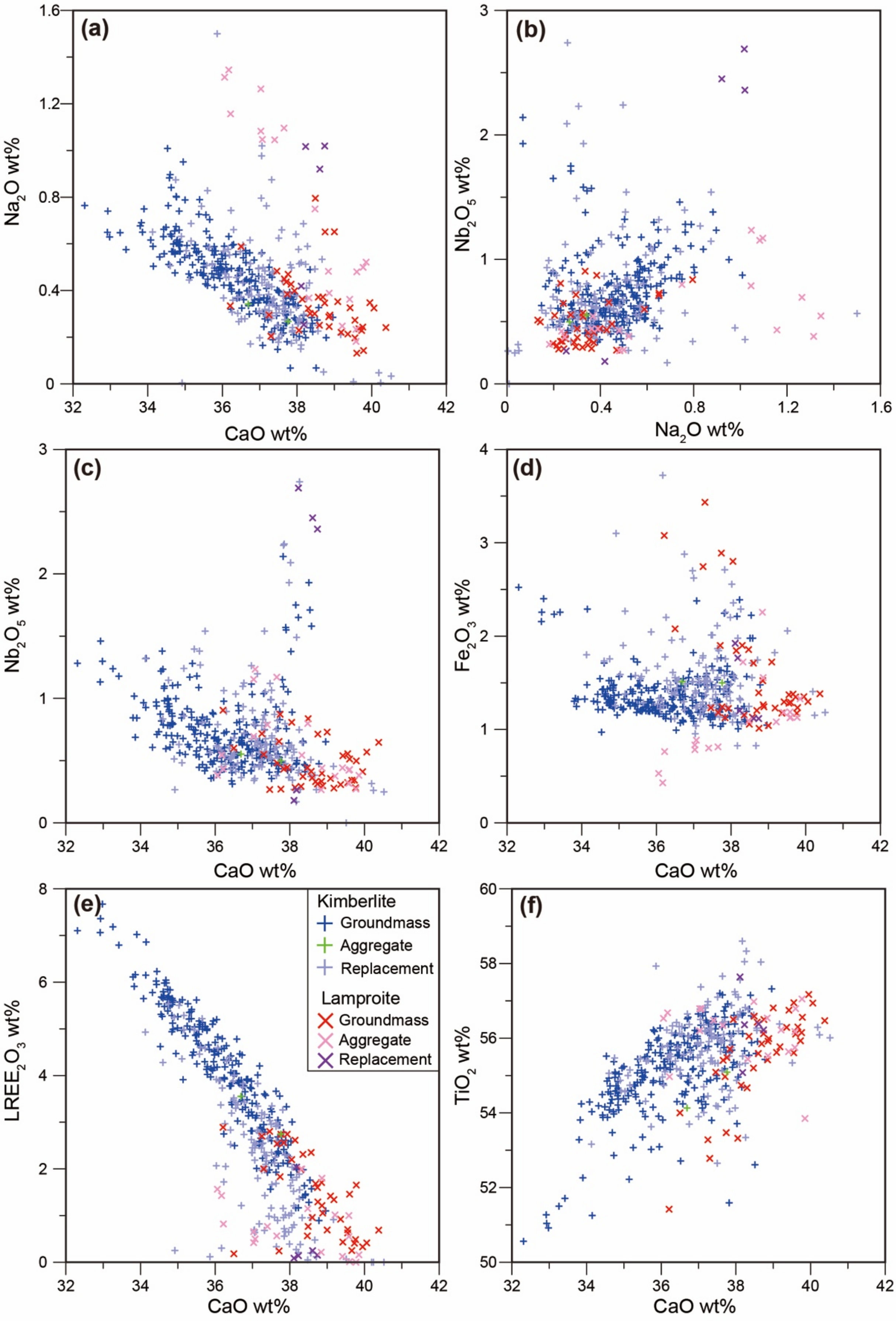

Fig. 8.8. Composition of primary perovskite. (a) CaO vs. Na_2O; (b) Na_2O vs. Nb_2O_5; (c) CaO vs. Nb_2O_5; (d) CaO vs. Fe_2O_3; (e) CaO vs. $LREE_2O_3$; (f) CaO vs. TiO_2, in wt%.

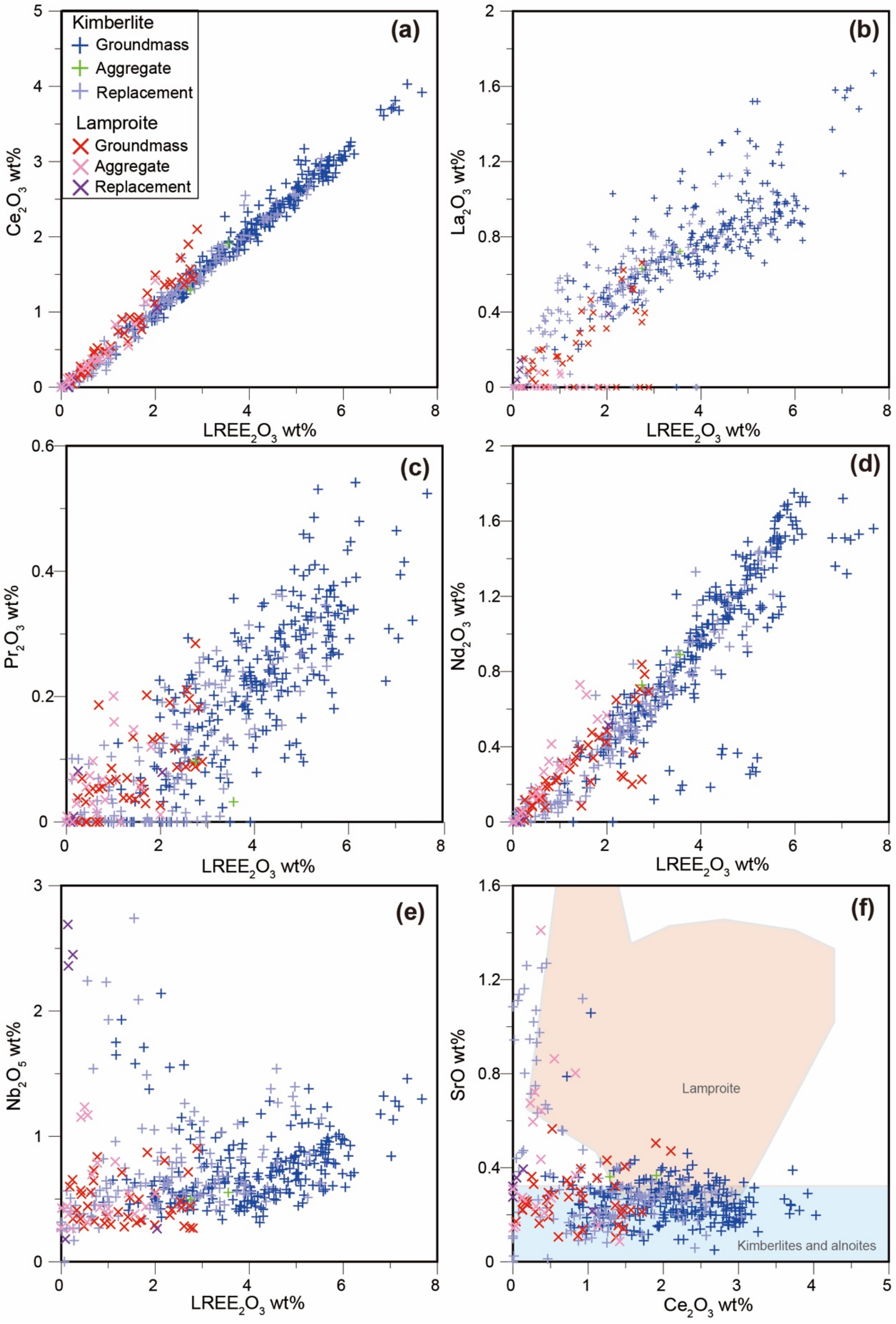

Fig. 8.9. Composition of primary perovskite, in wt%. (a) LREE$_2$O$_3$ vs. Ce$_2$O$_3$; (b) LREE$_2$O$_3$ vs. La$_2$O$_3$; (c) LREE$_2$O$_3$ vs. Pr$_2$O$_3$; (d) LREE$_2$O$_3$ vs. Nd$_2$O$_3$; (e) LREE$_2$O$_3$ vs. Nb$_2$O$_5$; (f) Ce$_2$O$_3$ vs. SrO, kimberlite,alnoite and lamproite fields according to Mitchell (1995).

The representative trace element composition of perovskite is shown in Table 8.3. The average chondrite REE normalized patterns of groundmass perovskite from SK-1 and SK-2 kimberlite and the melt in equilibrium are shown in Fig. 8.10 and 8.11. The chondrite normalized trace element patterns (Fig. 8.10) are similar between different perovskite grains and between SK-1 and SK-2. They show more differences in Th, Ta content between different perovsakite grains (Fig. 8.10). They show slightly higher heavy rare-earth elements (HREE) than perovskite from kimberlites worldwide from Chakhmouradian et al. (2013). The calculated melt in equilibrium for perovskite (Fig. 8.11) is also enriched in HREE than average whole rock kimberlite composition from Chakhmouradian et al. (2013).

Table 8.3. Representative trace element composition of primary perovskite by in situ LA-ICP-MS.

Kimberlite	SK-1				SK-2			
Plot	#8l	#8c	#8g	#8j	#12a	#7f	#10b	#7i
(ppm)								
Na	5101	2317	4407	5460	2533	2175	499	3866
Mg	677	3266	720	1295	22441	9798	25569	80213
K	340	180	294	355	625	348	50	436
Sc	7	10	7	8	10	22	9	17
Ti	329670	321007	332248	334736	339292	337973	329730	329730
V	133	118	137	146	120	224	63	174
Fe	7470	7899	7689	15372	16856	76517	19705	44178
Rb	0	0.6	0.1	0.3	7	3.0	0.3	2.1
Sr	2354	2129	2325	2164	2561	2418	281	2166
Y	481	451.8	417.1	493.3	434	407.1	409.5	439.8
Zr	1416	1675	1204	1564	1269	1322	1641	1042
Nb	6191	4193	5433	6867	3513	2985	6156	4501
Ba	30	48	30	67	79	1164	132	228
La	7968	4657	7618	7932	4479	4296	6803	6556
Ce	24398	11034	25444	24406	10615	8827	19746	19390
Pr	3358	1218	3357	3306	1127	963	2546	2584
Nd	13216	4269	13090	12974	4100	3568	9860	9983
Sm	1752	660.3	1690.3	1718.8	607	547.2	1299.1	1331.0
Eu	370	190.5	354.9	368.3	177	159.2	270.3	294.1
Gd	843	415.6	793.5	855.6	392	357.6	654.2	684.6
Tb	74	42.53	67.87	72.66	40	37.29	58.14	60.68
Dy	273	188.08	246.35	274.71	179	158.73	222.35	228.83
Ho	32	24.98	28.45	32.04	23	21.35	26.83	27.81
Er	54	45.81	47.91	56.23	43	39.56	46.25	47.55
Tm	4	4.42	3.57	4.33	4	3.37	3.62	3.68
Yb	16	19.35	14.94	17.22	18	15.97	16.73	16.10
Lu	1	1.76	1.23	1.52	2	1.43	1.49	1.35
Hf	77	69	65	90	49	48	68	45
Ta	817	98	750	913	119	79	608	488
Pb	754	78	797	937	19	35	102	276
Th	7320	45	8228	8126	40	33	4108	3097
U	242	101	221	265	99	65	250	202

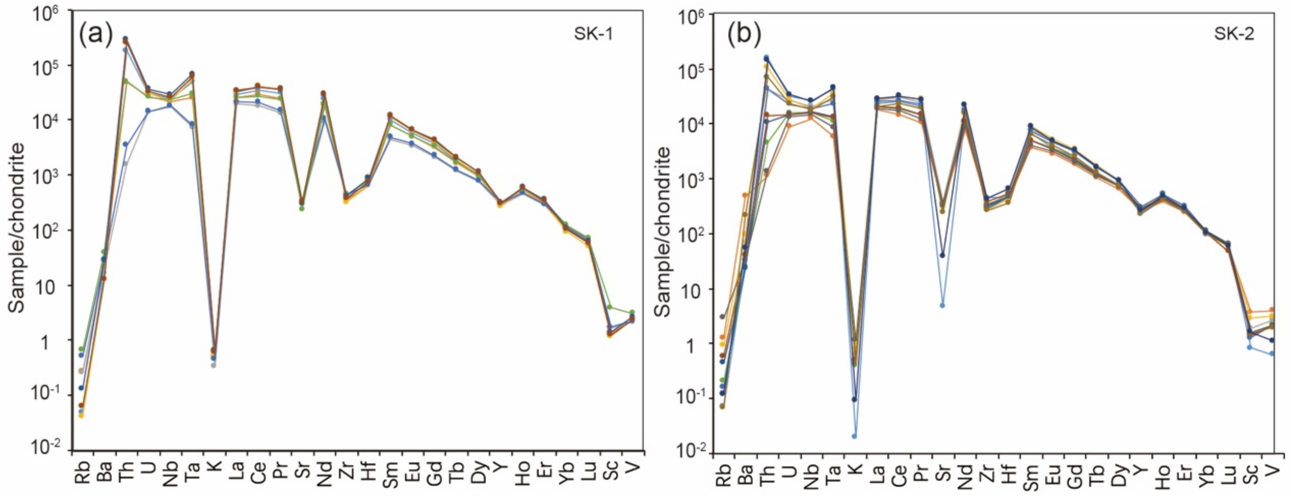

Fig. 8.10. Trace element composition (normalised to chondrite of McDonough and Sun, 1995) of primary perovskite from (a) SK-1 and (b) SK-2 kimberlites, by in situ LA-ICP-MS.

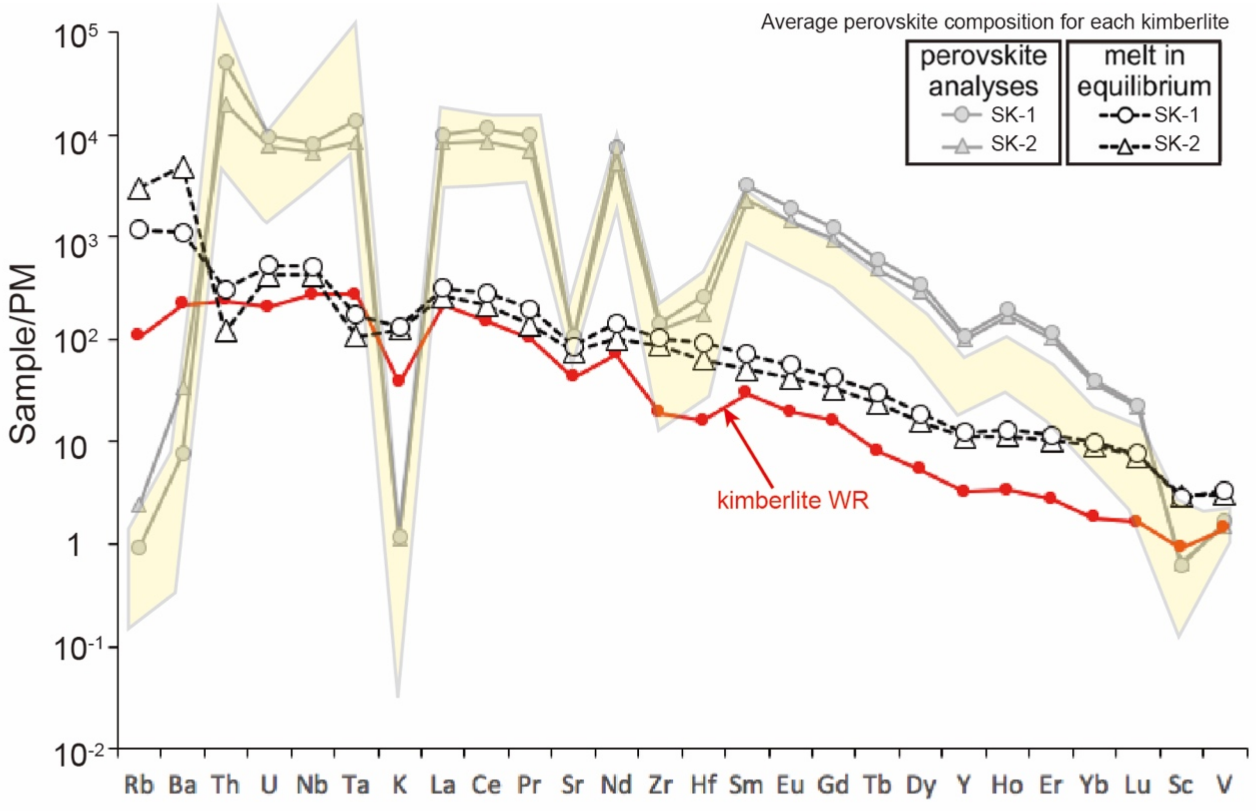

Fig. 8. 11. Composition of average groundmass perovskite from SK-1 and SK-2 kimberlite normalized to the primitive mantle following McDonough and Sun (1995). The melt in equilibrium for perovskite was calculated from the KD published by Chakhmouradian et al. (2013). The ochre field corresponds to data from perovskite from kimberlites worldwide (Chicken Park; Iron Mountain, Udachnaya and Grizzly kimberlites; from Chakhmouradian et al. (2013)). The average whole rock kimberlite (WR) composition has also been taken from Chakhmouradian et al. (2013) calculated from 75 pipes worldwide.

Comparison between primary and secondary perovskite

Comparison between primary and secondary perovskite was carried out in SK-1 and SK-2 kimberlites. Groundmass perovskite from SK-1 has the cores slightly enriched in REE (4.9-8.4 wt% $\sum LREE_2O_3$) and the rims have only 1.9-3.7 wt% $\sum LREE_2O_3$. Groundmass perovskite from SK-2 have 4.0- 5.5 wt% $\sum LREE_2O_3$ in the centers and 0.9-2.6 wt% $\sum LREE_2O_3$ in the borders. Nb is slightly enriched in the cores (0.5-1.1 wt% Nb_2O_5) compared to the rims 0.4-0.6 wt% Nb_2O_5 in the rims in both kimberlites. Groundmass perovskite in SK-1 and SK-2 has similar ΔNNO value (0.73 - 3.40 in SK-1 and 1.07 to 3.82 in SK-2).

Compositional trends of type 1 groundmass perovskite are similar for both kimberlites (Table 8.2., Fig. 8.12). Hence, the cores of the perovskite crystals from SK-1 are slightly enriched in REE (4.9 wt %–8.4 wt % $\sum LREE_2O_3$), whereas their rims have only 1.9 wt %–3.7 wt % $\sum LREE_2O_3$; similarly, perovskite crystals from SK-2 have 4.0 wt %–5.5 wt % $\sum LREE_2O_3$ in the centres and 0.9 wt %–2.6 wt % $\sum LREE_2O_3$ in the borders. Nb is also slightly enriched in the cores compared to the rims (0.6 wt %–1.1 wt % Nb_2O_5 in the cores and 0.4 wt %–0.6 wt % Nb_2O_5 in the rims in SK-1; 0.5 wt %–0.8 wt % Nb_2O_5 in the cores and 0.4 wt %–0.6 wt % Nb_2O_5 in the rims in SK-2). Type 1 perovskite in both kimberlites has Fe_2O_3 contents ranging 1.0 wt %–1.7 wt % (Table 8.2., Fig. 8.12).

Type 2 perovskite from the SK-2 kimberlite has different composition than type 1 perovskite. It is depleted in LREE (<1 wt % $\sum LREE_2O_3$) and Nb (<0.1 wt % Nb_2O_5) but it has higher Fe contents (2.0 wt %–4.0 wt % Fe_2O_3) than type 1 perovskite(Table 8.2., Fig. 8.12).

Frequency histograms of log fO_2 expressed relative to the NNO buffer (ΔNNO) calculated using the perovskite oxybarometer developed by Bellis and Canil (Bellis and Canil, 2007) are shown in Fig. 8.13. Type 1 perovskite in SK-1 and SK-2 has similar ΔNNO values (from −0.73 to −3.40 in SK-1 and from −1.07 to −3.82 in SK-2) but type 2 perovskite has very high ΔNNO values (from 1.03 to 10.52) and was formed in a highly oxidizing environment.

8.2.4. U-Pb dating

We also carried out the U-Pb dating on perovskite from SK-1 and SK-2 kimberlites in order to obtain the syn-eruption age of the kimberlites. Results of the U-Pb analysis are shown in Table 8.4 and Fig. 8.14. Perovskite from SK-1 shows a regression through all points (n=21) yielding an age of 1007±42Ma (95% confidence level; MSWD=51). Perovskite from SK-2 shows a regression through all points (n=18) yielding an age of 927±100Ma (MSWD=45), uncertainty is huge.

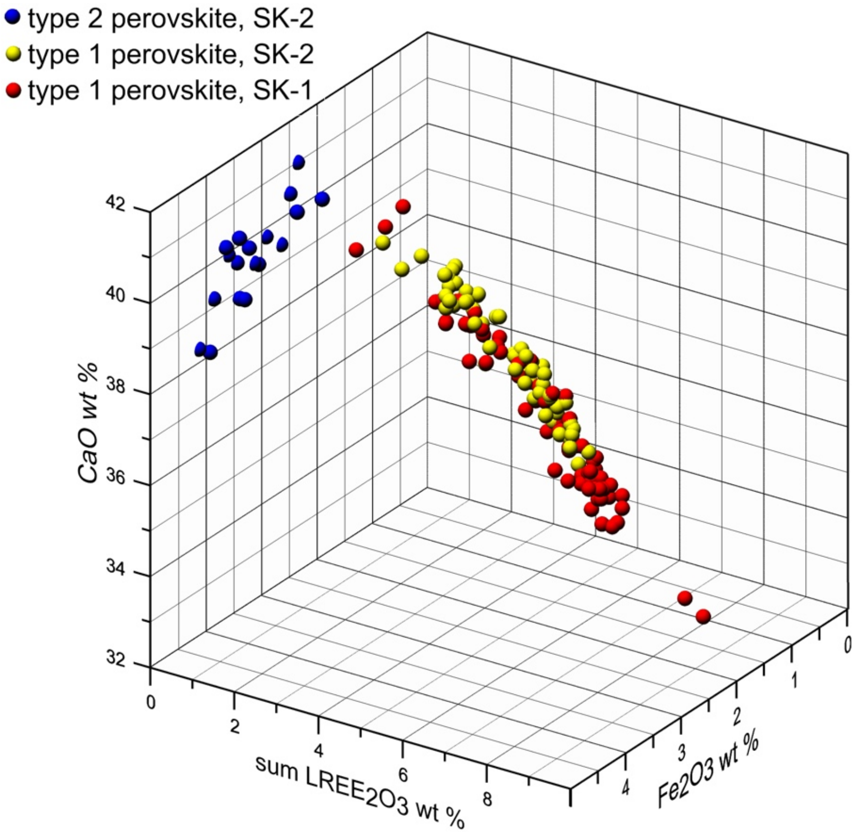

Fig. 8. 12. CaO- Σ LREE$_2$O$_3$-Fe$_2$O$_3$ (wt %) plot of type 1 perovskite from SK-1 and SK-2 and type 2 perovskite from SK-2 kimberlite.

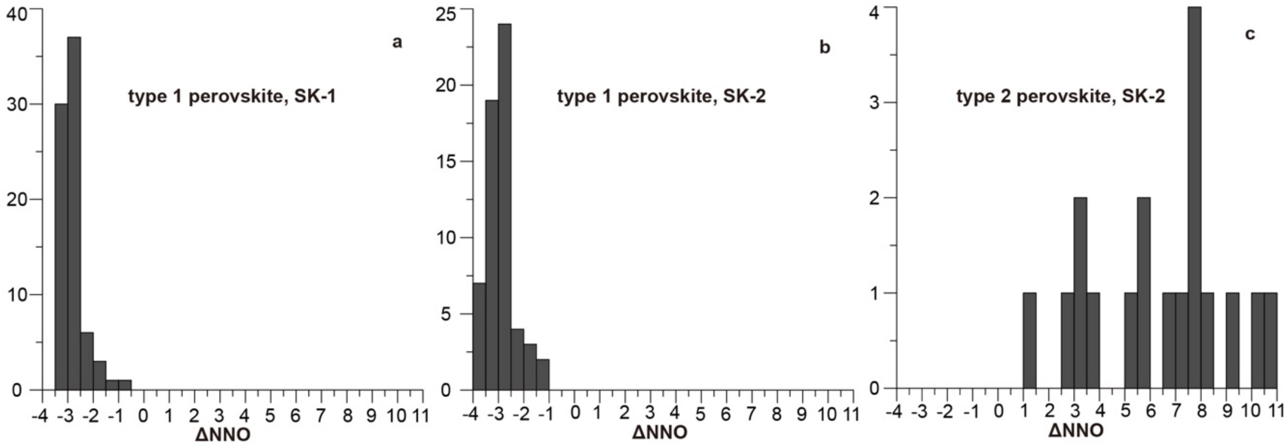

Fig. 8.13. Frequency histograms of log fO$_2$ expressed relative to the NNO buffer (ΔNNO) calculated using the perovskite oxybarometer developed by Bellis and Canil (Bellis and Canil, 2007). (a) type 1 perovskite from SK-1; (b) type 1 perovskite from SK-2; (c) type 2 perovskite from SK-2.

Table 8.4. U–Pb isotopic compositions of LIMA grains analysed in situ by LA-ICP-MS.

Kimberlite	Label	^{207}Pb/^{206}Pb	±2σ	^{207}Pb/^{235}U	±2σ	^{208}Pb/^{238}U	±2σ	^{208}Pb/^{232}Th	±2σ
SK-1	21-1_A_M4	0.3373	0.0054	13.5183	0.0018	0.2905	0.0018	1.5906	0.0490
	21-2_J_P13	0.2899	0.0041	9.9434	0.0018	0.2488	0.0018	0.0783	0.0021
	21-2_k_P14	0.2098	0.0021	6.2953	0.0012	0.2176	0.0012	0.0623	0.0011
	21-2_L_P15	0.2183	0.0024	6.5933	0.0013	0.2191	0.0013	0.0643	0.0013
	21-2_M_P16	0.2260	0.0026	6.9310	0.0014	0.2224	0.0014	0.0666	0.0014
	21-2_N_P17	0.1739	0.0020	4.8765	0.0013	0.2034	0.0013	0.0606	0.0012
	21-5d_p	0.1578	0.0014	4.1918	0.0009	0.1927	0.0009	0.0508	0.0008
	21-5e_p	0.2391	0.0027	6.8879	0.0013	0.2089	0.0013	0.0789	0.0017
	21-5f_p	0.2415	0.0017	7.2095	0.0009	0.2166	0.0009	0.0524	0.0005
	21-5G_p	0.2528	0.0020	8.2499	0.0011	0.2369	0.0011	0.0473	0.0005
	21-5h_p	0.1903	0.0016	5.1330	0.0009	0.1958	0.0009	0.0464	0.0006
	21-5i_p	0.2948	0.0028	9.8158	0.0012	0.2416	0.0012	0.0571	0.0010
	21-5j_p	0.2916	0.0026	9.4421	0.0012	0.2349	0.0012	0.0517	0.0009
	21-5k_p	0.3415	0.0023	12.6994	0.0011	0.2698	0.0011	1.1900	0.0129
	21-a_P1	0.1984	0.0031	5.5687	0.0013	0.2034	0.0013	0.0657	0.0016
	8021-2_C_P7	0.3091	0.0038	10.9411	0.0017	0.2567	0.0017	0.0689	0.0016
	8021-2_E_P8	0.1807	0.0025	5.3412	0.0015	0.2144	0.0015	0.0660	0.0017
	8021-2_F_P9	0.1634	0.0022	4.6431	0.0014	0.2061	0.0014	0.0584	0.0014
	8021-2_G_P10	0.3090	0.0044	11.4426	0.0019	0.2686	0.0019	0.0635	0.0018
	8021-2_H_P11	0.3154	0.0066	10.8541	0.0024	0.2496	0.0024	0.1047	0.0044
	8021-2_I_P12	0.3542	0.0056	15.2237	0.0024	0.3118	0.0024	0.0793	0.0025
SK-2	44-12_A_2_P	0.2265	0.0046	6.1154	0.0020	0.1963	0.0020	0.0930	0.0033
	44-12_A_3_P	0.2501	0.0043	7.3038	0.0019	0.2122	0.0019	0.1250	0.0038
	44-12_C_1_P	0.3019	0.0035	11.2777	0.0018	0.2710	0.0018	0.0687	0.0014
	44-12_E_4_P	0.3575	0.0038	13.1014	0.0017	0.2659	0.0017	0.9514	0.0184
	44-12_F_5_P	0.2054	0.0034	6.0359	0.0018	0.2132	0.0018	0.0717	0.0022
	44-2_H_6_P	0.2008	0.0034	5.5688	0.0016	0.2012	0.0016	0.0540	0.0017
	44-2_H_7_P	0.1901	0.0034	4.8707	0.0016	0.1859	0.0016	0.0563	0.0020
	44-5_b_2_P	0.1803	0.0026	4.5543	0.0013	0.1837	0.0013	0.0591	0.0016
	44-5_b_3_P	0.2085	0.0017	5.9621	0.0009	0.2075	0.0009	0.0642	0.0009
	44-5_c_4_P	0.2371	0.0038	6.0336	0.0015	0.1850	0.0015	0.1156	0.0035
	44-5_c_5_P	0.2834	0.0057	7.9523	0.0021	0.2042	0.0021	0.1650	0.0066
	44-5_c_6_P	0.3247	0.0051	9.7885	0.0019	0.2192	0.0019	0.4059	0.0126
	44-5_d_7_P	0.2033	0.0019	5.6718	0.0010	0.2025	0.0010	0.0692	0.0012
	44-5_d_9_P	0.2439	0.0028	6.6672	0.0012	0.1983	0.0012	0.0571	0.0013
	8044-7_f_P1	0.2590	0.0049	7.7866	0.0023	0.2180	0.0023	0.3963	0.0126
	8044-7_G_P2	0.3064	0.0052	10.6912	0.0024	0.2531	0.0024	1.9096	0.0632
	8044-7_H_P3	0.1703	0.0022	4.8627	0.0014	0.2071	0.0014	0.0618	0.0014
	8044-7_I_P4	0.1951	0.0025	5.6023	0.0014	0.2083	0.0014	0.0661	0.0014
	8044-7_J_P5	0.1868	0.0037	5.2212	0.0019	0.2027	0.0019	0.1298	0.0046
	8044-7_K_P6	0.1723	0.0020	4.7702	0.0013	0.2009	0.0013	0.0677	0.0013

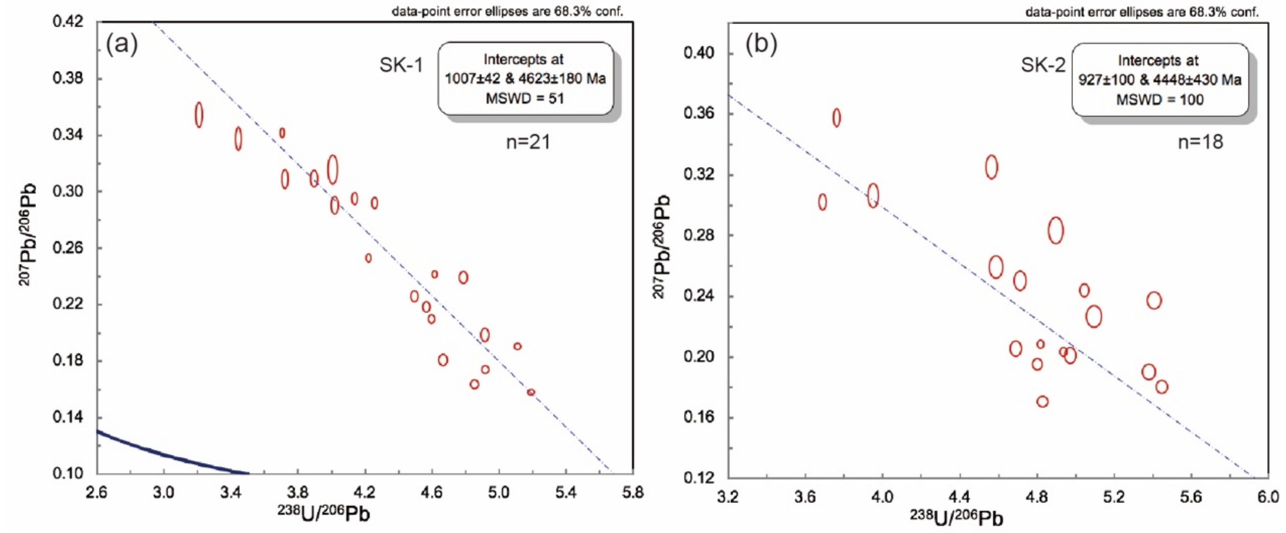

Fig. 8.14. ^{207}Pb/^{206}Pb vs 2^{38}U/^{206}Pb Concordia diagrams for in-situ LA-ICP-MS analyses of perovskite grains from. (a) SK-1 kimberlite n=21; (b) SK-2 kimberlite, n=18 rejecting the more outlying grains. Errors are shown as ellipses at 1σ.

8.3. ALTERATION PRODUCTS OF PEROVSKITE

8.3.1. Textural patterns

We describe the different alteration styles of groundmass perovskite and spinel from SK-1 and SK-2 kimberlites (Eastern Dharwar craton, India).

Groundmass perovskite (type 1 perovskite) from SK-1 is euhedral, zoned and slightly replaced by anatase following grain borders and small cracks (Fig. 8.15a).

Groundmass perovskite (type 1 perovskite) from SK-2 is euhedral to subhedral and it has oscillatory zoning. This perovskite is partially or nearly totally replaced by kassite [$CaTi_2O_4(OH)_2$] accompanied by abundant aeschynite-(Ce), ideally [$(Ce,Ca,Fe,Th)(Ti,Nb)_2(O,OH)_6$] (Fig. 8.15b-d). The ensemble may also be replaced by Mn-rich ilmenite along small cracks (Fig. 8.15d).

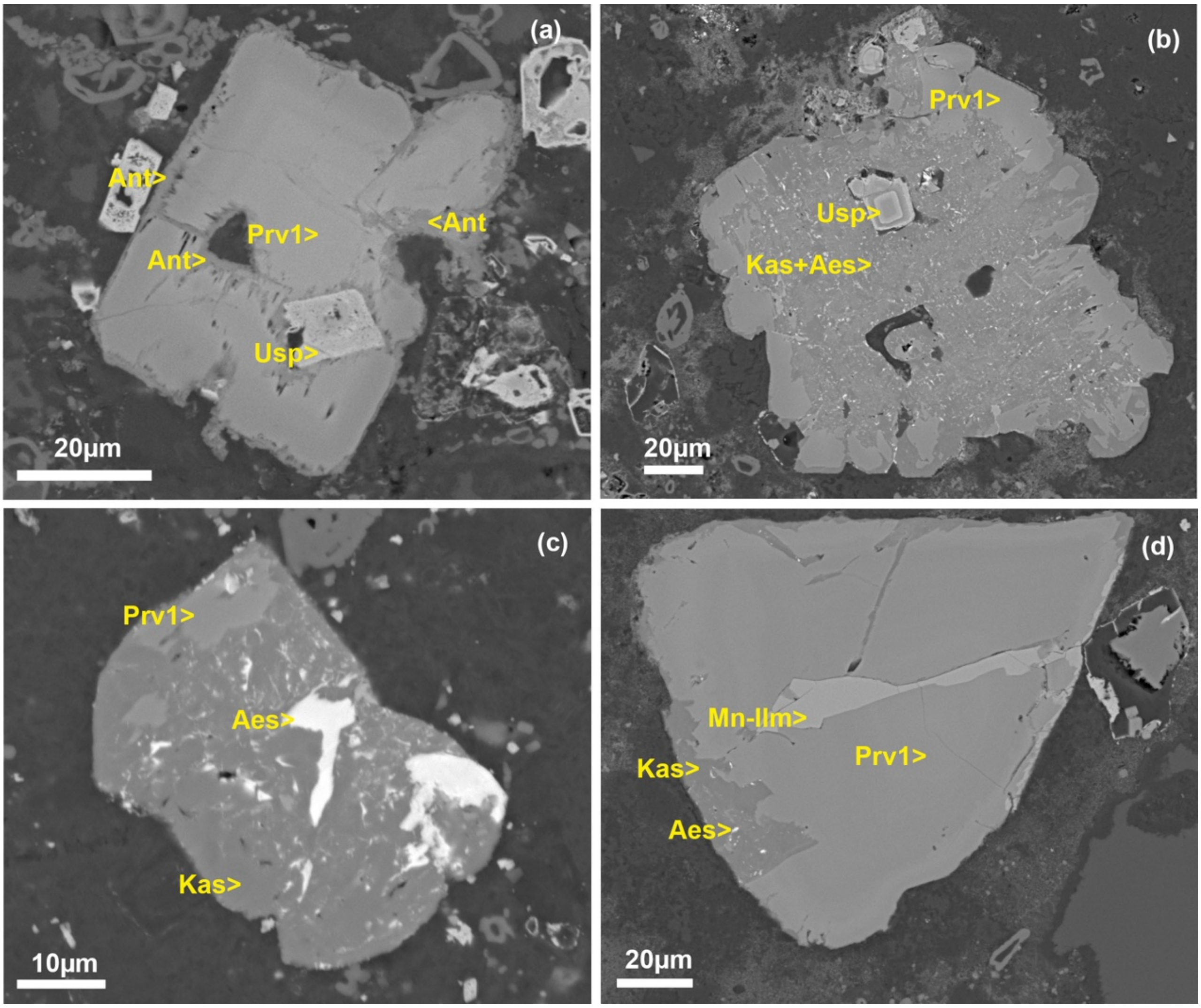

Fig. 8.15. Representative SEM (BSE) images of the groundmass from SK-1 and SK-2 kimberlites. (a) Type 1 perovskite (Prv1) with an ulvöspinel inclusion (Usp) from SK-1 kimberlites being replaced by anatase (Ant) along borders and fractures. (b) Type 1 groundmass perovskite from SK-2 kimberlite, replaced by kassite (Kas) with aeschynite (Aes); (c) Type 1 groundmass perovskite from SK-2, replaced by kassite with aeschynite; (d) Type 1 perovskite from SK-2, altered to kassite and aeschynite (Kas + Aes) in grain borders; the ensemble is replaced by Mn-rich ilmenite (Mn-ilm) along fractures and grain borders.

8.3.2. MicroRaman Study

Identity of anatase was confirmed by microRaman spectroscopy and its spectrum was compared with that of submicroscopic anatase, mixed with calcite, altering perovskite in carbonatites (Pereira et al., 2005; Martins et al., 2014) (Fig. 8.16a). Calcite has a peak at 1088 cm^{-1} which corresponds to the vibration of the CO_3 group (Martins et al., 2014). However, calcite is absent from the products of alteration of the perovskite from Siddanpalli.

Kassite [$CaTi_2O_4(OH)_2$] has a very similar chemical composition to cafetite ($CaTi_2O_5 \cdot H_2O$). The identification of kassite from the SK-2 kimberlite was confirmed by comparing the kassite Raman spectrum with the available spectrum of kassite standards (Martins et al., 2014; Fig. 8.16b).

Finally, the Raman analysis was helpful to establish the identity of aeschynite-(Ce). In this case, most of the bands have similarities with those from the published standards of members of the aeschynite group. Minor differences in the positions of the bands can be explained because the studied aeschynite is Ta-poor and La- and Nd-rich when compared with the standard aeschynites (Paschoal et al., 2003; Tomašić et al., 2004).

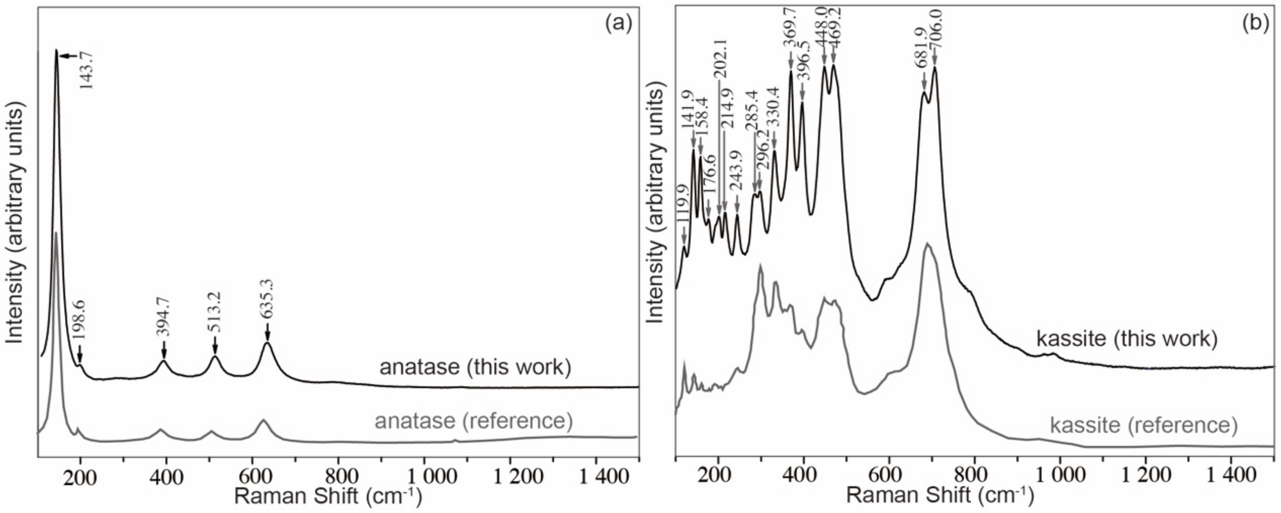

Fig. 8. 16. Representative Raman spectrum analysed in: (a) anatase from SK-1 kimberlite (this work) compared with anatase reference standard from Martins et al. (2014), the last presents a peak at 1088 cm−1 which corresponds to calcite; (b) kassite from SK-2 kimberlite (this work) compared with kassite reference standard adapted from Martins et al. (2014).

8.3.3. Chemical composition

Kassite replacing type 1 perovskite in SK-2 has a stoichiometric composition (Table 8.2), whereas the associated aeschynite-(Ce) tends to concentrate LREE and, to a lesser extent, Nb. The aeschynite-(Ce) produces the next average structural formula: $(Ca_{0.39}Ce_{0.33}La_{0.13}Nd_{0.12}Pr0_{.04})_{\sum 1.01}(Ti_{1.8}2Nb_{0.07}Fe^{3+}_{0.02}Zr_{0.02})_{\sum 1.93}(O,OH)_6$ (Table 8.2). Y, Er, Dy and Pb contents in aeschynite-(Ce) have been analysed but they are below detection limit. Therefore, the aeschynite-group minerals from SK-2 kimberlite are poor in Nb, U and Th when compared to similar minerals typically occurring as metamictic phases in carbonatites (Nasir et al., 2009) and metasomatised rocks (Macdonald et al., 2015). However, their compositions are similar to those of the late Ti-REE minerals described in the Iron Mountain kimberlite field (Mitchell and Chakhmouradian, 1998).

8.4. DISCUSSION

8.4.1. Primary perovskite

Groundmass perovskite crystallizes directly from the kimberlite magma (Mitchell, 1986). The crystallization of magmatic perovskite is produced later than that of macrocrystal spinel; and simultaneously with “reaction” Fe-rich spinel and groundmass spinels of the magnesian ulvöspinel-magnetite series in kimberlite (Chakhmouradian and Mitchell, 2000). As it is a main carrier of U and Th, this mineral has turn out to be very useful to date both kimberlite and carbonatite eruptions (Cox and Wilton, 2006; Batumike *et al.*, 2008; Simonetti *et al.*, 2008). Additionally, Sr and Nd isotopes can be useful to assess the origin of the magma which has led to the crystallization of the perovskite (Donnelly, 2012).

Perovskite is a principal host of LREE in SiO_2-undersaturated ultramafic and alkaline rocks (Mitchell, 2002) and is a mineral that may be produced along different crystallization stages of these magmas. Therefore, the chemical and textural study of these generations can provide information about several stages of magmatic crystallization (Chakhmouradian and Mitchell, 2001; Chalapathi Rao et al., 2011). The crystallization of magmatic perovskite is produced later than that of macrocrystal spinel; and simultaneously with “reaction” Fe-rich spinel and groundmass spinels of the magnesian ulvöspinel—magnetite series in kimberlite (Chakhmouradian and Mitchell, 2000).

There are published emplacement ages of Siddanapalli kimberlites, but all of them are about SK-1, indicating that the emplacement took place during the Mesoproterozoic and close to 1.1 Ga. Kumar *et al.* (2007) determined that the age of emplacement was 1093±4 Ma by using Rb-Sr on phlogopite; Gopalan and Kumar (2008) obtained an age of 1063±41 using K-Ca of phlogopite while Chalapathi Rao *et al.* (2013) give the age in 1093 ±18 Ma using U-Pb of perovskite. The 1007±42Ma on groundmass perovskite from SK-1 kimberlite from this work is coherent with the age from these previous works.

8.4.2. Primary and secondary perovskite

However, perovskite cannot be formed only by magmatic processes. A metasomatic origin has been inferred for perovskite from carbonatites (Kukharenko et al., 1965; Lepekhina et al., 2009) and perovskite from skarns is also widely described as a hydrothermal product (Mitchell, 2002).

Two types of perovskite occur in the SK-1 and SK-2 Indian kimberlites. The first type crystallized directly from the kimberlite magma, whereas a hydrothermal origin was inferred from the second. Additionally, two different replacement trends of groundmass perovskite have been identified. Type 1 groundmass perovskite is replaced by anatase in SK-1 and by kassite along with aeschynite-(Ce) in SK-2. The different sequences are related to alteration under different $f(CO_2)$ and $f(H_2O)$ conditions. In some cases, perovskite may be strongly altered to secondary minerals, resulting in a redistribution of REE and, potentially, U, Pb and Th. Therefore, U-Pb dating studies involving perovskite require a detailed petrographic characterisation to confirm its primary (i.e. magmatic) origin.

Perovskite is a valuable mineral recorder of the crystallization conditions of the kimberlites. It commonly crystallizes directly from the kimberlite magma (Mitchell, 1986). Therefore, pristine primary perovskite grains in both kimberlites and carbonatites are often used for geochemical investigations and, in particular for U-Pb dating (Mitchell and Chakhmouradian, 1998; Chakhmouradian and Mitchell, 2000, 2001; Heaman and Kjarsgaard, 2000; Heaman *et al.*, 2004; Cox and Wilton, 2006; Paton *et al.*, 2007; Batumike *et al.*, 2008; Simonetti *et al.*, 2008; Woodhead *et al.*, 2009; Zurevinski *et al.*, 2011; Chalapathi Rao *et al.*, 2013; Castillo-Oliver *et al.*, 2016). However, it has been proved that different perovskite generations can occur in the same kimberlite. Simultaneous occurrence of two populations of primary perovskite has been explained by magma mingling (Castillo-Oliver et al., 2016). In addition, primary magmatic perovskite can be altered (Mitchell and Chakhmouradian, 1998; Chakhmouradian and Mitchell, 2000) during subsolidus processes to secondary minerals that may redistribute REE and potentially, U, Pb and Th (Yang et al., 2009). Our petrographic data shows that two types of texturally fresh (i.e. pristine) perovskite occur in the studied Indian kimberlites. Groundmass type 1 crystals may be interpreted as primary magmatic perovskite. However, type 2 perovskite occurs along with calcite and serpentine filling porosity produced by replacement of Ti-rich spinels. This assemblage suggests that type 2 perovskite could be produced by subsolidus hydrothermal phenomena and thus not necessarily related to the primary perovskite. Similar pristine secondary hydrothermal perovskites have been described in carbonatites and cannot be used to obtain the age of the intrusive (Lepekhina et al., 2009). Therefore, our observations further restrict the use of groundmass perovskite for geochronological purposes, since they show for the first time that pristine perovskite can be also formed in kimberlites by hydrothermal processes. Therefore, an accurate petrographic study is necessary to exclude perovskite affected by subsolidus processes. Hence, we suggest taking additional cautions when using perovskite grains in concentrates.

8.4.3. Alteration of perovskite

The alteration of perovskite is strongly dependent upon pH, f (CO_2) and temperature. It is expected to occur in late-stage hydrothermal alteration processes and in the subaerial weathering environment (Mitchell, 2002). The replacement of perovskite occurs at the late stage of groundmass formation, resulting from a decrease in f (O_2) and temperature (<350 °C) at low pressure ($P < 2$ kbars) and over a wide range of a(Mg^{2+}) values (Chakhmouradian and Mitchell, 2000). The replacement of olivine by serpentine as well as the replacements of perovskite and spinel suggest that P (CO_2) and P (H_2O) remained relatively high (Mitchell and Chakhmouradian, 1998).

The two Indian kimberlites studied here have significant differences regarding their subsolidus history, mainly represented by the higher complexity of perovskite alteration in SK-2. The alteration process took place under different fluid/rock ratios in each kimberlite, in a relatively closed system. Under these conditions, Ti-rich minerals are unstable and, in particular, Ti-rich spinels are easily replaced in both kimberlites by mixtures of Ti-rich hydrogarnets, calcite and serpentine. A relatively low SiO_2 and high-water activities were necessary to avoid the crystallization of titanite and to favour the crystallization of hydrogarnets. Slight replacement of perovskite by anatase in SK-1 could be indicative of a decrease of temperature under conditions of medium to high *f* (CO_2), following the thermodynamic calculations data (Martins et al., 2014). However, the same experimental data suggest that the strong replacement of perovskite by kassite in SK-2 needs a high *f (*H_2O) and a low activity in alkalis. The formation of kassite or anatase during perovskite replacement may also involve different rates of Ca-leaching, as kassite formation is favoured by lower Ca-leaching (Mitchell and Chakhmouradian, 1998). The LREE-rich perovskite is more unstable during these processes than pure end-member perovskite. Therefore, aeschynite-(Ce) inherits the composition of the replaced LREE-bearing perovskite cores and it is Nb-poor because the cores were also Nb-poor. Aeschynite-(Ce) could also concentrate U, and the randomly distribution of this mineral in the replacement products coupled with the possible zoning in these crystals could be responsible of errors when determining ages in altered perovskites, as are those of SK2.

Perovskite may be unstable in CO_2-rich fluid environments characteristic of the final stage of some carbonatites and kimberlites worldwide (Mitchell and Chakhmouradian, 1998; Chakhmouradian and Mitchell, 2000; Pereira et al., 2005). Products of perovskite replacement in kimberlites may include kassite, anatase and titanite along with calcite, ilmenite and unidentified LREE-Ti oxides (Mitchell and Chakhmouradian, 1998; Martins et al., 2014). Similarly, carbonatitic perovskite is replaced by anatase with calcite and finally by ilmenite and ancylite (Mitchell and Chakhmouradian, 1998). In consequence, only pristine unaltered perovskite has been used to establish U-Pb age (Heaman and Kjarsgaard, 2000; Heaman et al., 2004; Chalapathi Rao et al., 2013) and Sr-Nd-Pb isotopic composition (Paton et al., 2007; Woodhead et al., 2009; Zurevinski et al., 2011) from different worldwide kimberlites.

Ti-rich minerals can supply information of petrological or economic interest. However, these minerals can be easily altered by subsolidus processes. In addition, the hydrothermal occurrences of these minerals in other geological environments suggest that these minerals can be produced by the reaction of the existing magmatic minerals with late hydrothermal or supergene fluids.

CHAPTER 9

CRICHTONITE GROUP (LIMA)

9. CRICHTONITE GROUP (LIMA)

9.1. INTRODUCTION

“LIMA” is an acronym used for members of the series lindsleyite-mathiasite [(Ba,Sr)(Zr,Ca)(Fe,Mg)$_2$(Ti,Cr,Fe)$_{18}$O$_{38}$ - (K,Ba,Sr)(Zr,Fe)(Mg,Fe)$_2$(Ti,Cr,Fe)$_{18}$O$_{38}$)] found as mantle metasomatic products in xenoliths in kimberlite. However, these minerals should be properly named as members of the crichtonite group.

The crichtonite group of minerals contains several series of isostructural end-members, all of them characterized by crystallizing in the trigonal system (with space group R3, Z = 3 and an unit-cell of *a*hex ~ 10.4 Å and *c*hex ~20.9 Å) and a common structural formula: $^{XII}A^{VI}B^{VI}C_{18}{}^{1V}T_2(W)_{38}$ (Armbruster and Kunz, 1990; Orlandi *et al.*, 1997), where dominant cations are: ^{XII}A = Ba, K, Pb, Sr, La, Ce, Na, Ca; ^{VI}B = Mn, Y, U, Fe, Zr, Sc; $^{VI}C_{18}$ = Ti, Fe, Cr, Nb, V, Mn, Al; $^{IV}T_2$ = Fe, Mg, Zn; W = O, (OH); ions known to dominate in natural samples are marked in bold.

Solid solutions are widespread and complete among the end-members of the crichtonite group; therefore, in spite the group has not a large number of mineral species known until the present, there is a large diversity of possible compositions in this group. However, only Ti, Fe and O are systematically present. Ti (^{VI}C) accounts for 10 to 16 apfu in most of the published compositions of members of the crichtonite group. The nomenclature of the group is based upon the combination of dominant cations in the sites ^{XII}A and ^{VI}B (Orlandi *et al.*, 1997). However, since Ti use to be the dominant cation in B, they are named in most of the cases according to the cation filling the A position: lindsleyite for Ba, mathiasite for K, crichtonite for Sr, loveringite for Ca, landauite for Na, senaite for Pb and davidite for U-REE. In spite the widespread use made for the acronym LIMA, we prefer use in this work the term “crichtonite-group minerals”, because many of the observed compositions in these minerals do not fit in the lindsleyite-mathiasite series. In fact, the plotted compositions of many “LIMA” do not have K or Ba as dominant cations, and therefore cannot be named as lindsleyite-mathiasite. Therefore, abuse of the term LIMA can be confused and creates an excessive simplification with a serious loss of valuable chemical information. Hence, we reserve the name “LIMA” to any member of the lindsleyite-mathiasite series, although we prefer the name “crichtonite-group minerals”.

“LIMA” minerals s.s. are usually found in xenolithic associations and are thought as being formed through metasomatism of upper mantle (Giuliani et al., 2014). These minerals have been studied in several localities. The majority of the studied LIMA minerals come from the kimberlites from South Africa (Jaersfontein, Kolonkwanen and Bultfontein), and were mainly found in their metasomatized peridotite xenoliths (Jones *et al.*, 1982; Haggerty, 1983; Konzett *et al.*, 2013; Giuliani *et al.*, 2014, 2018) or in heavy mineral concentrates (Haggerty *et al.*, 1983; Griffin *et al.*, 2014). There are few works on LIMA in other localities; Almeida *et al.* (2014) studied LIMA minerals from the peridotite xenoliths in the Alto Paranaíba Igneous Province in Brazil. There are also several studies about LIMA in kimberlites from Shandong in China (Liu *et al.*, 1990; Lu and Zhou, 1994; Lu *et al.*, 1996, 1998; Zhou *et al.*, 1996). LIMA minerals were also found as inclusions in diamonds in Yakutia in Russia (Sobolev *et al.*, 1997) and in Namibia (Leost *et al.*, 2003).

9.2. TEXTURAL PATTERNS

Crichtonite-group minerals were found in a few cases, only in some of the studied kimberlites in the next types of textural associations: A) in metasomatized mantle xenoliths or B) xenocrysts. Crichtonite-group minerals were found only in four occurrences in this work: in xenoliths in the Dutoit-Span kimberlite in South Africa and xenocrysts in the SK-1, SK-2 Siddanpalli kimberlites and in the KL-4 Kalyandurg kimberlite in India.

Crichtonite-group-bearing xenolith found in the Dutoit-Span kimberlite is consisf of basically by phlogopite and LIMA (anhedral crystals having around 3mm in diameter; Fig. 9.1a). However, LIMA minerals are replaced by another Ca-richer crichtonite group minerals (Fig. 9.1b) which is probably loveringite (no EMPA analysis are available yet), and then by geikielite. Diopside and apatite associations occur between phlogopite and ilmenite, probably in association with the crichtonite-group minerals (Fig. 9.1b).

Ilmenite is replaced, in some cases, by mineral associations of perovskite, ulvöspinel and Zr-Ca-Ti oxide (Fig. 9.1b, c)

The LIMA xenocrysts have an anhedral appearance and dimensions averaging 0.1 to 2mm (Fig. 9.1d). The mathiasite grains shows a reaction rim, being replaced by a first rim of geikielite followed by another rim of ulvöspinel that covers and replaces the rim of geikielite; finally, a part of the ulvöspinel rim is also mantled by subhedral perovskite (Fig. 9.1e). The contacts between mathiasite and geikielite show a fibrous texture (¨brush texture¨) which consists probably of fine bands of mathiasite and geikielite (Fig. 9.1f).

9.3. CHEMICAL COMPOSITIONS

Chemical composition of crichtonite-group minerals was analysed by EMP in the SK-1, SK-2 and KL-4 kimberlites. Representative compositions of mathiasite from SK-1 and SK-2 and crichtonite s.s. from KL-4 are presented in Table 9.1. Unfortunately, there are not quantitative chemical data from the Ca-rich member yet.

The analyzed mathiasite grains show little variation in major-element composition between the SK-1 and SK-2 kimberlite, compositions are also similar in the same kimberlite body. All of the analyzed LIMA minerals from the SK-1 and SK-2 kimberlites have their A position dominated by K over Ba and Ca, indicating that these crichtonite group minerals are dominated by the mathiasite end-member. Individual grains of mathiasite are compositionally homogeneous. Mathiasite grains from SK-1 and SK-2 also show similar compositions (Fig 9.2). The average formula of mathisite from SK-1 is the next:

$$(K_{0.431}Ca_{0.265}Ba_{0.131}Sr_{0.117}Ce_{0.065}La_{0.016})_{1.024}(Zr_{0.751}Fe_{0,229}Mn_{0.020})_{1.000}(Mg_{1.485}Fe_{0,509}Zn_{0.006})_{2.000}(Ti_{13.292}Cr_{3.270}Fe_{1.267}V_{0.151}Nb_{0.105}Al_{0.087}Ni_{0.056}Si_{0.004}Ta_{0.004})_{18,232}O_{38},$$

and that from SK-2 is as follows:

$$(K_{0.442}Ca_{0.256}Ba_{0.131}Sr_{0.115}Ce_{0.062}La_{0.015})_{1.020}(Zr_{0.749}Fe_{0.234}Mn_{0.017})_{1.000}(Mg_{1.482}Fe_{0.512}Zn_{0.006})_{2.000}(Ti_{13.320}Cr_{3.195}Fe_{1.335}V_{0.153}Nb_{0.113}Al_{0.073}Ni_{0.005}Si_{0.004}Ta_{0.005})_{18.202}O_{38}.$$

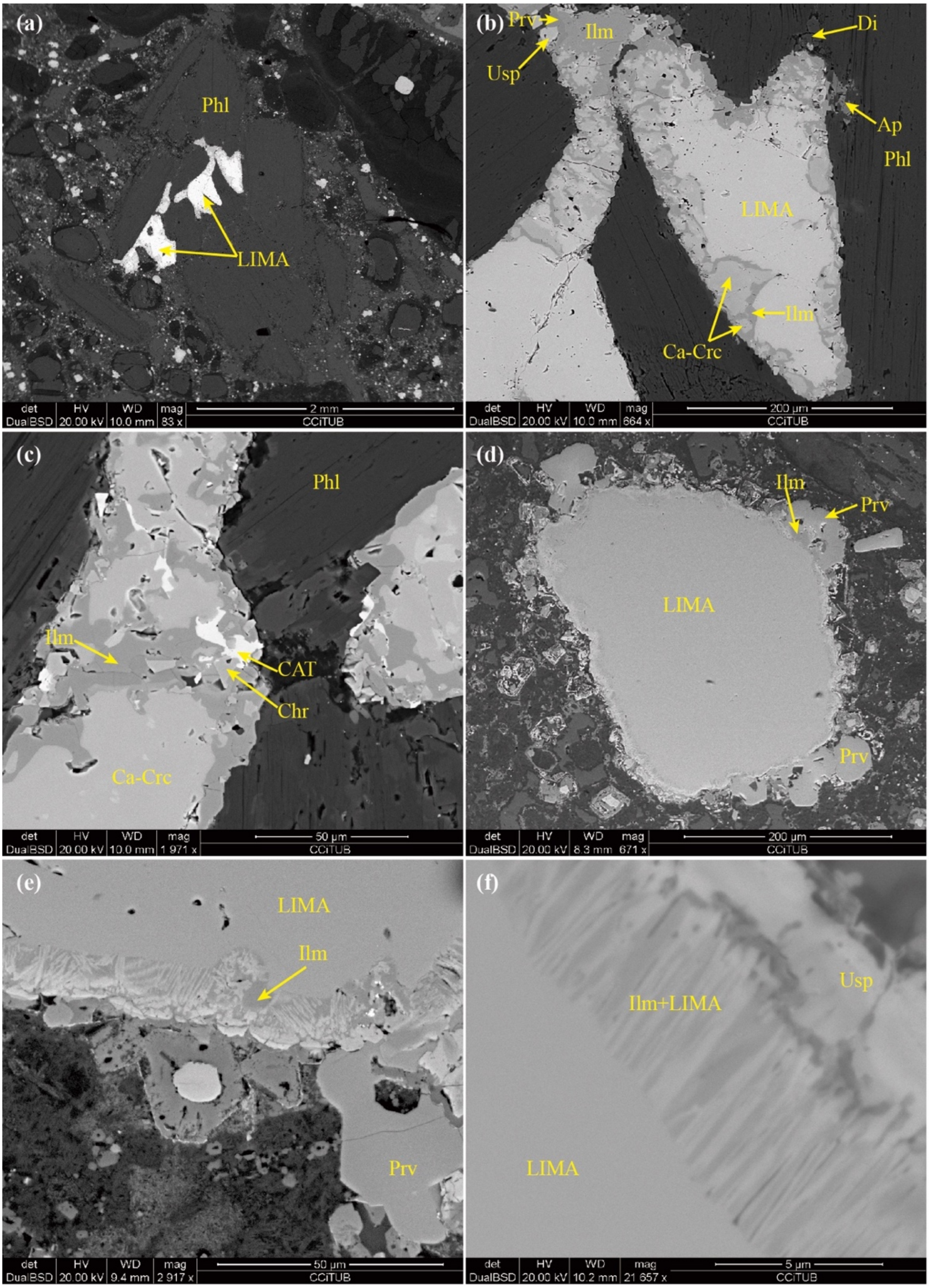

Fig. 9.1. Back-scattered electron (BSE) imagings of LIMA minerals. (a) LIMA grains in a xenolith with phlogopite (Phl), in the Dutoit-Span kimberlite. (b) LIMA replaced by a Ca-richer crichtonite mineral (Ca-Crc, probably loveringite) and geikielitic ilmenite (Ilm) which is replaced by perovskite (Prv) and ulvöspinel (Usp); diopside (Di) and apatite are found in the contact between ilmenite and phlogopite. (c) Ca-rich crichtonite group mineral (probably, loveringite) replaced by ilmenite, a Ca-Zr-Ti oxide (CAT, possibly zirconolite), chromite (Chr) and perovskite. (d-e) Anhedral LIMA xenocryst mantled by ilmenite and perovskite in the SK-2 Siddanpalli kimberlite. (f) LIMA mantled by a rim of LIMA+ilmenite (geikielite), then by a rim of ulvöspinel, in the SK-1 Siddanpalli kimberlite.

However, the crichtonite-group mineral in KL-4 kimberlite is a crichtonite s.s., because the A position is dominated by Sr (Table 9.1), followed by Ba and Ca, while the K content is minority. Its average formula can be written as:

$(Sr_{0.560}Ba_{0.251}Ca_{0.208}K_{0.089}Ce_{0.054}La_{0.054})_{1.192}(Zr_{0.726}Fe_{0.256}Mn_{0.018})_{1.000}(Mg_{1.592}Fe_{0.400}Zn_{0.008})_{2.000}(Ti_{12.636}Cr_{3.522}Fe_{1.537}Nb_{0.046}Al_{0.572}Si_{0.008})_{18.320}O_{38}$.

The analyses have been plotted in the Ba-K-(Ca+REE+Pb+Sr+Na) triangular diagram (Fig. 9.2). The mathiasite grains from SK-1 and SK-2 kimberlites studied in the present work have similar compositions to members of the crichtonite group of minerals from Jagersfontein, South Africa, while there are quiet differences with those found in China and Brazil (Fig. 9.2). However, as can be seen in this figure, most of the analyses of previous authors are not strictly members of the lindsleyite-mathiasite series, because Ba or K are not dominant in the A position. In our analyses, the mathiasite end-member is dominant in most of the mathiasite grains, but never achieves more than 0.5 apfu. Contrastingly, Sr may be more than 0.5 apfu in the KL-4 kimberlites and in these cases the mineral can be clearly classified as crichtonite s.s.

The representative trace element composition of the studied mathiasite crystals is shown in Table 9.2. The chondrite and primitive mantle normalized trace element patterns (Fig. 9.3) are similar between different mathiasite grains and between SK-1 and SK.-2. They show more differences in heavy rare-earth elements (HREE) content between different mathisite grains (Fig. 9.3). Mathiasite grains are also homogenous when studied by back-scattered electron SEM imaging (Fig. 9.1d).

Table 9.1. Representative chemical composition of minerals of the crichtonite group from the SK-1, SK-2 and KL-4 kimberlites.

	SK-1				SK2				KL-4	
	8021-2_D	8021-8_A	8021-11_E	Average of 20 crystals	8044_H	8044-5_A	8044-7_D	Average of 15 crystals	8038_D	Average of 4 analyses
SiO_2	0.03	bdl	bdl	-	bdl	0.03	bdl	-	bdl	-
Al_2O_3	0.14	0.38	0.20	0.26	0.14	0.25	0.20	0.22	1.63	1.67
Cr_2O_3	13.69	14.52	15.35	14.52	13.73	15.45	13.53	14.14	15.43	15.35
Ce_2O_3	0.65	0.42	0.75	0.62	0.99	0.57	0.28	0.59	0.40	0.45
La_2O_3	bdl	0.06	0.27	0.15	0.26	0.26	0.13	0.14	0.47	0.52
TiO_2	61.95	63.37	60.78	62.02	60.52	61.51	62.00	61.94	57.61	57.89
MgO	3.22	3.63	3.45	3.50	3.34	3.49	3.61	3.48	3.56	3.68
Na_2O	bdl	bdl	bdl	bdl	bdl	bdl	bdl	bdl	bdl	bdl
BaO	1.34	0.99	1.17	1.17	1.69	1.18	1.02	1.17	1.89	1.90
V_2O_3	0.69	0.75	0.61	0.66	0.78	0.62	0.69	0.67	bdl	bdl
FeO	9.07	8.28	8.01	8.41	9.58	7.97	8.54	8.70	8.83	9.04
MnO	0.11	0.09	0.09	0.08	0.11	0.04	0.06	0.07	0.04	0.08
NiO	bdl	bdl	bdl	0.02	bdl	0.05	bdl	bdl	na	na
Ta_2O_5	0.12	bdl	0.06	0.05	bdl	bdl	0.09	0.07	na	na
ZnO	bdl	bdl	bdl	bdl	bdl	0.04	bdl	bdl	0.06	0.04
SrO	0.53	0.66	0.93	0.71	0.79	0.83	0.68	0.69	3.36	3.33
ZrO_2	5.54	4.95	5.69	5.41	5.23	5.30	5.27	5.38	5.41	5.13
Nb_2O_5	0.90	0.43	1.26	0.82	0.97	0.97	0.86	0.87	0.35	0.35
K_2O	1.36	1.21	1.00	1.19	1.20	1.02	1.32	1.21	0.21	0.24
CaO	0.67	1.07	0.81	0.87	0.60	0.94	0.79	0.84	0.70	0.71
Total	100.00	100.83	100.43	100.44	99.91	100.55	99.08	100.15	99.95	100.36
(apfu)	Cations on basis of 38 O									
Ti	13.379	13.430	13.085	13.292	13.202	13.175	13.423	13.320	12.632	12.636
Cr	3.107	3.234	3.473	3.270	3.148	3.478	3.079	3.195	3.556	3.522
Fe	2.178	1.951	1.917	2.005	2.323	1.898	2.056	2.080	2.153	2.193
Mg	1.378	1.525	1.472	1.485	1.444	1.482	1.549	1.482	1.547	1.592
Zr	0.776	0.680	0.794	0.751	0.740	0.736	0.740	0.749	0.769	0.726
V	0.158	0.170	0.141	0.151	0.181	0.142	0.160	0.153	0.000	0.000
Nb	0.117	0.055	0.163	0.105	0.127	0.125	0.112	0.113	0.046	0.046
Al	0.046	0.127	0.068	0.087	0.047	0.085	0.068	0.073	0.560	0.572
Ni	-	-	-	0.006	-	0.011	-	-	-	-
Si	0.009	-	-	-	-	0.010	-	-	-	-
Mn	0.026	0.022	0.023	0.020	0.027	0.011	0.015	0.017	0.010	0.018
Zn	-	-	-	-	-	0.009	-	-	0.013	0.008
Ta	0.009	-	0.005	0.004	-	-	0.007	0.005	-	-
total M	21.183	21.195	21.141	21.176	21.239	21.162	21.208	21.187	21.285	21.312
K	0.498	0.435	0.364	0.431	0.442	0.372	0.485	0.442	0.078	0.089
Ca	0.205	0.323	0.249	0.265	0.186	0.287	0.244	0.256	0.219	0.219
Ba	0.151	0.109	0.131	0.131	0.192	0.132	0.115	0.131	0.216	0.215
Sr	0.089	0.107	0.154	0.117	0.132	0.137	0.113	0.115	0.568	0.560
Ce	0.068	0.044	0.079	0.065	0.105	0.060	0.030	0.062	0.054	0.054
La	-	0.007	0.028	0.016	0.027	0.027	0.014	0.015	0.054	0.054
Na	-	-	-	-	-	-	-	-	-	-
total A	1.011	1.024	1.004	1.024	1.086	1.015	1.000	1.020	1.189	1.192
Al+Zn+Si	0.081	0.150	0.091	0.106	0.074	0.105	0.083	0.090	0.570	0.590
Zn+Mn	0.026	0.022	0.023	0.020	0.027	0.020	0.015	0.017	0.023	0.026
Ti/Nb	114.134	243.812	80.053	134.931	103.992	105.432	120.048	120.054	273.897	281.586
Ti/Zr	17.252	19.750	16.480	17.746	17.852	17.905	18.150	17.819	16.429	17.431
Ca+REE+Pb+Sr+Na	0.366	0.480	0.510	0.463	0.451	0.511	0.400	0.447	0.895	0.887

*bdl: below detection limit; nd: not analysed

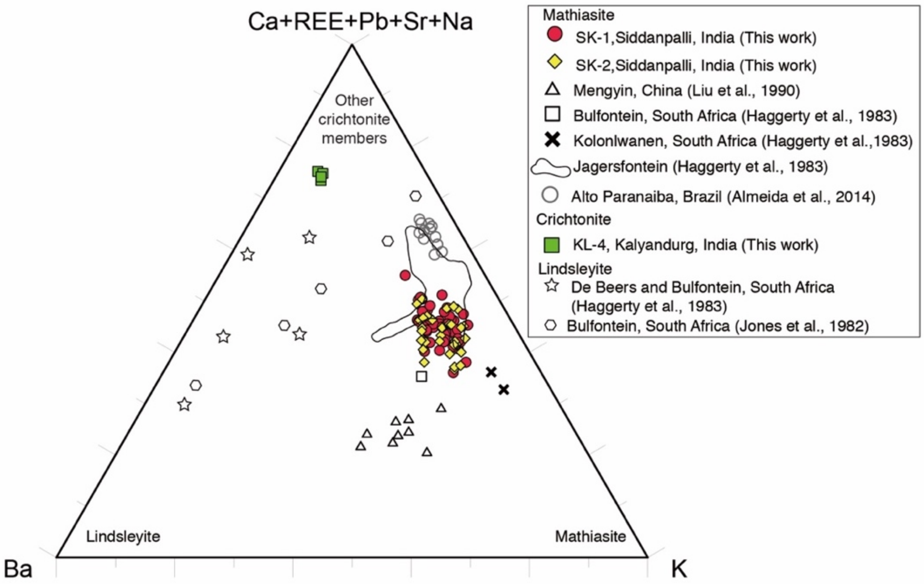

Fig. 9.2. Ba-K-(Ca+REE+Pb+Sr+Na) triangular diagram showing the composition (in apfu) of the minerals of the crichtonite group studied in this work: mathiasite from SK-1 and SK-2 and crichtonite s.s. from the KL-4 kimberlite from India, compared witth the mathiasite and lindsleyite compositions provided by other authors (Jones et al., 1982; Haggerty et al., 1983; Liu et al., 1990; Almeida et al., 2014). However, note that many of the historical data do not fit in the Ba- or K-rich domains corresponding to strictly lindsleyite-mathiasite compositions.

Table 9.2. Representative trace element composition of mathiasite from the SK-1 and SK-2 kimberlites.

	SK-1			SK-2		
Plot	#10b	#12a	#12c	#7d	#11c	#12c
(ppm)						
Na	1021	1125	978	835	873	775
K	8940	10143	9441	10965	11200	8453
Sc	128	140	134	140	145	148
V	1771	2281	1856	2514	2335	2457
Rb	4.4	5.6	5.0	6.0	5.8	5.4
Sr	6030	4967	4887	4300	4227	3402
Y	32.5	32.6	37.8	34.2	43.6	56.2
Nb	8934	8525	7667	6407	6644	5959
Ba	9578	9093	9309	7339	8998	7174
La	1970	1399	1682	1239	1131	782
Ce	1724	1192	1484	1194	1102	903
Pr	101	70	87	74	68	67
Nd	194	136	169	152	144	176
Sm	9.8	8.2	9.6	9.9	10.0	18.1
Eu	4.6	3.7	4.4	4.3	4.7	8.6
Gd	11.2	10.2	11.3	10.7	11.7	16.8
Tb	1.20	1.19	1.37	1.39	1.59	2.33
Dy	7.70	8.00	8.97	8.19	10.64	15.51
Ho	1.60	1.65	1.77	1.76	2.13	2.92
Er	4.46	4.54	5.18	4.75	5.78	7.77
Tm	0.67	0.69	0.76	0.68	0.85	1.21
Yb	4.85	4.73	5.47	4.55	5.87	7.94
Lu	0.67	0.62	0.74	0.59	0.78	1.07
Hf	855	848	783	886	898	649
Ta	829	743	419	694	376	504
Pb	204	160	174	134	174	170
Th	88	75	97	57	87	68
U	585	505	512	364	556	489

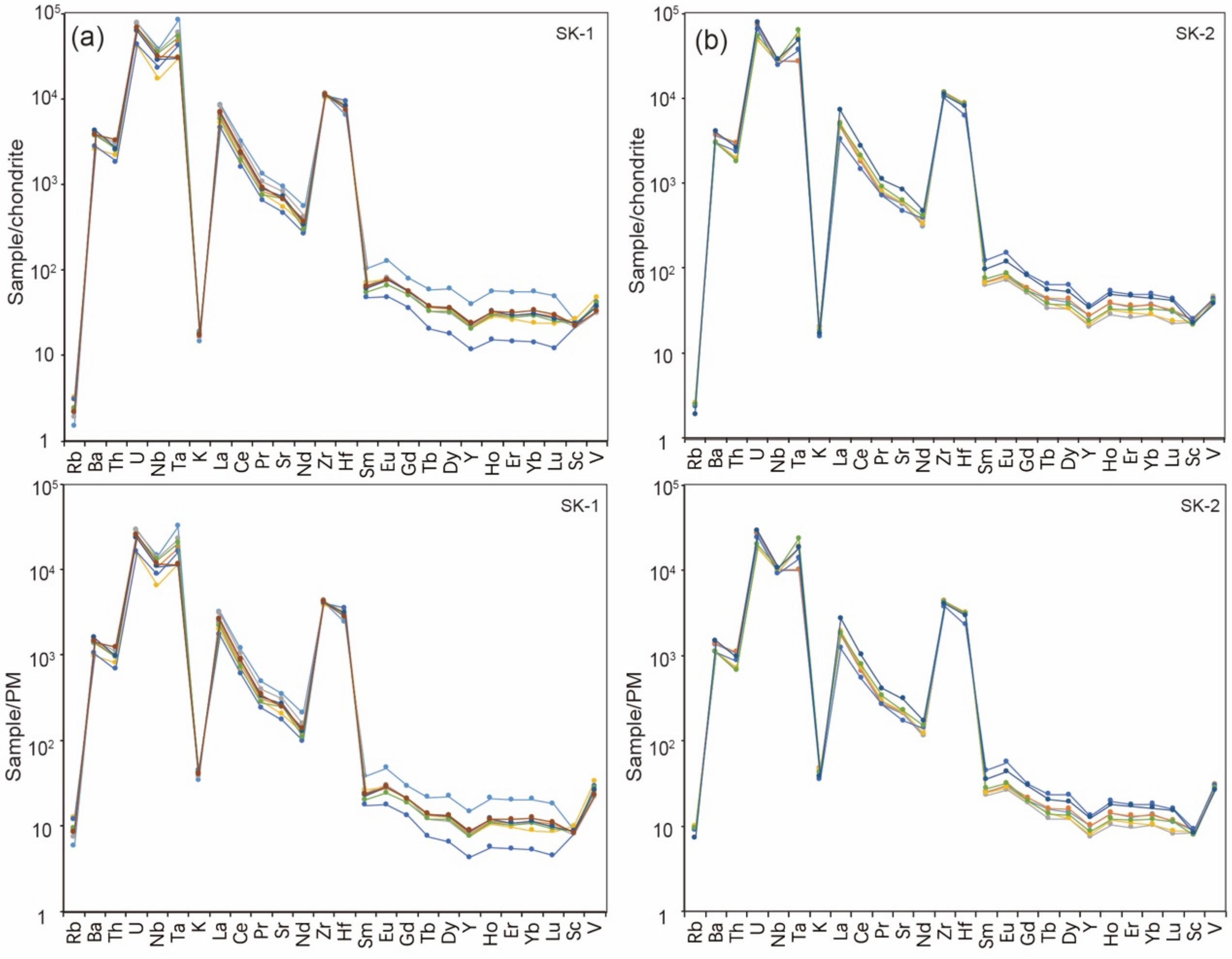

Fig. 9.3. Trace element composition normalised to chondrite (a-b) and normalised to primitive mantle (PM, c-d) of mathiasite from SK-1 and SK-2 kimberlites, by in situ LA-ICP-MS. Chondrite and primitive mantle data from McDonough and Sun (1995).

9.4. U-PB DATING

In situ U-Pb dating of mathiasite from the SK-1 and SK-2 kimberlites of the Siddanpalli kimberlite field from India was carried out in this work by LA-ICP-MS in order to date the mantle metasomatism event. Results of the U-Pb analysis are shown in Table 9.3 and Fig. 9.4 and Fig. 9.5.

Little spread of ratio ^{207}Pb/^{206}Pb is documented in mathiasite grains from the SK-1 kimberlite, and most grains return values of ^{207}Pb/^{206}Pb around 0.321. The insufficient spread of ^{207}Pb/^{206}Pb means that the resulting age has no sense for mathiasite grains from SK-1 (Fig. 9.4). Textural relations indicate that mathiasite is a mantle xenocryst; however, the calculated age around 600Ma is 400Ma younger than the perovskite age which is the kimberlite magma age. Therefore, the fact that the calculated age is 300 to 400 Ma younger than the external geological constraint indicates that it is a wrong age. The same issue was detected during previous dating of LIMA megacrysts from the Jagersfontein kimberlite (Griffin et al., 2014).

In contrast, mathiasite grains from the SK-2 kimberlite show sufficient spread and show a nice Concordia regression (Fig. 9.5). However, the uncertainty is huge. A regression through all points (n=18) of mathiasite from SK-2 yield an age of 807±170Ma (95% confidence level; MSWD=30). Rejection of the more outlying grains improves the regression to less uncertainty (922±92Ma; MSWD=9; n=12).

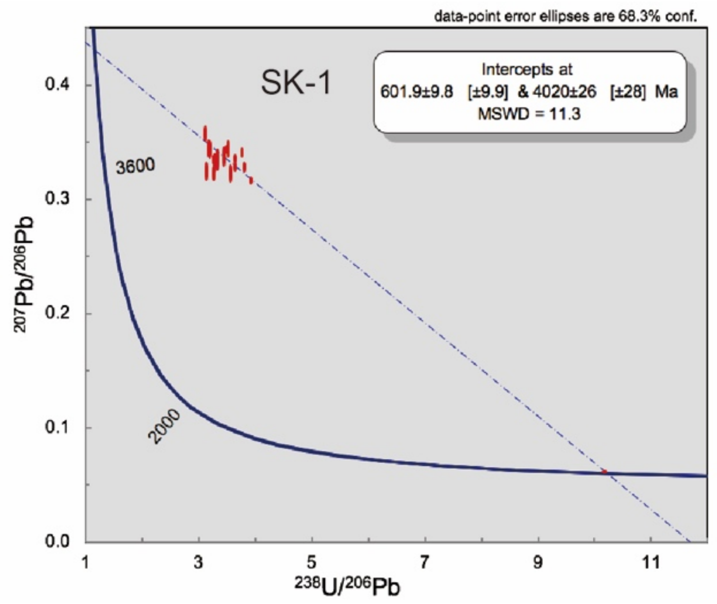

Fig. 9.4. ^{207}Pb/^{206}Pb vs 2^{38}U/^{206}Pb Concordia diagrams for in-situ LA-ICP-MS analyses of LIMA xenocrystic grains from the SK-1 kimberlite, n=20, while the calculated age is not coherent. Errors are shown as ellipses at 1σ.

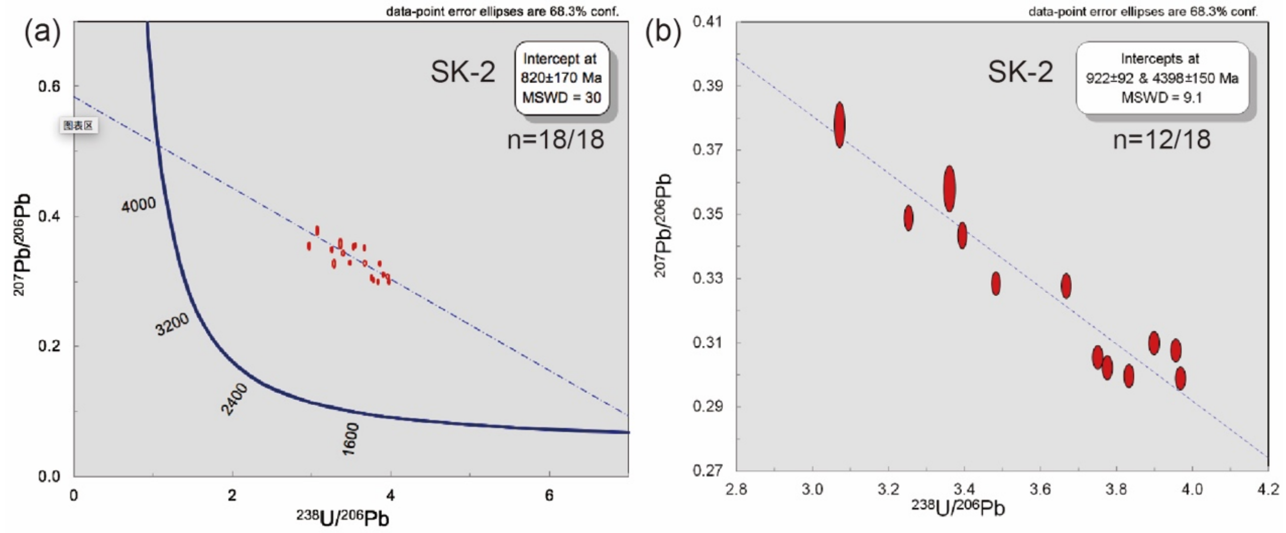

Fig. 9.5. ^{207}Pb/^{206}Pb vs. ^{238}U/^{206}Pb Concordia diagrams for in-situ LA-ICP-MS analyses of LIMA xenocrystic grains from the SK-2 kimberlite. (a) n=18; (b) n=12 rejecting the more outlying grains. Errors are shown as ellipses at 1σ.

Table 9.3. U–Pb isotopic compositions of grains of the crichtonite group analysed in situ by LA-ICP-MS.

Kimberlite	Label	$^{207}\mathrm{Pb}/^{206}\mathrm{Pb}$	±2σ	$^{207}\mathrm{Pb}/^{235}\mathrm{U}$	±2σ	$^{208}\mathrm{Pb}/^{238}\mathrm{U}$	±2σ	$^{208}\mathrm{Pb}/^{232}\mathrm{Th}$	±2σ
SK-1	21-1_A_M4	0.3373	0.0054	13.5183	0.0018	0.2905	0.0018	1.5906	0.0490
	21-1_A_M5	0.3443	0.0049	14.9685	0.0018	0.3152	0.0018	1.8262	0.0485
	21-1_D_M6	0.3321	0.0052	13.9758	0.0019	0.3051	0.0019	1.1392	0.0337
	21-1_G_m7	0.3247	0.0049	14.3120	0.0020	0.3197	0.0020	1.3485	0.0402
	21-1a_m	0.3406	0.0023	12.4583	0.0010	0.2653	0.0010	1.3090	0.0136
	21-1a_m2	0.0614	0.0005	0.8315	0.0004	0.0983	0.0004	0.0306	0.0004
	21-1D_m1	0.3289	0.0024	12.4532	0.0012	0.2746	0.0012	1.0033	0.0117
	21-1D_m2	0.3279	0.0027	11.8674	0.0013	0.2625	0.0013	0.9614	0.0139
	21-1G_m1	0.3347	0.0021	14.1910	0.0013	0.3075	0.0013	1.1669	0.0101
	21-1G_m2	0.3423	0.0022	14.8382	0.0013	0.3144	0.0013	1.1843	0.0109
	21-2_D_M2	0.3226	0.0039	13.6517	0.0019	0.3069	0.0019	1.3754	0.0321
	21-2_D_M3	0.3574	0.0045	15.8002	0.0020	0.3206	0.0020	1.4663	0.0356
	21-5B_m	0.3357	0.0022	12.6906	0.0011	0.2744	0.0011	1.1622	0.0113
	21-9_B_M4	0.3435	0.0049	14.8066	0.0019	0.3129	0.0019	1.9635	0.0470
	21-9B_m	0.3435	0.0020	13.5411	0.0010	0.2861	0.0010	1.4643	0.0104
	21-9C_m	0.3163	0.0020	11.1195	0.0010	0.2551	0.0010	0.8922	0.0081
	21-9D_m	0.3822	0.0031	15.2520	0.0013	0.2894	0.0013	1.5742	0.0218
	21-D_M1	0.3439	0.0047	13.4739	0.0015	0.2839	0.0015	1.5268	0.0360
	21-H_M2	0.3227	0.0048	12.5251	0.0016	0.2813	0.0016	1.2273	0.0321
	21-H_M3	0.3348	0.0060	13.8534	0.0020	0.2998	0.0020	1.5594	0.0506
SK-2	44-1_A_1_M	0.2990	0.0023	10.3876	0.0011	0.2520	0.0011	0.9053	0.0144
	44-1_A_2_M	0.2997	0.0024	10.7829	0.0012	0.2609	0.0012	0.9485	0.0157
	44-11_C_4_m	0.3278	0.0026	12.3222	0.0012	0.2726	0.0012	1.4995	0.0207
	44-11H_C_3_m	0.3285	0.0025	13.0057	0.0012	0.2871	0.0012	1.6144	0.0202
	44-2_C_3_M	0.3099	0.0024	10.9580	0.0012	0.2564	0.0012	1.0429	0.0140
	44-2_C_4_M	0.3077	0.0024	10.7227	0.0012	0.2527	0.0012	1.0336	0.0142
	44-4a_m	0.3490	0.0026	14.7918	0.0014	0.3074	0.0014	1.2575	0.0160
	44-5_A_3_M	0.3435	0.0027	13.9559	0.0014	0.2946	0.0014	1.4257	0.0243
	44-5_B_4_M	0.3055	0.0025	11.2319	0.0013	0.2666	0.0013	1.2070	0.0215
	44-5_B_5_M	0.3023	0.0025	11.0400	0.0013	0.2648	0.0013	1.1751	0.0218
	8044-6_A_M1	0.3780	0.0047	16.9633	0.0019	0.3256	0.0019	1.9242	0.0386
	8044-6_A_M2	0.3581	0.0048	14.6852	0.0018	0.2976	0.0018	1.6069	0.0351
	44-10_A_1_m	0.3537	0.0027	13.8141	0.0013	0.2833	0.0013	1.7662	0.0227
	44-12_E_1_M	0.3555	0.0023	13.8114	0.0012	0.2819	0.0012	1.6727	0.0152
	44-12_C_2_M	0.3273	0.0022	11.6914	0.0011	0.2592	0.0011	1.5705	0.0157
	44-10_B_2_m	0.3517	0.0025	13.2455	0.0011	0.2732	0.0011	1.8110	0.0212
	8044-7_d_M1	0.3550	0.0036	16.4853	0.0020	0.3368	0.0020	1.8625	0.0354
	8044-6_D_M3	0.3271	0.0038	13.7407	0.0017	0.3047	0.0017	1.6636	0.0311

9.5. DISCUSSION

LIMA minerals have been described as mantle xenoliths not only from kimberlites but also from ultramafic lamprophyres (i.e., Rezvukhin *et al.*, 2017). In fact, they may occur in different textural types: a) as euhedral inclusions in Cr-rich pyrope, thus indicating a metasomatic origin in the mantle for these garnets (Varlamov *et al.*, 1996; Wang *et al.*, 1999; Vrána, 2008; Rezvukhin *et al.*, 2016b; a, 2017), or b) as anhedral grains, interstitial between mantle silicates (without garnet). In many of these associations they may be found with other oxides, mainly Nb- or Cr-rutile, and may be accompanied with carbonates and apatite. In the studied cases, the mantle xenoliths show evidences of percolation of metasomatic agents (magmas and/or fluids) that produced different generations of crichtonite-group minerals, differing mainly in the main cation in the A position, starting with mathiasite (K), then crichtonite s.s. (Sr) or loveringite (Ca). They are accompanied at least by diopside and apatite; the occurrence of apatite is a proof of the existence of volatiles associated with the percolating magma. In other places, the association of crichtonite minerals with carbonates and apatite allowed also other authors explain these associations by percolation of Ca-Sr-Na-LREE-Zr-bearing carbonate-silicate metasomatic agents through Mg- and Cr-rich depleted peridotite protoliths (Rezvukhin *et al.*, 2018).

The most noticeable geochemical data provided by these minerals is the existence of large amounts of incompatible elements in mantle associations, as are Sr, Ba, K, REE, Ti, Zr, Nb, Ta, Al and Zn. Hence, these minerals indicate that the mantle was metasomatized by LILE-HFSE-rare earth element (REE)-rich fluids or magmas (Erlank *et al.*, 1987; Giuliani *et al.*, 2014). There are noticeable differences between the crichtonite minerals in Sk1/SK2 and KL-4, since the last is enriched in Sr and Al. The former Al-rich crichtonite-group minerals were found in inclusions in garnets, as in the Aldanskaya lamprophyre (Rezvukhin *et al.*, 2018), with 1-2 wt% Al_2O_3, whereas the interstitial crichtonite grains found in the Kapvaal craton had tenors less than 1 wt% Al_2O_3; however, the contents of Al in KL-4 are also relatively high, around 1.67 wt% Al_2O_3.

Crichtonite-group minerals are important reservoirs for a large number of incompatible elements in the source regions of kimberlites, even if they occur only in small amounts, because they have high concentrations of LILE, HFSE and LREE This mantle metasomatism may occur under different mantle conditions. Experimental studies confirm the stability of crichtonite minerals in low-T peridotite assemblages with T ranging from 720 to 820°C and a P range of ~34–42 kbar (~110–130 km), which corresponds to a mantle domain in the uppermost part of the diamond stability field; however, they may be formed well inside the diamond stability (Foley *et al.*, 1994; Konzett, 2005), including conditions up to 11 Gpa and 1500-1600ºC, being therefore potentially stable also in the asthenosphere to depth of up to 450km (Konzett, 2005).

The LIMA minerals found in xenoliths from the Dutoit-Span kimberlite show two members of the crichtonite minerals in disequilibrium, with the LIMA grains replaced by another member of the crichtonite group but enriched in Ca (Fig. 9.1a-c). Giuliani et al. (2018) also observed elemental and isotopic heterogeneity between coeval LIMA minerals, thus suggesting that those mantle rocks were metasomatized by multiple fluids or magmas at broadly the same time (i.e. within thousands to millions of years), which could be due to interaction between one or more Ti-rich silicate melts and a previously metasomatized, phlogopite-rich, lithospheric mantle. These authors concluded that mantle metasomatic assemblages produced by the infiltration of broadly coeval fluids with variable compositions and fluids infiltrating a rock do not necessarily cause equilibration at the cm scale. Following these authors, disequilibrium should be preserved for up to hundreds of Myr at mantle lithosphere temperatures, unless subsequently affected by transient heating and/or fluid infiltration events (Giuliani et al., 2018). High uncertainty in U-Pb age for is frequently found when using LIMA grains for dating. It seem to be a large uncertainty 922±92 Ma because is almost 10% error. However, the U-Pb age of a LIMA grain from Jagersfontein, obtained by Griffin et al. (2014), is 161±49 Ma, thus representing almost 30% of error.

Perovskite ages from SK-1 and SK-2 kimberlite, as is explained in the chapter 8, show a regression 1007±42 Ma for SK-1 and 975±66 Ma for SK-2. The 1007±42 Ma age on perovskite obtained by us in the SK-1 kimberlite is similar to the ages obtained by previous authors (for this SK-1 kimberlite body; Kumar et al., 2007; Gopalan and Kumar, 2008; Chalapathi Rao et al., 2013). Perovskite age should indicate kimberlite emplacement age, while LIMA mineral age should indicate the age of the mantle metasomatism event. The mathiasite age of 922±92 Ma from SK-2 is within the uncertainty range of the corresponding perovskite age. They are suggested as reflecting the timing of an metasomatic event just before the kimberlite emplacement, and this could explain the existence of disequilibria not only between the crichtonite minerals and the rest of minerals, but also the lack of equilibria at microscale inside the crichtonite minerals..

Crichtonite-group minerals are not so commonly found as other minerals currently used for age determination minerals (for instance, phlogopite or perovskite). Although Giuliani et al. (2014) obtained apparently good results for U-Pb dating using LIMA. U-Pb dating for LIMA carried out both in this work and other works has high errors (eg. Griffin et al., 2014). The existence of common Pb in the mineral and the frequent existence of subsequent metasomatic processes resulting in large recrystallizations of the mineral may disturb the U-Pb dating. We conclude that LIMA and similar minerals are, in most of cases, not an ideal target for U-Pb dating.

CHAPTER 10

MICA GROUP

10. MICA GROUP

10.1. INTRODUCTION

Mica group minerals are phyllosilicates composed by infinite sheets of polymerized SiO_4 tetrahedra, in which a layer of octahedral coordinated cation is sandwiched between two layers of tetrahedral coordinated cations; in addition, substitutions of the 25% of Si by Al and Fe^{3+} in the tetrahedral positions are compensated by entrance of interlayer cations of 10-12 coordination (Fig. 10.1).

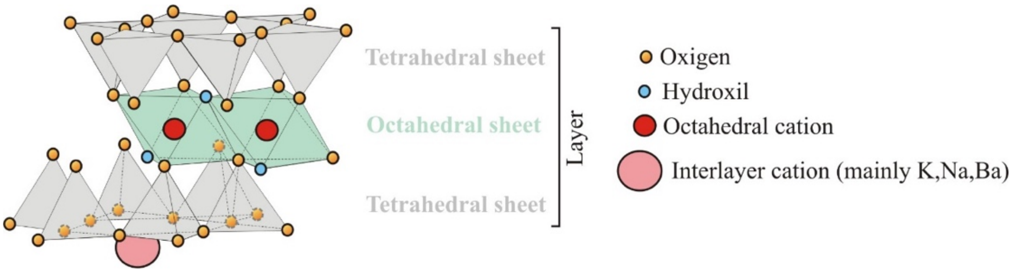

Fig. 10.1. Structure of the micas. Based on (Grim, 1968).

The general formula of mica group mineral is : $X_2Y_{4-6}Z_8O_{20}(W)_4$, where X could be large cations and cationic groups as K, Na, Ca, Ba, NH_4, Cs, Rb or a vacancy; Y could be Al, Mg, Fe^{2+}, Fe^{3+}, Mn^{2+}, Mn^{3+}, Cr, Ti, Li, V, Ni, Cu, and others; Z is mainly Si and Al but Fe^{3+} , Ti, B, P and Be may also occur; W is OH, F, Cl, S or O (Rieder et al., 1999). As in the case of other sheet silicates, members of the mica group may be dioctahedral or trioctahedral, based on the degree of occupancy of the 3 possible cations in the octahedral layer: in the case of the dioctahedral micas, only 2 of the 3 positions are occupied by trivalent cations; in case of the trioctahedral micas, all the three positions are occupied by divalent cations (Rieder et al., 1999).

Micas in kimberlites and related rocks are mainly restricted to the trioctahedral series, including the following micas:

Phlogopite $KMg_3(AlSi_3O_{10})(OH)_2$
Fluorophlogopite $KMg_3(AlSi_3O_{10})(F)_2$
Eastonite $KMg_2Al(Al_2Si_2O_{10})(OH)_2$
Annite $KFe^{2+}_3(AlSi_3O_{10})(OH)_2$
Siderophyllite $KFe^{2+}_2Al(Al_2Si_2O_{10})(OH)_2$
Tetraferriannite $KFe^{2+}_3((Fe^{3+},Al)Si_3O_{10})(OH)_2$
Tetraferriphlogopite $KMg_3(Fe^{3+}Si_3O_{10})(OH,F)_2$
Aspidolite $NaMg_3(AlSi_3O_{10})(OH)_2$
Cloroferrokinoshitalite $(Ba,K)(Fe^{2+},Mg)_3(Al_2Si_2O_{10})(Cl,OH,F)_2$
Ferrokinoshitalite $(Ba,K)(Fe^{2+})_3(Al_2Si_2O_{10})(OH,F)_2$
Kinoshitalite $(Ba,K)(Mg)_3(Al_2Si_2O_{10})(OH,F)_2$
Oxykinoshitalite $(Ba,K)(Mg,Ti,Fe^{3+},Fe^{2+})_3((Si,Al)_4O_{10})(O,OH,F)_2$
Oxyphlogopite $K(Mg,Ti,Fe)_3[(Si,Al)_4O_{10}](O,F)_2$

10.2. TEXTURAL PATTERNS

Minerals of the mica group were found, in the 79 studied kimberlites, as some of the following petrographic varieties:

1) Component of xenoliths
2) Macrocrysts and microcrysts
3) Primary micas as microphenocryst and groundmass.
4) Reaction rims replacing garnet xenocrysts

10.2.1. Micas as component of xenoliths

Mica is found in xenoliths which have been sampled by kimberlite or related magmas after encountered them during the ascent from the source in the mantle to the Earth surface. Therefore, in this category both mantle xenoliths and crustal xenoliths are included, although the more significative are those coming from the mantle. Phlogopite is found in many mantle-derived xenoliths, as in glimmerites, MARID (metasomatized mantle rocks made up by Mica-Amphibole-Rutile-Ilmenite-Diopside; (Dawson and Smith, 1977), PIC (metasomatized mantle rocks made up by Phlogopite-Ilmenite-Clinopyroxene; Grégoire et al., 2002) and peridotitic xenoliths (Grégoire et al., 2002). Moreover, annite is also found in granitic xenoliths.

10.2.2. Micas as macrocrysts and microcrysts

Macrocrystal and microcrystal micas have been commonly found in the studied kimberlites. They are subhedral isolated crystals, rounded or corroded, sometimes broken (Fig. 10.2a-b); they may display deformation features. Macrocryst and microcryst are non-genetic terms, based on the crystal size range, used in previous works to classify crystals in kimberlites and related rocks. However, there is no agreement on the size limits between both descriptive groups. For instance, crystals can be described as macrocryst when having more than 0.5 mm (Mitchell, 1995), more than 0.3 mm (Giuliani et al., 2016) or more than 1mm (Scott Smith et al., 2018). In this work macrocryst and microcryst are used to describe these isolated micas when their origin, xenocrystic or primary, cannot be clearly established.

Macrocrystal mica could occur as phenocrysts or xenocrysts. However, there are no significant differences in composition between macrocrystal micas from kimberlites and from orangeites (Mitchell, 1995). Although Reguir et al. (2009) suggested that trace element of macrocrystic phlogopite can be used to distinguish between kimberlites and carbonatites, major elements of macrocrysts cannot be used for the discrimination. Therefore, this work focus on the study of the micas as microphenocrysts and groundmass crystals, which can be surely primary.

10.2.3. Primary micas

Phlogopite is one of the typical primary minerals in kimberlites and related rocks. Primary phlogopite occurs as rare small microphenocrysts or as extremely fine-grained component of the groundmass in the melt-bearing pyroclasts (formerly pelletal lapilli) in volcaniclastic rocks. Microphenocrysts in volcaniclastic rocks (Fig. 10.2c) are less zoned than in coherent rocks. Groundmass phlogopite is found frequently together with clinopyroxene and apatite in melt-bearing pyroclasts as ultra-fine grained (frecuently aprox. 4-20µm) euhedral-subhedral tabular crystals (Fig. 10.2d).

In coherent rocks, micas commonly occurs as microphenocrysts (typically 0.2-1 mm) and as fine-grained groundmass phlogopite (typically 0.01-0.2 mm). The limit between microphenocrysts and groundmass micas is distinct in some cases. Microphenocrysts are often euhedral with tabular habit. Flow-aligned texture is displayed in many occurrences (Fig. 10.2e), while in other cases it is randomly oriented. Microphenocrysts may exhibit very complex zoning (Fig. 10.2f). It is common that the outermost rim is identical in composition to the groundmass phlogopite (Fig.10.3a).

Groundmass phlogopite is euhedral to anhedral. It may be unzoned (Fig. 10.3b) or zoned (Fig.10.3c), but the zoning has less complexity than that found in the microphenocrysts. When zoned, the composition of the zoned groundmass phlogopite may be equivalent to that of the corresponding external rims of zoned microphenocrysts (Fig. 10.3a). Inclusions of other groundmass minerals such as spinels, perovskite and apatite are frequently observed (Fig. 10.2f, 10.3a-d). Poikilitic plate phlogopite could reach a larger size (up to 1mm) and include a lot of earlier-formed crystals (Fig. 10.3e).

Primary phlogopite is also found many times together with other groundmass minerals (eg. spinels) in veins that crosscut xenocrysts such as ilmenite and olivine (Fig. 10.3f). Extreme fine grained (~$\leqslant$ 1μm) phlogopite occur together with spinels (commonly magnesio ulvöspinel-ulvöspinel- magnetite) forming phlogopite-spinel globular bodies (“magmaclasts”,Fig. 10.4a).

10.2.4. Reaction rims replacing garnet xenocrysts

Mica is also found in the reaction rims produced by replacement of garnet xenocrysts. Hence, its composition is highly influenced by the composition of the precursor garnet. For instance, mica is annite in reaction rims mantling almandine xenocrysts in BK-9 Damtshaa kimberlite (Fig. 10.4b), while mica is phlogopite in the reaction rim replacing pyrope in the Mir kimberlite (Fig. 10.4c). Moreover, phlogopite enriched in Cr (2.6-4.3 wt% Cr_2O_3) is found in the reaction rim mantling Cr-rich (12.4 wt% Cr_2O_3) pyrope in Snap Lake kimberlite (Fig. 10.4d).

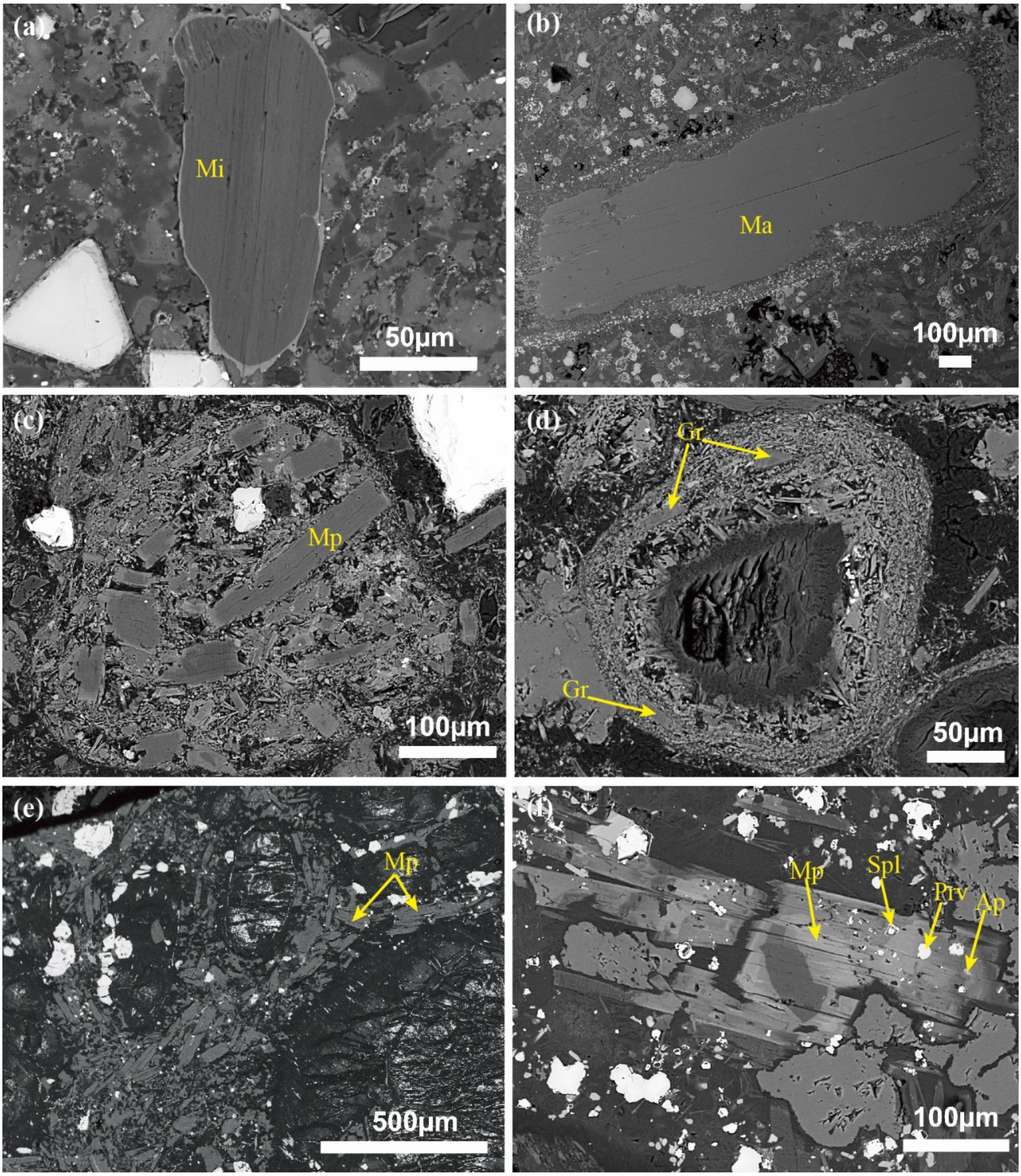

Fig. 10.2. Back-scattered electron (BSE) imagings of micas. (a) Rounded microcrystal (Mi) of phlogopite in Jackson inlet kimberlite. (b) Corroded macrocrystal (Ma) of phlogopite in the Monastery coherent kimberlite. (c) Microphenocrysts of phlogopite (Mp) in Ville-Marie volcaniclastic kimberlite. (d) Groundmass phlogopite (Gr) in melt-bearing pyroclast in Ville-Marie volcaniclastic kimberlite. e) Flow-aligned texture displayed by microphenocrysts (Mp) from Gate-Adah coherent kimberlite. (f) Complex zoning shown in a microphenocryst (Mp) from Bultfontein coherent kimberlite, containing inclusions of spinel (Spl), perovskite (Prv) and apatite (Ap).

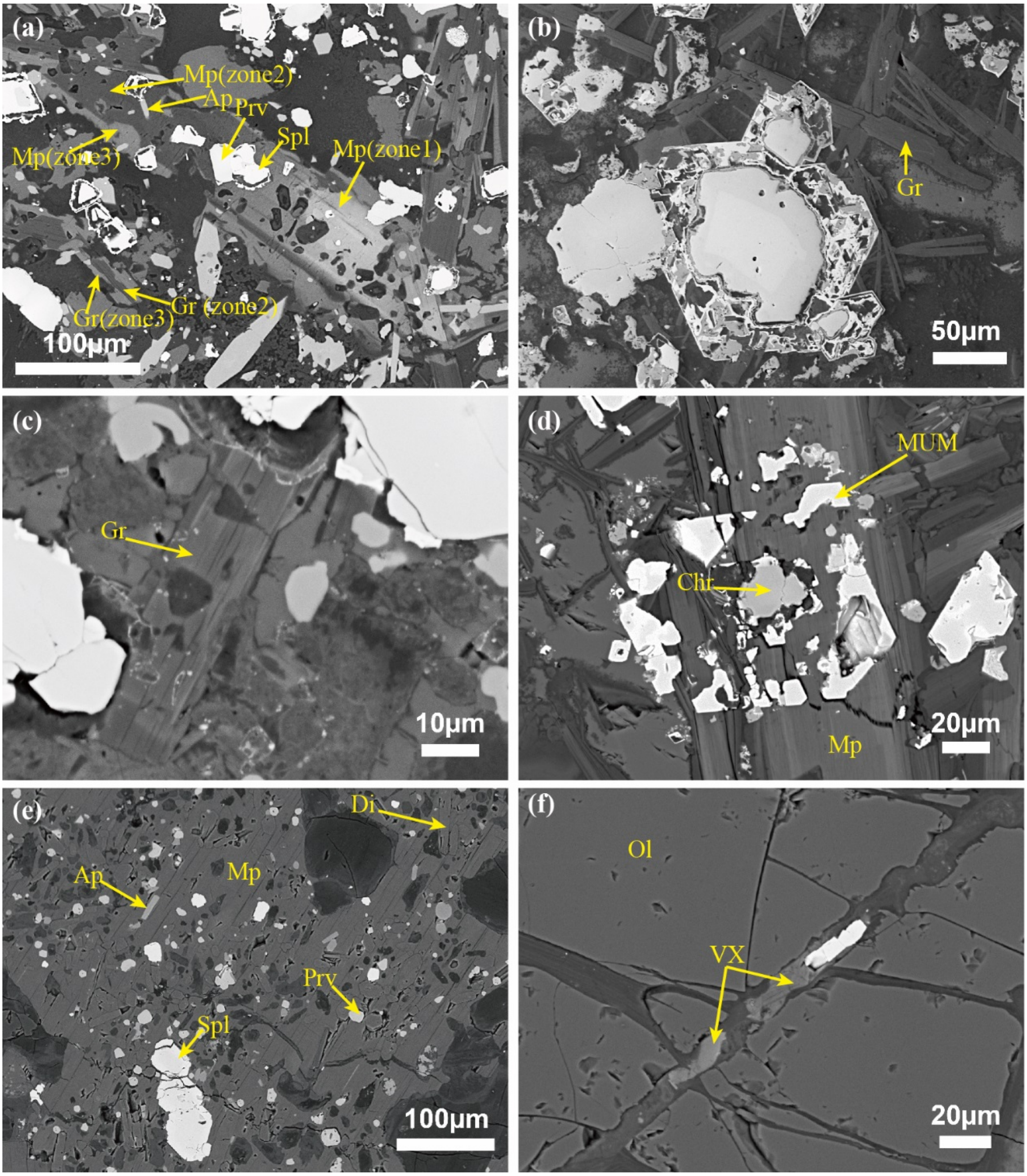

Fig. 10.3. Back-scattered electron (BSE) imagings of micas. (a) Microphenocryst (Mp) mica show 3 compositional zonings (zone 1-zone3), same composition of zone 2 and zone 3 are also found in zoned groundmass (Gr) mica in Helam orangeite; microphenocrysts have inclusions of spinel (Spl), perovskite (Prv) and apatite (Ap). (b) Unzoned groundmass (Gr) mica in Birch Mountains kimberlite. (c) Groundmass (Gr) mica showing zonation in Dutoit Span kimberlite. (d) Microphenocryst phlogopite with inclusions of spinel group minerals with a core of chromite (Chr) and border of MUM, in Emakowskaya kimberlite. (e) Microphenocrystal of poikilitic mica containing inclusions of spinel (Spl), perovskite (Prv) and apatite (Ap) in Kelsey Lake lamproite. (f) Mica (VX) found in vein crosscuts olivine (Ol) xenocryst in Letlhakane DK1 coherent kimberlite.

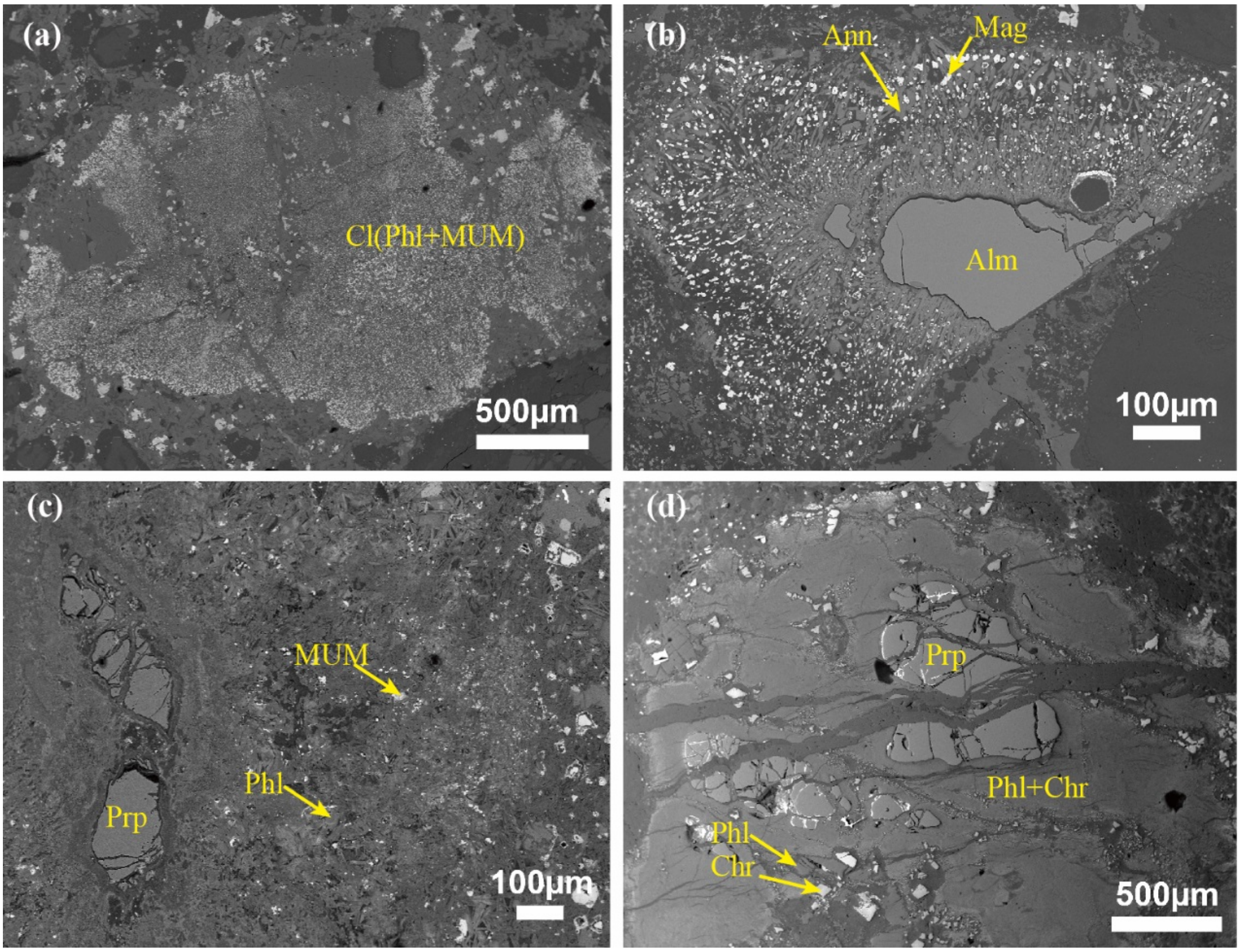

Fig. 10.4. Back-scattered electron (BSE) imagings of micas. (a) Phlogopite-MUM spinel (Phl+MUM) globular body (Cl), Banakoro "B" kimberlite. (b) Annite (Ann) and magnetite (Mag) form the reaction rim of almandine (Alm), in Damtshaa BK9 "A" volcaniclastic kimberlite. (c) Phlogopite (Phl) and MUM spinel form the reaction rim of pyrope (Prp), in Mir kimberlite. (d) Cr-rich phlogopite (Phl) and chromite (Chr) form the reaction rim of Cr-rich pyrope (Prp), Snap Lake kimberlite.

10.3. CHEMICAL COMPOSITION OF PRIMARY MICA

The accurate determination of structural formulas is complicate in the case of micas. Since Fe^{2+}/Fe^{3+} ratio is not determined by microprobe analysis, its estimation for micas is always a problem. The commonly used Fe^{2+}/Fe^{3+} estimation method for many minerals proposed by Droop (1987) often fails for micas due to the presence of cation vacancies in these minerals (Mitchell, 1995; Brod et al., 2001). There are also previous works that calculated Fe^{2+} and Fe^{3+} assuming that Ti occurs only in octahedral position (Lee et al., 2003). However, phlogopite compositions from present work suggest that is possible to have Ti both in octahedral and tetrahedral positions. In addition, Mg can be found in octahedral and interlaminar position, thus avoiding use of those methods to calculate Fe^{2+} and Fe^{3+}. Many previous works assumed total iron as Fe^{2+} (Mitchell, 1986, 1995), while the others assume all Fe^{3+} to fill the deficiency of tetrahedral site and the rest iron as Fe^{2+} in octahedral position (Tappe *et al.*, 2004b, 2006). Iron is recalculated as Fe^{3+} to fill the deficiency of tetrahedral site and the rest iron as Fe^{2+} in octahedral position in this work. The majority of groundmass phlogopite and some compositional zoning domains of microphenocrysts are too small to analyse their trace elements content by LA-ICP-MS. 955 EMPA analyses from primary micas from kimberlite, orangeites, lamproites and UML have been used for our compositional study.

The compositional range of primary micas in the studied samples (including kimberlites, orangeites, lamproites and UMLs) fit in solid solution between members of the series between phlogopite [$KMg_3(Si_3Al)O_{10}(OH)_2$] - annite [$KFe^{2+}_3(Si_3Al)O_{10}(OH)_2$] - tetraferriphlogopite [$KMg_3(Si_3Fe^{3+})O_{10}(OH)_2$] - tetraferriannite [$KFe^{2+}_3(Si_3Fe^{3+})O_{10}(OH)_2$] (Fig. 10.5). The majority fall into phlogopite and tetraferriphlogopite dominant fields (Fig. 10.5).

Low apfu contents of Si and Al (Si+Al < 8 on basis of 22 oxygens in tetrahedral site) request the entrance of Fe^{3+} in tetrahedral position (Fig. 10.6a), termed as tetraferriphlogopite when there is more Fe^{3+} than Al in tetrahedral position. Moreover, solid solution with the kinoshitalite [$BaMg_3(Si_2Al_2O_{10})(OH)_2$] end member is also frequently found in kimberlite micas as the presence of substitution of K by Ba in interlayer position, but no analyses fall into kinoshitalite domain (more Ba than K in interlayer position), although some of them are close to the limit (Fig. 10.6b). In some occurrences, fluortetraferriphlogopite (when tetraferriphlogopite has F > 1 apfu on basis of 22 oxygens) is also present in groundmass mica, for instance, in the south pipe of Karowe AK6 kimberlite.

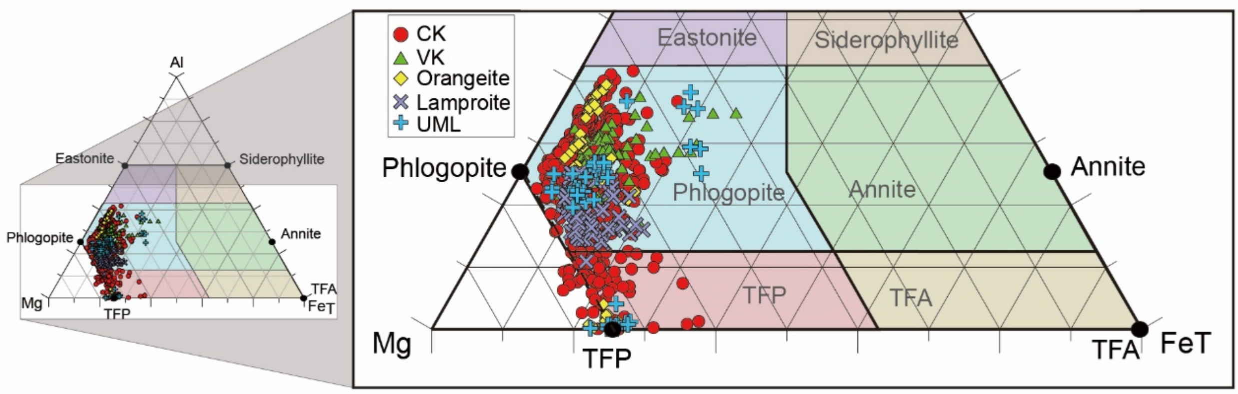

Fig. 10.5. Composition of primary micas of studied coherent kimberlites (CK), volcaniclastic kimberlites (VK), orangeites, lamproites and ultramafic lamprophyres (UML) plotted in the ternary system Al-Mg-Fe_T. Limits between constituents modified from Mitchell (1995) and Brod et al. (2001) based on dominant-constituent rule of Nickel (1992) and Hatert and Burke (2008). TFP: tetraferriphlogopite; TFA: tetraferriannite.

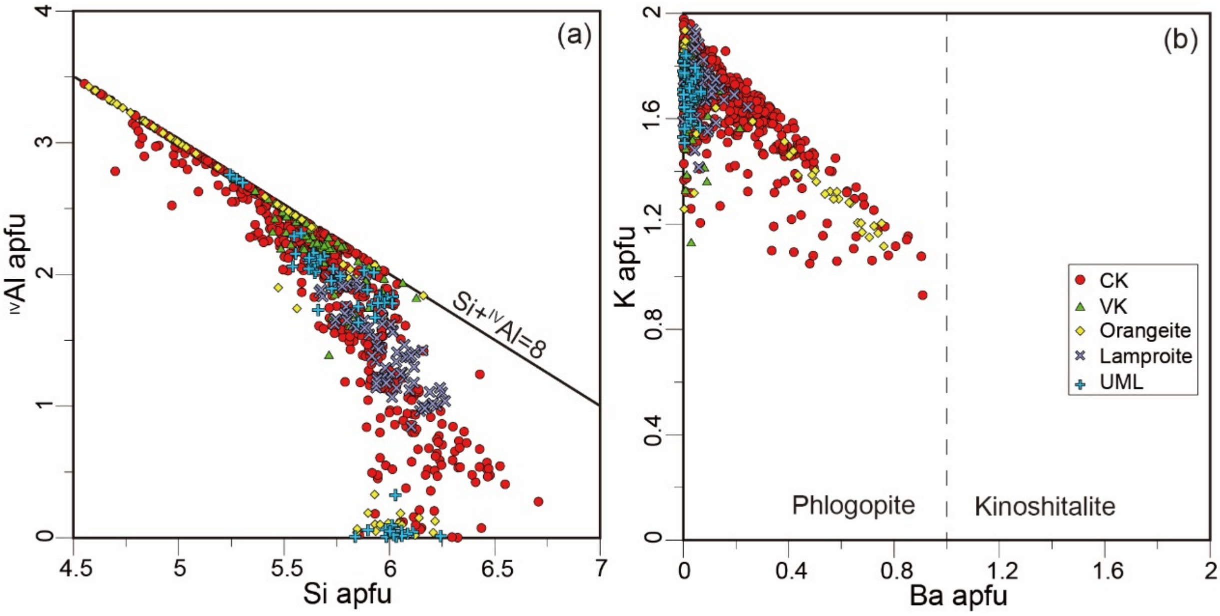

Fig. 10.6. Composition of primary micas of studied coherent kimberlites (CK), volcaniclastic kimberlites (VK), orangeites, lamproites and ultramafic lamprophyres (UML) plotted in the binary diagrams: (a) ^{IV}Al (apfu) vs. Si (apfu). (b) K (apfu) vs. Ba (apfu). Based on 24 (O, OH, F).

First of all, an extent overlap of the compositions of the studied primary micas from kimberlites, orangeites, lamproites and UMLs is observed (Fig. 10.5-10.9).

Micas from kimberlites have wider compositional range than those previously described as the kimberlite mica field (Fig. 10.7). Micas from volcaniclastic kimberlite have a more limited compositional range than those from coherent kimberlites. Micas from volcaniclastic kimberlite have a relatively limited and high-medium Al content (7.94-18.41 wt% Al_2O_3), while coherent kimberlite micas have a very wide range of Al content that vary from 0 to 22.8 wt% Al_2O_3. Tetraferriphlogopite may be present in coherent kimberlites but lacks in volcaniclastic kimberlites. Ti content range is similar while Fe content is also more limited in micas from volcaniclastic kimberlites (0.3-5.1 wt% TiO_2 and 3.0-16.6 wt% FeO_T) than in coherent kimberlites (0-5.5 wt% TiO_2 and 1.9-21.9 wt% FeO_T).

Lamproites (excluding those classified as orangeites) in the studied samples also have a relatively limited composition (Fig. 10.7). Al content is relatively low (5.2-12.8 wt% Al_2O_3) but only one of them is tetraferriphlogopite and its Al content is not so low as in tetraferriphlogopite from kimberlites, orangeites and UMLs. Ti and Fe contents are also relatively limited (0.5-4.8 wt% TiO_2, 4.6-13.2 wt% FeO_T).

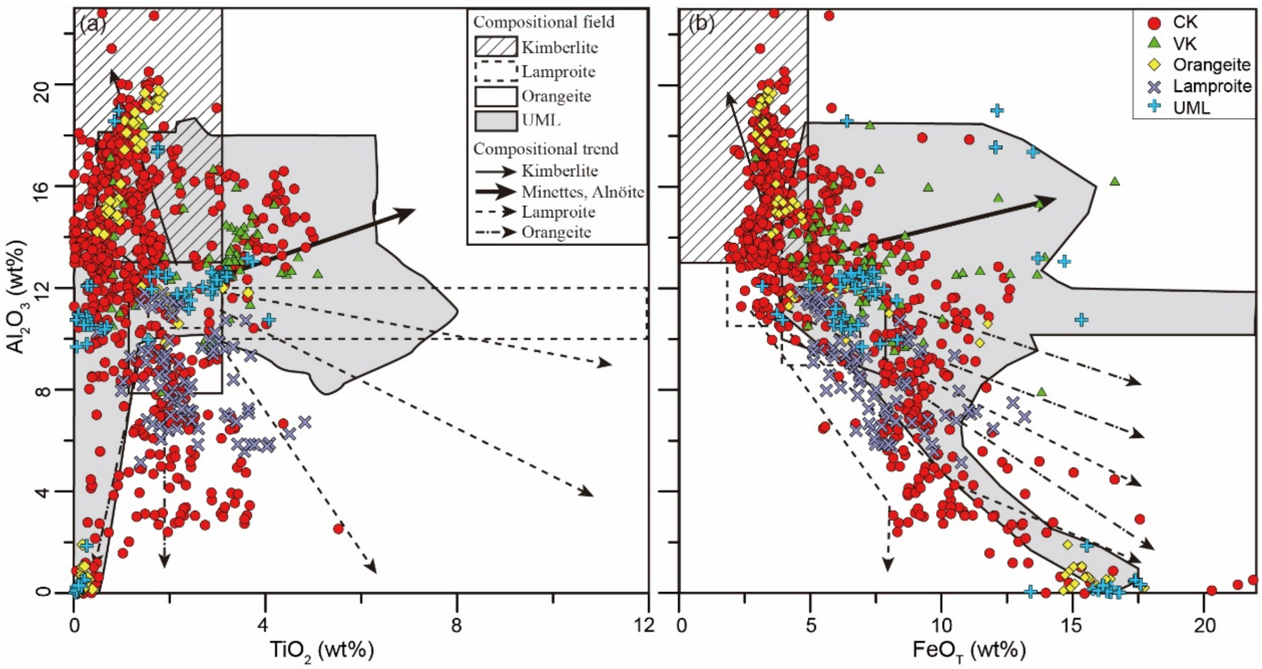

Fig. 10.7. Al_2O_3 vs. TiO_2 (wt%) and Al_2O_3 vs. FeO_T (wt%) compositional variation of micas from coherent kimberlites (CK), volcaniclastic kimberlites (VK), orangeites, lamproites and ultramafic lamprophyres (UML), compared with the compositional fields and trends for kimberlites, lamproites, orangeites and minette micas from Mitchell (1995). UML field from (Mitchell et al. (1999) and Tappe et al. (2004, 2006, 2014).

The higher Cr contents are found in kimberlites (volcaniclastic and coherent kimberlites, 0-1.9 wt% Cr_2O_3, Fig. 10.8a). Mica from UMLs (0-0.8 wt% Cr_2O_3) and orangeites (0-0.7 wt% Cr_2O_3) is also found slightly enriched in Cr (Fig. 10.8a), while lamproites remain Cr-free ($Cr_2O_3 < 0.1$ wt%, Fig. 10.8a).

The majority of micas have #Mg [$\#Mg=Mg/(Mg+Fe^{2+})$] above 0.8. The lower #Mg is found in UMLs and volcaniclastic kimberlites (Fig, 10.8b).

The highest Na contents are obtained in coherent kimberlites (0-2.8 wt% Na_2O, Fig. 10.8c). A relatively slight Na enrichment in micas is also found in lamproites (0-1.2 wt% Na_2O) and volcaniclastic kimberlites (0.1-0.9 wt% Na_2O), while Na contents remain low in orangeites (0-0.5 wt% Na_2O) and UMLs (0-0.5 wt% Na_2O).

The higher F contents occur in coherent kimberlites (0-6.4 wt% F) and lamproites (0-4.8 wt% F, Fig. 10.8d), while F content is relatively low in volcaniclastic kimberlites (0-1.4 wt% F), orangeites (0-1.4 wt% F) and UMLs (0.1-1.3 wt% F). Some micas from coherent kimberlites show a positive correlation between Na and F (Fig. 10.9a).

Coherent kimberlites (with 0-12.5 wt% BaO), and orangeites (with 0-15.1 wt% BaO) return the highest Ba contents (Fig.10.9b-d). Slight Ba enrichment is found in some micas from lamproites (0-4.3 wt% BaO) and coherent kimberlites (0-3.9 wt% BaO), while Ba contents remain low in UML micas (0-1.2 wt% BaO).

No very clear correlation between Ba and F is observed (Fig. 10.9b), but very high Ba contents use to be found in micas with low F content as in some coherent kimberlites and orangeites, while micas containing higher F proportions have low Ba tenors, as in some coherent kimberlites and lamporites (Fig. 10.9b). In addition, no very clear correlation between Ba and Mg and between Ba and Al_2O_3 is observed (Fig. 10.9b), while a slight positive correlation between Ba and Al is displayed in some micas from coherent kimberlites and orangeites.

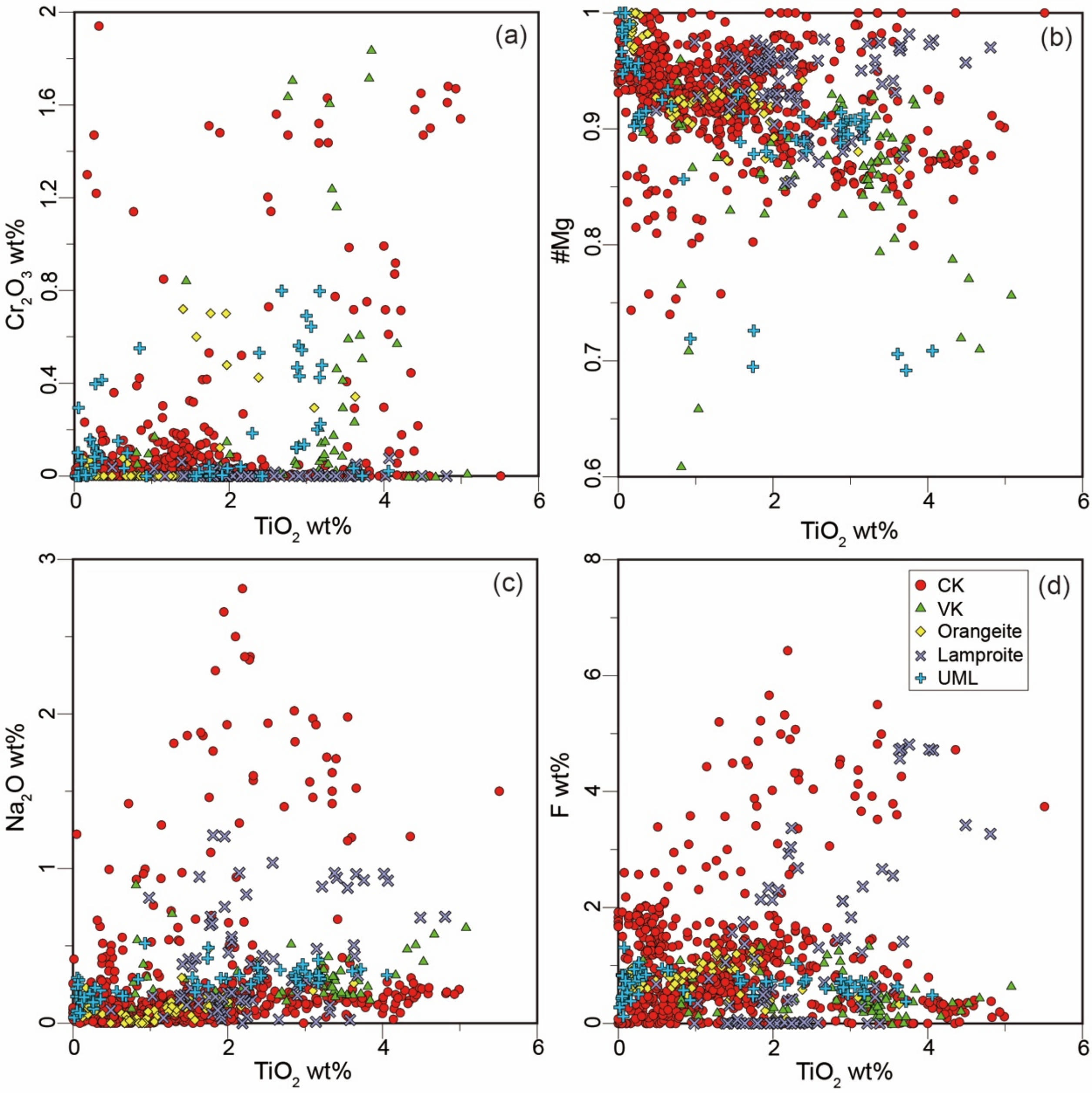

Fig. 10.8. Composition of primary micas of coherent kimberlites (CK), volcaniclastic kimberlites (VK), orangeites, lamproites and ultramafic lamprophyres (UML) plotted in binary systems. (a) Cr_2O_3 (wt%) vs. TiO_2 (wt%). (b) #Mg [#Mg=Mg/(Mg+Fe^2)] vs. TiO_2 (wt%). (c) Na_2O (wt%) vs. TiO_2 (wt%). (d) F (wt%) vs. TiO_2 (wt%).

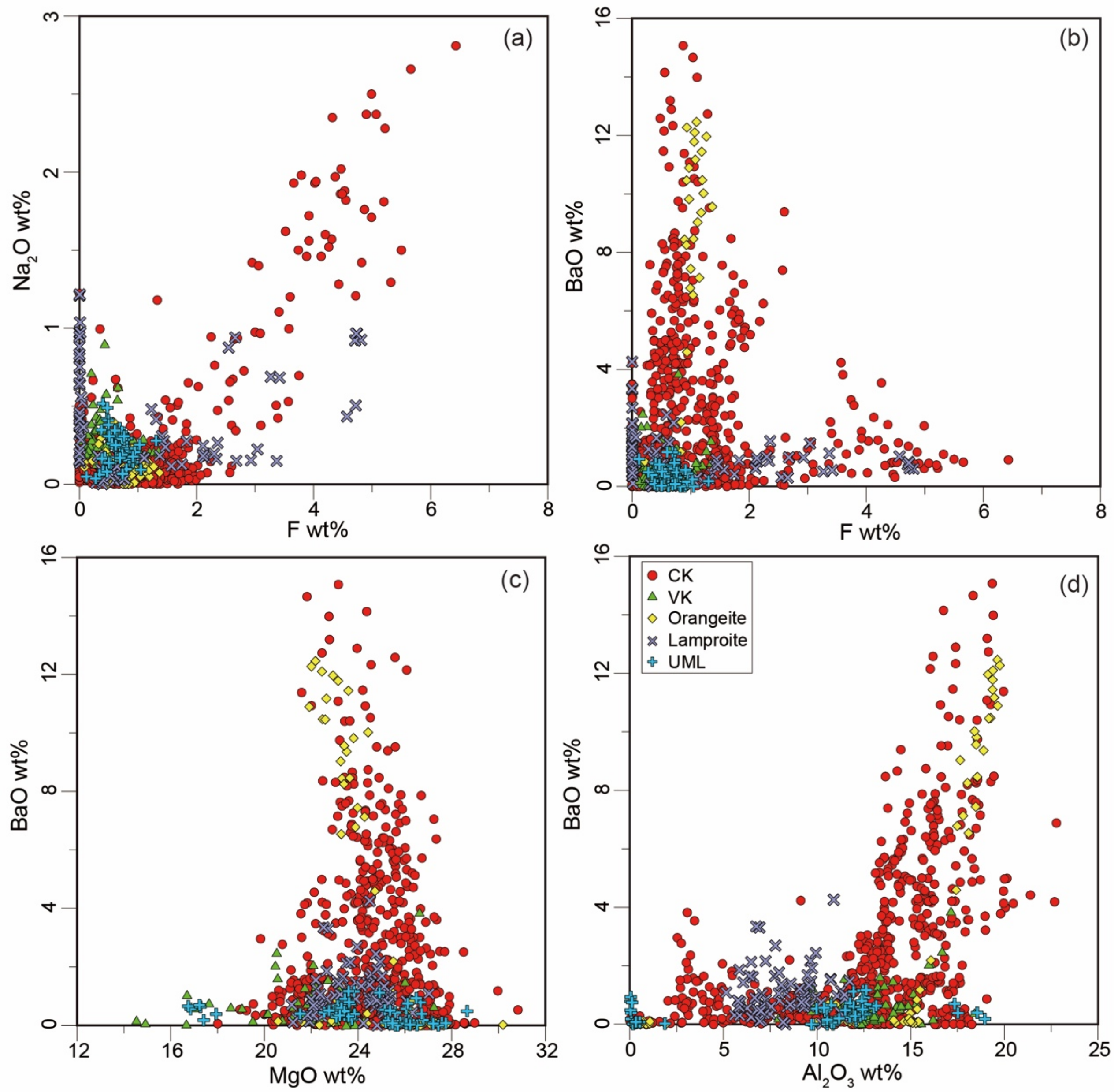

Fig. 10.9. Composition of primary micas of coherent kimberlites (CK), volcaniclastic kimberlites (VK), orangeites, lamproites and ultramafic lamprophyres (UML) plotted in binary system. (a) Na_2O (wt%) vs. F (wt%). (b) BaO (wt%) vs. F (wt%). (c) BaO (wt%) vs. MgO(wt%). (d) BaO (wt%) vs. Al_2O_3 (wt%).

Tetraferriphlogopite is found in coherent kimberlites, lamproites, orangeites and UMLs, while tetraferriphlogopite is lacking is volcaniclastic kimberlites. However, tetraferriphlogopite has been observed only in a case in lamproite. Tetraferriphlogopite is Al depleted (Al_2O_3 < 6.1 wt%) as the low proportions of Si and Al in tetrahedral position force the entrance of Fe^{3+} in this site. Tetraferriphlogopite crystals (Fig. 10.10) have a wider compositional range in coherent kimberlites (0-6.1 wt% Al_2O_3, 0-5.5 wt% TiO_2, 8.1-21.9 wt% FeO_T) than in orangeites (0.1-1.9 wt% Al_2O_3, 0.1-1.4 wt% TiO_2, 14.6-17.7 wt% FeO_T) and UMLs (0-1.9 wt% Al_2O_3, 0-0.3 wt% TiO_2, 13.4-17.6 wt% FeO_T). There is a clear positive correlation between Na and F contents in tetraferriphlogopite in coherent kimberlites (Fig. 10.11a), while F and Na content are low in tetraferriphlogopite from orangeites, lamproites and UMLs. Relatively high Ba content in tetraferriphlogopite is found in coherent kimberlites with F around 4 wt% (Fig. 10.11b), while F and Na contents are low in orangeites, lamproites and UMLs..

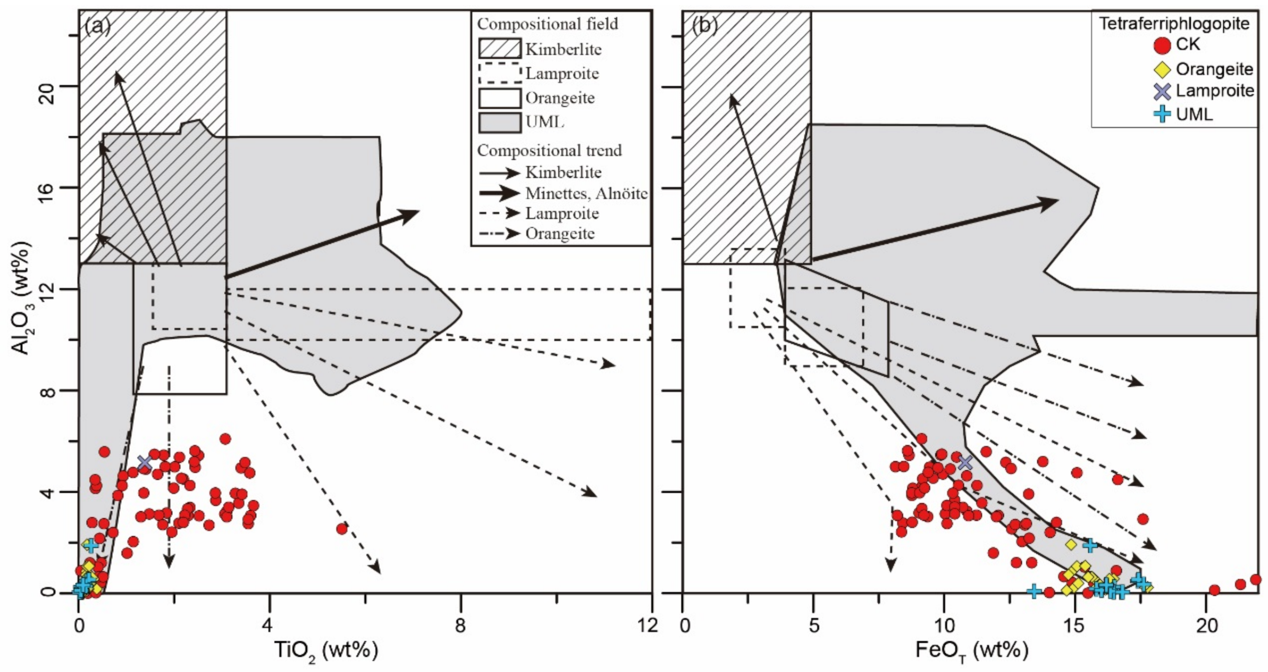

Fig. 10.10. Al_2O_3 vs. TiO_2 (wt%) and Al_2O_3 vs. FeO_T (wt%) compositional variation of tetraferriphlogopite from coherent kimberlites (CK), orangeites, lamproites and ultramafic lamprophyres (UMLs). Compositional fields and trends for kimberlites, lamproites, orangeites and minette micas from Mitchell (1995). UML field from (Mitchell et al. (1999) and Tappe et al. (2004, 2006, 2014).

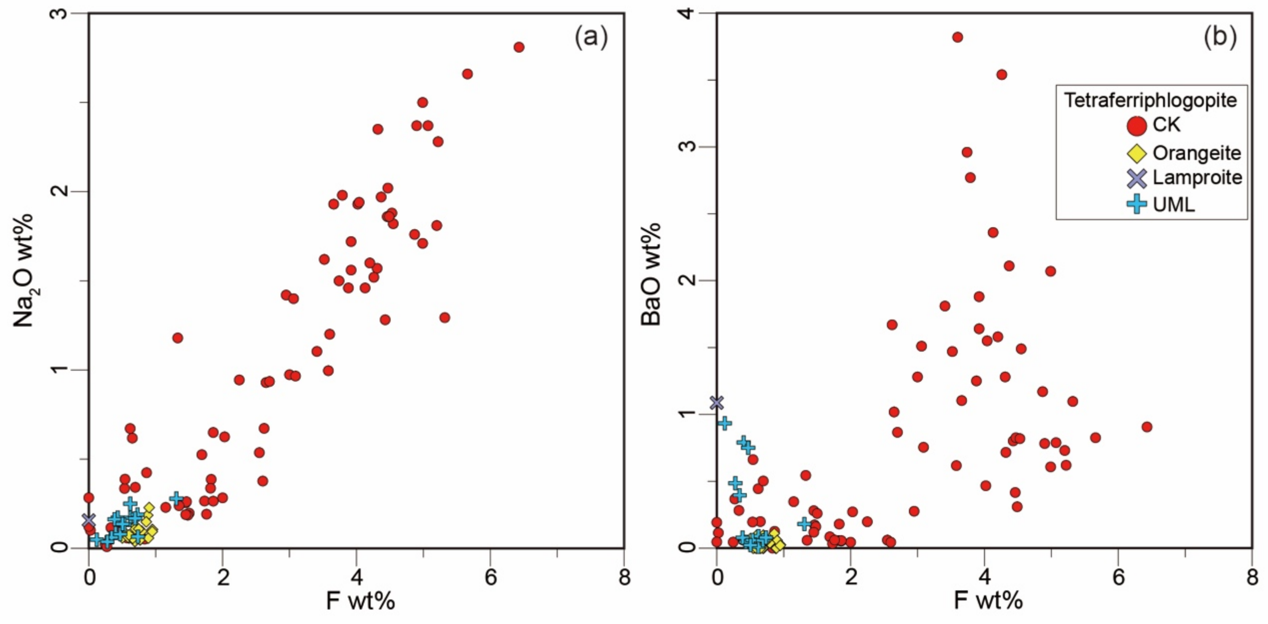

Fig. 10.11. Composition of tetraferriphlogopite of coherent kimberlites (CK), orangeites, lamproites and ultramafic lamprophyres (UML) plotted in binary system. (a) Na_2O (wt%) vs. F (wt%). (b) BaO (wt%) vs. F (wt%).

Table 10.1. List of studied samples and different compositional zonings presented in micas.

	Sample	Region	Location	Name	Rock	Zoned macrocryst	Microphenocryst	Groundmass
Angola	CU-79-70,5A, CU-79-113A		Cucumbi		VK			
Angola	TZ-G18-47, TZ-G18-252		Tchiuzo		VK			1
Botswana	10052	SD	Jwaneng	Centre pipe	VK			
Botswana	10053	SD	Jwaneng	North pipe	VK			
Botswana	10054	SD	Jwaneng	South pipe	VK			
Botswana	10055	CD	Orapa	AK1, "A"	VK			1
Botswana	10056	CD	Orapa	AK1, "B"	VK	1,2		3
Botswana	10057	CD	Orapa	AK1, "C"	VK			1
Botswana	10058	CD	Letlhakane	DK1	VK			1
Botswana	10060	CD	Damtshaa	BK9, "A"	VK			1
Botswana	10061	CD	Damtshaa	BK9, "B"	VK			
Canada	7999	Quebec	Temiskaming	Ville-Marie	VK		1,2,3(Ba)	1,2,3(Ba)
Canada	9168	Ontario	Temiskaming	Seed	VK			
Canada	9359	NWT	SW Slave	Drybones Bay	VK			1
USA	8015	Michigan	Lake Ellen	Lake Ellen	VK			
USA	9346	Utah	San Juan Co.	Alhambra Rock	VK		1,2	1,2
USA	9966	Tennessee	Tazewell	Norris metakimberlite	VK			
Venezuela	7544		Guaniamo		VK/CK			
Russia	10077	NR	Lomonosovskaya		VK			
Russia	10079	NR	Pionerskaya		VK			1
Russia	9985	Yakutia	Pobeda ('Victory')		VK			1
Russia	9959	Yakutia	Leningrad		VK			
Angola	CC-47-46		Cacuilo	K47	CK			
Botswana	10049	CD	Karowe	AK6, South pipe	CK			1(TFP, FTFP), 2
Botswana	10050	CD	Karowe	AK6, Center pipe	CK			
Botswana	10051	CD	Karowe	AK6, North pipe	CK			
Botswana	10059	CD	Letlhakane	DK1	CK			1(TFP)
South Africa	7707	NCP		Riverton	CK		1,2,3,4,5 (TFP)	2,3,4,5 (TFP)
South Africa	9156	FSP		Bultfontein	CK		1,2,3,4(Ba),5,6	4,5,6
South Africa	9311	NCP	Kimberley	Big Hole	CK	1,2		
South Africa	9351	NCP	Kimberley		CK			a1,a2,b1,b2(TFP)
South Africa	9364	NCP	Kimberly	DutoitSpan	CK	1,2		2
South Africa	9725	FSP		Monastery	CK	1,2		2(Ba),3
South Africa	9630	FSP	Kaalvallei	"occurence A"	CK			1(TFP)
Lesotho	9607			P200	CK			1(TFP)
Guinea	8870			Banakoro	CK		1,2 (Ba),3,4	3,4
Guinea	8871			Banakoro	CK	1,2,3		3,4(TFP)
Canada	9353, 9354	Québec	Temiskaming	Notre Dâme du Nord	CK	1,2		
Canada	9577	Ontario	Bucke Township		CK			1(Ba),2
Canada	6934	NWT	Somerset island		CK			
Canada	7448	NWT	Diavik		CK			1
Canada	7449	NWT	LDG Ekati	Point Lake	CK		1(Ba),2,3	2,3
Canada	9613	NWT	SW Slave	Snap Lake	CK		1,2(Ba)	1,2(Ba)
Canada	7454	Alberta	Birch Mountains		CK		1(Ba),2,3	3
Canada	9360	Nanavut	Baffin Island	Jackson inlet	CK	1,2(Ba)		

Table 10.1. (continued)

	Sample	Region	Location	Name	Rock	Zoned macrocryst	Microphenocryst	Groundmass
USA	7314	Colorado	Larimer Co.	Chicken Park	CK			1(Ba),2
USA	10070	Pennsylvania	Fayette Co.	Gate-Adah	CK	1,2	2,3,4(Ba),5	2,3,4(Ba),6
USA	9348	Colorado	Kelsey Lake		CK		1(Ba),2,3(TFP)	1(Ba),2,4(TFP)
USA	9345	Colorado	Laramie Co		CK		1(Ba),2,3	2,3
USA	9352	Michigan	Menominee	Site 73	CK			
USA	9576	Colorado	Larimer Co.	Sloan #2	CK		1(Ba),1	1(Ba),2
Russia	10037	Yakutia	Udachnaya		CK			
Russia	10065	Yakutia	Obnazhonnaya		CK			1
Russia	4928	Yakutia	Mir		CK			1
Russia	9611	Kola Peninsula	Emakowskaya		CK		1,2(Ba),3,4	3,4
India	8021	RKF	Siddanpalli cluster	SK-1	CK			
India	8044	RKF	Siddanpalli cluster	SK-2	CK			
India	8029	RKF	Siddanpalli cluster	SK-3	CK			
India	8030, 8040, 8041	WKF	Chigicherla cluster	CC-4	CK			alt
India	8022, 8023	WKF	Chigicherla cluster	CC-5	CK			1(TFP)
India	8036	WKF	Kalyandurg	KL-3	CK			1 (TFP)
India	8037, 8038	WKF	Kalyandurg	KL-4	CK			1 (Ba),2
India	8027	WKF	Wajrakarur village	P-1	CK			
India	8043	WKF	Lattavaram village	P-3	CK			1(Ba),2
China	9333	Shandong province	Mengyin	Red Flag #1	CK			1(Ba),2
China	9737,9738, 9740	Shandong province	Mengyin	Shengli	CK			1(Ba),2,3
China	9573, 9574	Liaoning province		Wafangdian	CK			1
South Africa	7881	NCP	Kimberley	Helam	Orangeite (Hammond and Mitchell, 2002)		1(Ba),2,3(TPF)	2,3(TPF)
South Africa	9375	FSP		Roberts Victor	Orangeite (Mitchell 1995)	1,2		2,3
South Africa	9952	NCP		Bellsbank	Orangeite (Mitchell 1995)			1
South Africa	9602	FSP	Kaalvallei	"occurence B"	Lamproite (this work)			1,2
USA	9341	Colorado	Kelsey Lake		Lamproite (this work)		1	1
USA	9340	Arkansas	Murfreesboro		Lamproite (McCandless et al. 1994)		1	1
India	8024	WKF	Chigicherla cluster	CC-1	Lamproite (this work)			1
India	8025	WKF	Wajrakarur village	P-2	Lamproite (Kaur&Mitchell 2013)			1
India	8035	WKF	Lattavaram village	P-4	Lamproite (Shaikh et al., 2018)			1 (TFP)
India	8045	WKF	Mulligiripally	P-5	Lamproite (Kaur et al., 2013)			1
Canada	10142	Quebec	Ugava Bay	Torngat	UML (Tappe et al., 2004)		1,2,3,4,5(TFP)	1,2,3,4,6(TFP)

SD: Southern District; CD: Central District; NCP: Northern Cape Province; FSP: Free State Province; NR: Northern Region; RKF: Raichur kimberlite field; WKF: Wajrakarur kimberlite field. VK: volcaniclastic kimberlite; CK: coherent kimberlite; UML: ultramafic lamprophyres; Ba: highest Ba content zone; TFP: tetraferriphlogopite

10.4. EXAMPLES OF MICAS WITHIN SINGLE KIMBERLITES AND RELATED ROCKS

Several individual occurrences are described separately due to the diversity of mica populations and the variety of complex zoning in every occurrences. Only several selected examples from the 79 studied kimberlites are presented in the following section, because they are enough representative to describe the general patterns of the ensemble.

10.4.1. Banankoro ("B") kimberlite, Guinea

A detailed petrographic study of generations of phlogopite and other minerals from an occurrence in Banankoro "B" kimberlite has been published by the author of this memory (Xu *et al.*, 2018b). In this case, seven different phlogopite generations have been identified, as macrocrysts, groundmass microcrysts, globular bodies and veinlets cutting globular bodies (Fig. 10.12-10.14, Table 10.2).

The core of phlogopite macrocrysts (Fig. 10.12a-b) is Al-poor (11.5-11.7 wt% Al_2O_3) and Ti-free (<0.3 wt% TiO_2). Phlogopite macrocryst core is replaced by a fist rim (Fig. 10.12a-b) which is Al-rich (around 14.2 wt% Al_2O_3) and Ti-rich (around 3.7 wt% TiO_2) (Fig. 10.13). This rim is mantled by a second rim (outermost rim, Fig. 10.12a-b), which is Ti-poor (1.4-2.1 wt% TiO_2) and Al-poor (10.8-12.9 wt% Al_2O_3). The last zoned unit has a similar composition to the core of groundmass phlogopite (Fig. 10.12c, 10.13).

The above mentioned cores of groundmass phlogopite (0.01-0.1 mm) are covered by Al-free (0-0.4 wt% Al_2O_3) and Ti-free (0.2-0.4 wt% TiO_2) tetraferriphlogopite rims (Fig. 10.12c, 10.13). This tetraferriphlogopite has 1.49-1.70 apfu Fe^{3+} in the tetrahedral position. The contents of Ba remain low in groundmass phlogopite, although the core could contain a little more Ba than the rim (0.2-0.6 wt% and 0-0.2 wt% BaO respectively, Fig. 10.13).

Phlogopite from the globular bodies (Fig. 10.12d) is very different as that found as macrocrysts and groundmass. It is Al-rich (12-14 wt% Al_2O_3) and Ti-poor (<0.5 wt% TiO_2). It is not zoned. It is associated with fine-grained spinel, also with a very different composition when compared with the spinel groundmass.

Phlogopite in veinlets crosscutting these phlogopite-spinel globular bodies (Fig. 10.12d) has the highest Al contents (12.2-16.4 wt% Al_2O_3, Fig.10.13) in this kimberlite and is Ti-poor to Ti-free (0.3-1-2 wt% TiO_2), containing up to 1.12 wt% BaO.

The majority of mica generations from this occurrence have low Cr, except the core of macrocrysts and veins crosscutting globular bodies, which are Cr-rich (Fig. 10.13). There is a positive correlation between Ba and F in phlogopite from globular bodies and its veins, while other phlogopite generations are F-free (Fig. 10.13).

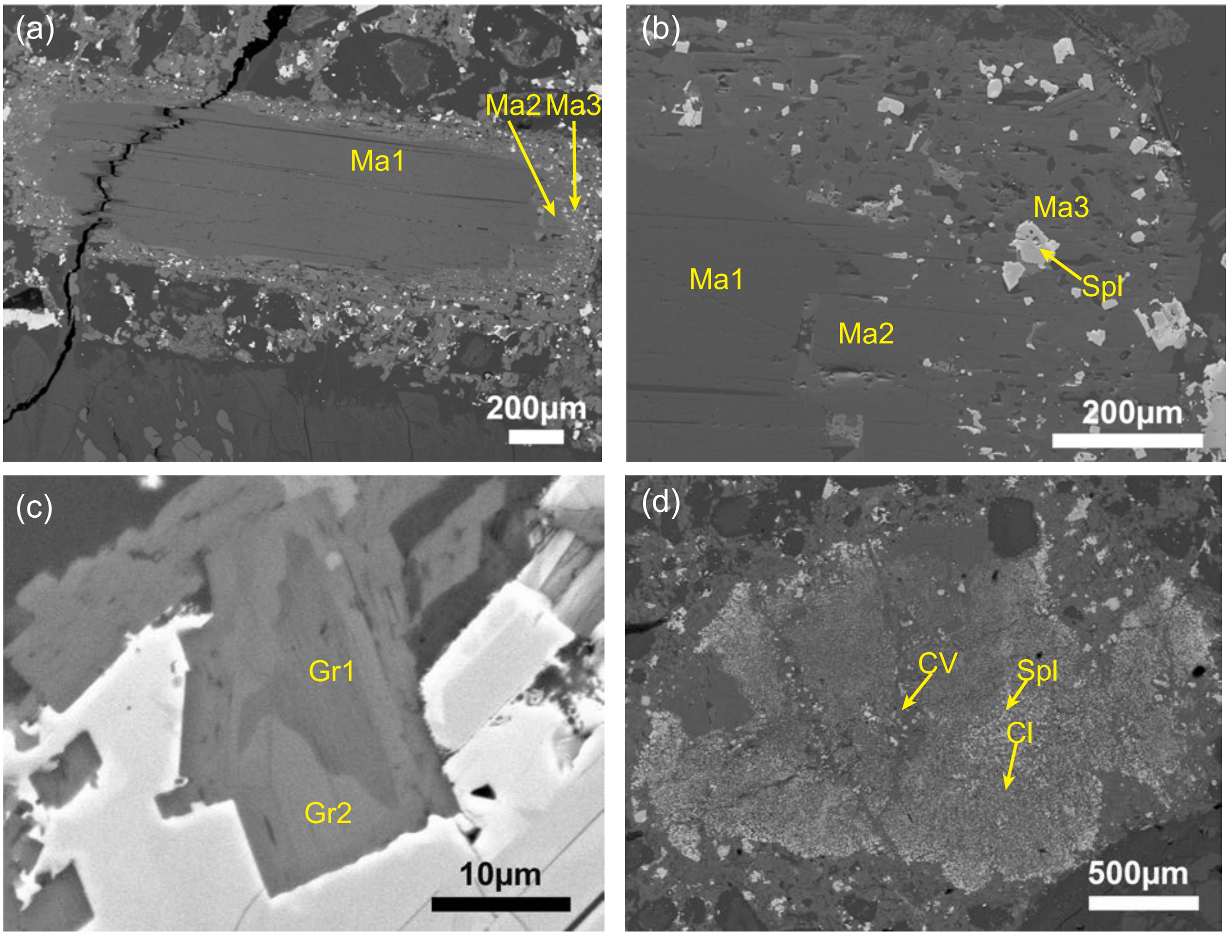

Fig. 10.12. Back-scattered electron (BSE) imagings of micas from the Banankoro kimberlite (occurrence A). a) Macrocrystal phlogopite core (Ma1) shows a first reaction rim (Ma2) and an outermost rim (M3). b) Detail of the above image. Spinel (Spl) is found as inclusions only in the outer phlogopite rim (Ma3); (c) Groundmass phlogopite showing a phlogopite core (Gr1) replaced by a tetraferriphlogopite rim (Gr2). (d) Globular body of phlogopite (Cl) and spinel (Spl) crosscut by veins of phlogopite (CV).

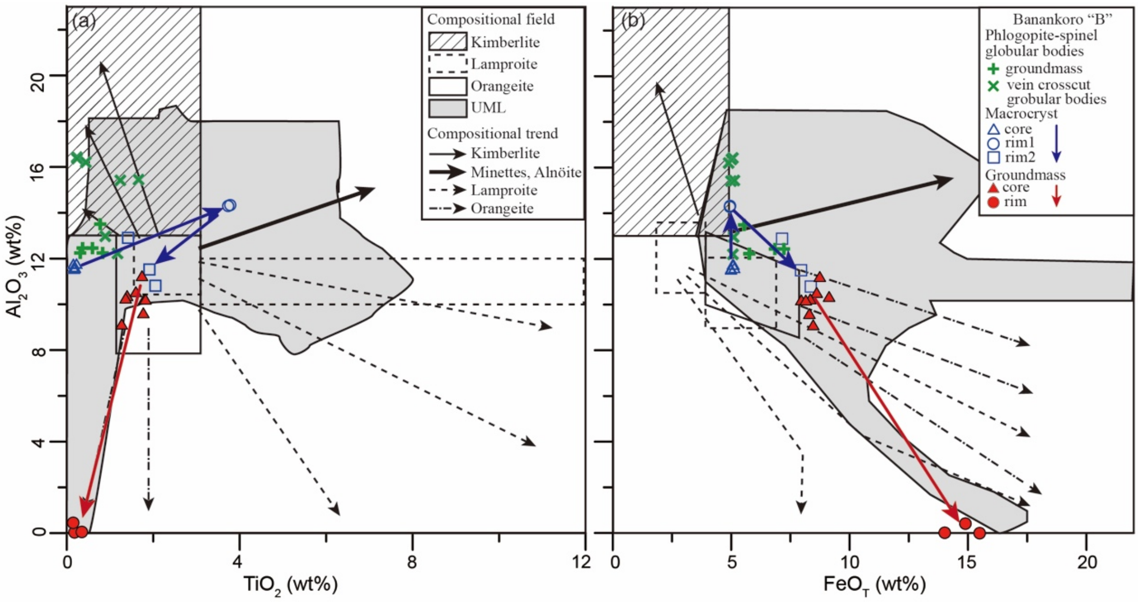

Fig. 10.13. Al_2O_3 vs. TiO_2 (wt%) and Al_2O_3 vs. FeO_T (wt%) compositional variation of phlogopite in Banankoro A. Compositional fields and trends for micas from kimberlites, lamproites, orangeites and minettes are from Mitchell (1995). UML field is from (Mitchell et al. (1999) and Tappe et al. (2004, 2006, 2014). TFP: tetraferriphlogopite.

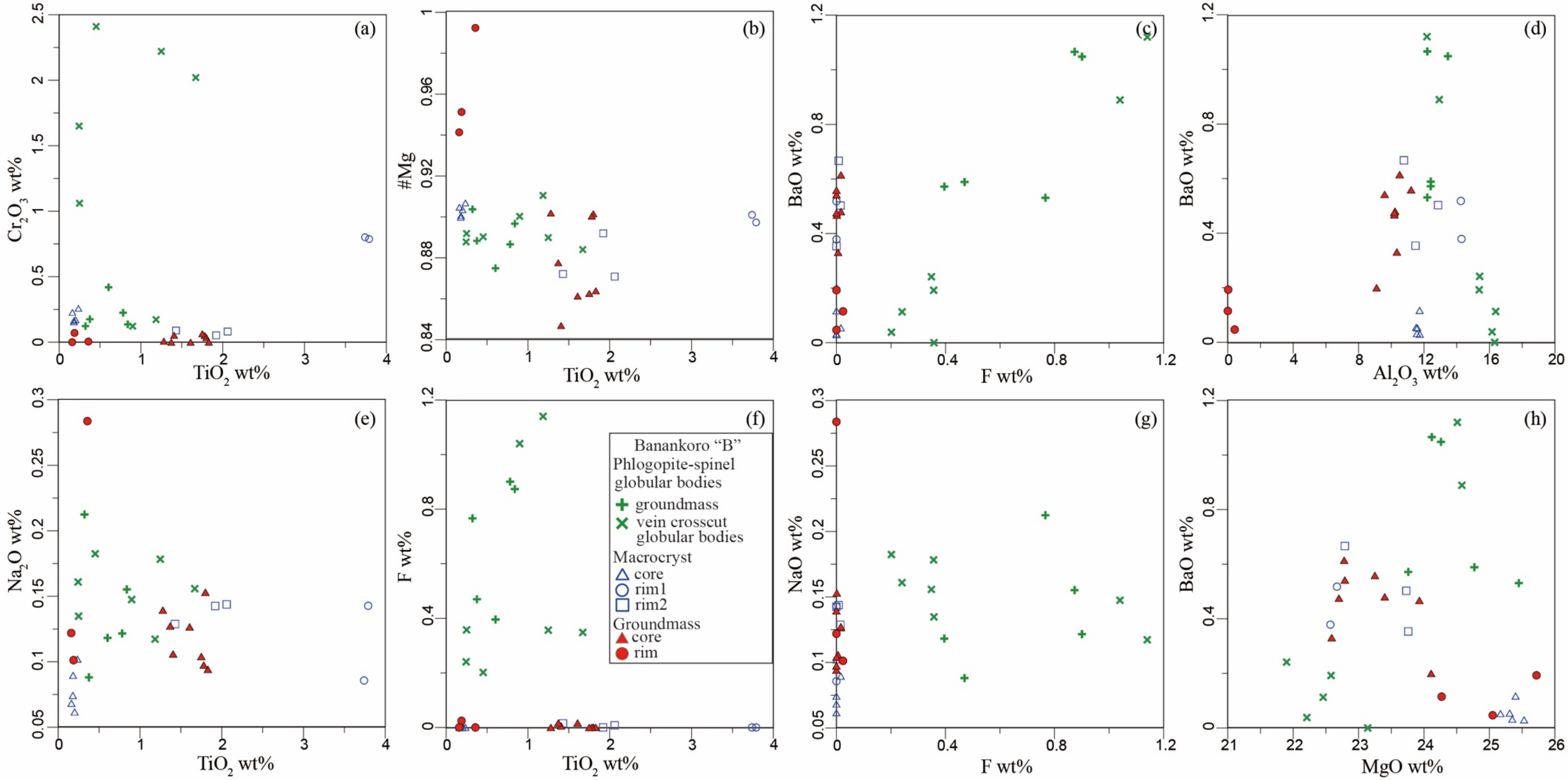

Fig. 10.14. Composition of micas in Banankoro "A". (a)TiO$_2$ (wt%) vs. Cr$_2$O$_3$ (wt%). (b) TiO$_2$ (wt%) vs. #Mg, #Mg=Mg/(Mg+Fe^{2+}). (c) F vs. BaO wt%. (d) Al$_2$O$_3$ vs. BaO. (e) TiO$_2$ (wt%) vs. Na$_2$O (wt%). (f) F (wt%) vs. TiO$_2$ (wt%). (g) Na$_2$O (wt%) vs. F (wt%). (h) BaO (wt%) vs. MgO (wt%).

Table 10.2. Representative compositions of micas from the Banankoro "B" kimberlite.

	1	2	3	4	5	6	7	8	9	10
	Banankoro "A"									
	Veinlet in olivine	Macrocryst			Clast		Groundmass			
(wt%)		core	rim1	rim2	groundmass	veinlet	core	core	rim	rim
SiO_2	40.24	41.81	38.42	39.08	38.60	39.37	40.73	40.47	41.78	42.24
Al_2O_3	12.20	11.73	14.25	11.48	12.41	16.32	10.23	10.19	bdl	0.03
FeO	4.83	4.77	4.44	5.13	5.55	5.00	5.82	4.66	2.22	0.35
Fe_2O_3	1.02	0.36	0.54	3.11	1.42	0.00	2.78	3.65	14.71	15.14
TiO_2	0.32	0.16	3.74	1.92	0.38	0.25	1.37	1.80	0.19	0.36
Cr_2O_3	0.12	0.23	0.80	0.05	0.18	1.06	bdl	0.04	0.07	bdl
V_2O_3	0.02	bdl	bdl	0.04	0.04	0.02	bdl	0.05	0.05	0.07
MnO	0.09	0.05	0.04	0.19	0.09	0.12	0.15	0.16	0.27	0.29
NiO	0.03	0.16	0.09	bdl	bdl	bdl	0.03	0.06	0.02	0.04
MgO	25.45	25.40	22.67	23.76	24.77	23.14	23.40	23.93	24.27	25.72
K_2O	9.21	9.88	8.94	9.29	8.95	9.86	9.20	9.09	9.80	9.22
BaO	0.53	0.12	0.52	0.35	0.59	bdl	0.48	0.47	0.11	0.19
Na_2O	0.21	0.07	0.09	0.14	0.09	0.13	0.13	0.15	0.10	0.28
CaO	0.04	0.01	0.05	0.04	0.02	bdl	0.04	0.08	0.05	0.16
SrO	0.06	bdl	0.13	0.05	0.09	bdl	0.07	bdl	0.05	bdl
F	0.77	bdl	bdl	bdl	0.47	0.36	0.02	bdl	0.02	bdl
H_2O	3.79	4.19	4.17	4.12	3.85	4.04	4.11	4.14	3.95	4.02
Total	98.62	98.96	98.90	98.76	97.29	99.54	98.55	98.95	97.65	98.15
(apfu)	Cations on basis of 24 (O, OH, F)									
Si	5.812	5.983	5.526	5.689	5.687	5.607	5.937	5.863	6.324	6.297
Al	2.077	1.978	2.415	1.970	2.155	2.393	1.757	1.740	-	-
Fe^{3+}	0.111	0.039	0.059	0.341	0.158	-	0.305	0.397	1.675	1.699
∑IV	8.000	8.000	8.000	8.000	8.000	8.000	8.000	8.000	8.000	8.000
Al	-	-	-	-	-	0.347	-	-	-	-
Ti	0.035	0.017	0.405	0.210	0.042	0.027	0.150	0.196	0.021	0.040
Cr	0.014	0.026	0.091	0.006	0.020	0.119	-	-	0.008	-
V	-	-	-	-	-	-	-	0.006	0.006	0.008
Mn	0.011	0.005	0.005	0.023	0.012	0.014	0.018	0.019	0.034	0.037
Fe^{2+}	0.584	0.570	0.534	0.625	0.684	0.596	0.709	0.565	0.281	0.044
Ni	-	0.018	0.010	-	-	-	-	0.007	0.002	-
Mg	5.480	5.419	4.861	5.157	5.238	4.913	5.085	5.168	5.476	5.716
∑VI	6.131	6.056	5.906	6.026	6.000	6.019	5.966	5.965	5.830	5.849
K	1.697	1.803	1.640	1.725	1.682	1.791	1.711	1.680	1.892	1.753
Ba	0.030	0.007	0.029	0.020	0.034	-	0.027	0.027	0.007	0.011
Na	0.059	0.019	0.024	0.040	0.025	0.037	0.036	0.043	0.030	0.082
Ca	0.006	-	0.007	0.007	-	-	0.006	0.012	0.008	0.026
Sr	-	-	0.011	-	0.007	-	0.006	0.000	0.004	-
∑A	1.798	1.831	1.711	1.796	1.752	1.829	1.786	1.761	1.941	1.873
F	0.350	-	-	-	0.219	0.161	0.007	-	0.012	-
OH	3.650	4.000	4.000	4.000	3.781	3.839	3.993	3.999	3.988	4.000

bdl: below detection limit; FeO and Fe_2O_3 recalculated

10.4.2. Karowe AK6 South pipe kimberlite, Botswana

Subhedral-anhedral groundmass mica from this pipe shows a compositional range between tetraferriphlogopite, fluortetraferriphlogopite (F > 2apfu, on basis 24 (O,OH, F)) and phlogopite (Table. 10.3). It shows a poor zoning, although some crystals display better zonation as shown in Fig. 10.15.

In some cases, it evolves within the tetraferriphlogopite field showing a slightly depletion of Ti and Ba accompanied by enrichment of Na and F (Gr a1-2, Fig. 10.15-17). In some other crystals, the tetraferriphlogopite core is mantled or replaced by phlogopite whith an enrichment in Al and a depletion of Ti, F, Na and Ba (Gr b1-2 and Gr c1-2, Fig. 10.15-17).

In general, tetraferriphlogopite from this occurrence has large variations in the Na_2O contents (0.7-2.5 wt% Na_2O) and is F-rich (2.6-5.3 wt% F). High Na and F tenors in micas were proposed as typical of lamproites (Mitchell, 1995).

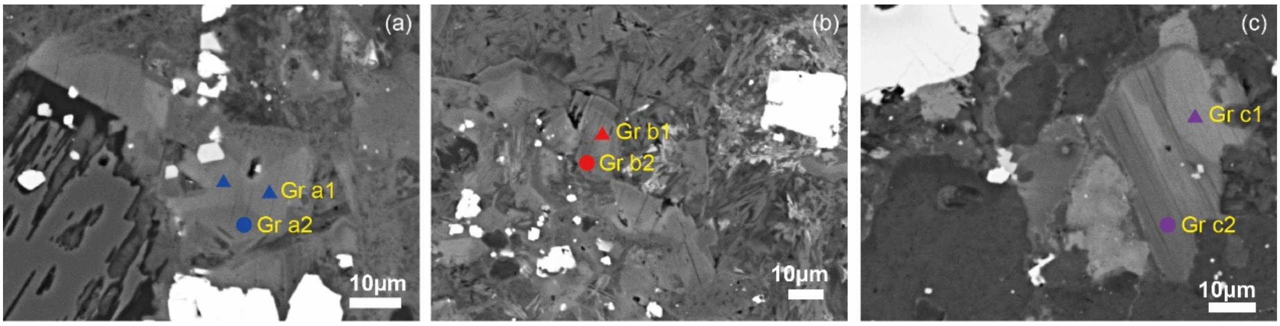

Fig. 10.15. Back-scattered electron (BSE) imagings of micas from Karowe AK6 South pipe kimberlite. (a-b) Groundmass mica showing a tetraferriphlogopite core (Gr a1, Gr b1) replaced by a phlogopite rim (Gr a2, Gr b2). (c) Groundmass mica showing a tetraferriphlogopite core (Gr c1) replaced by another tetraferriphlogopite rim (Gr c2).

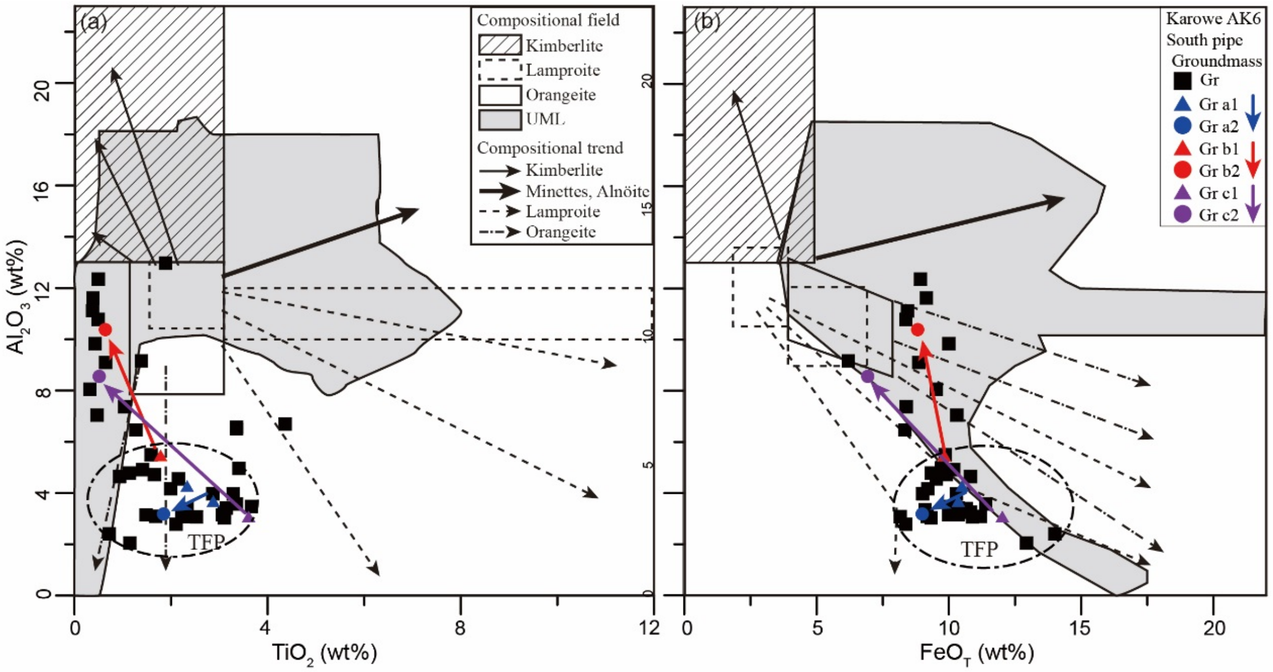

Fig. 10.16. Al_2O_3 vs. TiO_2 (wt%) and Al_2O_3 vs. FeO_T (wt%) compositional variation of groundmass (Gr) mica in south pipe of Karowe AK6. Some analyses (Gr a1-2, Grb1-2, Grc1-2) correspond with the points indicated in Fig. 10.15. Compositional fields and trends for micas from kimberlites, lamproites, orangeites and minettes are from Mitchell (1995). UML field is from (Mitchell et al. (1999) and Tappe et al. (2004, 2006, 2014). TFP: tetraferriphlogopite.

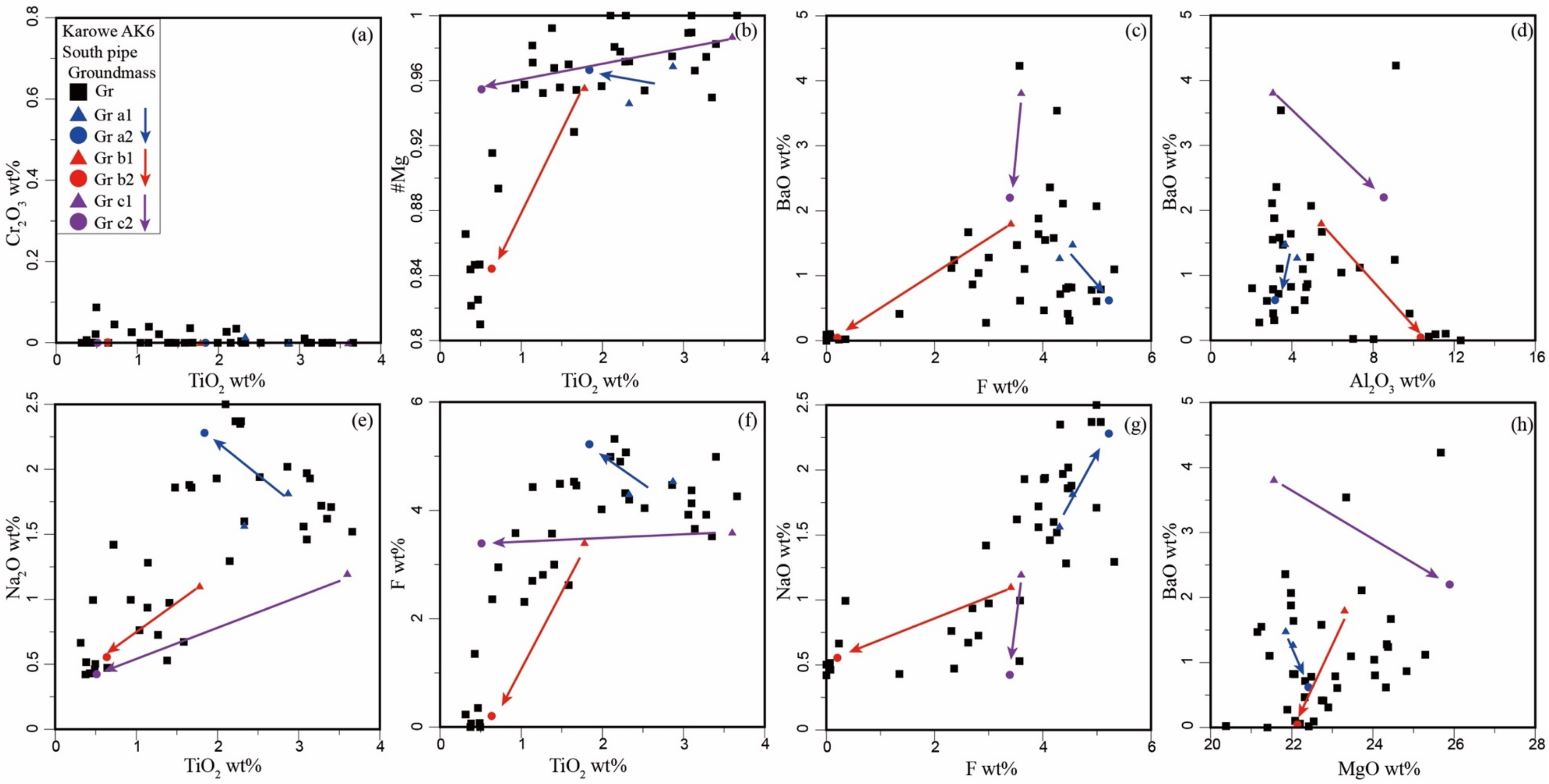

Fig. 10.17. Composition of groundmass (Gr) mica in the south pipe of Karowe Ak-6. Some analyses (Gr a1-2, Grb1-2, Grc1-2) are the points indicated in Fig. 10.15. (a) TiO_2 (wt%) vs. Cr_2O_3 (wt%). (b) TiO_2 (wt%) vs. #Mg, #Mg=Mg/(Mg+Fe^{2+}). (c) F (wt%) vs. BaO (wt%). (d) Al_2O_3 (wt%) vs. BaO (wt%). (e) TiO_2 (wt%) vs. Na_2O (wt%). (f) F (wt%) vs. TiO_2 (wt%). (g) Na_2O (wt%) vs. F (wt%). (h) BaO (wt%) vs. MgO (wt%).

Table 10.3. Representative compositions of micas from Karowe AK6 and Riverton kimberlites.

	1	2	3	4	5	6	7	8	9	10	11
	Karowe AK6						Riverton				
	Groundmass						Micropehnocryst				
(wt%)	a1	a2	b1	b2	c1	c2	a1	a2	a3	a4	a5
SiO_2	42.00	44.74	41.42	41.02	39.33	41.26	41.74	39.83	36.15	39.99	41.50
Al_2O_3	3.67	3.17	5.45	10.35	3.07	8.53	10.77	12.66	16.11	13.76	0.43
FeO	1.24	1.38	1.92	7.28	0.49	2.19	3.29	3.22	3.39	3.43	1.35
Fe_2O_3	10.15	8.48	8.80	1.73	12.82	5.30	1.79	1.46	0.00	0.00	15.90
TiO_2	2.87	1.84	1.78	0.64	3.60	0.51	0.34	3.16	1.38	0.33	0.46
Cr_2O_3	bdl	bdl	bdl	bdl	bdl	bdl	0.20	1.52	0.16	bdl	bdl
V_2O_3	0.03	bdl	0.03	0.04	0.02	bdl	bdl	0.29	0.13	bdl	bdl
MnO	0.07	0.04	0.13	0.26	0.10	0.08	bdl	bdl	bdl	0.06	0.13
NiO	bdl	0.03	bdl	bdl	0.03	bdl	0.18	0.18	0.03	bdl	bdl
MgO	21.85	22.41	23.30	22.14	21.56	25.89	25.69	22.52	24.27	26.94	26.11
K_2O	9.42	9.92	9.24	9.87	8.25	9.13	10.48	10.03	8.77	9.90	8.32
BaO	1.49	0.62	1.81	0.05	3.82	2.20	0.11	0.09	4.36	0.64	0.06
Na_2O	1.82	2.28	1.10	0.56	1.20	0.42	0.11	0.13	0.08	0.03	0.34
CaO	0.04	0.03	0.48	0.43	0.05	0.08	bdl	0.02	0.02	0.03	0.06
SrO	0.06	bdl	0.04	bdl	bdl	0.07	0.07	bdl	bdl	bdl	bdl
F	1.92	2.20	1.44	0.09	1.52	1.43	0.62	0.51	0.75	0.42	1.82
H_2O	1.89	1.64	2.47	3.99	2.24	2.54	3.89	3.94	3.72	4.01	3.18
Total	98.51	98.77	99.40	98.44	98.09	99.63	99.27	99.56	99.33	99.55	99.66
(apfu)	Cations on basis of 24 (O, OH, F)										
Si	6.226	6.525	6.084	6.019	5.982	5.969	5.987	5.705	5.314	5.693	6.152
Al	0.641	0.545	0.943	1.790	0.550	1.454	1.820	2.137	2.686	2.307	0.074
Fe^{3+}	1.132	0.930	0.972	0.191	1.467	0.577	0.193	0.157	0.000	0.000	1.774
Ti	0.000	0.000	0.000	0.000	0.000	0.000	0.000	0.000	0.000	0.000	0.000
∑IV	8.000	8.000	8.000	8.000	8.000	8.000	8.000	8.000	8.000	8.000	8.000
Al	-	-	-	-	-	-	0.000	0.000	0.104	0.002	0.000
Ti	0.320	0.202	0.197	0.070	0.412	0.056	0.036	0.340	0.153	0.035	0.052
Cr	-	-	-	-	-	-	0.022	0.172	0.018	-	-
V	0.004	-	0.003	0.005	0.002	-	-	0.033	0.016	-	-
Mn	0.009	0.005	0.016	0.032	0.012	0.010	-	-	-	0.008	0.017
Fe^{2+}	0.153	0.169	0.236	0.894	0.063	0.265	0.395	0.385	0.417	0.408	0.168
Ni	-	0.003	-	-	0.003	-	0.020	0.021	0.004	-	-
Mg	4.829	4.872	5.102	4.843	4.889	5.584	5.493	4.809	5.286	5.546	5.754
∑VI	5.315	5.251	5.554	5.845	5.382	5.915	5.971	5.762	6.000	6.000	6.000
K	1.781	1.845	1.731	1.847	1.601	1.685	1.917	1.833	1.644	1.798	1.573
Ba	0.087	0.035	0.104	0.003	0.228	0.125	0.006	0.005	0.251	0.036	0.003
Na	0.523	0.645	0.314	0.158	0.354	0.119	0.031	0.036	0.022	0.009	0.097
Ca	0.006	0.004	0.075	0.068	0.008	0.013	-	0.002	0.003	0.004	0.009
Sr	0.005	-	0.003	-	-	0.006	0.006	-	-	-	-
Mg							0.000	0.000	0.032	0.172	0.016
∑A	2.402	2.530	2.228	2.076	2.191	1.947	1.962	1.876	1.954	2.021	1.702
F	2.133	2.407	1.584	0.094	1.732	1.551	0.282	0.231	0.350	0.190	0.853
OH	1.867	1.593	2.416	3.906	2.269	2.449	3.718	3.769	3.650	3.810	3.147

bdl: below detection limit; FeO and Fe_2O_3 recalculated

10.4.3. Riverton kimberlite, South Africa

Riverton kimberlite has microphenocrysts (0.3-0.6 mm) of phlogopite that display a complex zoning (Fig. 10.18-20, Table 10.3). It shows five concentrically zoned domains, among which the outermost three are also observed in groundmass phlogopite.

Microphenocryst core (zone 1) has slight variations in Al (10.5-13.2 wt% Al_2O_3) and is Ti free to -poor (0.3-0.8 wt% TiO_2), Fe-rich (2.7-6.3 wt% FeO_T), Ba-free (0-0.8 wt% BaO) and Cr-free to -rich (0.2-1.5 wt% Cr_2O_3).

The first rim (zone 2) has also slight variations in Al, which is Al-rich (12.4-14.3 wt% Al_2O_3); Ti is enriched in this domain (2.8-4.1 wt% TiO_2), as well as Fe (4.4-5.3 wt% FeO_T) and Cr (0.9-1.5 wt% Cr_2O_3), whereas Ba is very poor (0.1-0.7 wt% BaO).

Zone 3 is slightly enriched in Al respect with the above zone (15.1-16.8wt% Al_2O_3) but impoverished in Ti (0.8-2.1 wt% TiO_2), Fe (3.2-4.4 wt% FeO_T) and Cr (<0.2 wt% Cr_2O_3); contrastingly, it is enriched in Ba (1.6-6.3 wt% BaO).

Zone 4 has high variations in Al (12.1-15.6 wt% Al_2O_3), Ti (0.3-3 wt% TiO_2), Fe (3.2-6.1 wt% FeO_T), Ba (0.1-1.6 wt% BaO) and Cr (0-1.6 wt% Cr_2O_3).

Zone 5 is the outermost rim, and is made up by tetraferriphlogopite enriched in F (1.4-2.6 wt% F).

The core (zone 1) may be a xenocrystal. Transit from zone 1 to zone 2 is characterized by the enrichment of Ti and Cr and a slight depletion of Mg; the transit from zone 2 to zone 3 reflects enrichment of Ba and Al and depletion of Cr and Ti. The entrance in zone 4 is characterized by the depletion of Ti, Al, Ba and enrichment of Mg. Finally, the pass from 4 to zone 5 is characterized by the depletion of Al and enrichment of Fe and F.

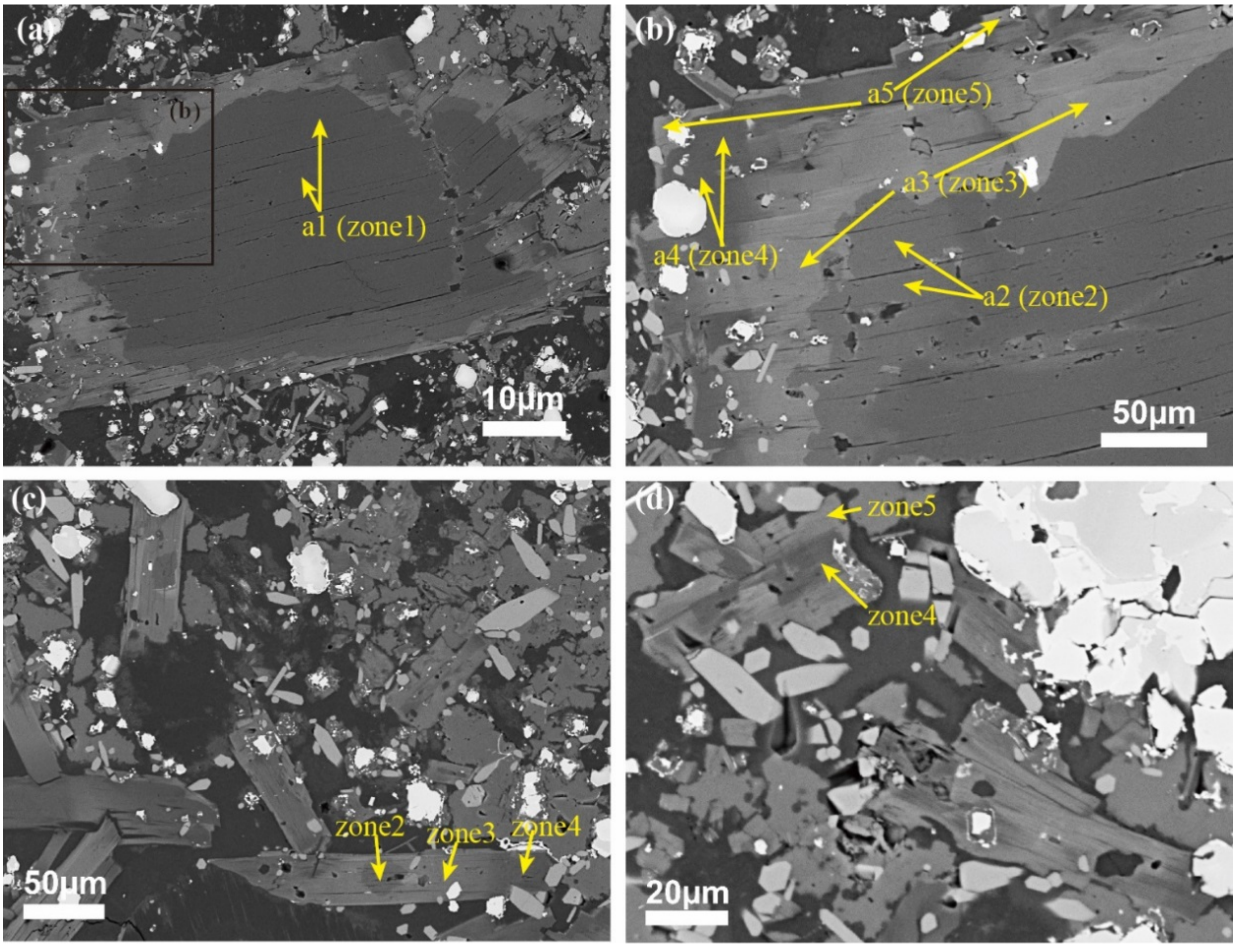

Fig. 10.18. Back-scattered electron (BSE) imagings of micas from Riverton kimberlite. (a-b) Mica micrrophenocrystal showing 5 compositional zones. The points a1 to a5 correspond to the analyses indicated in Fig. 10.19-20. (c-d) Groundmass micas with compositional zones 2 to 5.

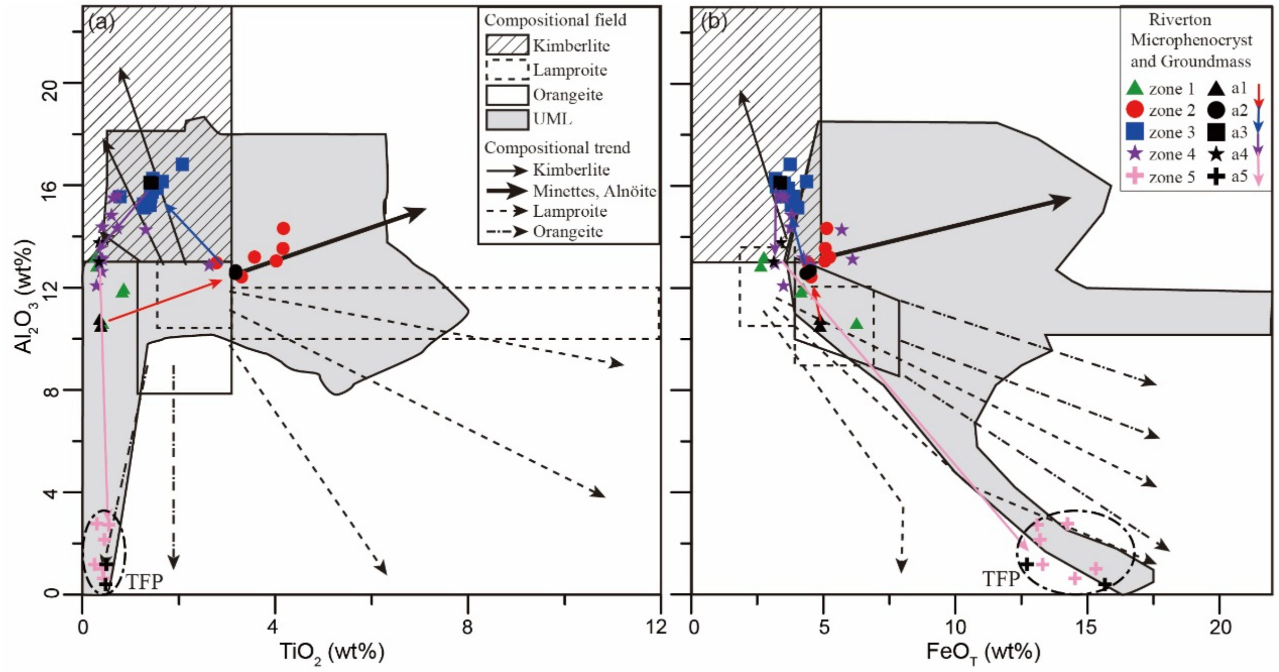

Fig. 10.19. Al_2O_3 vs. TiO_2 (wt%) and Al_2O_3 vs. FeO_T (wt%) diagrams showing the compositional variation (5 zones) of microphenocryst and groundmass mica in Riverton kimberlite. Analyses a1-2 are points indicated in Fig. 10.18. Compositional fields and trends of micas for kimberlites, lamproites, orangeites and minettes from Mitchell (1995). UML field from (Mitchell et al. (1999) and Tappe et al. (2004, 2006, 2014). TFP: tetraferriphlogopite.

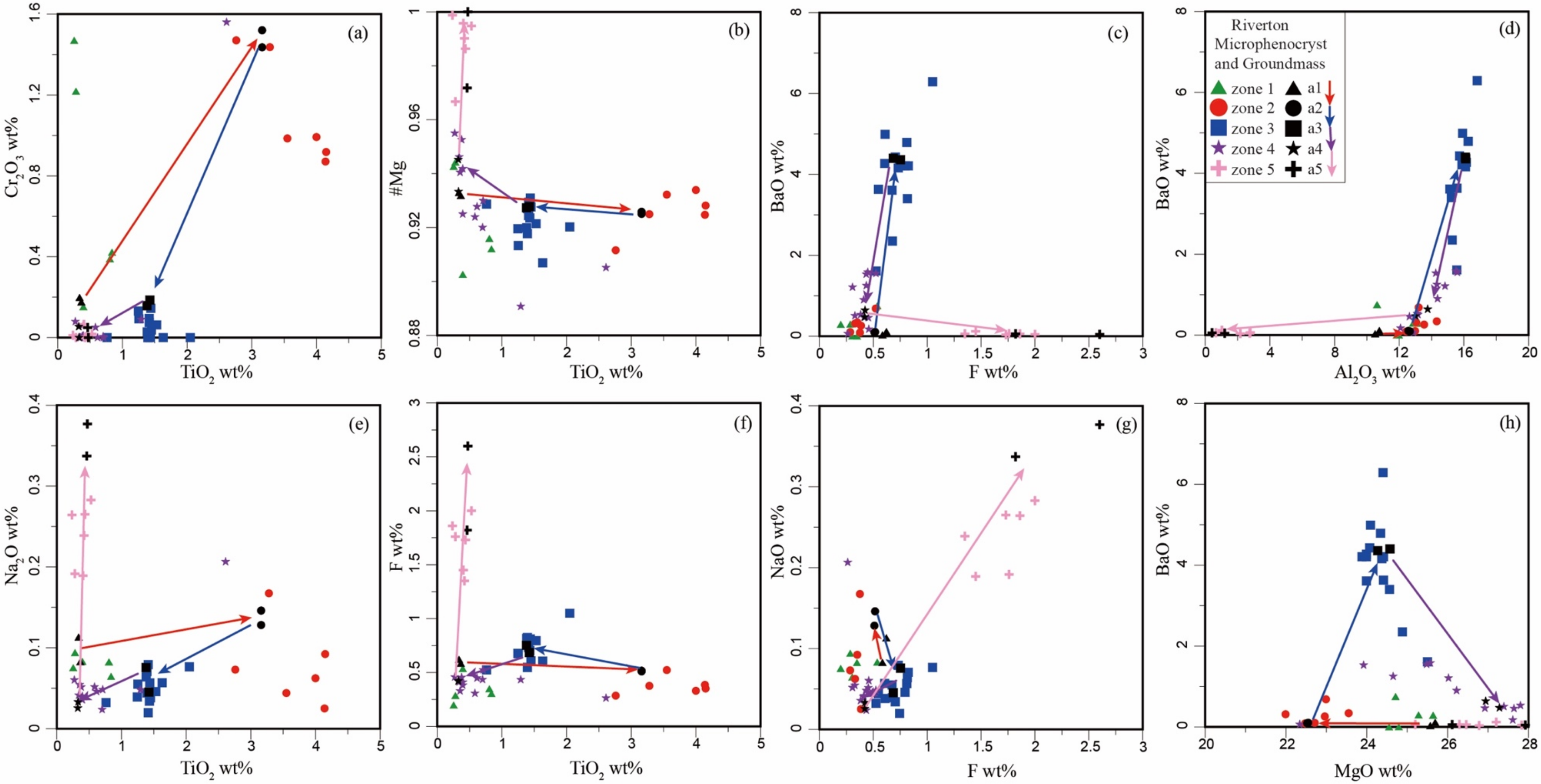

Fig. 10.20. Composition of the five zones of microphenocrystic and groundmass micas in Riverton kimberlite. Some analyses (a1-2) are those indicated in Fig. 10.18. (a) TiO_2 (wt%) vs. Cr_2O_3 (wt%). (b) TiO_2 (wt%) vs. #Mg, #Mg=Mg/(Mg+Fe^{2+}). (c) F (wt%) vs. BaO (wt%). (d) Al_2O_3 (wt%) vs. BaO (wt%). (e) TiO_2 (wt%) vs. Na_2O (wt%). (f) F (wt%) vs. TiO_2 (wt%). (g) Na_2O (wt%) vs. F (wt%). (h) BaO (wt%) vs. MgO (wt%

10.4.4. Bultfontein kimberlite, South Africa

Microphenocrysts (or macrocrysts) and groundmass micas in Bultfontein kimberlite have very complex zoning (labelled as zone 1 to zone 6, following crystallization order, Fig. 10.21-23, Table 10.4). These crystals have a corroded core composed by two different phlogopite compositional zones.

Zone 1 has low Ti contents (0.4-1.5wt% TiO_2). It is Al-poor (11.1-12.8wt% Al_2O_3); Cr contents are low (0.1-0.8 wt% Cr_2O_3).

The second zone is strongly enriched in Ti (2.5-3.6 wt% TiO_2) with respect the former and there are also slightly enrichments in Al (12.3-13.3 wt% Al_2O_3) and Cr (0.7-1.6 wt% Cr_2O_3), with a depletion of Mg. Zone 1 and zone 2 are Ba-free (<0.4 wt% BaO) and they are free of spinel inclusions.

Compared with the above unit, zone 3 is Ti-poor (0.6-1.3wt% TiO_2), but is strongly enriched in Al (17.2-17.6wt% Al_2O_3) and Ba (4.6-5.4 wt% BaO); it is impoverished in Cr (<0.2 wt% Cr_2O_3).

Zone 4 is characterized by a strong enrichment in Ba (6.5-8.4 wt% BaO) and Al (17.7-22.3 wt% Al_2O_3).

Contrastingly, although zone 5 is Ba rich (2.3-5.0 wt% BaO) it is depleted in Ba respect to zone 4.

Depletion of Al and Ba, accompanied by slight enrichment of Mg and F, is shown in the transit from zone 5 to zone 6.

Finally, phlogopite crystals from fine-grained spinel-phlogopite globular bodies have similar compositions as those from phlogopite of zone 5.

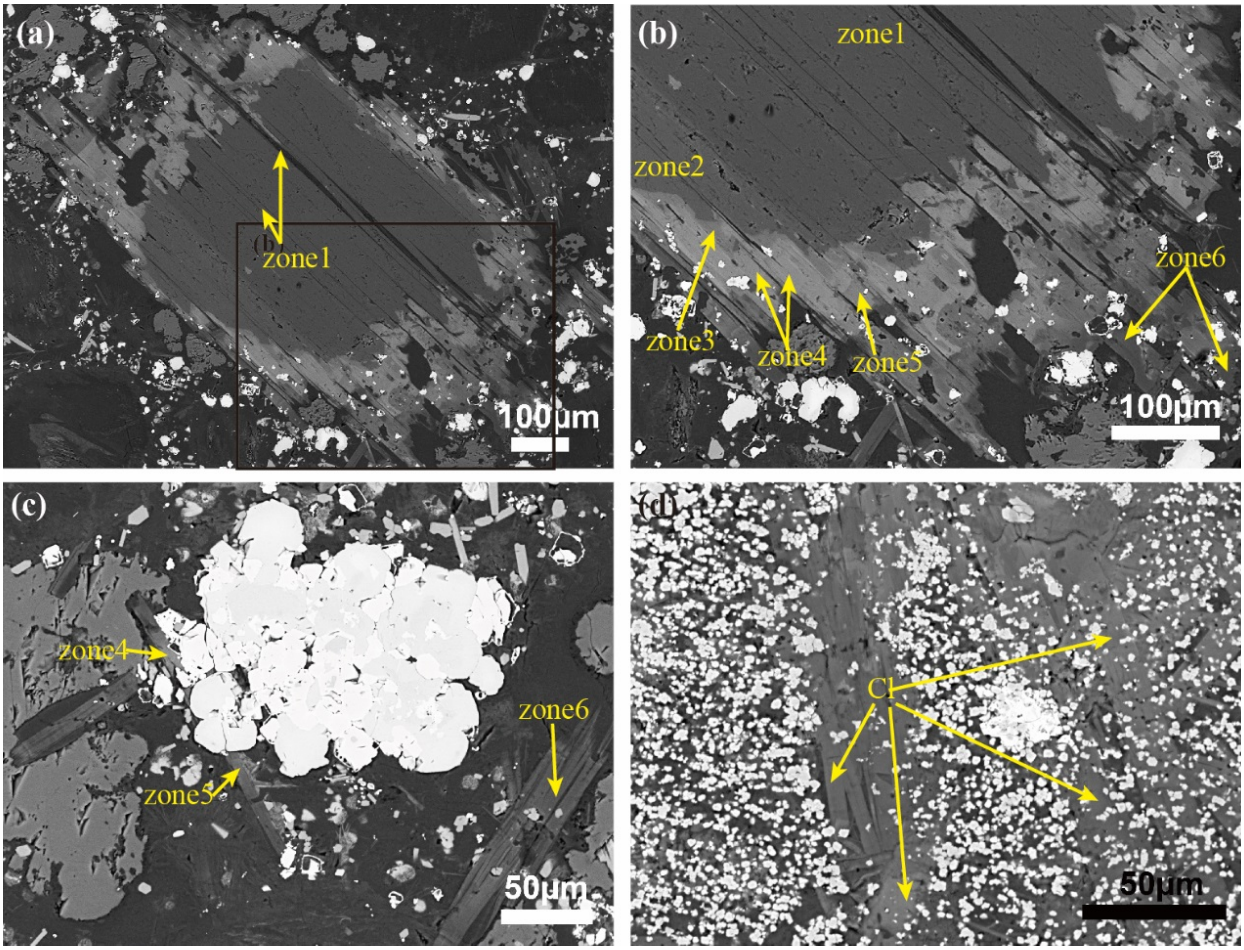

Fig. 10.21. Back-scattered electron (BSE) images of micas from the Bultfontein kimberlite. (a-b) Mica microphenocrystals showing six compositional zones. (c) Groundmass micas displaying compositional zones 4 to 6. (d) Detail of phlogopite in spinel-phlogopite globular body (Cl).

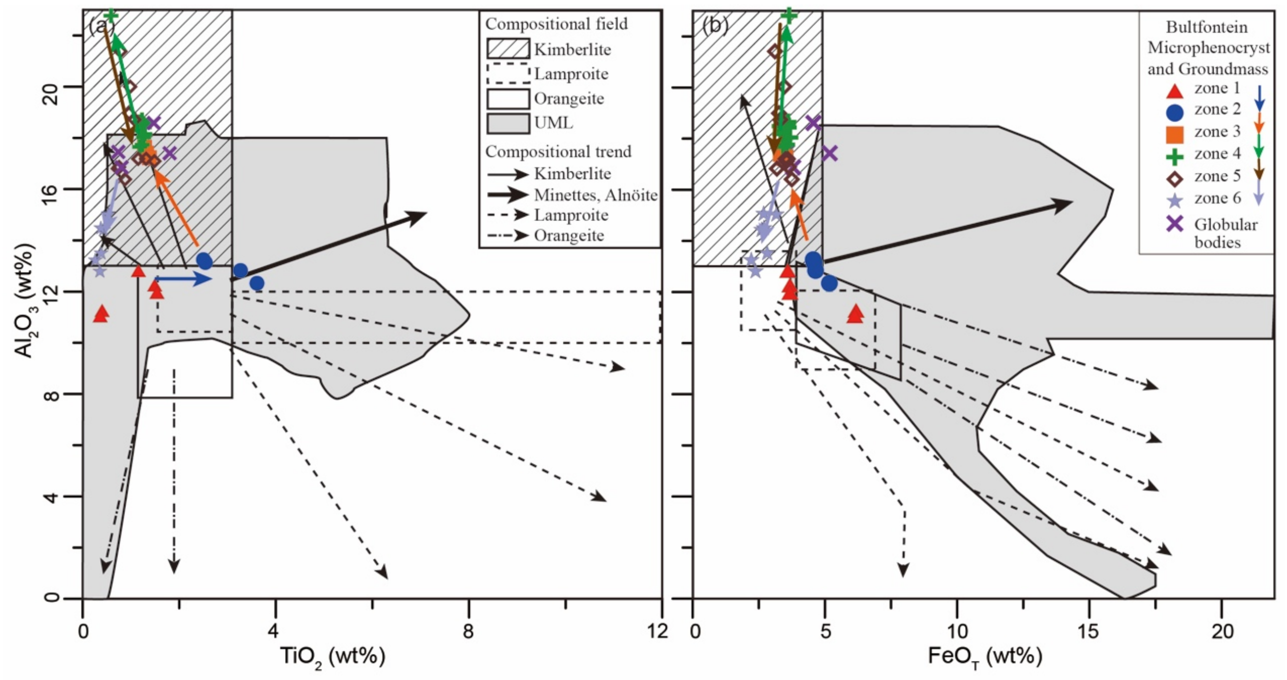

Fig. 10.22. Al_2O_3 vs. TiO_2 (wt%) and Al_2O_3 vs. FeO_T (wt%) compositional variation in the six zones of microphenocrystic and groundmass mica in Bultfontein kimberlite. Compositional fields and trends for micas from kimberlites, lamproites, orangeites and minette micas adapted from Mitchell (1995). UML field from (Mitchell et al. (1999) and Tappe et al. (2004, 2006, 2014)

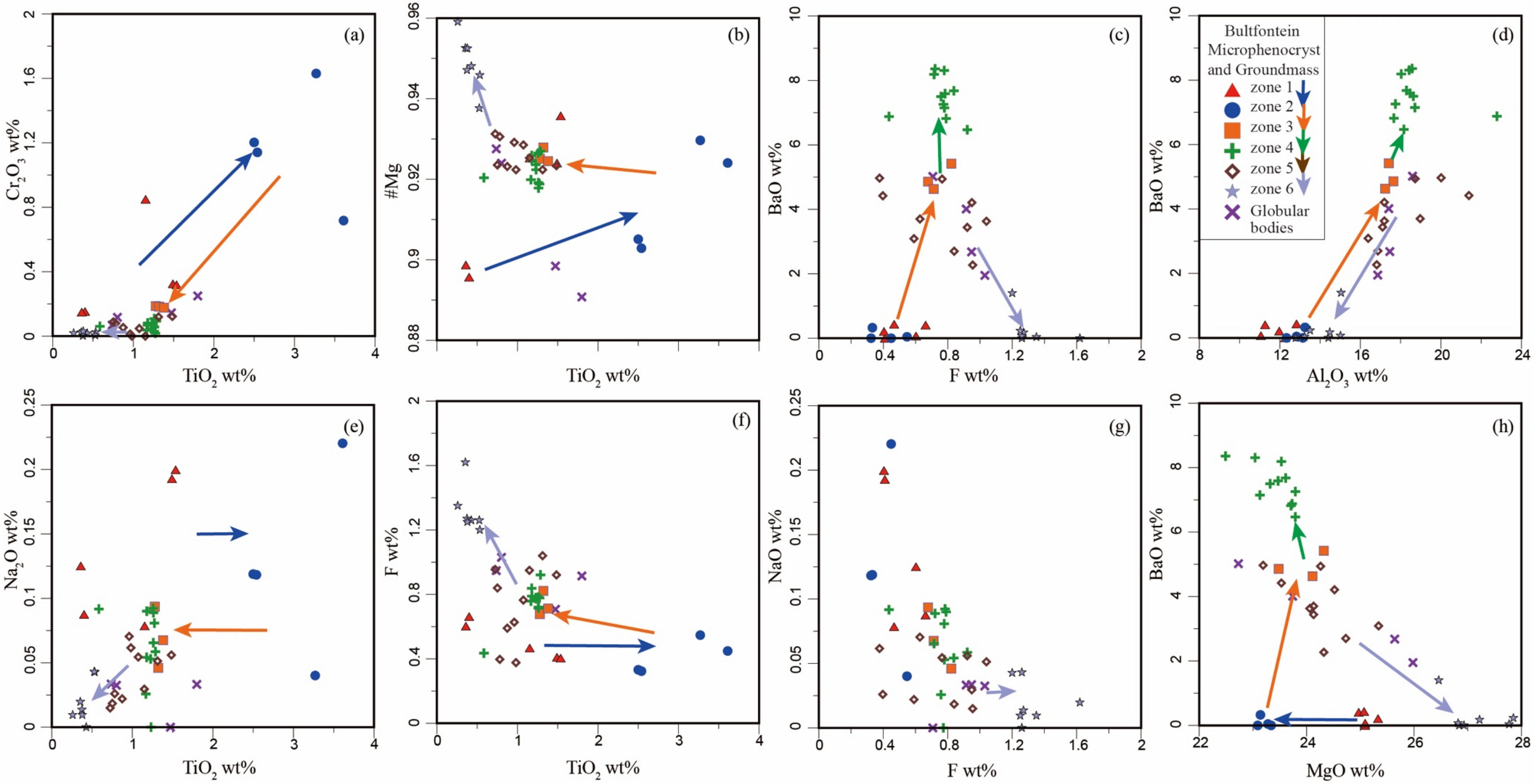

Fig. 10.23. Compositional variation in the six zones of microphenocrysts and groundmass mica in Bultfontein kimberlite. (a) TiO_2 (wt%) vs. Cr_2O_3 (wt%). (b) TiO_2 (wt%) vs. #Mg, #Mg=Mg/(Mg+Fe^{2+}). (c) F (wt%) vs. BaO (wt%). (d) Al_2O_3 (wt%) vs. BaO (wt%). (e) TiO_2 (wt%) vs. Na_2O (wt%). (f) F (wt%) vs. TiO_2 (wt%). (g) Na_2O (wt%) vs. F (wt%). (h) BaO (wt%) vs. MgO (wt%).

Table 10.4. Representative compositions of mica from Bultfontein, Point Lake and Snap Lake kimberlite.

	1	2	3	4	5	6	7	8	9	10	11	12	13
	Bultfontein							Point Lake			Snap Lake		
	Micropehnocryst and Groundmass						Clast	Micropehnocryst and Groundmass					Rim of garnet
(wt%)	zone 1	zone 2	zone 3	zone 4	zone 5	zone 6		zone 1	zone 2	zone 3	zone 1	zone 2	
SiO_2	42.36	40.63	35.40	34.66	38.61	39.69	34.18	29.97	34.77	38.69	37.19	32.53	38.65
Al_2O_3	11.06	13.14	17.23	17.66	16.81	15.01	18.59	19.15	18.27	16.91	15.48	17.61	14.97
FeO	5.04	4.43	3.51	3.44	3.20	3.18	4.58	3.20	3.10	3.18	3.32	3.55	4.06
Fe_2O_3	1.22	0.19	0.00	0.00	0.00	0.00	0.00	0.00	0.00	0.00	0.00	0.00	0.00
TiO_2	0.36	2.54	1.38	1.18	0.72	0.53	1.47	1.27	0.90	0.75	0.17	0.95	0.43
Cr_2O_3	0.15	1.14	0.18	0.08	0.03	bdl	0.14	0.03	bdl	bdl	0.05	0.04	4.27
V_2O_3	bdl	bdl	bdl	bdl	bdl	bdl	bdl	bdl	bdl	bdl	bdl	bdl	bdl
MnO	bdl	0.02	bdl	0.02	0.04	0.06	0.04	bdl	bdl	0.03	bdl	bdl	0.03
NiO	0.05	0.03	0.05	bdl	bdl	bdl	bdl	bdl	bdl	bdl	0.07	0.05	bdl
MgO	25.09	23.09	24.11	23.71	24.32	26.82	22.73	22.46	24.09	25.04	26.28	23.65	22.41
K_2O	10.33	10.24	8.71	8.28	9.44	10.03	8.35	5.43	8.43	10.02	9.41	6.80	9.07
BaO	bdl	bdl	4.63	6.82	2.27	bdl	5.02	12.73	5.66	0.53	3.29	10.41	0.14
Na_2O	0.13	0.12	0.07	0.09	bdl	0.04	bdl	0.16	0.04	bdl	bdl	0.13	0.62
CaO	bdl	bdl	bdl	bdl	0.05	0.07	bdl	0.31	0.09	0.06	bdl	bdl	bdl
SrO	bdl	0.03	bdl	0.03	bdl	bdl	0.03	0.20	0.06	0.02	0.07	0.12	0.09
F	0.60	0.32	0.71	0.79	0.95	1.26	0.71	1.29	0.48	0.22	0.65	1.12	0.31
H_2O	3.94	4.06	3.75	3.68	3.75	3.65	3.72	3.23	3.85	4.13	3.82	3.41	4.02
Total	100.32	99.99	99.72	100.45	100.20	100.34	99.55	99.43	99.74	99.57	99.79	100.37	99.07
(apfu)	Cations on basis of 24 (O, OH, F)												
Si	6.018	5.778	5.196	5.126	5.515	5.599	5.058	4.677	5.116	5.487	5.402	4.951	5.563
Al	1.852	2.202	2.804	2.874	2.485	2.401	2.942	3.323	2.884	2.513	2.598	3.049	2.437
Fe^{3+}	0.131	0.020	0.000	0.000	0.000	0.000	0.000	0.000	0.000	0.000	0.000	0.000	0.000
Ti	0.000	0.000	0.000	0.000	0.000	0.000	0.000	0.000	0.000	0.000	0.000	0.000	0.000
∑IV	8.000	8.000	8.000	8.000	8.000	8.000	8.000	8.000	8.000	8.000	8.000	8.000	8.000
Al	0.000	0.000	0.176	0.204	0.345	0.095	0.300	0.199	0.284	0.313	0.051	0.109	0.102
Ti	0.038	0.272	0.152	0.131	0.078	0.056	0.164	0.150	0.099	0.080	0.019	0.109	0.047
Cr	0.017	0.128	0.020	0.010	0.003	-	0.017	0.004	-	-	0.005	0.004	0.486
V	-	-	-	-	-	-	-	-	-	-	-	-	-
Mn	-	0.003	-	0.003	0.005	0.007	0.005	-	-	0.003	-	-	0.004
Fe^{2+}	0.599	0.527	0.431	0.425	0.382	0.375	0.567	0.418	0.381	0.377	0.403	0.452	0.489
Ni	0.006	0.004	0.005	-	-	-	-	-	-	-	0.008	0.006	-
Mg	5.314	4.895	5.215	5.225	5.179	5.467	4.947	5.226	5.229	5.222	5.509	5.318	4.808
∑VI	5.983	5.828	6.000	6.000	5.993	6.000	6.000	5.998	6.000	6.000	6.000	6.000	5.942
K	1.872	1.857	1.631	1.562	1.720	1.805	1.576	1.081	1.582	1.813	1.743	1.320	1.665
Ba	-	-	0.266	0.395	0.127	-	0.291	0.778	0.326	0.030	0.187	0.621	0.008
Na	0.034	0.033	0.019	0.026	-	0.012	-	0.047	0.011	-	-	0.039	0.172
Ca	-	-	-	-	0.008	0.011	-	0.052	0.015	0.009	-	-	-
Sr	-	0.002	-	0.003	-	-	0.002	0.018	0.005	0.002	0.006	0.011	0.007
Mg	0.000	0.000	0.060	0.003	0.000	0.174	0.067	0.000	0.056	0.072	0.181	0.048	0.000
∑A	1.910	1.892	1.976	1.992	1.860	2.005	1.937	1.976	1.996	1.926	2.126	2.039	1.853
F	0.271	0.145	0.331	0.369	0.431	0.562	0.331	0.637	0.224	0.097	0.299	0.539	0.141
OH	3.729	3.855	3.669	3.631	3.569	3.438	3.669	3.363	3.776	3.903	3.701	3.461	3.859

bdl: below detection limit; FeO and Fe_2O_3 recalculated

10.4.5. Point Lake kimberlite, Canada

Microphenocrystic phlogopite and groundmass phlogopite have three compositional zonings (from core to outermost rim: zone 1 to zone 3, Fig. 10.24-26, Table 10.4) which display a depletion of Ba accompanied by a slight depletion of Al and F. All of them plot within kimberlite mica field (Fig. 10.26).

The core of microphenocrysts has the highest Ba contents in this kimberlite (10.4-15.1 wt% BaO) and is also very enriched in Al (18.6-19.4 wt% Al_2O_3); F contents are noticeable (0.9-1.3 wt% F).

Zone 2 is slightly impoverished in some of these elements when compared with the above zone: Ba is strongly depleted (3.6-8.3 wt% BaO) as well as F (0.3-0.5 wt% F), but the Al contents remain constant (18.0-19.3 wt% Al_2O_3).

Finally, the zone 3 is Ba-free (0-0.5 wt% BaO), and is also slightly impoverished in Al (13.9-17.3wt% Al_2O_3) and in F (0.1-0.3 wt% F).

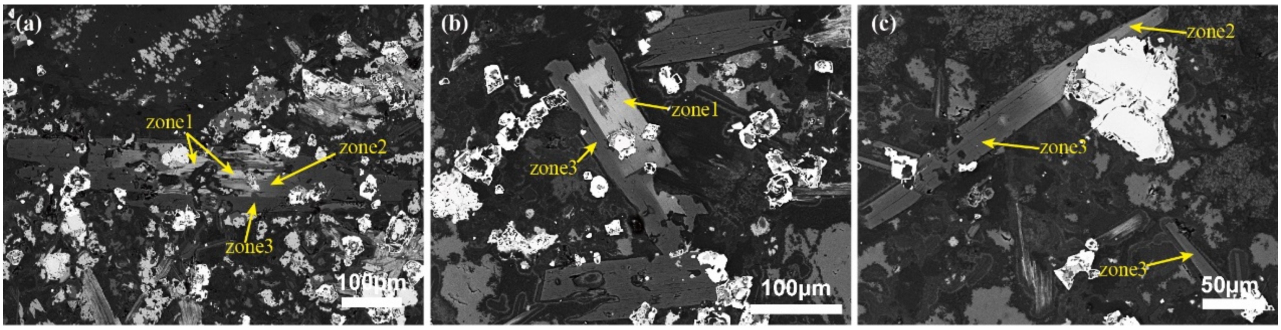

Fig. 10.24. Back-scattered electron (BSE) imagings of micas from Point Lake kimberlite. (a-b) Microphenocrystic mica showing three compositional zones. (b-c) Groundmass micas displaying the compositional zones 1 to 3.

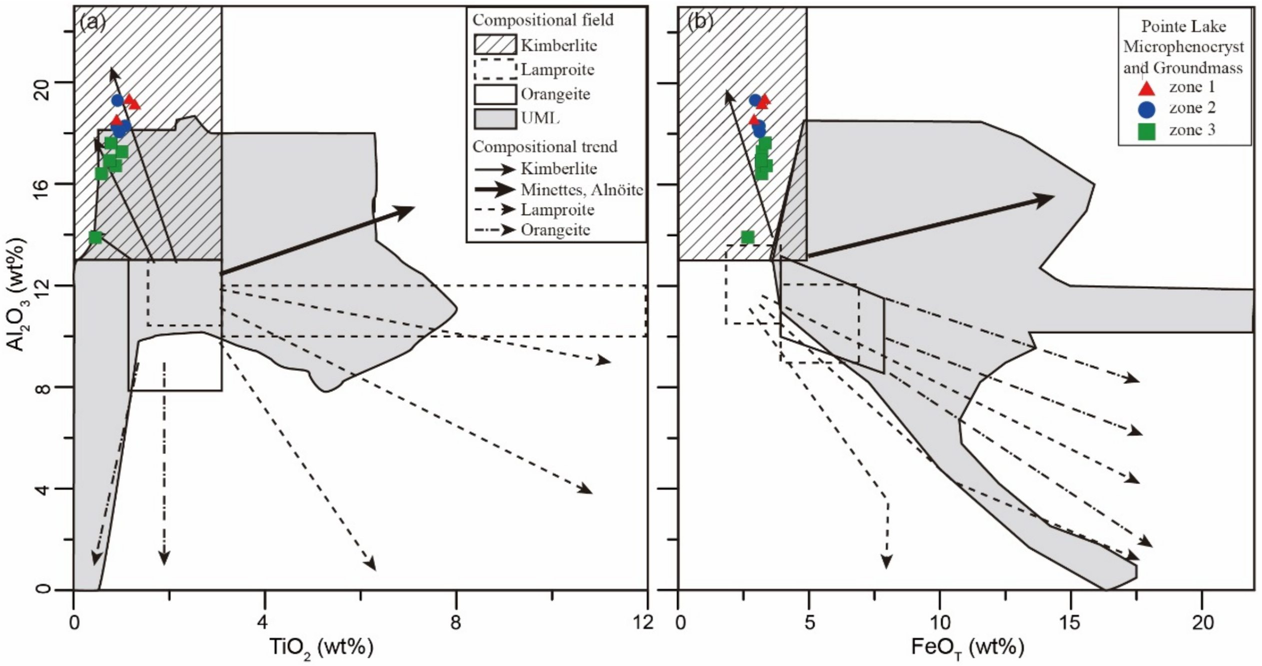

Fig. 10.25. Al_2O_3 vs. TiO_2 (wt%) and Al_2O_3 vs. FeO_T (wt%) compositional variation in the three zones of microphenocrystic and groundmass micas in Point Lake kimberlite. Compositional fields and trends for kimberlites, lamproites, orangeite sand minette micas are adapted from Mitchell (1995). UML field is taken from (Mitchell et al. (1999) and Tappe et al. (2004, 2006, 2014)

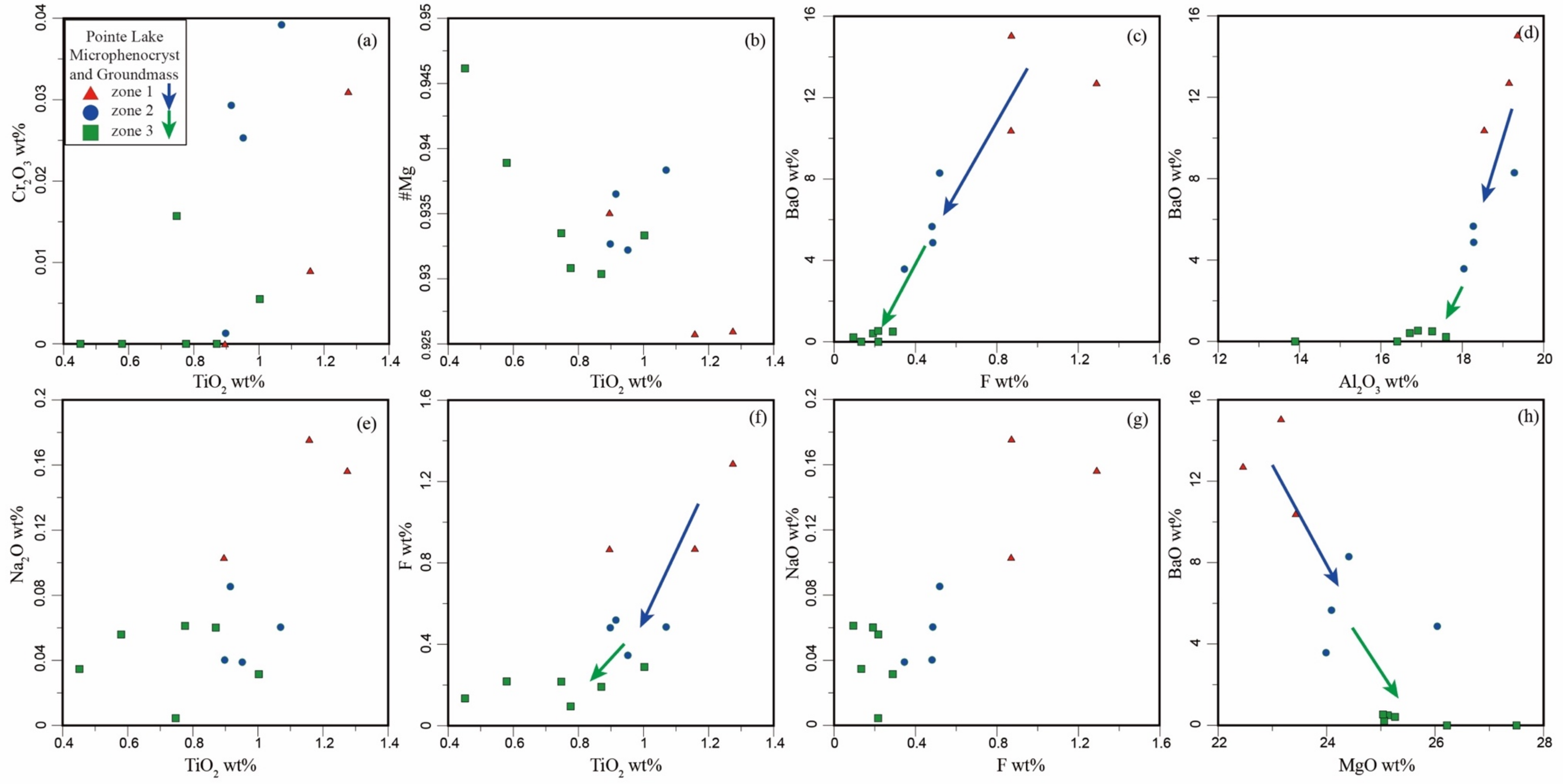

Fig. 10.26. Compositional variations in the three zones of microphenocrystic and groundmass micas in Point Lake kimberlite. (a) TiO_2 (wt%) vs. Cr_2O_3 (wt%). (b) TiO_2 (wt%) vs. #Mg, #Mg=Mg/(Mg+Fe^{2+}). (c) F (wt%) vs. BaO (wt%). (d) Al_2O_3 (wt%) vs. BaO (wt%). (e) TiO_2 (wt%) vs. Na_2O (wt%). (f) F (wt%) vs. TiO_2 (wt%). (g) Na_2O (wt%) vs. F (wt%). (h) BaO (wt%) vs. MgO (wt%).

10.4.6. Snap Lake, Canada

Microphenocrystic phlogopite shows an enrichment of Ba from core (zone 1, 2.8-6.6wt% BaO) to rim (zone 2, 6.4-10.4 wt% BaO, Fig. 10.27-29, Table 10.4).

Phlogopite in the reaction rim of Cr-rich pyrope is remarkably enriched in Cr (Fig. 10.27-29).

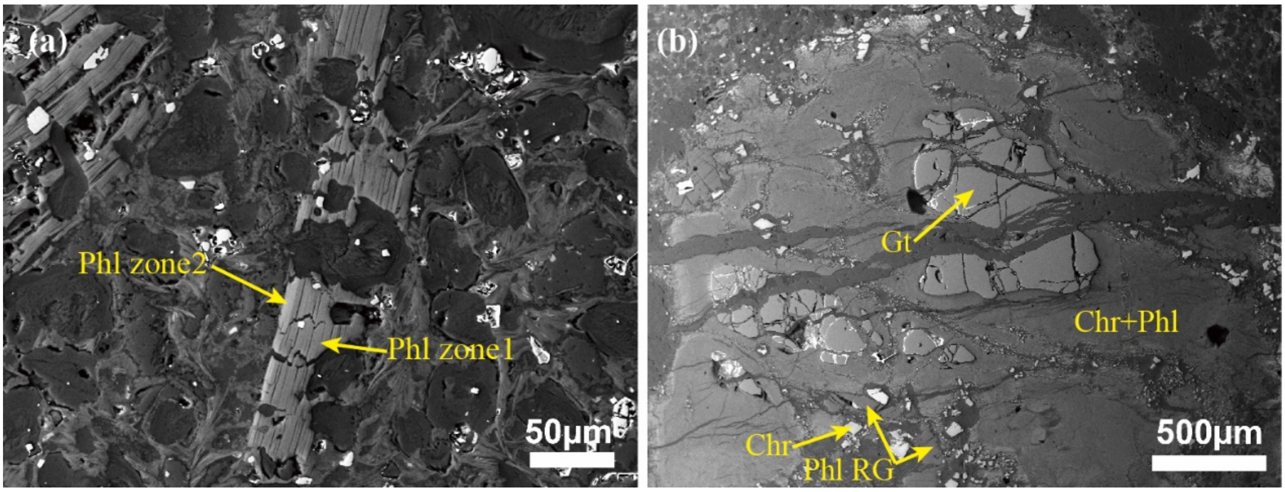

Fig. 10.27. Back-scattered electron (BSE) imagings of micas from Span Lake kimberlite. (a) Microphenocrystic phlogopite (Phl) shows 2 compositional zones (1-2). (b) Cr-rich garnet (Gt) xenocryst replaced by a reaction rim of cryptocrystalline chromite with phlogopite (Chr+Phl) and microcrystic chromite (Chr) with phlogopite (Phl RG).

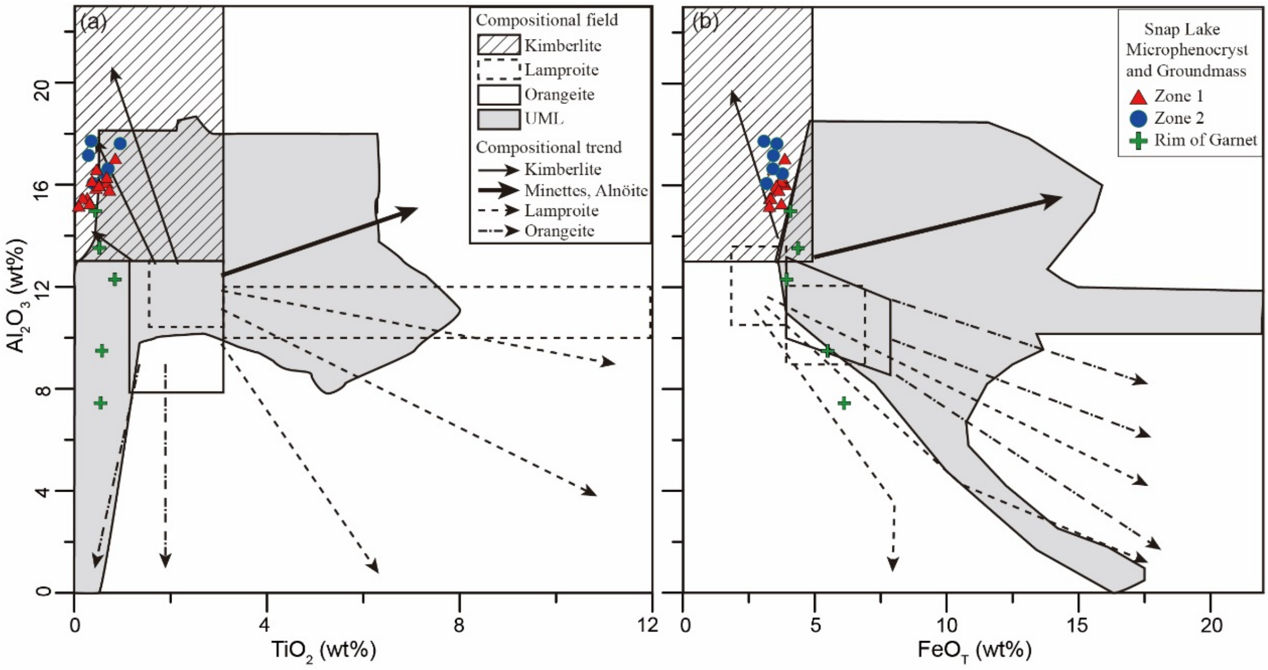

Fig. 10.28. Al_2O_3 vs. TiO_2 (wt%) and Al_2O_3 vs. FeO_T (wt%) compositional variation of microphenocrystic and groundmass phlogopite (zones 1-2) and phlogopite in reaction rims replacing garnet in Snap Lake kimberlite. Compositional fields and trends of micas for kimberlites, lamproites, orangeites and minettes adapted from Mitchell (1995). UML field from (Mitchell et al. (1999) and Tappe et al. (2004, 2006, 2014).

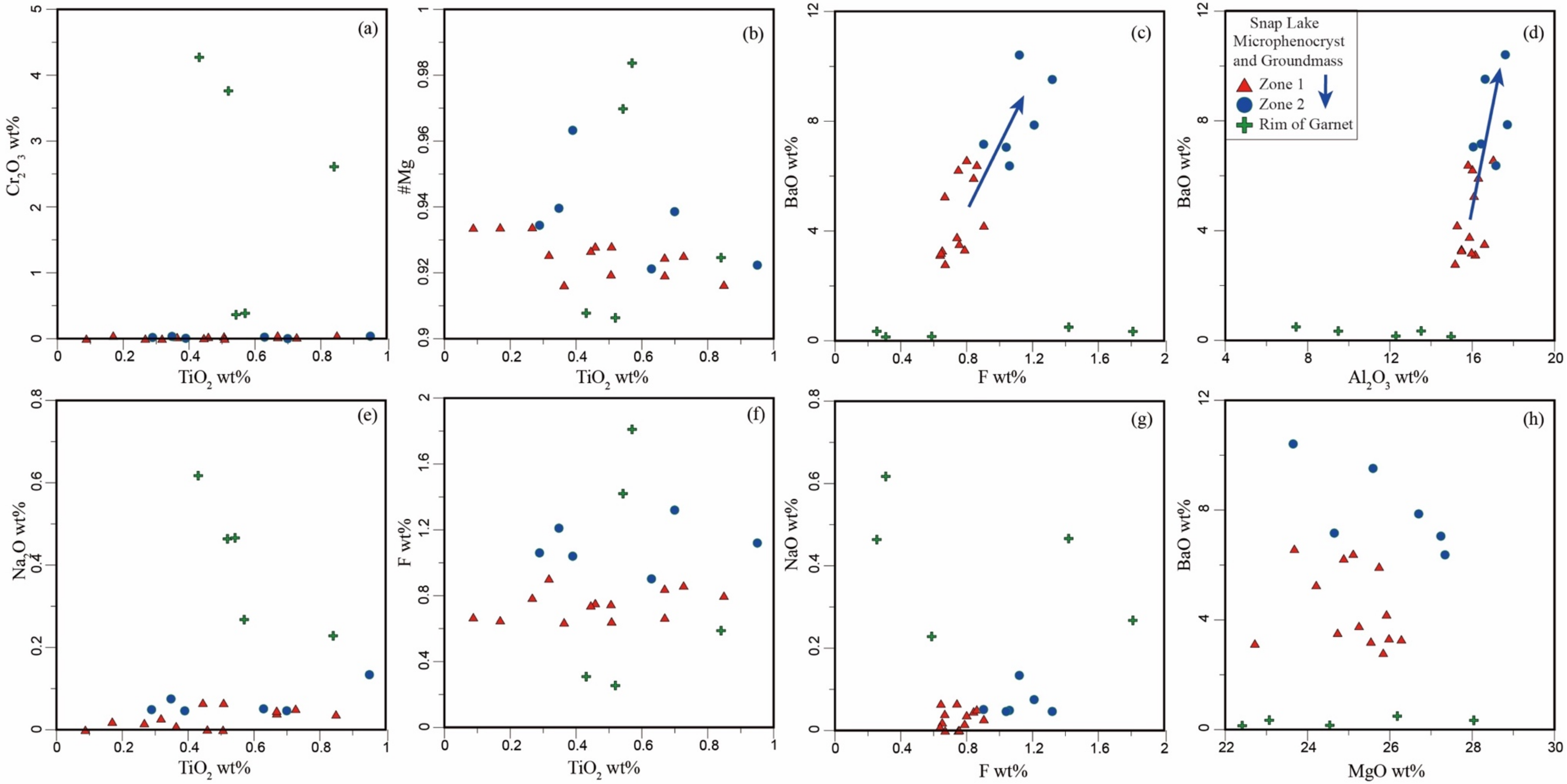

Fig. 10.29. Compositional variation of microphenocrystic and groundmass phlogopite (zones 1-2) and phlogopite in reaction rim replacing garnet in Snap Lake kimberlite. (a) TiO_2 (wt%) vs. Cr_2O_3 (wt%). (b) TiO_2 (wt%) vs. #Mg, #Mg=Mg/(Mg+Fe^{2+}). (c) F (wt%) vs. BaO (wt%). (d) Al_2O_3 (wt%) vs. BaO (wt%). (e) TiO_2 (wt%) vs. Na_2O (wt%). (f) F (wt%) vs. TiO_2 (wt%). (g) Na_2O (wt%) vs. F (wt%). (h) BaO (wt%) vs. MgO (wt%).

10.4.7. Shengli and Red Flag #1 kimberlites, Mengyin, China

Groundmass crystals of phlogopite from the Shengli kimberlite and their zoning reflecting the change of the Ba contents, with an early enrichment in cores followed by replacing units with Ba depletion (Fig. 10.30-32, Table 10.5). Some crystals show clear zoning, for instance, the points labelled as a1-a3 in Fig. 10.30. The core is Ba-rich (4.2-8.1 wt% BaO) replaced by the firs rim of higher Ba content (8.8-10.5 wt% BaO). The outermost rim is Ba poor to rich (0.6-2.5 wt% BaO). There is a good positive correlation between Al and Ba but no correlation between Ba and F. Cr content remain low.

Groundmass phlogopite (0.05-0.1mm) from Red Flag #1 kimberlite has a core with a slight higher BaO content than the rim (Fig. 10.30-32, Table 10.5). This depletion of Ba is accompanied by a depletion of Al (core has 2.0-2.8 wt% BaO and 12.2-13.2 wt% Al_2O_3, rim has 0.2-1.8 wt% BaO and 8.5-12.0 wt% Al_2O_3).

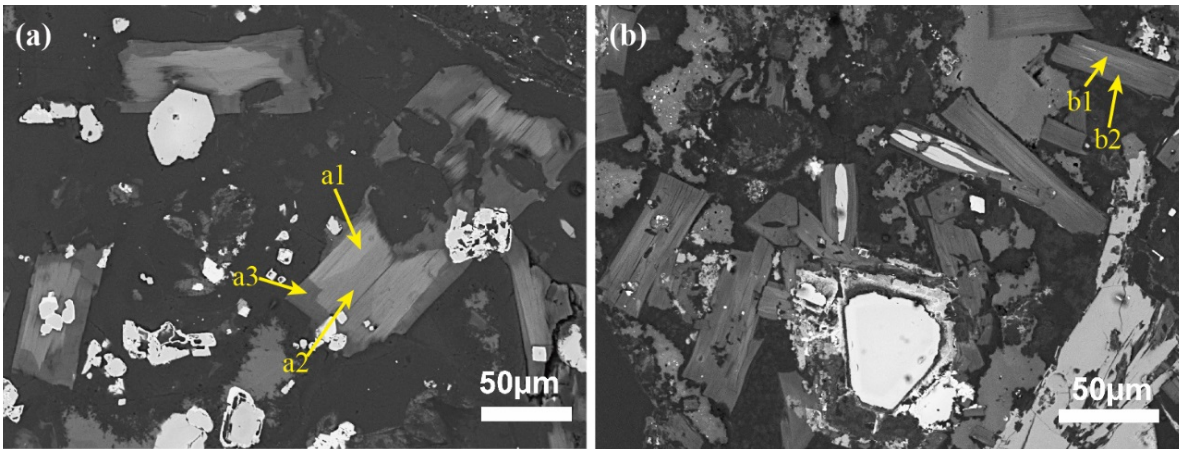

Fig. 10.30. Back-scattered electron (BSE) imagings of micas from Shengli (a) and Red Flag #1 (b) kimberlite. Punts of analyses a1-3 and b1-2 are illustrated in Fig 10.31-32.

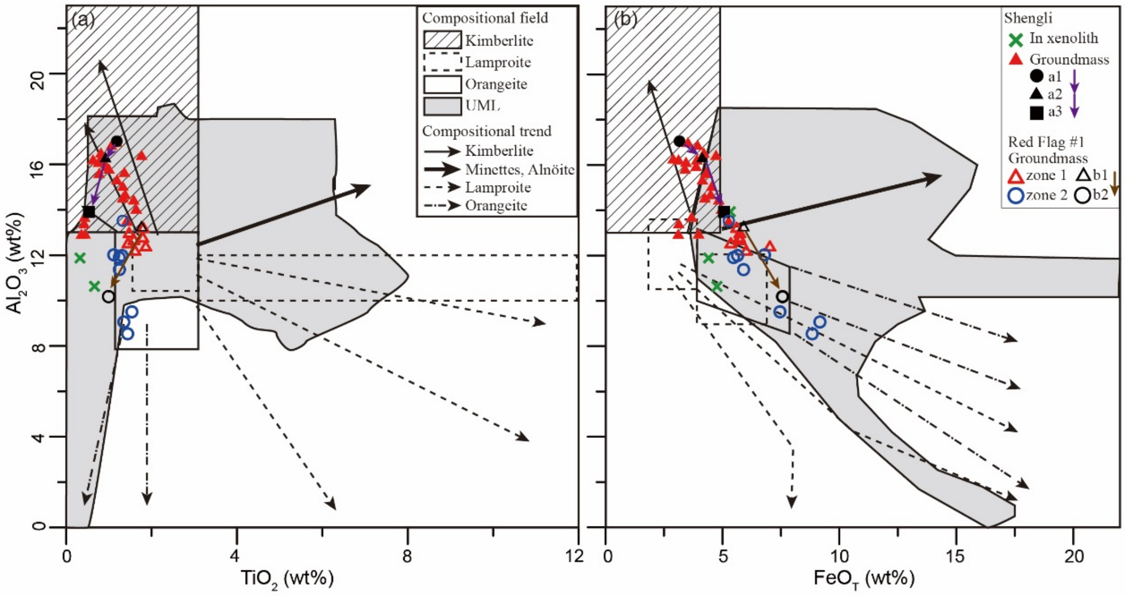

Fig. 10.31. Al_2O_3 vs. TiO_2 (wt%) and Al_2O_3 vs. FeO_T (wt%) compositional variation of groundmass mica in Shengli and Red Flag #1 kimberlite. Compositional fields and trends for kimberlites, lamproites, orangeites and minette micas, adapted from Mitchell (1995). UML field from (Mitchell et al. (1999) and Tappe et al. (2004, 2006, 2014). Points of analyses a1-3 and b1-2 are those illustrated in Fig 10.30.

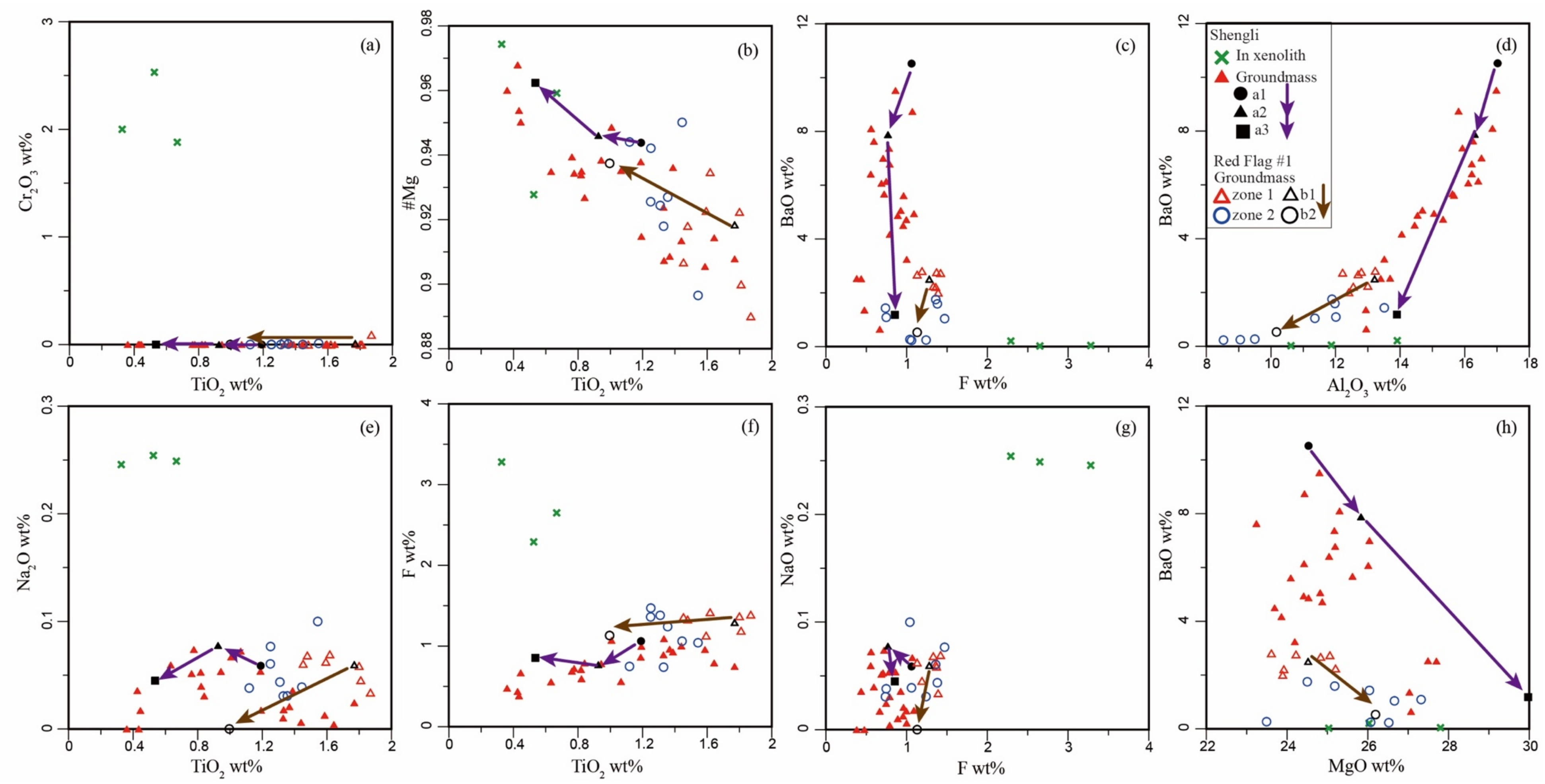

Fig. 10.32. Composition of groundmass phlogopite in Shengli and Red Flag #1 kimberlite. (a) TiO_2 (wt%) vs. Cr_2O_3 (wt%). (b) TiO_2 (wt%) vs. #Mg, #Mg=Mg/(Mg+Fe^{2+}). (c) F (wt%) vs. BaO (wt%). (d) Al_2O_3 (wt%) vs. BaO (wt%). (e) TiO_2 (wt%) vs. Na_2O (wt%). (f) F (wt%) vs. TiO_2 (wt%). (g) Na_2O (wt%) vs. F (wt%). (h) BaO (wt%) vs. MgO (wt%). Points of analyses a1-3 and b1-2 are illustrated in Fig 10.30.

Table 10.5. Representative compositions of micas from Shengli, Red Flag and Letlhakane kimberlite.

	1	2	3	4	5	6	7	8	9	10
	Shengli			Red Flag		Letlhakane DK1				
	Groundmass					Volcaniclastic rock		Coherent rock		
(wt%)				zone 1	zone 2	Groundmass		Groundmass		Vein
SiO_2	30.48	35.74	38.71	38.20	40.55	42.00	41.61	45.91	43.28	42.11
Al_2O_3	17.02	14.69	13.40	13.23	9.05	10.55	10.77	2.42	2.75	3.41
FeO	2.60	3.02	1.64	4.68	3.66	1.98	5.02	0.00	0.94	0.50
Fe_2O_3	0.61	1.62	1.65	1.01	6.10	3.30	1.76	9.27	10.16	10.48
TiO_2	1.19	1.39	0.43	1.81	1.36	0.80	0.32	1.95	3.55	2.30
Cr_2O_3	bdl	bdl	bdl	bdl	bdl	0.10	bdl	0.06	bdl	bdl
V_2O_3	0.12	0.19	0.07	bdl	bdl	0.04	0.02	bdl	0.05	0.02
MnO	bdl	0.06	0.07	0.08	0.09	0.07	0.09	0.05	0.15	0.09
NiO	bdl	0.04	bdl	0.02	0.04	0.07	bdl	0.02	0.02	0.02
MgO	24.53	24.82	27.70	23.61	26.07	27.24	24.77	23.84	20.77	22.69
K_2O	5.53	8.53	9.04	9.30	8.18	9.16	8.37	9.43	8.75	7.98
BaO	10.52	5.06	2.52	2.81	0.25	0.65	0.83	0.83	2.77	1.32
Na_2O	0.06	0.04	0.04	0.05	0.03	0.20	0.15	2.66	1.98	2.07
CaO	0.03	0.53	0.05	0.08	0.05	0.06	1.12	0.09	0.16	0.92
SrO	0.12	0.04	0.05	bdl	bdl	0.06	bdl	0.07	bdl	0.07
F	1.06	0.93	0.44	1.19	1.24	1.10	1.11	5.66	3.79	4.59
H_2O	3.32	3.63	3.97	3.53	3.60	3.74	3.64	1.52	2.26	1.87
Total	97.20	100.32	99.77	99.60	100.26	101.12	99.60	103.78	101.39	100.44
(apfu)	Cations on basis of 24 (O, OH, F)									
Si	4.782	5.268	5.556	5.602	5.813	5.904	5.984	6.549	6.392	6.237
Al	3.147	2.552	2.266	2.286	1.529	1.748	1.825	0.407	0.479	0.595
Fe^{3+}	0.072	0.180	0.178	0.112	0.658	0.349	0.191	0.995	1.129	1.168
Ti	0.000	0.000	0.000	0.000	0.000	0.000	0.000	0.049	0.000	0.000
∑IV	8.000	8.000	8.000	8.000	8.000	8.000	8.000	8.000	8.000	8.000
Al	0.000	0.000	0.000	0.000	0.000	0.000	0.000	0.000	0.000	0.000
Ti	0.140	0.154	0.046	0.200	0.146	0.085	0.035	0.160	0.394	0.256
Cr	-	-	-	-	-	0.012	-	0.007	-	-
V	0.016	0.022	0.009	-	-	0.004	0.003	-	0.006	0.002
Mn	-	0.007	0.008	0.010	0.011	0.008	0.011	0.006	0.018	0.011
Fe^{2+}	0.342	0.372	0.196	0.574	0.439	0.233	0.604	0.000	0.116	0.062
Ni	-	0.005	-	0.003	0.004	0.007	-	0.003	0.003	0.002
Mg	5.502	5.439	5.741	5.162	5.399	5.651	5.311	5.070	4.573	5.010
∑VI	6.000	6.000	6.000	5.948	6.000	6.000	5.963	5.246	5.110	5.344
K	1.107	1.604	1.655	1.740	1.496	1.642	1.535	1.716	1.648	1.508
Ba	0.647	0.292	0.142	0.161	0.014	0.036	0.047	0.046	0.160	0.077
Na	0.018	0.010	0.010	0.013	0.009	0.053	0.042	0.736	0.567	0.594
Ca	0.005	0.083	0.008	0.013	0.008	0.009	0.173	0.013	0.026	0.146
Sr	0.011	0.003	0.004	-	-	0.005	-	0.006	-	0.006
Mg	0.236	0.015	0.186	0.000	0.173	0.058	0.000	0.000	0.000	0.000
∑A	2.023	2.008	2.004	1.928	1.699	1.803	1.798	2.517	2.404	2.331
F	0.526	0.432	0.198	0.552	0.562	0.489	0.505	2.553	1.770	2.150
OH	3.474	3.568	3.802	3.448	3.438	3.511	3.495	1.447	2.230	1.850

bdl: below detection limit; FeO and Fe_2O_3 recalculated

10.4.8. Letlhakane DK1 volcaniclastic and coherent kimberlite

Letlhakane DK1 volcaniclastic kimberlite has groundmass phlogopite (<5μm, Fig. 10.33-35, Table 10.5) which is Al poor (10.6-11.2wt% Al_2O_3), Fe-rich (5.0-7.0 wt% FeO_T), Ti and Ba -free to -poor (0.3-1.0 wt% TiO_2, 0.2-0.8 wt% BaO), F-poor (0.8-1.1 wt% F) and Cr-free (<0.1wt% Cr_2O_3). Macrocryst has similar composition as phlogopite in mantle xenolith.

Groundmass mica is tetraferriphlogopite in Letlhakane DK1 coherent kimberlite (Fig. 10.33-35, Table 10.5). Groundmass tetraferriphlogopite has variable tenors in Na (1.0-2.8 wt% Na_2O) and is F-rich (3.1-6.4 wt% F). There is a positive correlation between Na and F, and a negative correlation between Ba and Mg. Tetraferriphlogopite crystals from veins crosscutting olivine xenocrysts have similar composition as those in the groundmass.

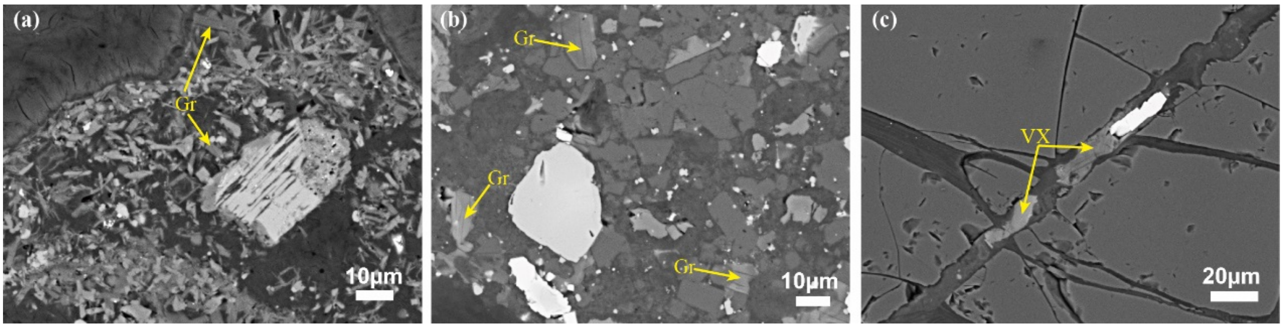

Fig. 10.33. Back-scattered electron (BSE) imagings of groundmass (Gr) micas and micas in vein in olivine xenocryst (VX) from Letlhakane DK1 volcaniclastic (a) and coherent (b-c) kimberlite.

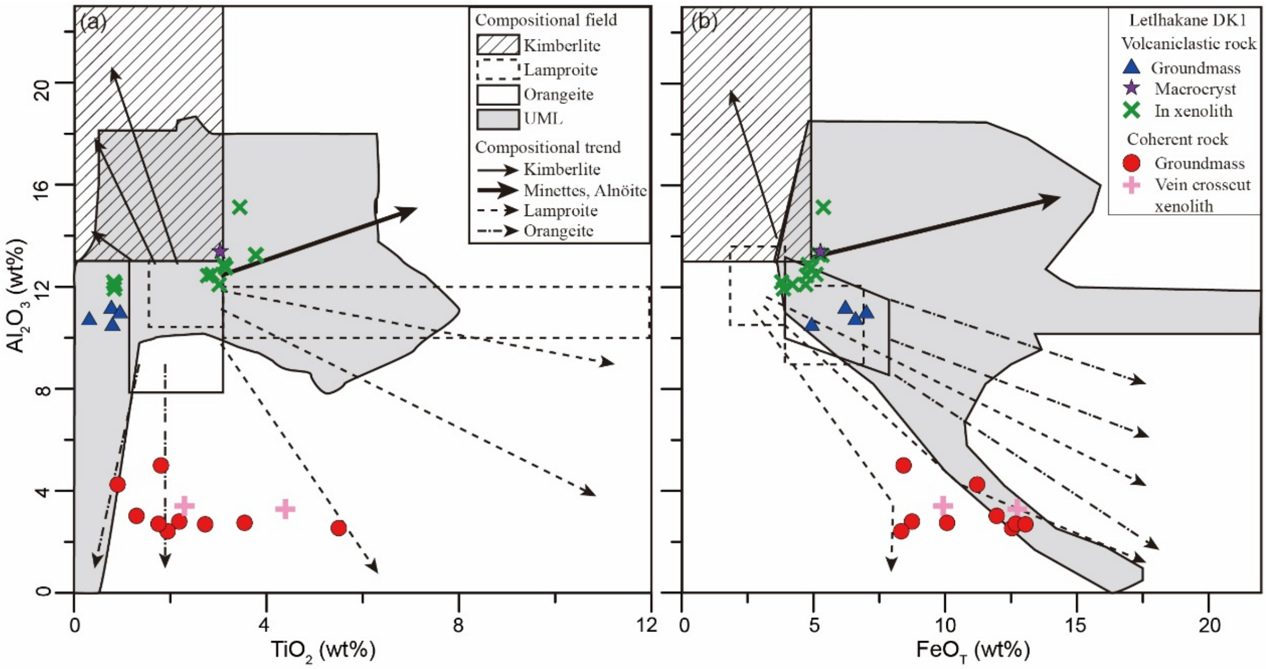

Fig. 10.34. Al_2O_3 vs. TiO_2 (wt%) and Al_2O_3 vs. FeO_T (wt%) compositional variation of micas from volcaniclastic and coherent domains of the Letlhakane DK1 kimberlite. Compositional fields and trends for kimberlites, lamproite, orangeite and minette micas used for comparison are from Mitchell (1995). UML field from (Mitchell et al. (1999) and Tappe et al. (2004, 2006, 2014).

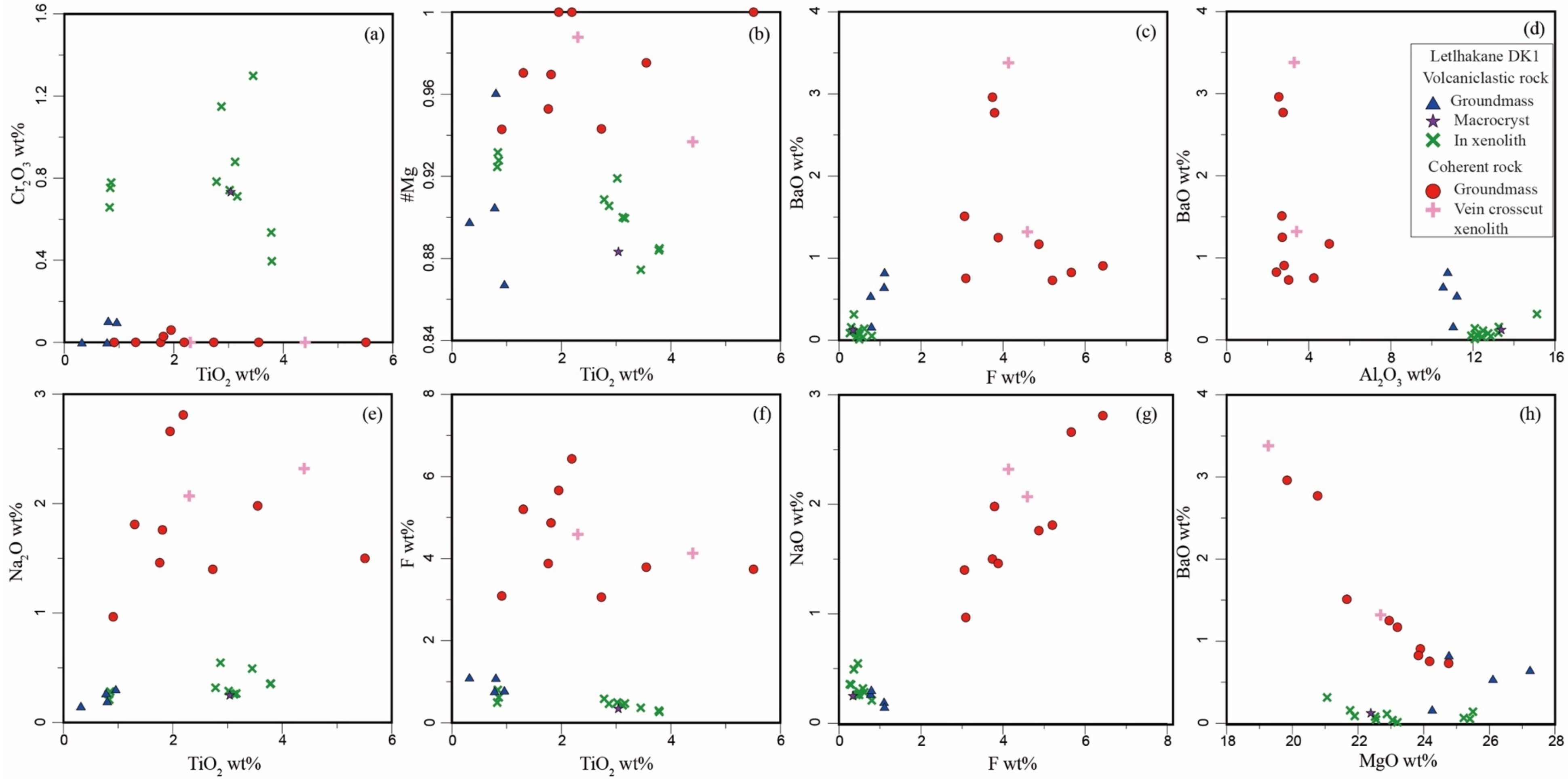

Fig. 10.35. Composition of mica in Letlhakane DK1 volcaniclastic and coherent kimberlite. (a) TiO_2 (wt%) vs. Cr_2O_3 (wt%). (b) TiO_2 (wt%) vs. #Mg, #Mg=Mg/(Mg+Fe^{2+}). (c) F (wt%) vs. BaO (wt%). (d) Al_2O_3 (wt%) vs. BaO (wt%). (e) TiO_2 (wt%) vs. Na_2O (wt%). (f) F (wt%) vs. TiO_2 (wt%). (g) Na_2O (wt%) vs. F (wt%). (h) BaO (wt%) vs. MgO (wt%).

10.4.9. Ville-Marie volcaniclastic kimberlite, Canada

Microphenocrysts (0.05-0.2 mm) from volcaniclastic kimberlite show three zoned units (Fig 10.36-38, Table 10.6). The core (zone1, MP 1) is Al-poor (about 12.4 wt% Al_2O_3) and Ba-free (<0.1 wt% BaO). Zone 2 (MP 2) replaces the above unit and is impoverished in Al (3.2-3.7 wt% Al_2O_3) and Ba-poor (0.2-0.8 wt% BaO). Zone 3 replaces the above units and is comparatively enriched in Al (15.3-16.7 wt% Al_2O_3) and Ba (2.1-2.5wt% BaO). From core to first rim an enrichment of Al, Ba and Ti is recorded. Macrocryst (> 0.3 mm) and groundmass (<0.0.5 mm) phlogopite have similar composition as the microphenocrysts.

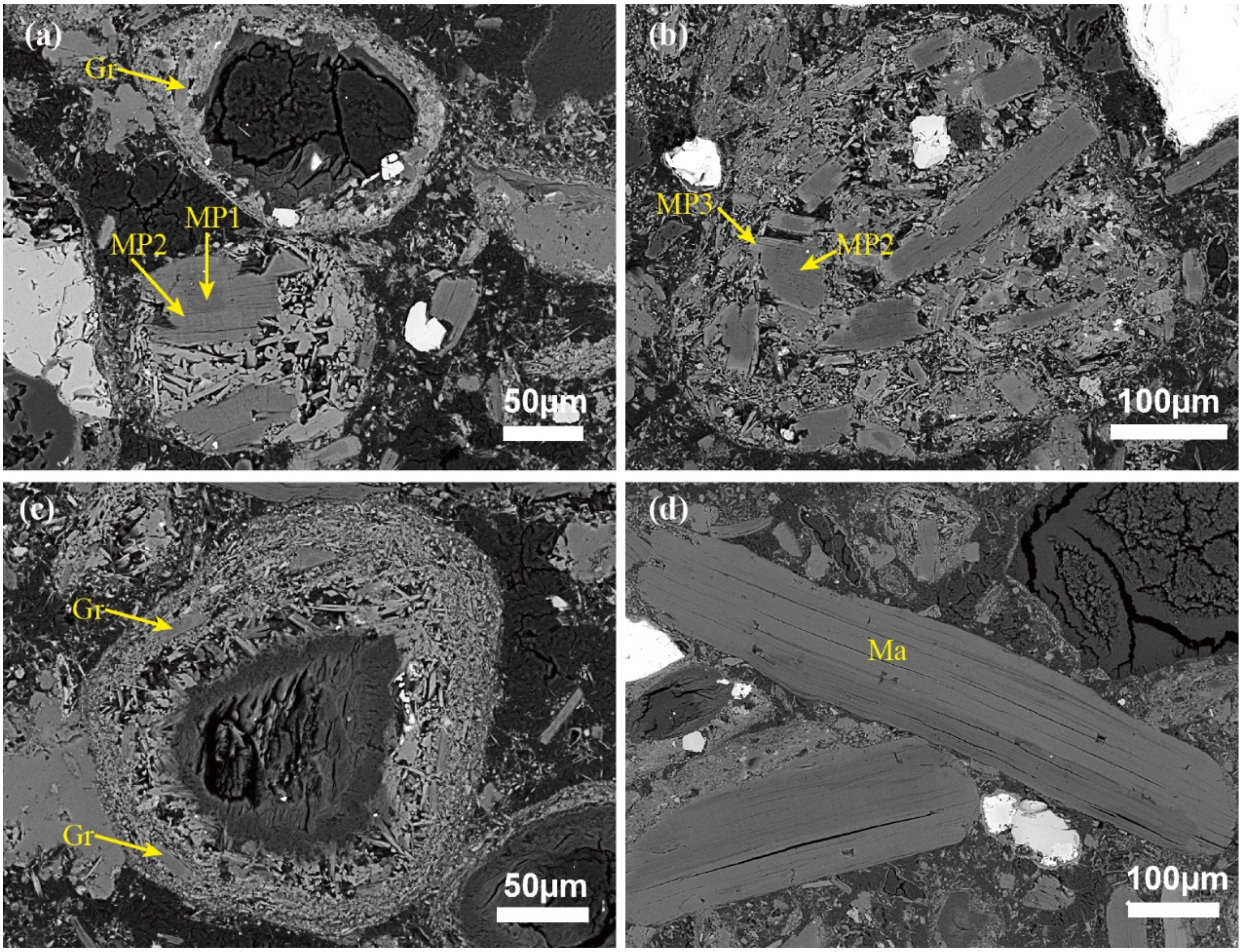

Fig. 10.36. Back-scattered electron (BSE) imagings of micas from Ville-Marie volcaniclastic kimberlite. (a-c) Groundmass mica (Gr) and microphenocrystic mica (MP) showing three compositional zones (MP1-MP3). (d) Macrocrystal mica crystals (Ma).

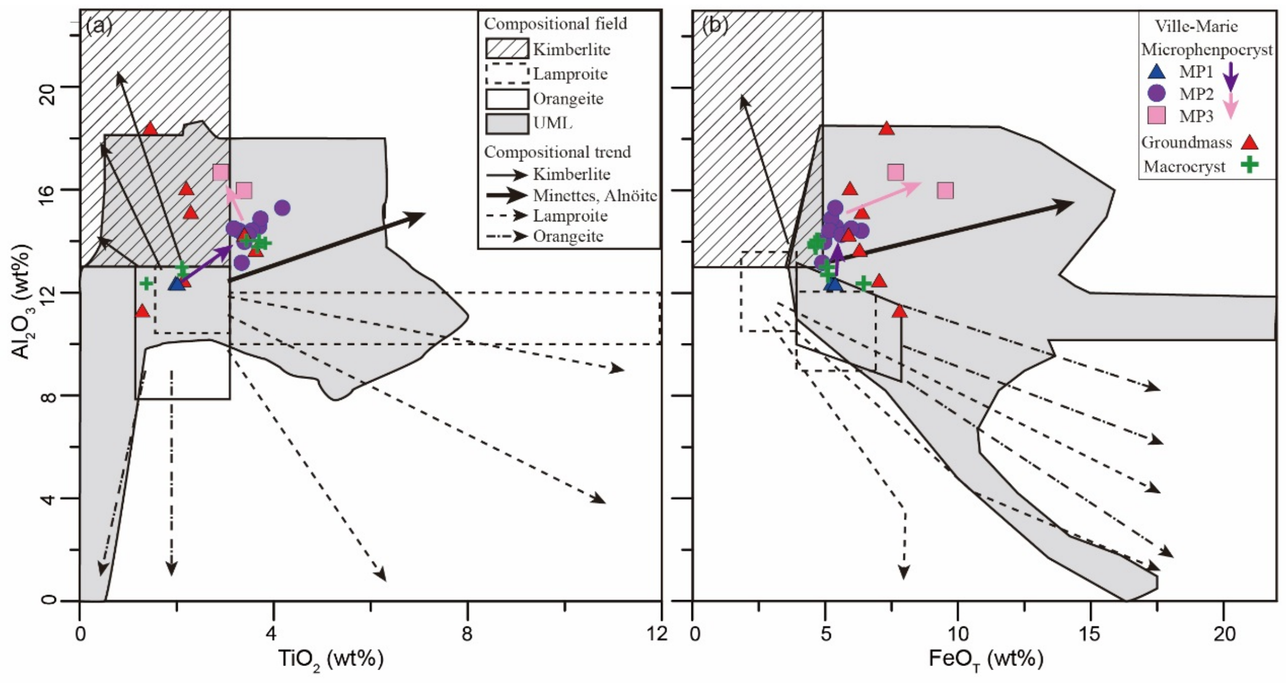

Fig. 10.37. Compositional diagrams Al_2O_3 vs. TiO_2 (wt%) and Al_2O_3 vs. FeO_T (wt%) compositional variation in micas found as microphenocrysts (MP1-3), groundmass (Gr) and macrocrysts (Ma) in Ville-Marie volcaniclastic kimberlite. Compositional fields and trends for micas from kimberlites, lamproites, orangeites and minette are adapted after Mitchell (1995). UML field adapted after (Mitchell et al. (1999) and Tappe et al. (2004, 2006, 2014).

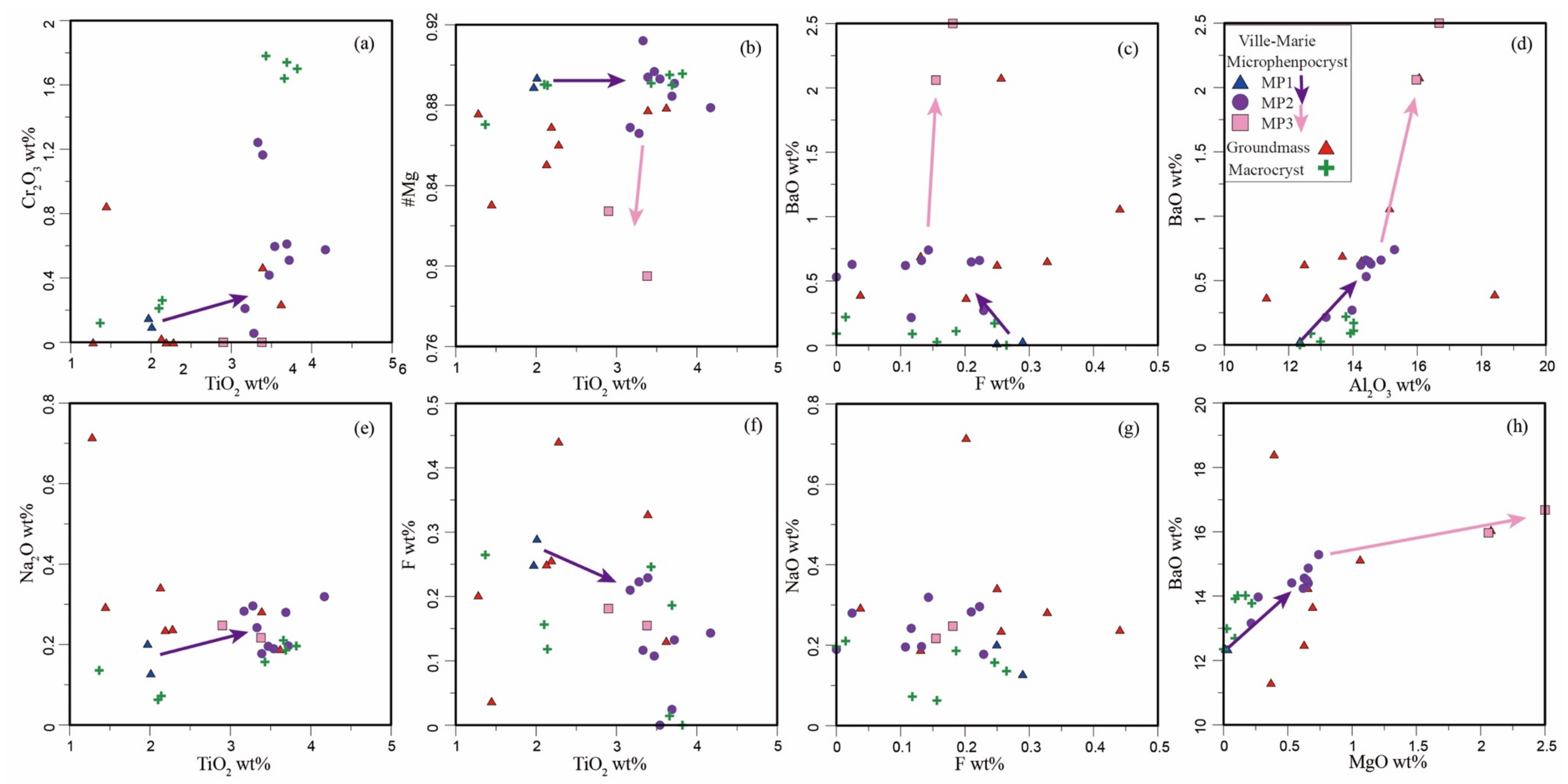

Fig. 10.38. Composition of microphenocrystic (MP1-3), groundmass (Gr) and macrocrystic (Ma) micas in Ville-Marie volcaniclastic kimberlite. (a) TiO$_2$ (wt%) vs. Cr$_2$O$_3$ (wt%). (b) TiO$_2$ (wt%) vs. #Mg, #Mg=Mg/(Mg+Fe^{2+}). (c) F (wt%) vs. BaO (wt%). (d) Al$_2$O$_3$ (wt%) vs. BaO (wt%). (e) TiO$_2$ (wt%) vs. Na$_2$O (wt%). (f) F (wt%) vs. TiO$_2$ (wt%). (g) Na$_2$O (wt%) vs. F (wt%). (h) BaO (wt%) vs. MgO (wt%).

Table 10.6. Representative compositions of micas from the Ville-Marie and Tchiuzo kimberlites and from the Helam and Roberts Victor orangeites.

	1	2	3	4	5	6	7	8	9	10	11	12
	Ville-Marie					Tchiuzo		Helam			Roberts Victor	
	Microphenocryst			Groundmass		Groundmass		Microphenocryst and Groundmass			Groundmass	
(wt%)	MP1	MP2	MP3					zone 1	zone 2	zone 3		
SiO_2	41.97	38.34	35.86	37.47	38.81	38.03	40.16	29.55	39.07	40.43	43.54	39.69
Al_2O_3	12.37	14.41	16.68	16.06	13.67	13.59	9.88	19.63	14.91	0.11	11.28	11.81
FeO	5.22	4.76	7.64	5.92	5.41	5.81	5.51	3.38	3.85	0.57	4.22	5.73
Fe_2O_3	0.00	0.43	0.00	0.00	0.97	1.55	4.25	0.00	0.00	17.54	0.00	1.33
TiO_2	1.97	3.54	2.90	2.19	3.62	3.27	2.70	1.83	0.68	0.12	1.96	3.63
Cr_2O_3	0.15	0.60	bdl	bdl	0.24	bdl	bdl	bdl	bdl	0.07	0.70	0.34
V_2O_3	bdl	bdl	bdl	bdl	bdl	bdl	bdl	bdl	bdl	bdl	0.03	0.07
MnO	0.02	0.08	0.12	0.10	0.04	0.12	0.15	0.00	0.04	0.13	0.07	0.03
NiO	0.07	0.06	0.03	0.04	0.07	0.04	bdl	bdl	0.02	0.06	0.13	0.18
MgO	23.49	22.30	20.53	22.09	22.02	22.20	22.18	22.18	26.19	26.72	22.86	20.58
K_2O	10.49	10.36	9.13	9.51	10.09	9.49	9.52	5.61	10.10	9.61	10.09	10.14
BaO	bdl	0.53	2.50	2.08	0.69	1.33	0.74	12.46	0.21	bdl	0.15	0.13
Na_2O	0.20	0.19	0.25	0.24	0.19	0.29	0.21	0.16	0.05	0.04	0.16	0.26
CaO	0.05	bdl	0.15	0.11	0.08	0.12	0.12	0.04	0.11	0.05	0.19	0.02
SrO	bdl	bdl	0.12	0.19	bdl	bdl	bdl	bdl	0.08	0.05	0.05	0.05
F	0.25	0.00	0.18	0.26	0.13	0.76	1.20	1.10	0.86	0.69	0.38	0.33
H_2O	4.12	4.17	4.00	4.02	4.11	3.78	3.55	3.32	3.81	3.70	4.06	3.94
Total	100.31	99.78	100.01	100.16	100.09	100.07	99.76	98.81	99.67	99.60	99.70	98.12
(apfu)	Cations on basis of 24 (O, OH, F)											
Si	5.943	5.512	5.261	5.425	5.579	5.510	5.841	4.607	5.558	6.016	6.161	5.815
Al	2.057	2.441	2.739	2.575	2.316	2.321	1.694	3.393	2.442	0.019	1.839	2.039
Fe^{3+}	0.000	0.047	0.000	0.000	0.104	0.169	0.465	0.000	0.000	1.964	0.000	0.147
Ti	0.000	0.000	0.000	0.000	0.000	0.000	0.000	0.000	0.000	0.000	0.000	0.000
∑IV	8.000	8.000	8.000	8.000	8.000	8.000	8.000	8.000	8.000	8.000	8.000	8.000
Al	0.007	0.000	0.145	0.165	0.000	0.000	0.000	0.214	0.058	0.000	0.042	0.000
Ti	0.210	0.383	0.320	0.239	0.391	0.356	0.295	0.215	0.073	0.014	0.209	0.400
Cr	0.017	0.068	-	-	0.027	-	-	-	-	0.009	0.078	0.040
V	-	-	-	-	-	-	-	-	-	0.000	0.003	0.008
Mn	0.002	0.009	0.015	0.012	0.005	0.014	0.018	0.000	0.005	0.017	0.008	0.004
Fe^{2+}	0.618	0.573	0.937	0.717	0.651	0.704	0.670	0.441	0.458	0.070	0.499	0.703
Ni	0.008	0.007	0.003	0.004	0.009	0.005	-	-	0.003	0.007	0.014	0.021
Mg	4.959	4.779	4.490	4.768	4.719	4.795	4.810	5.131	5.397	5.884	4.822	4.495
∑VI	5.821	5.818	5.910	5.905	5.802	5.876	5.804	6.000	6.000	6.000	5.676	5.670
K	1.895	1.900	1.709	1.756	1.850	1.754	1.766	1.116	1.833	1.824	1.821	1.895
Ba	-	0.030	0.144	0.118	0.039	0.076	0.042	0.761	0.011	-	0.008	0.008
Na	0.056	0.053	0.070	0.066	0.053	0.081	0.059	0.049	0.014	0.011	0.044	0.073
Ca	0.007	-	0.023	0.016	0.013	0.019	0.019	0.006	0.017	0.008	0.028	0.004
Sr	-	-	0.010	0.016	-	-	-	-	0.006	0.004	0.004	0.004
Mg	0.000	0.000	0.000	0.000	0.000	0.000	0.000	0.025	0.157	0.044	0.000	0.000
∑A	1.961	1.985	1.956	1.973	1.955	1.930	1.886	1.957	2.039	1.891	1.907	1.983
F	0.112	0.000	0.084	0.117	0.060	0.349	0.552	0.542	0.385	0.324	0.171	0.153
OH	3.888	4.000	3.916	3.883	3.940	3.651	3.448	3.458	3.615	3.676	3.829	3.847

bdl: below detection limit; FeO and Fe_2O_3 recalculated

10.4.10. Tchiuzo, volcaniclastic kimberlite, Angola

In volcaniclastic Tchiuzo kimberlite, phlogopite has clearly different composition depending if it occurs in groundmass, in xenoliths or macrocrysts (Fig. 10.39-41, Table 10.6). Groundmass phlogopite is relatively impoverished in Al (7.9-13.6 wt% Al_2O_3) and enriched in Ba (0.2-1.6 wt% BaO) and F (0.5-1.3 wt% F) in comparison with phlogopite in xenoliths and macrocrysts.

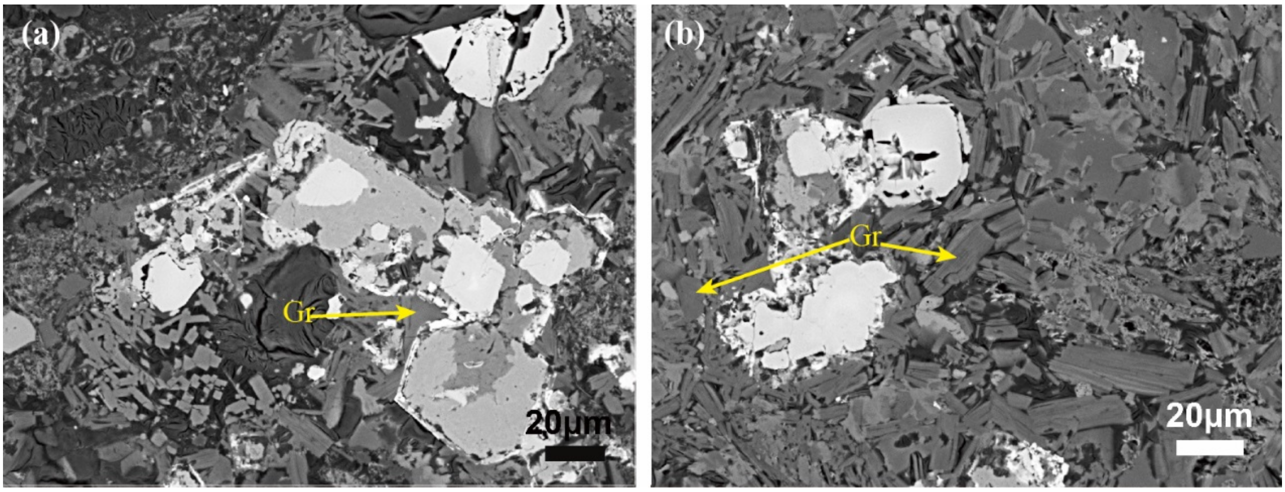

Fig. 10.39. Back-scattered electron (BSE) imagings of groundmass phlogopite (Gr) from the Tchiuzo volcaniclastic kimberlite (a-b).

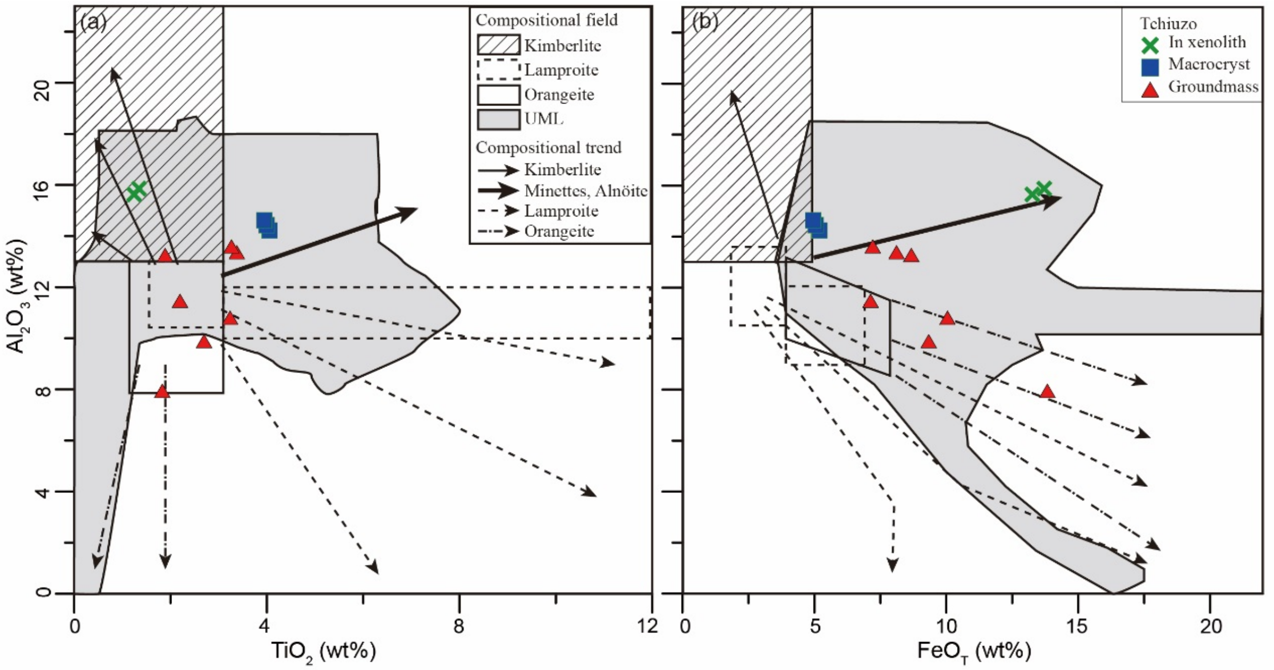

Fig. 10.40. Al_2O_3 vs. TiO_2 (wt%) and Al_2O_3 vs. FeO_T (wt%) compositional variation of mica in groundmass, macrocrysts and xenoliths in Tchiuzo volcaniclastic kimberlite. Compositional fields and trends for micas in kimberlites, lamproites, orangeites and minettes adapted from Mitchell (1995). UML field adapted from (Mitchell et al. (1999) and Tappe et al. (2004, 2006, 2014)

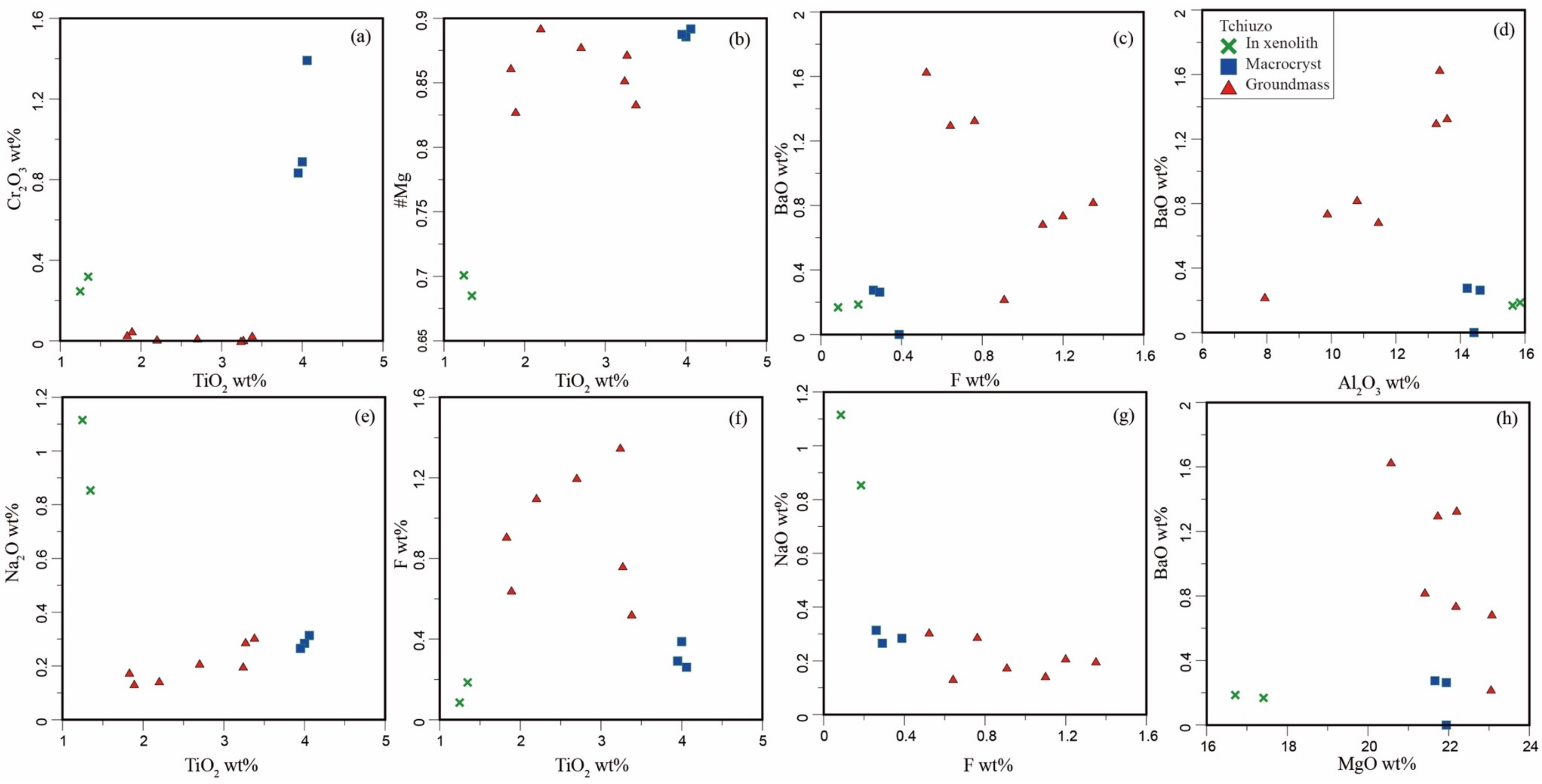

Fig. 10.41. Composition of mica in groundmass, macrocrysts and xenoliths in Tchiuzo volcaniclastic kimberlite. (a) TiO_2 (wt%) vs. Cr_2O_3 (wt%). (b) TiO_2 (wt%) vs. #Mg, #Mg=Mg/(Mg+Fe^{2+}). (c) F (wt%) vs. BaO (wt%). (d) Al_2O_3 (wt%) vs. BaO (wt%). (e) TiO_2 (wt%) vs. Na_2O (wt%). (f) F (wt%) vs. TiO_2 (wt%). (g) Na_2O (wt%) vs. F (wt%). (h) BaO (wt%) vs. MgO (wt%).

10.4.11. Helam orangeite, South Africa

Primary micas are microphenocrystic and groundmass mica which display three different compositional zonings (Fig. 10.42-44, Table 10.6). Core (zone 1) of microphenocrysts and groundmass mica is strongly enriched in Al rich (17.4-19.8 wt% Al_2O_3) and Ba (4.6-12.5 wt% BaO). Zone 1 phlogopite is mantled by a new generation of phlogopite slightly impoverished in these elements (14.1-16.1 wt% Al_2O_3 and 0-2.2 wt% BaO; zone 2). The outermost rim (zone 3, Fig. 10.42a,b,c) is tetraferriphlogopite.

Phlogopite macrocrysts in Helam orangeite are corroded and replaced by primary micas (Fig. 10.41d).

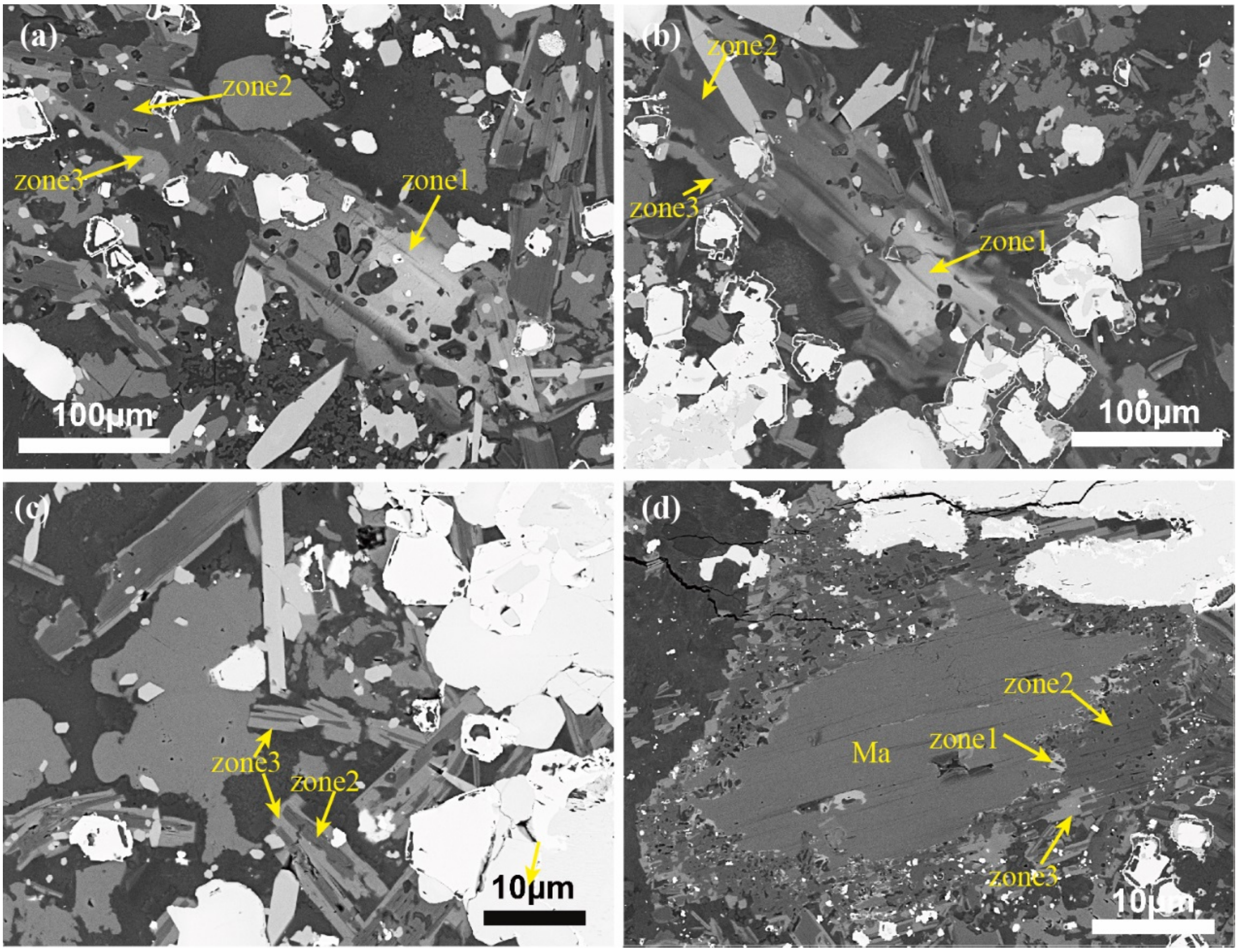

Fig. 10.42. Back-scattered electron (BSE) images of micas from the Helam orangeite. (a-b) Microphenocrystals of mica show 3 compositional zones (zone 1 to zone 3). (c) Groundmass micas compositional zone 2 to zone 3. (d) Macrocrystal of mica replaced by primary micas of compositional zones 1 to 3.

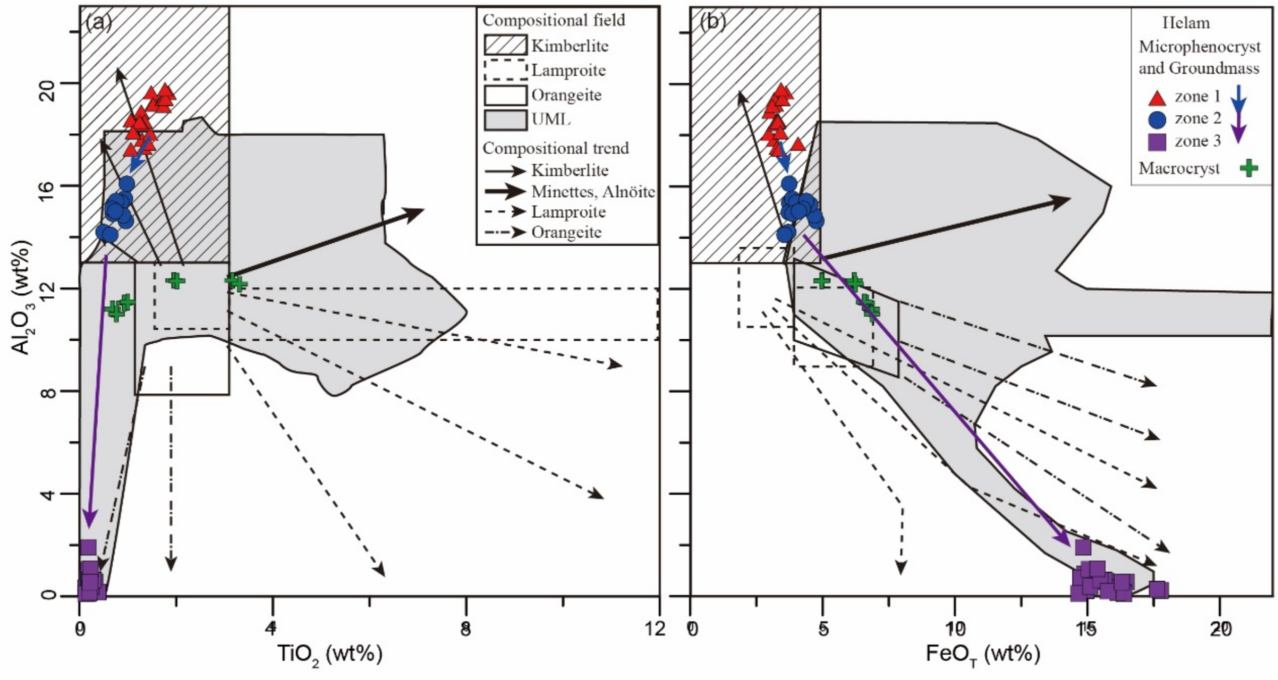

Fig. 10.43. Al_2O_3 vs. TiO_2 (wt%) and Al_2O_3 vs. FeO_T (wt%) diagrams showing compositional variations of microphenocrysts and groundmass (zones 1-3) and macrocryst mica in the Helam orangeite. Compositional fields and trends for micas from kimberlites, lamproites, orangeites and minettes are from Mitchell (1995). UML field is from Mitchell et al. (1999) and Tappe et al. (2004, 2006, 2014).

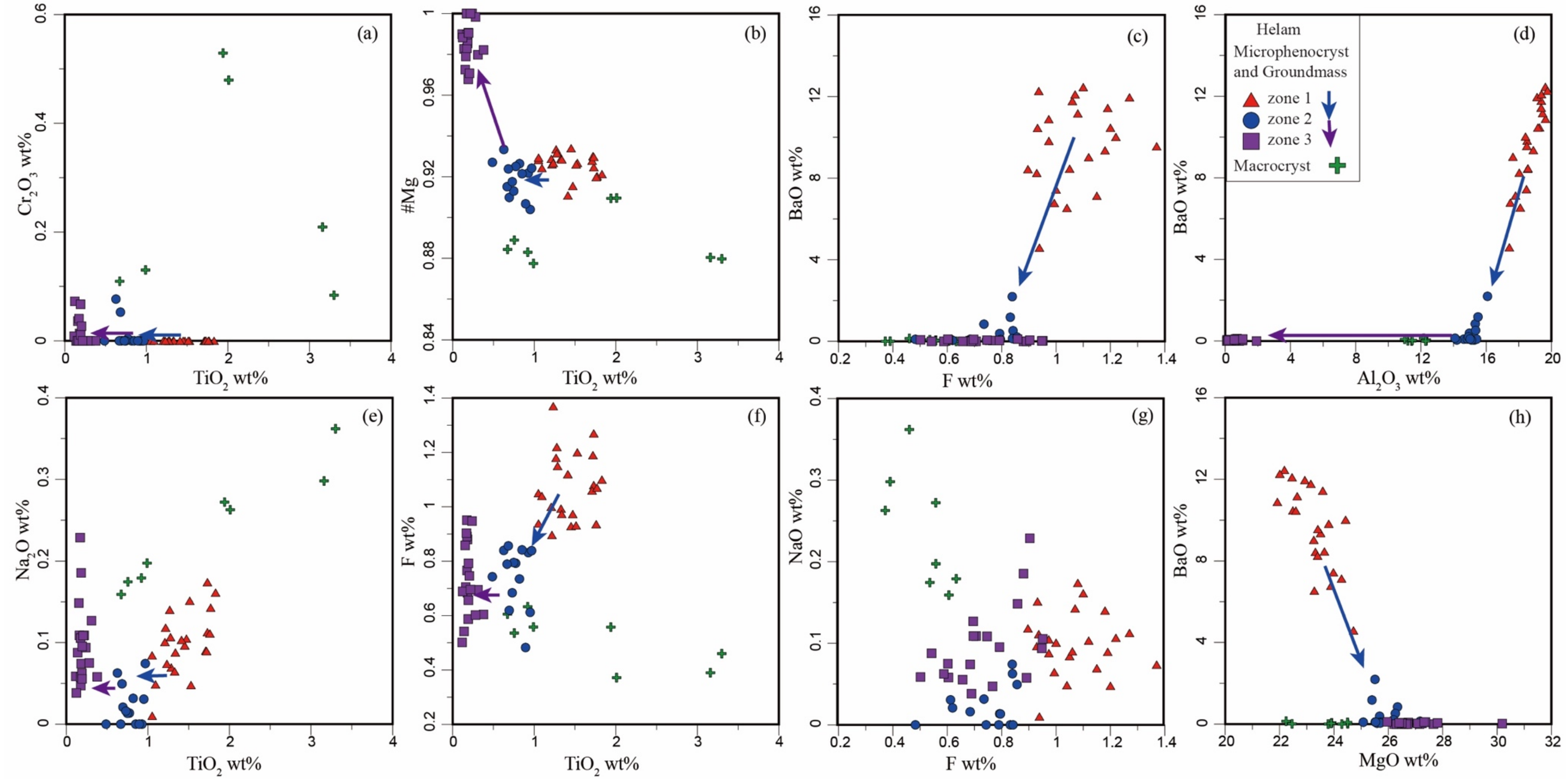

Fig. 10.44. Composition of microphenocrysts and groundmass (zones 1-3) and macrocrystic mica in Helam orangeite. (a) TiO_2 (wt%) vs. Cr_2O_3 (wt%). (b) TiO_2 (wt%) vs. #Mg, #Mg=Mg/(Mg+Fe^{2+}). (c) F (wt%) vs. BaO (wt%). (d) Al_2O_3 (wt%) vs. BaO (wt%). (e) TiO_2 (wt%) vs. Na_2O (wt%). (f) F (wt%) vs. TiO_2 (wt%). (g) Na_2O (wt%) vs. F (wt%). (h) BaO (wt%) vs. MgO (wt%).

10.4.12. Roberts Victor orangeite, South Africa

Groundmass phlogopite in Robert Victor orangeite is Al-poor (11-12.1 wt% Al_2O_3), but no tetraferriphlogopite is found (Fig. 10.45-47, Table 10.6). It is slightly zoned, F-free to F-poor (0.1-0.6 wt% F), Ti-poor to -rich (1.4-3.1 wt% TiO_2), Na-poor (0.1-0.5 wt% Na_2O). Macrocrysts show different compositions between phlogopite and annite. Macrocrystic annite (xenocrystic) is replaced by a rim of primary phlogopite which has similar composition to the groundmass phlogopite (Fig. 10.44-46).

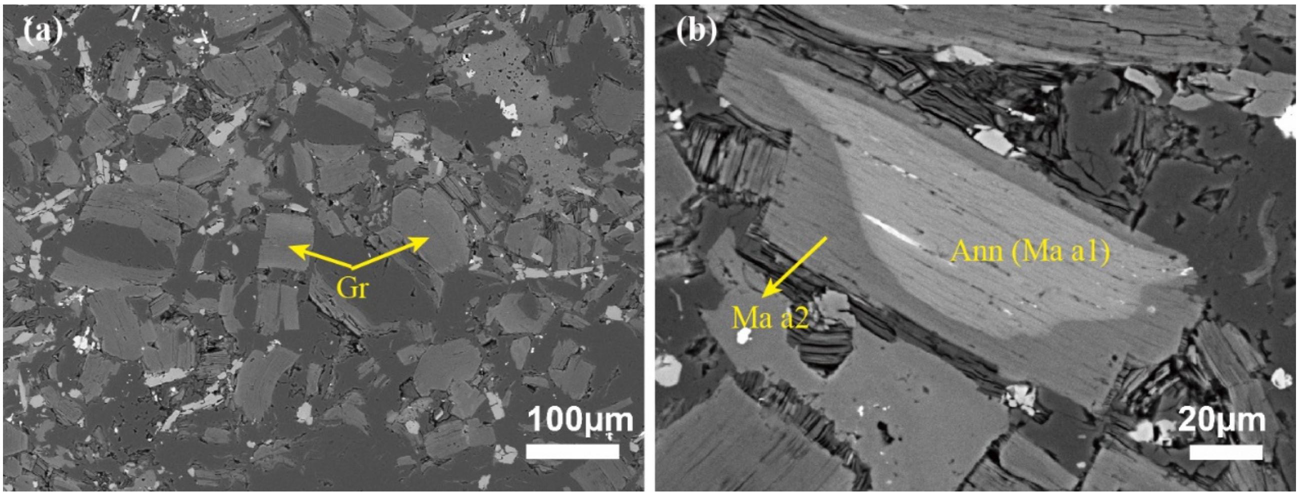

Fig. 10.45. Back-scattered electron (BSE) imagings of micas from Roberts Victor orangeite. (a) Groundmass phlogopite (Gr). (b) Macrocryst of annite (Ann, Ma a1) replaced by a rim of primary phlogopite (Ma a2).

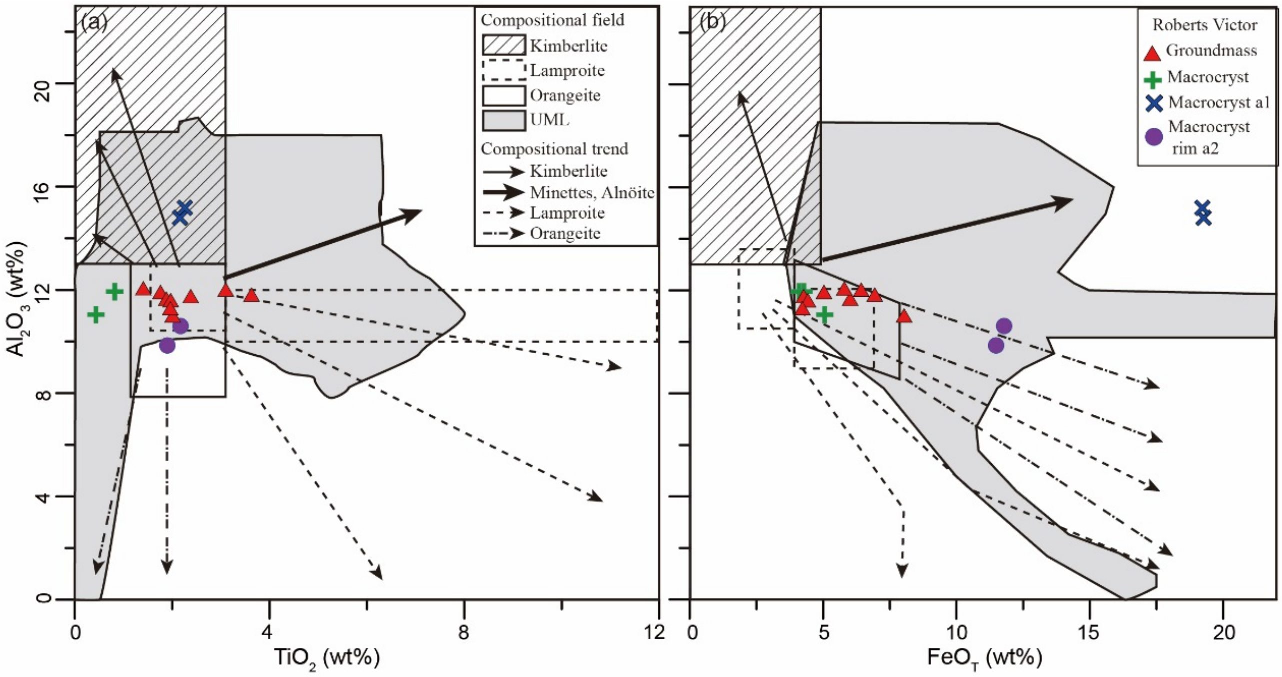

Fig. 10.46. Al_2O_3 vs. TiO_2 (wt%) and Al_2O_3 vs. FeO_T (wt%) compositional variation of mica in Roberts Victor orangeite. Compositional fields and trends for micas from kimberlites, lamproites, orangeites and minettes are from Mitchell (1995). UML field is from (Mitchell et al. (1999) and Tappe et al. (2004, 2006, 2014). Macrocryst a1 and rim a2 are indicated in Fig. 10.4.

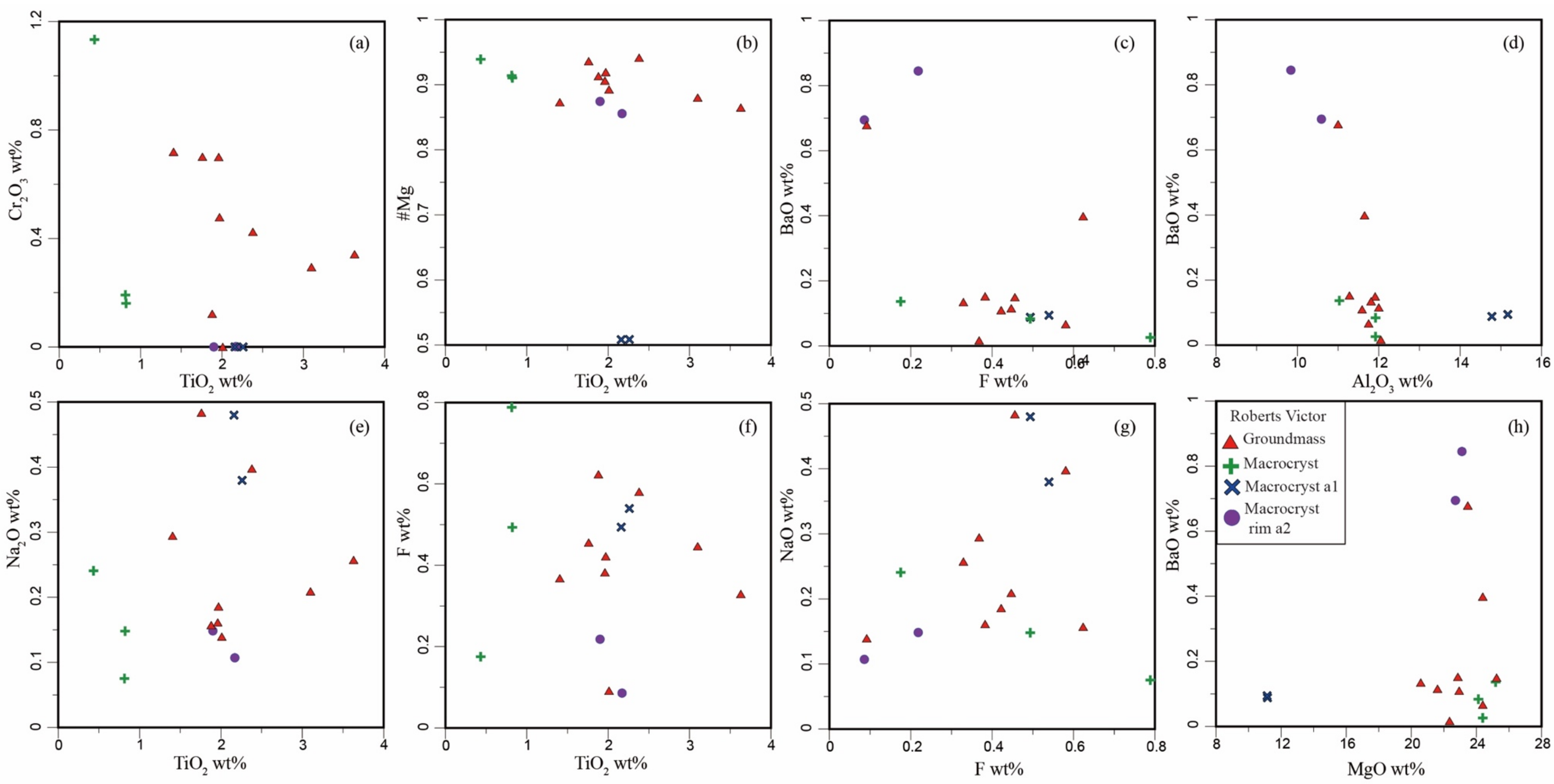

Fig. 10.47. Composition of mica in Roberts Victor orangeite. (a) TiO_2 (wt%) vs. Cr_2O_3 (wt%). (b) TiO_2 (wt%) vs. #Mg, #Mg=Mg/(Mg+Fe^{2+}). (c) F (wt%) vs. BaO (wt%). (d) Al_2O_3 (wt%) vs. BaO (wt%). (e) TiO_2 (wt%) vs. Na_2O (wt%). (f) F (wt%) vs. TiO_2 (wt%). (g) Na_2O (wt%) vs. F (wt%). (h) BaO (wt%) vs. MgO (wt%). Macrocrystic annite a1 and rim a2 are indicated in Fig. 10.45.

10.4.13. Murfreesboro lamproite, USA

Groundmass phlogopite in Murfreesboro lamproite is Al-poor (7.0-10.8 wt% Al_2O_3) but tetraferriphlogopite is absent (Fig. 10.48-50, Table 10.7). It is Ti-free to Ti-rich (0.5-3.7 wt% TiO_2), F-free to F-rich (0-2.4 wt% F). It is Cr-free and Na-free. No clear zoning pattern is observed.

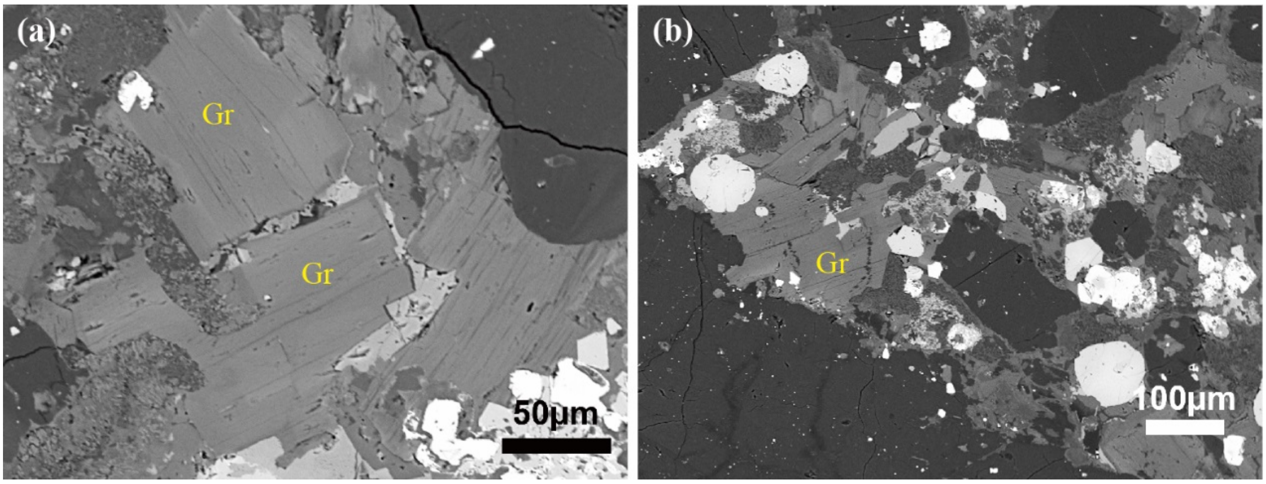

Fig. 10.48. Back-scattered electron (BSE) imagings of groundmass (Gr) micas from Murfreesboro lamproite (a-b).

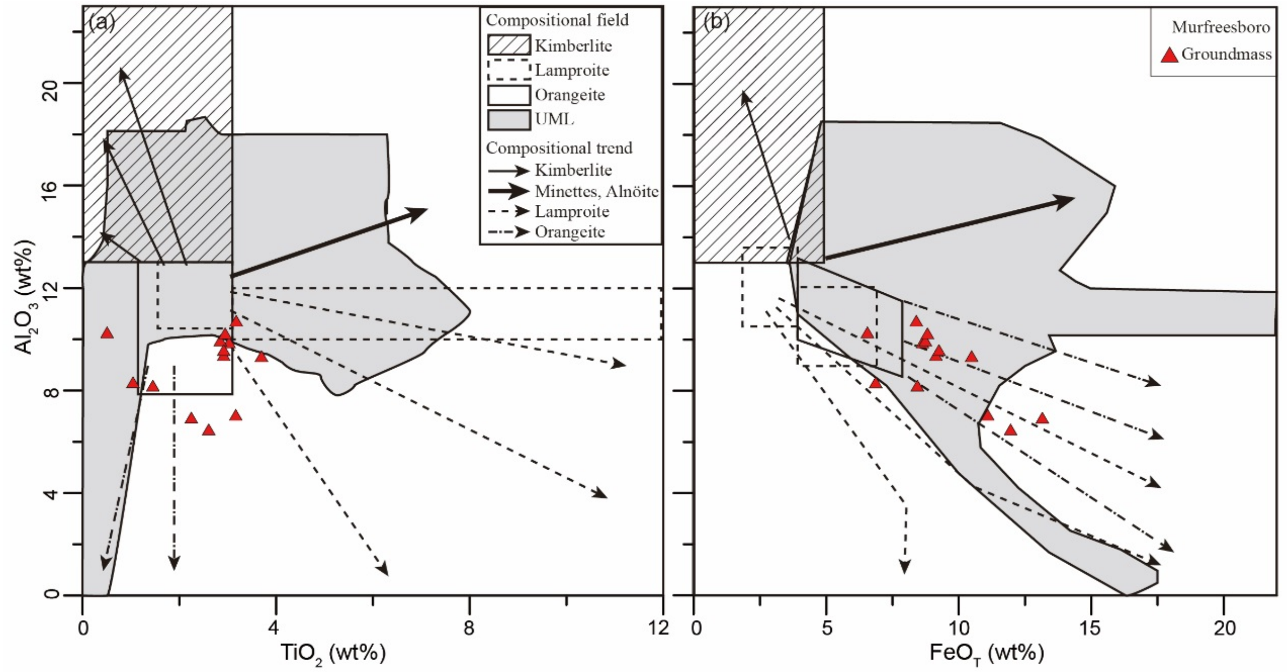

Fig. 10.49. Al_2O_3 vs. TiO_2 (wt%) and Al_2O_3 vs. FeO_T (wt%) compositional variation of groundmass micas from the Murfreesboro lamproite. Compositional fields and trends for micas from kimberlites, lamproites, orangeites and minettes are adapted from Mitchell (1995). UML field is adapted from (Mitchell et al. (1999) and Tappe et al. (2004, 2006, 2014).

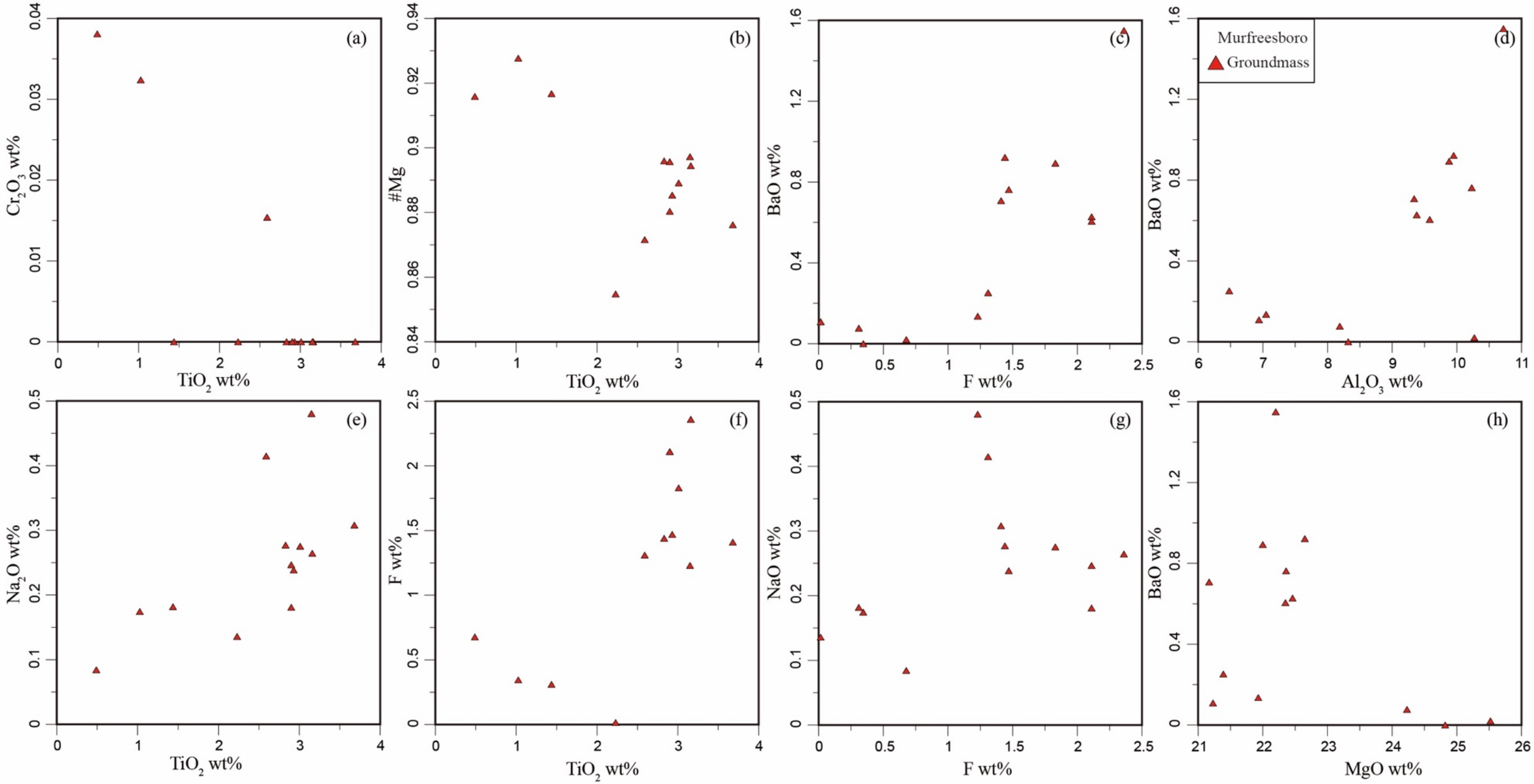

Fig. 10.50. Composition of groundmass micas from the Murfreesboro lamproite. (a) TiO_2 (wt%) vs. Cr_2O_3 (wt%). (b) TiO_2 (wt%) vs. #Mg, #Mg=Mg/(Mg+Fe^{2+}). (c) F (wt%) vs. BaO (wt%). (d) Al_2O_3 (wt%) vs. BaO (wt%). (e) TiO_2 (wt%) vs. Na_2O (wt%). (f) F (wt%) vs. TiO_2 (wt%). (g) Na_2O (wt%) vs. F (wt%). (h) BaO (wt%) vs. MgO (wt%).

Table 10.7. Representative compositions of mica from Murfreesboro, Chigicherla CC1, Wajrakarur P-2 and Mulligiripally P-5 lamproites and Torngat UML.

	1	2	3	4	5	6	7	8	9	10	11	12	13	14
	Murfreesboro		Chigicherla CC1		Wajrakarur P-2			Mulligiripally P-5		Torngat				
	Groundmass					Microphenocryst		Groundmass		Microphenocryst and Groundmass				
(wt%)										zone 1	zone 2	zone 3	zone 4	zone 5
SiO_2	41.46	39.77	39.75	39.14	41.77	40.31	42.75	40.92	40.75	37.20	42.45	39.03	40.73	39.34
Al_2O_3	6.48	10.23	9.93	10.72	9.57	6.75	6.40	7.49	8.32	13.04	10.97	12.32	10.37	0.05
FeO	5.62	5.16	1.99	3.04	2.28	1.06	1.47	6.77	3.55	13.39	2.50	4.86	3.29	0.00
Fe_2O_3	7.07	4.10	4.63	4.42	3.44	8.03	5.89	6.62	5.65	1.43	1.41	2.63	3.63	18.64
TiO_2	2.59	2.93	1.98	3.58	1.42	3.38	1.96	2.16	2.30	3.72	0.08	2.97	0.64	0.02
Cr_2O_3	bdl	bdl	bdl	bdl	bdl	bdl	bdl	bdl	bdl	bdl	bdl	0.14	bdl	bdl
V_2O_3	0.03	0.05	0.05	0.06	bdl	0.06	0.03	0.04	0.02	bdl	bdl	bdl	bdl	bdl
MnO	0.11	0.11	0.10	0.09	0.03	0.04	0.03	0.12	0.07	0.22	0.04	0.04	0.12	0.06
NiO	0.08	0.06	bdl	0.07	bdl	bdl	bdl	0.03	0.04	0.02	0.14	0.02	0.10	0.03
MgO	21.39	22.36	24.76	23.10	25.12	22.53	23.37	22.09	23.24	16.85	27.16	23.29	26.06	28.66
K_2O	9.38	9.31	9.23	9.00	9.63	9.00	9.54	8.65	9.54	8.98	9.76	9.07	9.50	8.45
BaO	0.25	0.76	2.44	1.52	1.34	3.35	1.66	0.35	1.06	0.56	0.12	0.59	0.57	0.49
Na_2O	0.08	0.02	0.15	0.32	0.06	bdl	0.03	0.10	0.05	bdl	bdl	bdl	bdl	bdl
CaO	0.05	bdl	0.03	0.05	0.08	0.07	0.03	bdl	0.03	0.09	bdl	0.07	bdl	bdl
SrO	1.31	1.47	0.59	0.60	bdl	bdl	bdl	bdl	bdl	0.38	0.84	0.50	0.91	0.28
F	0.41	0.24	bdl	bdl	0.38	0.97	1.21	0.15	0.38	0.35	0.17	0.38	0.18	bdl
H_2O	3.46	3.42	3.84	3.85	4.17	4.07	4.10	4.10	4.11	3.84	3.84	3.93	3.74	3.91
Total	99.77	99.99	99.47	99.57	99.28	99.63	98.47	99.59	99.12	100.07	99.47	99.83	99.84	99.92
(apfu) Cations on basis of 24 (O, OH, F)														
Si	6.095	5.794	5.788	5.683	5.981	5.948	6.006	5.938	6.249	5.547	6.017	5.623	5.852	5.838
Al	1.123	1.756	1.704	1.834	1.290	1.431	1.622	1.172	1.103	2.292	1.832	2.092	1.756	0.009
Fe^{3+}	0.782	0.449	0.508	0.483	0.728	0.621	0.372	0.890	0.648	0.161	0.151	0.285	0.393	2.081
Ti	0.000	0.000	0.000	0.000	0.000	0.000	0.000	0.000	0.000	0.000	0.000	0.000	0.000	0.002
$\sum$IV	8.000	8.000	8.000	8.000	8.000	8.000	8.000	8.000	8.000	8.000	8.000	8.000	8.000	7.930
Al	0.000	0.000	0.000	0.000	0.000	0.000	0.000	0.000	0.000	0.000	0.000	0.000	0.000	0.000
Ti	0.286	0.321	0.217	0.391	0.237	0.252	0.153	0.374	0.215	0.417	0.009	0.322	0.069	0.000
Cr	-	-	-	-	-	-	-	-	-	-	-	0.015	-	-
V	0.004	0.006	0.006	0.007	-	0.002	0.000	0.007	0.003	-	-	-	-	-
Mn	0.014	0.013	0.013	0.012	0.015	0.009	0.003	0.005	0.003	0.027	0.005	0.005	0.014	0.007
Fe^{2+}	0.691	0.629	0.243	0.369	0.828	0.434	0.274	0.131	0.179	1.670	0.296	0.585	0.396	0.000
Ni	0.009	0.007	0.002	0.008	-	-	-	0.000	0.000	0.003	0.015	0.003	0.012	0.004
Mg	4.688	4.857	5.375	5.000	4.814	5.057	5.385	4.948	5.093	3.746	5.671	5.003	5.506	5.989
$\sum$VI	5.693	5.833	5.855	5.787	5.905	5.759	5.817	5.466	5.495	5.863	6.000	5.933	6.000	6.000
K	1.759	1.730	1.714	1.667	1.613	1.776	1.766	1.691	1.779	1.708	1.765	1.667	1.741	1.600
Ba	0.015	0.044	0.139	0.086	0.020	0.060	0.075	0.193	0.095	0.033	0.006	0.034	0.032	0.028
Na	0.118	0.067	0.019	0.006	0.043	-	0.106	0.277	0.342	-	-	-	-	-
Ca	0.013	-	0.023	0.050	0.015	0.008	0.009	-	0.005	0.001	-	0.000	-	-
Sr	0.004	0.000	0.003	0.004	-	-	-	-	-	0.007	0.000	0.006	0.000	0.000
Mg	0.000	0.000	0.000	0.000	0.000	0.000	0.000	0.000	0.000	0.000	0.069	0.000	0.076	0.352
$\sum$A	1.908	1.845	1.898	1.814	1.691	1.955	1.963	2.171	2.224	1.850	1.886	1.813	1.898	1.990
F	0.609	0.677	-	-	0.000	0.000	0.000	0.000	0.000	0.178	0.374	0.227	0.415	-
OH	3.391	3.323	3.729	3.724	4.000	4.000	4.000	4.000	4.000	3.822	3.626	3.773	3.585	3.870

bdl: below detection limit; FeO and Fe_2O_3 recalculated

10.4.14. Chigicherla CC1, Wajrakarur P-2, Mulligiripally P-5 lamproites, India

Groundmass phlogopite in Chigicherla CC-1 pipe (classified as lamproite with our data and in agreement with Azhar M. Shaikh by personal communication) is Al-poor (7.8-10.7 wt% Al_2O_3) but tetraferriphlogopite is absent. It has variable tenors in Ti (1.2-3.6 wt% TiO_2) and F (0.3-0.8 wt%), as seen in Fig. 10.51-53, Table 10.7). It is Cr-free and Na-free. No clear zoning is observed.

Groundmass phlogopite in Wajrakarur P-2 lamproite has similar composition as those of the microphenocrystic phlogopite, which is Al-poor (5.9-10.9 wt% Al_2O_3). It has variable contents of Ti (1.0-3.4 wt% TiO_2) and Na (0.2-1.2 wt% Na_2O, Fig. 10.50-52, Table 10.7), whereas Cr is lacking.

Microphenocrystic phlogopite in Mulligiripally P-5 lamproite is Al-poor (6.8-8.3 wt% Al2O3) but the tetraferriphlogopite component is absent. It is Ti-poor (2.0-2.5 wt% TiO_2), and the F tenors are very low (<0.1 wt% F). It is Cr-free and the Na contents are also very low (0.2-0.6 wt% Na_2O, Fig. 10.50-52, Table 10.7). No clear zoning is observed.

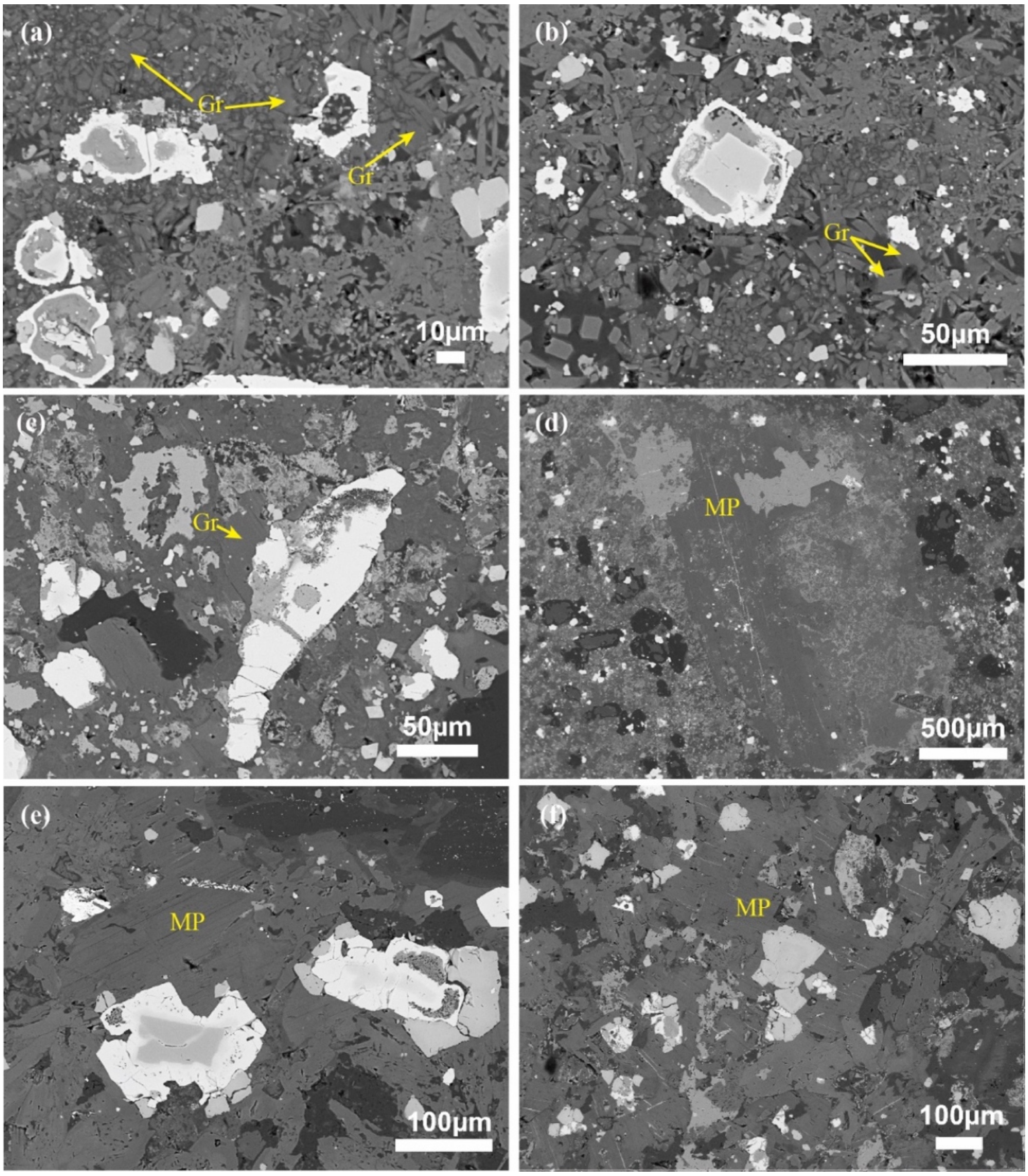

Fig. 10.51. Back-scattered electron (BSE) images of microphenocrysts (MP) and groundmass (Gr) micas from Chigicherla CC1 (a-b), Wajrakarur P-2 (c-d) and Mulligiripally P-5 (e-f) lamproites.

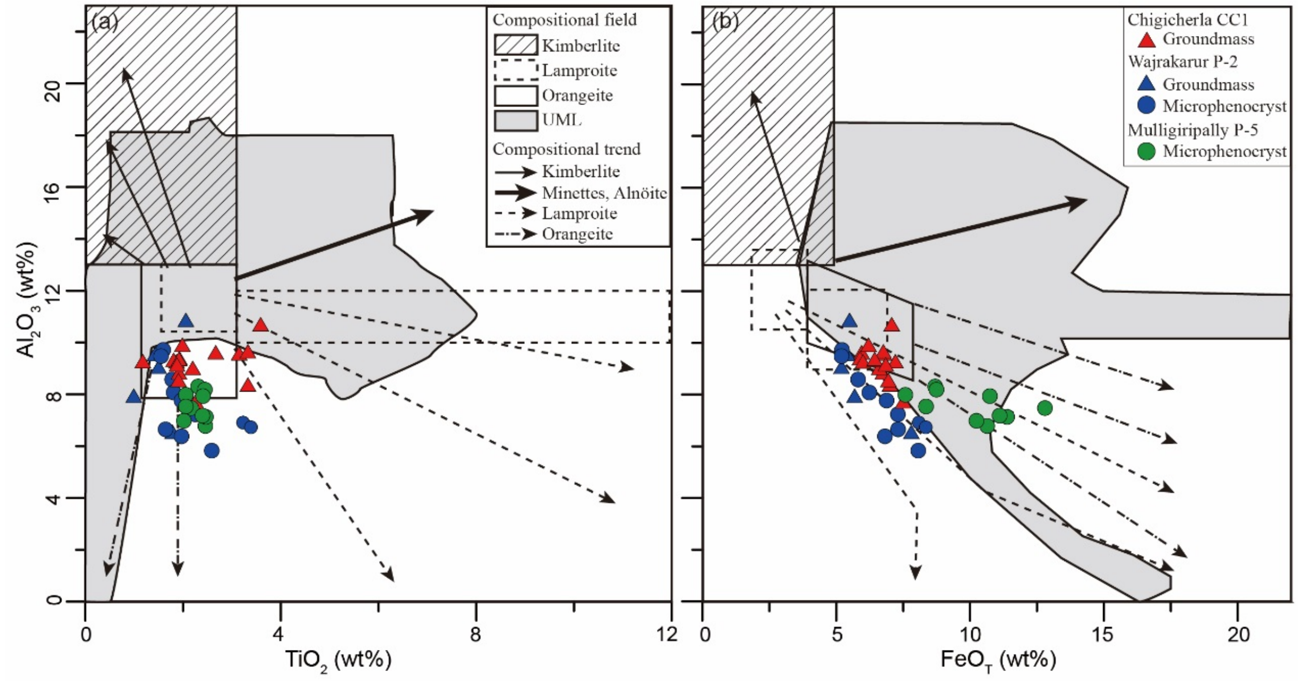

Fig. 10.52. Al_2O_3 vs. TiO_2 (wt%) and Al_2O_3 vs. FeO_T (wt%) compositional variation of microphenocrysts and groundmass micas from Chigicherla CC1, Wajrakarur P-2 and Mulligiripally P-5 lamproites. Compositional fields and trends for micas from kimberlites, lamproites, orangeites and minettes are adapted from Mitchell (1995). UML field is adapted from (Mitchell et al. (1999) and Tappe et al. (2004, 2006, 2014).

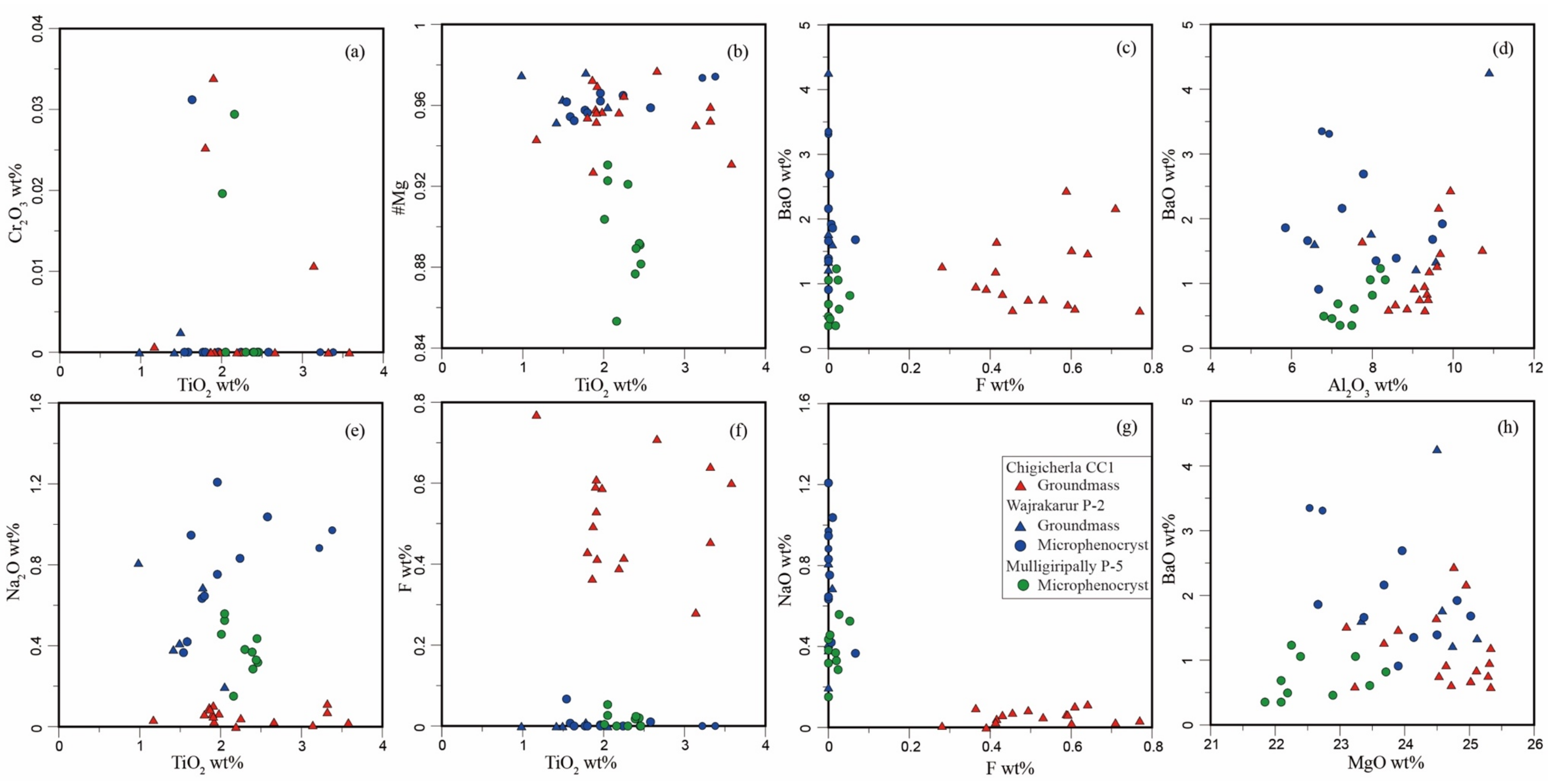

Fig. 10.53. Composition of microphenocryst and groundmass micas from Chigicherla CC1, Wajrakarur P-2 and Mulligiripally P-5 lamproites. (a) TiO_2 (wt%) vs. Cr_2O_3 (wt%). (b) TiO_2 (wt%) vs. #Mg, #Mg=Mg/(Mg+Fe^{2+}). (c) F (wt%) vs. BaO (wt%). (d) Al_2O_3 (wt%) vs. BaO (wt%). (e) TiO_2 (wt%) vs. Na_2O (wt%). (f) F (wt%) vs. TiO_2 (wt%). (g) Na_2O (wt%) vs. F (wt%). (h) BaO (wt%) vs. MgO (wt%).

10.4.15. Torngat UML, Canada

Microphenocrystic and groundmass phlogopite show complex zonings (6 compositional zones, Fig. 10.54-56, Table 10.7). Zone 1 is found as core of microphenocrysts; it has strong variations in the contents of Al (10.8-19.0 wt% Al_2O_3), Ti (0.9-4.1 wt% TiO_2) and Fe (12.1-14.7wt% FeO_T).

Zone 2 has similar compositions in Al (9.7-18.6 wt% Al_2O_3), but is strongly impoverished in Ti (0-0.6 wt% TiO_2) and Fe (3.2-7.7 wt% FeO_T). Inclusions of groundmass chromite occur in zone 2. No clear crystallization order between zone 1 and zone 2 is observed. Zone 1 and zone 2 are mantled by zone 3.

Zone 3 is Al-poor (10.0-12.6 wt% Al_2O_3), and slightly enriched in Al (1.5-3.2 wt% TiO_2) and Fe (6.0-8. 3wt% FeO_T).

Zone 3 is mantled by a thin rim of zone 4 which has less Ti and Al than zone 3 (0.6-0.7 wt% TiO_2 and 10.4-10.5 wt% Al_2O_3).

The outermost rim zone 5 corrodes the above units and is made up by tetraferriphlogopite.

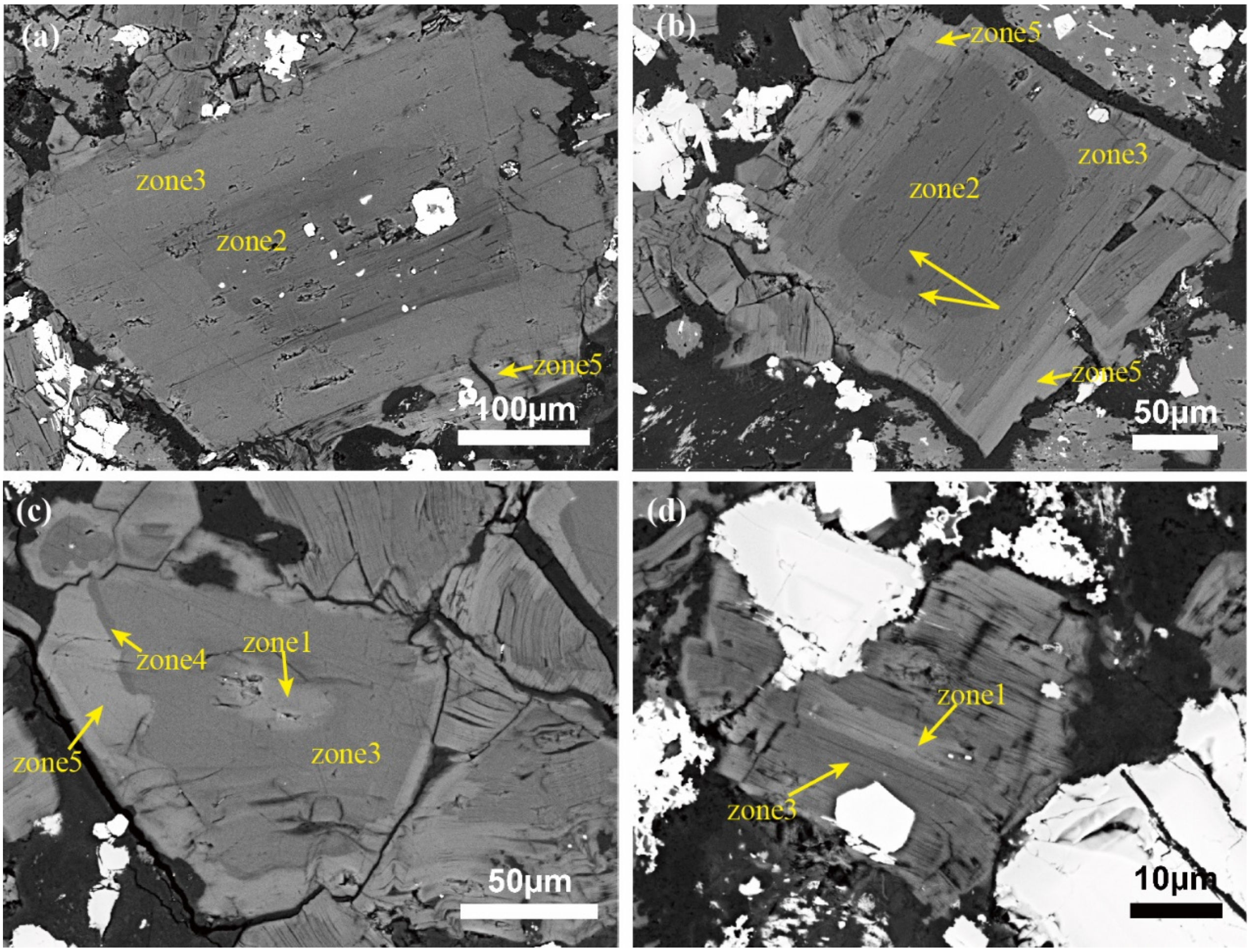

Fig. 10.54. Back-scattered electron (BSE) imagings of microphenocrystic and groundmass micas from Torngat UML showing 5 different compositional zones (zone 1-zone5).

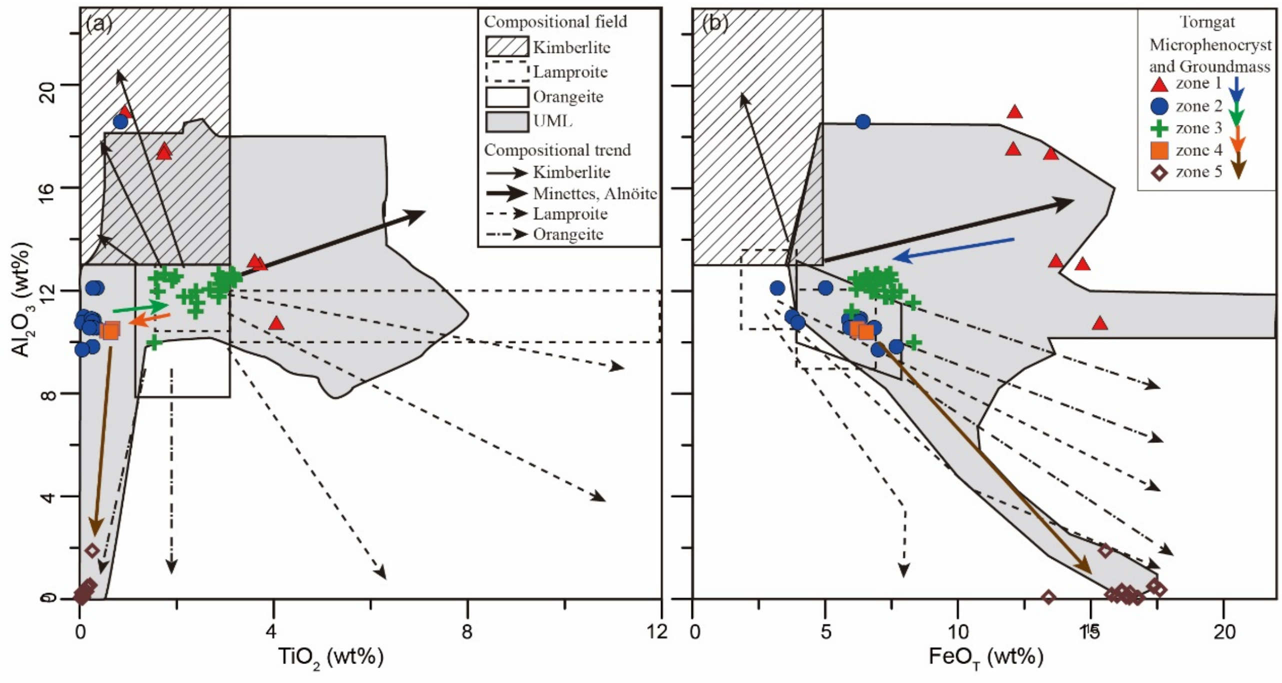

Fig. 10.55. Al_2O_3 vs. TiO_2 (wt%) and Al_2O_3 vs. FeO_T (wt%) compositional variation of microphenocrystic and groundmass micas from Torngat UML showing 5 different compositional zones (zones 1-5). Compositional fields and trends for micas from kimberlites, lamproites, orangeites and minettes are adapted from Mitchell (1995). UML field adapted from (Mitchell et al. (1999) and Tappe et al. (2004, 2006, 2014).

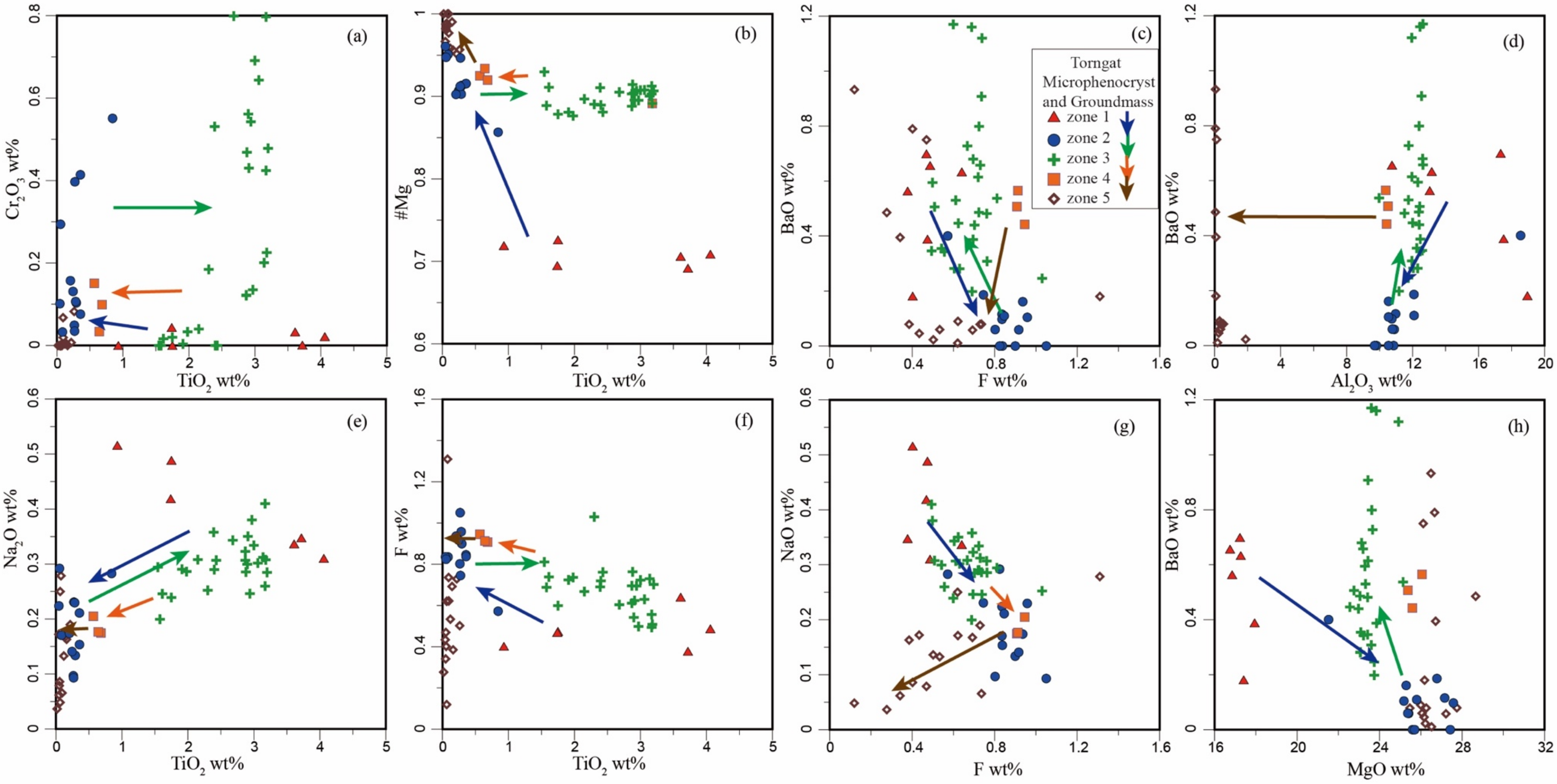

Fig. 10.56. Composition of microphenocrystic and groundmass micas from Torngat UML showing 5 different compositional zones (zones 1 - 5). (a) TiO_2 (wt%) vs. Cr_2O_3 (wt%). (b) TiO_2 (wt%) vs. #Mg, #Mg=Mg/(Mg+Fe^{2+}). (c) F (wt%) vs. BaO (wt%). (d) Al_2O_3 (wt%) vs. BaO (wt%). (e) TiO_2 (wt%) vs. Na_2O (wt%). (f) F (wt%) vs. TiO_2 (wt%). (g) Na_2O (wt%) vs. F (wt%). (h) BaO (wt%) vs. MgO (wt%).

10.5. DISCUSSION

10.5.1. Composition of micas in kimberlite and related rocks

The composition of micas in the study rocks has a diversity of compositions, but most of the published studies deal on the variations of some major or minor components, without taking into account the mineral species involved. However, the problem of the representation of mineral compositions in complex series as those present in the micas from kimberlites and related rocks has not been solved. In these rocks, micas can be a combination of many different end-members. Moreover, there are some instrumental limitations, as the determination of the halogen content, the analysis of light elements, and the problems derived from the microprobe analyses in strongly cleavaged minerals. In addition, there are difficulties to resolve the problem of the Fe oxidation state, to calculate the water and to establish the correct number of vacancies in every position.

In this study we had used different systems to create the structural formulas, with similar results. The next problem was how to represent the mineral compositions, because the mineral composition of micas in kimberlites and related rocks is very diverse. However, a quick examination revealed that most of the analyses could be represented in terms of the next end-members:

*phlogopite
*annite
* eastonite
*siderophyllite
*tetraferriphlogopite
*tetraferriannite
*kinoshitalite
*ferrokinoshitalite

Most of the compositional variations of these micas can be modeled in terms of the ratios Mg/Fe and the aluminum contents (Al^{IV}, Al^{VI} and total Al), and taking also into account the Ba contents in the A position. One must take into account that only members of the phlogopite-annite and tetraferriphlogopite-tetraferriannite series occur strictly as mineral species in these rocks. However, Al may occur in octahedral position thus providing an eastonite/siderophyllite component, or Ba in the A position in amounts that does not achieve 1 apfu (on basis of 24 (O,OH,F)). Therefore, we have designed a new graphic to show in mineralogical terms the most common compositional variations (using apfu values and not wt% as in most of the existing diagrams), representing in the X axis the values of Al^{IV} versus the values of the ratio $(Al^{VI}-Ba+(Mg/(Mg+Fe^{2+})))*(1+Al^{IV})$ in the Y axis. Most of the available analysis roughly plot on a line in this graphic, thus reflecting progressive variations in chemical compositions in the tetraferriphlogopite-tetraferriannite-phlogopite-annite domains, with minor deviations towards the fields of eastonite-siderophyllite or, alternatively, kinoshitalite-ferrokinoshitalite (Fig. 10.57). However, neither octahedral Al or Ba are higher than 0.5 apfu, and therefore the Al-rich or Ba-rich terms as eastonite or kinoshitalite are never achieved.

The contents in Fe^{2+} tend to be lower than those of the Mg, and therefore the series are more restricted to the terms tetraferriphlogopite-phlogopite-eastonite-kinoshitalite. In fact, the extreme high Fe ($Fe/(Fe+Mg) \geq 0.2$) content in macrocrysts is suggested to be restricted to carbonatites rather than in kimberlites (Reguir et al., 2009). In our calculations all octahedral Fe has been assumed to be Fe^{2+}.

Other minor components are Ti, F and Na, but their variations will be discussed in the corresponding dominant terms.

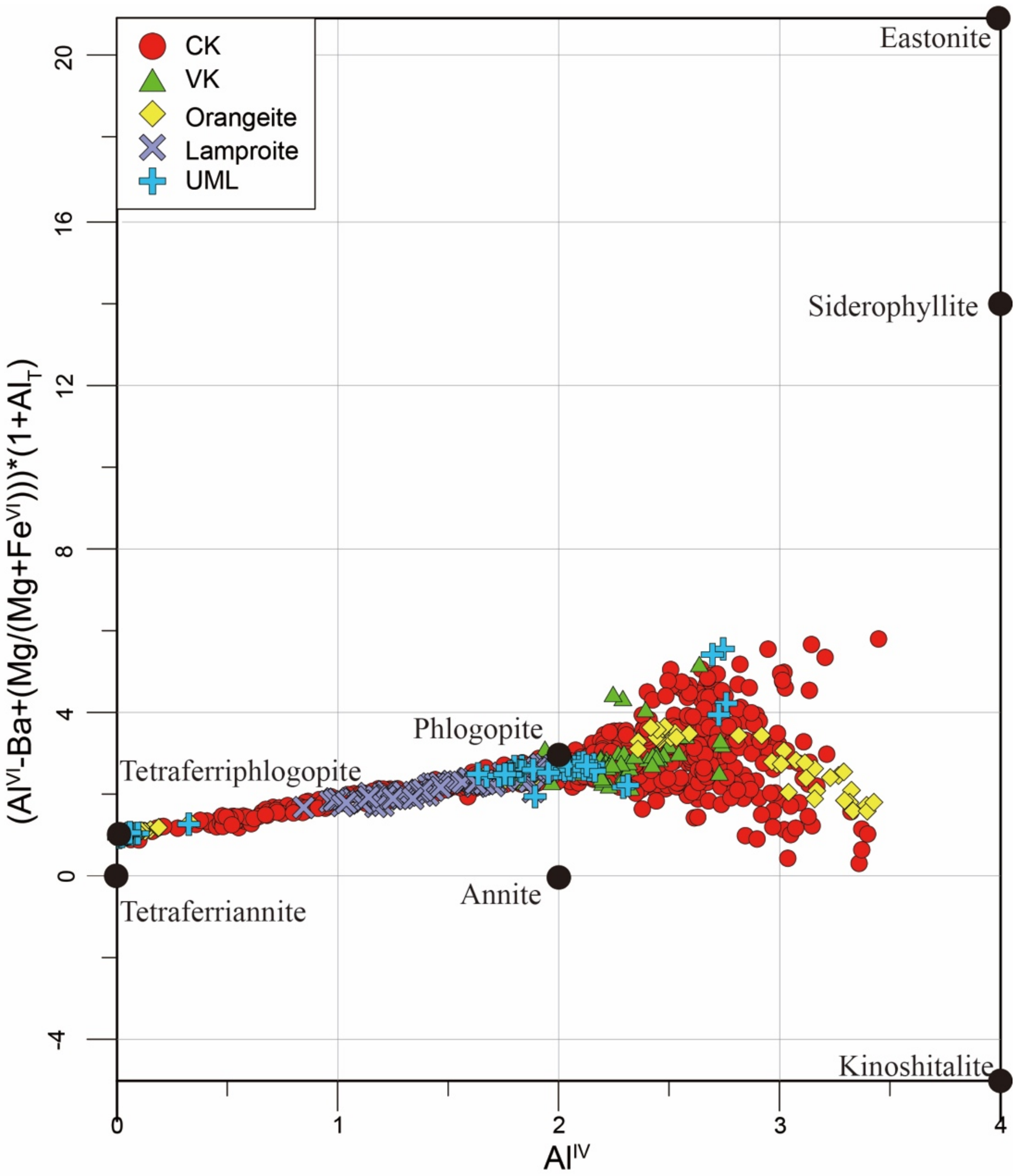

Fig. 10.56. Compositional variations in micas from kimberlites and related rocks, in the diagram tetrahedral Al (AI^{IV}) versus the values of the ratio (Al^{VI}-Ba+(Mg/(Mg+Fe^{VI})))*(1+ Al_T), on basis of 24 (O,OH,F).

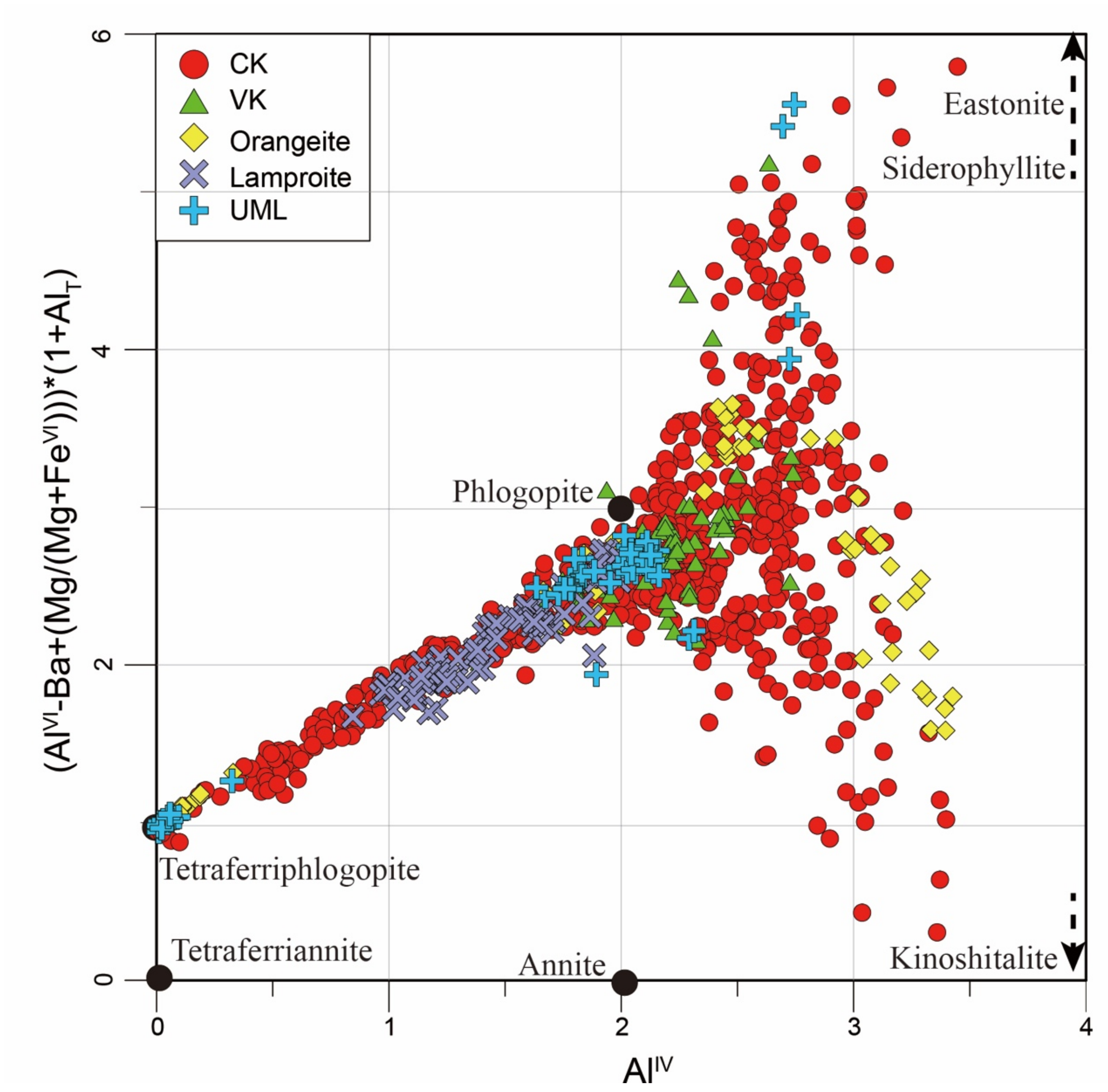

Fig. 10.56 (continuation, detail). Compositional variations in micas from kimberlites and related rocks, in the diagram tetrahedral Al (AI^{IV}) versus the values of the ratio (Al^{VI}-Ba+(Mg/(Mg+Fe^{VI})))*(1+Al_T).

10.5.1.1. Tetraferriphlogopite

Tetraferriphlogopite is a rare mica, and was discovered in many carbonatites and their related glimmerites, as in Kovdor in Russia and Siilinjärvi in Finnland (Puustinen, 1973). It has been further described in many rocks, as orangeites , lamproites (Kaur and Mitchell, 2013) and aillikites (Digonnet et al., 2000).

Tetraferriphlogopite occurs as core of groundmass mica in some occurrences in kimberlites and related rocks (eg. Karowe AK6 kimberlite), while it occurs as outermost rim in groundmass mica in other occurrences (eg. Banankoro kimberlite). This could indicate differences in the melt evolutionary history.

The majority of the analysed tetraferriphlogopite crystals are F-rich; some of them fit in the fluorotetraferriphlogopite domain (eg. Karowe kimberlite). In addition, some of them are Na-rich and they are relatively Ba-poor. In general, there is a positive correlation between Na and F in tetraferriphlogopite from coherent kimberlite (Fig. 10.11a). A similar occurrence of this F- and Na-enriched tetraferriphlogopite has been found in alkali-enriched and halogen-bearing carbonate melt inclusion in olivine in a kimberlite (Golovin *et al.*, 2007; Abersteiner *et al.*, 2018b). This Na enrichment in tetraferriphlogopite has been explained by a crystallization from a volatile (F)-rich melt/fluid. In fact, some authors proposed that the last derivatives of the kimberlite melt have an alkaline carbonatitic composition (Golovin et al., 2007): in comparison with the early kimberlite melts, the late melts evolve near the surface to have higher contents of Ca, Fe, alkalis, and volatiles (CO_2, H_2O, F, Cl, and S) at lower concentrations of SiO_2, MgO, Al_2O_3, Cr_2O_3 and TiO_2. However, as indicated, the tetraferriphlogopite may occur in the cores, intermediate rims or external rims of the crystals, thus suggesting a more complex history.

Mitchell (1995) suggested that tetraferriphlogopite in kimberlite is due to relatively oxidizing conditions with Fe^{3+} as total iron, which is associated with addition of groundwater to magma and/or rapid carbon dioxide loss. However, Mössbauer spectroscopy and X-ray absorption near-edge spectroscopy (XANES) studies show that tetraferriphlogopite could have both Fe^{2+} and Fe^{3+} and the last in both tetrahedral and octahedral positions (Cruciani et al., 1995). The formation of tetraferriphlogopite is due to low availability of Al in melt (Lee et al., 2003). Thereby, the tetraferriphlogopite origin is more likely due to low availability of Si and Al in melt rather than a more oxidizing condition. Al deficiency could also be relative to peralkalinity of the parental magma (Mitchell, 1995).

In the 79 studied kimberlites and related rocks, the presence of tetraferriphlogopite is always accompanied by the development of spinel trends C or E (trend 2 in other works) if the groundmass spinel is zoned and some trend is shown. These data also suggest a deficit in Al during the stages of crystallization of tetraferriphlogopite.

10.5.1.2. High-Ba phlogopite

(Guo and Green, 1990), with the support of experimental data, proposed that the Ba content in the phlogopite from the mantle should increase along with the Ti content when the temperature (independently of the pressure) would be increased. However, the occurrence of Ba-rich and Ti-poor phlogopites in mantle xenoliths (Arima, 1988) poses a question over this interpretation.

Ba is allowed incorporate into the phlogopite structure during ascent of the kimberlite magmas in the earliest stages of kimberlite genesis (Barnett and Laroulandie, 2017). Groundmass phenocrysts nucleated during a rapid cooling inducting all available Ba in the chemical environment to be immediately fractionated into the phlogopite structure in the near surface environment (Barnett and Laroulandie, 2017).

The highest Ba contents (BaO >12 wt%) in the study rocks were found in Point Lake kimberlite (up to 15.1 wt% BaO), Laramie Co. kimberlite (up to 14.7 wt% BaO) and Bucke Township (up to 14.2 wt% BaO). In these cases the highest Ba content are in the cores of microphenocrysts. High Ba tenors tend to be associated with F enrichments; similar behaviour has also been observed in Finish kimberlites (O’Brien and Tyni, 1999) and in the Igwisi Hills kimberlites (Willcox et al., 2015).

However, the highest Ba may occur in cores of microphenocrysts (eg. Point Lake kimberlite and Helam orangeite in this study), but also in rims (eg. Snap Lake kimberlite in this study, or P-3 Wajrakarur by Shaikh et al., 2018) or intermediate zones (eg. Riverton, Bultfontein or Shengli kimberlites in this study). Replacement of K phlogopite in rims has been described in other kimberlites, i.e. the Igwisi Hills in Tanzania, and in some cases the crystal may became replaced in full, as in West Greenland (Nielsen et al., 2009).

Groundmass phlogopite enriched in Ba was proposed as typical for kimberlites (Mitchell, 1995; Giuliani et al., 2016). However, Ba enrichment is also found in microphenocrystal phlogopite in Helam orangeite, and many kimberlites (nearby 20%) were found to have negligible Ba contents in this study. Moreover, Ba contents cannot to be used to distinguish between kimberlites and carbonatites because of significant overlap (Reguir et al., 2009).

Ba-rich phlogopites have also been described in carbonatite veinlets in fergusite from the Dunkeldyk potassium-rich basaltoid complex (south-eastern Pamirs, Solovova et al., 2009). These authors note that the available experimental studies suggest that the mineral-forming media of such Ba-rich phlogopites was a residual melt enriched in volatiles (including F) and fluid-mobile elements.

An important problem to discuss in Ba-rich micas is the source of this element. Two main sources of Ba could be invoked: a) a continental contamination (by extraction from K-bearing minerals as feldspars, micas or amphiboles from the host rocks) and b) a mantle provenance.

A crustal provenance could be a possibility, taking into account that metasomatic processes on the host rocks, similar to the fenitization, occur in many kimberlites (Smith et al., 2004). Therefore, the possibility of crustal contamination during the kimberlite emplacement cannot be ruled out and has been proposed in some cases (i.e., Caro et al., 2004). However, a Ba enrichment by extraction of this element from the structure of the feldspars or micas from the host rocks should be accompanied by other enrichments in elements present in the same crustal K-bearing minerals, as Pb; moreover, there are no much evidences of simultaneous Si/Al enrichments. For instance, the crustal contamination suggested to explain the occurrence of magmatic alkaline halides and sulfides in the Udachnaya kimberlite has been found recently erroneous (Kamenetsky *et al.*, 2014; Abersteiner *et al.*, 2018c).

Barium is a large cation and should be a highly incompatible trace element in the peridotitic upper mantle. However, Ba may be enriched in different mineral manifestations in the metasomatized mantle rocks. In these domains, Ba is present in the structures of the mica and amphibole groups, although BaO contents in phlogopites from mantle xenoliths rarely exceed 0.8 wt% (Smith *et al.*, 1979b; Delaney *et al.*, 1980). Other possible Ba carriers include the LIMA minerals (lindsleyite-mathiasite series; chapter 9 in this work; Haggerty, 1983; Haggerty et al., 1983, 1986) and Ba-K titanate minerals (Jones et al., 1982; Haggerty et al., 1986; Grey et al., 1987). Accepting that the Ba can have a mantle source, a possible source should be some kind of interaction with these metasomatized rocks or a direct partial melting of them.

10.5.1.3. High-Al phlogopite

Mica is a principal host for Al in primary mineral assemblage in kimberlites and related rocks. Therefore, the Al content in the primary micas can reflect the Al content of the melt. However, the crystallization of micas took place in all of the cases after the crystallization of the spinels, and this process may have depleted the Al content in the melt.

For a long time, the authors studying kimberlites had used the model of mica evolution proposed by Mitchell (1995), suggesting that mica composition in kimberlite groundmass is enriched in Al, Ba, plus F, Zr and Nb, and depleted in Fe, Ti, plus Na, Sr and Ni. Last studies did not propose many variations (Giuliani et al., 2016). Following these authors, the dominant and characteristic trend is Al enrichment in micas of kimberlite and the typical kimberlite mica field should be above 13 wt% Al_2O_3 (Fig. 10.6; Mitchell, 1995), while the half of this kimberlite mica field is overlapped with the mica field of UML (Tappe et al., 2004, 2006, 2014). However, the Al entrapment in micas can be made in two paths: via enrichment in tetrahedral Al coupled by Ba entrance in A (kinoshitalite component) or via simultaneous enrichment of Al in tetrahedral and octahedral positions (eastonite-siderophyllite component in Fig. 10.56). A true eastonitic component is never achieved in the studied micas from the selected occurrences, being $Al^{VI}< 1$ apfu (on basis of 24 (O,OH,F)); however, a proportion of the eastonite-siderophyllite end member is usually present in different positions of the crystallization sequences. High Al contents are found in kimberlites (both in coherent and volcaniclastic), but also in ultramafic lamprophyres and in some orangeites. Many kimberlites have unzoned or Al-depleted micas, as in some archetypical kimberlites of the Kimberley area (less than 12.83 wt% Al_2O_3; (Muramatsu, 1983) or southern India (6.24-12.78 wt%; Chalapathi Rao et al., 2011). Thy et al. (1987) concluded that Al^{VI} should be absent in lamproites and common kimberlites in after study kimberlites and lamproites from Greenland. However, many worldwide kimberlites contain significative Al^{VI}, whereas it is absent in other lamproites. Therefore, the occurrence of high-Al phlogopite cannot be used as an argument to classify these rocks.

Finally, Al contents in phlogopite could be a result of the primary magmatic composition of the kimberlite, but also could be a result of crustal contamination.

10.5.1.4. High-Ti phlogopite

High Ti contents in phlogopite xenoliths have been proposed to be related with a crystallization at high temperature in the mantle, independently of the pressure (Tronnes et al., 1985).

In the classical diagrams by Mitchell (1995), the Ti contents were proposed as a discriminant factor between kimberlites and lamproites, being lower in kimberlites. However, our study demonstrates that Ti may have very high values in kimberlites (see, for instance, Fig. 10.7).

High Ti and Cr found as a rim in complex macrocrysts crystallised from kimberlite magma from the Bultfontein kimberlite are interpreted as the result of an early crystallization of kimberlite magma in the upper mantle previously to the eruption of the kimberlite, and could have similar composition as batches of magma that never achieved the surface ("failed kimberlites", Giuliani et al., 2016).

10.5.1.5. High-Cr phlogopite

High Cr contents are not very common in kimberlites although in this study were found in Banankoro “B” (up to 0.8 wt%), Chicken Park (up to 1.1 wt% Cr_2O_3), Karowe AK6 (up to 1.5 wt% Cr_2O_3), Riverton (up to 1.6 wt% Cr_2O_3), Gate-Adah (up to 1.7 wt% Cr_2O_3), Kimberley (up to 1.9 wt% Cr_2O_3) and Bultfontein (up to 1.6 wt% Cr_2O_3), being all of them coherent kimberlite rocks. High Cr content in volcaniclastic rock were found in Ville-Marie (up to 1.2 wt% Cr_2O_3), Orapa AK1 "B" (up to 1.8 wt% Cr_2O_3) and Damtshaa BK9 “B” (up to 1.6 wt% Cr_2O_3).

Macrocrysts from kimberlites are enriched in Cr when compared with micas from carbonatites (Reguir et al., 2009). As indicated in the above section, high Ti-Cr zones of phlogopite macrocrysts from Bulfontein have composition similar to high Cr-Ti polymict breccia xenoliths that are interpreted as failed kimberlite intrusions (Giuliani et al., 2016), whereas phlogopite from mantle peridotite xenoliths is typically low in Cr-Ti.

10.5.2. Crystallization sequence

Macrocrystic micas can have both origins, xenocrystic or primary. It is undoubtable that the disaggregation of mantle xenoliths could produce large volumes of mica macrocrysts, while macrocrysts in orangeite magma have been interpreted as crystallized prior to emplacement the magma and be cogenetic with microphenocrysts (Mitchell, 1995). In fact, in many cases it is difficult to assert the origin of an isolate macrocryst weather is xenocrystic or primary. Cores of microphenocrysts, in some cases, may be free of inclusions of groundmass minerals such as spinel, apatite and perovskite, thus making difficult to define a xenocrystic or primary origin.

Cores of microphenocrysts, less frequently, and the external rims of microphenocrysts, more frequently, are poikilitic showing inclusions of groundmass minerals (spinel, apatite and perovskite). Therefore, these generations of micas formed relatively late in the crystallization sequence of the magma, syn- and/or to post the formation of the these groundmass minerals. Groundmass mica commonly has identical composition with the outermost or the last few zonings, thus crystallized at the same time as them.

Micas, however, may be replaced by secondary minerals as chlorite, vermiculite and expansive clays, which can replace completely the mica crystals.

10.5.3. Complex zoning trends

Micas in kimberlites and related rocks present very complex compositional zoning, mainly reflected in the proportions of Fe^{2+}, Al (total), Fe^{3+}, Ti and Ba. However, as indicated, there are also important variations in the contents of Na, F and Cr; it is also important to note the differences in behaviour of Al^{IV} and Al^{VI}. Most of the studies developed to the present have been carried out in terms of some of the major components, in particular, Al and Ti. The classical trends proposed by Mitchell (1995) are based on binary diagrams Al_2O_3-TiO_2. However, these diagrams use wt% and not atomic proportions, and therefore they are not indicative of the molar mineral composition and does not provide information about the distribution of octahedral and tetrahedral aluminium. To help to solve this problem, as indicated before, we have created in this study some new diagrams that could be used to show the mineralogical composition of the micas (see Fig. 10.56). In these diagrams Ti is not used because it is not a major component and Ti never achieves more than 1 apfu (on basis of 24 (O,OH,F)). These low contents do not account for the dominance of other types of micas, such as oxy-micas.

These diagrams can also be used to explain in mineralogical terms the evolution of micas in kimberlites and related rocks. Therefore, we selected several examples of the studied rocks to check the use of these diagrams. One must take into account that approximately half of the study rocks have unzoned micas, which use to be nearby the composition of the phlogopite end member, with minor annite or eastonite components. Therefore, these diagrams are only showing variations of representative samples among the complexly zoned micas.

Zoning may be different between macrocrysts and microcrysts in some cases, at least in some stages. Banankoro macrocrystic phlogopite has an early enrichment towards the eastonite end member (showing an increase in Al^{IV} and Al^{VI}; Fig. 10.57a). One must take into account that the composition of mica in the globular bodies is distinctly enriched in eastonitic component. This suggest a partial reaction trend (1) between two different mingling magmas that should be crystallizing different micas.

However, the eastonitic trend is reversed and finally, the Banankoro micas evolve towards tetraferriphlogopite, thus indicating a trend of decreasing Al, which is the contrary to the archetypical kimberlites of Mitchell (1995). However, similar trends with Al enrichment in the early stages and late evolution towards tetraferriphlogopite are also seen in Karowe AK6 (Fig. 10.57b), Riverton (Fig. 10.57v) and Bultfontein (Fig. 10.57d) kimberlites. In the Karowe AK6 and Riverton kimberlites there are no evidences of globular bodies with Al-rich micas. In the Karowe AK6 kimberlite, early micas are Al-poor, and evolve first towards phlogopite and then reverse to tetraferriphlogopite. However, globular bodies are present in the Bultfontein kimberlite, and their micas are also extremely Al-rich. Groundmass micas from the Bultfontein kimberlite also have a pattern of zoning similar to that of their equivalent micas in Banankoro. Hence, this type of early trend of Al enrichment (part octahedral and part tetrahedral) can be produced by some kind of reaction with some agent external to the kimberlite magma. In the cases of Banankoro and Bultfontein kimberlites, the existence of distinct batches of different magmas and the existence of different micas in both of them could explain some reaction grade between these magmas. In the other two cases, a possibility could be crustal contamination with Al-rich minerals, such as feldspars.

The behaviour of barium in micas is very different depending on each kimberlite. A Ba enrichment in micas (kinoshitalite/ferrokinoshitalite molecule) is only possible when is coupled with an Al^{IV} enrichment. However, the Point kimberlites evolve from kinoshitalite-rich component to phlogopite but finally to eastonite, thus indicating an impoverishment in Ba but an enrichment in Al^{VI} (Fig. 10.57e). The contrary trend can be seen in the Snap Lake kimberlite, which become enriched in both Al^{IV} and Ba, but not in Al^{VI} (Fig. 10.57f). Note that the vector of Al enrichment in the last case is very different to the vector of Al enrichment which is typical during eastonitic enrichments, where Al^{IV} enrichment is also accompanied with Al^{VI} enrichment.

The reaction with xenoliths and xenocrysts can produce high-Al micas, as can be seen in the reaction rims of phlogopite around garnets. However, these rims of micas tend also to evolve towards low-Al micas (Fig. 10.57f).

Mica evolution can be very different in groundmass micas from the same craton, as in the Chinese kimberlites of Shengli and Red Flag #1 (Fig. 10.58a).

On the other hand, micas from volcaniclastic kimberlites can be extremely enriched in Al (showing typical trends of enrichment in eastonite component), and therefore in this case it could be explained by crustal contamination (Fig. 10.58b).

The trends in orangeites may be more evolved than in kimberlites. The Helam orangeite evolves from kinoshitalite-rich mica towards phlogopite and finally to tetraferriphlogopite, thus indicating a decrease of Ba and Al^{VI} (Fig. 10.58c).

Trends in ultramafic lamprophyres evolve from eastonite-rich compositions to phlogopite and finally to tetraferriphlogopite (Fig. 10.58d).

The complex zonings could be related to rapid cooling process, degasifications and changing of fluid composition. Variation of evolutionary trends is depend upon local environment crystallization conditions such as redox conditions, water content and cooling conditions (Mitchell, 1995).

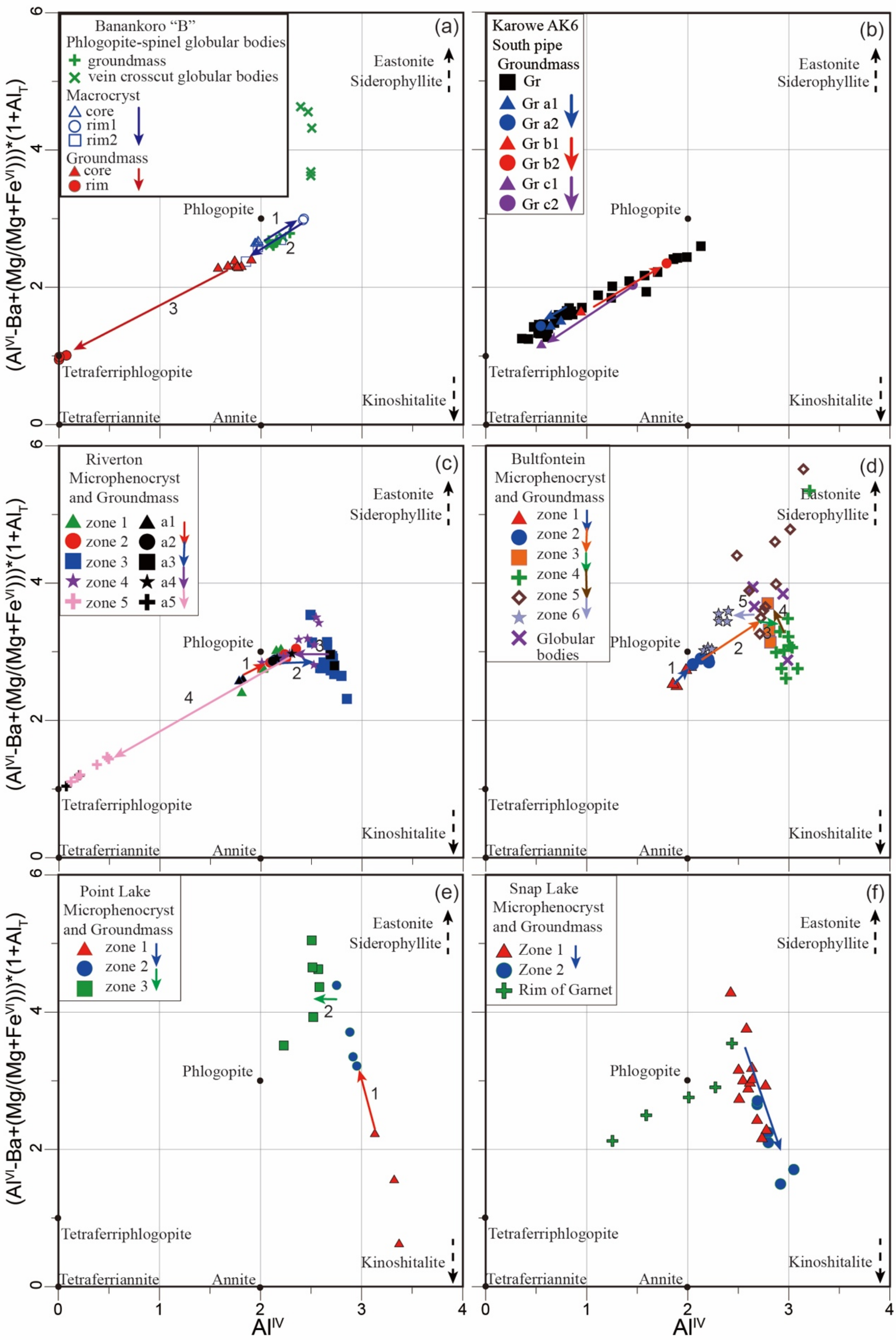

Fig. 10.57. Evolution of macrocrystic and microcrystic groundmass micas in selected zoned crystals from kimberlites.

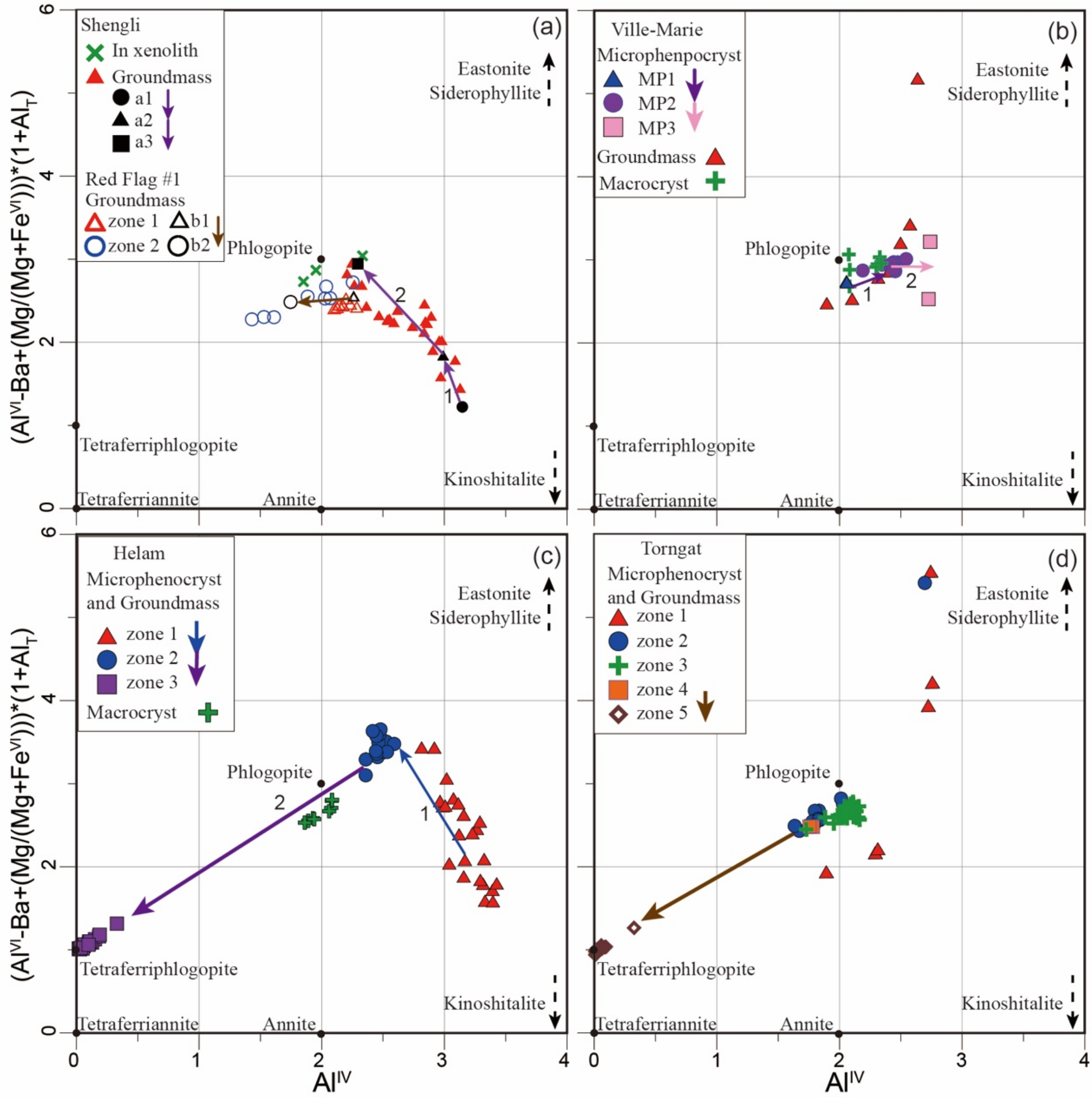

Fig. 10.58. Evolution of macrocrystic and microcrystic groundmass micas in selected zoned crystals from coherent kimberlites (a), volcanoclastic (b), orangeites (c) and ultramafic lamprophyres (d).

10.5.4. Considerations about using micas for rock classification

Tetraferriphlogopite has been reported as typical of lamproite (including orangeites, Mitchell, 1995; Kaur and Mitchell, 2013, 2016; Shaikh et al., 2018) and may also be found in some carbonatites (Brod et al., 2001; Lee et al., 2003). Tetraferriphlogopite is used for the discrimination between aillikite, orangeite and kimberlite (Mitchell and Bergman, 1991; Mitchell, 1995; Tappe et al., 2005). Mitchell (1995) suggests that tetraferriphlogopite could be found in kimberlites but should be less common. However, the wide population studied in this work demonstrate that the presence of tetraferriphlogopite in kimberlites is more common than stated. Moreover, not all lamproites (including orangeites) have tetraferriphlogopite.

Micas are one of the three mineral groups used for the discrimination between kimberlite, orangeites and UML (Tappe et al., 2005). However, extent compositional overlap between primary micas from the studied kimberlites, orangeites, lamproites and UMLs is observed (Fig. 10.4-10.8). Moreover, tetraferriphlogopite which was suggested as typical for UMLs and lamproites, is also frequently found in kimberlite. Ba-rich phlogopite which was proposed as typical for kimberlite is also found in lamproites. Moreover, the prevailing evolutionary trends proposed for micas in these rocks (Mitchell, 1995) are not consistent with our results in the most of the 79 occurrences studied in this work. Moreover, groundmass mica has very different composition in different lithofacies (volcaniclastic or coherent) rocks from the same pipe (i.e. Letlhakane DK1 Fig. 10.3-35). All of these inconsistences indicate the useless of micas for the classification between kimberlite and related rocks.

CHAPTER 11

CLINOPYROXENE GROUP

11. CLINOPYROXENE GROUP

11.1. INTRODUCTION

The pyroxene group of minerals are chain silicates, with a rhombic or monoclinic symmetry and a general structural formula that can be written as XYZ_2O_6 (Morimoto, 1988), where X are mainly cations in 8 coordination (mainly Ca and Na, but also Mn, K, Li and sometimes Mg and Fe2+), Y are cations in 6 coordination (mainly Al, Ti, Fe^{2+}, Fe^{3+}, Cr, V, Sn, Sc, Ni, Mn) and Z are cations in 4 coordination (mainly Si, rarely Al). They are divided into orthopyroxene subgroup (orthorhombic) and clinopyroxene subgroup (monoclinic). Classification is based on the infilling of the positions X, Y and Z. The pyroxene group minerals discovered up to the present moment are listed in Table 11.1.

Pyroxenes are largely used in diamond explorations as kimberlite indicator mineral (KIM), based on the chemical differences that exist between the mantle pyroxenes and their crustal equivalents (i.e., Stephens and Dawson, 1977; Quirt, 2004).

Moreover, xenocrystic clinopyroxenes are other commonly used as DIM's, as recorders of the characteristics of the underlying mantle (eg. Nimis, 1998; Cookenboo and Grutter, 2007; Zozulya et al., 2008).

The occurrence of pyroxene is also important in the discrimination between kimberlites and related rocks (Tappe et al., 2005). Primary clinopyroxene does not occur in coherent kimberlite (Mitchell, 1995; Tappe *et al.*, 2005; Kamenetsky et al., 2009). Therefore, some coherent rocks containing primary groundmass clinopyroxene have been reclassified as lamproite in this work.

11.2. TEXTURAL PATTERNS

Clinopyroxene subgroup minerals have been found in this work in the following parageneses:

A) Clinopyroxene in xenoliths;
B) Clinopyroxene xenocrysts;
C) Primary groundmass clinopyroxene in coherent lamproites;
D) Primary groundmass clinopyroxene in peletal lapilli in volcaniclastic kimberlites;
E) Clinopyroxene produced by replacement;
F) Clinopyroxene in globular bodies.

Different paragenesis of pyroxenes found in different studied kimberlites and related rocks are listed in Table 11.2.

Table 11.1. Classification of the pyroxene group minerals, based on the original IMA classification (Morimoto, 1988) expanded with the recent finding of new minerals after the database (MINDAT, 2019).

	Mineral names	End member	Solid solution
Orthopyroxenes			
	Protoenstatite	$Mg_2Si_2O_6$	$(Mg,Fe)_2Si_2O_6$
	Enstatite	$Mg_2Si_2O_6$	
	Ferrosilite	$Fe^{2+}{}_2Si_2O_6$	
	Donpeacorite		$(Mn,Mg)MgSi_2O_6$
Clinopyroxenes			
A.	***Mg-Fe pyroxenes***		
	Clinoenstatite	$Mg_2Si_2O_6$	$(Mg,Fe)_2Si_2O_6$
	Clinoferrosilite	$Fe^{2+}{}_2Si_2O_6$	
	Pigeonite	$(Mg,Fe,Ca)_2Si_2O_6$	
B.	***Mn-Mg pyroxenes***		
	Kanoite	$MnMgSi_2O_6$	
C.	***Ca pyroxenes***		
	Diopside	$CaMgSi_2O_6$	
	Hedenbergite	$CaFe^{2+}Si_2O_6$	
	Augite		$(Ca_x,Mg_y,Fe_z)(Mg_{y1},Fe_{z1})Si_2O_6$
	Johannsenite	$CaMn^{2+}Si_2O_6$	
	Petedunnite	$CaZnSi_2O_6$	
	Esseneite	$CaFe^{3+}[AlSiO_6]$	
	Kushiroite	$CaAl[AlSiO_6]$	
D.	***Ca-Na pyroxenes***		
	Omphacite		$(Ca,Na)(R^{2+},Al)Si_2O_6$
	Aegirine-augite		$(Ca,Na)(R^{2+},Fe^{3+})Si_2O_6$
E.	***Na pyroxenes***		
	Jadeite	$NaAlSi_2O_6$	$Na(Al,Fe^{3+})Si_2O_6$
	Aegirine	$NaFe^{3+}Si_2O_6$	
	Kosmochlor	$NaCrSi_2O_6$	
	Jervisite	$NaSc^{3+}Si_2O_6$	
	Natalyite	$NaV^{3+}Si_2O_6$	
	Namansilite	$NaMn^{3+}Si_2O_6$	
F.	***Li pyroxenes***		
	Spodumene	$LiAlSi_2O_6$	

Table 11.2. Textural types of clinopyroxene studied in this work.

	Sample	Region	Location	Name	Rock	In xenolith (A1-A3)	Xenocryst (B)	Groundmass lamproite (C)	Groundmass VK (D)	Replacement (E)	Globular bodies (F)
Angola	CU-79-70,5A, CU-79-113A		Cucumbi		VK	A1			D	E	
Angola	TZ-G18-47, TZ-G18-252		Tchiuzo		VK				D		
Angola	CC-47-46		Cacuilo	K47	CK	A1					
Botswana	10052	SD	Jwaneng	Centre pipe	VK		B				
Botswana	10053	SD	Jwaneng	North pipe	VK						
Botswana	10054	SD	Jwaneng	South pipe	VK	A1	B				
Botswana	10055	CD	Orapa	AK1, "A"	VK	A1;A2;A3	B		D	E	
Botswana	10056	CD	Orapa	AK1, "B"	VK	A3			D		
Botswana	10057	CD	Orapa	AK1, "C"	VK	A1;A3	B		D		
Botswana	10058	CD	Letlhakane	DK1	VK	A1;A2;A3			D		
Botswana	10060	CD	Damtshaa	BK9, "A"	VK	A2;A3	B				
Botswana	10061	CD	Damtshaa	BK9, "B"	VK	A2;A3	B		D	E	
Botswana	10049	CD	Karowe	AK6, South pipe	CK	A2					
Botswana	10050	CD	Karowe	AK6, Center pipe	CK						
Botswana	10051	CD	Karowe	AK6, North pipe	CK	A2;A3					
Botswana	10059	CD	Letlhakane	DK1	CK	A2					F
South Africa	7707	NCP		Riverton	CK						
South Africa	9156	FSP		Bultfontein	CK	A2					
South Africa	9311	NCP	Kimberley	Big Hole	CK	A1;A2					
South Africa	9351	NCP	Kimberley		CK						
South Africa	9364	NCP	Kimberly	DutoitSpan	CK	A2					
South Africa	9725	FSP		Monastery	CK						
South Africa	9630	FSP	Kaalvallei	"occurence A"	CK						
South Africa	9602	FSP	Kaalvallei	"occurence B"	Lamproite (this work)			C			
South Africa	7881	NCP	Kimberley	Helam	Orangeite (Hammond and Mitchell, 2002)						
South Africa	9375	FSP		Roberts Victor	Orangeite (Mitchell 1995)						
South Africa	9952	NCP		Bellsbank	Orangeite (Mitchell 1995)						
Lesotho	9607			P200	CK						
Guinea	8870			Banakoro	CK						
Guinea	8871			Banakoro	CK						
Canada	7999	Quebec	Temiskaming	Ville-Marie	VK	A3			D	E	
Canada	9168	Ontario	Temiskaming	Seed	VK						
Canada	9359	NWT	SW Slave	Drybones Bay	VK						
Canada	10142	Quebec	Ugava Bay	Torngat	UML (Tappe et al., 2004)						
Canada	9353, 9354	Québec	Temiskaming	Notre Dâme du Nord	CK	A2				E	
Canada	9577	Ontario	Bucke Township		CK						
Canada	6934	NWT	Somerset island		CK						
Canada	7448	NWT	Diavik		CK						
Canada	7449	NWT	LDG Ekati	Point Lake	CK						
Canada	9613	NWT	SW Slave	Snap Lake	CK						
Canada	7454	Alberta	Birch Mountains		CK						
Canada	9360	Nanavut	Baffin Island	Jackson inlet	CK						

Table 11.2. (continued)

	Sample	Region	Location	Name	Rock	In xenolith (A1-A3)	Xenocryst (B)	Groundmass lamproite (C)	Groundmass VK (D)	Replacement (E)	Globular bodies (F)
USA	8015	Michigan	Lake Ellen	Lake Ellen	VK						
USA	9346	Utah	San Juan Co.	Alhambra Rock	VK						
USA	9966	Tennessee	Tazewell	Norris metakimberlite	VK						
USA	7314	Colorado	Larimer Co.	Chicken Park	CK						
USA	10070	Pennsylvania	Fayette Co.	Gate-Adah	CK						
USA	9348	Colorado	Kelsey Lake		CK						
USA	9345	Colorado	Laramie Co		CK						
USA	9352	Michigan	Menominee	Site 73	Ck						
USA	9576	Colorado	Larimer Co.	Sloan #2	CK						
USA	9341	Colorado	Kelsey Lake		Lamproite (this work)			C			
USA	9340	Arkansas	Murfreesboro		Lamproite (McCandless et al. 1994)			C			
Venezuela	7544		Guaniamo		VK/CK						
Russia	10077	NR	Lomonosovskaya		VK				D		
Russia	10079	NR	Pionerskaya		VK				D		
Russia	9985	Yakutia	Pobeda ('Victory')		VK						
Russia	9959	Yakutia	Leningrad		VK						
Russia	10037	Yakutia	Udachnaya		CK						
Russia	10065	Yakutia	Obnazhonnaya		CK						
Russia	4928	Yakutia	Mir		CK						
Russia	9611	Kola Peninsula	Emakowskaya		CK						
India	8021	RKF	Siddanpalli cluster	SK-1	CK						
India	8044	RKF	Siddanpalli cluster	SK-2	CK						
India	8029	RKF	Siddanpalli cluster	SK-3	CK						
India	8030, 8040, 8041	WKF	Chigicherla cluster	CC-4	CK						
India	8022, 8023	WKF	Chigicherla cluster	CC-5	CK						
India	8036	WKF	Kalyandurg	KL-3	CK						
India	8037, 8038	WKF	Kalyandurg	KL-4	CK						
India	8027	WKF	Wajrakarur village	P-1	CK						
India	8043	WKF	Lattavaram village	P-3	CK						
India	8024	WKF	Chigicherla cluster	CC-1	Lamproite (this work)			C			
India	8025	WKF	Wajrakarur village	P-2	Lamproite (Kaur&Mitchell 2013)						
India	8035	WKF	Lattavaram village	P-4	Lamproite (Shaikh et al., 2018)			C			
India	8045	WKF	Mulligiripally	P-5	Lamproite (Kaur et al., 2013)			C			
China	9333	Shandong province	Mengyin	Red Flag #1	CK						
China	9737,9738, 9740	Shandong province	Mengyin	Shengli	CK						
China	9573, 9574	Liaoning province		Wafangdian	CK						

SD: Southern District; CD: Central District; NCP: Northern Cape Province; FSP: Free State Province; NR: Northern Region; RKF: Raichur kimberlite field; WKF: Wajrakarur kimberlite field. VK: volcaniclastic kimberlite; CK: coherent kimberlite; UML: ultramafic lamprophyres.

11.2.1. Xenolitic /xenocrystic clinopyroxene (types A and B)

Clinopyroxene occurs in both mantle xenoliths and crustal xenoliths. Clinopyroxene found in mantle xenoliths may be present in MARID-PIC suite xenoliths (A1) and peridotitic xenoliths (A2). Clinopyroxene is also found in crustal xenoliths, i.e., in basaltic xenoliths (A3).

MARID/PIC xenoliths (Fig. 11.1a) studied in the present work occur with the following mineral associations: phlogopite + clinopyroxene + ilmenite; phlogopite + clinopyroxene; phlogopite + ilmenite + rutile + clinopyroxene and clinopyroxene + ilmenite.

Peridotitic xenoliths (Fig. 11.1b) studied in the present work present the following mineral associations: phlogopite + clinopyroxene + chromite; clinopyroxene + pyrope + phlogopite; olivine + clinopyroxene; olivine + clinopyroxene + orthopyroxene + phlogopite + ilmenite; orthopyroxene + clinopyroxene + ilmenite; olivine + clinopyroxene + phlogopite; clinopyroxene + orthopyroxene + chromite; olivine + clinopyroxene + orthopyroxene; phlogopite + LIMA + clinopyroxene + ilmenite; phlogopite + richterite + orthopyroxene + olivine + clinopyroxene; olivine + clinopyroxene + phlogopite + spinel ss + orthopyroxene; clinopyroxene + phlogopite + spinel ss + orthopyroxene; clinopyroxene as inclusions in olivine xenocrysts and clinopyroxene as inclusions in pyrope.

Moreover, clinopyroxene is also found in basaltic xenoliths together with ilmenite (Fig. 11.1c). Rounded or fragmented anhedral grains (Fig. 11.1d) are found in many kimberlites.

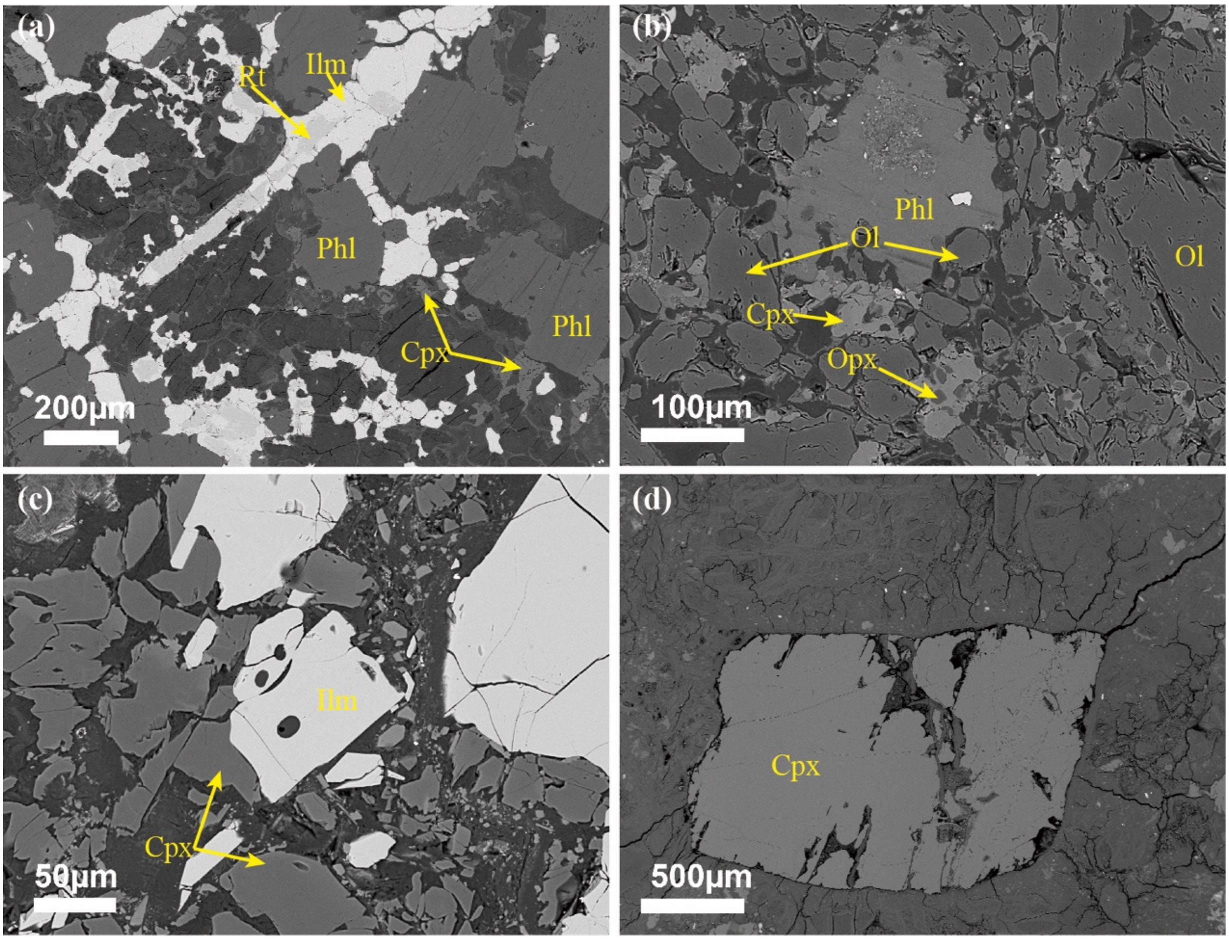

Fig. 11.1. Back-scattered electron (BSE) images of xenocrystic and xenolitic clinopyroxene. (a) Clinopyroxene (Cpx) in MARID xenolith with rutile (Rt), ilmenite (Ilm) and phlogopite (Phl), in the Letlhakane DK1 volcaniclastic kimberlite. (b) Clinopyroxene in peridotitic xenolith with olivine (Ol), phlogopite, and orthopyroxene (Opx), in the Big Hole coherent kimberlite. (c) Clinopyroxene (Cpx) in basaltic xenolith with ilmenite, in the Damtshaa BK9 “B” volcaniclastic kimberlite. (d) Anhedral clinopyroxene xenocryst, in the south pipe of the Jwaneng volcaniclastic kimberlite.

11.2.2. Primary groundmass clinopyroxene in lamproite (type C)

Primary clinopyroxene in coherent lamproites is found as a prismatic euhedral-subhedral groundmass mineral (1µm - 50µm, Fig. 11.2a-c). It is produced in late stages in the groundmass crystallization sequence, because it may mantle ulvöspinel and perovskite of the groundmass, but it can be included in lately formed phlogopite plates.

11.2.3. Primary groundmass clinopyroxene in peletal lapilli in volcaniclastic kimberlite (type D)

Primary clinopyroxene is commonly found in volcaniclastic kimberlite as very fine groundmass minerals in peletal lapilli in volcaniclatic kimberlite (Fig. 11.2d-e). Grain size is very fine, from less than 1µm to 5µm. Clinopyroxene, sometimes accompanied by phlogopite and apatite, is the principal groundmass mineral in magmaclasts (peletal lapilli), frequently developed around a xenocrystal or a phenocrystal core.

11.2.4. Clinopyroxene produced by replacement (type E)

Clinopyroxene is also found replacing other minerals. For instance, clinopyroxene has been observed replacing orthopyroxene xenocrysts; it may replace clinopyroxene of different composition or can occur in intergranular veinlets in xenoliths made up by olivine + orthopyroxene (Fig. 11.3f).

11.2.5. Clinopyroxene in globular bodies (type G)

Clinopyroxene is the main mineral produced by crystallization in globular (spherical or ellipsoidal) domains of 100-500 µm in diameter; the resulting crystals are arranged in a geode-like disposition, with the crystals growing towards the center of the body (Fig. 11.3). The central part of these bodies is occupied by serpentine-group minerals.

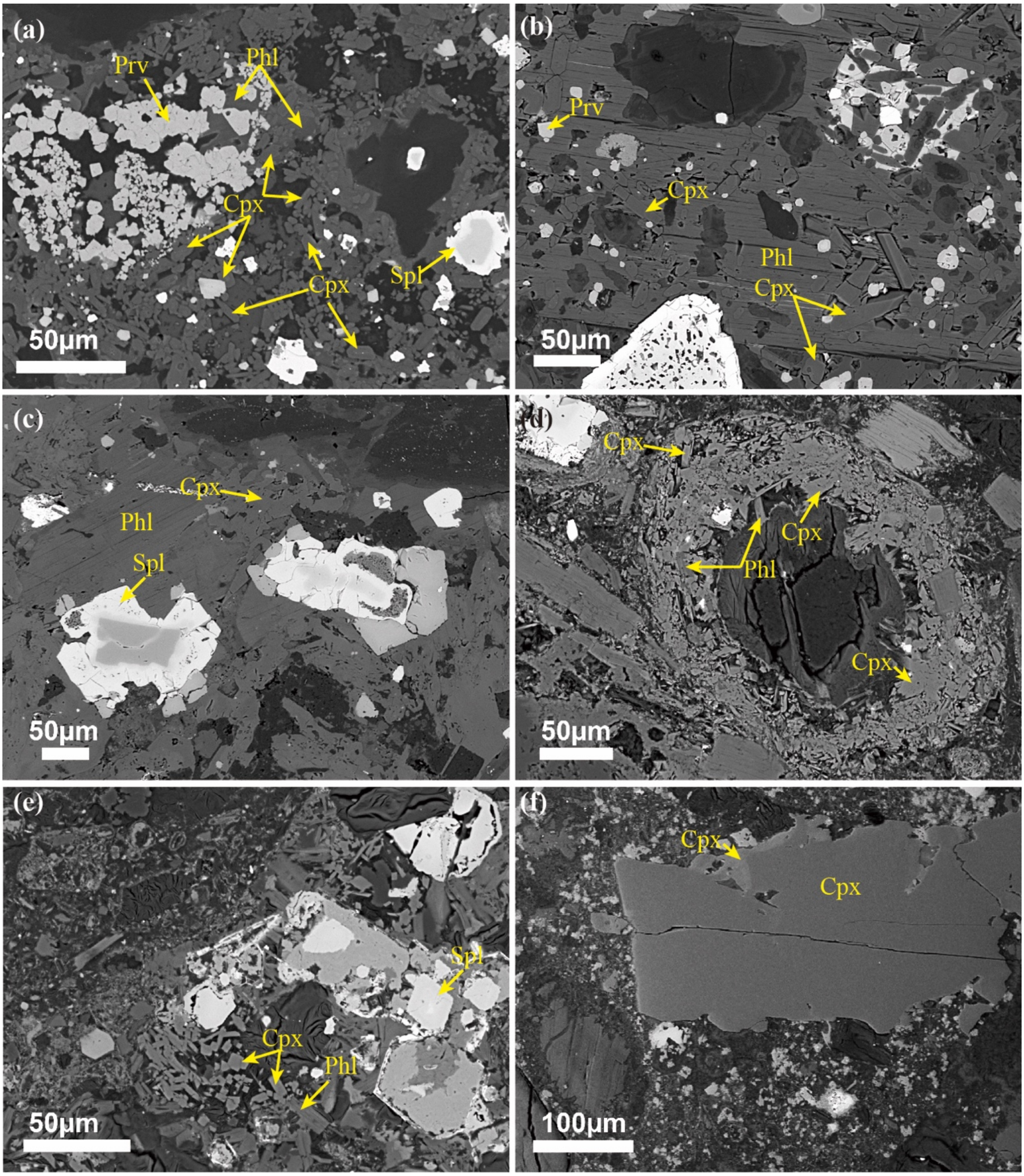

Fig. 11.2. Back-scattered electron (BSE) imagings of clinopyroxene. (a) Groundmass clinopyroxene (Cpx) together with other groundmass minerals as perovskite (Prv), spinel-group mineral (Spl), and phlogopite (Phl), in the Lattavaram P4 lamproite. (b) Groundmass euhedral clinopyroxene and perovskite included in poikilitic phlogopite (Phl), in the Kelsey Lake "B" lamproite. (c) Euhedral groundmass clinopyroxene together with phlogopite, in the Mulligiripally P5 lamproite. (d) Clinopyroxene in peletal lapilli together with phlogopite, in the Ville-Marie volcaniclastic kimberlite. (e) Clinopyroxene, phlogopite and spinel-group mineral as groundmass in the Tchiuzo volcaniclastic kimberlite. (f) Clinopyroxene xenocryst replaced by another clinopyroxene of different composition, in the Cucumbi volcaniclastic kimberlite.

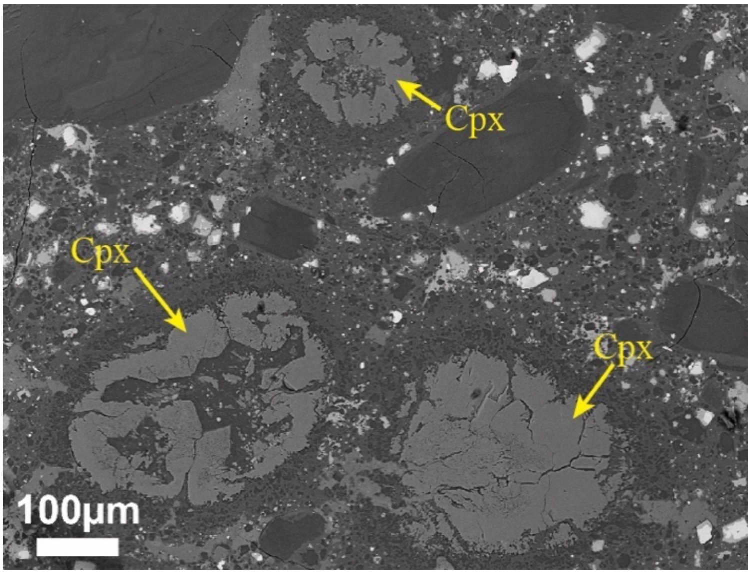

Fig. 11.3. Back-scattered electron (BSE) imagings of clinopyroxene in globular bodies in the north pipe of the Karowe AK6 coherent kimberlite.

11.3. CHEMICAL COMPOSITION

The analysed pyroxenes have been classified by using the classification diagrams of Morimoto (1988), with the preliminary diagram Q-J being used to discriminate the dominant types of pyroxene (Fig. 11.4a) and the quadrilateral and alkaline and calc-alkaline pyroxenes being used to classify them, respectively, with the Fig. 11.4b and 11.4c.

11.3.1. Xenolitic /xenocrystic clinopyroxenes (types A and B)

All the clinopyroxene crystals in the studied MARID xenoliths have compositions of quadrilateral Ca-Mg-Fe clinopyroxenes and are represented in the diopside and augite fields (Fig. 11.4). The majority of these crystals are Mg-rich and Fe-poor.

The majority of clinopyroxenes in the studied peridotitic xenoliths are also diopside and augite, although some analysed grains plot in the pigeonite field and are slightly enriched in Na.

Clinopyroxene in basaltic xenoliths is represented both in the Ca-Mg-Fe and the Ca-Na clinopyroxene fields, having compositions of augite, pigeonite, aegirine-augite and augite. Therefore, the analysed basalt xenoliths are very diverse in tectonic setting and can have compositions of calc-alkaline and alkaline suites.

The studied xenocrysts correspond to Ca-Mg-Fe clinopyroxenes, ranging from diopside (in most of kimberlites and related rocks) to augite and pigeonite, with many similarities between the pyroxenes from basalts and those from MARID.

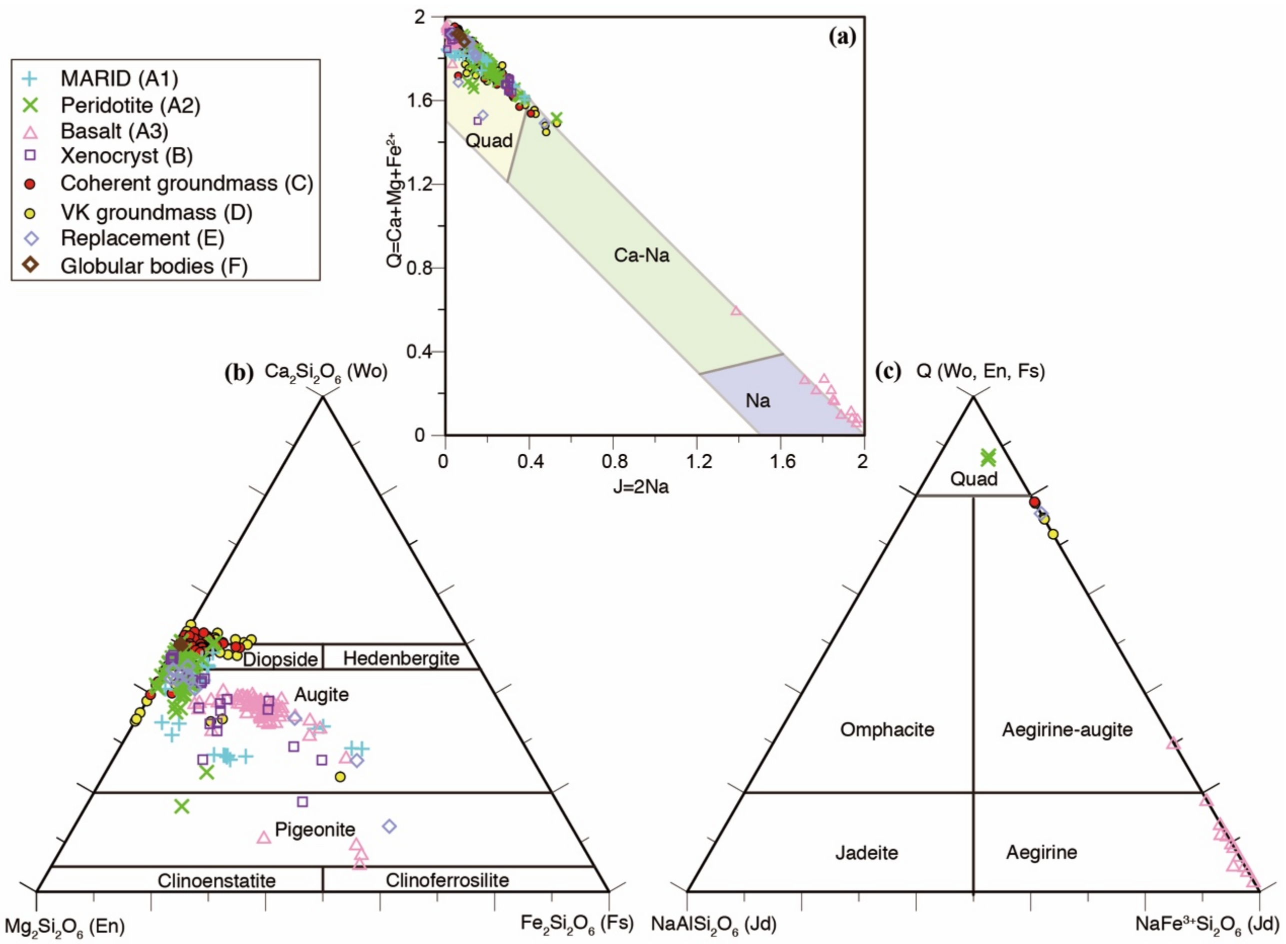

Fig. 11.4. Classification of clinopyroxenes of the studied samples using the diagrams of Morimoto (1988). (a) Q-J preliminar classification diagram. (b) $Ca_2Si_2O_6$-$Mg_2Si_2O_6$-$Fe_2Si_2O_6$ classification of the quadrilateral clinopyroxenes (Quad field in (a), Morimoto, 1988). (c) Q (Wo, En, Fs)-$NaAlSi_2O_6$-$NaFe^{3+}Si_2O_6$ classification diagram for alkaline clinopyroxene classification diagram (fields Ca-Na and Na in the Q-J preliminar diagram; Morimoto, 1988).

Cr-rich (>1wt% Cr_2O_3) compositions are found in part of the clinopyroxenes from MARID or peridotitic xenoliths and xenonocrysts. Contrastingly, all the clinopyroxene grains from basaltic xenolith are Cr-poor (<1wt% Cr_2O_3, Fig. 11.5a-c). The majority of Cr-rich clinopyroxenes have Ca/(Ca+Mg) ratios between 0.4-0.5, Mg/(Mg+Fe) between 0.8-1.0 and Al_2O_3 <4 wt% (Fig. 11.5a-c), while Cr-poor clinopyroxenes have Ca/ (Ca+Mg) between 0.1-0.6, Mg/(Mg+Fe) between 0.4-1.0 and 0-9 wt% Al_2O_3 (Fig. 11.5a-c).

Peridotitic clinopyroxenes have remarkable variations in the aluminium contents (0-9 wt% Al_2O_3, 0-0.4 apfu Al), while clinopyroxenes in MARID are more impoverished in this element, with 0-3 wt% Al_2O_3 (0-0.1apfu, Fig. 11.5c-e). Relatively low Al and Ca clinopyroxene found in basaltic xenoliths are compensated with Na and Fe^{3+} enrichment, thus producing aegirine (Fig. 11.5e). However, the majority of the analysed clinopyroxenes have Na_2O < 4 wt%, with exception of the alkaline clinopyroxene from alkaline basaltic xenoliths having 9-14 wt% Na_2O.

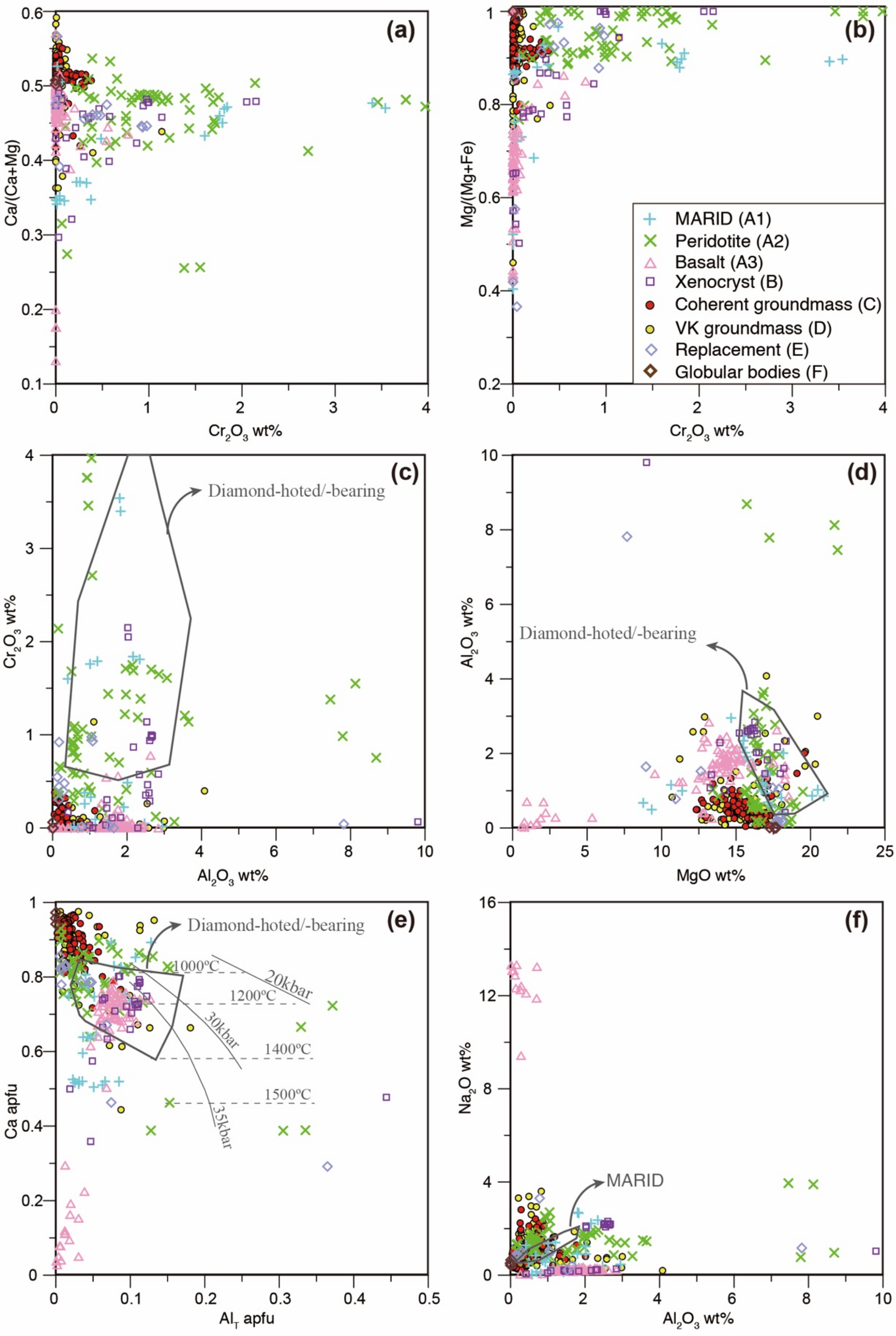

Fig. 11.5. Composition of the studied clinopyroxenes based on the following ratios: (a) Cr_2O_3 vs. Ca/(Ca+Mg); (b) Cr_2O_3 vs. Mg/(Mg+Fe); (c) Al_2O_3 vs. Cr_2O_3; (d) MgO vs. Al_2O_3; (e) Al_T vs. Ca; (f) Al_2O_3 vs. Na_2O projections. Diamond hoted/-bearing clinopyroxene field and Lines repre- senting isobars (solid) and isotherms (dashed) from Nimis (1998). MARID field from Fitzpayne *et al.* (2018).

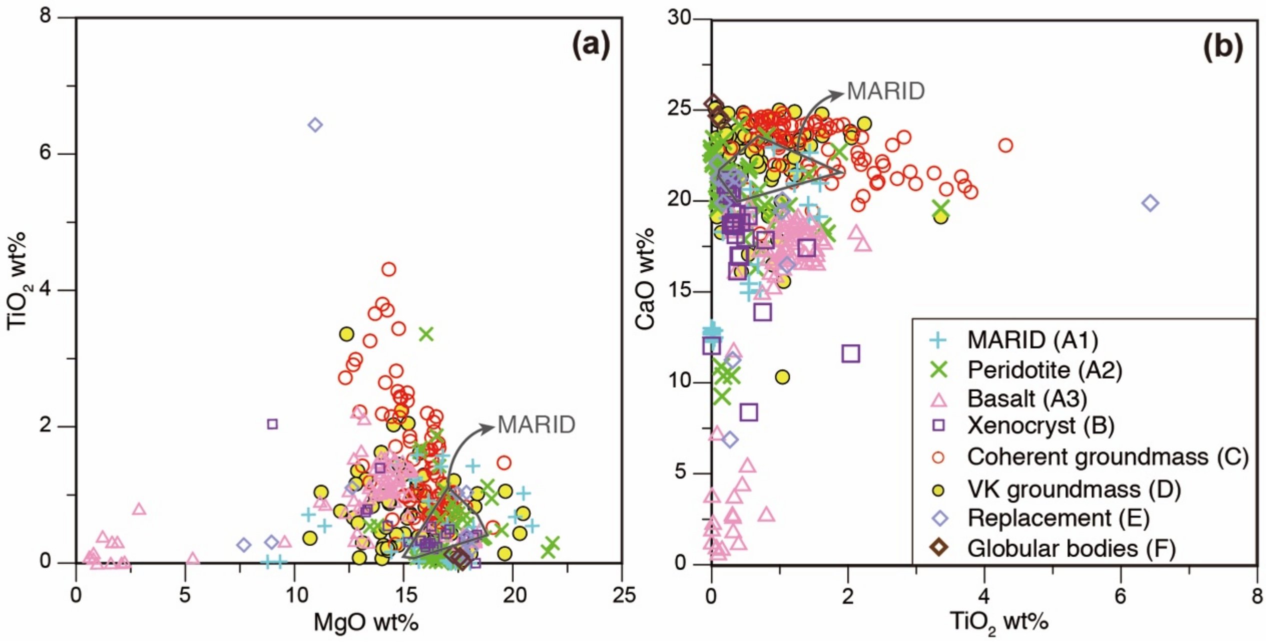

Fig. 11.6. Plot of the compositions of the studied clinopyroxenes in the following binary diagrams: (a) MgO vs. TiO_2; (b) TiO_2 vs. CaO. MARID field from Fitzpayne *et al.* (2018).

The majority of clinopyroxene from types A and B (xenolithic and xenocrystic) have 0-2 wt% TiO_2 (Fig. 11.6a). Although one analysis of groundmass pyroxene in volcaniclastic kimberlites returned 3.4 wt% TiO_2, the most of the TiO_2 values in this environment are lower than 2 wt%. High TiO_2 contents in clinopyroxene are found in relatively high Ca clinopyroxene (Fig. 11.6b); hence, this element may be slightly enriched in the coherent groundmass of lamproites (Fig. 11.6a).

No evident correlation exists between #Mg and Na_2O, Ca/(Ca+Mg), Al_2O_3 and TiO_2 (Fig. 11.7), while positive correlation between #Mg and CaO, and negative correlation between #Mg and MnO is observed (Fig. 11.7).

Most of the analysed xenocrysts could correspond to disaggregation of MARID xenoliths, because most of their values overlap systematically with those of the calc-alkaline basalts and MARID (Fig. 11.7, 11.8).

The majority of clinopyroxenes in xenoliths (including in MARID, peridotitic and basaltic xenoliths) and xenocrysts have high Al/Ti ratio (Al/Ti>1) as the field of primary clinopyroxene of UML (Fig. 11.9) determined by Tappe *et al.* (2006).

Finally, the proportions of K_2O can be significative (more than 1 wt%) in some of the analysed samples, and tend to be higher in some mantle xenoliths, but also in many of the crystals from coherent lamproite or volcaniclastic kimberlite.

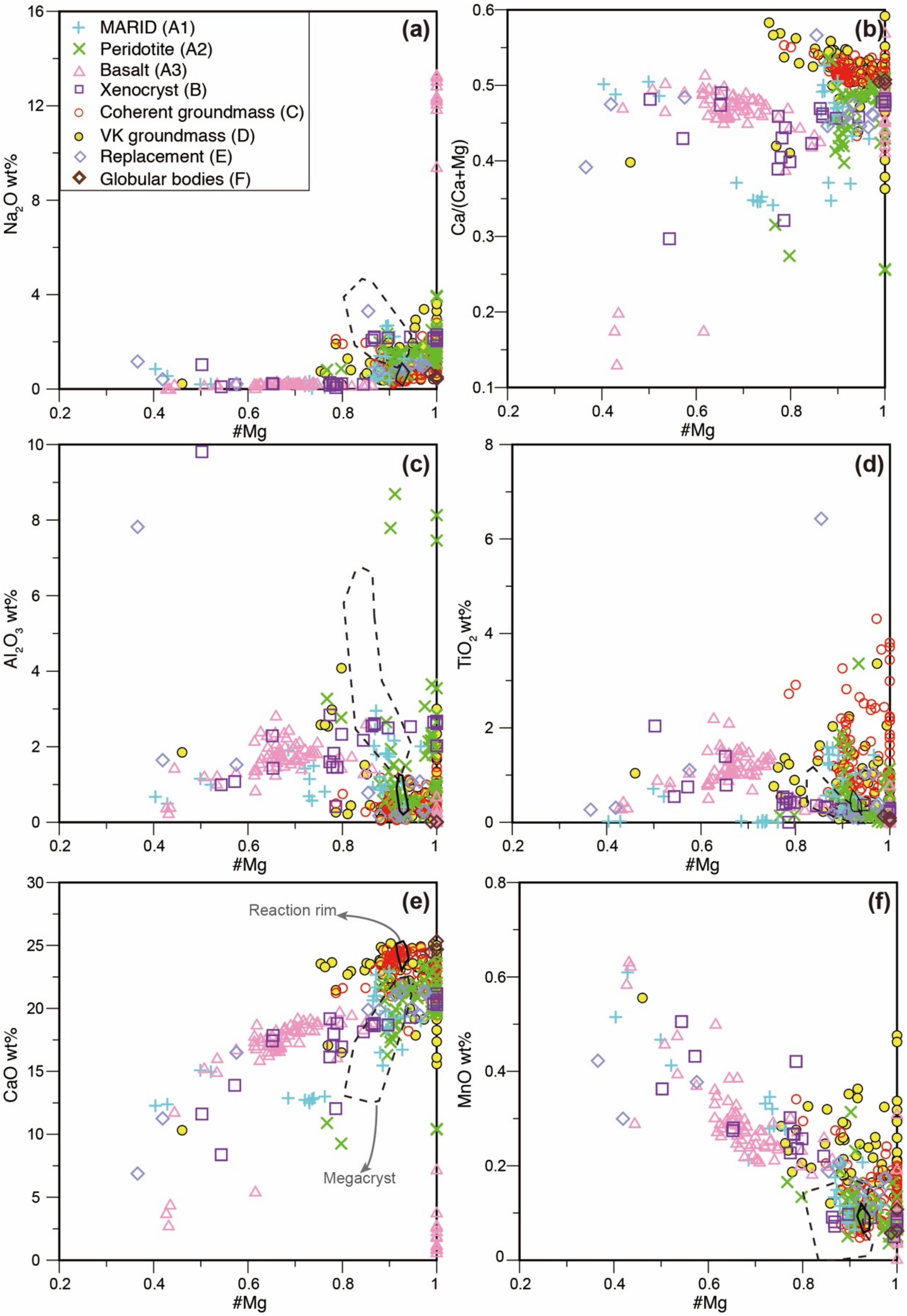

Fig. 11.7. Plot of the compositions of the studied clinopyroxenes in the following binary diagrams respect to #Mg (#Mg=Mg/(Mg+Fe^{2+})): (a) vs. Na_2O; (b) vs. Ca/(Ca+Mg); (c) vs. Al_2O_3; (d) vs. TiO_2; (e) vs. CaO; (f) vs. MnO. Fields of macrocrysts and reaction rim are from Bussweiler *et al.* (2016).

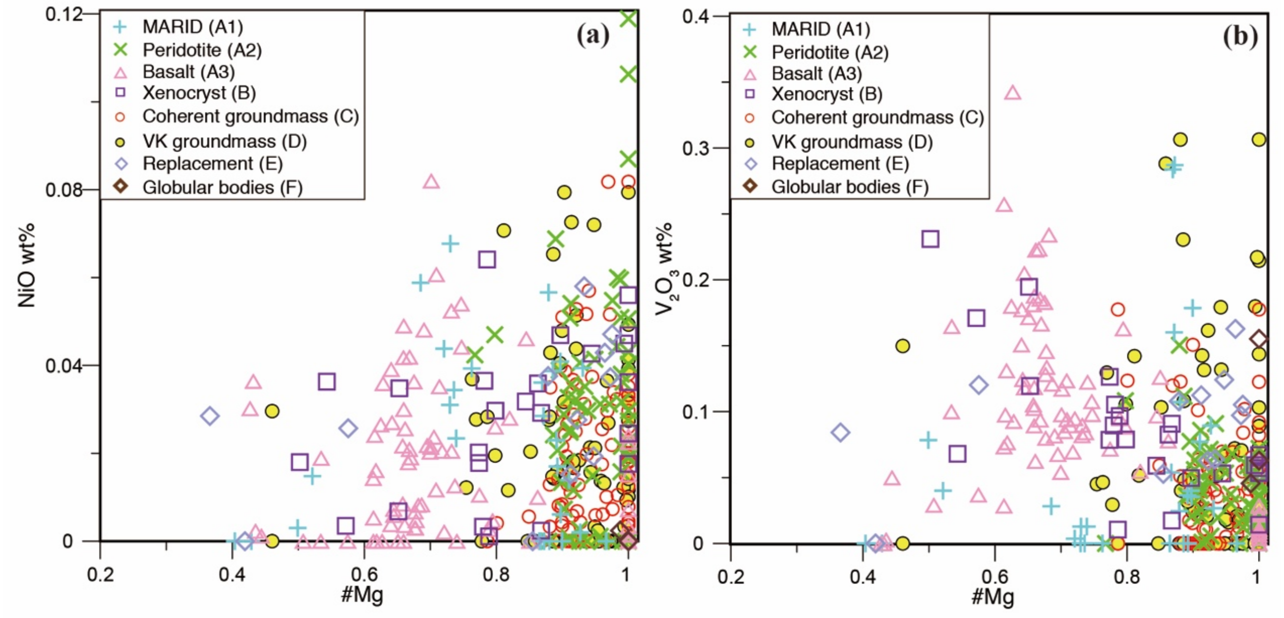

Fig. 11.8. Plot of the compositions of the studied clinopyroxenes in the following binary diagrams respect to #Mg (#Mg=Mg/(Mg+Fe^{2+})): (a) vs. NiO wt%; (b) vs. V_2O_3 wt%.

11.3.2. Primary clinopyroxene (Types C and D)

The majority of groundmass clinopyroxene in both coherent rocks (lamproites) and volcaniclastic rocks (kimberlites) are quadrilateral Ca-Mg-Fe-dominant clinopyroxenes that plot in the diopside and augite fields (Fig. 11.4). They are Cr-poor (<1wt% Cr_2O_3).

Groundmass clinopyroxene in lamproites has Ca/(Ca+Mg) about 0.4-0.6 and Mg/(Mg+Fe) around 0.8-1 (Fig. 11.5a-b, while groundmass clinopyroxene in volcaniclastic kimberlites has similar proportions in the ratios Ca/(Ca+Mg) and Mg/(Mg+Fe), around =0.4-0.6 and 0.5-1 respectively (Fig. 11.5a-b). Al_2O_3 content ranges from 0 to 2 wt% in lamproites and 0 to 4 wt% in kimberlites (Fig. 11.5d-c). Ca proportions are between 0.7-1 apfu in lamproites and 0.4-1 in volcaniclastic kimberlites (Fig. 11.5e), whereas Na tenors are between 0.2-2.8 in lamproites and 0.2-3.6 apfu in kimberlites (Fig. 11.5f).

Clinopyroxene from all these rocks has similar composition in terms of TiO_2-MgO and CaO-TiO_2 plots (Fig. 11.6), although clinopyroxene in lamproites could get slightly higher Ti contents (0.3-4.3 wt% TiO_2 in lamproites and 0.1-3.4 wt% TiO_2 in kimberlites). No evident correlation between #Mg and Na_2O, Ca/(Ca+Mg), Al_2O_3, TiO_2, CaO and MnO is observed (Fig. 11.7).

11.3.3. Clinopyroxene of replacement (type E)

Clinopyroxene replacing other minerals shows a wide compositional range (Fig. 11.4), because it is formed by the interaction between xenocrysts and kimberlite melt. Therefore, its composition depends on both the composition of the xenocryst, the composition of the melt and the grade of magma/rock interaction.

11.3.4. Clinopyroxene of globular bodies (type F)

Clinopyroxene found in globular bodies in coherent kimberlites has composition close to pure diopside (Fig. 11.4). It has low Cr (0-0.1 wt% Cr_2O_3), Ti (0-0.1wt% TiO_2), Al (<0.1 wt%Al_2O_3), Na (0.4-0.7wt% Na_2O) and Mn (0.1-0.5; Fig. 11.5). It has 0.50-0.51 of Ca/(Ca+Mg) and 0.99-1.00 of Mg/(Mg+Fe).

11.4. DISCUSSION

11.4.1. Crystallization Sequence

Mantle and crustal xenoliths with clinopyroxene are incorporated in kimberlitic and related magmas from its origin in deep mantle or during the magma ascent. Clinopyroxene xenocrysts are considered as derived from disaggregation of xenoliths.

Groundmass clinopyroxene in coherent rock of lamproites formed a bit before to/or contemporaneous to groundmass phlogopite as the former is included in/or cocrystallised with the later one. It can be an important component of the rocks and therefore its crystallization may remove from the magma significative proportions of Al, Mg, Ti and Ca.

Groundmass clinopyroxenes in volcaniclastic kimberlites are one of the main constituents of groundmass of peletal lapilli; they were formed frequently together with groundmass phlogopite and apatite and they can be considered as crystallized from the kimberlite magma.

Globular bodies seem to be formed independently of the rest of the minerals of the intrusion and could be formed by crystallization of a mingling magma or by crystallization in cavities in association with late-magmatic or hydrothermal processes.

11.4.2. Xenolitic and xenocrystic pyroxene

Both peridotitic and eclogitic clinopyroxenes are found as inclusions in diamonds and therefore they can be potentially DIM’s (Cookenboo and Grütter, 2010). Only mantelic clinopyroxenes from MARID and peridotitic xenolith have been studied in this work, and clinopyroxene from eclogitic xenoliths was not available. However, an eclogitic origin for some clinopyroxene xenocrysts cannot be excluded, as four xenocrysts plot in the eclogitic clinopyroxene field (Fig. 11.9b). Peridotitic clinopyroxenes are chrome diopside, while eclogitic clinopyroxenes are Cr-poor and Na-rich omphacitic with distinctive enrichment in K (0.6-1.3 wt% K_2O, Cookenboo and Grütter, 2010). The studied Cr-rich clinopyroxene has compositions similar to those of pyroxene in lherzolite xenoliths, although Cr-rich clinopyroxene is also found in MARID xenoliths (Mitchell, 1986). Nearly half part of analysed clinopyroxenes in peridotitc xenolith are Cr-rich (<1wt%, Fig. 11.5a), while no omphacitic clinopyroxene is found (Fig. 11.4). However, many Cr-rich clinopyroxene megacrysts in orangeite are probable derived from eclogites (Moore and Gurney, 1991).

Chrome diopside in diamond inclusion typically contain 0.5-4.5 wt% Cr_2O_3 and <4.0 wt% Al_2O_3 (Cookenboo and Grütter, 2010). Most of the studied clinopyroxenes in peridotitic and MARID xenoliths and xenocrysts plot in the peridotitic clinopyroxene inclusions of the diamond field (Fig. 11.10b). However, there are not remarkable compositional differences between pyroxenes found as inclusions in diamond and non-diamond associated grains (Stephens and Dawson, 1977). Cr-rich diopside megacrysts have been also considered to be formed by deep crystallization of a previously failed kimberlite (Bussweiler *et al.*, 2016).

11.4.3. Primary pyroxene

Primary clinopyroxene was suggested to occur as primary liquidus phase, as microcrystalline aggregates of diopside formed during late stages in kimberlite groundmass, or as result of reaction between kimberlitic and related magmas and xenoliths (Mitchell, 1986). The formation of diopside or, alternatively, monticellite, was suggested as depending on the silica activity and the temperature of crystallization (Mitchell, 1986). However, primary magmatic diopside should be lacking in kimberlitic magmas (Tappe *et al.*, 2005) according to the current IUGS classification for the kimberlites; many of the described crystals in coherent kimberlites were xenocrystic (Kamenetsky *et al.*, 2009a). Therefore, studied coherent kimberlite-like samples which contain primary groundmass clinopyroxene have been reclassified as lamproites in this work. However, clinopyroxene is a typical groundmass mineral in peletal lapilli in volcaniclastic kimberlites. Unfortunately, our results indicate that there are no evident compositional differences between primary groundmass clinopyroxenes between those from coherent lamproites and those from volcaniclastic kimberlites (Fig. 11.4-11.10). Although some clinopyroxenes in volcaniclastic kimberlites could be enriched in Al relative to pyroxenes from lamproites, in many other cases both domains overlap (Fig. 11.9).

Diopside is a common primary mineral component of the groundmass in volcanic kimberlite (VK) found in magmaclast groundmass, diopside-phlogopite mantle and interclast groundmass (Hetman, 2008; Mitchell *et al.*, 2009; Sparks, 2013). These pyroxenes have low contents in Al, Ti, Cr and Na, explained in terms of low grades of crustal contamination and a formation in a low pressure context, under activity of deuteric fluids (Mitchell *et al.*, 2009). Porritt *et al.* (2012) demonstrated that the presence of silicic lithics of the basement can provide chemical components to promote formation of diopside. Clinopyroxene found in the halo around an altered xenolith has higher Al contents, indicating that the reaction with xenoliths caused the Al enrichment in the final liquids; this Al-enrichment of the late-stage residual fluids should post-date the crystallisation of the Al-depleted tetraferriphlogopite (Scott Smith *et al.*, 1984). However, our textural study indicated that phlogopite and diopside could crystallize simultaneously in these facies.

Ca/(Ca+Mg) values reflect the temperature of crystallization (Lindsley and Dixon, 1976; Mitchell, 1986). Increasing of the Ca/(Ca+Mg) ratios and decreasing those of of Mg/(Mg+Fe) could be due to fractional crystallization of parent magma with decreasing of temperature (Mitchell, 1986). The ratios Mg/(Mg+Fe) decrease if silicates are the minerals that are crystallizing,, but these ratios could remain constant or decrease depending on the amount of ilmenite crystallized (Schulze, 1984). For constant Mg/(Mg+Fe) in pyroxene, ilmenite fractionation cannot exceed 15wt% (Mitchell, 1986). Different pyroxene compositional trends could be caused by crystallization of different amounts of ilmenite (Mitchell, 1986).

Rim of megacrysts are formed by reaction with the hosting kimberlite magma (Bussweiler *et al.*, 2016).

Primary pyroxene in lamproite and orangeite have similar compositions, although titanian aegirine is not found in lamproite (Mitchell, 1995). Both lamproite and orangeite have low Ti and Al content (Mitchell, 1995).

Clinopyroxene megacryst (dominantly subcalcic diopside, aluminous augite and salite) in alkaline rocks (eg. alnöite, minette, nephelinite, basanite and alkaline basalt) is richer in Al and FeO than kimberlite megacrysts (Mitchell, 1986). UML pyroxenes (such as those in alnöite or aillikite) typically have higher Al and Ti contents (eg. 0.9-4.5wt% or 0.3-10.1 wt% Al_2O_3; Mitchell, 1995) and are solid solutions between diopside, $CaAlAlSiO_6$ and $CaTiAl_2O_6$; their Al^{VI} contents typically differ from those in orangeite and lamproite. However, clinopyroxene is absent in the UML sample studied in this work, from Torngat.

11.4.4. Use of clinopyroxene for the classification for kimberlite and related rocks

Primary pyroxenes are considered as absent in coherent kimberlites (Mitchell, 1995; Tappe *et al.*, 2005). Therefore, some coherent rocks containing primary groundmass clinopyroxenes have been reclassified as lamproites in our study. However, as indicated, clinopyroxene is a common groundmass mineral in peletal lapilli in volcaniclastic kimberlites. These differences in one of principal groundmass mineral in volcaniclastic and coherent kimberlites suggest that a different classification rule must be established for the classification for kimberlite and related rocks.

Groundmass clinopyroxene in lamproites has low Al content (the majority Al <0.05 apfu) and the majority plots in lamproite and orangeite fields defined by (Mitchell, 1995), although it extends to higher Ti content than that originally proposed (Fig. 11.9). On the other hand, part of groundmass clinopyroxene in volcaniclastic kimberlite has high Al/Ti (>1) as clinopyroxenes from UML, but a part of them has low Al/Ti (<1), similar to those from lamproites and orangeites (Fig. 11.9). No correlation exists between Al_2O_3, Cr_2O_3 and Na_2O (Fig. 11.5c, 11.5f and 11.10b).

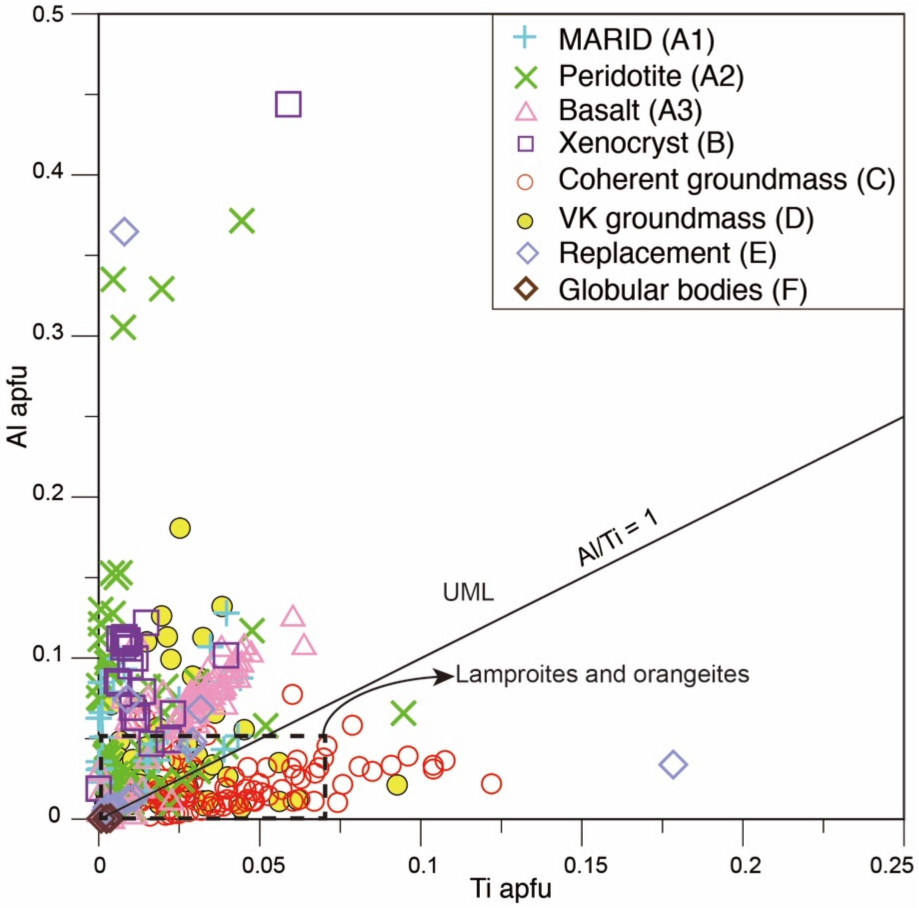

Fig. 11.9. Projection of the compositions of the studied clinopyroxenes in the Ti vs. Al diagram. Field of lamproites and orangeites according to Mitchell (1995). Field of UML according to Tappe *et al.* (2006).

11.4.5. Use of clinopyroxene for the diamond exploration

All the studied clinopyroxenes from both peridotite and eclogite xenoliths plot out of the compositions found in Cr-diopside from diamond inclusions when using the (Ca+Al)/(Na+Ti) diagram. However, the majority of studied clinopyroxene xenocrysts and those from MARID and peridotitic xenoliths plot in the same field of the peridotitic clinopyroxene found as inclusion in diamond (Fig. 11.10; Cookenboo and Grütter, 2010). Therefore, the use of these diagrams seems largely confusing.

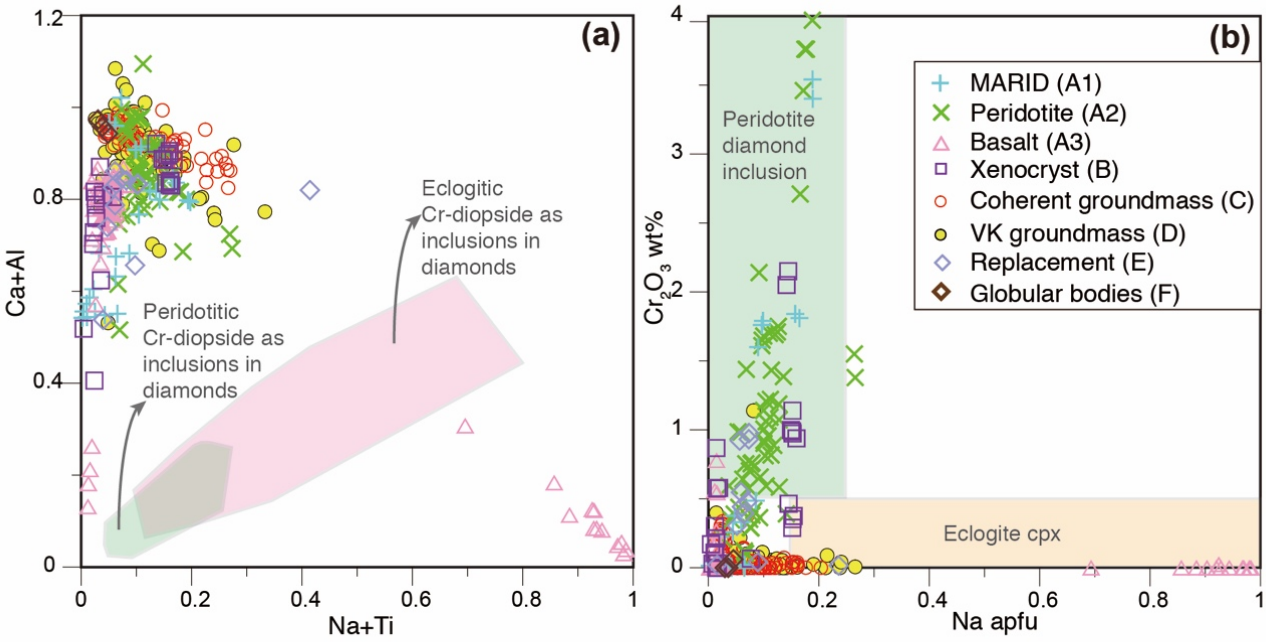

Fig. 11.10. Plots of the studied clinopyroxene compositions: (a) Na+Ti vs. Ca+Al and (b) Na (apfu) vs. Cr_2O_3 (wt%) projection. Fields of Cr-diopside from peridotite and eclogite found as inclusions in diamond according to Cookenboo and Grütter (2010).

11.4.6. Potassium in pyroxenes

The occurrence of relatively high amounts of K in different types of pyroxenes creates some questions. Potassium is a large cation and cannot enter in crustal conditions in the structure of pyroxene. However, under conditions of high and ultrahigh pressure K can be accommodated in substitution of Ca in clinopyroxenes, and this occurrence has been found in kimberlite xenoliths and diamond inclusions (Ricard *et al.*, 1989; Harlow and Veblen, 1991; Sobolev *et al.*, 1998; Kaminsky *et al.*, 2000; Stachel *et al.*, 2000; Pokhilenko *et al.*, 2004), xenoliths in lamproites (Jaques *et al.*, 1990) and ultrahigh pressure eclogites (Sobolev and Shatsky, 1990); the extent of this substitution has been proposed as a geobarometer (Ashchepkov *et al.*, 2017). In fact, the contents of K in pyroxene in these conditions seems not very high: experimental data and thermodynamic modeling suggested that at pressures of ~5 GPa (120-150 km of depth), clinopyroxene may accommodate up to 1 wt.% K_2O. In case of higher pressure, the contents could be higher, 3-5.75 wt% in the range 7-10 GPa as demonstrated by experiments (i.e., Safonov *et al.*, 2006 and references therein). Finally, some recent findings of natural occurrences of K-rich pyroxene in mantle xenoliths seems to confirm that at higher pressures the K contents in mantle pyroxenes can be even higher than in the diamond findings (1.97

wt% K_2O, Plá Cid *et al.*, 2003; 2.34 wt.% K_2O, Ghorbani and Middlemost, 2000).

Moreover, the fact that such K-enriched pyroxenes were found as inclusions in diamond, suggested use of K in pyroxene as a diamond-indicator.

In the case of the studied pyroxenes (Fig. 11.11), xenocrystic and xenolithic pyroxenes coming from some peridotite xenoliths have remarkable K contents, around 1 wt% K_2O, which could indicate a formation at nearby 5 GPa (120-150 km of depth). However, many pyroxene grains from the volcaniclastic kimberlites and from the groundmass of coherent lamproites returned not only similar values, but even higher (more than 2 wt% K_2O). These results pose a problem, because these values could correspond to very deep associations (nearby 6 Gpa) and this cannot be the case, because these rocks crystallized near the surface. There are two possibilities to explain this paradox: a) there are fine-grained intergrowths of groundmass phlogopite with these pyroxenes, or b) potassium-bearing clinopyroxene may result simply from a high K activity in the crystallizing magma, as suggested by Harlow and Veblen (1991). In any case, caution must be done when analyzing pyroxenes from kimberlites.

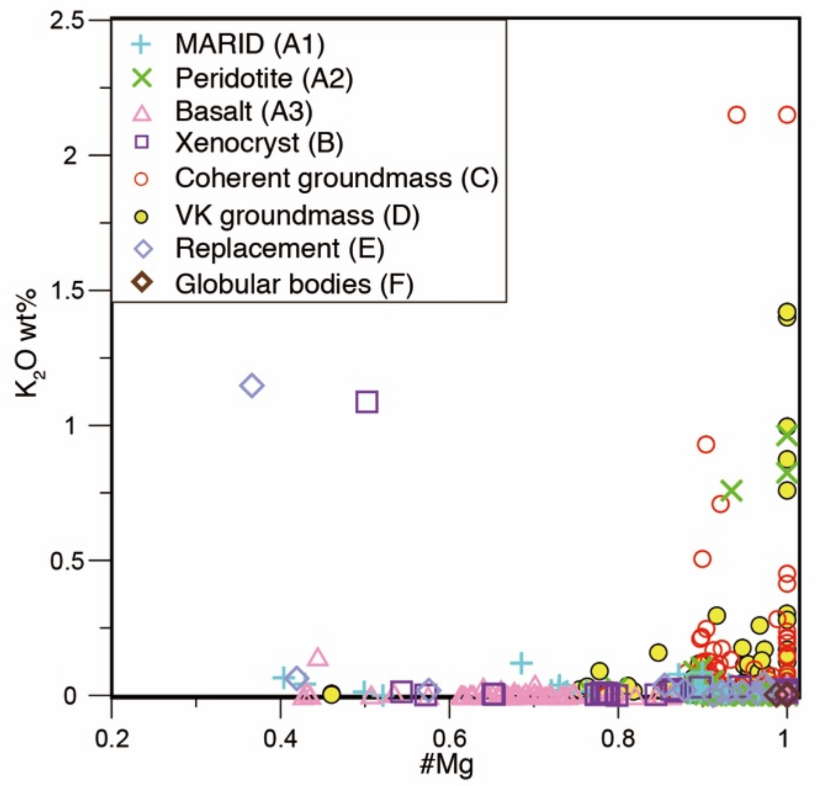

Fig. 11.11. Plot of the compositions of the studied clinopyroxenes in the binary diagrams K_2O (in wt%) respect to #Mg (#Mg=Mg/(Mg+Fe^{2+})).

CHAPTER 12

TITANIUM GARNETS

12. TITANIUM GARNETS

12.1. INTRODUCTION

Primary Ti-rich garnet was proposed as a key mineral for the classification of ultramafic lamprophyres, such as aillikites (Tappe *et al.*, 2004b) and orangeites (Dongre et al., 2016). Ti-rich garnets classified as andradite, schorlomite, zirconian schorlomite and kimzeyite occur in the Torngat aillikite dykes (Tappe *et al.*, 2004b); kimzeyite and Ti-andradite from Aillik Bay are considered as primary magmatic minerals and are indicators of the aillikitic affinity of these rocks (Tappe et al., 2006). A primary magmatic origin has also been suggested for the Ca-Ti-Fe rich garnets found in orangeite from Swartruggens (Hammond and Mitchell, 2002). However, Ti-rich hydrogarnets can be produced by subsolidus reactions in a wide span of environments, as in metapyroxenites (Müntener and Hermann, 1994), serpentinites (Amthauer and Rossman, 1998), basalts from the oceanic seafloor (Laverne et al., 2006) and magmatic alkaline rocks and carbonatites (Schingaro et al., 2016).

Therefore, the Ti-rich minerals can supply information of petrological or economic interest. However, these minerals can be easily altered by subsolidus processes. In addition, the hydrothermal occurrences of these minerals in other geological environments suggest that these minerals can be produced by the reaction of the existing magmatic minerals with late hydrothermal or supergene fluids.

Different alteration styles of groundmass Ti-rich oxide (perovskite and spinel) from SK-1 and SK-2 kimberlites (Eastern Dharwar craton, India) are described in this work, including the neoformation of pristine perovskite and Ti-rich hydrogarnets by subsolidus processes.

12.2. TEXTURAL PATTERNS

Ti-rich spinel-group minerals in groundmass from SK-1 are strongly altered to a cryptocrystalline mixture of serpentine-group minerals, calcite, magnetite and anhedral Ti-rich andradite (Fig.12.1a-b).

Similar mineral associations occur in the SK-2 kimberlite. In this case, however, the groundmass atoll spinels are replaced by mixtures of Ti-rich hydrogarnets, calcite and serpentine, but this late association include significative proportions of a late euhedral secondary perovskite (type 2 perovskite) which has different compositions with that primary in the groundmass (Fig.12.1c-d).

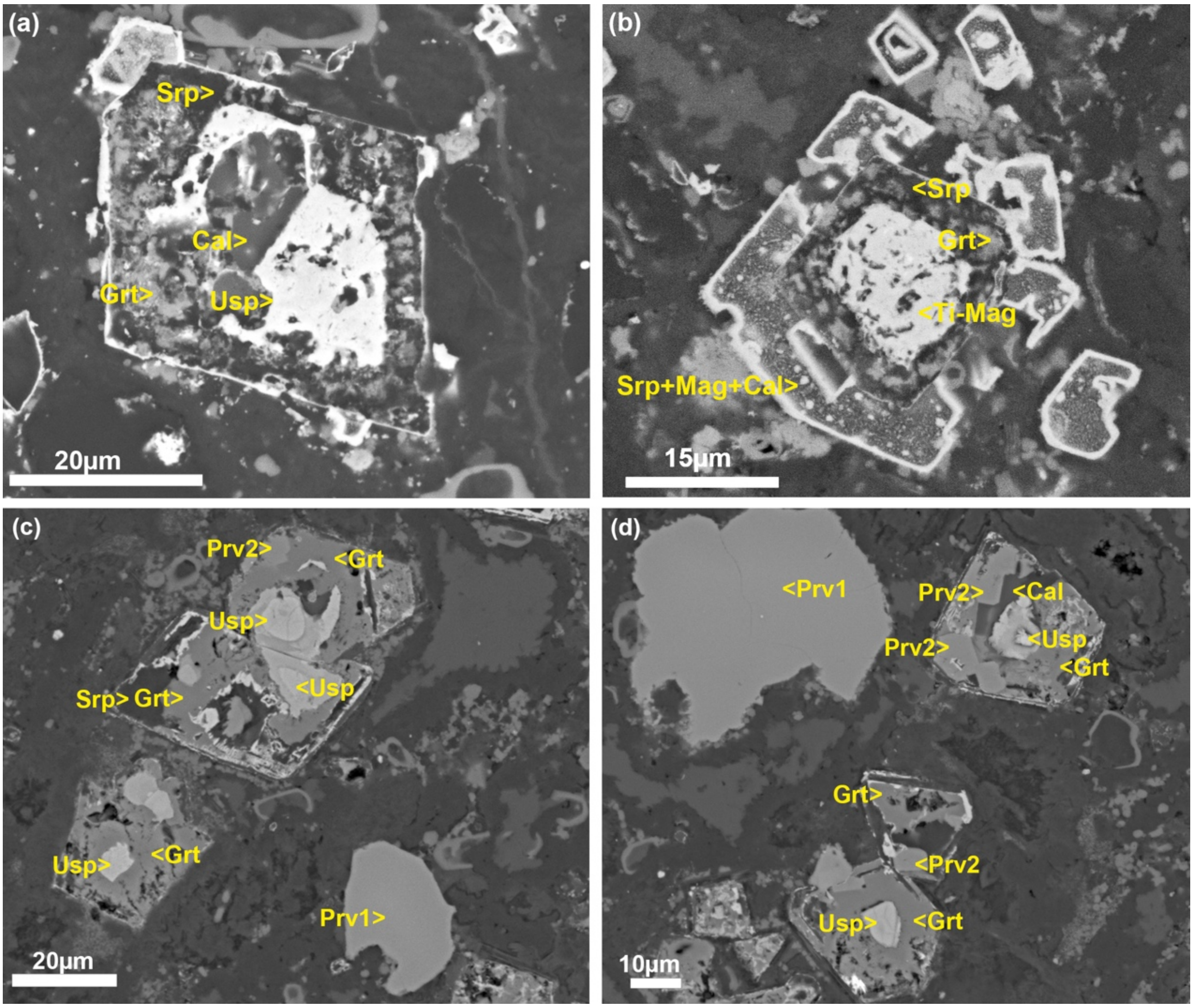

Fig. 12.1. Representative SEM (BSE) images of textural patterns of the titanium garnet from SK-1 and SK-2 kimberlites. (a) Euhedral atoll spinel from SK-1, replaced by serpentine (Srp), calcite (Cal) and cryptocrystalline Ti-rich garnets (Grt), with a relict of ulvöspinel (Usp) in the centre of the crystal. (b) Atoll spinel from SK-1, altered to serpentine, calcite, magnetite (Mag) and cryptocrystalline Ti-rich garnets, with a relict of titanomagnetite (Ti-Mag) in the centre. (c) Groundmass atoll spinel from SK-2 altered to type 2 perovskite (Prv2), Ti-rich garnets and serpentine, showing ulvöspinel relicts and primary type 1 perovskite (Prv1). (d) Atoll groundmass spinel from SK-2 altered to type 2 euhedral perovskite, Ti-rich garnets and calcite, showing relicts of ulvöspinel and type 1 perovskite (Prv1).

12.3. MICRORAMAN STUDY

Raman spectra of Ti-rich garnet from SK-2 kimberlite is also recorded (Fig. 12.2) and shows a peak at 3576 cm^{-1} which corresponds to the OH vibration (Laverne et al., 2006). The spectrum was compared with those of other hydrogarnets (Downs, 2006; Ghosh et al., 2017). The existance of the OH vibration indicates that these Ti-rich garnets can be classified better as Ti-rich hydrogarnets.

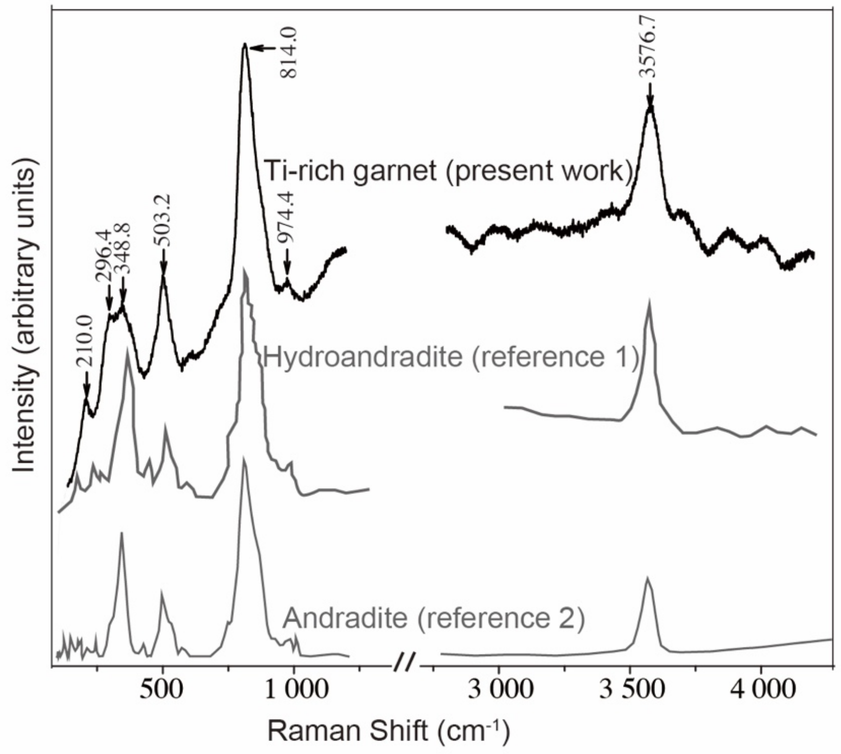

Fig. 12.2. Representative Raman spectrum analysed in Ti-rich garnet from SK-2 kimberlite, compared with grossular-hydroandradite reference 1 adapted from Ghosh et al. (2017) and andradite reference 2 adapted from the RRUFF Project database (R060350; Downs, 2006).

12.4. CHEMICAL COMPOSITION

Ti-rich hydrogarnets from the SK-2 kimberlite were analysed by EMPA, while those from the SK-1 pipe are too small to be analysed (Table 12.1). According to the IMA nomenclature for garnet group minerals (Grew et al., 2013), schorlomite end member has 2 apfu Ti in Y position, while andradite end member has 2 apfu Fe^{3+} in Y position. The Ti-rich garnets (12.9 wt %–26.3 wt % TiO_2) studied in the present work could correspond to a theoretical hydrous andradite (when it has < 1 apfu Ti) and hydrous schorlomite (when it has > 1 apfu). However, Ti-rich hydroandradite from the SK-2 kimberlite returns low total (88 wt %–96 wt %) and Si is also very low (1.6–1.9 apfu), thus suggesting the substitution of Si by OH in Z position and the existence of H_2O molecules. They plot inside the field of Ti andradites from ultramafic lamprophyres (Dongre et al., 2016; Fig. 12.3).

12.5. DISCUSSION

The occurrence of abundant Ti-rich garnets in the groundmass of the rock could suggest an aillikitic affinity during a preliminary examination, based on the International Union of Geological. Sciences (IUGS) rock classification (Tappe et al., 2005). Ti-rich garnets in groundmass from Indian kimberlites have been used to classify the rocks as orangeites (Dongre et al., 2016). Those Ti-rich garnets have similar composition to the Ti-rich garnets studied in the current work, which also plot inside the field of high Ti-andradite from kimberlite-UML rocks (Fig.12.3). However, hydrogarnets from SK-1 and SK-2 kimberlites replace Ti-rich oxides and are accompanied by hydrothermal minerals such as serpentine and type 2 perovskite, thus indicating that they were produced by late hydrothermal processes. Therefore, these garnets cannot be representative of the parental magma composition. In fact, Ti-rich hydrogarnets have also been found in ophiolite sequences as a result of hydrothermal alteration (Ghosh et al., 2017). Hence, attention must be paid to the position of Ca-Ti-rich garnet in the mineral sequence before using it to classify the rock based on its occurrence.

Table 12.1. Representative EMPA analysis of Ti-rich garnet from SK-2 kimberlites.

(wt%)	#1	#2	#4	#5	#15	#17	#19	#20	#21
SiO_2	20.20	25.44	21.62	21.86	21.51	23.18	20.69	21.24	20.00
Al_2O_3	0.63	0.69	0.98	0.98	0.85	0.89	0.85	0.84	0.92
Cr_2O_3	0.32	0.83	1.23	0.77	2.81	0.37	2.63	1.25	2.22
TiO_2	26.33	23.39	14.80	14.60	15.50	13.30	15.64	14.46	16.02
MgO	0.80	1.46	0.08	0.20	0.17	0.47	0.14	0.10	0.68
Na_2O	bdl	0.04	bdl	bdl	bdl	bdl	bdl	bdl	bdl
BaO	0.10	0.11	bdl	bdl	bdl	bdl	bdl	0.10	0.11
MnO	0.13	0.09	0.07	0.09	0.06	0.08	0.10	0.08	0.22
FeO	13.62	11.88	14.34	15.16	13.07	16.04	12.42	15.13	14.95
SrO	bdl	bdl	bdl	bdl	bdl	bdl	bdl	bdl	bdl
ZrO_2	0.79	0.77	0.20	0.28	0.18	0.30	0.54	0.40	0.35
K_2O	0.01	0.01	0.02	0.01	0.01	0.01	0.01	bdl	bdl
CaO	30.61	30.24	34.92	34.82	35.19	34.12	35.24	34.94	32.91
Total	93.86	95.22	88.26	88.77	89.35	88.77	88.25	88.53	88.39
Recalculated analyses									
Fe_2O_3	15.14	13.20	15.94	16.85	14.52	17.83	13.80	16.81	16.61
FeO	0.00	0.00	0.00	0.00	0.00	0.00	0.00	0.00	0.00
Total	95.12	96.28	89.88	90.47	90.81	90.55	89.66	90.26	90.06
(apfu)	Cation for 3 (Ca+K+Na+Sr+Ba+Mn+Mg)								
Si	1.773	2.194	1.724	1.739	1.697	1.863	1.631	1.688	1.643
Al	0.065	0.070	0.092	0.092	0.079	0.084	0.079	0.079	0.090
Cr	0.022	0.056	0.078	0.048	0.175	0.024	0.164	0.078	0.144
Ti	1.738	1.517	0.888	0.874	0.920	0.804	0.927	0.865	0.990
Mg	0.105	0.188	0.010	0.024	0.020	0.056	0.016	0.012	0.084
Na	0.000	0.006	0.000	0.000	0.000	0.000	0.000	0.000	0.000
Ba	0.004	0.004	0.000	0.000	0.000	0.000	0.000	0.003	0.004
Mn	0.010	0.006	0.005	0.006	0.004	0.006	0.007	0.005	0.015
Fe^{3+}	1.000	0.857	0.956	1.009	0.862	1.078	0.819	1.006	1.027
Sr	0.000	0.000	0.000	0.000	0.000	0.000	0.000	0.000	0.000
Zr	0.034	0.032	0.008	0.011	0.007	0.012	0.021	0.016	0.014
K	0.001	0.001	0.002	0.001	0.001	0.001	0.001	0.000	0.000
Ca	2.878	2.794	2.983	2.968	2.974	2.937	2.976	2.975	2.897

"bdl": below detection limit

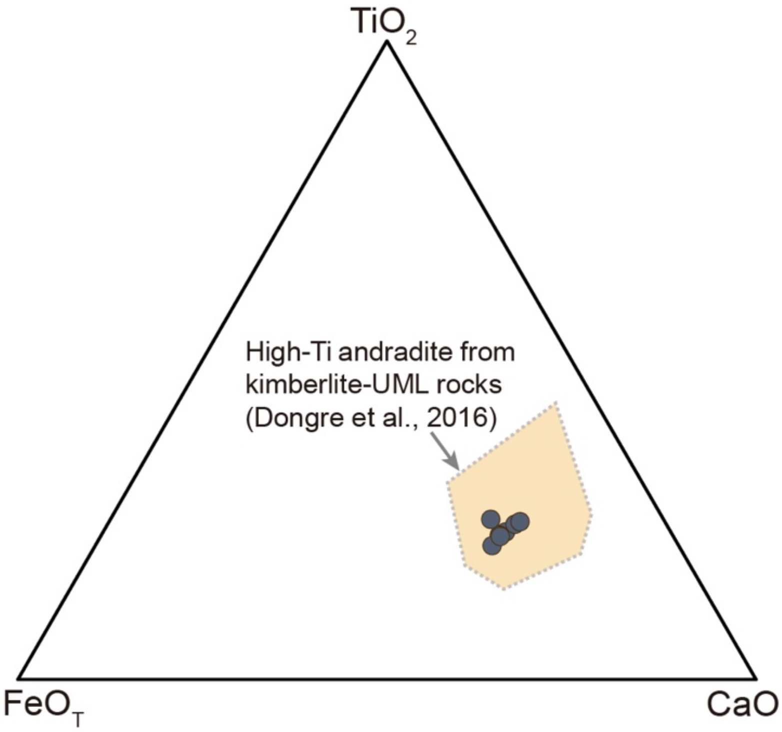

Fig. 12.3. Compositional variation of TiO_2, FeOT and CaO for Ti-rich garnet from SK-2 kimberlite pipe compared with Ti-rich andradites from ultramafic lamprophyres (Dongre et al., 2016).

CHAPTER 13

DJERFISHERITE

13. DJERFISHERITE

13.1 INTRODUCTION

Djerfisherite [$K_6(Fe,Cu,Ni)_{25}S_{26}Cl$] is a complex Cl-bearing potassium sulfide. The occurrence of complex alkaline sulfides as djerfisherite has been documented in many geological environments, but some varieties are characteristic of some Si-poor magmatic rocks, as some meteorites (Fuchs, 1966), carbonatites (Kogarko *et al.*, 1991; Korobeinikov *et al.*, 1998); kimberlites (Clarke *et al.*, 1994; Sharygin *et al.*, 2007, 2008); metasomatized mantle rocks (Dawson *et al.*, 1995); melt inclusions in basaltic rocks (Solovova *et al.*, 1996); and ultramafic lamprophyes (Panina *et al.*, 2001). Djerfisherite is also found in chloride-carbonate “nodules” in kimberlite (Kamenetsky *et al.*, 2014).

13.2. TEXTURAL PATTERNS

Djerfisherite was found in this study as having the following textural patterns:

1) Kimberlite groundmass djerfisherite
2) As daughter phase in melt inclusions in ilmenite xenocrysts
3) As a metasomatic product in mantle xenoliths.

Djerfisherite has been found in the groundmass of a very fresh kimberlite from Menominee in USA. It occurs as anhedral grains up to 400 μm in diameter (Fig. 13.1a-b). It is partly pseudomorphised by a sequence of valleriite ($(Fe^{2+},Cu)_4(Mg,Al)_3S_4(OH,O)_6$) and galena, followed by magnetite and cronstedtite ($((Fe^{2+},Fe^{3+})_3(Si,Fe^{3+})_2O_5(OH)_4)$).

Djerfisherite was also found in a metasomatized xenolith consisting of hastingsite, phlogopite, ilmenite, magnetite and calcite (Fig. 13.1c-d), coming from the Notre Dâme du Nord kimberlite. It is formed as a late product, along with calcite, ilmenite and magnetite; all these minerals occur interstitially among the silicate grains. Djerfisherite seems to be mantling and replacing another mineral which is totally altered (probably olivine).

Finally, djerfisherite was discovered as a component of a recrystallized melt inclusion, 15μm in length, in an ilmenite xenocryst from the Kaalvallei A lamproite (Fig. 13.1e-f). Djesfisherite is euhedral less than 5μm in diameter, and is found together with euhedral nepheline and an anhedral Na-Ca-K carbonate (probably, gregoryite, ($(Na_2,K_2,Ca)CO_3$) in the inclusion. All these minerals can be interpreted as daughter crystals.

13.3. CHEMICAL COMPOSITION

The composition of djerfisherite has been analysed in groundmass djerfisherite from the Menominee coherent kimberlite (Table 13.1). In this case, djerfisherite is relatively Ni-rich (5.5-7.9 apfu Ni) and Cu-poor (0.4-1.2 apfu Cu); its average structural formula is $[K_{5.86}Na_{0.03}Ca_{0.03}][Fe_{17.46}Ni_{6.64}Cu_{0.80}Co_{0.15}]S_{26}Cl_{1.00}$. The composition of the studied djerfisherite is compared with that of other worldwide occurrences in Fig. 13.2.

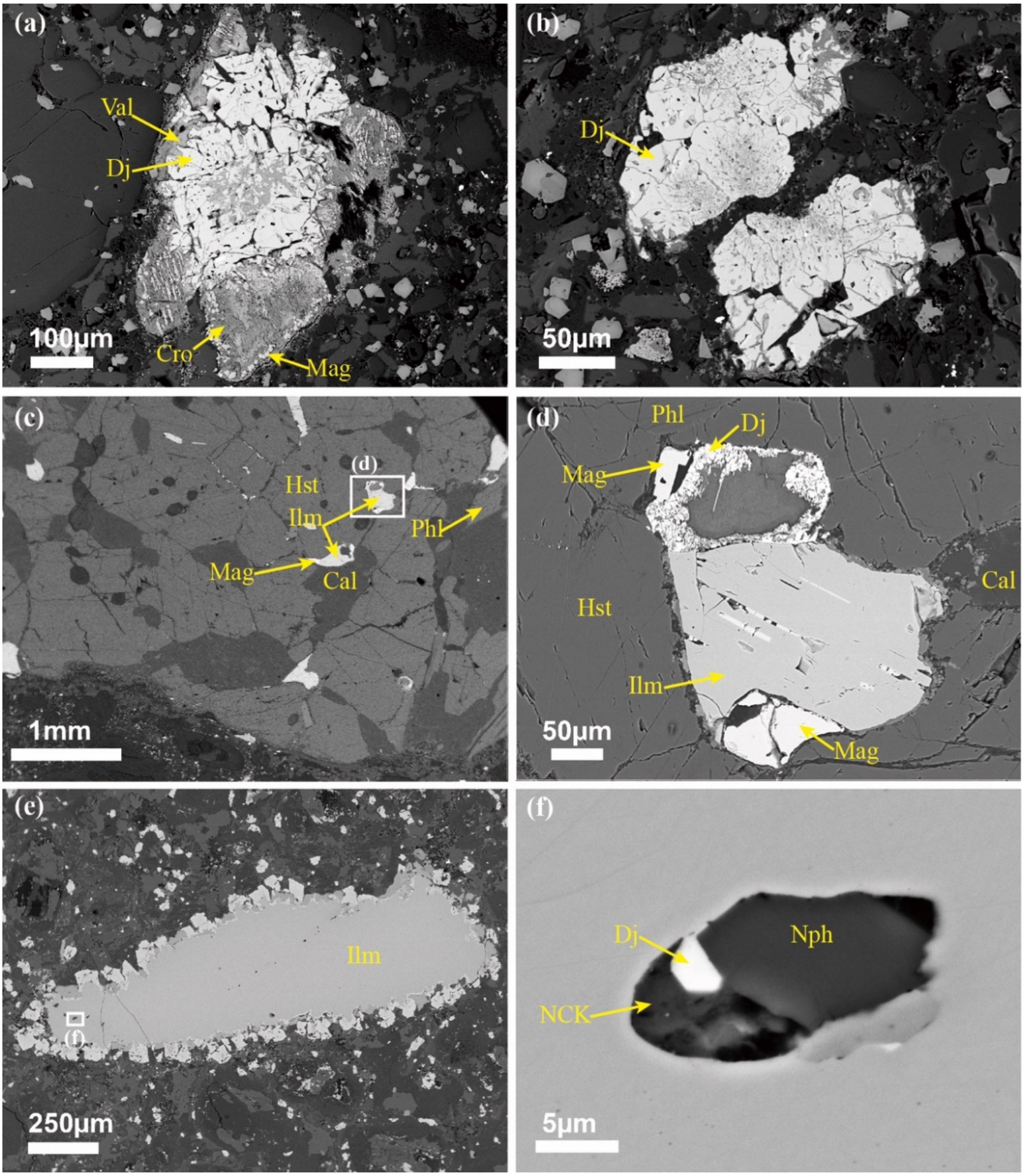

Fig. 13.1. Representative SEM (BSE) images of djerfisherite. (a-b) Groundmass djerfisherite (Dj) replaced by valleriite (Val), magnetite (Mag) and cronstedtite (Cro), from the Menominee kimberlite. (e-d) Djerfisherite as a late replacement product in a mantle xenolith made up by hastingsite (Hst), phlogopite (Phl), ilmenite (Ilm), magnetite (Mag) and calcite (Cal). (e-f) Djerfisherite in a recrystallized melt inclusion in an ilmenite xenocryst from the Kaalvalley "B" lamproite, together with nepheline (Nph) and a Na-Ca-K carbonate (NCK), probably gregoryite.

Table 13.1. Representative EMP chemical analyses of djerfisherite from the Menominee kimberlite.

No.	#3	#4	#6	#17	#26	#28
(wt %)						
Si	0.03	bdl	bdl	bdl	bdl	0.02
Al	0.01	bdl	0.02	0.02	0.01	0.01
Ca	0.04	bdl	0.02	0.06	0.04	0.03
K	8.99	8.85	8.83	8.95	8.99	8.93
Mg	bdl	0.03	bdl	bdl	bdl	0.02
Na	0.03	bdl	0.07	0.07	0.05	bdl
Cu	1.23	1.31	1.16	3.04	1.61	2.05
Ni	16.61	16.33	16.42	12.96	18.33	17.77
Co	0.52	0.48	0.51	0.16	0.27	0.24
Fe	37.98	37.85	38.06	39.01	35.68	35.64
Pb	0.33	0.35	0.36	0.32	0.36	0.32
S	32.69	32.60	32.61	32.63	32.65	32.66
Cl	1.36	1.39	1.39	1.38	1.39	1.41
Total	99.82	99.20	99.45	98.60	99.37	99.10
(apfu)	Cations on basis of 26 S					
Si	0.027	0.000	0.000	0.000	0.000	0.015
Al	0.006	0.000	0.015	0.020	0.005	0.008
Ca	0.028	0.000	0.011	0.036	0.026	0.019
K	5.864	5.789	5.774	5.849	5.871	5.830
Mg	0.000	0.029	0.000	0.000	0.000	0.021
Na	0.032	0.000	0.073	0.075	0.051	0.003
Cu	0.494	0.527	0.467	1.222	0.647	0.823
Ni	7.217	7.115	7.152	5.642	7.974	7.728
Co	0.226	0.209	0.222	0.070	0.117	0.105
Pb	0.040	0.043	0.044	0.040	0.044	0.040
Fe	17.344	17.333	17.424	17.848	16.314	16.291
S	26.000	26.000	26.000	26.000	26.000	26.000
Cl	0.978	1.003	1.002	0.995	1.001	1.015

bdl: below detection limit

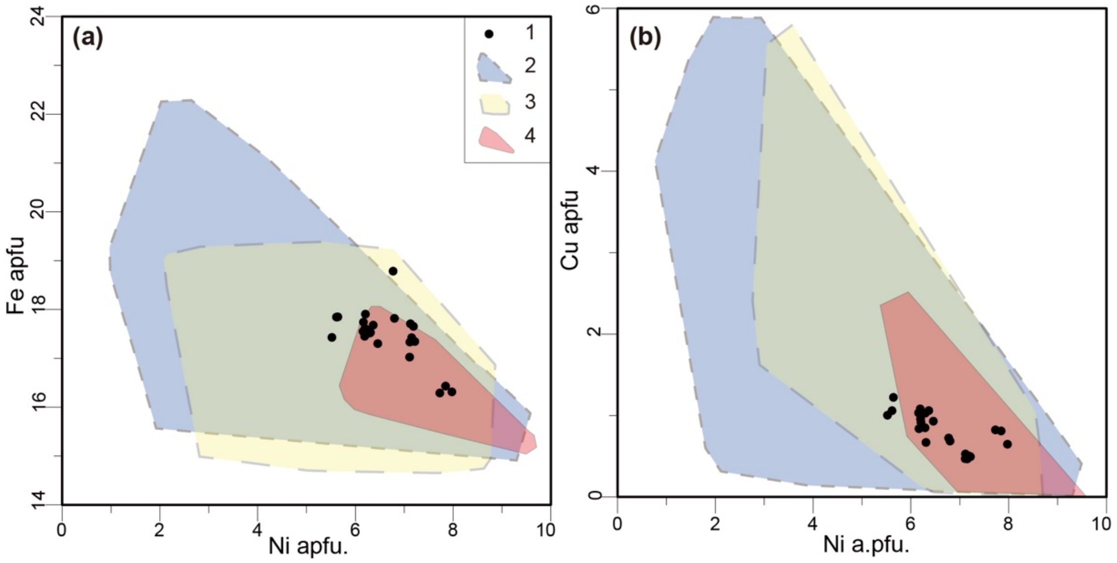

Fig. 13.2. Diagrams showing the composition of djerfisherite. a) Ni vs. Fe and b) Ni vs. Cu plots. 1, djerfisherite from the groundmass of the Menominee kimberlite (this work); 2, djerfisherite from kimberlite groundmass and from melt inclusions in kimberlitic olivine from the Udachnaya-East pipe (Golovin et al., 2007; Sharygin et al., 2007); 3, djerfisherite from xenoliths from the Siberian kimberlites (Dobrovol'skaya et al., 1975; Distler et al., 1987; Solov'eva et al., 1988; Bulanova et al., 1990; Misra et al., 2004; Sharygin et al., 2007); 4, djerfisherite from sulfide inclusions in the Siberian diamonds (Bulanova et al., 1990; Zedgenizov et al., 1998).

13.4. DISCUSSION

Sharygin *et al*, (2007) suggested a late magmatic origin of djerfisherite in the Udachnaya-East kimberlite groundmass, formed at shallow depths and at T≤ 800ºC. A similar origin has been suggested for the groundmass djerfisherite from Lac de Gras field (Chakhmouradian and Mitchell, 2001). Djerfisherite has been also found in mantle xenoliths as interstitial rims around Fe–Ni–Cu sulfides and around sulfide globules (Dobrovol'skaya *et al.*, 1975; Distler *et al.*, 1987; Spetsius *et al.*, 1987; Solov'eva *et al.*, 1988; Bulanova *et al.*, 1990; Misra *et al.*, 2004; Sharygin *et al.*, 2007), as xenocrysts/megacrysts around primary sulfide globules and as daughter phase in melt inclusions (Dobrovol'skaya *et al.*, 1975; Bulanova *et al.*, 1980, 1990; Distler *et al.*, 1987; Spetsius *et al.*, 1987; Zedgenizov *et al.*, 1998; Golovin *et al.*, 2003, 2007; Logvinova *et al.*, 2008; Kamenetsky *et al.*, 2009b) and as inclusions in diamond (Zedgenizov *et al.*, 1998).

However, the experimental data indicated that djerfisherite is not stable at pressures higher than 3 Gpa, so that djerfisherite included in diamond and mantle xenoliths could not crystallize in the deep part of the cratonic lithospheric mantle (Minin *et al.*, 2015). Therefore, djerfisherite included in diamond and mantle xenoliths might form by interaction between xenoliths and kimberlitic melts (Sharygin *et al.*, 2012; Minin *et al.*, 2015). Some authors propose that djerfisherite should form as replacement of pre-existing Fe–Ni–Cu sulfides by metasomatic K–Cl bearing melts/fluids in the kimberlite melt (Abersteiner *et al.*, 2019b). Another djerfisherite formation mechanism is direct crystallisation of djerfisherite from the kimberlite melt in groundmass or due to infiltration of kimberlite melt into xenoliths (Abersteiner *et al.*, 2019b).

Groundmass djerfisherite in Udachnaya-East kimberlite is not contaminated by crustal components because the isotopic analysis of S returned data within the mantle range and are thus magmatic (Kitayama *et al.*, 2017). These authors proposed thaat djerfisherite crystallized in the late magmatic stages of the kimberlite evolution, forming during the kimberlite eruption, when the evolved kimberlitic magma became sufficiently enriched in S, Na, K and Cl (Kitayama *et al.*, 2017). In fact, the presence of djerfisherite occurrences in groundmass kimberlite are explained by Cl enrichment in the forming melt (Sharygin *et al.*, 2007; Minin *et al.*, 2015).

However, some points obtained in the present study argue against the above interpretations:

a) The djerfisherite in the Menominee kimberlite groundmass is mantled by at the least the last spinels, as magnetite, and could be produced during intermediate stages of crystallization of the groundmass; however, it is also noticeable that djerfisherite does not contain inclusions of typical groundmass minerals. The common occurrence of djerfisherite at the Menominee pipe indicates a high activity of volatiles (S and Cl) and alkalis during intermediate stages of the melt crystallization, as well as very low Si activity, which could also explain the common occurrence of spinel *s.s.* instead of phlogopite.

b) Djerfisherite replacing the xenoliths is not associated with the typical groundmass minerals of the kimberlite, and therefore this metasomatic process should be produced before the arrival of the kimberlite magma. Therefore, the djerfisherite is associated with older metasomatic processes. These processes are associated with the entrance of a fluid-rich carbonatic magma.

c) The occurrence of djerfisherite as a daughter crystal trapped in melt inclusions in xenocrystic ilmenite, as in the case of Menominee. In particular, one must take into account that the containing ilmenite is xenocrystic and probably associated with metasomatic processes in the mantle, being replaced by the groundmass ilmenite minerals. Therefore, they must be formed in the mantle and under the activity of alkaline carbonatitic magmas.

In any case, these occurrences point to a formation by metasomatic processes in the mantle in presence of volatile-rich alkaline magmas, including those kimberlitic and lamproitic. This higher volatile content probably led to more rapid eruption, thus favouring the diamond preservation

(Ogilvie-Harris *et al.*, 2009).

The occurrence of djerfisherite in kimberlites also provides evidence that the infiltrating kimberlite melt was enriched in K and Cl and, therefore, lamphophyric and kimberlitic melts were more enriched in alkalis and halogens tan the whole-rock composition, as suggested by Abersteiner *et al.* (2019b).

CHAPTER 14

GENERAL DISCUSSION

14. GENERAL DISCUSSION

The textural and chemical characteristics of the minerals of kimberlites and related rocks were studied in the above sections, as well as the consequences of these particularities. In the following discussions the aim to establish the paragenetic sequence in the kimberlites and related rocks, and the general conclusions that can be extracted. These paragenetic sequences have implications on the understanding of the petrogenesis of these rocks, which is important for the understanding of the processes forming and preserving diamond.

Moreover, in addition to the classic interest for kimberlites, orangeites and lamproites, the aillikites and other ultramafic lamprophyres are proven to be diamondiferous (e.g., Tappe *et al.*, 2008) and therefore they must be studied carefully.

Many minerals from kimberlites, such as ilmenite, spinels, rutile and perovskite, are important carriers of petrogenetic information. Xenocrystic Ti-rich oxides in kimberlitic rocks, such as Cr-rich rutile, Ti-rich spinel and ilmenite, provide information about the metasomatic processes in the cratonic lithospheric mantle (Ragozin *et al.*, 2014; Rezvukhin *et al.*, 2016a). In addition, Ti-rich oxides from kimberlite groundmass, such as Ti-rich spinel (Roeder and Schulze, 2008) and perovskite (Bellis and Canil, 2007), could supply information about the evolution of kimberlitic magmas. Finally, perovskite (Batumike et al., 2008; Castillo-Oliver et al., 2016) and rutile (Tappe et al., 2014; Malkovets et al., 2016) could also be used to determine the kimberlite emplacement age. However, in many cases these minerals undergo complex alteration processes during the hydrothermal or supergene late stages of the kimberlite crystallization sequence that could disturb the petrogenetic interpretations based on geochemical data. Therefore, it is important to establish the paragenetic sequence and to determine the different generations or disturbances that can experiment these minerals in the different rocks.

14.1. PARAGENETIC SEQUENCE

General paragenetic sequences of crystallization in kimberlites and related rocks are established in this section, based on the synthesis of the individual paragenetic sequences obtained in the 79 occurrences considered representative of the worldwide kimberlites and related rocks studied in this work (Fig. 14.1-5). Sequences were obtained on the basis of the textural relationship between the main minerals. Not all the studied samples show the entire sequence, and many of them only show a part, or parts, of this sequence.

The majority of kimberlites contain large amounts of xenoliths and xenocrysts; even in those that are coherent rocks (formerly called hypabyssal) xenoliths and xenocrysts of different sizes are observed. Xenoliths are incorporated in magma since its original places in the mantle, during the magma ascent and near the earth surface, including mantle xenoliths and crustal xenoliths. Mantle xenoliths in the studied samples are peridotitic xenoliths, eclogitic xenoliths and MARID/PIC/glimmeritic xenoliths. These rocks record different stages of metasomatism in the mantle, as is demonstrated by the occurrence of significative mineral associations with large-ion lithophile elements (LILE).

Diverse types of xenocrystals are produced by disaggregation of the corresponding xenoliths; therefore, their mineral composition can be considered as daughter of the parental xenoliths.

The intrusive process can be described as developed in a succession of stages: early magmatic, intermediate magmatic, late magmatic and post-magmatic (hydrothermal and supergene).

Peridotite xenoliths

Minerals identified in the different (metasomatized) peridotitic xenoliths include olivine, orthopyroxene, clinopyroxene (diopside), garnet (pyrope), chromite (MCC, AMC), LIMA, mica (phlogopite), ilmenite (Fe^{3+}-rich, Mg-rich and ilmenite s.s.) and diamond. A large euhedral octahedral diamond (8 mm in diameter) of gem quality was located by us in a sample of metasomatized peridotite from Diavik mine, Canada. Previously reported occurrences of diamond include the Finsch kimberlite in South Africa (Shee *et al.*, 1982).

Eclogitic xenoliths

Eclogitic xenoliths were merely studied in this work, although they may contain omphacitic clinopyroxene, almandine-pyrope garnet, rutile, diamond, kyanite, etc. In our study we appreciated that some samples of Cr-rich kyanite-bearing eclogitic xenoliths from the Robert Victors mine were extremely rich in diamond inclusions, with more than 2 large euhedral crystals (more than 6 mm in diameter)/ 20 cm^3. Diamond-bearing eclogites were reported in many places, as in Yakutia, Russia (Loz'ko *et al.*, 1983) or in Orapa, Botswana (Robinson *et al.*, 1984).

MARID/PIC/Glimmerites

MARID/PIC/glimmerites xenoliths represent intense metasomatized peridotites produced by mantle refertilization (Dawson and Smith, 1977; Peterson and LeCheminant, 1993; Fitzpayne *et al.*, 2017). The examples found in the studied kimberlites and related rocks are made up by different proportions of several generations of clinopyroxenes (diopside-augite, some of them metasomatic) accompanied by different proportions of metasomatic minerals as phlogopite (dominant in glimmerites and common in MARID and PIC), K-richterite (common in MARID), rutile (common in MARID) and ilmenite (Mg-rich; common in MARID and PIC).

Rutile may be replaced by ilmenite, as in the Letlhakane DK1 volcaniclastic kimberlite, and this generation of ilmenite is considered as pre-kimberlitic.

No diamond has been found in this study in MARID/PIC/glimmerite xenoliths and we did not find descriptions of diamond in these associations.

Basaltic xenoliths

Basaltic and granitic xenoliths are identified in this study as the most common crustal xenoliths. Basaltic xenoliths contain clinopyroxenes (diopside, augite and aegirine), Ti-poor magnetite, ilmenite (Fe^{3+}-rich, Mn rich and ilmenite s.s.), while other minerals (probably, plagioclase and olivine) are highly altered. Basaltic xenoliths are commonly found in samples from Orapa, Karowe, Letlhakane and Damtshaa from Botswana where basalt is present in the country rocks.

The occurrence, in some cases, in the same fragment, of different types of pyroxenes (including aegirine) and different types of ilmenites (in particular, Mn-rich ilmenite, supposed to be hydrothermal) is a strong argument suggesting that the host rock and the xenoliths suffered hydrothermal alkaline alterations, similar to those found during the fenitization if host rocks by carbonatites. These processes could lead to enrichment in alkalis in the host rock, and loss of silica and calcium, that could be introduced in the kimberlite. This contamination could account for the development of groundmass diopside in the most contaminated rocks, i.e., the volcaniclastic kimberlites. Furthermore, the basalt should be contaminated with Mn thus producing Mn-rich ilmenite. Similar processes have been described in fenitized basalts, e.g. Basu and Bhattacharyya (2014).

Granitic xenoliths

Granitic xenoliths are made up by minor quartz, abundant K-feldspar, albitized plagioclase, annite, amphibole (magnesiohornblende, hastingsite), zircon, apatite, magnetite and different types of ilmenite (ilmenite s.s., Mn-rich ilmenite and pyrophanite).

A significative point is the occurrence of hastingsite $[\{Na\}\{Ca_2\}\{Fe^{2+}{}_4Fe^{3+}\}(Al_2Si_6O_{22})(OH)_2]$, an alkaline amphibole which is rare in granites but common in alkaline rocks (including A granites and similar rocks; e.g., Davidson, 1982; Pagano *et al.*, 2016) and fenites (e.g., Lowers *et al.*, 2004; Doroshkevich *et al.*, 2010) or by replacement of alkaline volcanism (e.g. Price *et al.*, 2003). This mineral can occur in addition to magnesiohornblende, which is more typical of granitic rocks. Therefore, as in the case of the basalts, these granites are affected by hydrothermal alteration inducted by the kimberlite intrusion and a process similar to fenitization took place. For a long time most of the authors declined study this process, which was supposed to be absent (Mitchell, 1986). However, Smith *et al.* (2004) also described a similar process in the Murowa and Sese pipes in Zimbabwe and suggest that this process can be more widespread worldwide than is now imagined. These authors also pointed out that during the fenitization process the hosting granites become strongly enriched in Mg, Cr, Ni, CO_2 and H_2O^+, with higher Ca, Mn, Nb, Sr, P, Fe^{3+} /Fe^{2+} ratio, U, Co, and Cu, with approximately equal TiO_2, K_2O, Na_2O, La, Ta, Rb, Zr, Zn impoverished in SiO_2, Al_2O_3, Ga and Y. Therefore, the Mn enrichment in the ilmenites of the hydrothermal stage cannot be produced by contamination from the host rock and should be related with some particularities of the evolution of the kimberlite magma.

Early intrusive stages

The first mineral liquidus from kimberlite magma is olivine; olivine is frequently zoned, with a core that can be xenocrystic and a phenocrystic rim. Along with the crystallization of olivine, at the early stage (magmatic stage 1), rutile is the first mineral to crystallise, then a spinel group mineral and geikielite or high-magnesian ilmenite. All these minerals have been observed as inclusion in olivine, and also as groundmass minerals. High magnesian ilmenites replacing rutile microphenocrysts are also observed.

Spinel group mineral in this stage is typically chromite MCC or AMC, less commonly spinel s.s. (only observed in the Menominee pipe). Ilmenite crystallised in this stage is typically Mg-rich, Fe^{3+}-rich geikielite and geikielite. However, when minerals of the ilmenite group replace pre-existing xenocrystic ilmenites or other xenocrystic Ti-rich minerals, the resulting ilmenites show wider compositional range. The chemical composition of these crystals is highly dependent on the composition of the replaced minerals and the interaction degree. A possible early stage mica phenocryst (phlogopite) may be crystallised as the core and first rim of some complexly zoned phlogopite without inclusions of groundmass spinel and perovskite, although it is sometimes ambiguous whether it is phenocrystic or xenocrystic.

Intermediate magmatic stage

This stage (stage 2) of magma crystallisation is characterised by the crystallization of groundmass spinel group minerals (MUM) and perovskite. However, in some occurrences, Mn-rich ilmenite crystallised before and is replaced by the MUM and perovskite. Spinel group mineral crystallised in this stage is typically MUM. MUM could crystallise a little before and then cocrystallised with perovskite, while perovskite could start to nucleate a little later. For instance, an ilmenite xenocrystal is firstly replaced/overgrown by MUM which is immediately followed by an intergrowth of MUM and perovskite, then mantled by perovskite.

Late magmatic stage

In a later stage (stage 3), magma crystallisation produces groundmass phlogopite, apatite, monticellite, primary carbonate and djerfisherite. Groundmass primary clinopyroxene can be formed in this stage, but is only present in lamproites and volcaniclastic kimberlites.

Monticellite [$CaMgSiO_4$], when present, crystallises simultaneously with phlogopite, because in some cases it includes and mantles phlogopite while in other occurrences it crystallised before phlogopite as it is included by phlogopite. Monticellite is a rare groundmass mineral, but has been described in other kimberlites worldwide (e.g., Kola, Beard *et al.*, 1998; Canada, Caro *et al.*, 2004; Kopylova *et al.*, 2010). Abersteiner *et al.* (2018) find also monticellite, in some cases dominant in the groundmass and associated with periclase, and concludes that this association can be formed by degasification of the forsterite in presence of a carbonatitic magma:

Forsterite + Carbonate (melt) ↔ Monticellite + Periclase + CO_2

Phlogopite crystallises in some occasions as poikilitic plates including other groundmass minerals such as diopside, apatite, perovskite and MUM. Groundmass clinopyroxene crystallises before groundmass phlogopite because is mantled by phlogopite, while it may crystallise contemporaneously with phlogopite forming groundmass of peletal lapilli in volcaniclastic kimberlite.

The position in the sequence of the Cl-bearing alkaline sulfides found in this study, as djerfisherite [$K_6(Fe,Cu,Ni)_{25}S_{26}Cl$], or rasvumite [$KFe_2S_3$] is difficult to be established in the available material, because these sulfides have been strongly replaced by secondary late minerals, including chlorite and hydrous sulfides as valleriite [$(Fe^{2+},Cu)_4(Mg,Al)_3S_4(OH,O)_6$]. However, these sulfides are widely spread in many worldwide kimberlites (e.g., Clarke *et al.*, 1994; Sharygin *et al.*, 2011), and may be very abundant and well preserved in some cases. For some authors, since it has been discovered in mantle xenoliths, it could be formed in the mantle; however, experiments carried out at high pressure demonstrated that this mineral is unstable above 3 Gpa (Minin *et al.*, 2016). Hence, these authors proposed that djerfisherite could be formed by interaction of kimberlite magma/fluid with the mantle xenoliths, and it is not a diamond-indicator mineral. Normally, djerfisherite uses to replace other sulfides, as pyrrhotite, following the next sequence of replacement:

pyrrhotite → rasvumite → djerfisherite, thus reflecting an increase in the alkalinity and in the activity of Cl in the evolved melt (Sharygin *et al.*, 2008).

The position of diopside in the sequence is under discussion. For some authors it is a microlitic mineral (Skinner and Marsh, 2004a). However, in some cases it forms as a late mineral and may occur filling voids, in association with serpentines. This is why Stripp *et al.* (2006), Walters *et al.* (2006) and Hayman *et al.* (2009) proposed a hydrothermal origin for this mineral, at low temperature. Probably diopside may represent a transitional stage between magmatic and hydrothermal and can be formed, as calcite and the ilmenites, by both mechanisms.

Similar problem can be found when trying to explain the paragenetic position of carbonates. Primary carbonate could be calcite or dolomite. Primary carbonate (calcite) crystallizes as tabular groundmass crystal in some occurrences; this tabular calcite could be pseudomorphic of nyerereite [$Na_2Ca(CO_3)_2$]. Nyerereite and other alkaline carbonates and sulfates, as well as alkaline sulfides, are strongly soluble in water and are dissolved easily during weathering. However, these alkaline minerals have been described as primary minerals in many unaltered kimberlites or were preserved as melt/fluid inclusions into resistant minerals that protected them of dissolution (e.g., Parthasarathy *et al.*, 2002; Sharygin *et al.*, 2006, 2008; Kamenetsky *et al.*, 2013; Golovin *et al.*, 2017). In other cases, calcite or dolomite can define banded or interstitial units. Therefore, they formed late in the sequence and could be either primary or secondary. Isotopic studies of them are suggesting that these minerals formed by both processes (Wilson *et al.*, 2007). Armstrong *et al.* (2004) pointed out that different calcite generations can be traced by using the contents of minor elements as Ba and Sr, which are concentrated in the crystals formed at higher temperatures.

A poorly studied aspect is the possibility to find vocanic glass in kimberlites. Porritt and Russell (2012) pointed out that although kimberlitic volcanic glass has never been described, this could be due to a very high instability of this glass. In fact, for other authors the fine-grained groundmass of serpentines or clay minerals mixtured with fine-grained calcite could be produced by devitrification of kimberlitic volcanic glass (Skinner and Marsh, 2004b; Stripp *et al.*, 2006). Perhaps thin dikes are good places to explore this possibility in future, as well as small melt inclusions encapsulated in late minerals, as magnetite.

Post-magmatic stage

An association of secondary minerals is produced during the subsolidus hydrothermal processes. Their crystallisation removes many of the primary magmatic minerals and the xenolitic crystals. No detailed study has been done for secondary minerals in this work, although different parageneses of the same mineral have been observed, such as serpentine and carbonates. As indicated above, secondary clinopyroxene may crystallise as geode-like texture. Perovskite can be altered in some cases to anatase or kassite, along with aeschynite. It is important to take into account that this process can break free Sr, Nb and REE from the perovskite, with all the resulting geochemical and geochronological implications

Groundmass atoll spinel group minerals can be altered to mixtures of serpentine, chlorite, titanium hydrogarnet, magnetite, and secondary perovskite. Therefore, perovskite may be formed in two stages, magmatic and hydrothermal.

Secondary apatite and carbonate crystallised in veins and interstital. Secondary ilmenite (Mg-rich, geikielite, Mn-rich and pyrophanite) crystallised as tabular crystal or replacing primary Ti-bearing oxides.

Minerals crystallised in this stage are related with a late fluid. However, there is a controversy about the nature of this fluid. The problem is associated with the question about the origin of serpentine in kimberlites: deuteric (Mitchell, 2013) or produced by convective circulation of external fluids (Wyatt *et al.*, 2004; Sparks, 2013; Afanasyev *et al.*, 2014), or a combination of these phenomena during the decrease of the temperature, as suggested by the occurrence of different generations of serpentine (Giuliani *et al.*, 2017). Based on the occurrence of secondary hydrothermal pyrophanite found in our study and based in the existence of hydrothermal fenitization of the host rocks and xenoliths leading to Mn, Cr and Nb metasomatism over the host rock, that can be reflected in crystallization of secondary pyrophanite in the host rocks. We conclude that pyrophanite (and therefore late geikielite too) must be deuteric. However, the fenitization processes can be bimetasomatic, as are registered in many magmatic processes, and therefore the kimberlitic rock can be contaminated with fluids of supergene origin and enriched in silica from the host rocks, as happens in the case of the fenitization related with carbonatites (Melgarejo *et al.*, 2012).

Other minerals as chlorite and smectite are commonly found in volcaniclastic kimberlites as pseudomorphs of olivine or in interpeletal lapilli space and can represent very late products. In particular, smectites can be supergene and unrelated with the kimberlite emplacement.

14.2. PRIMARY MINERAL ASSOCIATIONS

The presence of groundmass minerals from the 79 studied kimberlites and related rocks is presented in Table 14.1. However, no correlation is observed between the different mineral occurrences. There is no regular relation which could occur during the magma ascent to close to the surface, which can also influence to the minerals which crystallise between the presence of perovskite and spinels (chromite and MUM). The mineralogy of the kimberlite depends on the original composition of the magma, as well as on the crystallization conditions and the differentiation processes. Moreover, other factors that can largely modify the original magma could be the assimilation of wall rock and xenoliths, mingling and mixing processes.

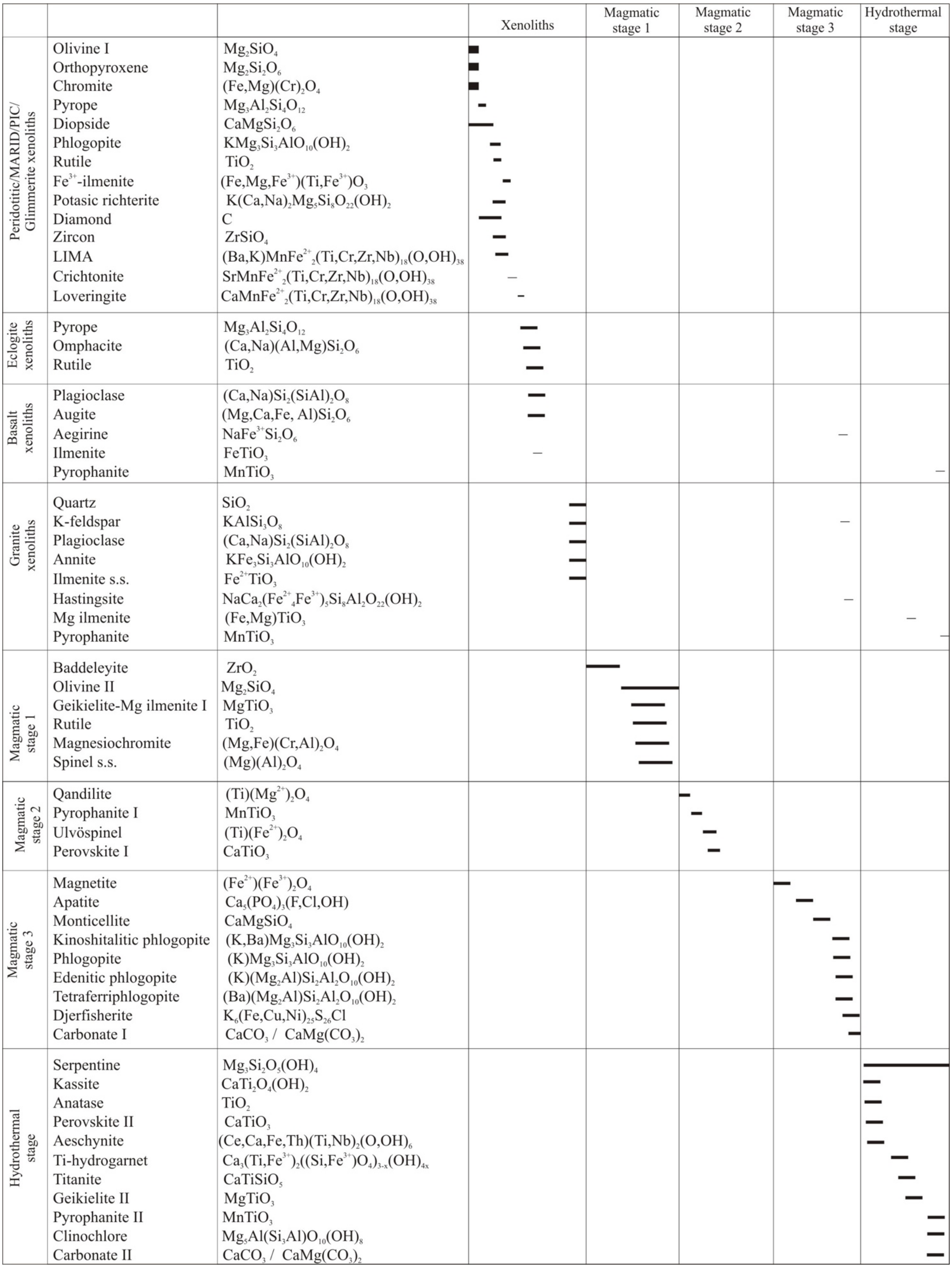

			Xenoliths	Magmatic stage 1	Magmatic stage 2	Magmatic stage 3	Hydrothermal stage
Peridotitic/MARID/PIC/ Glimmerite xenoliths	Olivine I	Mg$_2$SiO$_4$	▬				
	Orthopyroxene	Mg$_2$Si$_2$O$_6$	▬				
	Chromite	(Fe,Mg)(Cr)$_2$O$_4$	▬				
	Pyrope	Mg$_3$Al$_2$Si$_4$O$_{12}$	▬				
	Diopside	CaMgSi$_2$O$_6$	▬				
	Phlogopite	KMg$_3$Si$_3$AlO$_{10}$(OH)$_2$	▬				
	Rutile	TiO$_2$	▬				
	Fe^{3+}-ilmenite	(Fe,Mg,Fe^{3+})(Ti,Fe^{3+})O$_3$	▬				
	Potasic richterite	K(Ca,Na)$_2$Mg$_5$Si$_8$O$_{22}$(OH)$_2$	▬				
	Diamond	C	▬				
	Zircon	ZrSiO$_4$	▬				
	LIMA	(Ba,K)MnFe$^{2+}_2$(Ti,Cr,Zr,Nb)$_{18}$(O,OH)$_{38}$	▬				
	Crichtonite	SrMnFe$^{2+}_2$(Ti,Cr,Zr,Nb)$_{18}$(O,OH)$_{38}$	–				
	Loveringite	CaMnFe$^{2+}_2$(Ti,Cr,Zr,Nb)$_{18}$(O,OH)$_{38}$	▬				
Eclogite xenoliths	Pyrope	Mg$_3$Al$_2$Si$_4$O$_{12}$	▬				
	Omphacite	(Ca,Na)(Al,Mg)Si$_2$O$_6$	▬				
	Rutile	TiO$_2$	▬				
Basalt xenoliths	Plagioclase	(Ca,Na)Si$_2$(SiAl)$_2$O$_8$	▬				
	Augite	(Mg,Ca,Fe, Al)Si$_2$O$_6$	▬				
	Aegirine	NaFe^{3+}Si$_2$O$_6$				–	
	Ilmenite	FeTiO$_3$	–				
	Pyrophanite	MnTiO$_3$					–
Granite xenoliths	Quartz	SiO$_2$	▬				
	K-feldspar	KAlSi$_3$O$_8$	▬			–	
	Plagioclase	(Ca,Na)Si$_2$(SiAl)$_2$O$_8$	▬				
	Annite	KFe$_3$Si$_3$AlO$_{10}$(OH)$_2$	▬				
	Ilmenite s.s.	Fe^{2+}TiO$_3$	▬				
	Hastingsite	NaCa$_2$(Fe$^{2+}_4$Fe^{3+})$_5$Si$_8$Al$_2$O$_{22}$(OH)$_2$				–	
	Mg ilmenite	(Fe,Mg)TiO$_3$					–
	Pyrophanite	MnTiO$_3$					–
Magmatic stage 1	Baddeleyite	ZrO$_2$		▬			
	Olivine II	Mg$_2$SiO$_4$		▬			
	Geikielite-Mg ilmenite I	MgTiO$_3$		▬			
	Rutile	TiO$_2$		▬			
	Magnesiochromite	(Mg,Fe)(Cr,Al)$_2$O$_4$		▬			
	Spinel s.s.	(Mg)(Al)$_2$O$_4$		▬			
Magmatic stage 2	Qandilite	(Ti)(Mg^{2+})$_2$O$_4$			▬		
	Pyrophanite I	MnTiO$_3$			▬		
	Ulvöspinel	(Ti)(Fe^{2+})$_2$O$_4$			▬		
	Perovskite I	CaTiO$_3$			▬		
Magmatic stage 3	Magnetite	(Fe^{2+})(Fe^{3+})$_2$O$_4$				▬	
	Apatite	Ca$_5$(PO$_4$)$_3$(F,Cl,OH)				▬	
	Monticellite	CaMgSiO$_4$				▬	
	Kinoshitalitic phlogopite	(K,Ba)Mg$_3$Si$_3$AlO$_{10}$(OH)$_2$				▬	
	Phlogopite	(K)Mg$_3$Si$_3$AlO$_{10}$(OH)$_2$				▬	
	Edenitic phlogopite	(K)(Mg$_2$Al)Si$_2$Al$_2$O$_{10}$(OH)$_2$				▬	
	Tetraferriphlogopite	(Ba)(Mg$_2$Al)Si$_2$Al$_2$O$_{10}$(OH)$_2$				▬	
	Djerfisherite	K$_6$(Fe,Cu,Ni)$_{25}$S$_{26}$Cl				▬	
	Carbonate I	CaCO$_3$ / CaMg(CO$_3$)$_2$				▬	
Hydrothermal stage	Serpentine	Mg$_3$Si$_2$O$_5$(OH)$_4$					▬
	Kassite	CaTi$_2$O$_4$(OH)$_2$					▬
	Anatase	TiO$_2$					▬
	Perovskite II	CaTiO$_3$					▬
	Aeschynite	(Ce,Ca,Fe,Th)(Ti,Nb)$_2$(O,OH)$_6$					▬
	Ti-hydrogarnet	Ca$_3$(Ti,Fe^{3+})$_2$((Si,Fe^{3+})O$_4$)$_{3-x}$(OH)$_{4x}$					▬
	Titanite	CaTiSiO$_5$					▬
	Geikielite II	MgTiO$_3$					▬
	Pyrophanite II	MnTiO$_3$					▬
	Clinochlore	Mg$_5$Al(Si$_3$Al)O$_{10}$(OH)$_8$					▬
	Carbonate II	CaCO$_3$ / CaMg(CO$_3$)$_2$					▬

Fig. 14.1. Paragenetic sequences of crystallization of minerals in coherent kimberlites.

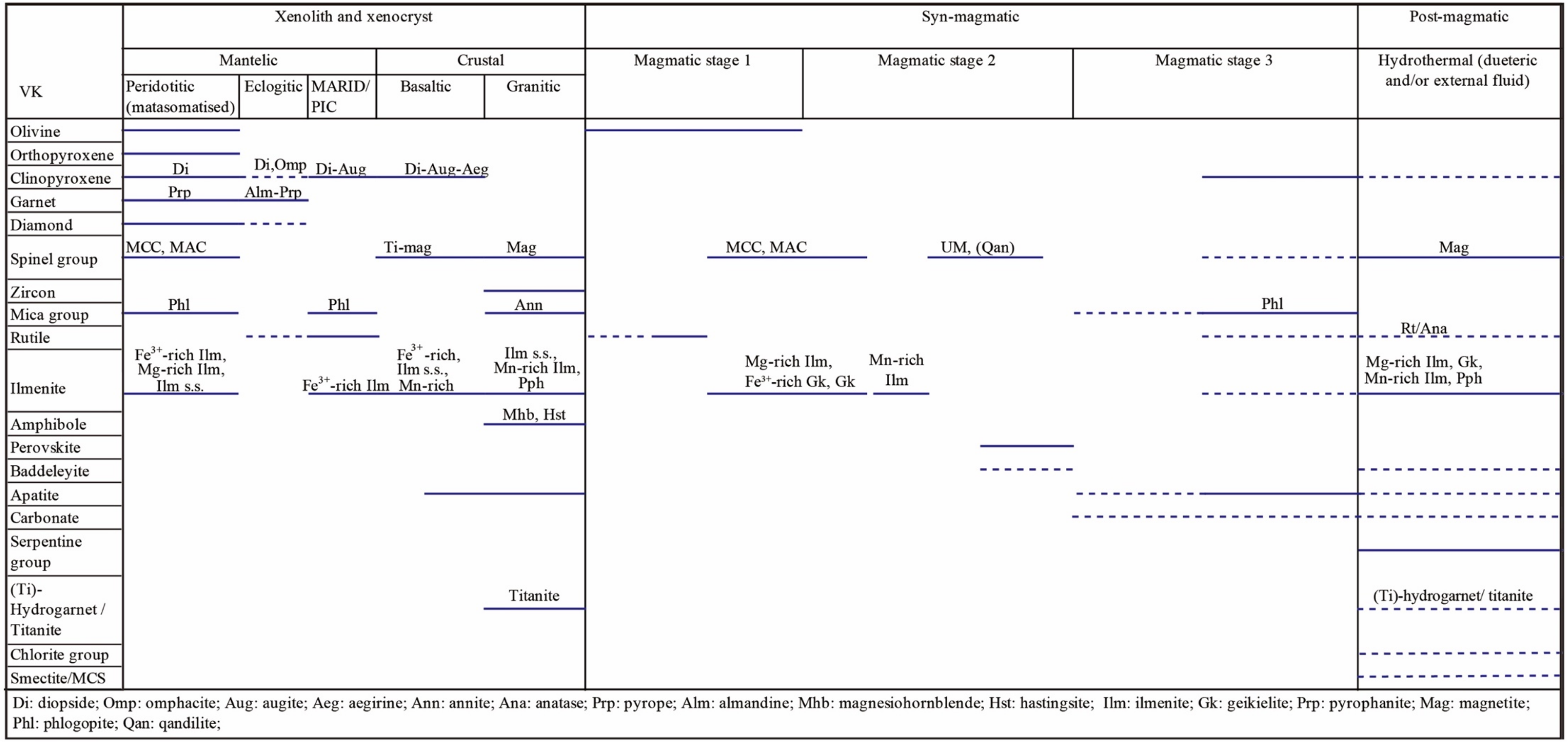

Fig. 14.2. Paragenetic sequences of crystallization of minerals in volcaniclastic kimberlites.

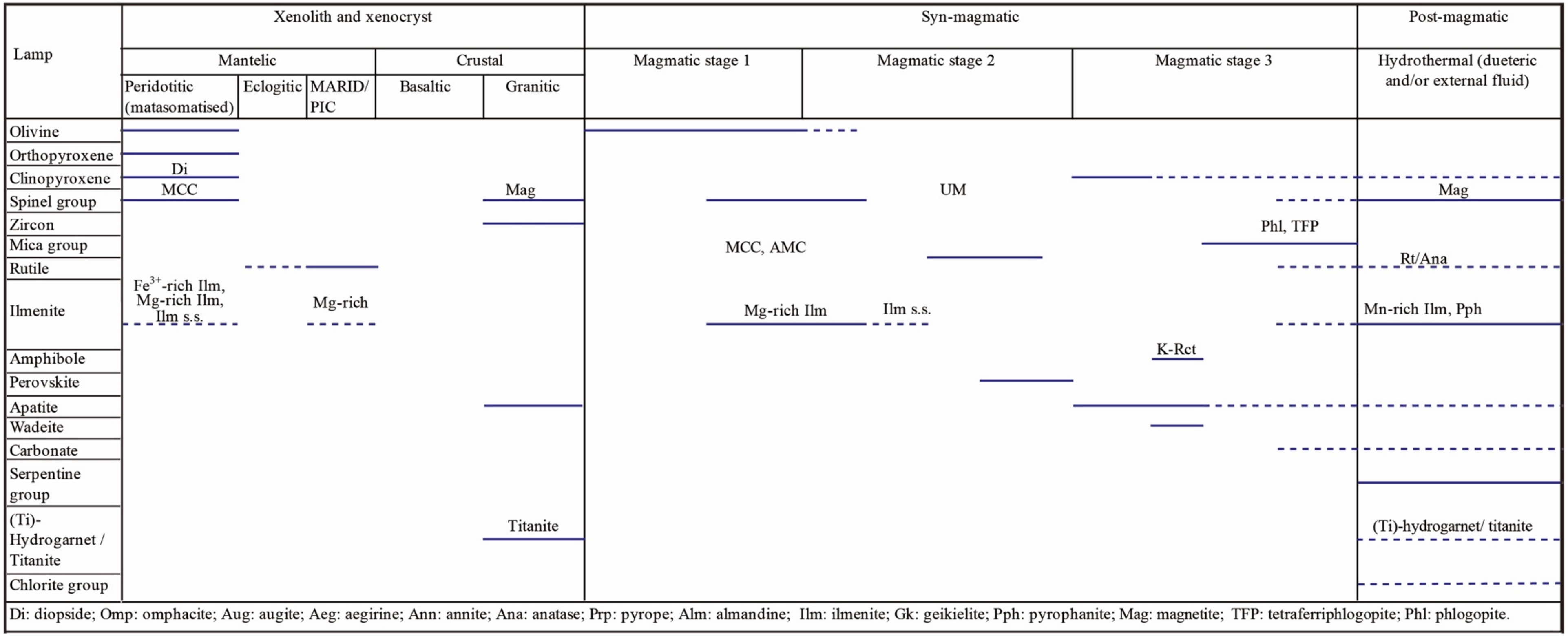

Fig. 14.3. Paragenetic sequences of crystallization of minerals in lamproites.

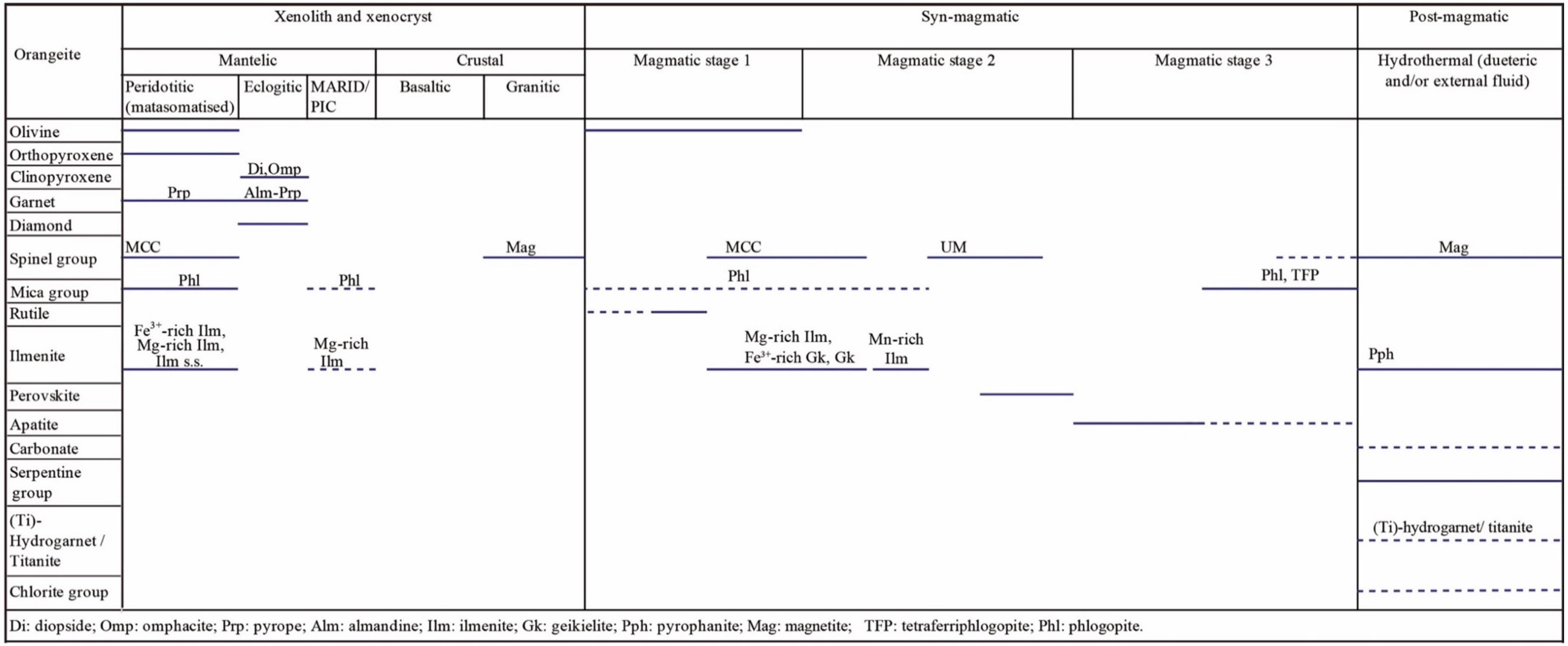

Fig. 14.4. Paragenetic sequences of crystallization of minerals in orangeites.

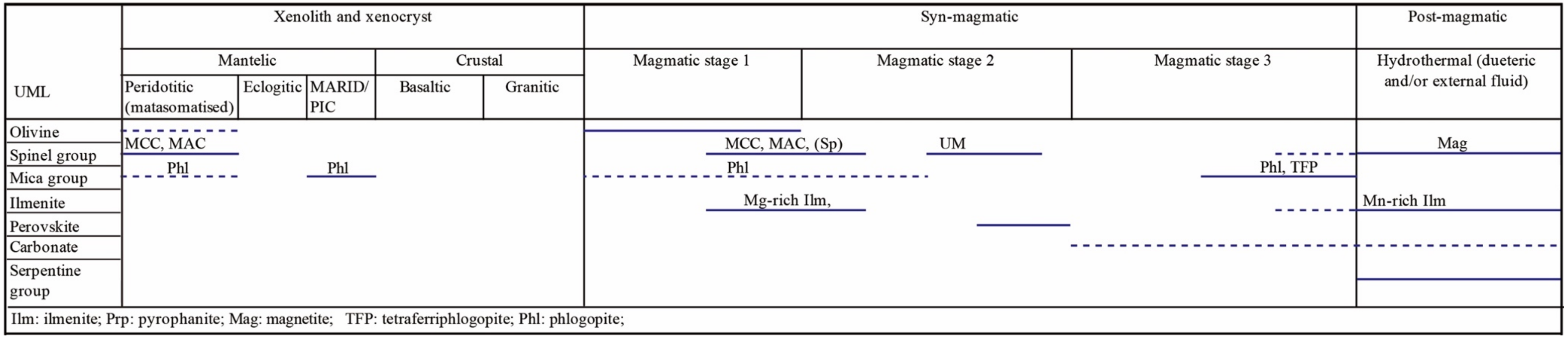

Fig. 14.5. Paragenetic sequences of crystallization of minerals in ultramafic lamprophyres.

Table 14.1. Principal primary mineral association in studied kimberlites and related rocks in this work (excluding olivine).

	Sample	**Region**	**Location**	**Name**	**Rock**	**Rutile**	**Spinel**			**Ilmenite**	**Perovskite**	**Phlogopite**	**Monticellite**	**Clinopyroxene**	**Tabular calcite**
Angola	CU-79-70,5A, CU-79-113A		Cucumbi		VK					C	Y			D	
Angola	TZ-G18-47, TZ-G18-252		Tchiuzo		VK		AMC	MCC	MUM	C,D	Y	Y		D	
Botswana	10052	SD	Jwaneng	Centre pipe	VK	Y		MCC	MUM	C					Y
Botswana	10053	SD	Jwaneng	North pipe	VK		AMC	MCC		C					
Botswana	10054	SD	Jwaneng	South pipe	VK	Y		MCC		C					
Botswana	10055	CD	Orapa	AK1, "A"	VK			MCC	MUM	C	Y	Y		D	Y
Botswana	10056	CD	Orapa	AK1, "B"	VK			MCC			Y	Y		D	
Botswana	10057	CD	Orapa	AK1, "C"	VK			MCC			Y	Y		D	
Botswana	10058	CD	Letlhakane	DK1	VK			MCC	MUM	C	Y	Y		D	
Botswana	10060	CD	Damtshaa	BK9, "A"	VK				MUM	C	Y	Y			
Botswana	10061	CD	Damtshaa	BK9, "B"	VK			MCC	MUM	C	Y			D	
Canada	7999	Quebec	Temiskaming	Ville-Marie	VK		AMC	MCC	MUM	C	Y	Y (Ba)		D	
Canada	9168	Ontario	Temiskaming	Seed	VK			MCC	MUM	C					
Canada	9359	NWT	SW Slave	Drybones Bay	VK	Y		MCC		C		Y			
USA	8015	Michigan	Lake Ellen	Lake Ellen	VK	Y			MUM	C					
USA	9346	Colorado	San Juan Co.	Alhambra Rock	VK				MUM			Y			
USA	9966	Tennessee	Tazewell	Norris metakimberlite	VK					C					
Venezuela	7544		Guaniamo		VK/CK				MUM						
Russia	10077	NR	Lomonosovskaya		VK		AMC	MCC			Y			D	
Russia	10079	NR	Pionerskaya		VK			MCC			Y	Y		D	
Russia	9985	Yakutia	Pobeda		VK		AMC	MCC	MUM		Y	Y			
Russia	9959	Yakutia	Leningrad		VK			MCC		C					

Table 14.1. (continued 1)

	Sample	Region	Location	Name	Rock	Rutile	Spinel			Ilmenite	Perovskite	Phlogopite	Monticellite	Clinopyroxene	Tabular calcite
Angola	CC-47-46		Cacuilo	K47	CK				MUM	C	Y				
Botswana	10049	CD	Karowe	AK6, South pipe	CK		AMC	MCC	MUM	C	Y	Y (TFP)			
Botswana	10050	CD	Karowe	AK6, Center pipe	CK				MUM	C	Y				
Botswana	10051	CD	Karowe	AK6, North pipe	CK				MUM	C,D	Y				
Botswana	10059	CD	Letlhakane	DK1	CK		AMC		MUM		Y	Y (TFP)	Y		
South Africa	7707	NCP		Riverton	CK		AMC	MCC	MUM	C	Y	Y (TFP)			
South Africa	9156	FSP		Bultfontein	CK			MCC	MUM	C,D	Y	Y (Ba)			
South Africa	9311	NCP	Kimberley	Big Hole	CK	Y		MCC	MUM	C					
South Africa	9351	NCP	Kimberley		CK			MCC	MUM		Y	Y (TFP)			
South Africa	9364	NCP	Kimberly	DutoitSpan	CK	Y		MCC	MUM	C	Y	Y			
South Africa	9725	FSP		Monastery	CK				MUM	C	Y	Y (Ba)			
South Africa	9630	FSP	Kaalvallei	"occurence A"	CK				MUM	C	Y	Y (TFP)			
Lesotho	9607			P200	CK		AMC		MUM	C		Y (TFP)	Y		
Guinea	8870			Banakoro "A"	CK			MCC	MUM		Y	Y (Ba)	Y		
Guinea	8871			Banakoro "B"	CK			MCC	MUM	C	Y	Y (TFP)			
Canada	9353, 9354	Québec	Temiskaming	Notre Dâme du Nord	CK		AMC	MCC	MUM	C					Y
Canada	9577	Ontario	Bucke Township		CK			MCC	MUM	C	Y	Y (Ba)			
Canada	6934	NWT	Somerset island		CK	Y			MUM	C	Y				
Canada	7448	NWT	Diavik		CK			MCC	MUM		Y	Y			
Canada	7449	NWT	LDG Ekati	Pointe Lake	CK		AMC	MCC	MUM	C	Y	Y (Ba)			
Canada	9613	NWT	SW Slave	Snap Lake	CK			MCC	MUM			Y (Ba)			
Canada	7454	Alberta	Birch Mountains		CK			MCC	MUM		Y	Y (Ba)			
Canada	9360	Nanavut	Baffin Island	Jackson inlet	CK			MCC	MUM		Y	Y (Ba)			Y
USA	7314	Colorado	Larimer Co.	Chicken Park	CK		AMC		MUM	C	Y	Y (Ba)			
USA	10070	Pennsylvania	Fayette Co.	Gate-Adah	CK		AMC	MCC	MUM	C	Y	Y (Ba)			
USA	9348	Colorado	Kelsey Lake		CK		AMC	MCC	MUM			Y (Ba,TFP)			
USA	9345	Wyoming	Laramie Co		CK			MCC	MUM		Y	Y (Ba)			Y
USA	9352	Michigan	Menominee	Site 73	Ck	Y			Sp,MUM,Qan	C					
USA	9576	Colorado	Larimer Co.	Sloan #2	CK		AMC	MCC		C	Y	Y (Ba)			
Russia	10037	Yakutia	Udachnaya		CK	Y		MCC	MUM	C					Y
Russia	10065	Yakutia	Obnazhonnaya		CK				MUM		Y	Y			
Russia	4928	Yakutia	Mir		CK			MCC	MUM	C	Y	Y			

Table 14.1. (continued 2)

	Sample	**Region**	**Location**	**Name**	**Rock**	**Rutile**	**Spinel**			**Ilmenite**	**Perovskite**	**Phlogopite**	**Monticellite**	**Clinopyroxene**	**Tabular calcite**
Russia	9611	Kola Peninsula	Emakowskaya		CK	Y		MCC	MUM			Y (Ba)			
India	8021	RKF	Siddanpalli cluster	SK-1	CK			MCC	MUM	C	Y				
India	8044	RKF	Siddanpalli cluster	SK-2	CK				MUM	C,D	Y				
India	8029	RKF	Siddanpalli cluster	SK-3	CK			MCC	MUM	C,D	Y				
India	8030, 8040, 8041	WKF	Chigicherla cluster	CC-4	CK			MCC	MUM	C,D	Y				
India	8022, 8023	WKF	Chigicherla cluster	CC-5	CK		AMC	MCC	MUM		Y	Y (TFP)			
India	8036	WKF	Kalyandurg	KL-3	CK		AMC	MCC	MUM		Y	Y (TFP)			
India	8037, 8038	WKF	Kalyandurg	KL-4	CK				MUM	C	Y	Y (Ba)			
India	8027	WKF	Wajrakarur village	P-1	CK		AMC	MCC			Y				
India	8043	WKF	Lattavaram village	P-3	CK			MCC	MUM	C		Y (Ba)			
China	9333	Shandong province	Mengyin	Red Flag #1	CK		AMC	MCC	MUM	C	Y	Y (Ba)			
China	9737,9738, 9740	Shandong province	Mengyin	Shengli	CK		AMC	MCC	MUM		Y	Y (Ba)			
China	9573, 9574	Liaoning province		Wafangdian	CK			MCC				Y			

Table 14.1. (continued 3)

	Sample	Region	Location	Name	Rock	Rutile	Spinel			Ilmenite	Perovskite	Phlogopite	Monticellite	Clinopyroxene	Tabular calcite
South Africa	7881	NCP	Kimberley	Helam	Oran (*2)				MUM	C	Y	Y(Ba,TFP)			
South Africa	9375	FSP		Roberts Victor	Oran (*3)			MCC			Y	Y			
South Africa	9952	NCP		Bellsbank	Oran (*3)			MCC	MUM			Y			
South Africa	9602	FSP	Kaalvallei	"occurence B"	Lamp (*1)				MUM	C,D	Y	Y		C	
USA	9341	Colorado	Kelsey Lake		Lamp (*1)			MCC	MUM		Y	Y		C	
USA	9340	Arkansas	Murfreesboro		Lamp (*5)		AMC	MCC	MUM		Y	Y		C	
India	8024	WKF	Chigicherla cluster	CC-1	Lamp (*1)			MCC	MUM		Y	Y		C	
India	8025	WKF	Wajrakarur village	P-2	Lamp (*6)			MCC	MUM		Y	Y			
India	8035	WKF	Lattavaram village	P-4	Lamp (*7)		AMC	MCC	MUM		Y	Y (TFP)		C	
India	8045	WKF	Mulligiripally	P-5	Lamp (*9)		AMC		MUM		Y	Y		C	
Canada	10142	Quebec	Ugava Bay	Torngat	UML (*4)			MCC	MUM	C	Y	Y (TFP)			

SD: Southern District; CD:Central District; NCP:Northern Cape Province; FSP:Free State Province; NR:Northern Region; RKF: Raichur kimberlite field; WKF: Wajrakarur kimberlite field. VK: volcaniclastic kimberlite; CK: coherent kimberlite; UML: ultramafic lamprophyres; Ba: highest Ba content zone; TFP: tetraferriphlogopite. *1:this work; *2: Gurney et al. 2005; *3:Mitchell 1995; *4:Tappe et al., 2004;*5:McCandless et al. 1994;*6:Kaur&Mitchell 2013;*7:Shaikh et al., 2018;*8:Kaur et al., 2013. Lamp: lamproite; Oran: orangeite; Y: precence. Types of ilmenite, diopside and spinel are expained in each chapter.

14.3. CLASSIFICATION OF KIMBERLITE AND RELATED ROCKS

Kimberlites, lamproites, orangeites and ultramafic lamprophyres (including aillikite) are volatile-rich silica-undersaturated mantle-derived rocks which exhibit a lot of similarities in their texture, chemical and mineralogical features. Although all of them could contain diamonds, the diamond content and exploitation potential are very different between them. Therefore, correct petrographic classification of these rocks is very important for their economical valuation. However, the classification between them is always ambiguous and controversial (Mitchell, 1995; Le Maitre, 2002; Tappe *et al.*, 2005; Downes *et al.*, 2006; Scott Smith *et al.*, 2018).

Chemical classifications

It is complicate to define a classification of kimberlites and related rocks, because these are rocks that experimented a long trip in the mantle and crust, having different grades of assimilation with the host rocks, that are very different taking into account the mantle inhomogeneities.

These rocks use to be plenty of xenoliths and xenocrysts, in proportions that became very high, in particular, in the crater facies. However, many authors attempted to define a classification based on chemical criteria. Authors of Russian school (Bogatikov *et al.*, 2001, 2007, 2009; Ilupin and Roshchina, 2002) and also from Canada (Hartzler, 2007) proposed to establish different categories of kimberlites based on the titanium contents (low-titanium kimberlites, intermediate titanium kimberlites, high titanium kimberlites), which should be correlated negatively with the diamond potential (Vasilenko *et al.*, 2002). The titanium is an element that tends to be immobile during hydrothermal processes and, in fact, in the fenitized xenoliths the titanium content remains constant when comparing the fresh and fenitized rocks. This means that the Ti is not removed from the pipe during the intrusive process. The problem, in our opinion, came from the fact that kimberlites contain different proportions of Ti-bearing minerals as ilmenites, spinels and perovskites and, as we had seen in this study, part of them are xenocrystic and are distributed in erratic amounts and in different grain sizes. Therefore, although Hartzler (2007) proposed to avoid the problem of xenoliths by hand-picking the groundmass, the groundmass is commonly contaminated with these xenoliths, perhaps because they contain small fragments and/or perhaps because the minerals of the groundmass have already reacted with the mantle xenocrysts and therefore they do not reflect the compositions of the original magma.

Mineralogical classifications

The presence and composition of phlogopite, spinel and clinopyroxene is proposed to be the key for the discrimination between kimberlite, orangeite and aillikite (Tappe *et al.*, 2005). However, the study of the composition of these minerals from 79 kimberlites and related rocks in this work demonstrated that there is an wide overlap of compositional range of these minerals in kimberlites and related rocks. Following the existing classification by the IUGS (Tappe *et al.*, 2005), tetraferriphlogopite should be typical of lamproites (including orangeites) and aillikites and absent in kimberlites. However, the wide population study among 79 kimberlites in this work demonstrate that many coherente kimberlites have tetraferriphlogopite, while tetraferriphlogopite is not observed in many of the studied orangeites, lamproites and volcaniclastic kimberlites (Table 14.1). Thus we suggest that tetraferriphlogopite could not be an useful mineral for rock classification.

A similar problem appears in the case of the groundmass spinel, which composition is used as another criterion for rock classification. The classification criterion is that the spinels from aillikites, orangeites and lamproites should follow the trend 2 while spinels from kimberlites should follow trend 1 (Mitchell, 1995; Tappe *et al.*, 2005). However, many of the studied kimberlites also show this trend 2 and, as we had seen, many of these pipes exhibit intermediate trends, or mixed trends.

Moreover, when applying the composition of phlogopites and spinels in the studied 79 worldwide kimberlites the compositions of these minerals plot in the compositional fields of lamproites and UMLs in a large number of kimberlites.

In fact, in many studies carried out by other authors in these pipes, these authors plot the composition of phlogopite and spinel in these compositional diagrams, but classify the rocks as kimberlites although they strictly plot in the lamproite or UML fields (e.g. Kononova *et al.*, 2011, Gaudet *et al.*, 2018).

Thus the existing classification diagram using phlogopite and spinel compositions is only useful to show their compositional range and evolution while is useless for classification. Some new classification guides and/or diagram must be stablished.

There are other problems. Groundmass minerals show differences in coherent kimberlite and volcaniclastic kimberlite. For instance, different composition of mica and presence of clinopyroxene. The presence of clinopyroxene was also proposed to discriminate between kimberlite, aillikite and orangeite (Tappe *et al.*, 2005). However, clinopyroxene is observed as one of the most common principal groundmass constituent in peletal lapilli in volcaniclastic kimberlite, but it is lacking in the same pipe in the corresponding coherent kimberlite. The difference in main groundmass mineral phase suggested that we need a different guide of classification for volcaniclastic kimberlites and coherent kimberlites.

Other inconsistency in the classification is the use of monticellite to preclude to classify a rock as lamproite (Le Maitre, 2002). Monticellite is only found in three kimberlites in this work. Monticellite is not found in samples from the P2 Indian lamproite studied in this work, but monticellite in P2 lamproite is reported by Kaur and Mitchell (2013) as partially- or completely-replaced by pectolite and hydrogarnet.

The classification for orangeites is also controversial and was changing in the ultimate years. Orangeites were known in origin as “micaceous kimberlite” (Wagner, 1914) and later, were termed as “group II kimberlite” (Skinner, 1989; Woolley *et al.*, 1996; Le Maitre, 2002). Orangeite were defined by IUGS (Le Maitre, 2002) as ultrapotassic, peralkaline volatile-rich (dominantly H_2O) rocks, characterized by phlogopite macrocrysts and microphenocrysts, together with “tetraferriphlogopite” to phlogopite groundmass micas. As its basically differentiated from kimberlite as it is phlogopite dominant and by its composition of phlogopite. Recently, orangeites have been proposed to be included into the lamproites (var. Kaapvaal) due to their petrographic similarity and common petrogenesis (Scott Smith *et al.*, 2018), as they should all derived from metasomatized (enriched) deep lithospheric mantle while kimberlite is derived from asthenospheric mantle (Mitchell, 2006). However, this reclassification of orangeite to lamproite is not widely accepted or used. The term “orangeite” is still commonly used in recent works (e.g. Giuliani *et al.*, 2015; Fitzpayne *et al.*, 2018, 2019; Sarkar *et al.*, 2018). Moreover, kimberlite and lamproite are also proposed to be related to a unifying petrogenetic model by interaction of a silica-poor carbonatite melt with differently metasomatised wall rocks in the lithospheric mantle (Shaikh *et al.*, 2018). In this work, composition and phase of groundmass minerals are quite and more similar for studied kimberlite and orangeites in this work than for orangeite and lamproite. Thus, we disagree with the substitution of term orangeite by lamproite.

In the case of the aillikites, one of the criteria for the definition could be the occurrence of titanian garnets. However, in the Indian kimberlites garnets are produced in large amounts in the late stages of crystallization, associated with secondary minerals, as a late product of replacement of spinels. These garnets are in fact hydrogarnets and we interpreted them as produced by the action of late Ca-rich fluids. Therefore, these garnets cannot be used in the classification of the rocks.

Moreover, as the classification role is changing along time in recent years, many intrusion bodies previously classified as kimberlites should be classified now in different categories depending on the criteria used. A review for the rock classification for known "kimberlites" is also needed to be done.

Therefore, a mineralogical classification of the kimberlites and related rocks should take into account only the primary magmatic minerals and avoid the use of xenolitic material. In a first approach, perhaps it is possible to partly retain the definitions by Tappe *et al.* (2005), by reserving the use of the term aillikite to rocks with Ca silicates in the groundmass (with the exception of melilite and plagioclase) and with a high proportion of calcite in the groundmass (less than 50 modal percent and more than 20 modal %. However, we suggest to avoid the use of the titanium garnet for the classification, with the exception of the cases when the mineral is primary. Spinel compositions are not useful in many of the cases and can create confusion.

The proposal by Tappe *et al.* (2005) could also be retained for the term lamproite, which could be defined in coherent rocks having diopside, alkali feldspar, primary amphiboles (notably potassium richterite) and/or feldspathoids. Again, we propose to avoid the use of spinels and phlogopites in classification.

Kimberlite could be reserved for the ultrapotassic ultrabasic rocks as proposed by Tappe *et al.* (2005), with less than 20 modal % of carbonates and without primary feldspars or feldspathoids, amphiboles or pyroxenes (for coherent rock). Again, we discourage the use of spinel and mica compositions.

Moreover, kimberlite and lamproite are also proposed to be related to a unifying petrogenetic model by interaction of a silica-poor carbonatite melt with differently metasomatised wall rocks in the lithospheric mantle (Shaikh *et al.*, 2018). In this work, composition and phase of groundmass minerals are quite and more similar for studied kimberlite and orangeites in this work than for orangeite and lamproite. Thus, we disagree with the substitution of term orangeite by lamproite.

The other question is the division of the kimberlites. In fact, there are not two equal kimberlites, and there are many textural and chemical variations inside the same pipe. However, this is an important question, because it can be associated with the diamond grade. As indicated, an empirical approach made in Siberian kimberlites suggest that the diamond grade correlates negatively with the Ti contents. Probably this is not an universal rule, because in Angola some of the richest pipes, as Catoca, are strongly enriched in ilmenite xenocrysts. However, Ti minerals can also be in the groundmass, in form of spinels, perovskite, groundmass ilmenite, rutile, minerals of the crichtonite group and phlogopite.

In some cases, Ti-garnet can be very abundant, although it has been interpreted as formed by alteration of spinels. In fact, spinels and perovskite are the dominant Ti-bearing minerals in the groundmass. They commonly occur in high modal proportions, and therefore they could be used to help classify the rock and define the Ti content related with the kimberlitic magma (not the total TiO_2 that is obtained in whole rock analyses, less precise because it is contaminated with the xenoliths).

Hence, the composition of the spinel may have petrogenetic value by reflecting the activity of some of the spinel components in the crystallizing kimberlitic magma. Hence, the following subtypes could be established based on the mineral parageneses found in this study:

a) Chromitic kimberlites, with AMC or MCC

b) Peraluminic kimberlites, with spinel s.s.
c) Titanian kimberlites, with ulvöspinel-qandilite (MUM but excluding magnetite)

Unfortunately, it is complicate to correlate nothing with the diamond grade, because this data is never provided by the mining companies, and many of the existing data can be suspicious. However, we believe that should be interesting to check the possible correlation between the diamond grade and these subtypes of kimberlites.

14.4. MANTLE METASOMATISM AND KIMBERLITE

LIMA minerals is formed by mantle metasomatism process. Mathiasite age and perovskite age indicating the mantle metasomatism and kimberlite emplacement age respectively. The similar age about 1000 Ma in SK-1 Indian kimberlite reported in this work indicate an metasomatism process shortly before or nearly at the same time as the kimberlite emplacement. MARID and PIC formed by intense mantle metasomatism. Metasomatism event by carbonated silicate melt shortly before and during entrainment by kimberlite magma registered in carbonate and Ti-rich vein cross-cutting MARID and PIC is also reported by Fitzpayne *et al.* (2018).

14.5. USE AND MISUSE OF KIMS AND DIMS

Minerals of the ilmenite group are classic indicator minerals of kimberlite (KIMs) and have been used as a guide for kimberlite exploration and to assess the survival of diamond, as diamond indicator minerals (DIMs). Magnesian ilmenite is a charact eristic mineral in kimberlite and is important for exploration due to its ease to concentrate and resistant to physical and chemical alteration (Mitchell, 1986). Occurrences of Mn-rich ilmenite have also been proposed as a guide for diamond exploration (Meyer and McCallum, 1986; Sobolev *et al.*, 1999; Kaminsky *et al.*, 2000, 2001, 2006; Kaminsky and Belousova, 2009) and are currently used for several exploration companies.

However, in this memory we demonstrated that acritical use of ilmenites as DIM cannot be a valid method because a) Mg-rich ilmenites can be produced in metasomatic processes in the mantle, but they are largely produced during the intrusive processes, including those of the late hydrothermal stages; b) there are no evidences of genetic links of Mg-ilmenites with diamond; c) high contents of elements as Cr and Nb can be produced by replacement of xenocrysts of minerals containing these elements, as chromite, crichtonite, zircon and perovksite; d) Mn-rich ilmenites are only produced in the latest magmatic and hydrothermal stages and, therefore, are not associated with the crystallization or the preservation of the diamond and cannot be used as a DIM.

Contrastingly, the potential of some textural patterns in ilmenite, as the occurrence of aluminous spinel exsolutions, is not enough explored yet, but this association can be indicative of decomposition of solid solutions formed in ultrahigh pressure domains that could also host diamond.

Use of many minerals as diamond indicator is based in the existence of high Cr contents, as in the cases of the next minerals: Cr-rutile (Malkovets *et al.*, 2016; Rezvukhin *et al.*, 2016a), Cr-pyrope (Sobolev et al., 1973), high Cr chromite (Gurney et al., 1993), Cr-rich picroilmenite (Sobolev et al., 1997) and Cr-diopside (Sobolev et al., 1997). However, many primary rutile studied in this work are also Cr-rich and are not associated with diamond formation.

Hence, the correct use of these minerals as KIMs and/or DIMs request a detailed petrographic study to certify whether their origin is mantelic primary magmatic, magmatic related with the intrusive processes, or secondary post-magmatic. Therefore, use of chemical analysis on concentrates of these minerals cannot provide meaningful information.

CHAPTER 15

CONCLUSIONS

15. CONCLUSIONS

1. Successive generations of the spinel group minerals, ilmenite group minerals, rutile, mica group minerals and clinopyroxene group minerals (mantle xenocrystic, primary magmatic early, primary magmatic late, as well as secondary hydrothermal) record the evolution of the kimberlites and related rocks from mantle to surface.

2. A general paragenetic sequence is established. Early crystallization in the first intrusive stage in kimberlites and related rocks produces olivine phenocrysts that may have trapped inclusions of co-crystallizing rutile, Mg-rich ilmenite to geikielite and chromite. Phlogopite microphenocrysts could start to crystallize in this stage. A second magmatic stage may produce saturation in pyrophanite. Lately in this stage, qandilite-ulvöspinel-magnetite start to crystallize, together with perovskite, along with phlogopite microphenocrysts. Finally, in the late stage, apatite, groundmass phlogopite, monticellite, djerfisherite and carbonate crystallize. Post-magmatic hydrothermal stages could produce geikielite, Mg-rich ilmenite, Mn-rich ilmenite, kassite, anatase, secondary perovskite, aeschynite, titanium garnet, serpentine, carbonates and clinochlore.

3. Ti-rich minerals in kimberlites and related rocks are the result of a continuous reaction of a progressively fractionated magma with early generations of Ti-rich minerals, formed both in the mantle or in the different stages of magmatic crystallization (rutile, ilmenites and perovskites); similar minerals are also produced during subsolidus hydrothermal processes.

4. Mantelic ilmenites are Fe^{3+}-rich and crustal ilmenites, Fe^{2+}-rich. Ilmenite formed during the early stages of intrusion is geikielitic, but there is a reaction trend between the magma and the above generations leading to Mg enrichment. During late magmatic processes Mn is enriched in the residual magmas, thus producing crystallization of pyrophanitic ilmenite and a new reaction trend of these Mn-enriched magmas with the early generations of ilmenites, producing progressive enrichments in Mn. Hydrothermal processes produce the repetition of this sequence and new reaction trends. Therefore Mg- or Mn-ilmenites cannot be used as DIM because they can be very late minerals formed during magmatic or subsolidus postmagmatic processes unrelated with the diamond formation or preservation.

5. The new generations of ilmenite retain high contents of the precursor mineral: Nb when replacing rutile or perovskite, Cr when replacing chromite or crichtonite, Zr when replacing crichtonite. Therefore, the trace composition of ilmenite cannot be used to extract petrogenetic information or be used for diamond exploration.

6. Perovskite may be found in two generations in the same intrusion: as primary magmatic and as secondary hydrothermal. Hence, we suggest taking additional cautions when using perovskite grains for U-Pb dating.

7. High uncertainty for U-Pb dating for LIMA minerals suggests that, in most of cases, they are not ideal target for U-Pb dating, because they are commonly replaced by Ti-rich minerals during the intrusive stages.

8. Titanium garnet has been found only as a secondary post magmatic mineral, thus, attention must be paid to the position of Ca-Ti-rich garnet in the mineral sequence before using it to classify the rock based on its occurrence, as proposed in the current IUGS classification rules.

9. Magma mingling processes have been identified at least in a case in kimberlites, based on the

simultaneous occurrence of spinels with different composition in the same groundmass. This can be another cause of heterogeneity in these rocks.

10. The generalized occurrence of clinopyroxene in volcaniclastic kimberlites and its absence in coherent kimberlites as one of principal groundmass component suggests that the same current IUGS classification rules cannot be used for coherent and volcaniclastic kimberlites.

11. The occurrence of djerfisherite in kimberlites also provides evidence indicating that the infiltrating kimberlite melt was enriched in K and has high activity of volatiles (S and Cl).

12. The kimberlites and related rocks are heterogeneous mixtures of xenocrystic material and intrusive magma, and reaction between the magmas and the xenoliths produces reactions and partial or complete replacement. Both types of heterogeneities have been observed at the scales of micrometre, thus making the kimberlites and related rocks extremely heterogenous. Therefore, there is no sense in using bulk rock composition and bulk isotope studies in these rocks.

13. Applying the composition of minerals from 79 kimberlite and related rocks in the classic and popular classification diagrams demonstrated that there is an extent overlap of compositional range of these minerals in kimberlite and related rock. Thus the existing IUGS classification diagrams using mineral compositions (eg. phlogopite and spinel) are only useful to show their compositional range and evolution while are useless for classification. New graphics for spinel group and mica group minerals from kimberlite and related rocks are provided in this memory. These new graphics allow us to visualize easier the different compositional types of these minerals.

14. Finally, a detailed petrographic study of the accessory minerals is necessary to be sure of their origin (mantelic, primary magmatic or secondary post-magmatic) in order to carry out a correct use of those minerals as KIMs and/or DIMs.

REFERENCES

REFERENCES

Abersteiner, A., Kamenetsky, V.S., Graham Pearson, D., Kamenetsky, M., Goemann, K., Ehrig, K. and Rodemann, T. (2018a) Monticellite in group-I kimberlites: Implications for evolution of parental melts and post-emplacement CO2 degassing. *Chemical Geology*, **478**, 76–88.

Abersteiner, A., Kamenetsky, V.S., Kamenetsky, M., Goemann, K., Ehrig, K. and Rodemann, T. (2018b) Significance of halogens (F, Cl) in kimberlite melts: Insights from mineralogy and melt inclusions in the Roger pipe (Ekati, Canada). *Chemical Geology*, **478**, 148–163.

Abersteiner, A., Kamenetsky, V.S., Golovin, A. V, Kamenetsky, M. and Goemann, K. (2018c) Was Crustal Contamination Involved in the Formation of the Serpentine-Free Udachnaya-East Kimberlite? New Insights into Parental Melts, Liquidus Assemblage and Effects of Alteration. *Journal of Petrology*, **59**, 1467–1492.

Abersteiner, A., Kamenetsky, V.S., Goemann, K., Giuliani, A., Howarth, G.H., Castillo-Oliver, M., Thompson, J., Kamenetsky, M. and Cherry, A. (2019a) Composition and emplacement of the Benfontein kimberlite sill complex (Kimberley, South Africa): Textural, petrographic and melt inclusion constraints. *Lithos*, **324–325**, 297–314.

Abersteiner, A., Kamenetsky, V.S., Goemann, K., Golovin, A. V., Sharygin, I.S., Giuliani, A., Rodemann, T., Spetsius, Z. V. and Kamenetsky, M. (2019b) Djerfisherite in kimberlites and their xenoliths: implications for kimberlite melt evolution. *Contributions to Mineralogy and Petrology*, **174**, 8.

Abzalov, M. (1998) Chrome–spinels in gabbro–wehrlite intrusions of the Pechenga area, Kola Peninsula, Russia: emphasis on alteration features. *Lithos*, **43**, 109–134.

Afanasyev, A.A., Melnik, O., Porritt, L., Schumacher, J.C. and Sparks, R.S.J. (2014) Hydrothermal alteration of kimberlite by convective flows of external water. *Contributions to Mineralogy and Petrology*, **168**, 1038.

Agee, J.J., Jr, J.R.G. and Taylor, L. a. (1982a) Petrogenesis of oxide minerals in kimberlite, Elliot County Kentucky. *American Mineralogist*, **67**, 28.

Agee, J.J., Garrison, J.R. and Taylor, L.A. (1982b) Petrogenesis of oxide minerals in kimberlite, Elliott County, Kentucky. *American Mineralogist*, **67**, 28–42.

Akaogi, M. (2007) Phase transitions of minerals in the transition zone and upper part of the lower mantle. Pp. 1–13 in: *Advances in High-Pressure Mineralogy Special Series 421* (E. Ohtani, editor). Geological Society of America.

Allsopp, H.L. and Barrett, D.R. (1975) Rb-Sr age determinations on South African kimberlite pipes. *Physics and Chemistry of the Earth*, **9**, 605–617.

Almeida, V. V., Janasi, V. de A., Svisero, D.P. and Nannini, F. (2014) Mathiasite-loveringite and priderite in mantle xenoliths from the Alto Paranaíba Igneous Province, Brazil: genesis and constraints on mantle metasomatism. *Central European Journal of Geosciences*, **6**, 614–632.

Amthauer, G. and Rossman, G.R. (1998) The hydrous component in andradite garnet. *American Mineralogist*, **83**, 835–840.

Andersen, D.J. and Lindsley, D.H. (1979) The olivine-ilmenite thermometer. Pp. 493–507 in: *Proceedings of the Lunar and Planetary Science Conference L0th, Volume 1*. Pergamon Press, Inc, New York.

Anovitz, L.M., Treiman, A.H., Essene, E.J., Hemingway, B.S., Westrum, E.F., Wall, V.J., Burriel, R. and Bohlen, S.R. (1985) The heat-capacity of ilmenite and phase equilibria in the system Fe-T-O. *Geochimica et Cosmochimica Acta*, **49**, 2027–2040.

Arai, S. (1992) Chemistry of chromian spinel in volcanic rocks as a potential guide to magma chemistry. *Mineralogical Magazine*, **56**, 173–184.

Arima, M. (1988) Barium-rich phlogopite in a mantle derived xenolith of the Upper Canada Mine kimberlite, Ontario, Canada: Implications for Ba-reservoir in the upper mantle. *Journal of Mineralogy, Petrology and Economic Geology*, **83**, 217–231.

Armbruster, T. and Kunz, M. (1990) Cation arrangement in a unusual uranium-rich senaite: crystal structure study at 130 K. *European Journal of Mineralogy*, **2**, 163–170.

Armstrong, J.P., Wilson, M., Barnett, R.L., Nowicki, T. and Kjarsgaard, B.A. (2004a) Mineralogy of primary carbonate-bearing hypabyssal kimberlite, Lac de Gras, Slave Province, Northwest Territories, Canada. *Lithos*, **76**, 415–433.

Armstrong, K.A. (1995) An investigation of the spinel mineralogy of the C-14 kimberlite, Kirkland Lake, Ontario. Queen's University, 185 pp.

Armstrong, K.A., Roeder, P.L. and Helmstaedt, H.H. (1997) Composition of spinels in the C14 kimberlite, Kirkland Lake, Ontario. *Russian Geology and Geophysics*, **38**, 454–466.

Armstrong, K.A., Nowicki, T.E. and Read, G.H. (2004b) Kimberlite AT-56: a mantle sample from the north central Superior craton, Canada. *Lithos*, **77**, 695–704.

Ashchepkov, I. V., Ntaflos, T., Kuligin, S.S., Malygina, E. V., Agashev, A.M., Logvinova, A.M., Mityukhin, S.I., Alymova, N. V., Vladykin, N. V., Palessky, S. V. and Khmelnikova, O.S. (2013) Deep-Seated Xenoliths from the Brown Breccia of the Udachnaya Pipe, Siberia. Pp. 59–73 in: *Proceedings of 10th International Kimberlite Conference*. Springer India, New Delhi.

Ashchepkov, I. V., Alymova, N. V., Logvinova, A.M., Vladykin, N. V., Kuligin, S.S., Mityukhin, S.I., Downes, H., Stegnitsky, Y.B., Prokopiev, S.A., Salikhov, R.F., Palessky, V.S. and Khmel'nikova, O.S. (2014) Picroilmenites in Yakutian kimberlites: variations and genetic models. *Solid Earth*, **5**, 915–938.

Ashchepkov, I.V., Ntaflos, T., Logvinova, A.M., Spetsius, Z.V., Downes, H. and Vladykin, N.V. (2017) Monomineral universal clinopyroxene and garnet barometers for peridotitic, eclogitic and basaltic systems. *Geoscience Frontiers*, **8**, 775–795.

Baldwin, S.L., Monteleone, B.D., Webb, L.E., Fitzgerald, P.G., Grove, M. and June Hill, E. (2004) Pliocene eclogite exhumation at plate tectonic rates in eastern Papua New Guinea. *Nature*, **431**, 263–267.

Barnes, S.J. and Roeder, P.L. (2001) The Range of Spinel Compositions in Terrestrial Mafic and Ultramafic Rocks. *Journal of Petrology*, **42**, 2279–2302.

Barnett, R.L. and Laroulandie, C. (2017) Barium and titanium enrichment of zoned phlogopite xenocrysts and phenocrysts in the Adamantin kimberlites , Québec , Canada . P. No. 4587 in: *11th International Kimberlite Conference Extended Abstract*.

Basu, S.K. and Bhattacharyya, T. (2014) Petrography and mineral chemistry of Alkaline-Carbonatite Complex in Singhbhum Crustal Province, Purulia region, Eastern India. *Journal of the Geological Society of India*, **83**, 54–70.

Batumike, J.M., Griffin, W.L., Belousova, E.A., Pearson, N.J., O'Reilly, S.Y. and Shee, S.R. (2008) LAM-ICPMS U-Pb dating of kimberlitic perovskite: Eocene-Oligocene kimberlites from the Kundelungu Plateau, D.R. Congo. *Earth and Planetary Science Letters*, **267**, 609–619.

Beard, A.D., Downes, H., Hegner, E., Sablukov, S.M., Vetrin, V.R. and Balogh, K. (1998) Mineralogy and geochemistry of Devonian ultramafic minor intrusions of the southern Kola Peninsula, Russia: implications for the petrogenesis of kimberlites and melilitites. *Contributions to Mineralogy and Petrology*, **130**, 288–303.

Becker, M. and Le Roex, A.P. (2006) Geochemistry of South African on- and off-craton, group I and group II kimberlites: Petrogenesis and source region evolution. *Journal of Petrology*, **47**, 673–703.

Begg, G.C., Griffin, W.L., Natapov, L.M., O'Reilly, S.Y., Grand, S.P., O'Neill, C.J., Hronsky, J.M.A., Djomani, Y.P., Swain, C.J., Deen, T. and Bowden, P. (2009) The lithospheric architecture of Africa: Seismic tomography, mantle petrology, and tectonic evolution. *Geosphere*, **5**, 23–50.

Bellis, A. and Canil, D. (2007) Ferric Iron in CaTiO3 perovskite as an oxygen barometer for kimberlitic magmas I: Experimental calibration. *Journal of Petrology*, **48**, 219–230.

Biagioni, C. and Pasero, M. (2014) The systematics of the spinel-type minerals: An overview. *American Mineralogist*, **99**, 1254–1264.

Bindi, L., Chen, M. and Xie, X. (2017) Discovery of the Fe-analogue of akimotoite in the shocked Suizhou L6 chondrite. *Scientific Reports*, **7**, 42674.

Black, L.P. and Gulson, B.L. (1978) The age of the Mud Tank carbonatite, Strangways Range, Northern Territory. *BMR Journal of Australian Geology & Geophysics*, **3**, 227–232.

Boctor, N.Z. and Boyd, F.R. (1980) Oxide minerals in the Liqhobong kimberlite , Lesotho. *American Mineralogist*, **65**, 631–638.

Bogatikov, O.A., Kononova, V.A., Pervov, V.A. and Zhuravlev, D.Z. (2001) Sources, Geodynamic setting of formation, and diamond-bearing potential of kimberlites from the Northern margin of the Russian plate: A Sr–Nd Isotopic and ICP-MS Geochemical Study. *Petrology*, **9**, 191–203.

Bogatikov, O.A., Kononova, V.A., Nosova, A.A. and Kondrashov, I.A. (2007) Kimberlites and lamproites of the East European Platform: Petrology and geochemistry. *Petrology*, **15**, 315–334.

Bogatikov, O.A., Kononova, V.A., Nosova, A.A. and Kargin, A. V. (2009) Polygenetic sources of kimberlites, magma composition, and diamond potential exemplified by the East European and Siberian cratons. *Petrology*, **17**, 606–625.

Bosi, F., Biagioni, C. and Pasero, M. (2019) Nomenclature and classification of the spinel supergroup. *European Journal of Mineralogy*, **31**, 183–192.

Bovkun, A. V., Garanin, V.K. and Kudryavtseva, G.P. (2001) Mineralogy of Oxides from Kimberlite Groundmass: Genetic and Applied Aspects (an Example from the Yakutian Diamond Province). *Revista Brasileira de Geociências*, **31**, 493–496.

Boyd, F.R. and Danchin, R.V. (1974) Discrete Nodules from the Artur De Paiva Kimberlite, Angola. *Carnegie Institution Washington Year Book*, **73**, 278–282.

Brenan, J.M., Shaw, H.F., Phinney, D.L. and Ryerson, F.J. (1994) Rutile-aqueous fluid partitioning of Nb, Ta, Hf, Zr, U and Th: implications for high field strength element depletions in island-arc basalts. *Earth and Planetary Science Letters*, **128**, 327–339.

Brod, J.A., Gaspar, J.C., de Araújo, D.P., Gibson, S.A., Thompson, R.N. and Junqueira-Brod, T.C. (2001) Phlogopite and tetra-ferriphlogopite from Brazilian carbonatite complexes: petrogenetic constraints and implications for mineral-chemistry systematics. *Journal of Asian Earth Sciences*, **19**, 265–296.

Brown, R.J., Manya, S., Buisman, I., Fontana, G., Field, M., Niocaill, C. Mac, Sparks, R.S.J. and Stuart, F.M. (2012) Eruption of kimberlite magmas: Physical volcanology, geomorphology and age of the youngest kimberlitic volcanoes known on earth (the Upper Pleistocene/Holocene Igwisi Hills volcanoes, Tanzania). *Bulletin of Volcanology*, **74**, 1621–1643.

Bulanova, G.P., Shestakova, O.E. and Leskova, N.V. (1980) Djerfisherite in diamond-hosted sulfide inclusions. *Dokl Akad Nauk*, **225**, 430–433.

Bulanova, G.P., Spetsius, Z.V. and Leskova, N.V. (1990) *Sulphides in Diamonds and Xenoliths from Yakutian Kimberlite Pipes (in Russian)*. P. in.: Nauka, Novosibirsk, 119 pp.

Burnham, A.D., Berry, A.J., Wood, B.J. and Cibin, G. (2012) The oxidation states of niobium and tantalum in mantle melts. *Chemical Geology*, **330–331**, 228–232.

Buse, B., Schumacher, J.C., Sparks, R.S.J. and Field, M. (2010) Growth of bultfonteinite and hydrogarnet in metasomatized basalt xenoliths in the B/K9 kimberlite, Damtshaa, Botswana: Insights into hydrothermal metamorphism in kimberlite pipes. *Contributions to Mineralogy and Petrology*, **160**, 533–550.

Bussweiler, Y., Stone, R.S., Pearson, D.G., Luth, R.W., Stachel, T., Kjarsgaard, B.A. and Menzies, A. (2016) The evolution of calcite-bearing kimberlites by melt-rock reaction: evidence from polymineralic inclusions within clinopyroxene and garnet megacrysts from Lac de Gras kimberlites, Canada. *Contributions to Mineralogy and Petrology*, **171**, 65.

Bussweiler, Y., Pearson, D.G., Stachel, T. and Kjarsgaard, B.A. (2018) Cr-rich megacrysts of clinopyroxene and garnet from Lac de Gras kimberlites, Slave Craton, Canada – implications for the origin of clinopyroxene and garnet in cratonic lherzolites. *Mineralogy and Petrology*, **112**, 583–596.

Campeny, M., Kamenetsky, V.S., Melgarejo, J.C., Mangas, J., Manuel, J., Alfonso, P., Kamenetsky, M.B., Bambi, A.C.J.M. and Gonçalves, A.O. (2015) Carbonatitic lavas in Catanda (Kwanza Sul, Angola): Mineralogical and geochemical constraints on the parental melt. *Lithos*, **232**, 1–11.

Campeny, M., Melgarejo, J.C., Mangas, J., Manuel, J. and Gonçalves, A.O. (2017) Recent carbonatitic magmatism in Angola: the dykes of the Chiva lagoon maar. *Boletín de la Sociedad Geológica Mexicana*, **69**, 209–222.

Carmody, L., Taylor, L.A., Thaisen, K.G., Tychkov, N., Bodnar, R.J., Sobolev, N. V., Pokhilenko, L.N. and Pokhilenko, N.P. (2014) Ilmenite as a diamond indicator mineral in the Siberian craton: a tool to predict diamond potential. *Economic Geology*, **109**, 775–783.

Caro, G., Kopylova, M.G. and Creaser, R.A. (2004) The hypabyssal 5034 kimberlite of the Gahcho Kue cluster, Southeastern Slave Craton, Northwest Territories, Canada: a granite-contaminated group-I kimberlite. *The Canadian Mineralogist*, **42**, 183–207.

de Carvalho, H. (1983) Notice explicative préliminaire sur la géologie de l'Angola. *Garcia de Orta, Série de Geologia, Lisboa*, **6**, 15–30.

Cas, R.A.F., Hayman, P., Pittari, A. and Porritt, L. (2008) Some major problems with existing models and terminology associated with kimberlite pipes from a volcanological perspective, and some suggestions. *Journal of Volcanology and Geothermal Research*, **174**, 209–225.

Castillo-Oliver, M., Galí, S., Melgarejo, J.C., Griffin, W.L., Belousova, E., Pearson, N.J., Watangua, M. and O'Reilly, S.Y. (2016) Trace-element geochemistry and U-Pb dating of perovskite in kimberlites of the Lunda Norte province (NE Angola): Petrogenetic and tectonic implications. *Chemical Geology,* **426**, 118–134.

Castillo-Oliver, M., Melgarejo, J.C., Galí, S., Pervov, V., Gonçalves, A.O., Griffin, W.L., Pearson, N.J. and O'Reilly, S.Y. (2017) Use and misuse of Mg- and Mn-rich ilmenite in diamond exploration: A petrographic and trace element approach. *Lithos*, **292–293**, 348–363.

Chakhmouradian, A.R. and Mitchell, R.H. (2000) Occurrence, alteration patterns and compositional variation of perovskite in kimberlites. *Canadian Mineralogist,* **38**, 975–994.

Chakhmouradian, A.R. and Mitchell, R.H. (2001) Three compositional varieties of perovskite from kimberlites of the Lac de Gras field (Northwest Territories , Canada). *Mineralogical Magazine,* **65**, 133–148.

Chakhmouradian, A.R., Reguir, E.P., Kamenetsky, V.S., Sharygin, V. V. and Golovin, A. V. (2013) Trace-element partitioning in perovskite: Implications for the geochemistry of kimberlites and other mantle-derived undersaturated rocks. *Chemical Geology*, **353**, 112–131.

Chalapathi Rao, N.V., Lehmann, B., Mainkar, D. and Belyatsky, B. (2011) Petrogenesis of the end-Cretaceous diamondiferous Behradih orangeite pipe: Implication for mantle plume-lithosphere interaction in the Bastar craton, Central India. *Contributions to Mineralogy and Petrology,* **161**, 721–742.

Chalapathi Rao, N.V., Wu, F.Y., Mitchell, R.H., Li, Q.L. and Lehmann, B. (2013) Mesoproterozoic U-Pb ages, trace element and Sr-Nd isotopic composition of perovskite from kimberlites of the Eastern Dharwar craton, southern India: Distinct mantle sources and a widespread 1.1Ga tectonomagmatic event. *Chemical Geology,* **353**, 48–64.

Chalapathi Rao, N.V., Lehmann, B., Belyatsky, B. and Warnsloh, J.M. (2017) The Late Cretaceous diamondiferous pyroclastic kimberlites from the Fort à la Corne (FALC) field, Saskatchewan craton, Canada: Petrology, geochemistry and genesis. *Gondwana Research,* **44**, 236–257.

Channer, D.M.D., Egorov, A. and Kaminsky, F. (2001) Geology and strcture of the Guaniamo diamandiferous kimberlite sheets, South-West Venezuela. *Revista Brasileira de Geociências,* **31**, 615–630.

Clarke, D.B., Chapman, C.A.T., MacKay, R.M. and Mitchell, R.H. (1994) Occurrence and origin of djerfisherite from the Elwin Bay Kimberlite, Somerset Island, Northwest Territories. *The Canadian Mineralogist,* **32**, 815–823.

Cookenboo, H.O. and Grütter, H.S. (2010) Mantle-derived indicator mineral compositions as applied to diamond exploration. *Geochemistry: Exploration, Environment, Analysis,* **10**, 81–95.

Cooper, S.A., Belousova, E.A., Griffin, W.L. and Morris, B.J. (2008) Age of FS66 Kimberlite Beneath Murray Basin , South Australia : Laser Ablation ICP-MS Dating of Kimberlitic Zircon , Perovskite , and Rutile. P. No. 9IKC-A-00106 in: *9th International Kimberlite Conference Extended Abstract.*

Cordani, U.G., Teixeira, W., D'Agrella-Filho, M.S. and Trindade, R.I. (2009) The position of the Amazonian Craton in supercontinents. *Gondwana Research*, **15**, 396–407.

Cox, R.A. and Wilton, D.H.C. (2006) U–Pb dating of perovskite by LA-ICP-MS: An example from the Oka carbonatite, Quebec, Canada. *Chemical Geology*, **235**, 21–32. Elsevier.

Creaser, R.A., Grütter, H., Carlson, J. and Crawford, B. (2004) Macrocrystal phlogopite Rb–Sr dates for the Ekati property kimberlites, Slave Province, Canada: evidence for multiple intrusive episodes in the Paleocene and Eocene. *Lithos*, **76**, 399–414.

Cruciani, G., Zanazzi, P.F. and Quartieri, S. (1995) Tetrahedral ferric iron in phlogopite: XANES and Mossbauer compared to single-crystal X-ray data. *European Journal of Mineralogy*, **7**, 255–266.

Danchin, R. V. and D'Orey, F. (1972) Chromian spinel exsolution in ilmenite from the Premier Mine, Transvaal, South Africa. *Contributions to Mineralogy and Petrology*, **35**, 43–49.

Davidson, A. (1982) Petrochemistry of the Blachford lake complex near Yellowknife, Northwest Territories. *Paper - Geological Survey of Canada*, **81–83**, 71–79.

Davis, G.L. (1977) The ages and uranium contents of zircons from kimberlites and associated rocks. Pp. 67–69 in: *International Kimberlite Conference: Extended Abstracts 2(1)*. University of Alberta.

Davis, G.L. (1978) Zircons from the mantle. *Unites State Geological Survey Open File Report*, **78–701**, 86–88.

Dawson, J.B. and Smith, J. V. (1977) The MARID (mica-amphibole-rutile-ilmenite-diopside) suite of xenoliths in kimberlite. *Geochimica et Cosmochimica Acta*, **41**, 309–323.

Dawson, J.B. and Stephens, W.E. (1975) Statistical Classification of Garnets from Kimberlite and Associated Xenoliths. *The Journal of Geology*, **83**, 589–607. The University of Chicago Press.

Dawson, J.B., Smith, J. V. and Steele, I.M. (1995) Petrology and Mineral Chemistry of Plutonic Igneous Xenoliths from the Carbonatite Volcano, Oldoinyo Lengai, Tanzania. *Journal of Petrology*, **36**, 797–826.

Deer, W.A., Howie, R.A. and Zussman, J. (1992) *An Introduction to the Rock-Forming Minerals*. P. in.: Longman, London, 696 pp.

Delaney, J.S., Smith, J.V., Carswell, D.A. and Dawson, J.B. (1980) Chemistry of micas from kimberlites and xenoliths—II. Primary- and secondary-textured micas from peridotite xenoliths. *Geochimica et Cosmochimica Acta*, **44**, 857–872.

Digonnet, S., Goulet, N., Bourne, J., Stevenson, R. and Archibald, D. (2000) Petrology of the Abloviak Aillikite dykes, New Québec: evidence for a Cambrian diamondiferous alkaline province in northeastern North America. *Canadian Journal of Earth Sciences*, **37**, 517–533.

Distler, V. V., Ilupin, I.P. and Laputina, I.P. (1987) Sulfides of deep-seated origin in kimberlites and some aspects of copper-nickel mineralization. *International Geology Review*, **29**, 456–464.

Dobrovol'skaya, M.G., Tsepin, A.I., Ilupin, I.P. and Ponomarenko, A.I. (1975) Djerfisherite from Yakutia kimberlites. Pp. 3–11 in: *Deposits, Minerals and Parageneses of Endogenic (In Russian)* (P.M. Tatarinov, editor). Nauka, Leningrad.

Dong, Z.X. (1994) *Kimberlites in China (in Chinese with English Abstract)*. P. in.: Science Press, Beijing, 318 pp.

Dongre, A.N., Jacob, D.E. and Stern, R.A. (2015) Subduction-related origin of eclogite xenoliths from the Wajrakarur kimberlite field, Eastern Dharwar craton, Southern India: Constraints from petrology and geochemistry. *Geochimica et Cosmochimica Acta*, **166**, 165–188.

Dongre, A.N., Viljoen, K.S., Chalapathi Rao, N.V. and Gucsik, A. (2016) Origin of Ti-rich garnets in the groundmass of Wajrakarur field kimberlites, southern India: insights from EPMA and Raman spectroscopy. *Mineralogy and Petrology*, **110**, 295–307.

Donnelly, C.L., Griffin, W.L., Yang, J.-H., O'Reilly, S.Y., Li, Q.-L., Pearson, N.J. and Li, X.-H. (2012) In situ U–Pb Dating and Sr–Nd Isotopic Analysis of Perovskite: Constraints on the Age and Petrogenesis of the Kuruman Kimberlite Province, Kaapvaal Craton, South Africa. *Journal of Petrology*, **53**, 2497–2522.

Doroshkevich, A.G., Ripp, G.S. and Moore, K.R. (2010) Genesis of the Khaluta alkaline-basic Ba-Sr carbonatite complex (West Transbaikala, Russia). *Mineralogy and Petrology*, **98**, 245–268.

Downes, P.J., Wartho, J.-A. and Griffin, B.J. (2006) Magmatic Evolution and Ascent History of the Aries Micaceous Kimberlite, Central Kimberley Basin, Western Australia: Evidence from Zoned Phlogopite Phenocrysts, and UV Laser 40Ar/39Ar Analysis of Phlogopite–Biotite. *Journal of Petrology*, **47**, 1751–1783.

Downs, R.T. (2006) The RRUFF Project: an integrated study of the chemistry, crystallography, Raman and infrared spectroscopy of minerals. Pp. O03-13 in: *Program and Abstracts of the 19th General Meeting of the International Mineralogical Association in Kobe, Japan*.

Droop, G.T.R. (1987) A general equation for estimating Fe3+ concentrations in ferromagnesian silicates and oxides from microprobe analyses, using stoichiometric criteria. *Mineralogical Magazine*, **51**, 431–435.

Eccles, D.R., Heaman, L.M., Luth, R.W. and Creaser, R.A. (2004) Petrogenesis of the Late Cretaceous northern Alberta kimberlite province. *Lithos*, **76**, 435–459.

Egorov, K.N., Rotman, A.Y., Zinchuk, N.N. and Nosyko, S.F. (2005) Petrogeochemical composition of kimberlites in northeastern Angola. *Doklady Earth Sciences*, **403**, 891–895.

Egorov, K.N., Roman'ko, E.F., Podvysotsky, V.T., Sablukov, S.M., Garanin, V.K. and D'yakonov, D.B. (2007) New data on kimberlite magmatism in southwestern Angola. *Russian Geology and Geophysics*, **48**, 323–336.

Erlank, A., Waters, F., Hawkesworth, C., Haggerty, S., Allsopp, H., Rickard, R. and Menzies, M. (1987) Evidence for mantle metasomatism in peridotite nodules from the Kimberley pipes, South Africa. Pp. 221–311 in: *Mantle Metasomatism* (M.A. Menzies and C.J. Hawkesworth, editors).

Farr, H. and Farr, H. (2018) Petrography , Sr-isotope geochemistry and geochronology of the Nxau. **112**. Mineralogy and Petrology.

Faure, S. (2010) World Kimberlites CONSOREM Database (Version 3). *Consortium de Recherche en Exploration Minérale CONSOREM, Université du Québec à Montréal*. <www.consorem.ca.>.

Fedortchouk, Y. and Canil, D. (2004) Intensive Variables in Kimberlite Magmas, Lac de Gras, Canada and Implications for Diamond Survival. *Journal of Petrology*, **45**, 1725–1745.

Fedortchouk, Y. and McIsaac, E. (2013) Surface Dissolution Features on Kimberlitic Chromites as Indicators of Magmatic Fluid and Diamond Quality. Pp. 297–308 in: *Proceedings of 10th International Kimberlite Conference Volumne 1* (D.G. Pearson, H.S. Grütter, J.W. Harris, B.A. Kjarsgaard, H. O'Brien, N.V. Chalapathi Rao and S. Sparks, editors). Springer, New Delhi, New Delhi.

Field, M. and Scott Smith, B.H. (1998) Textural and genetic classification schemes of kimberlites: new perspective. Pp. 214–216 in: *Extended Abstracts of the Seventh International Kimberlite Conference*. Cape Town, South Africa.

Fitzpayne, A., Giuliani, A., Hergt, J., Phillips, D. and Janney, P. (2017) New constraints on the origins of MARID and PIC rocks based on mineral and bulk-rock geochemical data: Implicationsfor mantle metasomatism and alkaline magmatism. P. No. 11IKC-4481 in: *11th International Kimberlite Conference Extended Abstract*.

Fitzpayne, A., Giuliani, A., Phillips, D., Hergt, J., Woodhead, J.D., Farquhar, J., Fiorentini, M.L., Drysdale, R.N. and Wu, N. (2018) Kimberlite-related metasomatism recorded in MARID and PIC mantle xenoliths. *Mineralogy and Petrology*, 1–14.

Fitzpayne, A., Giuliani, A., Maas, R., Hergt, J., Janney, P. and Phillips, D. (2019) Progressive metasomatism of the mantle by kimberlite melts: Sr–Nd–Hf–Pb isotope compositions of MARID and PIC minerals. *Earth and Planetary Science Letters*, **509**, 15–26.

Foley, S., Höfer, H. and Brey, G. (1994) High-pressure synthesis of priderite and members of the lindsleyite-mathiasite and hawthorneite-yimengite series. *Contributions to Mineralogy and Petrology*, **117**, 164–174.

Friel, J.J., Harker, R.I. and Ulmer, G.C. (1977) Armalcolite stability as a function of pressure and oxygen fugacity. *Geochimica et Cosmochimica Acta*, **41**, 403–410.

Fuchs, L.H. (1966) Djerfisherite, Alkali Copper-Iron Sulfide: A New Mineral from Enstatite Chondrites. *Science*, **153**, 166–167.

Gaspar, J.C. and Wyllie, P.J. (1983) Ilmenite (high Mg,Mn,Nb) in the carbonatites from the Jacupiranga complex, Brazil. *American Mineralogist*, **68**, 960–971.

Gaspar, J.C. and Wyllie, P.J. (1984) The alleged kimberlite-carbonatite relationship: evidence from ilmenite and spinel from Premier and Wesselton mines and the Benfontein sill, South Africa. *Contributions to Mineralogy and Petrology*, **85**, 133–140.

Gaudet, M., Kopylova, M., Muntener, C., Zhuk, V. and Nathwani, C. (2018) Geology of the Renard 65 kimberlite pipe, Québec, Canada. *Mineralogy and Petrology*, **112**, 433–445.

Gernon, T.M., Field, M. and Sparks, R.S.J. (2012) Geology of the Snap Lake kimberlite intrusion, Northwest Territories, Canada: field observations and their interpretation. *Journal of the Geological Society*, **169**, 1–16.

Ghorbani, M.R. and Middlemost, E.A.K. (2000) Geochemistry of pyroxene inclusions from the Warrumbungle Volcano, New South Wales, Australia. *American Mineralogist*, **85**, 1349–1367.

Ghosh, B., Morishita, T., Ray, J., Tamura, A., Mizukami, T., Soda, Y. and Ovung, T.N. (2017) A new occurrence of titanian (hydro)andradite from the Nagaland ophiolite, India: Implications for element mobility in hydrothermal environments. *Chemical Geology*, **457**, 47–60. Elsevier B.V.

Giuliani, A. (2018) Insights into kimberlite petrogenesis and mantle metasomatism from a review of the compositional zoning of olivine in kimberlites worldwide. *Lithos*, **312–313**, 322–342.

Giuliani, A., Kamenetsky, V.S., Kendrick, M.A., Phillips, D., Wyatt, B.A. and Maas, R. (2013) Oxide, sulphide and carbonate minerals in a mantle polymict breccia: Metasomatism by proto-kimberlite magmas, and relationship to the kimberlite megacrystic suite. *Chemical Geology,* **353**, 4–18.

Giuliani, A., Phillips, D., Maas, R., Woodhead, J.D., Kendrick, M.A., Greig, A., Armstrong, R.A., Chew, D., Kamenetsky, V.S. and Fiorentini, M.L. (2014) LIMA U–Pb ages link lithospheric mantle metasomatism to Karoo magmatism beneath the Kimberley region, South Africa. *Earth and Planetary Science Letters*, **401**, 132–147.

Giuliani, A., Phillips, D., Woodhead, J.D., Kamenetsky, V.S., Fiorentini, M.L., Maas, R., Soltys, A. and Armstrong, R.A. (2015) Did diamond-bearing orangeites originate from MARID-veined peridotites in the lithospheric mantle? *Nature Communications*, **6**, 6837.

Giuliani, A., Phillips, D., Kamenetsky, V.S. and Goemann, K. (2016) Constraints on kimberlite ascent mechanisms revealed by phlogopite compositions in kimberlites and mantle xenoliths. *Lithos*, **240–243**, 189–201.

Giuliani, A., Soltys, A., Phillips, D., Kamenetsky, V.S., Maas, R., Goemann, K., Woodhead, J.D., Drysdale, R.N. and Griffin, W.L. (2017) The final stages of kimberlite petrogenesis: Petrography, mineral chemistry, melt inclusions and Sr-C-O isotope geochemistry of the Bultfontein kimberlite (Kimberley, South Africa). *Chemical Geology*, **455**, 342–356.

Giuliani, A., Woodhead, J.D., Phillips, D., Maas, R., Davies, G.R. and Griffin, W.L. (2018) Titanates of the lindsleyite–mathiasite (LIMA) group reveal isotope disequilibrium associated with metasomatism in the mantle beneath Kimberley (South Africa). *Earth and Planetary Science Letters*, **482**, 253–264.

Gogineni, S. V., Melton, C.E. and Giardini, A.A. (1978) Some petrological aspects of the Prairie Creek diamond-bearing kimberlite diatreme, Arkansas. *Contributions to Mineralogy and Petrology*, **66**, 251–261.

Golovin, A. V., Sharygin, V. V., Pokhilenko, N.P., Mal'kovets, V.G., Kolesov, B.A. and Sobolev, N. V. (2003) Secondary melt inclusions in olivine from unaltered kimberlites of the Udachnaya-East pipe, Yakuti. *Doklady Earth Sciences*, **388**, 93–96.

Golovin, A. V., Sharygin, V. V. and Pokhilenko, N.P. (2007) Melt inclusions in olivine phenocrysts in unaltered kimberlites from the Udachnaya-East pipe, Yakutia: Some aspects of kimberlite magma evolution during late crystallization stages. *Petrology*, **15**, 168–183.

Golovin, A. V., Sharygin, I.S. and Korsakov, A. V. (2017) Origin of alkaline carbonates in kimberlites of the Siberian craton: Evidence from melt inclusions in mantle olivine of the Udachnaya-East pipe. *Chemical Geology*, **455**, 357–375.

Golubkova, A.B., Nosova, A.A. and Larionova, Y.O. (2013) Mg-ilmenite megacrysts from the Arkhangelsk kimberlites, Russia: Genesis and interaction with kimberlite melt and postkimberlite fluid. *Geochemistry International*, **51**, 353–381.

Gopalan, K. and Kumar, A. (2008) Phlogopite K–Ca dating of Narayanpet kimberlites, south India: Implications to the discordance between their Rb–Sr and Ar/Ar ages. *Precambrian Research*, **167**, 377–382.

Graham, I., Burgess, J.L., Bryan, D., Ravenscroft, P.J., Thomas, E., Doyle, B.J., Hopkins, R. and Armstrong, K.A. (1999) Exploration History and Geology of the Diavik Kimberlites, Lac de Gras, Northwest Territories, Canada. Pp. 262–279 in: *Proceedings of the VIIth International Kimberlite Conference Volumne 1* (J.J. Gurney, J.L. Gurney, M.D. Pascoe and S.H. Richardson, editors). Red Roof Design, Cape Town, South Africa.

Green, D.H. and Sobolev, N. V. (1975) Coexisting garnets and ilmenites synthesized at high pressures from pyrolite and olivine basanite and their significance for kimberlitic assemblages. *Contributions to Mineralogy and Petrology*, **50**, 217–229.

Grégoire, M., Bell, D. and Le Roex, A. (2002) Trace element geochemistry of phlogopite-rich mafic mantle xenoliths: their classification and their relationship to phlogopite-bearing peridotites and kimberlites revisited. *Contributions to Mineralogy and Petrology*, **142**, 603–625.

Grew, E.S., Locock, A.J., Mills, S.J., Galuskina, I.O., Galuskin, E.V. and Hålenius, U. (2013) IMA report: Nomenclature of the garnet supergroup. *American Mineralogist*, **98**, 785–810.

Grey, I.E., Madsen, I.C. and Haggerty, S.E. (1987) Structure of a new upper-mantle, magnetoplumbite-type phase, Ba(Ti3Cr4Fe4Mg)O19. *American Mineralogist*, **72**, 633–636.

Griffin, W., Moore, R.O., Ryan, C., Gurney, J. and Win, T. (1997) *Geochemistry of magnesian ilmenite megacrysts from Southern African kimberlites*. P. in: *Geologiya I Geofizika*. 398-419 pp.

Griffin, W.L. and Ryan, C.G. (1995) Trace elements in indicator minerals: area selection and target evaluation in diamond exploration. *Journal of Geochemical Exploration*, **53**, 311–337.

Griffin, W.L., Ryan, C.G., Gurney, J.J., Sobolev, N.V. and Win, T.T. (1994) Chromite macrocrysts in kimberlites and lamproites: geochemistry and origin. Pp. 366–377 in: *Proceedings of 5th International Kimberlite Conference Volune 1* (H.A.O. Meyer and O.H. Leonardos, editors). Comphania de Pequisa de Rescursos Minerals, Special Publication 1/A Jan/94, Araxá Brazil.

Griffin, W.L., Powell, W.J., Pearson, N. and O'Reilly, S.Y. (2008) GLITTER: data reduction software for laser ablation ICP-MS. Pp. 204–207 in: *Laser Ablation–ICP–MS in the Earth Sciences. Mineralogical Association of Canada Short Course Series* (P. Sylvester, editor).

Griffin, W.L., Pearson, N.J., Andersen, T., Jackson, S.E., O'Reilly, S.Y. and Zhang, M. (2014) Sources of cratonic metasomatic fluids: In situ LA-MC-ICPMS analysis of Sr, Nd, Hf and Pb isotopes in Lima from the Jagersfontein Kimberlite. *American Journal of Science*, **314**, 435–461.

Grim, R.F. (1968) *Clay Mineralogy*. P. in.: McGraw-Hill, New York, 596 pp.

Guo, J. and Green, T.H. (1990) Experimental study of barium partitioning between phlogopite and silicate liquid at upper-mantle pressure and temperature. *Lithos*, **24**, 83–95.

Gurney, J.J. and Zweistra, P. (1995) The interpretation of the major element compositions of mantle minerals in diamond exploration. *Journal of Geochemical Exploration*, **53**, 293–309.

Gurney, J.J., Helmstaedt, H. and Moore, R.O. (1993) A review of the use and application of mantle mineral geochemistry in diamond exploration. *Pure and Applied Chemistry*, **65**, 2423–2442.

Haggerty, S.E. (1975a) The chemistry and genesis of opaque minerals in kimberlites. *Physics and Chemistry of the Earth*, **9**, 295–307.

Haggerty, S.E. (1975b) The chemistry and genesis of opaque minerals in kimberlites. *Physics and Chemistry of the Earth*, **9**, 295–307.

Haggerty, S.E. (1983) The mineral chemistry of new titanates from the jagersfontein kimberlite, South Africa: Implications for metasomatism in the upper mantle. *Geochimica et Cosmochimica Acta*, **47**, 1833–1854.

Haggerty, S.E. (1991) Oxide mineralogy of the upper mantle. Pp. 355–416 in: *Oxide Minerals: Petrologic and Magnetic Significance. Reviews in Mineralogy (Volume 25)* (D.H. Lindsey, editor). de Gruyter, New York.

Haggerty, S.E. (1995) Upper mantle mineralogy. *Journal of Geodynamics*, **20**, 331–364.

Haggerty, S.E., Hardie, R.B. and McMahon, B.M. (1979) The mineral chemistry of ilmenite nodule associations from the Monastery diatreme. Pp. 249–256 in: *The Mantle Sample: Inclusion in Kimberlites and Other Volcanics*. American Geophysical Union, Washington, D. C.

Haggerty, S.E., Smyth, J.R., Erlank, A.J., Rickard, R.S. and Danchin, R.V. (1983) Lindsleyite (Ba) and mathiasite (K): two new chromium-titanates in the crichtonite series from the upper mantle. *America Mineralogist*, **68**, 494–505.

Haggerty, S.E., Erlank, A.J. and Grey, I.E. (1986) Metasomatic mineral titanate complexing in the upper mantle. *Nature*, **319**, 761–763.

Hall, A.J., McConville, P., Boyce, A.J. and Fallick, A.E. (1994) A high-chromium corundum (ruby) inclusion in diamond from the São Luiz alluvial mine, Brazil. *Mineralogical Magazine*, **58**, 490–493.

Hammond, A.L. and Mitchell, R.H. (2002) Accessory mineralogy of orangeite from Swartruggens, South Africa. *Mineralogy and Petrology*, **76**, 1–19.

Harlow, G.E. and Davies, R.M. (2005) Diamonds. *Elements*, **1**, 67–70.

Harlow, G.E. and Veblen, D.R. (1991) Potassium in Clinopyroxene Inclusions from Diamonds. *Science*, **251**, 652–655.

Hartzler, J.R. (2007) The geological exploration of kimberlitic rocks in Québec. McGill University, 102 pp.

Hatert, F. and Burke, E.A.J. (2008) The IMA-CNMNC dominant-constituent rule revisited and extended. *The Canadian Mineralogist*, **46**, 717–728.

Hayman, P.C., Cas, R.A.F. and Johnson, M. (2009) Characteristics and alteration origins of matrix minerals in volcaniclastic kimberlite of the Muskox pipe (Nunavut, Canada). *Lithos*, **112**, 473–487.

Heaman, L.M. and Kjarsgaard, B.A. (2000) Timing of eastern North American kimberlite magmatism: Continental extension of the Great Meteor hotspot track? *Earth and Planetary Science Letters*, **178**, 253–268.

Heaman, L.M., Kjarsgaard, B.A. and Creaser, R.A. (2003) The timing of kimberlite magmatism in North America: implications for global kimberlite genesis and diamond exploration. *Lithos*, **71**, 153–184.

Heaman, L.M., Kjarsgaard, B.A. and Creaser, R.A. (2004) The temporal evolution of North American kimberlites. *Lithos*, **76**, 377–397.

Hearn Jr., B.C. (2004) The Homestead kimberlite, central Montana, USA: mineralogy, xenocrysts, and upper-mantle xenoliths☆. *Lithos*, **77**, 473–491.

Hetman, C.M. (2008) Tuffisitic Kimberlite (TK): A Canadian perspective on a distinctive textural variety of kimberlite. *Journal of Volcanology and Geothermal Research*, **174**, 57–67.

Hetman, C.M., Scott Smith, B., Robey, J., Nkotsi, T., Mohapi, M. and Mohapi, T. (2018) Letšeng diamond mine, Lesotho: a variant of Kimberley-type pyroclastic kimberlite emplacement. *Mineralogy and Petrology*, **112**, 365–382.

Hill, R.J., Craig, J.R. and Gibbs, G. V. (1979) Systematics of the spinel structure type. *Physics and Chemistry of Minerals*, **4**, 317–339.

Hoda, S.Q. and Krishnamurthy, P. (2014) No TitleGeochemistry, Mineralogy and economic potential of titano-magnetite rock from the Samchampi carbonatite-alkaline rock complex, Karbi-Anglong district, Assam, India. *Journal of Applied Geochemistry*, **16**, 132–141.

Hoese. (2009) The use of perovskite to explore characteristics of kimberlite. Macquarie University, 52 pp.

Huang, Y., Qin, S., Zhou, X., Deng, C., Zhao, D., Yang, J., Guo, Y., Gao, Y. and Li, G. (1992) *Kimberlites and Diamonds in the North China Craton (in Chinese)*. P. in.: Geological Publishing House, Beijing, 206 pp.

Hutchison, M.T. (2018) Diamond exploration and regional prospectivity of Western Australia. *Mineralogy and Petrology*, **112**, 737–753.

Ilupin, I.V. and Roshchina, I.A. (2002) Petrochemistry and geochemistry of kimberlites from different provinces of the World. *Russian Journal Of Earth Sciences*, **4**, 433–452.

Ionov, D.A., Doucet, L.S., Xu, Y., Golovin, A. V. and Oleinikov, O.B. (2018) Reworking of Archean mantle in the NE Siberian craton by carbonatite and silicate melt metasomatism: Evidence from a carbonate-bearing, dunite-to-websterite xenolith suite from the Obnazhennaya kimberlite. *Geochimica et Cosmochimica Acta*, **224**, 132–153.

Irvine, T.N. (1965) Chromian spinel as a petrogenetic indicator: Part 1. Theory. *Canadian Journal of Earth Sciences*, **2**, 648–672. NRC Research Press.

Irvine, T.N. (1967) Chromian Spinel as a Petrogenetic Indicator: Part 2. Petrologic Applications. *Canadian Journal of Earth Sciences*, **4**, 71–103.

Janse, A.J.. (2007) Global rough diamond production since 1870. *Gems & Gemology*.

Janse, A.J.A. (Bram. and Sheahan, P.A. (1995) Catalogue of world wide diamond and kimberlite occurrences: a selective and annotative approach. *Journal of Geochemical Exploration*, **53**, 73–111.

Jaques, A.L. and Foley, S.F. (1985) The origin of Al-rich spinel inclusions in leucite from the leucite lamproites of Western Australia. *American Mineralogist*, **70**, 11431150.

Jaques, A.L., O’Neill, H.S.C., Smith, C.B., Moon, J. and Chappell, B.W. (1990) Diamondiferous peridotite xenoliths from the Argyle (AK1) lamproite pipe, Western Australia. *Contributions to Mineralogy and Petrology*, **104**, 255–276.

Jones, A.P., Smith, J. V. and Dawson, J.B. (1982) Mantle Metasomatism in 14 Veined Peridotites from Bultfontein Mine, South Africa. *The Journal of Geology*, **90**, 435–453.

Kamenetsky, V.M., Crawford, A.J. and Meffre, S. (2001) Factors Controlling Chemistry of Magmatic Spinel: an Empirical Study of Associated Olivine, Cr-spinel and Melt Inclusions from Primitive Rocks. *Journal of Petrology*, **42**, 655–671.

Kamenetsky, V.S., Kamenetsky, M.B., Sobolev, A. V., Golovin, A. V., Sharygin, V. V., Pokhilenko, N.P. and Sobolev, N. V. (2009a) Can pyroxenes be liquidus minerals in the kimberlite magma? *Lithos*, **112**, 213–222.

Kamenetsky, V.S., Maas, R., Kamenetsky, M.B., Paton, C., Phillips, D., Golovin, A. V. and Gornova, M.A. (2009b) Chlorine from the mantle: Magmatic halides in the Udachnaya-East kimberlite, Siberia. *Earth and Planetary Science Letters*, **285**, 96–104.

Kamenetsky, V.S., Grütter, H., Kamenetsky, M.B. and Gömann, K. (2013) Parental carbonatitic melt of the Koala kimberlite (Canada): Constraints from melt inclusions in olivine and Cr-spinel, and groundmass carbonate. *Chemical Geology*, **353**, 96–111.

Kamenetsky, V.S., Golovin, A. V., Maas, R., Giuliani, A., Kamenetsky, M.B. and Weiss, Y. (2014) Towards a new model for kimberlite petrogenesis: Evidence from unaltered kimberlites and mantle minerals. *Earth-Science Reviews*, **139**, 145–167. Elsevier B.V.

Kaminsky, F., Zakharchenko, O., Davies, R., Griffin, W., Khachatryan-Blinova, G. and Shiryaev, A. (2001) Superdeep diamonds from the Juina area, Mato Grosso State, Brazil. *Contributions to Mineralogy and Petrology*, **140**, 734–753.

Kaminsky, F. V., Zakharchenko, O.D., Griffin, W.L., Channer, D.M.D. and Khachatryan-Blinova, G.K. (2000) Diamond from the Guaniamo area, Venezuela. *The Canadian Mineralogist*, **38**, 1347–1370.

Kaminsky, F. V., Zakharchenko, O.D., Khachatryan, G.K., Griffin, W.L. and Channer, D.M.D. (2006) Diamond from the Los Coquitos area, Bolivar State, Venezuela. *The Canadian Mineralogist*, **44**, 323–340.

Kaminsky, F. V., Sablukov, S.M., Belousova, E.A., Andreazza, P., Tremblay, M. and Griffin, W.L. (2010) Kimberlitic sources of super-deep diamonds in the Juina area, Mato Grosso State, Brazil. *Lithos*, **114**, 16–29.

Kaminsky, F. V, Sablukov, S.M., Sablukova, L.I., Shchukin, V.S. and Canil, D. (2002) Kimberlites from the Wawa area, Ontario. *Canadian Journal of Earth Sciences*, **39**, 1819–1838.

Kaminsky, F.V. and Belousova, E.A. (2009) Manganoan ilmenite as kimberlite/diamond indicator mineral. *Russian Geology and Geophysics*, **50**, 1212–1220.

Kargin, A.V., Sazonova, L.V., Nosova, A.A., Lebedeva, N.M., Tretyachenko, V.V. and Abersteiner, A. (2017) Cr-rich clinopyroxene megacrysts from the Grib kimberlite, Arkhangelsk province, Russia: Relation to clinopyroxene–phlogopite xenoliths and evidence for mantle metasomatism by kimberlite melts. *Lithos*, **292–293**, 34–48.

Kaur, G. and Mitchell, R.H. (2013) Mineralogy of the P2-West ‘Kimberlite’, Wajrakarur kimberlite field, Andhra Pradesh, India: kimberlite or lamproite? *Mineralogical Magazine*, **77**, 3175–3196.

Kaur, G. and Mitchell, R.H. (2016) Mineralogy of the P-12 K-Ti-richterite diopside olivine lamproite from Wajrakarur, Andhra Pradesh, India: implications for subduction-related magmatism in eastern India. *Mineralogy and Petrology*, **110**, 223–245.

Kaur, G., Korakoppa, M.M., Fareeduddin and Pruseth, K.L. (2013) Petrology of P-5 and P-13 “Kimberlites” from Lattavaram Kimberlite Cluster, Wajrakarur Kimberlite Field, Andhra Pradesh, India: Reclassification as Lamproites. Pp. 183–194 in: *Proceedings of 10th International Kimberlite Conference* (D.G. Pearson, H.S. Grütter, J.W. Harris, B.A. Kjarsgaard, H. O’Brien, N.V.C. Rao and S. Sparks, editors). Springer India, New Delhi.

Keshav, S. and Sen, G. (2003) A rare composite xenolith from Salt Lake Crater, Oahu: high-pressure fractionation and implications for kimberlitic melts in the Hawaiian mantle. *Contributions to Mineralogy and Petrology*, **144**, 548–558.

Kinny, P.D., Compston, W., Bristow, J.W. and Williams, I.S. (1989) Archaean mantle xenocrysts in a Permian kimberlite: Two generations of kimberlitic zircon in Jwaneng DK2, southern Botswana. Pp. 833–842 in: *Kimberlite and Related Rocks. Geological Society of Australia Special Publication, Vol. 14* (J. Ross, editor).

Kinny, P.D., Griffin, B.J., Heaman, L.M., Brakhfogel, F.F. and Spetsius, Z.V. (1997) SHRIMP U-Pb ages of perovskite from Yakutian kimberlitesv. *Russian Geology and Geophysics*, **38**, 97–105.

Kitayama, Y., Thomassot, E., Galy, A., Golovin, A., Korsakov, A., D’Eyrames, E., Assayag, N., Bouden, N. and Ionov, D. (2017) Co-magmatic sulfides and sulfates in the Udachnaya-East pipe (Siberia): A record of the redox state and isotopic composition of sulfur in kimberlites and their mantle sources. *Chemical Geology*, **455**, 315–330.

Kogarko, L.N., Plant, D.A., Henderson, C.M.B. and Kjarsgaard, B.A. (1991) Na-rich carbonate inclusions in perovskite and calzirtite from the Guli intrusive Ca-carbonatite, polar Siberia. *Contributions to Mineralogy and Petrology*, **109**, 124–129.

Kononova, V.A., Bogatikov, O.A. and Kondrashov, I.A. (2011) Kimberlites and lamproites: Criteria for similarity and differences. *Petrology*, **19**, 34–54.

Konzett, J. (2005) Phase Relations and Stability of Magnetoplumbite- and Crichtonite-Series Phases under Upper-Mantle P-T Conditions: an Experimental Study to 15 GPa with Implications for LILE Metasomatism in the Lithospheric Mantle. *Journal of Petrology*, **46**, 749–781.

Konzett, J., Wirth, R., Hauzenberger, C. and Whitehouse, M. (2013) Two episodes of fluid migration in the Kaapvaal Craton lithospheric mantle associated with Cretaceous kimberlite activity: Evidence from a harzburgite containing a unique assemblage of metasomatic zirconium-phases. *Lithos*, **182–183**, 165–184.

Kopylova, M., Navon, O., Dubrovinsky, L. and Khachatryan, G. (2010a) Carbonatitic mineralogy of natural diamond-forming fluids. *Earth and Planetary Science Letters*, **291**, 126–137.

Kopylova, M.G., Mogg, T. and Scott Smith, B. (2010b) Mineralogy of the Snap Lake Kimberlite, Northwest Territories, Canada, and Compositions of Phlogopite as Records of its Crystallization. *The Canadian Mineralogist*, **48**, 549–570.

Kopylova, M.G., Gaudet, M., Kostrovitsky, S.I., Polozov, A.G. and Yakovlev, D.A. (2016) Origin of salts and alkali carbonates in the Udachnaya East kimberlite: Insights from petrography of kimberlite phases and their carbonate and evaporite xenoliths. *Journal of Volcanology and Geothermal Research*, **327**, 116–134.

Korobeinikov, A.N., Mitrofanov, F.P., Gehor, S., Laajoki, K., Pavlov, V.P. and Mamontov, V.P. (1998) Geology and Copper Sulphide Mineralization of the Salmagorskii Ring Igneous Complex, Kola Peninsula, NW Russia. *Journal of Petrology*, **39**, 2033–2041.

Kostrovitsky, S.I., Malkovets, V.G., Verichev, E.M., Garanin, V.K. and Suvorova, L.V. (2004) Megacrysts from the Grib kimberlite pipe (Arkhangelsk Province, Russia)☆. *Lithos*, **77**, 511–523.

Kostrovitsky, S.I., Alymova, N. V., Yakovlev, D.A., Serov, I. V., Ivanov, A.S. and Serov, V.P. (2006) Specific features of picroilmenite composition in various diamondiferous fields of the Yakutian province. *Doklady Earth Sciences*, **406**, 19–23.

Kramers, J.D. and Smith, C.B. (1983) A feasibility study of U−Pb and Pb−Pb dating of kimberlites using groundmass mineral fractions and whole-rock samples. *Chemical Geology*, **41**, 23–38.

Kressall, R., Fedortchouk, Y. and McCammon, C.. (2015) Application of Fe-Ti oxide dissolution experiments to the petrogenesis of the Ekati Diamond Mine kimberlites, Northwest Territories, Canada. P. Abstract V23B-3139 in: *American Geophysical Union Fall Meeting*.

Kuehner, S. and Irving, A. (1998) Corundum-kyanite eclogite, grospydite and epidote amphibolite of probable subducted slab origin from Paleogene diamondiferous pipes in SW Wyoming. Pp. 475–477 in: *International Kimberlite Conference Extended Abstracts, 7(1)*.

Kukharenko, A.A., Orlova, M.P., Bulakh, A.G., Bagdasarov, E.A., Rimski-Korsakov, O.M., Nefedov, E.I., Ilyinskiy, G.A., Sergeev, A.B. and Abakumova, N.B. (1965) *The Caledonian Ultramafic Alkaline and Carbonatite Complexes of the Kola Peninsula and Northern Karelia*. P. in.: Moscow Nedra.

Kumar, A., Padma Kumari, V.M., Dayal, A.M., Murthy, D.S.N. and Gopalan, K. (1993) Rb-Sr ages of Proterozoic kimberlites of India: evidence for contemporaneous emplacement. *Precambrian Research*, **62**, 227–237.

Kumar, A., Heaman, L.M. and Manikyamba, C. (2007) Mesoproterozoic kimberlites in south India: A possible link to ∼1.1Ga global magmatism. *Precambrian Research*, **154**, 192–204.

Lappin, M.A. (1978) The evolution of a grospydite from the Roberts Victor mine, South Africa. *Contributions to Mineralogy and Petrology*, **66**, 229–241.

Laverne, C., Grauby, O., Alt, J.C. and Bohn, M. (2006) Hydroschorlomite in altered basalts from Hole 1256D, ODP Leg 206: The transition from low-temperature to hydrothermal alteration. *Geochemistry, Geophysics, Geosystems*, **7**.

Leblanc, M., Dautria, J.-M. and Girod, M. (1982) Magnesian ilmenitite xenoliths in a basanite from Tahalra, Ahaggar (Southern Algeria). *Contributions to Mineralogy and Petrology*, **79**, 347–354.

Lee, D.C., Maddren, J. and Griffin, B.J. (2004) The importance of chromite morphology in diamond exploration. P. 5 in: *8th International Kimberlite Conference Long Abstract*. Victoria.

Lee, M.J., Garcia, D., Moutte, J. and Lee, J.I. (2003) Phlogopite and tetraferriphlogopite from phoscorite and carbonatite associations in the Sokli massif, Northern Finland. *Geosciences Journal*, **7**, 9–20.

Lee, M.J., Lee, J.I. and Moutte, J. (2005) Compositional variation of Fe−Ti oxides from the Sokli complex, northeastern Finland. *Geosciences Journal*, **9**, 1–13.

Lensky, N.G., Niebo, R.W., Holloway, J.R., Lyakhovsky, V. and Navon, O. (2006) Bubble nucleation as a trigger for xenolith entrapment in mantle melts. *Earth and Planetary Science Letters*, **245**, 278–288.

Leost, I., Stachel, T., Brey, G.P., Harris, J.W. and Ryabchikov, I.D. (2003) Diamond formation and source carbonation: mineral associations in diamonds from Namibia. *Contributions to Mineralogy and Petrology*, **145**, 15–24.

Lepekhina, E.N., Antonov, A.V., Savva, E.V., Belyatsky, B.V. and Sergeev, S.A. (2009) Perovskite from the Tiksheozero carbonatite: age and genesis. P. in: *Perovskite from the Tiksheozero Carbonatite: Age and Genesis. Extended Abstract: Geochemistry of Magmatic Rocks — School Geochemistry of Alkaline Rocks*. Vernadsky Institute of Geochemistry and Analytical Chemistry, Russian Academy of Sciences, Moscow.

Lindsley, D.H. and Dixon, S.A. (1976) Diopside-enstatite equilibria at 850 degrees to 1400 degrees C, 5 to 35 kb. *American Journal of Science*, **276**, 1285–1301.

Liu, J., Guan, Y., Liu, X. and Ren, X. (1990) A study of mathiasite from the Shandong kimberlite of China. *Acta Mineralogica Sinica*, **10**, 221–226 (in Chinese with English abstract).

Liu, L., Zhang, J., Green, H.W., Jin, Z. and Sun, Y. (2004) UHP Ilmenite Exsolution from Iron-bearing Rutile in Eclogite from the Altyn Tagh, NW China. P. abstract id. T21A-0504 in: *American Geophysical Union, Fall Meeting 2004*.

Logvinova, A.M., Wirth, R., Fedorova, E.N. and Sobolev, N. V. (2008) Nanometre-sized mineral and fluid inclusions in cloudy Siberian diamonds: new insights on diamond formation. *European Journal of Mineralogy*, **20**, 317–331.

Lowers, H.A., Harrison, W.J., Wendlandt, R.F. and Meeker, G.P. (2004) Origin of fibrous amphiboles in the Iron Hill carbonatite complex, Gunnison County, Colorado. *Abstracts with Programs - Geological Society of America*, **36**, 246.

Loz'ko, Y.Y., Serenko, V.P., Koptil, V.I., Rudintskaya, Y.S. and Tsepin, A.I. (1983) Diamond-bearing kyanite eclogites from the Sytykanskaya kimberlite pipe, Yakutiya. *International Geology Review*, **25**, 381–394.

Lu, Q. and Zhou, H.. (1994) A new progress in research on mathiasite in Mengying, Shandong, III. Oxide minerals containing the large ions Cr, Ti and Fe in the upper mantle. *Acta Mineralógica Sinica*, **14**, 343–347 (in Chinese with English abstract).

Lu, Q., Zhou, H., Liu, H. and Lei, X. (1996) Metasomatism of incompatible elements from upper mantle. *Earth Sience – Journal of China University of Geosiences*, **21**, 553–556 (in Chinese with English abstract).

Lu, Q., Zhou, H., Liu, H. and Lei, X. (1998) Oxides and related minerals in upper mantel-relationship among complex oxides in kimberlites and an investigation on metasomatism in upper mantle. *Acta Mineralogica Sinica*, **18**, 483–495 (in Chinese with English abstract).

Ludwig, K.R. (2003) Isoplot/ex version 4.0: a geochemical toolkit for microsoft excel. Berkeley Geochronological Center Special Publication 4.

Macdonald, R., Bagiński, B., Kartashov, P.M., Zozulya, D. and Dzierżnowski, P. (2015) Hydrothermal alteration of chevkinite-group minerals. Part 2. Metasomatite from the Keivy massif, Kola Peninsula, Russia. *Mineralogical Magazine*, **79**, 1039–1059.

Le Maitre, R.W. (2002) *Igneous Rocks: a Classification and Glossary of Terms: Recommendations of the International Union of Geological Sciences Subcommission on the Systematics ofIgneous Rocks.* P. in.: Cambridge University Press, Cambridge, 236 pp.

Malkovets, V.G., Griffin, W.L., O'Reilly, S.Y. and Wood, B.J. (2007) Diamond, subcalcic garnet, and mantle metasomatism: Kimberlite sampling patterns define the link. *Geology*, **35**, 339.

Malkovets, V.G., Rezvukhin, D.I., Belousova, E.A., Griffin, W.L., Sharygin, I.S., Tretiakova, I.G., Gibsher, A.A., O'Reilly, S.Y., Kuzmin, D.V., Litasov, K.D., Logvinova, A.M., Pokhilenko, N.P. and Sobolev, N.V. (2016) Cr-rich rutile: A powerful tool for diamond exploration. *Lithos*, **265**, 304–311.

Mariano, A.N. and Roeder, P.L. (1983) Kerimasi: A Neglected Carbonatite Volcano. *The Journal of Geology*, **91**, 449–455.

Martins, T., Chakhmouradian, A.R. and Medici, L. (2014) Perovskite alteration in kimberlites and carbonatites: The role of kassite, CaTi2O4(OH)2. *Physics and Chemistry of Minerals*, **41**, 473–484.

Masun, K.M. (1999) he petrography and mineralogy of the lac de Gras Kimberlite Field, Slave Province, Northwest Territories: a comparative Study. 327 pp.

Masun, K.M., Doyle, B.J., Ball, S. and Walker, S. (2004) The geology and mineralogy of the Anuri kimberlite, Nunavut, Canada. *Lithos*, **76**, 75–97.

Mazzone, P. and Haggerty, S.E. (1986) Corganites and corgaspinites. Two new types of aluminous assemblages from the Jagersfontein kimberlite pipe. Pp. 279–281 in: *International Kimberlite Conference Extended Abstracts 4(1)*.

Mazzone, P. and Stephen E, H. (1989) Peraluminous xenoliths in kimberlite: Metamorphosed restites produced by partial melting of pelites. *Geochimica et Cosmochimica Acta*, **53**, 1551–1561.

McCammon, C.A. (2001) Oxidation during metasomatism in ultramafic xenoliths from the Wesselton kimberlite, South Africa: implications for the survival of diamond. *Contributions to Mineralogy and Petrology*, **141**, 287–296.

McCandless, T.E., Waldman, M.A. and Gurney, J.J. (1994) Macrodiamonds and microdiamonds from Murfreesboro lamproites, Arkansas: morphology, mineral inclusions, and carbon isotope geochemistry. Pp. 78–97 in: *Proceedings of 5th International Kimberlite Conference Volume 2* (H. 0. A. Meyer and 0. H. Leonardos, editors). Companhia de Pesquisa de Recursos Minerais (CPRM), Rio de Janeiro.

McDonough, W.F. and Sun, S. -s. (1995) The composition of the Earth. *Chemical Geology*, **120**, 223–253.

McMahon, B.M. and Haggerty, S.E. (1979) The Oka carbonatite complex: magnetite compositions and the related role of titanium in pyrochlore. Pp. 382–399 in: *Kimberlites, Diatremes and Diamonds: Their Geology, Petrology, and Geochemistry* (F.R. Boyd and H.O.A. Meyer, editors). American Geophysical Union, Washington, D.C.

Meinhold, G. (2010) Rutile and its applications in earth sciences. *Earth-Science Reviews*, **102**, 1–28.

Melcher, F., Grum, W., Simon, G., Thalhammer, T. V. and Stumpfl, E.F. (1997) Petrogenesis of the Ophiolitic Giant Chromite Deposits of Kempirsai, Kazakhstan: a Study of Solid and Fluid Inclusions in Chromite. *Journal of Petrology*, **38**, 1419–1458.

Melgarejo, J.C., Costanzo, A., Bambi, A.C.J.M., Gonçalves, A.O. and Neto, A.B. (2012) Subsolidus processes as a key factor on the distribution of Nb species in plutonic carbonatites: The Tchivira case, Angola. *Lithos*, **152**, 187–201.

Meyer, H.O.A. and McCallum, M.E. (1986) Mineral Inclusions in Diamonds from the Sloan Kimberlites, Colorado. *The Journal of Geology*, **94**, 600–612.

Meyer, H.O.A. and Mitchell, R.H. (1988) Sapphire-bearing ultramafic lamprophyre from Yogo, Montana: an ouachitite. *The Canadian Mineralogist*, **26**, 81–88.

Milani, L., Bolhar, R., Cawthorn, R.G. and Frei, D. (2017) In situ LA–ICP-MS and EPMA trace element characterization of Fe–Ti oxides from the phoscorite–carbonatite association at Phalaborwa, South Africa. *Mineralium Deposita*, **52**, 747–768.

Milligan, R.S. (2014) Reaction of iron tiranium oxide minerals with kimberlite magma; a case study for Orapa kimberlite cluster. Dalhousie University, Halifax, Nova Scotia, 85 pp.

MINDAT. (2019) . <https://www.mindat.org> (9 March 2019).

Minin, D., Sharygin, I., Litasov, K., Sharygin, V., Shatskiy, A. and Ohtani, E. (2016) High-pressure behavior of djerfisherite; implication for its origin in diamonds and mantle xenoliths. P. Abstract MR33A-2674 in: *American Geophysical Union Fall Meeting, 2016*.

Minin, D.A., Sharygin, I.S., Litasov, K.D., Sharygin, V. V., Shatskiy, A. and Ohtani, E. (2015) High-pressure stability of djerfisherite: implication for its origin in diamonds and mantle xenoliths. P. 14 in: *Advances in High Pressure Research II: Deepest Understanding 2015* (K.D. Litasov and E. Ohtani, editors). Novosibirsk-Irkutsk.

Minin, V.A., Prugov, V.P., Podgornykh, N.M., Kovyazin, S. V. and Kholodova, L.D. (2011) Composition of chromites from kimberlites of the Botuobinskaya pipe in Yakutia. *Geology of Ore Deposits*, **53**, 626–638.

Misra, K.C., Anand, M., Taylor, L.A. and Sobolev, N. V. (2004) Multi-stage metasomatism of diamondiferous eclogite xenoliths from the Udachnaya kimberlite pipe, Yakutia, Siberia. *Contributions to Mineralogy and Petrology*, **146**, 696–714.

Mitchell, R.H. (1973) Magnesian Ilmenite and Its Role in Kimberlite Petrogenesis. *The Journal of Geology*, **81**, 301–311.

Mitchell, R.H. (1978) Manganoan magnesian ilmenite and titanian clinohumite from the Jacupiranga carbonatite, São Paulo, Brazil. *American Mineralogist*, **63**, 544–547.

Mitchell, R.H. (1986) *Kimberlites: Mineralogy, Geochemistry, and Petrology*. P. in.: Plenum Press, New York, 442 pp.

Mitchell, R.H. (1995) *Kimberlites, Orangeites, and Related Rocks*. P. in.: Plenum Press, New York, N.Y., 410 pp.

Mitchell, R.H. (1997) *Kimberlites, Orangeites, Lamproites, Melilities, and Minettes: A Petrographic Atlas*. P. in.: Almaz Press Inc, Thunnder Bay, Ontario, Canada, 243 pp.

Mitchell, R.H. (2002) *Perovskites modern and ancient*. P. in.: Almaz Press, Thunder Bay, 320 pp.

Mitchell, R.H. (2006) Potassic magmas derived from metasomatized lithospheric mantle: Nomenclature and relevance to exploration for diamond-bearing rocks. *Journal of the Geological Society of India*, **67**, 317–327.

Mitchell, R.H. (2008) Petrology of hypabyssal kimberlites: Relevance to primary magma compositions. *Journal of Volcanology and Geothermal Research*, **174**, 1–8.

Mitchell, R.H. (2013) Paragenesis and Oxygen Isotopic Studies of Serpentine in Kimberlite. Pp. 1–12 in: *10th International Kimberlite Conference* (D.G. Pearson, H.S. Grütter, J.W. Harris, B.A. Kjarsgaard, H. O'Brien, N.V. Chalapathi Rao and S. Sparks, editors). Springer, New Delhi.

Mitchell, R.H. and Bergman, S.C. (1991) *Petrology of Lamproites*. P. in.: Springer, Boston, MA, Boston, MA, 447 pp.

Mitchell, R.H. and Chakhmouradian, A.R. (1998) Instability of perovskite in a CO2-rich environment: Examples from carbonatite and kimberlite. *Canadian Mineralogist*, **36**, 939–952.

Mitchell, R.H. and Clarke, D.B. (1976) Oxide and sulphide mineralogy of the Peuyuk kimberlite, Somerset Island, N.W.T., Canada. *Contributions to Mineralogy and Petrology*, **56**, 157–172.

Mitchell, R.H., Scott-Smith, B.H. and Larsen, L.M. (1999) Mineralogy of ultramafic dikes from the Sarfartoq, Sisimiut and Maniitsoq areas, West Greenland. Pp. 574–583 in: *Proceedings of the 7th International Kimberlite Conference Vol 2* (J.J. Gurney, J.L. Gurney, M.D. Pascoe and S.H. Richardson, editors). Red Roof Design, Cape Town.

Mitchell, R.H., Skinner, E.M.W. and Scott Smith, B.H. (2009) Tuffisitic kimberlites from the Wesselton Mine, South Africa: Mineralogical characteristics relevant to their formation. *Lithos*, **112**, 452–464.

Mitchell, R.H., Welch, M.D. and Chakhmouradian, A.R. (2017) Nomenclature of the perovskite supergroup: A hierarchical system of classification based on crystal structure and composition. *Mineralogical Magazine*, **81**, 411–461.

Moore, A. and Belousova, E. (2005) Crystallization of Cr-poor and Cr-rich megacryst suites from the host kimberlite magma: implications for mantle structure and the generation of kimberlite magmas. *Contributions to Mineralogy and Petrology*, **149**, 462–481.

Moore, A.E. (1987) A model for the origin of ilmenite in kimberlite and diamond: implications for the genesis of the discrete nodule (megacryst) suite. *Contributions to Mineralogy and Petrology*, **95**, 245–253.

Moore, R. and Gurney, J. (1991) Garnet megacrysts from group II kimberlites in southern africa. P. 298–300. Retrieved from https://www.ikcabstracts.c in: *5th International Kimberlite Conference: Extended Abstracts*.

Morimoto, N. (1988) Nomenclature of Pyroxenes. *Mineralogy and Petrology*, **39**, 55–76.

Motsamai, T., Harris, J.W., Stachel, T., Pearson, D.G. and Armstrong, J. (2018) Mineral inclusions in diamonds from Karowe Mine, Botswana: super-deep sources for super-sized diamonds? *Mineralogy and Petrology*, **112**, 169–180.

Muan, A., Hauck, J. and Lofall, T. (1972) Equilibrium studies with a bearing on lunar rocks. Pp. 185–196 in: *Proceedings 3rd of the Lunar Science Conference 1*.

Muggeridge, M.T. (1995) Pathfinder sampling techniques for locating primary sources of diamond: Recovery of indicator minerals, diamonds and geochemical signatures. *Journal of Geochemical Exploration*, **53**, 183–204.

Muntener, C. and Gaudet, M. (2018) Geology of the Renard 2 pipe to 1000 m depth, Renard Mine, Québec, Canada: insights into Kimberley-type pyroclastic kimberlite emplacement. *Mineralogy and Petrology*, **112**, 421–432.

Müntener, O. and Hermann, J. (1994) Titanian andradite in a metapyroxenite layer from the Malenco ultramafics (Italy): implications for Ti-mobility and low oxygen fugacity. *Contributions to Mineralogy and Petrology*, **116**, 156–168.

Muramatsu, Y. (1983) Geochemical investigations of kimberlites from the Kimberley area, South Africa. *Geochemical Journal*, **17**, 71–86.

Nasir, S., Theye, T. and Massonne, H.J. (2009) REE-Rich Aeschynite in Apatite-Dolomite Carbonatite, Eastern Oman Mountains. *The Open Mineralogy Journal*, **3**, 17–27.

Nayak, S.S. and Kudari, S.A.D. (1999) Discovery of diamond-bearing kimberlites in Kalyandurg area, Anantapur district, Andhra Pradesh. *Current Science*, **76**, 1077–1079.

Nickel, E.H. (1992) Solid solutions in mineral nomenclature. *Mineralogy and Petrology*, **46**, 49–53.

Nickel, E.H. (1995) Definition of a mineral. *Canadian Mineralogist*, **33**, 689–690.

Nickel, E.H. and McAdam, R.C. (1963) Niobian perovskite from Oka, Quebec; a new classification for minerals of the perovskite group. *The Canadian Mineralogist*, **7**, 683–697.

Nielsen, T.F.D., Jensen, S.M., Secher, K. and Sand, K.K. (2009) Distribution of kimberlite and aillikite in the Diamond Province of southern West Greenland: A regional perspective based on groundmass mineral chemistry and bulk compositions. *Lithos*, **112**, 358–371.

Nimis, P. (1998) Evaluation of diamond potential from the composition of peridotitic chromian diopside. *European Journal of Mineralogy*, **10**, 505–520.

Nixon, P.H. (1995) A review of mantle xenoliths and their role in diamond exploration. *Journal of Geodynamics*, **20**, 305–329.

Nixon, P.H. and Boyd, F.R. (1979) Garnet bearing lherzolites and discrete nodule suites from the Malaita Alnoite, Solomon Islands, S.W. Pacific, and their bearing on oceanic mantle composition and geotherm. Pp. 400–423 in: *The Mantle Sample: Inclusion in Kimberlites and Other Volcanics*. American Geophysical Union, Washington, D. C.

Nosova, A.A., Sazonova, L. V., Kargin, A. V., Smirnova, M.D., Lapin, A. V. and Shcherbakov, V.D. (2018) Olivine in ultramafic lamprophyres: chemistry, crystallisation, and melt sources of Siberian Pre- and post-trap aillikites. *Contributions to Mineralogy and Petrology*, **173**, 55.

Nowicki, T.E., Moore, R.O., Gurney, J.J. and Baumgartner, M.C. (2007) Diamonds and Associated Heavy Minerals in Kimberlite: A Review of Key Concepts and Applications. *Developments in Sedimentology*, **58**, 1235–1267.

O’Brien, H.E. and Tyni, M. (1999) Mineralogy and Geochemistry of Kimberlites and Related Rocks from Finland. Pp. 625–636 in: *Proceedings of the 7th International Kimberlite Conference Vol 2* (J.J. Gurney, J.L. Gurney, M.D. Pascoe and S.H. Richardson, editors). Red Roof Design, Cape Town.

O’Reilly, S.Y. and Griffin, W.L. (2006) Imaging global chemical and thermal heterogeneity in the subcontinental lithospheric mantle with garnets and xenoliths: Geophysical implications. *Tectonophysics*, **416**, 289–309.

Ogilvie-Harris, R.C., Field, M., Sparks, R.S.J. and Walter, M.J. (2009) Perovskite from the Dutoitspan kimberlite, Kimberley, South Africa: implications for magmatic processes. *Mineralogical Magazine*, **73**, 915–928.

Okamoto, K. and Maruyama, S. (2004) The Eclogite–Garnetite transformation in the MORB + H2O system. *Physics of the Earth and Planetary Interiors*, **146**, 283–296.

Orlandi, P., Pasero, M., Duchi, G. and Olmi, F. (1997) Dessauite, (Sr,Pb) (Y,U) (Ti,Fe3+)20O38 , a new mineral of the crichtonite group from Buca della Vena Mine, Tuscany, Italy. *American Mineralogist*, **82**, 807–811.

Paces, J.B., Zartman, R.E., Taylor, L.A., Futa, K. and Kwak, L.M. (1990) Pb isotop evidence for multiple episodes of lower crustal growth and modification in granulite nodules from superior Province, Michgan. P. A119 in: *Program with Abstracts, Geological Society of America Conference*. Dallas,Texas.

Pagano, D.S., Galliski, M.Á., Márquez-Zavalía, M.F., Novák, M. and Škoda, R. (2016) Petrography, Mineralogy, and Origin of the Syenite Pegmatitic Segregation Veins From La Peña Alkaline Complex, Mendoza, Argentina. *The Canadian Mineralogist*, **54**, 803–825.

Palke, A.C., Renfro, N.D. and Berg, R.B. (2016) Origin of sapphires from a lamprophyre dike at Yogo Gulch, Montana, USA: Clues from their melt inclusions. *Lithos*, **260**, 339–344.

Panina, L.I., Sazonov, A.M. and Usol'tseva, L.M. (2001) Melilitic and monticellite- bearing rocks of the Krestovskaya intrusion (northern Siberian Platform) and their genesis. *Geologiya i Geofizika (Russian Geology and Geophysics)*, **42**, 1314–1332.

Parfenoff, A. (1982) Un Minéral traceur pour la prospection alluvionnaire, l'ilménite : Relations entre ilménites magnésiennes, basaltes alcalins, kimberlites et diamant, BTGM. *Doc. Bur. Rech. Geol. Mineres*, No. 37.

Parthasarathy, G., Chetty, T.R.K. and Haggerty, S.E. (2002) Thermal stability and spectroscopic studies of zemkorite: A carbonate from the Venkatampalle kimberlite of southern India. *American Mineralogist*, **87**, 1384–1389.

Paschoal, C.W.A., Moreira, R.L., Fantini, C., Pimenta, M.A., Surendran, K.P. and Sebastian, M.T. (2003) Raman scattering study of RETiTaO6 dielectric ceramics. *Journal of the European Ceramic Society*, **23**, 2661–2666.

Pasteris, J.D. (1980) Opaque oxide phases of the De Beers Pipe kimberlite (Kimberley, South Africa) and their petrologic significance, Ph.D. thesis. Yale University.

Pasteris, J.D. (1981) The significance of groundmass ilmenite and megacryst ilmenite in kimberlites. *Contributions to Mineralogy and Petrology*, **75**, 315–325.

Pasteris, J.D. (1982) Representation of compositions in complex titanian spinels and application to the De Beers kimberlite. *American Mineralogist*, **67**, 244–250.

Pasteris, J.D. (1983) Spinel zonation of the De Beers kimberlite, South Africa: possible role of phlogopite. *Canadian Mineralogist*, **21**, 41–58.

Pasteris, J.D. (1984) Kimberlites: Complex Mantle Melts. *Annual Review of Earth and Planetary Sciences*, **12**, 133–153.

Paton, C., Hergt, J.M., Phillips, D., Woodhead, J.D. and Shee, S.R. (2007) New insights into the genesis of Indian kimberlites from the Dharwar Craton via in situ Sr isotope analysis of groundmass perovskite. *Geology*, **35**, 1011–1014.

Pereira, V.P., Conceicao, R.V., Formoso, M.L.L. and Pires, A.C. (2005) Alteration of perovskite to anatase in silica-undersaturated rocks of the Catalao I carbonatite complex, Brazil; a Raman study. *Revista Brasileira de Geociências*, **35**, 239–244.

Persikov, E.S., Bukhtiyarov, P.G. and Sokol, A.G. (2015) Change in the viscosity of kimberlite and basaltic magmas during their origin and evolution (prediction). *Russian Geology and Geophysics*, **56**, 885–892.

Peterson, T.D. and LeCheminant, A.N. (1993) Glimmerite xenoliths in Early Proterozoic ultrapotassic rocks from the Churchill province. *The Canadian Mineralogist*, **31**, 801–819.

Plá Cid, J., Nardi, L.V.S., Stabel, L.Z., Conceição, R.V. and Balzaretti, N.M. (2003) High-pressure minerals in mafic microgranular enclaves: evidences for co-mingling between lamprophyric and syenitic magmas at mantle conditions. *Contributions to Mineralogy and Petrology*, **145**, 444–459.

Pokhilenko, N.P., Sobolev, N.V., Reutsky, V.N., Hall, A.E. and Taylor, L.A. (2004) Crystalline inclusions and C isotope ratios in diamonds from the Snap Lake/King Lake kimberlite dyke system: evidence of ultradeep and enriched lithospheric mantle. *Lithos*, **77**, 57–67.

Porritt, L.A. and Russell, J.K. (2012) Kimberlite ash: Fact or fiction. *Physics and Chemistry of the Earth*, **45–46**, 24–32.

Porritt, L.A., Cas, R.A.F., Schaefer, B. and McKnight, S.W. (2012) Textural analysis of strongly altered kimberlite: Examples from the Ekati diamond mine, Northwest Territories, Canada. *Canadian Mineralogist*, **50**, 625–641.

Price, R.C., Cooper, A.F., Woodhead, J.D. and Cartwright, I. (2003) Phonolitic Diatremes within the Dunedin Volcano, South Island, New Zealand. *Journal of Petrology*, **44**, 2053–2080.

Priestley, K., McKenzie, D. and Debayle, E. (2006) The state of the upper mantle beneath southern Africa. *Tectonophysics*, **416**, 101–112.

Proenza, J., Gervilla, F., Melgarejo, J. and Bodinier, J.-L. (1999) Al- and Cr-rich chromitites from the Mayari-Baracoa ophiolitic belt (eastern Cuba); consequence of interaction between volatile-rich melts and peridotites in suprasubduction mantle. *Economic Geology*, **94**, 547–566.

Puustinen, K. (1973) Tetraferriphlogopite from the Siilinjärvi carbonatite complex, Finland. *Bulletin of the Geological Society of Finland*, **44**, 35–42.

Quirt, D.H. (2004) Cr-diopside (clinopyroxene) as a kimberlite indicator minerals for diamond exploration in glaciated terrains. P. Paper A-10, 14p. in: *Summary of Investigations 2004, Volume 2, Saskatchewan Geological Survey, Sask. Industry Resources, Misc. Rep. 2004-4.2.*

Ragozin, A.L., Zedgenizov, D.A., Shatskii, V.S., Orihashi, Y., Agashev, A.M. and Kagi, H. (2014) U-Pb age of rutile from the eclogite xenolith of the Udachnaya kimberlite pipe. *Doklady Earth Sciences*, **457**, 861–864.

Ranger, I.M., Heaman, L.M., Pearson, D.G., Muntener, C. and Zhuk, V. (2018) Punctuated, long-lived emplacement history of the Renard 2 kimberlite, Canada, revealed by new high precision U-Pb groundmass perovskite dating. *Mineralogy and Petrology*, **112**, 639–651.

Rapopo, M. and Sobie, P. (2018) The Liqhobong kimberlite cluster: an update on the geology. *Mineralogy and Petrology*, **112**, 339–350.

Reguir, E.P., Chakhmouradian, A.R., Halden, N.M., Malkovets, V.G. and Yang, P. (2009) Major- and trace-element compositional variation of phlogopite from kimberlites and carbonatites as a petrogenetic indicator. *Lithos*, **112**, 372–384. Elsevier B.V.

Reid, A.M., Donaldson, C.H., Dawson, J.B., Brown, R.W. and Ridley, W.I. (1975) The Igwisi Hills extrusive “kimberlites.” *Physics and Chemistry of the Earth*, **9**, 199–218.

Reis, B. (1972) Preliminary Note on the Distribution and Tectonic Control of Kimberlites in Angola. Pp. 276–281 in: *Proceedings of 24th International Geological Congress, Sect 4*.

Reubi, O., Nicholls, I.. and Kamenetsky, V.. (2003) Early mixing and mingling in the evolution of basaltic magmas: evidence from phenocryst assemblages, Slamet Volcano, Java, Indonesia. *Journal of Volcanology and Geothermal Research*, **119**, 255–274.

Rezvukhin, D.I., Malkovets, V.G., Sharygin, I.S., Kuzmin, D.V., Litasov, K.D., Gibsher, A.A., Pokhilenko, N.P. and Sobolev, N.V. (2016a) Inclusions of Cr- and Cr-Nb-Rutile in pyropes from the Internatsionalnaya kimberlite pipe, Yakutia. *Doklady Earth Sciences*, **466**, 173–176.

Rezvukhin, D.I., Malkovets, V.G., Sharygin, I.S., Kuzmin, D. V., Gibsher, A.A., Litasov, K.D., Pokhilenko, N.P. and Sobolev, N. V. (2016b) Inclusions of crichtonite group minerals in pyropes from the Internatsionalnaya kimberlite pipe, Yakutia. *Doklady Earth Sciences*, **466**, 206–209.

Rezvukhin, D.I., Malkovets, V.G., Sharygin, I.S., Tretiakova, I.G., Griffin, W.L. and O’Reilly, S.Y. (2018) Inclusions of crichtonite-group minerals in Cr-pyropes from the Internatsionalnaya kimberlite pipe, Siberian Craton: Crystal chemistry, parageneses and relationships to mantle metasomatism. *Lithos*, **308–309**, 181–195.

Rezvukhin, D.L., Nikolenko, E.L., Sharygin, L. and Malkovets, V.G. (2017) Oxide mineral inclusions in Cr-Pyropes from the Aldanska Ya lamprophye dyke, Yakutia. Pp. 205–208 in: *Proc. Intemational Conference on Magmatism Ofthe Earth and Related Strategic Metal Deposits Miass, Russia*.

Ricard, R.S., Harris, J.W., Gurney, J.J. and Cardoso, P. (1989) Mineral inclusions in diamonds from the Koffiefontein Mine. *Geological Society of Australia Special Publications*, **14**, 1054–1062.

Rieder, M., Cavazzini, G., D’yakonov, Y.S., Frank-Kamenetskii, V.A., Gottardi, G., Guggenheim, S., Koval’, P. V., Müller, G., Neiva, A.M.R., Radoslovich, E.W., Robert, J.-L., Sassi, F.P., Takeda, H., Weiss, Z. and Wones, D.R. (1999) Nomenclature of the micas. *Mineralogical Magazine*, **63**, 267–279.

Robinson, D.N., Gurney, J.J. and Shee, S.R. (1984) Diamond Eclogite and Graphite Eclogite Xenoliths from Orapa, Botswana. *Developments in Petrology*, **11**, 11–24.

Robles-Cruz, S.E. (2008) Kimberlites associated with the Lucapa structure, Angola. University of Barcelona, 112 pp.

Robles-Cruz, S.E., Watangua, M., Isidoro, L., Melgarejo, J.C., Galí, S. and Olimpio, A. (2009) Contrasting compositions and textures of ilmenite in the Catoca kimberlite, Angola, and implications in exploration for diamond. *Lithos*, **112**, 966–975. Elsevier B.V.

Rock, N.M.S. (1986) The Nature and Origin of Ultramafic Lamprophyres: Aln ites and Allied Rocks. *Journal of Petrology*, **27**, 155–196.

Roeder, P.L. and Reynolds, I. (1991) Crystallization of Chromite and Chromium Solubility in Basaltic Melts. *Journal of Petrology*, **32**, 909–934.

Roeder, P.L. and Schulze, D.J. (2008) Crystallization of groundmass spinel in kimberlite. *Journal of Petrology*, **49**, 1473–1495.

Roeder, P.L., Campbell, I.H. and Jamieson, H.E. (1979) A re-evaluation of the olivine-spinel geothermometer. *Contributions to Mineralogy and Petrology*, **68**, 325–334.

le Roex, A.P. (2003) Petrogenesis of Group I Kimberlites from Kimberley, South Africa: Evidence from Bulk-rock Geochemistry. *Journal of Petrology*, **44**, 2261–2286.

Roman'ko, E.F., Egorov, K.N., Podvysotskii, V.T., Sablukov, S.M. and D'yakonov, D.B. (2005) A new diamondiferous kimberlite region in southwestern Angola. *Doklady Earth Sciences*, **406**, 817–821.

Rudnick, R.L. (2000) Rutile-Bearing Refractory Eclogites: Missing Link Between Continents and Depleted Mantle. *Science*, **287**, 278–281.

Russell, J.K., Porritt, L.A., Lavallé, Y. and Dingwell, D.B. (2012) Kimberlite ascent by assimilation-fuelled buoyancy. *Nature*, **481**, 352–356.

Russell, S., Folco, L., Grady, M.M., Zolensky, M.E., Jones, R., Righter, K., Zipfel, J. and Grossman, J.N. (2004) The Meteoritical Bulletin, No. 88. *Meteoritics & Planetary Science*, **39**, A215–A272.

Safonov, O.G., Perchuk, L.L. and Litvin, Y.A. (2006) Effect of carbonates on crystallization and composition of potassium-bearing clinopyroxene at high pressures. *Doklady Earth Sciences*, **408**, 580–585.

Saleh, G.M. (2006) The chromite deposits associated with ophiolite complexes, Southeastern Desert, Egypt: Petrological and geochemical characteristics and mineralization. *Chinese Journal of Geochemistry*, **25**, 307–317.

Samsonov, A. V, Nosova, A.A., Tretyachenko, V. V, Larchenko, V.A. and Larionova, Y.O. (2009) Collisional sutures in the early precambrian crust as a factor responsible for localization of diamondiferous kimberlites in the northern East European Platform. *Doklady Earth Sciences*, **425**, 226–230.

Sarkar, C., Kjarsgaard, B.A., Pearson, D.G., Heaman, L.M., Locock, A.J. and Armstrong, J.P. (2018) Geochronology, classification and mantle source characteristics of kimberlites and related rocks from the Rae Craton, Melville Peninsula, Nunavut, Canada. *Mineralogy and Petrology*, **112**. Mineralogy and Petrology.

Schingaro, E., Lacalamita, M., Mesto, E., Ventruti, G., Pedrazzi, G., Ottolini, L. and Scordari, F. (2016) Crystal chemistry and light elements analysis of Ti-rich garnets. *American Mineralogist*, **101**, 371–384.

Schulze, D.J. (1984) Cr-poor megacrysts from the Hamilton Branch kimberlite, Elliot County, Kentucky. Pp. 97–108 in: *Proceedings of 3rd International Kimberlite Conference Volume 2* (J. Kornprobst, editor). Elsevier Press, New York.

Schulze, D.J. (2001) Origins of Chromian and Aluminous Spinel Macrocrysts from Kimberlites in Southern Africa. *The Canadian Mineralogist*, **39**, 361–376.

Schulze, D.J., N., A.P.F., Hearn Jr, B.C. and Hetman, C.M. (1995) Origin and Significance of Ilmenite Megacrysts and Macrocrysts from Kimberlite. *International Geology Review*, **37**, 780–812.

Scott Smith, B.H. (2008) Canadian kimberlites: Geological characteristics relevant to emplacement. *Journal of Volcanology and Geothermal Research*, **174**, 9–19.

Scott Smith, B.H. (2017) Kimberlites – from Mantle to Mine. 2–4.

Scott Smith, B.H., Danchin, R.V., HarrisS, J.W. and Stracke, K.J. (1984) Kimberlites Near Orroroo, South Australia. Pp. 121–142 in: *Proceedings of 3rd International Kimberlite Conference Volume 1* (J. Kornprobst, editor). Elsevier Press, New York.

Scott Smith, B.H., Nowicki, T.E., Russell, J.K., Webb, K.J., Mitchell, R.H., Hetman, C.M., M, H., Skinner, E.M.W. and Robey, J.A. (2013) Kimberlite Terminology and Classification12 pt12 pt. Pp. 1–17 in: *Proceedings of 10th International Kimberlite Conference* (D.G. Pearson, H.S. Grütter, J.W. Harris, B.A. Kjarsgaard, H. O'Brien, N.V. Chalapathi Rao and S. Sparks, editors). Springer, New Delhi.

Scott Smith, B.H., Nowicki, T.E., Russell, J.K., Webb, K.J., Mitchell, R.H., Hetman, C.M. and Robey, J. V. (2018) *A Glossary of Kimberlite and Related Terms*. P. in.: Scott-Smith Petrology Inc., North Vancouver, BC, Canada, Part1-144 pp; Part 2-59 pp; Part 3-56 pp.

Semytkivska, N. (2010) Picro-ilmenites: An experimental study in simple and complex systems to investigate P-T- fO2-composition relations at high pressures. ETH ZURICH, 148 pp.

Shaikh, A.M., Kumar, S.P., Patel, S.C., Thakur, S.S., Ravi, S. and Behera, D. (2018) The P3 kimberlite and P4 lamproite, Wajrakarur kimberlite field, India: mineralogy, and major and minor element compositions of olivines as records of their phenocrystic vs xenocrystic origin. *Mineralogy and Petrology*, **0**, 1–16.

Sharygin, I.S., Golovin, A. V. and Pokhilenko, N.P. (2011) Djerfisherite in Kimberlites of the Kuoikskoe field as an indicator of enrichment of Kimberlite melts in chlorine. *Doklady Earth Sciences*, **436**, 301–307.

Sharygin, I.S., Golovin, A.V. and Pokhilenko, N.P. (2012) Djerfisherite in xenoliths of sheared peridotite in the Udachnaya-East pipe (Yakutia): origin and relationship with kimberlitic magmatism. *Russian Geology and Geophysics*, **53**, 247–261.

Sharygin, I.S., Litasov, K.D., Shatskiy, A., Safonov, O.G., Golovin, A. V., Ohtani, E. and Pokhilenko, N.P. (2017) Experimental constraints on orthopyroxene dissolution in alkali-carbonate melts in the lithospheric mantle: Implications for kimberlite melt composition and magma ascent. *Chemical Geology*, **455**, 44–56.

Sharygin, V. V., Golovin, A. V., Pokhilenko, N.P. and Kamenetsky, V.S. (2007) Djerfisherite in the Udachnaya-East pipe kimberlites (Sakha-Yakutia, Russia): paragenesis, composition and origin. *European Journal of Mineralogy*, **19**, 51–63.

Sharygin, V. V., Kamenetsky, V.S. and Kamenetsky, M.B. (2008) Potassium sulfides in kimberlite-hosted chloride-"nyerereite" and chloride clasts of Udachnaya-East Pipe, Yakutia, Russia. *The Canadian Mineralogist*, **46**, 1079–1095.

Sharygin, V. V., Sobolev, N. V. and Channer, D.M.D. (2009) Oscillatory-zoned crystals of pyrochlore-group minerals from the Guaniamo kimberlites, Venezuela. *Lithos*, **112**, 976–985.

Sharygin, V.V., Kamenetsky, V.S. and Kamenetsky, M.B. (2006) Alkali carbonates and sulfides in kimberlite-hosted chloride-carbonate nodules (Udachnaya pipe, Russia). *Geochimica et Cosmochimica Acta*, **70**, A576.

Shee, S.R., Gurney, J.J. and Robinson, D.N. (1982) Two diamond-bearing peridotite xenoliths from the finsch kimberlite, South Africa. *Contributions to Mineralogy and Petrology*, **81**, 79–87.

Sigmarsson, O., Laporte, D., Carpentier, M., Devouard, B., Devidal, J.-L. and Marti, J. (2013) Formation of U-depleted rhyolite from a basanite at El Hierro, Canary Islands. *Contributions to Mineralogy and Petrology*, **165**, 601–622.

Simonetti, A., Heaman, L.M. and Chacko, T. (2008) Use of discrete-dynode secondary electron multipliers with Faradays - a 'reduced volume' approach for in-situ U-Pb dating of accessory minerals within petrographic thin sections by LA-MC-ICP-MS. Pp. 24–264 in: *Laser Ablation-ICP-MS in the Earth Sciences* (P. Ylvester, editor). Mineralogical Association of Canada Short Course Series 40.

Skinner, E.M.. (1989) Contrasting Group I and Group II kimberlite petrology: towards a genetic model for kimberlites. Pp. 528–544 in: *4th International Kimberlite Conference* (J.E. Glover and P.G. Harris, editors). Geological Society of Australia, Perth.

Skinner, E.M.W. and Marsh, J.S. (2004a) Distinct kimberlite pipe classes with contrasting eruption processes. *Lithos*, **76**, 183–200.

Skinner, E.M.W. and Marsh, J.S. (2004b) Distinct kimberlite pipe classes with contrasting eruption processes. *Lithos*, **76**, 183–200.

Skinner, E.M.W., Apter, D.B., Morelli, C. and Smithson, N.K. (2004) Kimberlites of the Man craton, West Africa. *Lithos*, **76**, 233–259.

Smith, C.B., McCallum, M.E., Coopersmith, H.G. and Eggler, D.H. (1979a) Petrochemistry and structure of kimberlites in the Front Range and Laramie Range, Colorado – Wyoming. Pp. 178–189 in: *Kimberlites, Diatremes, and Diamonds; Their Geology, Petrology, and Geochemistry* (F.R. Boyd and H.O.A. Meyer, editors). Amer. Geophys. Union, Washington.

Smith, C.B., Allsop, H.L., Kramers, J.D., Hutchinson, G. and Roddick, J.C. (1985) Emplacement ages of Jurassic-Cretaceous South African kimberlites by the Rb-Sr method on phlogopite and whole-rock samples. *Transactions of the Geological Society of South Africa*, **88**, 249–266.

Smith, C.B., Colgan, E.A., Hawthorne, J.B. and Hutchinson, G. (1988) Emplacement age of the Cross kimberlite, southeastern British Columbia, by the Rb–Sr phlogopite method. *Canadian Journal of Earth Sciences*, **25**, 790–792.

Smith, C.B., Sims, K., Chimuka, L., Duffin, A., Beard, A.D. and Townend, R. (2004) Kimberlite metasomatism at Murowa and Sese pipes, Zimbabwe. *Lithos*, **76**, 219–232.

Smith, J.V., Hervig, R.L., Akermand, D. and Dawson, J.B. (1979b) K, Rb, and Ba in micas from kimberlite and peridotitic xenoliths, and implications for origin of basaltic rocks. Pp. 241–251 in: *Kimberlites, Diatremes, and Diamonds* (F.R. Boyd and H.O.A. Meyer, editors). American Geophysical Union, Washington D. C.

Smyth, J.R. and Hatton, C.J. (1977) A coesite-sanidine grospydite from the Roberts Victor kimberlite. *Earth and Planetary Science Letters*, **34**, 284–290.

Smyth, J.R., Mccormick, T.C. and Caporuscio, F.A. (1984) Petrology of a Suite of Eclogitic Inclusions from the Bobbejaan Kimberlite I. Two Unusual Corundum-Bearing Kyanite Eclogites. Pp. 109–119 in: *Proceedings of 3rd International Kimberlite Conference Volume 2* (J. Kornprobst, editor).

Snowden, D.V. (1981) Mineralogy and petrology of two kimberlites at Dutoitspan mine, Kimberley. Rhodes University, Grahamstown, 134 pp.

Sobolev, N. V. and Shatsky, V.S. (1990) Diamond inclusions in garnets from metamorphic rocks: a new environment for diamond formation. *Nature*, **343**, 742–746.

Sobolev, N. V. and Yefimova, E.S. (2000) Composition and Petrogenesis of Ti-Oxides Associated with Diamonds. *International Geology Review*, **42**, 758–767.

Sobolev, N. V., Kuznetsova, I.K. and Zyuzin, N.I. (1968) The Petrology of Grospydite Xenoliths from the Zagadochnaya Kimberlite Pipe in Yakutia. *Journal of Petrology,* **9**, 253–280.

Sobolev, N. V., Lavrent'ev, Y.G., Pokhilenko, N.P. and Usova, L. V. (1973) Chrome-rich garnets from the kimberlites of yakutia and their parageneses. *Contributions to Mineralogy and Petrology*, **40**, 39–52.

Sobolev, N. V., Kaminsky, F. V., Griffin, W.L., Yefimova, E.S., Win, T.T., Ryan, C.G. and Botkunov, A.I. (1997) Mineral inclusions in diamonds from the Sputnik kimberlite pipe, Yakutia. *Lithos*, **39**, 135–157.

Sobolev, N. V., Yefimova, E.S., Channer, D.M.D., Anderson, P.F.N. and Barron, K.M. (1998) Unusual upper mantle beneath Guaniamo, Guyana shield, Venezuela: Evidence from diamond inclusions. *Geology*, **26**, 971.

Sobolev, N. V., Yefimova, E.S. and Koptil, V.I. (1999) Mineral inclusions in diamonds in the Northeast of the Yakutian diamondiferous province. Pp. 816–823 in: *Proceedings of the 7th International Kimberlite Conference Vol 2* (S.H. Gurney, J. J., Gurney, J. L., Pascoe, M. D. & Richardson, editor).

Solov'eva, L. V., Barankevich, V.G., Zav'yalova, L.L. and Lipskaya, V.I. (1988) Metasomatic alterations in ferromagnesian eclogites from the Udachnaya pipe. *Dokl Akad Nauk*, **303**, 1450–1454.

Solovova, I.P., Girnis, A. V. and Ryabchikov, I.D. (1996) Inclusions of carbonate and silicate melts in minerals of alkali basaltoids from the East Pamirs. *Petrology*, **4**, 319–341.

Solovova, I.P., Girnis, A. V., Ryabchikov, I.D. and Kononkova, N.N. (2009) Mechanisms of formation of barium-rich phlogopite and strontium-rich apatite during the final stages of alkaline magma evolution. *Geochemistry International*, **47**, 578–591.

Soltys, A., Giuliani, A. and Phillips, D. (2018) A new approach to reconstructing the composition and evolution of kimberlite melts: A case study of the archetypal Bultfontein kimberlite (Kimberley, South Africa). *Lithos*, **304–307**, 1–15.

Sparks, R.S.J. (2013) Kimberlite Volcanism. *Annual Review of Earth and Planetary Sciences*, **41**, 497–528.

Sparks, R.S.J., Baker, L., Brown, R.J., Field, M., Schumacher, J., Stripp, G. and Walters, A. (2006) Dynamical constraints on kimberlite volcanism. *Journal of Volcanology and Geothermal Research*, **155**, 18–48.

Sparks, R.S.J., Brooker, R.A., Field, M., Kavanagh, J., Schumacher, J.C., Walter, M.J. and White, J. (2009) The nature of erupting kimberlite melts. *Lithos*, **112**, 429–438.

Spetsius, Z. V., Bulanova, G.P. and Leskova, N. V. (1987) Djerfisherite and its genesis in kimberlitic rocks. *Dokl Akad Nauk*, **293**, 199–202.

Spetsius, Z.V. (2004) Petrology of highly aluminous xenoliths from kimberlites of Yakutia. *Lithos*, **77**, 525–538.

Sridhar, M., Chowdhary, V.S., Nayak, S.S. and Augustine, P.F. (2004) Discovery of kimberlite pipes in Gadwal area, Mahuhbubnagar district, Andhra Pradesh. *Journal of the Geological Society of India*, **31**, 1288–1291.

Stachel, T., Brey, G.P. and Harris, J.W. (2000) Kankan diamonds (Guinea) I: from the lithosphere down to the transition zone. *Contributions to Mineralogy and Petrology*, **140**, 1–15.

Stachel, T., Brey, G.P. and Harris, J.W. (2005) Inclusions in Sublithospheric Diamonds: Glimpses of Deep Earth. *Elements*, **1**, 73–78.

Stephens, W.E. and Dawson, J.B. (1977) Statistical Comparison between Pyroxenes from Kimberlites and Their Associated Xenoliths. *The Journal of Geology*, **85**, 433–449.

Storey, C.D., Smith, M.P. and Jeffries, T.E. (2007) In situ LA-ICP-MS U–Pb dating of metavolcanics of Norrbotten, Sweden: Records of extended geological histories in complex titanite grains. *Chemical Geology*, **240**, 163–181.

van Straaten, B.I., Kopylova, M.G., Russell, J.K., Webb, K.J. and Scott Smith, B.H. (2008) Discrimination of diamond resource and non-resource domains in the Victor North pyroclastic kimberlite, Canada. *Journal of Volcanology and Geothermal Research*, **174**, 128–138.

Stripp, G.R., Field, M., Schumacher, J.C., Sparks, R.S.J. and Cressey, G. (2006) Post-emplacement serpentinization and related hydrothermal metamorphism in a kimberlite from Venetia, South Africa. *Journal of Metamorphic Geology*, **24**, 515–534.

Tang, Y.-J., Zhang, H.-F., Ying, J.-F. and Su, B.-X. (2013) Widespread refertilization of cratonic and circum-cratonic lithospheric mantle. *Earth-Science Reviews*, **118**, 45–68.

Tappe, S., Jenner, G.A., Foley, S.F., Heaman, L., Besserer, D., Kjarsgaard, B.A. and Ryan, B. (2004a) Torngat ultramafic lamprophyres and their relation to the North Atlantic Alkaline Province. *Lithos*, **76**, 491–518.

Tappe, S., Jenner, G.A., Foley, S.F., Heaman, L., Besserer, D., Kjarsgaard, B.A. and Ryan, B. (2004b) Torngat ultramafic lamprophyres and their relation to the North Atlantic Alkaline Province. *Lithos*, **76**, 491–518.

Tappe, S., Foley, S.F., Jenner, G.A. and Kjarsgaard, B.A. (2005) Integrating ultramafic lamprophyres into the IUGS classification of igneous rocks: Rationale and implications. *Journal of Petrology*, **46**, 1893–1900.

Tappe, S., Foley, S.F., Jenner, G.A., Heaman, L.M., Kjarsgaard, B.A., Romer, R.L., Stracke, A., Nancy, J. and Hoefs, J. (2006) Genesis of Ultramafic Lamprophyres and Carbonatites at Aillik Bay, Labrador: a Consequence of Incipient Lithospheric Thinning beneath the North Atlantic Craton. *Journal of Petrology*, **47**, 1261–1315.

Tappe, S., Foley, S.F., Kjarsgaard, B.A., Romer, R.L., Heaman, L.M., Stracke, A. and Jenner, G.A. (2008) Between carbonatite and lamproite—Diamondiferous Torngat ultramafic lamprophyres formed by carbonate-fluxed melting of cratonic MARID-type metasomes. *Geochimica et Cosmochimica Acta,* **72**, 3258–3286.

Tappe, S., Steenfelt, A., Heaman, L.M. and Simonetti, A. (2009) The newly discovered Jurassic Tikiusaaq carbonatite-aillikite occurrence, West Greenland, and some remarks on carbonatite–kimberlite relationships. *Lithos,* **112**, 385–399.

Tappe, S., Kjarsgaard, B.A., Kurszlaukis, S., Nowell, G.M. and Phillips, D. (2014) Petrology and Nd–Hf Isotope Geochemistry of the Neoproterozoic Amon Kimberlite Sills, Baffin Island (Canada): Evidence for Deep Mantle Magmatic Activity Linked to Supercontinent Cycles. *Journal of Petrology,* **55**, 2003–2042.

Tappe, S., Romer, R.L., Stracke, A., Steenfelt, A., Smart, K.A., Muehlenbachs, K. and Torsvik, T.H. (2017) Sources and mobility of carbonate melts beneath cratons, with implications for deep carbon cycling, metasomatism and rift initiation. *Earth and Planetary Science Letters,* **466**, 152–167.

Tappert, R., Foden, J., Heaman, L., Tappert, M.C., Zurevinski, S.E. and Wills, K. (2019) The petrology of kimberlites from South Australia: Linking olivine macrocrystic and micaceous kimberlites. *Journal of Volcanology and Geothermal Research,* **373**, 68–96.

Thy, P., Stecher, O. and Korstgård, J.A. (1987) Mineral chemistry and crystallization sequences in kimberlite and lamproite dikes from the Sisimiut area, central West Greenland. *Lithos,* **20**, 391–417.

Timmerman, S., Honda, M., Phillips, D., Jaques, A.L. and Harris, J.W. (2018) Noble gas geochemistry of fluid inclusions in South African diamonds: implications for the origin of diamond-forming fluids. *Mineralogy and Petrology,* **112**, 181–195.

Tollo, R.P. and Haggerty, S.E. (1987) Nb-Cr rutile in the Orapa kimberlite, Botswana. *Canadian Mineralogist,* **25**, 251–264.

Tomašić, N., Gajović, A., Bermanec, V. and Rajić, M. (2004) Recrystallization of metamict Nb–Ta–Ti–REE complex oxides: a coupled X-Ray-Diffraction and Raman Spectroscopy study of aeschynite-(Y) and polycrase-(Y). *The Canadian Mineralogist,* **42**, 1847–1857.

Tompkins, L. a. and Haggerty, S.E. (1985) Groundmass oxide minerals in the Koidu kimberlite dikes, Sierra Leone, West Africa. *Contributions to Mineralogy and Petrology,* **91**, 245–263.

Treiman, A.H. and Essene, E.J. (1985) The Oka carbonatite complex, Quebec: Geology and evidence for silicate-carbonate liquid immiscibility. *American Mineralogist,* **70**, 1101–1113.

Tronnes, R.., Edgar, A.. and Arima, M. (1985) A high pressure-high temperature study of TiO2 solubility in Mg-rich phlogopite: implications to phlogopite chemistry. *Geochimica et Cosmochimica Acta,* **49**, 2323–2329.

Tschauner, O., Ma, C., Lanzirotti, A. and Newville, M. (2017) Riesite, a new high pressure polymorph of TiO2 that forms upon shock-release - comparison to (Zr,Ti)O2 in pseudotachylites. P. in: *Goldschmidt2017 Abstract*. Paris.

Ulrych, J., Pivec, E. and Rutsek, J. (1986) Spinel zonation in melilite rocks of the Ploucnice river region, Czechoslovakia. *Neues Jahrbuch Mineralogie, Abhandlungen,* **155**, 129–146.

Ustinov, V.N., Feijo Bartolomeu, A.M., Zagainy, A.K., Felix, J.T., Mikoev, I.I., Stegnitskiy, Y.B., Lobkova, L.P., Kukui, I.M., Nikolaeva, E. V. and Antonov, S.A. (2018) Kimberlites distribution in Angola and prospective areas for new discoveries. *Mineralogy and Petrology,* **112**, 383–396.

Varlamov, D.A., Garanin, V.K. and Kostrovskiy, S.I. (1996) Exotic high-titanium minerals as inclusions in garnets from lower crustal and mantle xenoliths. *Trans. Russs. Acad. Sci. Earth Sci.,* **345**, 352–355.

Vasilenko, V.., Zinchuk, N.., Krasavchikov, V.., Kuznetsova, L.., Khlestov, V.. and Volkova, N.. (2002) Diamond potential estimation based on kimberlite major element chemistry. *Journal of Geochemical Exploration,* **76**, 93–112.

Viljoen, K.S., Robinson, D.N., Swash, P.M., Griffin, W.L., Otter, M.L., Ryan, C.G. and Win, T.T. (1994) Diamond- and graphite-bearing peridotite xenoliths from the Roberts Victor kimberlite, South Africa. Pp. 285–303 in: *Proceedings of the Fifth International Kimberlite Conference. Companhia de Pesquisa de Recursos Minerais Special Publication 1* (H.O.A. Meyer and O.H. Leonardos, editors). Araxa, Brasil.

Viljoen, K.S., Schulze, D.J. and Quadling, A.G. (2005) Contrasting Group I and Group II Eclogite Xenolith Petrogenesis: Petrological, Trace Element and Isotopic Evidence from Eclogite, Garnet-Websterite and Alkremite Xenoliths in the Kaalvallei Kimberlite, South Africa. *Journal of Petrology*, **46**, 2059–2090.

Vrána, S. (2008) Mineral inclusions in pyrope from garnet peridotites, Kolín area, central Czech Republic. *Journal of GEOsciences*, 17–30.

Wagner, P.A. (1914) *The Diamond Fields of Southern Africa*. P. in.: Transvaal leader, Johannesburg, 347 pp.

Walters, A.L., Phillips, J.C., Brown, R.J., Field, M., Gernon, T., Stripp, G. and Sparks, R.S.J. (2006) The role of fluidisation in the formation of volcaniclastic kimberlite: Grain size observations and experimental investigation. *Journal of Volcanology and Geothermal Research*, **155**, 119–137.

Wang, L., Essene, E.J. and Zhang, Y. (1999) Mineral inclusions in pyrope crystals from Garnet Ridge, Arizona, USA: implications for processes in the upper mantle. *Contributions to Mineralogy and Petrology*, **135**, 164–178.

Weiss, Y. and Goldstein, S.L. (2018) The involvement of diamond-forming fluids in the metasomatic ‘cocktail’ of kimberlite sources. *Mineralogy and Petrology*, **112**, 149–167.

Whitmeyer, S.J. and Karlstrom, K.E. (2007) Tectonic model for the Proterozoic growth of North America. *Geosphere*, **3**, 220.

Wiedenbeck, M., Allé, P., Corfu, F., Griffin, W.L., Meier, M., Oberli, F., Quadt, A. VON, Roddick, J.C. and Spiegel, W. (1995) Three natural zircon standards for U-Th-Pb, Lu-Hf, trace element and REE analyses. *Geostandards and Geoanalytical Research*, **19**, 1–23.

Willcox, A., Buisman, I., Sparks, R.S.J., Brown, R.J., Manya, S., Schumacher, J.C. and Tuffen, H. (2015) Petrology, geochemistry and low-temperature alteration of lavas and pyroclastic rocks of the kimberlitic Igwisi Hills volcanoes, Tanzania. *Chemical Geology*, **405**, 82–101.

Wilson, M.R., Kjarsgaard, B.A. and Taylor, B. (2007) Stable isotope composition of magmatic and deuteric carbonate phases in hypabyssal kimberlite, Lac de Gras field, Northwest Territories, Canada. *Chemical Geology*, **242**, 435–454.

Withers, A.C., Essene, E.J. and Zhang, Y. (2003) Rutile/TiO2II phase equilibria. *Contributions to Mineralogy and Petrology*, **145**, 199–204.

Woodhead, J., Hergt, J., Phillips, D. and Paton, C. (2009) African kimberlites revisited: In situ Sr-isotope analysis of groundmass perovskite. *Lithos*, **112**, 311–317. Elsevier B.V.

Woolley, A.R., Bergman, S.C., Edgar, A.D., Le Bas, M.J., Mitchell, R.H., Rock, N.M.S. and Scott Smith, B.H. (1996) Classification of lamprophyres, lamproites, kimberlites, and the kalsilitic, melilitic, and leucitic rocks. *Canadian Mineralogist*, **34**, 175–186.

Wyatt, B.A. (1979) Manganoan ilmenite from Premier kimberlite. P. (Extented Abstract) in: *Kimberlite Symposium II*. Cambridge.

Wyatt, B.A. and Lawless, P.J. (1984) Ilmenite in Polymict Xenoliths from the Bultfontein and De Beers Mines, South Africa. Pp. 43–56 in: *Proceedings of the 3rd International Kimberlite Conference, Vol 2.* (J. Kornprobst, editor). Elsevier.

Wyatt, B.A., Baumgartner, M., Anckar, E. and Grutter, H. (2004) Compositional classification of “kimberlitic” and “non-kimberlitic” ilmenite. *Lithos*, **77**, 819–840.

Xiaoying, G. and Posukhova, T. V. (2010) Chromium spinels in North Chinese kimberlites, Huabei platform. *Moscow University Geology Bulletin*, **65**, 234–243.

Xu, J., Melgarejo, J.C. and Castillo-Oliver, M. (2018a) Ilmenite as a recorder of kimberlite history from mantle to surface: examples from Indian kimberlites. *Mineralogy and Petrology*, 1–13.

Xu, J., Melgarejo, J.C., Castillo-Oliver, M., Arqués, L. and Santamaria, J. (2018b) Ilmenite generations in kimberlite from Banankoro, Guinea Conakry. *Neues Jahrbuch für Mineralogie - Abhandlungen*, **195**, 191–204.

Xu, J., Melgarejo, J. and Castillo-Oliver, M. (2018c) Styles of Alteration of Ti Oxides of the Kimberlite Groundmass: Implications on the Petrogenesis and Classification of Kimberlites and Similar Rocks. *Minerals*, **8**, 51.

Yang, Y.H., Wu, F.Y., Wilde, S.A., Liu, X.M., Zhang, Y.B., Xie, L.W. and Yang, J.H. (2009) In situ perovskite Sr-Nd isotopic constraints on the petrogenesis of the Ordovician Mengyin kimberlites in the North China Craton. *Chemical Geology*, **264**, 24–42.

Zedgenizov, D.A., Logvinova, A.M., Shatskii, V.S. and Sobolev, N. V. (1998) Inclusions in microdiamonds from some kimberlite diatremes of Yakutia. *Dokl Akad Nauk*, **359**, 204–208.

Zhang, H.F., Menzies, M.A., Mattey, D.P., Hinton, R.W. and Gurney, J.J. (2001) Petrology, mineralogy and geochemistry of oxide minerals in polymict xenoliths from the Bultfontein kimberlites, South Africa: Implication for low bulk-rock oxygen isotopic ratios. *Contributions to Mineralogy and Petrology*, **141**, 367–379.

Zhou, H., Liu, Q., Lei, X. and Liu, H. (1996) Geochemical similarity of kimberlite between China and South Africa from the view of Ti-oxide minerals of upper mantle. *Earth Science – Journal of China University of Geosciences*, **21**, 557–562 (in Chinese with English abstract).

Zhu, T. and Gao, S.-P. (2014) The Stability, Electronic Structure, and Optical Property of TiO 2 Polymorphs. *The Journal of Physical Chemistry C*, **118**, 11385–11396.

Zozulya, D.R., Peltonen, P. and O'Brien, H. (2008) Pyrope and Cr-diopside as indicators of mantle structure and diamond depth facies in the Kola region. *Geology of Ore Deposits*, **50**, 524–534.

Zuev, V.M., Khar'kiv, A.D., Zinchuk, N.N. and Mankenda, A. (1988) Slightly eroded kimberlite pipes of Angola. *Geologiya i Geofizika*, **3**, 56–63.

Zurevinski, S.E., Heaman, L.M. and Creaser, R.A. (2011) The origin of Triassic/Jurassic kimberlite magmatism, Canada: Two mantle sources revealed from the Sr-Nd isotopic composition of groundmass perovskite. *Geochemistry, Geophysics, Geosystems*, **12**.